Pavement Deterioration and PE Pipe Behaviour Resulting from Open-cut and HDD Pipeline Installation Techniques

by

Adedamola Adedeji Adedapo

A thesis
presented to the University of Waterloo
in fulfillment of the
thesis requirement for the degree of
Doctor of Philosophy
in
Civil Engineering

Waterloo, Ontario, Canada, 2007

AUTHOR'S DECLARATION

I hereby declare that I am the sole author of this thesis. This is a true copy of the thesis, including any required final revisions, as accepted by my examiners.
I understand that my thesis may be made electronically available to the public.

Adedamola A Adedapo

Abstract

The damaging impact of continuous utility cuts on flexible pavement performance has been shown to be a major problem for urban roads and pavement mangers due to high reconstruction and maintenance costs. Horizontal directional drilling (HDD) is a trenchless construction method that does not require continuous trenching. HDD pipe installation techniques can reduce reinstatement costs, shorten construction periods, and lower social costs due to reduced user traffic delays. In this thesis, a detailed field study and numerical investigations was completed to quantify pavement deterioration and polyethylene (PE) pipe performance when pipelines are installed under flexible pavements using both traditional open-cut and HDD construction methods.

Two 200mm SDR-17 DIPS HDPE pipes were installed 1.5m below a flexible pavement using open-cut and HDD construction technique. A state-of-the-art instrumentation and data acquisition systems were developed to measure HDD drill rig, PE pipes and pavement responses during pipe installations and for a period of about three years afterwards. Field data from (GPR) surveys, falling weight deflectometer (FWD) tests, surface distress surveys, and ground surface elevation survey were used to evaluate pavement deterioration due to the pipeline installations. The mechanisms of ground deformations during HDD and open-cut pipe installation were numerically investigated with *FLAC*^{3D}, a commercial finite difference program. A hybrid constitutive model consisting of the traditional Duncan-Chang hyperbolic model and Mohr-Coulomb perfectly plastic model was developed and implemented in *FLAC*^{3D} to simulate the non-linear stress-strain and stress dependent behavior of granular materials.

Field test results show that the HDD installed pipe have significantly lower construction induced strains and ring deflections when compared to the open cut-and-cover installation and the mechanism of pipe deformation differs for the two construction techniques. The two pipes performed satisfactory over the long-term monitoring period as deflections and strain levels were below acceptable limits and there was no apparent deterioration of the pipe.

Pipe deflections resulting from environmental effects (freeze and thaw) were found to be more significant than those due to material creep. Furthermore, the modified Iowa's and Plastic Pipe Institute's (PPI) ring deflection equations were found to over estimate pipe deflection for the open-cut and HDD installed pipes by about 114 and 50 percent, respectively.

Results from field tests found that the HDD installation did not results in any observable change in the condition of the pavement structure performance, while the structure and integrity of pavement section in the vicinity of the open-cut was adversely impacted by utility cut excavation. It was determined numerically that when an unsupported excavation is created within a typical flexible pavement structure, distress zones that extend laterally from the face of the excavation to a distance of approximately 80% of the depth of excavation is developed. The results of the analyses suggests that better restoration techniques are required to eliminate the adverse effect caused by the stress relief within the pavement structure during a utility cut. Furthermore, the area of potential pavement deterioration should be extended beyond the edge of the utility cut to encompass the 'distress zones' when determining fees to cover pavement damage and restoration costs.

Results obtained from numerical simulations advanced the understanding of the mechanism, magnitude, and extent of deformation within the pavement structure during HDD pipe installation in frictional and cohesive subgrade soils. Relationship between HDD annular bore pressures and displacements have been incorporated into design Charts and Tables for use in estimating maximum allowable bore pressures for HDD installation beneath flexible pavements. Critical bore pressures that would limit ground deformations and prevent excessive pavement deformations are presented. Critical bore pressures were compared to estimated allowable bore pressures obtained from the widely used Delft Geotechnics equation. The Delft Geotechnics equation was found to over estimate allowable bore pressure for HDD installation beneath flexible pavement.

HDD pipeline installations under flexible pavement were found to have significantly lower restoration costs, social costs and maintenance cost than open-cut pipeline installations.

Acknowledgements

I am very grateful to my supervisor Dr. Mark Knight for his continued support, guidance, encouragements and friendship throughout the course of my graduate studies in Waterloo. Thank you for given me the opportunities to travel and present my work in many conferences around the world. I will also like to thank my co-supervisor Dr. Leo Rothenburg for his invaluable advice and suggestions. Very specially thanks to Dr. Susan Tighe for her friendship and interest in the research project and for providing the FWD and other pavement performance data for the CPATT test track. I thank the examining committee members Dr. Sam Ariaratnam, Dr. Gregory Glinka, Dr. Balvant Rajani and Dr. Jeff West for their interest, advice and for reviewing this thesis.

Financial supports provided by Centre for Pavement and Transportation Technology (CPATT) and Centre for Advancement of Trenchless Technologies (CATT), Natural Sciences and Engineering Research Council of Canada (NSERC) and the University of Waterloo are gratefully acknowledged. As well as the scholarships and bursaries received from NSERC, University of Waterloo, Ontario Graduate Scholarship, Faculty of Engineering and JNE Consulting Ltd.

I will like to acknowledge the excellent technical assistance provided by Mr. Ken Bowman and Mr. Terry Ridgway during the field investigation program. I thank my friend and programming guru Mr. Karl (Terzaghi) Lawrence for his help and all my colleague in the Geotechnical Engineering Group in Waterloo for their friendship. I thank Wayne and Pat Fox and the Nigerian committee in Kitchener-Waterloo for keeping me warm and making my stay in Waterloo memorable. I thank Dr. Robert Kenyon, the management and staff of KGS Group Consulting Engineers for their support and encouragement at the final stage of this thesis.

Deepest thanks to the wonderful grandmas, my father-in-law and my siblings for their affection and continuous support. I thank God for the children he gave to us while in Waterloo, Adeoluwa and Ifeoluwa, you are very precious to me. I look forward to more play time with you. Finally, I appreciate the love, encouragement, support and patience of my darling wife and best friend, Remilekun. Thank you for cheering me up, this dissertation will not be possible without you. Thank you, I will always love you.

Dedication

To the glory of God

To my darling wife Remilekun, I will always love you

To our children Adeoluwa and Ifeoluwa, I cherish you

Table of Contents

List of Figures

List of Tables

Chapter 1: Introduction

1.1 Description of Problem

The deteriorating conditions and under-capacity of aging underground infrastructure including water and wastewater distribution and collection systems, gas, petroleum and chemical pipelines, electrical and communication network and other utility corridors have resulted in an increased number of pavement utility cut worldwide. A report published by the New York City Transportation Commissioner indicated that more than 250,000 cuts are made each year in the street of New York City alone and this number increases by about 8% annually (Khogali and Mohamed, 1999). An American Public Works Association (APWA, 1991) study reported that about 180,000 utility cuts permits are issued annually in Chicago, IL alone; Jones (1999) also reported that that over 100,000 cuts are made annually in Camden Borough, a district of London, UK. Similar trends have been reported in other cities around the world.

Although some cities have developed guidelines for utility cut opening and restoration; nevertheless, unsatisfactory pavement performances were still observed even when 'good practice' guidelines were followed (Khogali and Mohamed, (1999); Lee and Lauter, (2000); Emery and Johnston (1986), Tighe et al, (2002)). Inadequate performance of restored utility cuts and trenches result in frequent maintenance and often require cities to reconstruct the road earlier than originally planned. The excessive cost associated with pavement rehabilitation due to utility cuts is putting a financial burden on cities and utility companies alike. For example, it has been estimated that the City of Toronto, Canada incurs over $3 million in cost annually for street maintenance program as a result of poor utility cut restoration (Emery and Johnston, 1987).

Interest in the impact of utility cuts on roadway performance has increased in the last two decades and a number of studies that dealt with the issue on utility cut excavations and restorations have been completed. Despite several studies, utility cut excavation and restoration still remains a major concern to road authorities and is one of the leading sources of contention between Municipalities and utility service providers (Schaefer et al, 2005). Public agencies initiated some of the previous studies while others were sponsored by utility companies. Most of the studies sponsored by public agencies attempt to quantify the financial impact of utility cut restoration on roadway performance while the majority utility companies' research has focused on the need for specific backfill/restoration specifications. Most of the previous studies reviewed were either oriented to the interest of a particular party or limited to a certain region. It is clear that the interpretations of the results from the studies, or the critical reviews, generally favor either the municipalities or the utilities company. These have limited the usefulness, validity and applicability of most of these studies. Moreover, the mechanisms that lead to poor performance of restored utility cuts are not well understood and have not been explored in detail in the previous studies.

Trenchless construction methods are rapidly becoming an economic alternative to cut-and-cover construction methods for pipeline installations. Trenchless technologies are a family of construction methods used for the installation, rehabilitation, replacement, repair, inspection, location, and leak detection of underground utility systems that do not require continuous trenching. Trenchless construction methods have reduced reinstatement costs, shortened construction periods, and lowered social costs due to reduced user traffic delays (Iseley and Tanwani, (1990), Tighe et al (1999)). Horizontal Directional Drilling (HDD) is a trenchless construction method used for the installation of underground utility systems under obstacles such as roads, railways, buildings, and rivers. It is based on mechanically cutting soil and rock formations using low volume and low-pressure drill fluid. The drilling fluid mixes with formation cuttings to produce easily displaceable *slurry* that entrains the cuttings and supports the bore. The pipe for the given service is pulled through the easily displaceable slurry. Horizontal directional drilling is the trenchless technology method considered in this research and an overview of the installation technique is presented in Chapter 2.

Although ground movements may occur during HDD installations, they are typically less than those that result from traditional open cut-and-cover installation. Improper design and/or lack of understanding of the ground displacement accompanying HDD installations could cause excessive displacement and damage of existing underground utilities and structures. These have resulted in losS of confidence in the installation technique by municipalities, regulators and designers. For example, Lueke and Ariaratnam (2003) stated that in January 2000, the City of Santa Clara, California placed a moratorium preventing the use of horizontal directional drilling as a result of increased number of incidents involving contractors that have humped roadways. Limited data exist to determine or estimate HDD induced ground movement resulting from bore slurry pressure build-up during installation underneath flexible pavement. In addition, the applicability of the existing method used by the HDD designer for estimating bore pressures that would limit ground deformation during HDD installation beneath flexible pavement has not been investigated.

In addition to problems associated with impact of construction methods on the performance of flexible pavement, this thesis also attempts to address problems related to the design of Polyethylene (PE) pipes. Polyethylene (PE) is one of the most widely used materials. Polyethylene is a viscoelastic material that deforms immediately upon application of an induced load. The material continues to deform or creep with time. The popularity of plastic pipes is due to constant improvements being made in manufacturing technologies and advantages over the conventional concrete and ductile iron pipes in terms of light-weightiness, connectivity/fusion, cost efficiency and long-term chemical stability (Massicotte, 2000).

The selection of appropriate pipe wall thickness expressed in terms of Standard Dimension Ratio (SDR) i.e. ratio of average outside diameter to minimum wall thickness, is currently based on limiting pipe deflection to some standard value set in various code of practice. In Canada for instance, pipe deflection is specified to be below 7.5% of the pipe outside diameter for non-pressure applications (CAN/CSA-b182.7-87). The most commonly used equation for estimating deflection is the *Iowa equation*, an empirical equation developed by Spangler (1938) and its modified version *Modified Iowa Equation* by Watkins (1966). The original *Iowa equation* was empirically derived from tests performed on buried corrugated

metal pipes and the equation is now being adopted by flexible plastic pipe manufacturer and designer without applying any correction factors to the computed deflections or taking into account the combined effect of insitu and backfill soil conditions encountered during various installation techniques.

Calculating pipe deflection has been, and continues to be a controversial subject (Masada, 2000), and to date, very little field data is available to validate the appropriateness of the existing equations for estimating PE pipe deflection especially for HDD installed pipes. As a first step to improve the design methodology, there is a need to better understand how PE pipes performs when subjected to loading conditions similar to that expected during and after installation using cut-and-cover and HDD techniques.

1.2 Research Objectives

The proposed research stemmed from a need to (*i*) objectively study issues related to utility cut excavation and restoration and its impact of pavement performance; and (*ii*) understand field performance of PE when installed using HDD and open-cut installation techniques.
Based on these, two primary goals were formulated for this thesis:

1). To determine the impact of traditional open cut-and-cover and Horizontal Directional Drilling (HDD) pipeline construction methods on flexible pavement, and

2). To determine polyethylene (PE) pipe performance when installed using traditional Cut-and-cover and Horizontal Directional Drilling (HDD) construction methods.

A two component research approach involving a detailed field study and numerical investigations were devised to achieve these objectives. The specific objectives of this research were to:

(a) Design and implement instrumentation to measure short-term (during installation) and long-term post installation response of PE pipes installed using HDD and traditional open cut-and-cover construction techniques.

(b) Advance the understanding of the influence of construction techniques on the behavior of PE pipe including pipe deflection and strains.

(c) Evaluate the appropriateness of the current design methodologies for calculating pipe deflection by comparing estimated values to measured field values.

(d) Design, develop and implement state-of-the-art pavement instrumentation and data acquisition capable of monitoring pavement response in real time with full remote access capabilities.

(e) Determine the causes and mechanisms of failure in and around utility cuts and their effects on the performance of flexible pavements. These findings would be necessary to quantify/predict deterioration and develop a realistic fees structure to cover additional maintenance cost resulting pavement utility cuts.

(f) Demonstrates *FLAC*^{3D} ability to simulate pipe installation using HDD and open cut-and-cover construction techniques beneath flexible pavement.

(g) Numerically simulate flexible pavement excavation and analytically evaluate its impact of the adjacent pavement structure.

(h) Generate a series of HDD simulations to identify and characterize key bore pressure-pavement displacement relationships during the HDD process. These relationships include the influence of the bore diameter, depth of cover, and pavement structure properties (e.g. thickness, modulus, shear strength) required to initiate and to propagate ground displacement outwardly from the bore.

(i) Develop bore pressure guides and tables to provide a first order approximation that can be used to set the maximum allowable bore pressures for new HDD installations beneath flexible pavement.

1.3 Thesis Organization

The following sections summarize the original contributions described in this thesis. The current state of pavement utility cut research and flexible PE pipe design was reviewed prior to conducting any field installations/investigations. Included in Chapter 2 is a review of previous work done on issues related to pavement utility cut; factors influencing pavement structure performance; and potential effects of pavement cuts. Followed by, the theories supporting calculation of loads and ring deflection on buried and HDD installed pipes and limitations of the current flexible pipe design practice. An overview of the HDD process and ground movement associated with the installation technique was also reviewed and presented in Chapter 2.

Flexible pavement structure consists mainly of granular material and the nature and amount of ground movements in granular materials are strongly influenced by their non-linear stress-strain behavior. A constitutive model capable of representing this important behavior was implemented for the numerical analysis. Detailed review of the plasticity theory; conventional Mohr-Coulomb linear elastic perfectly-plasticity model and the hyperbolic stress-strain relationship are presented in Chapter 3; followed by description and formulation of proposed Mohr-Coulomb non-linear elastic perfectly-plasticity constitutive model employed for the numerical modeling.

The proposed Mohr-Coulomb non-linear elastic perfectly-plasticity model described in Chapter 3 was implemented in *FLAC*^{3D} - a finite difference based program. The numerical formulation of *FLAC*^{3D} program and the implementation of the proposed constitutive model in *FLAC*^{3D} are presented in Chapter 4. To validate the constitutive model, a series of drained triaxial compression tests were simulated and results obtained from *FLAC*^{3D} were compared with measured laboratory test results. A rough strip footing on a cohesionless material was also simulated with the new constitutive model and the foundation response was compared to experimental data (Duncan 1962). Chapter 4 concludes with a code-to-code comparison of results obtained from the analysis of circular flexible pipe buried in a silty-sand using *FLAC*^{3D} and CANDE'89, a well established finite element program.

The field investigation program are described in Chapter 5, the descriptions include Center for Pavement and Transportation Technology (CPATT) field test facility, HDPE pipe and pavement instrumentation, field-scale installations and long-term monitoring program. The results of the field-scale investigations including those obtained from the long-term monitoring are also presented and discussed in the Chapter. Chapter 5 concludes with a summary of research contributions from the field investigation program.

A series of Horizontal Directional Drilling installations beneath flexible pavement simulated with *FLAC*^{3D} are presented in Chapter 6. Detailed description of the numerical model and modeling approach used for the simulations are also presented in the Chapter. This is followed by a validation of the *FLAC*^{3D} numerical model with closed form solution derived from cavity expansion theory and measured response from field-scale HDD installation. Simulations are completed for different subgrade materials, depths of cover and bore diameters. Bore pressures required to initiate and to propagate displacement fields outwards away from the bore are compared to maximum allowable bore pressures estimated with the Delft Geotechnics equations. Results obtained from the numerical analysis are presented as charts and tables. The Chapter concludes with discussions on the limitations, validity and practical significance of the simulation results.

The stages involved in the installation of small diameter utility pipes underneath flexible pavement using traditional open-cut installation technique were simulated with *FLAC*^{3D} and are presented in Chapter 7. The objectives of the numerical simulated presented in Chapter 7 were to analytically investigate the behavior of flexible pavement structure during excavation of utility cut/trench and the influence of backfill compaction on the performance of the installed pipe. The installation stages simulated numerically include trench excavation, preparation of the bedding, pipe placement and trench backfilling with compacted soil in small lifts. The field-scale open-cut pipe installation described in Chapter 5 was modeled analytically with *FLAC*^{3D} and the pipe responses obtained from the analysis were compared with measured field data. The results obtained from the simulations and discussion of the key findings including the impact of trench excavation on pavement structure performance is presented. Chapter 7 concludes with a summary and practical significance of the numerical simulations of open-cut installation.

Conclusions and recommendation for future work are presented in Chapter 8. The chapter details the contributions of the individual chapters presented in this dissertation.

Chapter 2: Background and Literature Review

2.1 Introduction

This Chapter includes a review of the current state of pavement utility cut research, an overview of horizontal directional drilling, and flexible PE pipe design. Previous work done on issues related to pavement utility cuts, factors influencing pavement structure performance and potential effects of pavement cuts are presented. This is followed by an overview of the HDD process and ground movement associated with the installation technique. The Chapter concludes with theories supporting calculation of loads and ring deflection on buried and HDD installed PE pipes, and limitations of current flexible pipe design practice.

2.2 Pavement Utility Cuts

Interest in the impact of utility cuts on roadway performance has increased in the last two decades and a number of studies that dealt with the issue of utility cut excavations and restorations have been completed. Public agencies initiated some of these studies while others were carried out under the direction of some of the utility companies. Most studies sponsored by public agencies attempt to quantify the financial impact of utility cut restoration of roadway performance while most utility companies' research has focused on the need for specific backfill/restoration specifications. The studies were either oriented to the interest of a particular party or limited to a certain region. It is clear that the interpretations of the results of the studies, or the critical reviews, generally favor either the municipalities or the utilities company.

The following Sections review factors influencing pavement structure performance, review potential effects of pavement cuts and presents a summary of important research on utility cut related issues done previously.

2.2.1 Factors Influencing Pavement Structure Performance

To determine key issues associated with potential impact of utility cuts on the future performance of pavements, it is important to understand the pavement systems structure as a whole and how they function. This includes the component materials, their characteristics and their contribution to the overall performance of the pavement structure. It is also essential to have knowledge of the materials used in utility cut restoration, their characteristics and the specific procedures used in their construction.

AMEC (2000) outlined some specific items that can be associated with the evaluation of different aspect of the existing pavement section and the utility cut repair section including:

(i) **Surfacing Materials**: Different materials influence pavement system performance. Surface treatments include asphalt concrete (AC), Portland cement concrete (PCC), aggregate bases and sub-bases, and surface stabilizing treatments (cement, fly ash, lime and others). Almost all the studies completed on utility cut to date considered structural systems comprised of AC overlying aggregate base (AB) and insitu subgrade soils.

(ii) **Soil Support Conditions**: The performance of existing and repaired pavement structural systems is strongly influenced by the underlying supporting soils. Subgrade or native supporting materials can include clays, sands, decomposed rock and borrowed fill materials, which have inherent or produced expansive or collapse characteristics. The supporting soils, the depth of cut, compaction and type of soil used to backfill a cut pavement section, are important to the future performance of either the existing or the cut pavement section. In most cases, the studies reviewed did not adequately characterize the soil support conditions.

(iii) **Climatic Conditions**: Climatic conditions such as sporadic, intense rainfall, freeze-thaw and wet-dry cycles can influence pavement performance. The studies reviewed were performed in various climatic environments, but climate was an inferred element in all of the studies.

(iv) **Traffic Volume**: The volume of traffic on an existing pavement section or a restored utility cut section has a major impact on the performance of either type of section. The traffic volume was generally characterized in the study by Shahin et al (1986) and Emery and Johnson (1987) where Falling Weight Deflectometer (FWD) procedures were used. The traffic volume was characterized by the type of street (arterial, collector or residential), lane designation, predominant vehicle type (bus, truck or passenger vehicle) or relative volume of traffic, with no specifics provided.

(v) **Present Pavement Condition**: The condition of the existing pavement section at the time the pavement cut is made is an important factor in assessing the impact of the pavement cut on the performance of the existing pavement section. Some of the studies reviewed including Lee and Lauther (1999), Tighe et al (2002) and Chow and Troyan (1999) initiated the analysis with a pavement survey, characterizing the condition of the existing pavement in terms of Pavement Condition Index (PCI) or a similar rating. The studies by Bodocsi et al (1995), Emery and Johnson (1987), Todres and Baker (1996) and many other did not attempt to quantify the present condition or age of the existing pavement. This lessens their usefulness in determining the actual impact of the utility cut repair on the rehabilitation requirements, and the cost of rehabilitation.

(vi) **Repair Conditions**: The conditions under which the pavement cut was made can influence the future performance of the repair section and the existing pavement. Typically, the studies reviewed including those by Emery and Johnson (1987), Todres and Wu (1990), Mangolds and Carapezza (1999) and Suhaibani et al (1992) evaluated pavement cuts made as part of common utility installations or

upgrades, not under emergency repair situations. The studies considered the much more common type of pavement cuts.

(vii) **Repair Entity and Procedures**: The specific equipment and procedures of the repair entity making the pavement cut can influence the future performance of the existing pavement section and the repaired section (Nichols-Vallerga, 2000). Typically, the studies did not address the repair entity (except in terms of the sponsoring agency) or the equipment used. However, several studies including those by Todres and Wu (1990) and Mangolds and Carapezza (1999) addressed the type of repair (T-section as compared to the more common straight cut without overlap). Studies completed by Emery and Johnson (1987), Todres (1999), Mangolds and Carapezza (1999) and Humphery and Parker (1998) also considered variations in the degree of compaction of the subgrade and/or the aggregate base supporting the surface pavement layer.

2.2.2 Potential Effects of Utility Cuts on Pavement Structure

There are many potential effects of trench cuts on existing pavement systems, their long-term performance and their rehabilitation requirements. These can be grouped in three general categories. A discussion of each categories and the extent to which they were addressed by the references reviewed are as follows.

(i) **Infiltration of Water**: Water or snowmelt can infiltrate at the interface between the repaired and the existing pavement sections. There could also be infiltration through the AC of either the existing or repaired section particularly low density, high permeability AC. The water typically weakens the unbound pavement layers (aggregate base, sub-base and subgrade), and can reduce the life of the existing and repaired pavement section. Moisture-induced effects can be more pronounced in freeze-thaw environments. The impact of moisture infiltration was directly addressed in only one of the studies reviewed in Mangolds and Carapezza (1991); the impact was not addressed in other studies, or was included only by completing field evaluations during both dry and wet climatic periods.

(ii) **Edge Effects at the Pavement Cut**: Sloughing of the subbase material and/or aggregate base adjacent to the pavement cut and inadequate compaction of the repair materials, particularly the subgrade soils, may result in the breaking down of the edge of the repaired and the adjacent existing pavement sections. This distress will allow more water to enter the pavement sections (existing and repaired), resulting in further degradation of pavement materials. The extent of this distress is dependent on the quality of the repair. Studies by Shahin et al (1986) and Humphrey and Parker (1998) addressed this issue.

(iii) **Quality of Materials and Construction Procedures**: If the quality of the materials and construction procedures used in the repair of a pavement cut are less than equivalent to the existing pavement section, a weaker pavement section will result. With traffic loading, this can result in the initial deterioration of the pavement cut, progressing to the adjacent pavement section. Studies by Emery and Johnston (1985), Todres and Saha (1996) and Mangolds and Carapezza (1991) characterized the placement conditions of the existing and repaired pavement sections. Todres (1999) and Humphrey and Parker (1998) theoretical studies considered differences in the degree of compaction and the composition of the aggregate base or subgrade.

Any one of these three processes can initiate pavement deterioration, independent of the age of the existing pavement, which can then progress to either of the other processes.

2.2.3 Summary of Previous Studies on Pavement Utility Cuts

Studies focusing on the impact of utility cut on road pavement have been carried out around the world. Review of some of the important research effort on utility cut is presented in the following Sub-Sections.

(i) City of Cincinnati and American Public Works Association (Bodocsi et al, 1995)

In an attempt to quantify the impact of utility cuts on pavements, the American Public Works Association (APWA) convened a committee in 1989 comprising representatives of City Agencies, to develop a research project "Recovering Costs of Pavements Cuts". The aim of that project was identified as the development of a method for calculating the real cost of pavement cuts and establishing an equitable fee structure to recover those costs. The determination of their proposed cost would include cost for pavement maintenance and anticipated rehabilitation for a minimum of two years after the cut.

The Cincinnati Infrastructure Institute at University of Cincinnati in cooperation with the City of Cincinnati was contracted to assist the APWA study by monitoring the impact of utility cuts on the performance and life span of the city's pavement. The study led to the development of methods for (a) evaluation of the condition of cuts and surrounding pavements based on subjective assessment i.e. visual inspection of distresses and objective measurements of strength i.e. deflection (b) development of a cost recovery policy, and (c) coordination with the city's street rehabilitation and maintenance program.

Results from the study indicated that there is a zone of weakness extending about 1.0m from the edge of the cut in all directions; reduction in flexible pavement service life due to utility cut varies between 47% and 60%; additional overlay thickness required for patched areas is about 1.75inches (45mm) resulting in an additional repair cost of about $950 to $1400 per patch. For the City of Cincinnati this correlates to $2M to $4.9M annually for repair of utility cut areas.

The causes of failure in and around utility cuts, their effects and the correctives measures that need to be taken to remedy structural deficiencies in and around that vicinity of the cuts were not considered in their study. These findings would be necessary in order to develop a realistic fees structure to cover restoration cost. This study was limited to the City of Cincinnati.

(ii) City of Ottawa-Carleton, Ontario (Lee and Lauter, 1999)

The study by the City of Ottawa-Carleton was conducted to determine the cost and impact of utility trenches (and appurtenances) on the semi-urban and urban Regional road network in Ottawa-Carleton, ON. The study relied mainly on the Municipality's Pavement Management System (PMS) database. In the PMS database for the regional road system, the overall pavement condition of a road section is defined as the pavement quality index (PQI), which is a function of the pavement roughness index (PRI), the structural adequacy index (SAI) and the surface distress index (SDI). Each of these indices is based on a scale of 0 to 10, with 10 being perfect. Statistical analyses were conducted using the PMS database. Comparable studies were then conducted based on objective field measurements to remove the subjectivity that has been the criticism of other previous studies. The concept of normalized life was also introduced, where normalized life is defined as the ratio of the number of years since the last rehabilitation of the pavement section and the number of years that the PMS database predicts that the pavement section will reach the critical PQI value.
Using data from the PMS database and the results of the field studies, correlations between PRI, SAI and SDI with normalized life were determined, typically resulting in poor correlation coefficients. However, when the three indices were combined to determine the PQI, much better correlations (0.80 and 0.85) were determined. How the indices are combined to compute the PQI value was not presented in the published report.

The study determined that the average pavement lifecycles were 13.7 and 12.4 years for roadway sections with and without trenching impacts, respectively. The difference in lifecycle varied from 0.2 years for pavements with a lifecycle of 5 years to 3.0 years for pavements with a lifecycle of about 25 years. It was also determined that at the roadway network level, utility trenching can be expected to reduce the network lifecycle by about 7.8%. However, when proportioned based on the contributing trenched area, the reduction in pavement lifecycle jumped to about 32.4 %. Finally, the study determined that the zone of weakness due to trenching extends 0.63 m (about 2 feet) beyond the edge of the trench.

(iii) Metropolitan Toronto, Ontario (Emery and Johnston 1985 & 1987)

The Metropolitan Toronto Roads and Traffic Departments contracted Trow Consulting Engineers, Ltd. to conducted series of studies to investigate utility cut restoration and their impact on the quality of urban pavements. To quantify their current impact, 43 recently restored utility cuts were randomly selected and inspected to determine the presence of discontinuities and voids using FWD.

The study showed that most of the utility cuts had discontinuity but few voids. Only 49 percent of the utility cut restorations had an overall quality and performance rating above minimum level. When the overall quality and performance rating was adjusted by removing surface conditions, 65% of the restored trenches had rating below the minimum level. It was recommended that unshrinkable fill be adopted in the utility cut restoration. Based on this recommendation, Metropolitan Toronto launched additional studies to investigate the possibility of using unshrinkable materials and a single stage restoration method. The outcome of these studies is the adoption of these materials as a backfill by Metropolitan Toronto. However, the use of a single stage restoration procedure did not present any economic advantages and its quality varied excessively with variability of workmanship. The adequacy of these materials with respect to frost action and freeze/thaw behavior was not evaluated.

(iv) City of Burlington, Vermont (Shahin, et al, 1986 & 1987)

The City of Burlington, Vermont hired ERES Consultants Inc. to study the effect of utility cut patching on pavement performance and rehabilitation costs. The study made use of a visual survey and a non-destructive evaluation using FWD. The Pavement Condition Index (PCI) procedure laid out in the US Army Corps of Engineers Technical Report M-294 by Shahin and Kohn (1981) was used to test and analyze pavements containing utility cuts.

It was determined from the study that pavement life was reduced by 39% to 73%, i.e. by an average factor of over 1.7 as results of utility cut patching. Similar to the APWA (1991) findings, it was determined that an area of weakness exists beyond the boundary of the utility

cut. The study concludes that although overlay increased pavement's stiffness modulus and service life, it didn't seem to correct the underlying distresses in the region of the utility cut.

The study did not consider the failure mechanism that contributed to the weakness observed around the periphery of the cut. The study achieved little success in presenting a quantitative measure of the goodness of fit of the derived curves and in discussing the adequacy of the limited data used to provide statistically significant conclusions (APWA, 1997).

(v) Southern California Gas Company (Todres and Wu, 1990; Todres and Baker, 1996; Todres and Saha, 1996; & Todres, 1999)

In response to concerns from the public sector on the impact of utility cut on pavement performance, Southern California Gas Company hired Are Inc. and the Institute of Gas Technology to conduct series of investigations to evaluate repair patches for asphalt paved streets. The studies included a theoretical analysis to assess critical elements of the repair and field experiments to confirm finding of the theoretical component. The theoretical analysis investigated cuts using a finite element program assuming linear elastic material properties, static loading conditions and employed an idealized circular cut shape in the analysis. The field study component was conducted at two selected pavement sections located on Carson Street and Florence Avenue in southern California.

Three pavement structures were investigated using finite element method (FEM):

(a) 2 inches (50mm) of asphalt concrete (AC), on 4 inches (100mm) of crushed stone base (CSB) on soil subgrade,
(b) 4 inches (100mm) of AC, on 8 inches (200mm) of CSB, on soil subgrade,
(c) 8 inches (200mm) of AC, on soil subgrade.

The cut was modeled as circular with a centrally applied load. Cut depth was taken constant at 900mm; and three cut diameters 600, 900, and 1200mm were explored. Two backfill densities (high and low) were investigated and the FE model was examined for structural responses to load. These responses included deflection, stresses and strains at surfaces and interfaces, both at the centerline and at various lateral distances.

The main conclusions derived from the studies were that soil backfill compaction is important in lighter pavement structures and that the size of cut is important in the structural responses in some cases. Other than the relative comparison of load carrying response of the different pavement configurations the studies did not address issues such as impact of utility cut on overall pavement life or maintenance costs. It also appears that the study assumed the adjacent pavement section and the underlying subgrade remain unaffected by the excavation. For the field experiments, sixteen cuts were placed in the wheel path of a heavily trafficked lane with a significant proportion of trucks and buses on Carson Street, Hawaiian Gardens, CA. Cuts were 1m wide by 1.3m deep and the existing pavement consisted of asphalt concrete on aggregate base on sand subbase. Conditions in the cut area were made more severe than in the surrounding pavement by reducing base thickness and having native subgrade directly below the aggregate base.

Comprehensive data were established on the pavement layers directly adjacent to each cut, and on the layer thicknesses and densities of all materials within the cuts. Base and asphalt were always compacted as well as possible. Backfill density targets were 85%, 90%, and 95% of modified Proctor maximum for the low, medium and high criteria, and were closely matched in the construction. For the two-year monitoring, surface profiles were determined over a two-dimensional grid that covered the cut and adjacent pavement, and non-destructive testing was performed by means of a falling weight deflectometer (FWD). The field test conducted on Florence Avenue, Downey, CA was similar in many respects to that described for Carson Street. Eighteen cuts were placed in the wheel path, and average daily traffic of the roadway was given as 3,200 including a fair number of trucks.

The studies concluded that standard section repairs are as good as T-section repairs, but that cold-mixed asphalt concrete (CMAC) is very deficient compared to hot-mixed asphalt concrete (HMAC) and that compaction has little effect on the performance of the patch. This is based on a limited comparison of cuts with nominal 80% versus 90% relative compaction. The study also concludes that there is no detrimental impact of the cut on the surrounding pavement. It should be noted that some comparisons are limited to single experiments, such as overlaying CMAC with HMAC.

(vi) Brooklyn Union Gas, New York (Mangolds and Carapezza, 1991)

The objectives of the study by Brooklyn Union Gas were to compare performance of cutback and non-cutback repairs, poorly and well-compacted backfill, and to evaluate moisture intrusion.

The investigation consisted of making and restoring 1m wide by 1m long by 1m deep cuts in a paved area at the Foster-Miller's facility which consist of 75mm of AC on 150mm of PCC a typical pavement configuration in New York City. Repeated loading was centrally applied by means of a hydraulic ram with load transferred to the pavement surface via a steel plate. Loading was 480 kPa. Twelve cuts were constructed, six cutback and six non-cutback. In each case three cuts had well compacted and three had poorly-compacted backfill. A failure criterion of 0.5 inches permanent deformation was adopted, and loading stopped at this point or at approximately 2.5 million cycles if the failure criterion had not been achieved.

The study concluded that well-compacted backfill resulted in acceptable pavement performance regardless of whether standard and T-section repairs are used. It also concluded that the use of T-section repairs does not prevent the infiltration of moisture because of the delamination of the AC and the breaking of the concrete.

(vii) University of Waterloo, Ontario (Tighe et al, 2002)

The study was conducted to assess the impact utility installations have on long-term pavement maintenance and service life so as to quantify the additional financial implications on road. The City of Waterloo, Ontario was used as pilot site to assess how cut-and-cover construction technique impact pavement life and long-term maintenance and rehabilitation costs. This assessment was accomplished through the use of eight case studies in which pipelines were placed under a municipal collector and a minor arterial roadway with 30-year life cycle.

Four of the studies were based on using open excavation while the other four were based on using trenchless technologies. The trenchless case studies were conducted with the

assumption that the pipe installation would results in a non-disturbed pavement structure. For cut-and-cover installations the trench was assumed to be 2m wide at the surface and to extend through the road base, subbase, and subgrade and backfilled using good construction practices. Initial pavement condition index (PCI) that utilizes both roughness in terms of RCI and types of distress was used as the performance measure. Pipe installations on a one-year old and seven-year old pavement were investigated. The Ontario Pavement Analysis of Costs, OPAC 2000 program, which is a mechanistic-empirical design program, was used to predict performance.

Results of the study suggested that pavement life can be reduced by approximately 30% once an excavation is made in a road and increased maintenance cost for excavating one-year old is approximately \$146 per m^2 and between \$85 and \$140 per m^2 for a seven-year old pavement structure. It also showed that the use of trenchless technology with good practices has the potential to significantly reduce road maintenance and rehabilitation cost, as well as, users delay costs.

(viii) Other Research Work

Other pavement utility cut research effort reviewed include field studies completed by Al-Suhaibani et al (1992) for City of Riyadh, Saudi Arabia; Nichols-Vallerga, (2000) for City of Seattle, Washington; and Tarakji (1995) and Chow and Troyan (1999) for City of San Francisco, California; and theoretical investigation by Humphrey and Parker (1998)

The causes of failure in and around utility cuts, their effects and the correctives measures that need to be taken to remedy structural deficiencies in and around that vicinity of the cuts were not considered in most of the previous studies. These findings are necessary to quantify/predict deterioration and develop a realistic fees structure to cover additional maintenance cost resulting pavement utility cut. There is also a need to objectively study issues related to utility cut excavation and restoration and impact on pavement performance.

2.3 Design of Flexible Pipes

The term "rigid" and "flexible" are somewhat arbitrary when applied to pipe. Generally, rigid pipes are pipes that are designed undergo only small deformations when subjected to loading. Pipes such as vitrified clay and concrete are considered as rigid. Rigid pipes are usually much stiffer than the soil in which they are installed. On the other hand, flexible pipes designed to deflect under load and are usually less stiff or only slightly stiffer than the surrounding soil (Petroff, 1990). Flexible pipes include corrugated metal pipes, plastic pipes, and some steel and ductile pipes. The relative stiffness between the soil and the pipe determines if a pipe is rigid or flexible.

Polyethylene (PE) is one of the most widely used materials for plastic pipes. Polyethylene pipe is a viscoelastic material that deforms immediately upon application of an induced load followed by a decreasing rate of deformation with time. The recoverable and irrecoverable portions of the deformation are attributed to the elastic and viscous properties of the PE pipe, respectively. Because the rate of permanent deformation is time dependent, PE pipe exhibits different short and long-term material properties. For example, as shown in Figure 2.1, the short term and long-term elastic modulus for High Density Polyethylene (HDPE) material at 23ºC are 800 and 200 MPa respectively. PE pipe performance design criteria are generally based on long-term material properties under constant stress. Material properties are also temperature dependent. Figure 2.1 shows that lower material temperatures yield significantly greater modulus of elasticity values.

2.3.1 Load on Buried Flexible Pipes

The load that ultimately reaches a buried pipe depends on the relative flexibility between the pipe and the soil. The trench load consists of the dead load of the backfill and any surcharge. The portion of the trench load that reaches the pipe embedment zone or a horizontal plane at the pipe crown depends on the shear strength of the soil, its stiffness and the width of the trench. Where the pipe and the soil are of equal stiffness, the trench load is spread uniformly over the pipe and soil. However when the soil is stiffer than the pipe, which is usually the case of flexible pipes, the pipe carries proportionately less load.

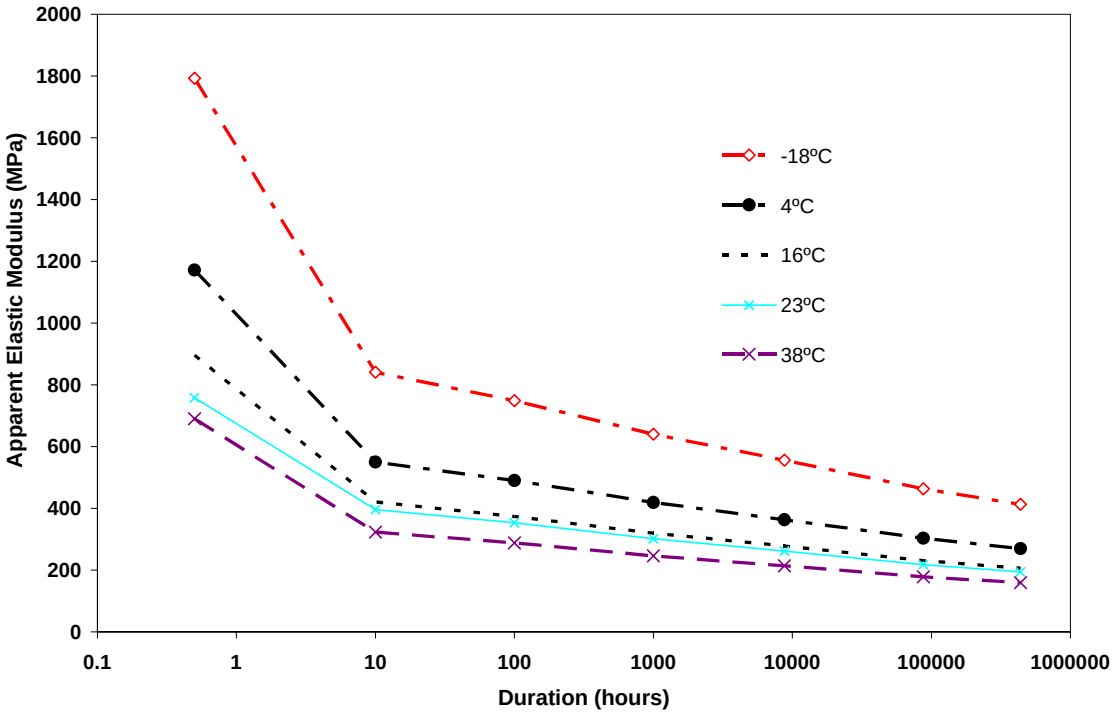

Figure 2.1: Apparent Modulus of Elasticity for HDPE at Various Temperatures
(Adapted from Performance Pipe, 2003)

This is a consequence of the pipe's deflection and the internal shear resistance of the soil (Spangler and Handy, 1982). As the pipe deflects the soil above the pipe displaces downward to accommodate the deflection. Internal shearing stresses within the soil develop and resist this downward movement, thus reducing the amount of load reaching the pipe. The load remaining in the soil above the pipe is shunted around the pipe into the soil besides the pipe. Consequently, the soil acts as an arch and carries a larger load than the pipe. This phenomenon, known as arching, is well documented by Lafebvre et al (1976).

Pipe designers often follow a conservative approach when designing piping systems. Soil arching effects are incorporated into design calculations by either using the earth loads predicted by the Marston load (P_M) equation or a modified soil load (P_C) equation that produces loads magnitude between the total earth pressure load i.e. prism load (P_E) and Marston loads (P_M) (Watkins and Anderson, 2000). The total earth/soil pressure or prism load per unit area is given by:

$$P_E = \gamma H \quad [2.1]$$

where γ is the unit weight of the overlying soil (kN/m^3), and H is the depth to the pipe crown in metres. The Marston load (P_M) is given by the following equation:

$$P_M = C_D \gamma B \quad [2.2]$$

where γ is the unit weight of the overlying soil (kN/m^3), B is the width of the trench at the crown of the buried pipe in metres, and C_D is a load coefficient given by:

$$C_D = \frac{1 - e^{-2ku'\frac{H}{B}}}{2ku'} \quad [2.3]$$

where u' is the friction angle between the backfill and trench walls, $k = \tan^2(45 + \frac{\phi}{2})$ is the Rankine earth pressure coefficient and ϕ is the internal friction angle of the soil. The modified load equation is often formulated using 40% of the difference between the prism load and the Marston load:

$$P_C = 0.6 P_M + 0.4 P_E \quad [2.4]$$

An alternative method proposed in Performance Pipe (2003) for calculating the modified arching vertical soil pressure suitable for most soils is given by:

$$P_C = F \gamma H \quad [2.5]$$

where $F = \frac{P_M + 0.4(P_E - P_M)}{P_E}$ is an arching coefficient.

2.3.2 Load on HDD Installed Flexible Pipes

Processes producing ring deflections in flexible PE pipes installed using HDD construction practices differ from those associated with buried pipe applications. In HDD installations, no

trench is excavated and backfill material is not placed under and above the product pipe. Instead, an oversized slurry filled bore, typically 1.5 times the diameter of the product pipe for smaller pipe, is reamed through the native soils leaving the surrounding in situ soils relatively undisturbed. Arching processes may still occur, but not in the same manner as with buried pipe construction practices. Here, arching may develop due to inward deflection of the bore. As with the downward movement of the backfilled material in buried pipes, the inward deflections of the bore generate frictional shear stresses in the overlying native soils and reduced earth and surface loadings. This is confirmed by results obtained from field study completed by Knight et al (2001) and Duyvestyn et al (2001b); excavations conducted on two HDD pipe installations revealed bore diameters (vertical and horizontal) fairly similar to reamer head diameters eight months and two years after installation. If arching processes were not active in the overlying and neighboring native soils, bore deflections (and hence bore diameters) would differ significantly from reamer diameters because of the higher vertical stresses (and hence vertical deflection) compared to lateral stresses. Here it is hypothesized that the lower stiffness pipe-slurry system distributes earth and surface loads to the surrounding stiffer native soils.

When a bore is created, the in situ stress field must redistribute around the discontinuum created by the presence of the bore in a manner similar to tunneling. The redistribution of stresses generally increases local stresses around the bore (Marshall, 2003). Earth and surface loads are transferred to the product pipe through the slurry occupying the annular space between the product pipe and the bore. If slurry were not present within the annular space or if the slurry material provided no supporting characteristics, loads could not be transferred to the product pipe unless the bore was to completely collapse around the pipe. However, if proper drilling practices are followed, slurry will always remain and completely fill the annular space as demonstrated in the field studies presented by Knight et al (2001) and Ariaratnam and Beljan (2005).

Bore slurry pressure measurement during field-scale HDD installations have shown that induced fluid pressures are generally greater than the overburden pressure at the crown of the bore (Duyvestyn et al, 2002). Hence the slurry pressure provides resistance to inward movements of the bore walls. During stoppages in drilling activities, these fluid pressures fall

off fairly rapidly potentially allowing inward bore movements. However, because a fluid phase exists within the annular space of the bore, inward bore deflections generate opposing slurry fluid pressures that are capable of supporting the bore and preventing collapse of the bore wall.

The primary sources of ovalization associated with HDD installations are believed to be buoyant deflection due to the presence of the fluid phase (slurry) in the bore, ring deflections due to earth and live loads in a deformed or collapse bore, deflection of the pipe as it is forced to negotiate curves in the bore, and finally, deflections due to stretching of the pipe as it is installed (PPI, 2000 and Polak et al, 2004). Ring deflection design limits (ovality limits) for PE pipes are governed by the intended purpose and SDR of the installed pipe. As shown in Table 2.1, non-pressure applications have higher design deflection limits than pipes used in pressure applications.

Table 2.1: Long-term Design Deflection Limits of Polyethylene Pipes (PPI, 2000)

SDR	21	17	15.5	13.5	11	9	7.3
Non-Pressure applications	7.5	7.5	7.5	7.5	7.5	7.5	7.5
Pressure Applications	7.5	6.0	6.0	6.0	5.0	4.0	3.0

2.3.3 Calculation of PE Pipe Ring Deflection

The performance of flexible pipe and its ability to support load is typically assessed by measuring the deflection from its initial shape. The allowable ring deflection for buried PE pipe is based on limiting tangential PE pipe strains in the outer surface of the pipe wall to no more than 1.0 to 1.5%. Ring deflection limits assume that pipe deflections are equal to the vertical compressive strain in the backfill adjacent to the pipe. The current design approach suggests that thicker walled i.e. lower SDR values, PE pipes have lower allowable ring deflections to limit tangential pipe strains to no more than 1.5% (Performance Pipe, 2003).

The deflection of a PE pipe is the sum total of two major components: the installation deflection and service deflection. Installation deflection is subject to control by the care used in the placement and compaction of the pipe embedment material in relation to the pipe's ring stiffness in case of buried pipe, or tensile load applied imposed on pipe during pullback for HDD installed pipe. The installation loads can result in either an increase or decrease in vertical pipe diameter; an increase in vertical pipe diameter is referred to as "rise" and is usually a result of the forces acting on the pipe during compaction of the embedment beside it (PPI, 2000). Installation deflection is not predictable by any of the mathematical formula, although there are empirical methods for accounting for it.

Service deflection reflects the response of the constructed pipe-soil system to the subsequent earth loading and induced/surcharge loadings, which often result in decrease in vertical diameter of the pipe. The most commonly used equation for the prediction of service deflection is the empirical equation developed by Spangler (1941) and its modified version Modified Iowa Equation by Watkins (1966). These and other equations used for estimating pipe deflection are presented below.

(i) Spangler's Iowa Equation

In the 1930's, Professor Spangler, of Iowa State University, developed a rational design procedure to predict the deflection of buried flexible conduit (Spangler, 1941). This design procedure calculated the horizontal deformation of the conduit as a function of the vertical load, the bedding support provided, and soil pressures acting laterally to resist the horizontal movement of the pipe. Based on the assumption the pipe was sufficiently rigid, the deformed shape would be that of an ellipse, Figure 2.2, he determined the vertical deflection would be approximately equal to the horizontal. Spangler's 'fill load' hypothesis assumed that pressure distribution around a circular flexible conduit is as shown in Figure 2.3. Since his original work, the soil term of his initial equation was modified to obtain what is referred to as the Modified Iowa Equation (Watkins, 1966).

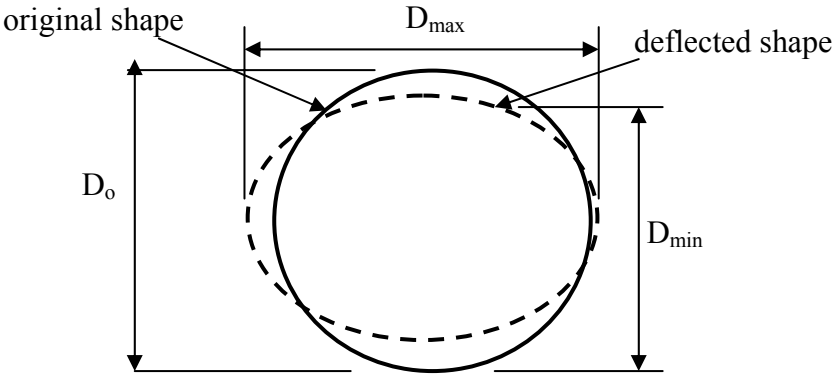

Figure 2.2: Typical PE Pipe Ring deflection

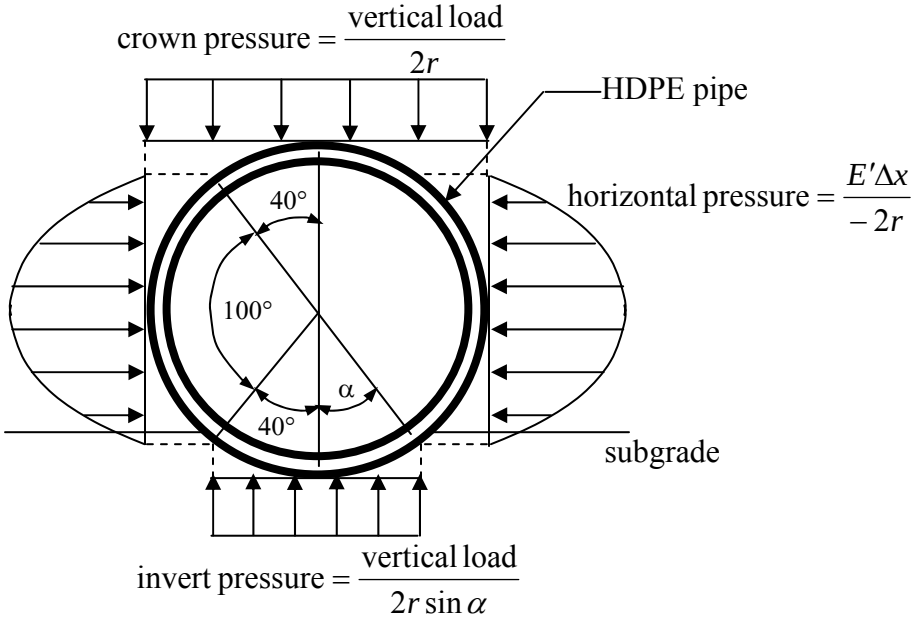

Figure 2.3: Basis of Spangler's derivation of the Iowa formula
(Spangler, 1941)

A common form of Spangler's Modified Iowa formula used by PE pipe designers for buried flexible pipe applications is:

$$\frac{\Delta}{D} = \left[\frac{KP_T L}{\frac{2}{3}E\left(\frac{1}{SDR-1}\right)^3 + 0.061E'} \right] \qquad [2.8]$$

where Δ is the ring deflection (mm); D is the average pipe diameter (mm); P_T is the total pressure (earth and live loads) at the pipe crown elevation (kPa); K is the bedding factor; L is the lag factor; E is the apparent modulus of elasticity of the pipe (kPa); SDR is the pipe standard dimension ratio, and E' is the modulus of soil reaction (kPa).

Spangler's bedding factor (K) depends on the bedding conditions of the backfill material and the diameter of the product pipe. Higher factors are attained for firm compacted bedding materials, pre-shaped bedding conditions, small bedding angles (α) and larger pipe diameters. A value of 0.1 is commonly used in calculations (Performance Pipe, 2003). Spangler's lag factor accounts for yielding of the soil along the sides of the flexible pipe in response to horizontal pressure long after the maximum vertical load has developed over the pipe. The experience of Spangler had shown that pipe ring deflection could increase by as much as 30% over 40 years (Uni-Bell, 1993). The deflection lag factor cannot be less than unity and has an upper limit of 2.0 and depends on the quality of the soil at the sides of the pipe (Spangler and Handy, 1982). Loose soils have higher deflection lag factors. Recommended values for lag factor range from 1.0 for short-term to 1.5 for long-term (Uni-Bell, 1993).

The modulus of soil reaction (E') represents the stiffness of the soil at the soil-pipe interface based on elastic theory and is defined as interface pressure divided by soil strain (Abdel-Sayed et al. 1994). Spangler's formula incorporates this modulus to account for lateral support provided by the surrounding backfilled soil on the pipe-soil system. The exact nature of this modulus is unknown; it is neither elastic modulus, nor a constant. E' value can not be obtained by testing a soil sample, but are empirically determined. The modulus of soil reaction is dependent on the loading configuration, depth of cover, relative stiffness of the

flexible pipe, type of flexible pipe, and properties of the surrounding soil (predominantly the type and degree of compaction). Howard (1977) published Tables that provide guidance for determining appropriate values of soil reaction, the published values are empirically based obtained, back calculated from existing installations in similar soils.

Subsequent to Spangler's research and acceptance of the modified equation, major changes have been made to the structural integrity of many flexible pipe products, such as substantially improved section properties, and the use of viscoelastic materials whose physical properties change as a function of time or temperature or both, resulting in deformations that are non-elliptical in shape (i.e. the vertical deflection is not equal to the horizontal deflection), and may increase with time. Recent trends in flexible pipe designs proposed by some manufacturers and designer have ignored the long established guidelines suggested for the use of Spangler's Equation, but continue to use his equation in their attempt to substantiate adequacy of their product. It is important to recognize the factors associated with the use of this equation for thermoplastic pipe, for instance:

- The equation was developed for thin wall corrugated metal pipe having a constant stiffness as a function of time using elastic theory.

- Ring deflection depends largely on modulus of soil reaction (E') and is subject to change along the length of the line due to installation variables.

- Spangler's Iowa formula predicts horizontal deflection, not vertical. Vertical deflection is estimated as being equal to predicted horizontal expansion.

- Construction induced deflection during installation caused by high compaction effort could be greater than load induced deflection and is not considered by the equation.

The use of the Modified Iowa equation to predict performance has a basic premise that the pipe deflection approximates an elliptical response and the vertical deflection is approximately equal to the calculated horizontal deflection. The estimated deflection should be adjusted to properly evaluate this equation for low stiffness pipe or high soil stiffness.

However, the formula that was derived from tests performed on corrugated metal pipes is now being adopted by flexible viscoelastic plastic pipe producers without applying correction factors for vertical to horizontal deflections and without correcting for the combined effect of insitu and backfill soil conditions.

(ii) Plastic Pipe Institute Formula (PPI, 2000)

The Plastic Pipe Institute published a handbook that provides some design considerations and calculations for HDD installed PE pipes. The designs assume that the slurry occupying the annular space between the bore and the installed pipe provides no side-support along the springline to restrain vertical deflection and that the primary resistance to deflection is provided by the long-term ring-stiffness of the pipe. However, as stated earlier, if the slurry material were to provide no support for an installed pipe, earth and surface loads could not be transmitted to the pipe unless complete collapse of the bore occurred. Even if complete collapse were to occur, the collapsed material would then provide some side support. Hence, PPI's assumption of the no side-support is excessively over-conservative.

Based on the assumption that the bore slurry provides no side support and that an imposed earth load on HDD installed pipe will be resisted primarily by the stiffness of the pipe, PPI suggests the use of the following pipe stiffness equation to calculate ring deflections due to earth load:

$$\frac{\Delta}{D} = \frac{0.0125 P_E}{\dfrac{E}{12(SDR-1)^3}} \qquad [2.9]$$

where Δ is the vertical ring deflection (m); D is the average pipe diameter (m); P_E is the total pressure (dead and live earth) at the pipe crown elevation (kPa); E is the apparent modulus of elasticity of the pipe (kPa) and SDR is the pipe dimension ratio. Equation 2.9 is an average of two ring deflection equations found in Watkins and Anderson (2000) given as

$$\frac{\Delta}{D} = \frac{0.0145 P_E}{\frac{EI}{D^3}} \qquad [2.10]$$

and

$$\frac{\Delta}{D} = \frac{0.0104 P_E}{\frac{EI}{D^3}} \qquad [2.11]$$

Equation 2.10 assumes that the pipe invert is supported on a rigid flat base and has a uniform crown pressure (P_E) as shown in Figure 2.4 while Equation 2.11 assumes that the invert and crown pressures are uniform and equal to P_E as in Figure 2.5. Both equations assume no lateral side support for the pipe-soil system. Equations 2.10 and 2.11 are based on parallel-plate load test and were derived from the use of strain energy theorem employing concepts of complementary energy and work (Watkins and Anderson 2000).

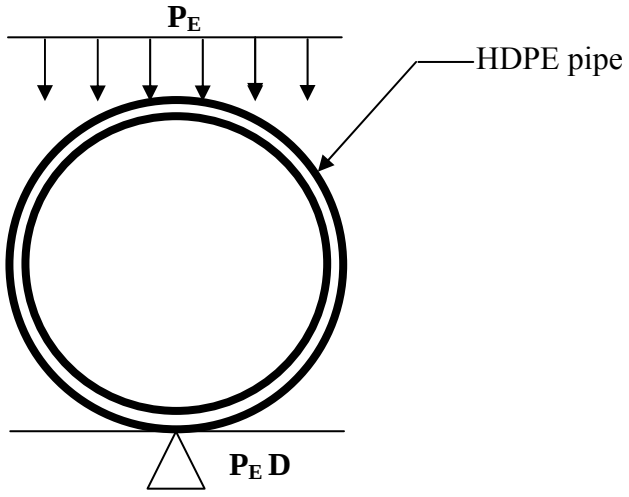

Figure 2.4: Rigid base pressure distribution for Equation 2.10

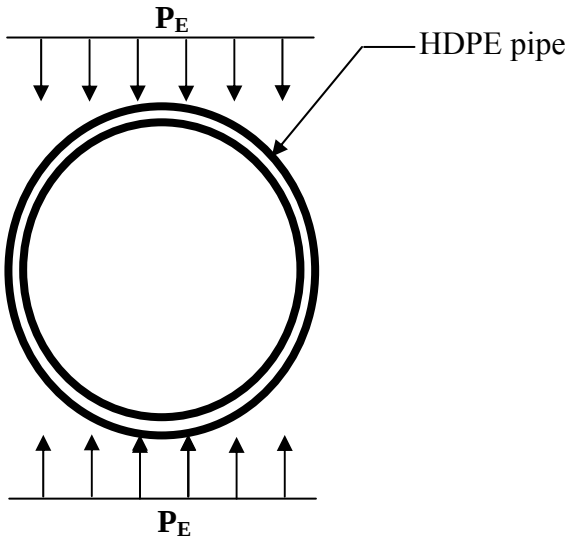

Figure 2.5: Rigid crown and invert pressure distribution for Equation 2.11

To account for arching effects, PPI (2000) suggested multiplying the total pressure (P_E) at the crown by an arching factor κ, given by:

$$\kappa = \frac{1 - e^{-2\frac{KH_c}{B}\tan\left(\delta/2\right)}}{2\frac{KH_c}{B}\tan\left(\delta/2\right)} \qquad [2.12]$$

where H_c is the depth of cover, $k = \tan^2(45 + \frac{\phi}{2})$ is the Rankine earth pressure coefficient and ϕ is the internal friction angle of the soil, B is the '*silo*' width (it is conservative to assume B equals the bore diameter), and δ is angle of wall friction (equal to ϕ for HDD applications).

PPI also provide equation for calculating pipe deflection due to buoyancy within the bore, the equation is based on the premise that a pressure difference is developed between the invert and the crown of the pipe when the pipe is submerged the drilling mud/slurry. And that the pressure difference applies a force, which deflects the invert upward toward the crown, thus creating ovality especially when the pipe is installed empty. The following equation was proposed for estimating buoyant deflection:

$$\frac{\Delta}{D} = \frac{0.088\gamma_s D(SDR-1)^4}{E(SDR)} \qquad [2.13]$$

where Δ is the vertical ring deflection (m); D is the average pipe diameter (m); γ_s is the unit weight of the bore slurry (kN/m^3); E is the apparent modulus of elasticity of the pipe (kPa) and SDR is the pipe dimension ratio.

2.4 Horizontal Directional Drilling

Horizontal directional drilling (HDD) is a construction method used to install new product pipe and underground service lines with minimal surface disturbance and disruption. This construction technique is increasing being used as the primary method for installation of underground infrastructure crossing environmental sensitive areas, roadways, railways and crowded urban areas. The horizontal directional drilling industry has grown significantly over the past 20 years and has achieved worldwide acceptance as an effective and economical alternative to open-cut excavation practices (Allouche et al. 2000, Gokhale et al 1999). A survey conducted by Allouche et al. (2000) revealed that almost three quarters of all HDD contractors are involved in municipal applications in which utility conduits are installed in engineered surface or subsurface structures that include embankments and pavement structure.

The HDD process is divided into three stages: pilot bore, pre-ream, and pullback of the product pipe. The pilot stage consists of drilling a pre-planned bore using a steerable slanted-face drill head that can be tracked from the surface. A schematic of the technique is shown in Figure 2.6. Typical pilot bore diameters range from 100mm to 150mm depending on the size of the drill bit and drill pipe used during the installation. The drill path is monitored by an electronic package housed in the pilot drill head (Figure 2.7). The electronic package (transmitter) detects the relation of the drill string to the earth's magnetic field and its inclination. This data is transmitted back to the surface where the receiver read and interprets

the signal to provide information about drill head location, orientation, depth, pitch and roll. Walkover receivers or wireline technology is used to track the path of the drill head.

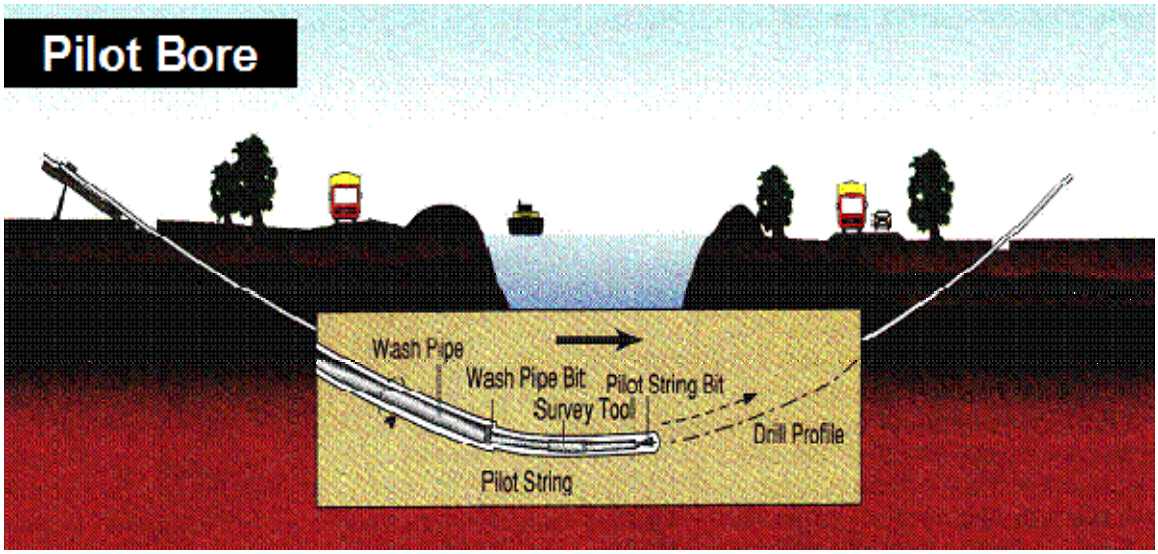

Figure 2.6: HDD Pilot bore drilling stage
(Adapted from DCCA, 1998)

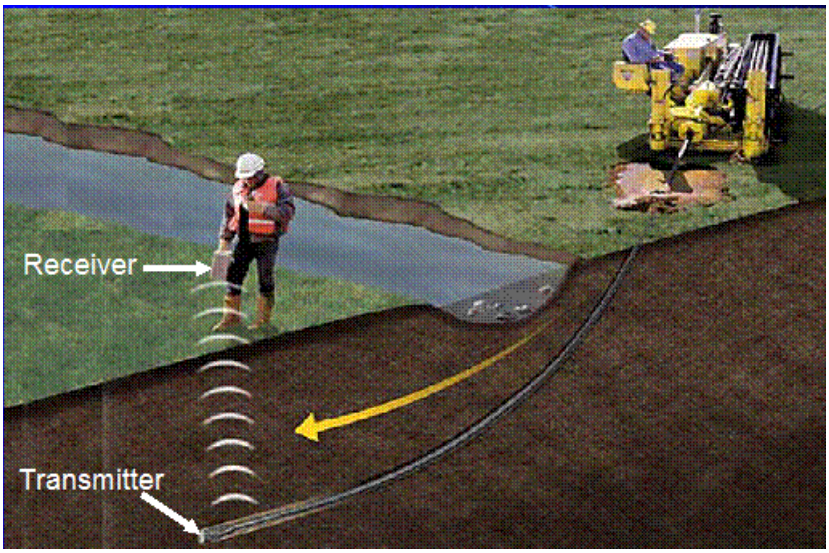

Figure 2.7: Walk over HDD drill head tracking device technique
(Adapted from DCCA, 1998)

Once the pilot bore is completed, the bore is enlarged to a suitable diameter for the product pipeline; the process of enlargement is the pre-ream stage. The pre-ream stage consists of installing a larger diameter reamer onto the drill string/pipe assembly and pulling (or pushing) it through the pilot bore, Figure 2.8. The soil cuttings created by the mechanical cutting action of the reamer during bore enlargement are mixed with raw drilling fluid to form flowable-slurry that can be easily transported out of the bore by the fluidic pressure gradient present within the bore.

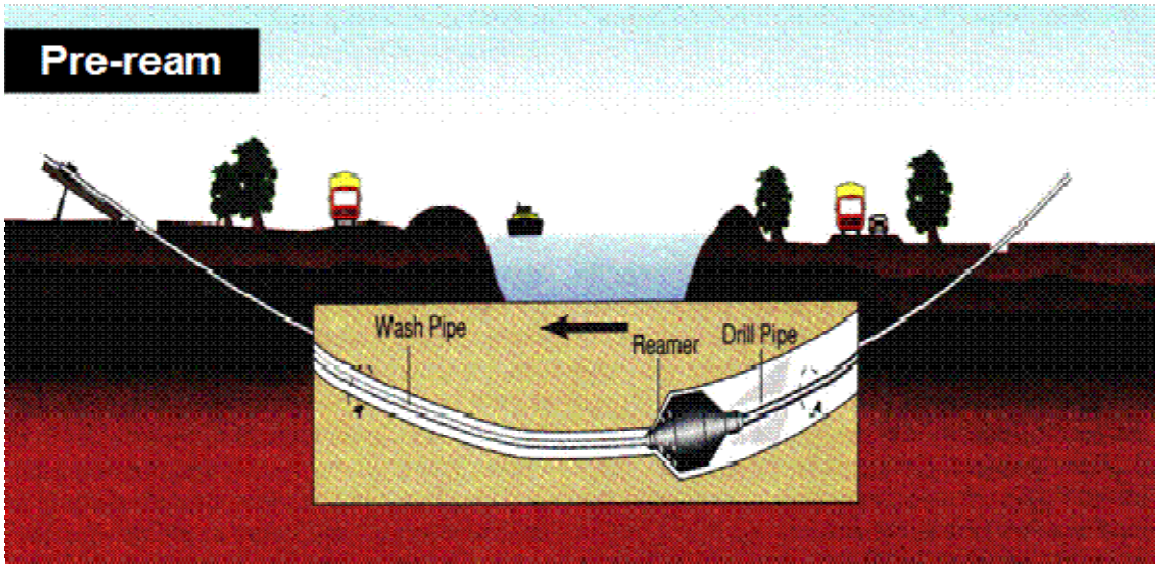

Figure 2.8: HDD Pre-reaming stage
(Adapted from DCCA, 1998)

Depending on subsurface conditions, installation parameters, drilling rig capabilities and characteristics of the product pipe, the bore can be pre-reamed with multiple reamer passes and or different sized reamer. It is recommended that the final bore diameter should be the lesser of 1.5 times the diameter of the product pipe or the diameter of the product pipe plus 300mm for bore diameters greater than 200mm (Bennett et al, 2001). Smaller installations require a minimum 50mm annular space around the entire product pipe.

Prior to the pipe installation (product pipe pullback stage), a volume of soil cutting equivalent to at least the volume of the product pipe must be removed from the bore. The removal of soil cutting (or more correctly bore slurry) is accomplished by inducing fluidic pressure gradient within the bore. Gelinas and Mathy (2001) noted that it is this induced pressure gradient that produces the majority of the ground deformation (heaving) during HDD installation especially in shallow bore.

Once the bore is enlarged to the desired diameter, the product pipe can be pulled through it. The product pipe is prefabricated on the opposite side of the drilling rig. A reamer is attached to the drill string, and then connected to the pipeline pull-head via a swivel, Figure 2.9. The swivel reduces the torsion on product pipe by preventing any translation of the reamer's rotation into the pipeline string thereby allowing for a smooth pull into the bore. The drilling rig then begins the pullback operation, rotating and pulling on the drill string while drilling fluid is released into the bore concurrently. The pullback continues until the reamer and pipeline break ground at the drilling rig.

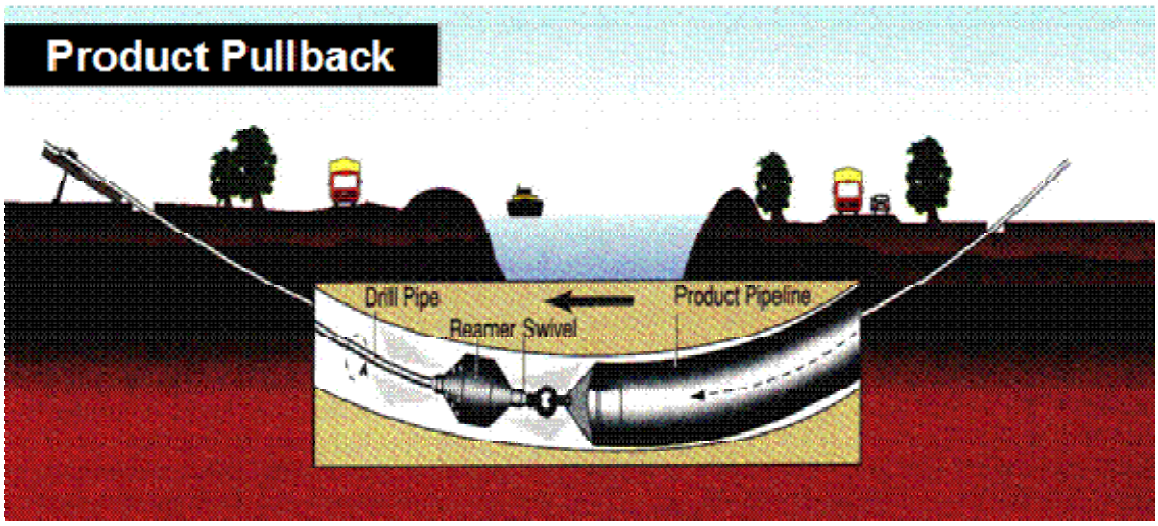

Figure 2.9: HDD Product pipe pull back stage
(Adapted from DCCA, 1998)

2.4.1 Ground Deformation Associated with HDD

Ground movements that may occur during HDD installation is of primary concern to municipalities and contractors especially in urban areas where underground right of ways have become increasingly crowded. Lueke and Ariaratnam (2003) stated that there have been an increased number of incidents where surface heave from HDD installation have damaged existing surface and subsurface structures. The frequency of such incidences have forced some municipalities to place restrictions on the use of horizontal directional drilling for utility installation.

Ground movements associated with horizontal directional drilling are directly related to the magnitude of pressure generated by the drilling fluid introduced into the bore to promote removal of soil cutting during installation process. Although pressure build-up within the bore can occur during pilot bore, prereaming, or pipe pullback, it is often during the reaming and pullback phases that most ground movements become substantial. The action of the reamer or collapsed bore may hinder the flow of slurry exiting the bore resulting in build-up of bore slurry pressure. To avoid excessive bore pressure build-up the slurry produced during HDD process should be able to exit the bore easily. Large soil cutting, inadequate quantity of drilling fluid and improper mixing of raw drilling fluid and soil cutting could all restrict the flow of slurry within the bore leading to excessive pressurization of the bore.

In cohesionless soils, plastic expansion of the bore may develop due to excessive bore slurry pressure and eventually result in the overlying soil being heaved. When heaving is accompanied by fracturing of the overlying soil, the bore pressure is dissipated and bore-fluids may rise to the ground surface. The term inadvertent return is given to the pooling bore-fluids on the ground surface. In cohesive soils, excessive bore pressure leads to development of hydraulic fracture. Hydraulic fracture is a tangential tensile failure of the host soil at the outer edge of the bore due to increased bore slurry pressure. Increased bore pressure will cause the annular tangential stresses to increase until the tensile strength of the soil is reached and fracture is initiated. Once a fracture is initiated, it will propagate out along the path of least resistance until the fluid pressure causing the propagation is relieved. Due to increase in geostatic insitu stresses with depth and lateral earth pressure coefficient that is often less than unity, fracture tends to develop at the crown of the bore and follow an upward direction towards the ground surface continuing until a stronger soil horizon or structure that

is capable of resisting the induced fluid pressure or the ground surface is encountered. The stress require to propagate fracture upward is generally lower than the initiating pressure.

New methods and instruments have been developed for monitoring bore slurry pressure during HDD installation e.g. Knight and Duyvestyn (2001), Ariaratnam et al (2000); and Baumert et al (2004). These instruments have improved the quality of data obtained from instrumented HDD field installations and have generally enhanced the understanding of mechanisms that causes ground movements and hydraulic fracturing during HDD installations. However, further research is still required to develop reasonable estimates of allowable bore slurry pressures to minimize ground movements induced during HDD installations. The research work presented herein is a step in that direction.

Chapter 3: Soil Constitutive Model

3.1 Introduction

The Mohr-Coulomb linear elastic-perfectly plastic model is one of the most widely used non-linear models for numerical analyses of soils and soil-structures interaction problems. It is generally assumed that the elastic response of the model is linear and isotropic. However recent field and laboratory studies have shown that even at very small strains, many soils exhibit non-linear stress-strain behavior (Burland, 1989, and Jardine et al, 1986). If the results of numerical simulations are to be realistic and meaningful, it is important that the stress-strain characteristics of the soil be represented reasonably. Since the nature and amount of ground movements in granular materials are strongly influenced by their non-linear stress-strain behavior, a constitutive model capable of representing this important behavior was implemented for the numerical analysis.

The proposed model is a variation of the conventional Mohr-Coulomb linear elastic-perfectly plastic model in which the secant elastic moduli are replaced by tangential elastic moduli that are hyperbolic function of the confining stress. The non-linear stress-strain behavior of granular materials has been simulated extensively using hyperbolic relationships. The widely used hyperbolic functions for simulation of stress-strain curves was formalized by Duncan and Chang (1970) using Konder (1963) findings that the plot of stress vs. strain in a triaxial compression test is very nearly a hyperbola. Although, the hyperbolic relationships by Duncan and Chang (1970) can reasonably simulate stress-strain behavior of soils in the elastic range (i.e. at working load before failure), it has shown that it does not accurately model the behavior of real soils at and after failure (Chen and Saleeb, 1994).

The conventional Mohr-Coulomb model, on the other hand, is capable of capturing soils behaviour at failure and it has been successfully used to calculate stability limits states for many geotechnical problems (Brinkgreve, 2005 and Smith, 1994). The proposed modified Mohr-Coulomb model described in this Chapter combines the good aspect of both models by using the hyperbolic stress-strain relationship to model soil's behavior before failure, and the Mohr-Coulomb perfectly-plastic model to determine the behaviour at and after failure.
In this chapter, review of the conventional Mohr-Coulomb linear elastic perfectly-plasticity model and the hyperbolic relationship are presented. The proposed Mohr-Coulomb non-linear elastic perfectly-plasticity model which combines the advantages of the two traditional models is described thereafter.

3.2 Mohr-Coulomb Linear Elastic Perfectly-Plastic Model

The Mohr-Coulomb linear elastic perfectly-plastic model is based on incremental elastic-perfectly plastic theory. Hence, it is important to present a brief description of the theory before describing the model in detail.

3.2.1 Incremental Elastic-Plastic Theory

The Mohr-Coulomb elastic perfectly plastic model is based on the assumption that soil is a perfectly elastic material under working load and perfectly plastic under ultimate failure condition. The model is derived from the flow theory of plasticity and only a brief description of the theory is presented here. Detailed discussion of the theory can be found in Hill (1950) and Desai and Christian (1977).

The theory of plasticity represents a necessary extension of the theory of elasticity and is concerned with the analysis of stresses and strains in the plastic, as well as, the elastic ranges. Its gives more realistic estimates of load carrying capacities of materials and provides a better understanding of the reaction of the structural element to the forces induced in the material (Chen and Han, 1988). Plasticity theory provides a mathematical relationship that characterize the elasto-plastic response of materials, once the stress-strain or constitutive relationship is known, equations of equilibrium and of compatibility can be used to determine the state of stress or strain when the materials is subjected to a prescribed force. The stress-

strain relationship for a material depends on many factors, including the homogeneity, isotropy, and continuity of the body material, its reaction to loading over a period and the rate and magnitude of loading (Chen and Baladi, 1985).

In the flow theory of plasticity, the incremental stress-strain relation is based on the fundamental assumptions of the existence of yield surface and a flow rule which specifies the general form of the stress-strain relationship. The yielding of a material obeying the theory of perfect plasticity is defined by the yield criterion or function f. The yield function f is a known function that specifies the limiting stress combination for which plastic flow takes place; this function is represented by a surface in the generalized stress space, and all stress points below the surface ($f < 0$) are characterized by elastic behavior and when $f = 0$ the material is in a plastic state. The function can be represented mathematically as

$$f(\sigma_{ij}) = 0 \qquad [3.1]$$

The yield surface is fixed in the stress space for a perfectly plastic material and any state of stress that satisfies Equation 3.1 lies on the yield surface since the stress point cannot move outside the surface i.e. $f \not> 0$, this requirement is termed *consistency condition*. If an increment of stress $\Delta\sigma_{ij}$ is applied and the stress state moves out of the current elastic region, a *loading* process is taking place. Further loading beyond the onset of plastic flows only causes the stress state to move along the tangential direction. Thus the condition for a continuation or further plastic flow, or the criterion for loading, is

$$f(\sigma_{ij}) = 0 \quad \text{and} \quad df = \frac{\partial f}{\partial \sigma_{ij}} d\sigma_{ij} = 0 \qquad [3.2]$$

and the criteria for unloading is

$$f(\sigma_{ij}) = 0 \quad \text{and} \quad df = \frac{\partial f}{\partial \sigma_{ij}} d\sigma_{ij} < 0 \qquad [3.3]$$

Thus, the yield function or surface $f(\sigma_{ij})$ is also called the *loading function* or *surface*.

The theory of plasticity assumes that the total incremental strains tensor, $\Delta\varepsilon_{ij}$, can be decomposed into elastic ($\Delta\varepsilon_{ij}^{e}$) and plastic ($\Delta\varepsilon_{ij}^{p}$) incremental strains tensors:

$$\Delta\varepsilon_{ij} = \Delta\varepsilon_{ij}^{e} + \Delta\varepsilon_{ij}^{p} \qquad [3.4]$$

The elastic response is normally assumed to be governed by an incremental form of generalized Hooke's or any other non-linear elastic model. The elastic relations between the elastic strain increments and stress increments can be written as

$$\Delta\sigma_{ij} = C_{ijkl}(\Delta\varepsilon_{kl}^{e}) \qquad [3.5]$$

where C_{ijkl} is the elastic tangential stiffness tensor.

The flow rule is the necessary kinematic assumption postulated for plastic flow. It gives the ratio or the relative magnitudes of the component of the plastic strain increments tensor $\Delta\varepsilon_{ij}^{p}$.

The flow rule also define the direction of the plastic strain increment vector, $\Delta\underline{\varepsilon}_{i}^{p}$, in the strain space as that normal to the plastic potential surface $g(\sigma_{ij}) = constant$ i.e.

$$\Delta\varepsilon_{ij}^{p} = d\lambda \frac{\partial g}{\partial \sigma_{ij}} \qquad [3.6]$$

where $d\lambda$ is a positive scalar factor or proportionality, which is non-zero only when plastic deformation occur. The function $g(\sigma_{ij}) = constant$ defines a surface (*hypersurface*) of plastic potential in nine-dimensional stress space. The concept of *plastic potential function* was first proposed by von Mises in 1928. When the yield function and the plastic potential function coincides ($f = g$); thus,

$$\Delta\varepsilon_{ij}^{p} = d\lambda \frac{\partial f}{\partial \sigma_{ij}} \qquad [3.7]$$

and plastic flow develops along the normal to the yield surface $\partial f / \partial \sigma_{ij}$. Equation 3.7 is called the *associated flow rule* because the plastic flow is connected or associated with the yield criterion, while Equation 3.6 with $f \neq g$ is called a *non-associated flow rule*. The

Mohr-Coulomb elastic perfectly plastic model described in the following section is characterized by a shear yield function and a non-associated shear flow rule. In addition the failure envelope is characterized by a tensile yield function with associated flow rule.

3.2.2 Mohr-Coulomb Yield Criterion in 3D

The yield function used in the implementation of the Mohr-Coulomb linear elastic perfectly plastic model is founded upon the Mohr's failure criterion. Mohr's criterion is based on the assumption that the maximum shear stress is the only decisive measure of impending failure and that intermediate principal stress σ_2 has no influence on the failure. The failure criterion also considers the limiting shear stress (τ) in a plane to be a function of the normal stress σ in the same plane at a point i.e.

$$|\tau| = f(\sigma) \qquad [3.8]$$

where $f(\sigma)$ is an experimentally determined function. According to this criterion, failure of material will occur for all states of stress for which the largest of the Mohr circles is tangent to the envelope, Figure 3.1. The simplest form of Mohr envelope $f(\sigma)$ is a straight line relation between τ and σ, illustrated in Figure 3.2. The equation for the straight-line envelope is known as Coulomb's equation. The terms c and ϕ are known as apparent cohesion and angle of internal friction respectively; both are material constants determined experimentally.

$$|\tau| = f(\sigma) = c - \sigma \tan\phi \qquad [3.9]$$

The failure criterion associate with Equation 3.9 is referred to the Mohr-Coulomb criterion in soil mechanics and for $\sigma_1 \le \sigma_2 \le \sigma_3$ the Mohr-Coulomb criterion can be written as

$$\frac{1}{2}(\sigma_1 - \sigma_3)\cos\phi = -c + \left[\frac{1}{2}(\sigma_1 + \sigma_3) - \frac{\sigma_1 - \sigma_3}{2}\sin\phi\right]\tan\phi \qquad [3.10]$$

or rearranging

$$\sigma_1 - \sigma_3 \frac{1+\sin\phi}{1-\sin\phi} = -2c\frac{\cos\phi}{1-\sin\phi} \qquad [3.11]$$

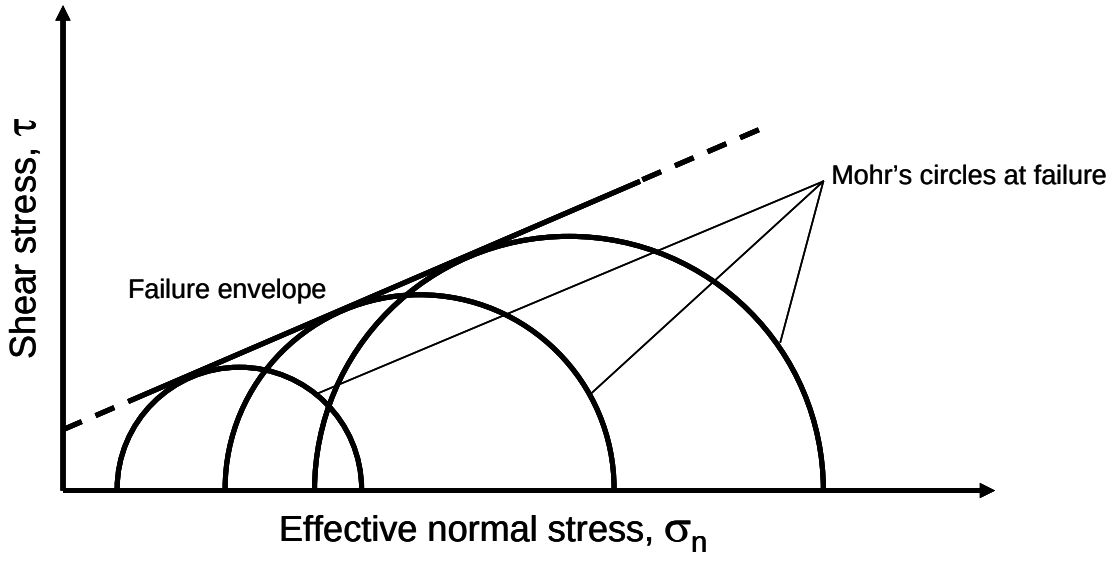

Figure 3.1: Mohr's circle failure envelope

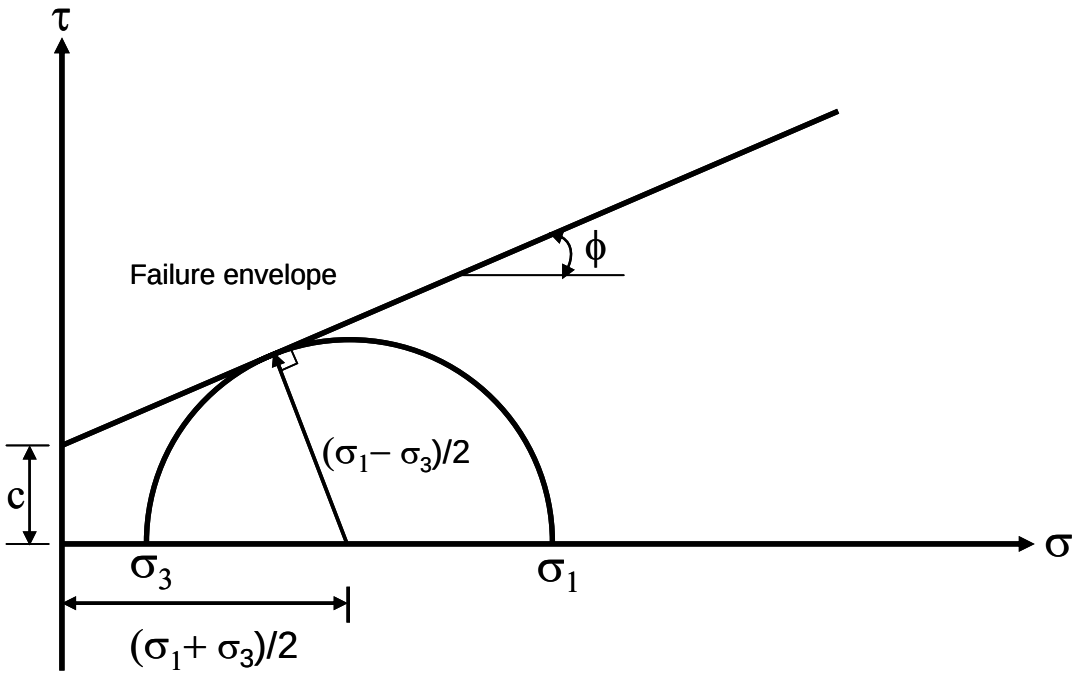

Figure 3.2: Simplified Mohr Envelop for $f(\sigma)$

If N_ϕ is defined as:

$$N_\phi = \frac{1+\sin\phi}{1-\sin\phi} \qquad [3.12]$$

Equation 3.11 can now be reduced to

$$\sigma_1 - \sigma_3 N_\phi = -2c\sqrt{N_\phi} \qquad \text{for } \sigma_1 \le \sigma_2 \le \sigma_3 \qquad [3.13]$$

The intermediate principal stress σ_2 has no influence of the failure. To demonstrate the shape of the three-dimensional failure surface of the Mohr-Coulomb criterion, Equation 3.10 will be expressed terms of stress invariants I_1, J_2 and θ as shown in the following Equation

$$\frac{1}{3}I_1\sin\phi + \sqrt{J}\sin\left(\theta + \frac{1}{3}\pi\right) + \frac{\sqrt{J_2}}{\sqrt{3}}\cos\left(\theta + \frac{\pi}{3}\right)\sin\phi - c\cos\phi = 0 \qquad [3.14]$$

where the angle of similarity θ is defined as

$$\cos 3\theta = \frac{3\sqrt{3}}{2}\frac{J_3}{J_2^{3/2}} = \frac{\sqrt{2}J_3}{\tau_{oct}^3}$$

$$J_2 = \frac{1}{3}(I_1^2 - 3I_2)$$

$$J_3 = \frac{1}{27}(2I_1^3 - 9I_1I_2 + 27I_3)$$

$$I_1 = \sigma_1 + \sigma_2 + \sigma_3$$

$$I_2 = \sigma_1\sigma_2 + \sigma_2\sigma_3 + \sigma_3\sigma_1$$

$$I_3 = \sigma_1\sigma_2\sigma_3$$

$$\tau_{oct} = \sqrt{\tfrac{2}{3}J_2}$$

Shield (1955) has shown that, the Mohr-Coulomb failure criterion as described by Equation 3.14 is an irregular hexagonal pyramid in the principal stress $(\sigma_1, \sigma_2, \sigma_3)$ space, Figure 3.3a. Its meridians are straight lines and its failure cross section in the $\pi-$plane $(\sigma_1 + \sigma_2 + \sigma_3 = 0)$ is an irregular hexagon as shown in Figure 3.3b. Cowan (1953) suggested combining the Mohr-Coulomb criterion with a maximum tensile strength cutoff to obtain a better approximation when tensile stresses occur. The tensile strength of the material cannot exceed

the value σ_3 which corresponds to the intersection of the straight lines $f = 0$ and $\sigma_1 = \sigma_3$ in the $f(\sigma_1, \sigma_3)$ plane as shown in Figure 3.4 for $\sigma_1 \le \sigma_2 \le \sigma_3$.

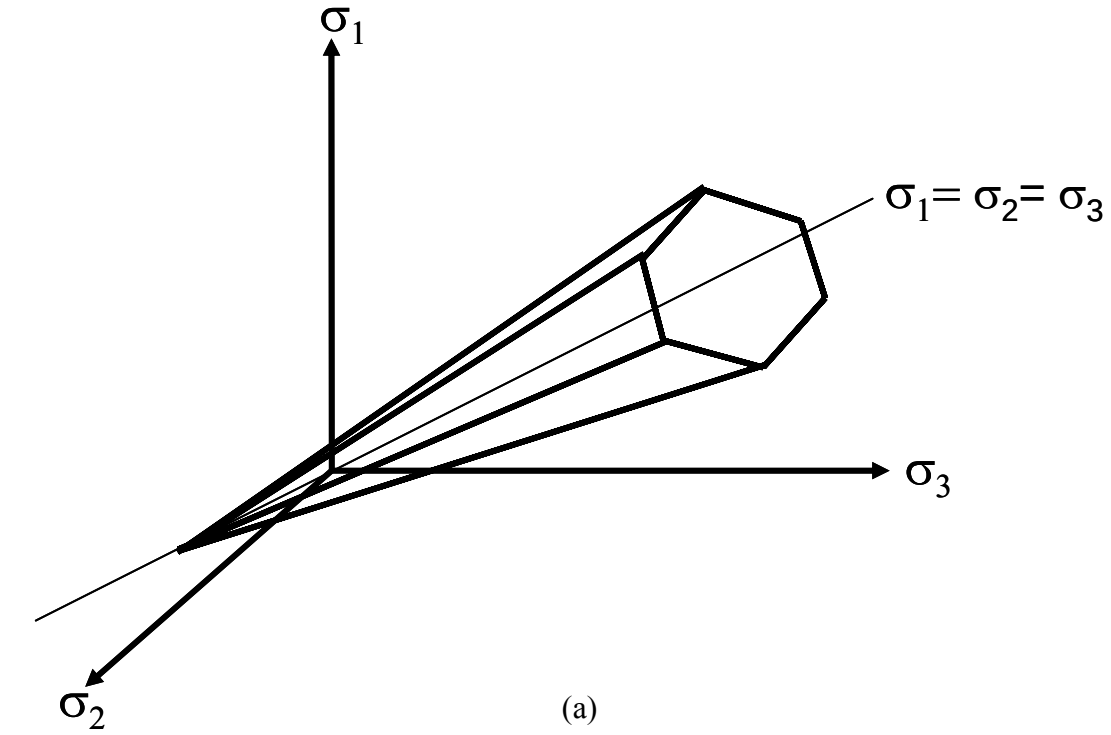

(a)

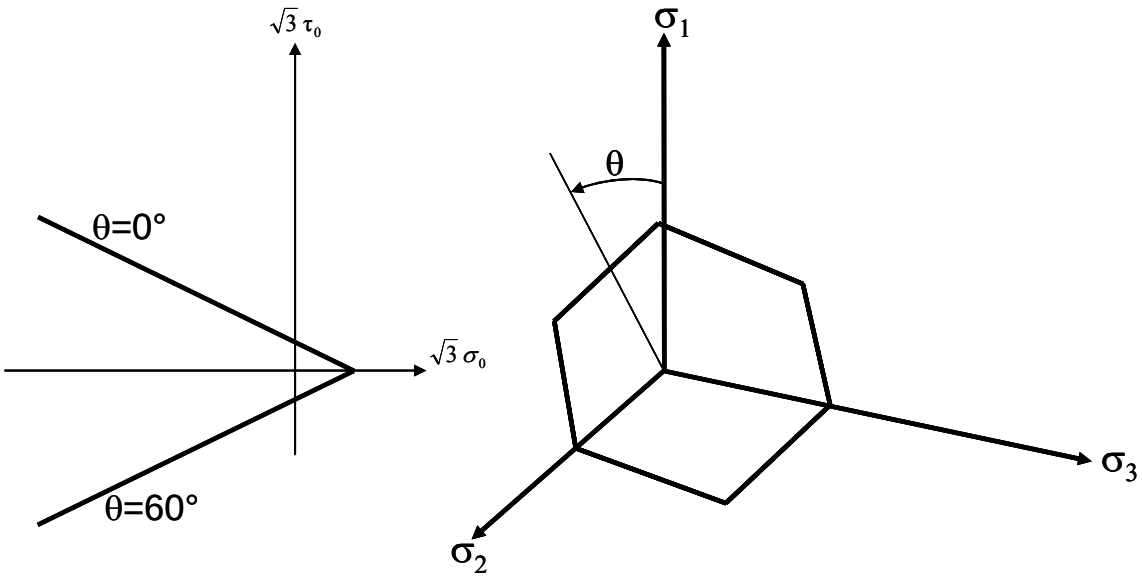

(b)

Figure 3.3: Mohr-Coulomb yield surface in principal stress space

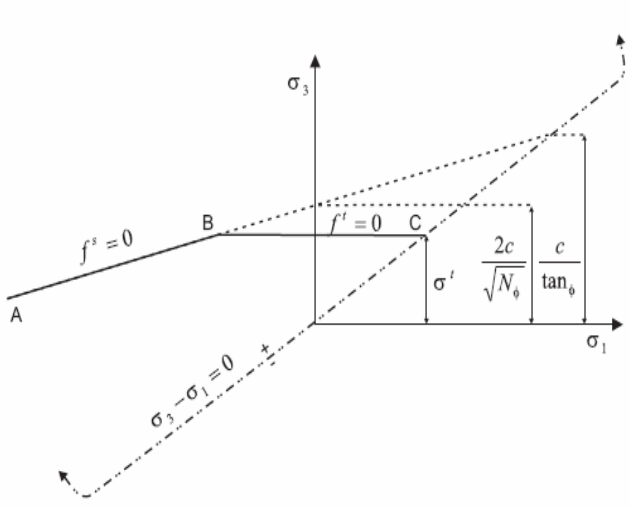

Figure 3.4: *FLAC*^{3D} Mohr-Coulomb failure criterion with tensile cutoff
(Itasca, 2002)

The Mohr-Coulomb criterion is simple and its validity is well established for many soils (Lade, 2005). However, the hexagonal failure surface is mathematically convenient in three-dimensional application only in problems where it is obvious which one of the six sides is to be used (Chen and Hen, 1988). If this information is not known, the corners/edges of the hexagon can cause considerable difficulty and give rise to complication (singularity) in obtaining numerical solution. In addition, the failure criterion neglects the effect of the intermediate principal stress. Nevertheless, for most part, the Mohr-Coulomb criterion has in the past been used to obtain reasonable solutions to important and practical problems in geotechnical engineering (Chen and Mizuno, 1990). Problem resulting from singularity at the corners are handled appropriately in Flac^{3D} formulation and will be explained in the next Chapter.

3.2.3 Mohr-Coulomb perfectly plastic model non-associated flow rule

In contrast with elasticity theory, where a one-to-one correspondence exists between the total stresses and the total elastic strains, such a unique relation does not exist between the plastic strains and the stresses. Instead, the plastic strains are assumed to be derived from the plastic

potential function $g(\sigma_{ij}) = constant$ according to Equation 3.6. Radenkovic (1961) proposed the following definition for plastic potential function g suitable for granular material:

$$\frac{1}{2}(\sigma_3 - \sigma_1) + \frac{1}{2}(\sigma_1 + \sigma_3)\sin\psi = constant \qquad \sigma_1 \le \sigma_2 \le \sigma_3 \qquad [3.15]$$

or rearranging

$$\sigma_1 - \sigma_3 \frac{1+\sin\psi}{1-\sin\psi} = constant \qquad [3.16]$$

If N_ψ is defined as:

$$N_\psi = \frac{1+\sin\psi}{1-\sin\psi} \qquad [3.17]$$

Then, Equation 3.16 can now be reduced to

$$\sigma_1 - \sigma_3 N_\psi = constant \qquad \text{for } \sigma_1 \le \sigma_2 \le \sigma_3 \qquad [3.18]$$

where ψ is the dilation angle. This plastic potential resembles the Mohr-Coulomb yield function f defined in Equation 3.13, the only difference being that the angle of internal friction ϕ in f is replaced by the dilatancy angle ψ. Equation 3.18 suggests that the intermediate principal stress σ_2 does not influence the condition for yielding; consequently, the flow rule predicts that there is no plastic straining in the direction of the intermediate principal stress.

3.3 The Hyperbolic Stress-Strain Relationship

Several advanced soil models based on hypoelasticity, hyperelasticity, plasticity and hypoplasticity have been proposed for the simulation of non-linear stress-strain behavior of soils (Lade, 2005; Kolymbas, 1991; and Desai and Siriwardane, 1984). However, the practical usefulness of these models is limited because they require determination of several complicated material constants that are not obtainable from conventional geotechnical laboratory tests.

Chen and Saleeb (1991) described the hyperbolic model presented herein as the simplest class of hypoelastic models. The incremental stress-strain relations are formulated directly as a simple extension of the isotropic linear elastic model with the elastic constants replaced by variable tangential moduli which are taken to be functions of the stress and/or strain invariants. The hyperbolic model is very attractive from both computational and practical view points. The material parameters involved in the models can be easily determined from standard laboratory tests using well defined procedures; and many of these parameters have broad data base. Also, the hyperbolic stress-strain relationships have been used in the analyses of a number of different types of static and quasi-static soil mechanics problem. The hyperbolic model is described in details in this section.

3.3.1 Tangential Young's Modulus

Ohde (1939) suggested that soil stiffness can be formulated as a stress-dependent parameter using power law while Kondner (1963) proposed the use of hyperbolae to represent the stress-strain behavior of cohesive and cohesionless soils. The hyperbolic model developed by Duncan and Chang (1970) was based on these two primary ideas from Ohde (1939) and Konder (1963). Figure 3.5 shows the proposed hyperbolas Duncan and Chang (1970) by which is represented mathematically with equation of the form

$$\sigma_1 - \sigma_3 = \frac{\varepsilon}{\frac{1}{\mathrm{E}_i} + \frac{\varepsilon}{(\sigma_1 - \sigma_3)_{ult}}} \qquad [3.19]$$

The parameters of the hyperbolic equation have physical significance. E_i is the initial tangent modulus or the initial slope of the stress-strain curve and $(\sigma_1 - \sigma_3)_{ult}$ is the asymptotic value of the deviator stress which is related closely to the strength of the soil. The values of E_i and $(\sigma_1 - \sigma_3)_{ult}$ for a given stress-strain curve can be determined easily. If the hyperbolic equation is transformed as shown in Figure 3.6, it represent a linear relationship between $\varepsilon/(\sigma_1 - \sigma_3)$ and ε. The values of $\varepsilon/(\sigma_1 - \sigma_3)$ is calculated from test data and are plotted against ε to determine the best-fit hyperbola for the stress-strain curve.

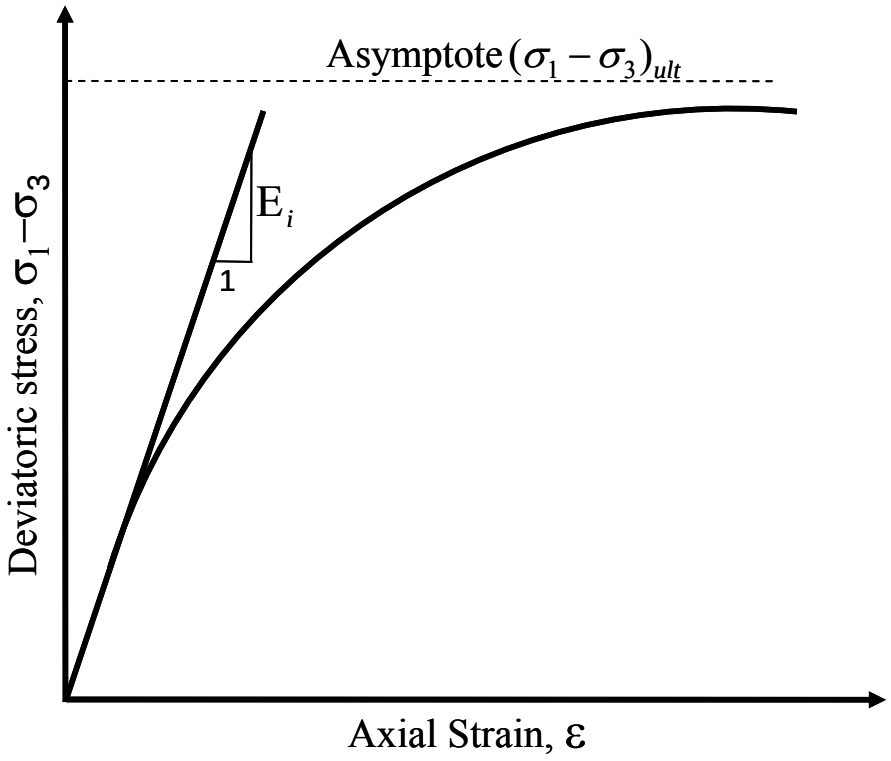

Figure 3.5: Hyperbolic representation of a stress strain curve by Duncan and Chang (1970)

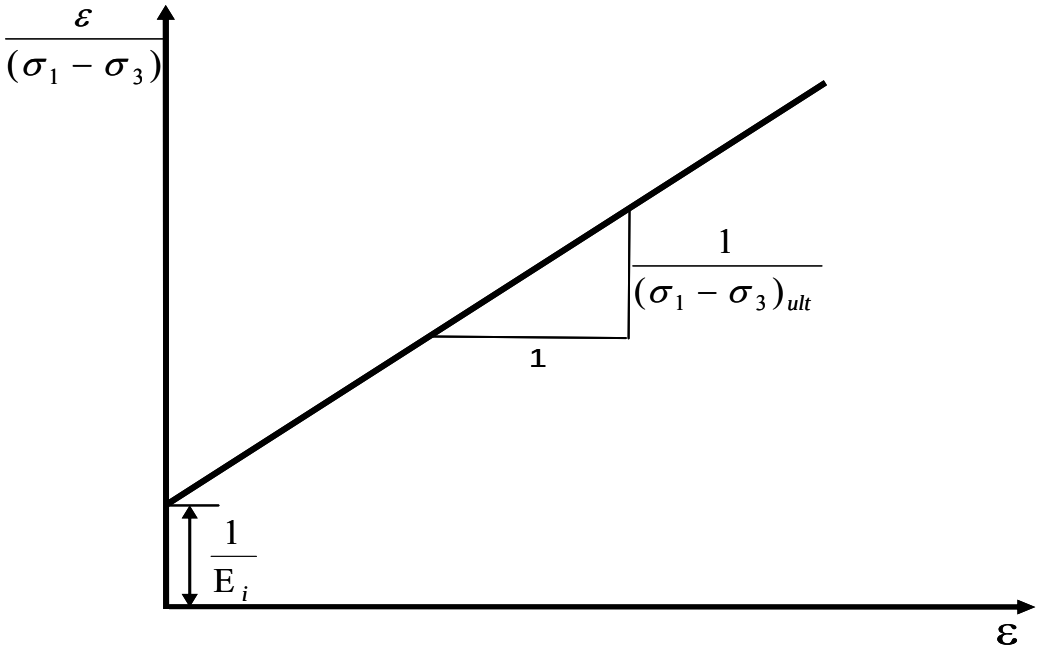

Figure 3.6: Transformed stress-strain curve for determining hyperbolic stress strain curve

For all soils except fully saturated soils tested under consolidated-undrained conditions, an increase in confining pressure will result in a steeper stress-strain curve and a higher strength,

and the values of E_i and $(\sigma_1 - \sigma_3)_{ult}$ therefore increases with increasing confining stress. This stress dependency is taken into consideration in the hyperbolic formulation by using the empirical correlation suggested by Janbu (1963) to represent the variation of E_i and $(\sigma_1 - \sigma_3)_{ult}$ with confining stress. The variation of E_i and confining stress (σ_3) is represented by the following equation

$$E_i = KP_a\left(\frac{\sigma_3}{P_a}\right)^n \qquad [3.20]$$

The parameter K is the modulus number, and n is the modulus exponent that determines the rate of variation of E_i with σ_3. Both K and n are dimensionless numbers that can be obtained from logarithmic plot of E_i/P_a and σ_3/P_a. P_a is atmospheric pressure expressed in the same unit as E_i.

The value of $(\sigma_1 - \sigma_3)_{ult}$ is often slightly greater than the compressive strength of soil (Duncan et al, 1980). This would be expected, because the hyperbola remains below the asymptote at all finite values of strain. The ultimate deviatoric stress, $(\sigma_1 - \sigma_3)_{ult}$ may be related to the compressive strength, $(\sigma_1 - \sigma_3)_f$ by means of a factor R_f termed as the failure ratio as shown by

$$(\sigma_1 - \sigma_3)_f = R_f(\sigma_1 - \sigma_3)_{ult} \qquad [3.21]$$

The variation of $(\sigma_1 - \sigma_3)_{ult}$ with σ_3 is accounted for by using Mohr-Coulomb failure criterion shown in Equation 3.22

$$(\sigma_1 - \sigma_3)_f = \frac{2c\cos\phi + 2\sigma_3\sin\phi}{1 - \sin\phi} \qquad [3.22]$$

in which c is the cohesion and ϕ is the angle of internal friction. The actual failure envelope is often curved, hence ϕ may also be varied with σ_3 as follows:

$$\phi = \phi_o - \Delta\phi \log \sigma_3 / P_a \qquad [3.23]$$

where ϕ_o is the value of ϕ for $\sigma_3 = P_a$, and $\Delta\phi_o$ is the reduction in ϕ for a tenfold increase in σ_3.

The instantaneous slope of the stress-strain curve is the tangent Young's modulus, E_t can be obtained by differentiating Equation 3.19 with respect ε and substituting Equations 3.20, 3.21, and 3.22 into the resulting expression for E_t. The resulting equation for E_t is

$$E_t = [1 - R_f S_L]^2 E_i \qquad [3.24]$$

where $S_L = \dfrac{(\sigma_1 - \sigma_3)}{(\sigma_1 - \sigma_3)_f}$ is the stress level, or fraction of strength mobilized.

Equation 3.24 can be employed very conveniently in the incremental stress analyses, and constitutes the essential component of the hyperbolic model. Because the tangent modulus is expressed in terms of stress only, it may be employed for analyses of problem involving any arbitrary initial stress condition without any additional complications.

3.3.2 Bulk Modulus

Isotropic materials require at least two elastic material properties to develop a complete stiffness relation and define the stress-strain behavior of an isotropic elastic material. Duncan et al (1980) proposed the use of Bulk modulus, K, which varies with confining stress, σ_3 according to the following expression:

$$K = K_b P_a \left(\frac{\sigma_3}{P_a} \right)^m \qquad [3.25]$$

in which K_b is the bulk modulus number and m is the bulk modulus exponent.

Selig (1988) proposed an alternative and more direct method for obtaining K from hydrostatic compression test as illustrated in Figure 3.7. Selig observed that the curve relating hydrostatic confining stress, σ_m, and the volumetric strain, ε_{vol}, can be reasonably represented by the hyperbolic equation

$$\sigma_m = \frac{K_i \varepsilon_{vol}}{1 - (\varepsilon_{vol} / \varepsilon_u)} \qquad [3.26]$$

where K_i is the initial tangent bulk modulus, and ε_u is the ultimate volumetric strain at large stress. The tangent bulk modulus K_t is determined by differentiating Equation 3.26 and substituting ε_{vol} also from Equation 3.26 into the resulting equation. The result is Selig's bulk modulus expression:

$$K_t = K_i [1 + \sigma_m / B_i \varepsilon_u]^2 \qquad [3.27]$$

To determine the parameters K_i and ε_u, the hydrostatic test data are plotted in a linearized hyperbolic form. Lin (1987) and Yang (1987) have demonstrated that the hyperbolic formulation for tangent bulk modulus represent soil behavior in a hydrostatic compression test better than the formulation proposed by Duncan et al (1980).

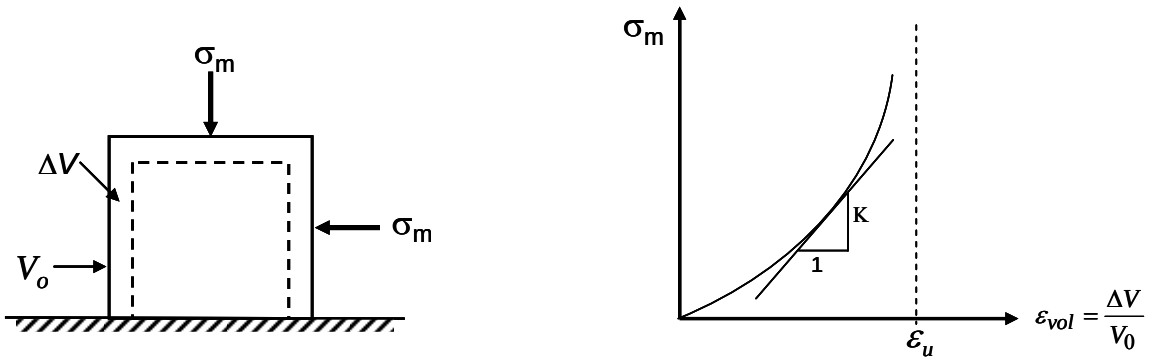

Figure 3.7: Determination of bulk modulus from hydrostatic compression test (after Selig, 1988)

3.3.3 Unloading and Reloading Conditions

In a triaxial test, soil exhibits stiffer behavior when the axial load is being reduced from its highest previous value (i.e. unloading: when the stress level is less than the maximum previous value) than when the axial load is being increased above its highest previous value (primary loading), as shown in Figure 3.8. This phenomenon is simulated in the hyperbolic model by using a higher value of tangent Young's modulus for unloading or reloading conditions than for primary loading conditions.

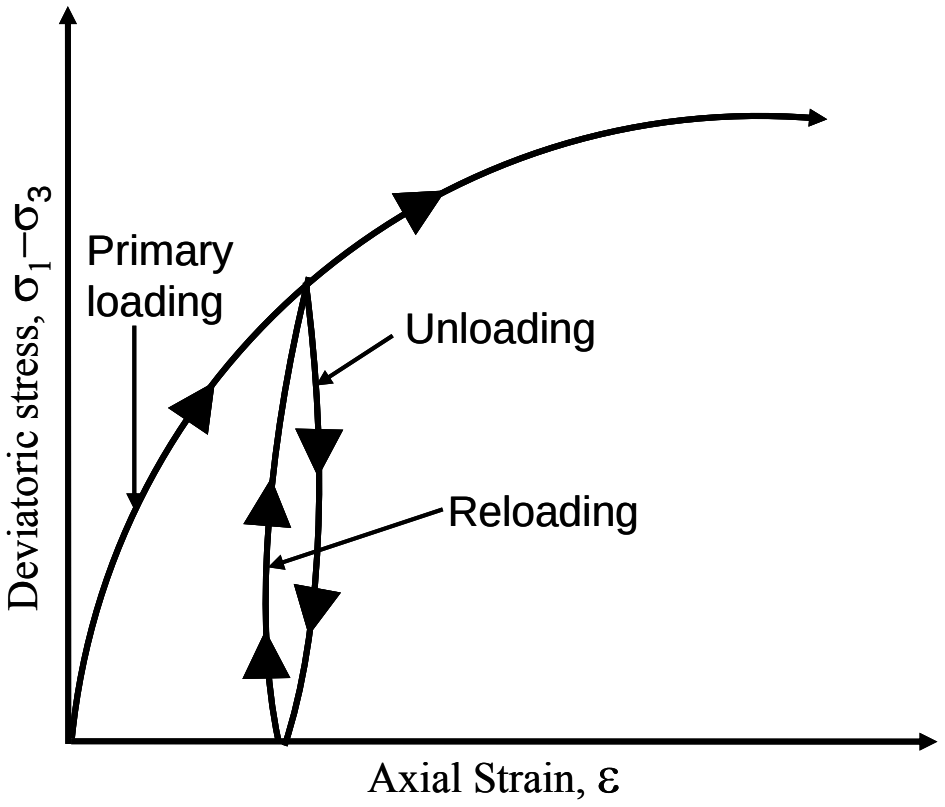

Figure 3.8: Approximate representation of Loading-Unloading in triaxial testing

This higher value is referred to as the "unloading-reload Young's modulus" and is represented by the E_{ur}. The value of E_{ur} is related to the confining pressure by the following Equation:

$$E_{ur} = K_{ur} P_a \left(\frac{\sigma_3}{P_a} \right)^n \quad [3.28]$$

where K_{ur} is the unload-reload modulus and the other parameters are has previous defined. The value of K_{ur} is always larger than the value of K for primary loading (Chen and Mizuno, 1990). K_{ur} may be 20% greater than K for dense sands; and for soft soils like loose sands, K_{ur} may be three times as large as K (Boscardin, et al 1990). On subsequent reloading there is always some hysteresis, but it is usually reasonable accurate to approximate the behavior during unloading-reloading stress changes as linear and elastic, i.e. ignoring any hysteresis effect.

The state of stress possible in a 3-D numerical simulation are more complex than those of a triaxial test and a more complex criterion for the unload-reload stress state is required. Duncan et al (1984), defined unload-reload condition using dimensionless quantity called the "stress state". The stress state S_S was defined by:

$$S_S = S_L \sqrt[4]{\frac{\sigma_3}{P_a}} \quad [3.29]$$

Filz et al (1990) modified the definition of the stress state to account for soils with a cohesion intercept in the strength envelope:

$$S_S = S_L \sqrt[4]{\frac{\sigma_3 + \frac{c}{\tan\phi}}{P_a}} \quad [3.30]$$

A state of stress is defined as being unload-reload if the stress state S_S is less than the maximum previous state of stress, $S_{S(\max past)}$.

3.4 Proposed Non-linear Elastic-Plastic Mohr-Coulomb Model

The Mohr-Coulomb model has been traditionally used as a linear elastic-plastic model; the non-linear elastic behaviour of soil can be captured with the Mohr-Coulomb model by varying the elastic moduli. Hyperbolic relationships proposed by Duncan and Chang (1970) provide a practical and convenient formulation for modeling non-linear and stress-dependent behavior of soils. They suggested equations that account for the influence confining stress on soil stiffness.

In the proposed stress-strain model, the conventional Mohr-Coulomb linear elastic-plastic model was modified to include non-linear soil's behavior and dependence of stiffness on confining stress. The constant elastic moduli that have been traditionally used in the Mohr-Coulomb linear elastic-plastic model were replaced with stress-dependent moduli based on Duncan and Chang (1970) hyperbolic relations. Although, the original Mohr-Coulomb model is capable of capturing soils behaviour at failure and it has been successfully used to calculate stability limits states for many geotechnical problems, its gives poor results when used to simulate soil behavior in the elastic range i.e. at working load before failure (Chen and Saleeb, 1991). On the other hand, hyperbolic model have been shown to capture granular material behavior under working load (Duncan and Chang, 1970). This important modification to the conventional Mohr-Coulomb model ensures that soil behavior is simulated more accurately both in the elastic, as well as, the plastic range.

When the stress level is below unity, or equivalently, when the value of the Mohr-Coulomb yield function $f < 0$, the stress-strain relationship is determined by using the elastic hyperbolic relations. When the stress level is equal to unity i.e. the Mohr-Coulomb yield function $f = 0$, the plasticity model is used to determine the stress-strain relationship. Detailed description of the proposed model and its implementation in *FLAC*^{3D} software are presented in Chapter 4.

3.5 Summary

A modification to the conventional Mohr-Coulomb linear elastic-plastic model has been presented in this Chapter. The proposed constitutive model is a hybrid of the traditional Duncan-Chang hyperbolic model and Mohr-Coulomb perfectly plastic model. The modified model combines the good aspect of both models by using the hyperbolic stress-strain relationship to model the soil's behavior before failure, and the conventional Mohr-Coulomb plastic model to determine the behaviour at and after failure. The model is based on elastic-plastic theory and it addresses most of the characteristics of granular material behavior relevant to ground movements around excavation and pressurized bore including non-linearity, stress dependency of the stress-strain relationship and path dependence.

The elastic response is assumed to be incremental linear, isotropic and specified by Hooke's law. The tangential elastic moduli are considered stress level dependent and hence the total elastic response is non-linear. The plastic shear mechanism assumes: (i) the ultimate strength and state of stress is limited by the Mohr-Coulomb failure criterion; (ii) a non-associative flow rule for shear failure and (iii) an associated rule for tensile failure.

The parameters required for the proposed model can be easily determined from standard soil tests. Furthermore, the wide data base available for the parameters is useful in assessing the reliability of the values determined from laboratory tests, or in estimating reasonable values for the soils involved in a particular problem where sufficient data is not available.

The major deviations of the model from observed soil behavior are: (i) the shape of the failure surface given by Mohr-Coulomb criterion, which is not curved and the neglects of the effect of the intermediate principal stress; (ii) the inability to capture volume change during pure shearing.

In the following chapter, the numerical analysis procedure used to solve the stress-deformation problems (i.e. equilibrium, compatibility and boundary conditions for the proposed stress-strain relationship, as well as the numerical implementation will be discussed.

Chapter 4: Numerical Analysis Procedure

4.1 Introduction

The numerical analyses described in this thesis were implemented using *FLAC^{3D} –Fast Lagrangian Analysis of Continua in 3 Dimensions*, version 3.0 computer code. *FLAC^{3D}* is based on the finite difference method, which is perhaps the oldest numerical technique used for the solution of sets of differential equations, given initial values and/or boundary values (Desai and Christian 1977). In the finite difference method, every derivative in the set of governing equations is replaced directly by an algebraic expression written in terms of the field variables (e.g., stress or displacement) at discrete points in space; these variables are undefined within elements. In contrast, the finite element method has a central requirement that the field quantities (stress, displacement) vary throughout each element in a prescribed fashion, using specific functions controlled by parameters. The formulation involves the adjustment of these parameters to minimize error terms or energy terms.

Similar to finite elements methods, *FLAC^{3D}* translate a set of differential equations into matrix equations for each element, relating forces at nodes to displacements at nodes; although these sets of equations are derived by the finite difference method, the resulting element matrices, for an elastic material, are identical to those of the finite element method (for constant-strain tetrahedra). It is pointless, then, to argue about the relative merits of finite elements or finite differences as the resulting equations are the same. The *"mixed discretization"* scheme used in *FLAC^{3D}* provides for accurate modeling of plastic collapse loads and plastic flow. This scheme is believed to be physically more justifiable than the *"reduced integration"* scheme commonly used with finite elements (Marti and Cundall 1982).

The full dynamic equations of motion used in *FLAC*^{3D} also has the advantage of achieving a numerically stable solution even when the problem is not statically stable, allowing examination of large strains and displacement prior to failure.

FLAC^{3D} is robust in the sense that it can handle any constitutive model with no adjustment to the solution algorithm. It is this attribute that makes implementation of the proposed constitutive model possible. The constitutive model proposed in the previous chapter were implemented in *FLAC*^{3D} and used in the analyses that will be presented in the subsequent Chapters of this thesis.

4.2 *FLAC*^{3D} Numerical Formulation

Once the grid is generated and the boundary conditions are set, the model is solved. The method of solution in *FLAC*^{3D} is characterized by the following three approaches:

(a) Finite difference approach in which first-order space and time derivatives of a variable are approximated by finite differences, assuming linear variations of the variable over finite space and time intervals, respectively.

(b) Discrete-model approach involves replacing the continuous medium by a discrete equivalent i.e. one in which all forces involved (applied and interactive) are concentrated at the nodes of a three-dimensional mesh used in the medium representation.

(c) Dynamic-solution approach. The inertial terms in the equations of motion are used as numerical means to reach the equilibrium state of the system under consideration.

The laws of motion for the continuum are, by means of these approaches, transformed into discrete forms of Newton's law at the nodes. The resulting system of ordinary differential equations is then solved numerically using an explicit finite difference approach in time. The spatial derivatives involved in the derivation of the equivalent medium are those appearing in the definition of strain rates in term of velocities. For the purpose of defining velocity variations and corresponding space intervals, the medium is discretized into constant strain-rate elements of tetrahedral shape whose vertices are the nodes of the mesh mentioned above. Figure 4.1 illustrates a tetrahedron.

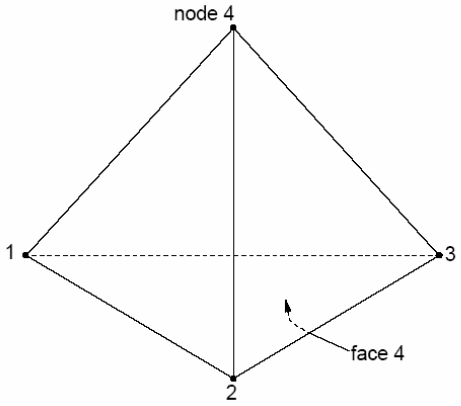

Figure 4.1: Tetrahedron used to discretized *FLAC*^{3D} Model Grid (Itasca, 2005)

The discretization process starts by grouping the continuous models into zones and then discretizing the zones (internally) into tetrahedral. Figure 4.2 illustrates how an eight-noded zone can be broken up into two (and only two) configuration of five tetrahedral.

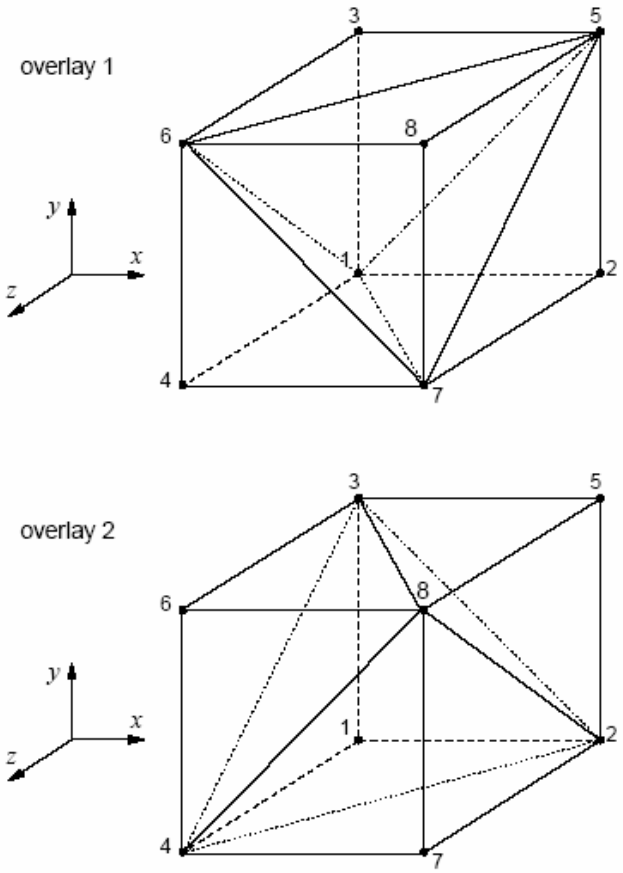

Figure 4.2: An 8-node zone with 2 overlays of 5 tetrahedra in each overlay (Itasca, 2005)

The advantage of having the two overlays is that nodal forces calculations are evaluated by averaging over the two overlays, which produces a *mixed discretization* process that ensures symmetric zones response for symmetric loading. *FLAC*^{3D} uses an explicit *"time-marching"* finite difference solution scheme. For every time step, the calculation sequence can be summarized as follows:

(a) New strain rates are derived from nodal velocities.
(b) Constitutive equations are used to calculate new stresses from the strain rates and stresses at the previous time.
(c) The equations of motion are invoked to derive new nodal velocities and displacements from stresses and forces.

This general calculation sequence is illustrated in Figure 4.3. The sequence is repeated at every time step, and the maximum *out-of-balance force* in the model is monitored. This force would either approach zero (indicating that the system is reaching an equilibrium state) or it would approach a constant (non-zero value, indicating that a portion or all of the system is at steady-state/plastic flow). The calculation may be interrupted at any point in order to analyze the solution.

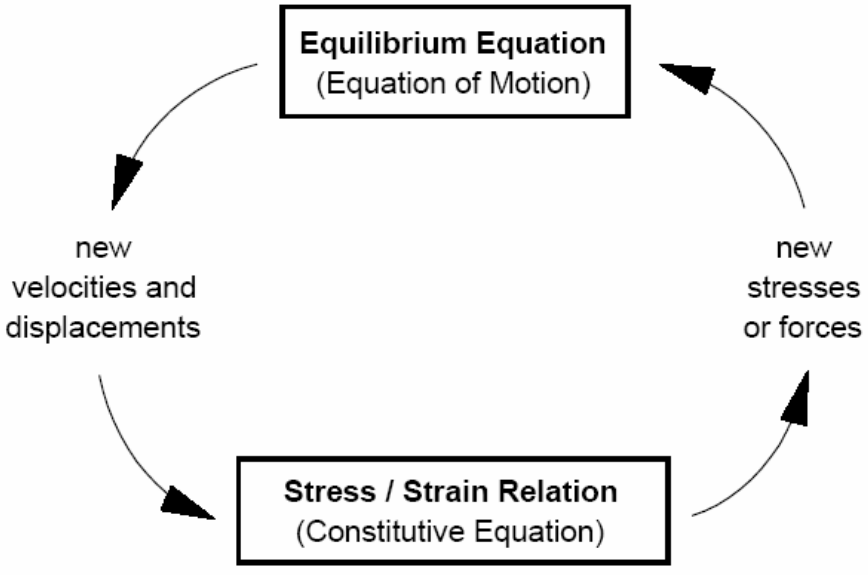

Figure 4.3: Basic explicit calculation cycle
(Itasca, 2005)

The formulation can be used in two strain modes: *"Eulerian"* termed small strain, or *"Lagrangian"* termed large-strain. In the small strain mode, movement and deformation are relative to a fixed coordinate, the coordinates are not updated and stress rotation corrections are not taken into consideration. In contrast, when in large-strain mode, the modal coordinate of the elements are updated at each time step by simply adding the incremental displacement. Hence, the grid moves and deforms with the material it represents.

4.2.1 Strain Rate Calculation

Starting from a known velocity field, the components of the strain rate tensor (ξ_{ij}) are computed for each tetrahedron in a zone, using the finite difference formulation in Equation 4.1, obtained by the application of Gauss divergence theorem.

$$\xi_{ij} = -\frac{1}{6V}\sum_{l=1}^{4}(\upsilon_i^l n_j^{(l)} + \upsilon_j^l n_i^{(l)})S^{(l)} \qquad [4.1]$$

where V and S are the volume and surface area of the tetrahedron respectively; $[n]$ is the exterior unit vector normal to the surface; υ is the velocity vector and the superscript l relates to the value at node l.

A procedure of mixed discretization is then applied and new diagonal strain-rate tensor components are calculated. The principle of mixed discretization technique is to give the element more volumetric flexibility by proper adjustment of the first invariants of the tetrahedral strain-rate tensor. In the approach, a coarser discretization in zones is superposed to the tetrahedral discretization, and the first strain rate invariant of a particular tetrahedron in a zone is evaluated as the volumetric-average value over all tetrahedra in the zone. The invariant gives a measure of the rate of dilation of the constant strain-rate tetrahedron.
For a particular tetrahedron, now locally labeled l in the zone

$$\xi_{ij}^l = \eta_{ij}^l + \frac{\xi^z}{3}\delta_{ij} \qquad [4.2]$$

where η^l is the deviatoric strain-rate tensor, and ξ^z, the average value for the zone of the first strain-rate invariant, is calculated from

$$\zeta^z = \frac{\sum_{k=1}^{n_t} \xi^{[k]} V^{[k]}}{\sum_{k=1}^{n_t} V^{[k]}} \qquad [4.3]$$

where n_t is the total number of tetrahedra involved in the zone computation, and $V^{[k]}$ is the volume of the tetrahedra k.

4.2.2 Stress Calculation

The constitutive equations are used in their incremental form H_{ij}^* to calculate stress increments for each tetrahedron in a zone:

$$\Delta\sigma_{ij} = \Delta\breve{\sigma}_{ij} + \Delta\sigma_{ij}^C \qquad [4.4]$$

where $\Delta[\breve{\sigma}_{ij}] = H_{ij}^*(\sigma_{ij}, \Delta\varepsilon_{ij})$ is the co-rotational stress increment in which H_{ij}^* is a given function; and $\Delta\varepsilon_{ij} = \xi_{ij}\Delta t$. The stress correction $\Delta\sigma_{ij}^C$ is not taken into consideration in small strain mode. In large strain mode, its value is given by:

$$\Delta\sigma_{ij}^C = (\omega_{ik}\sigma_{kj} - \sigma_{ik}\omega_{kj})\Delta t \qquad [4.5]$$

where $\omega_{ij} = -\frac{1}{6V}\sum_{l=1}^{4}(\upsilon_i^l n_j^{(l)} + \upsilon_j^l n_i^{(l)})S^{(l)}$ is the rate of rotation tensor.

For consistence, the technique of discretization is also applied to the stress tensor. The first invariant of the stress tensor, derived after application of the strain-rate increment, is evaluated as a volumetric average for the zone. In this process, the stress tensor of a particular tetrahedron l in a zone is first estimated and decomposed into deviatoric and volumetric parts:

$$\sigma_{ij}^l = s_{ij}^l + \sigma^l\delta_{ij} \qquad [4.6]$$

where $[s]^l$ is the deviatoric stress-rate tensor, and $\sigma^{[l]} = 1/3\sigma_{ii}^{[l]}$ is the mean normal stress. The first invariant for the zone is calculated as the volumetric average value over all tetrahedra in the zone:

$$\sigma^z = \frac{\sum_{k=1}^{n_t} \sigma^{[k]} V^{[k]}}{\sum_{k=1}^{n_t} V^{[k]}} \qquad [4.7]$$

where n_t is the total number of tetrahedra involved in the zone computation, and $V^{[k]}$ is the volume of the tetrahedra k. Finally, the tetrahedron stress-rate tensor components are calculated using:

$$\sigma_{ij}^l = s_{ij}^l + \sigma^z \delta_{ij} \qquad [4.8]$$

4.2.3 Nodal Mass and Out-of-Balance Force Calculation

The tetrahedron contribution m^l to the nodal mass at local node l is evaluated using:

$$m^l = \frac{\alpha_1}{9V} \max\left([n_i^{(l)} S^l]^2, i = 1,3\right) \qquad [4.9]$$

where $\alpha_1 = K + 4/3G$, K is the bulk modulus and G is the shear modulus; V and S are the volume and surface area of the tetrahedron respectively and $[n]$ is the exterior unit vector normal to the surface. The magnitude of the time-step is set equal to unity for this derivation.

The nodal mass $M^{<l>}$ at global node l is computed as the sum of contributions Equation 4.9 at the node of all tetrahedra having that node in common:

$$M^{<l>} = [[m]]^{<l>} \qquad [4.10]$$

In the small-strain mode, the nodal mass calculation is only carried out once before cycling; while it is updated every 10 steps in large-strain mode. The tetrahedron contribution $[p]^l$ to the out-of-balance force at local node l is computed from the stresses and body forces using:

$$p_i^l = \frac{1}{3}\sigma_{ij} n_j^{(l)} S^l + \frac{1}{4}\rho b_i V \qquad [4.11]$$

where ρ is the mass per unit volume, $[b]$ is the body force per unit mass and the other terms are previously defined.

The sum of contributions Equation 4.11 at global node l of all tetrahedra having a node in common is evaluated. Averaging over two overlays is carried out when appropriate, and the contributions $[P]^{<l>}$ of applied loads and concentrated forces are added. Thus providing the expression for the out-of-balance force $[F]^{<l>}$ at global node l as:

$$[F]^{<l>} = [[p_i]]^{<l>} + P_i^{<l>} \qquad [4.12]$$

The out-of-balance force is monitored to detect whether the system has reached a state of equilibrium or steady flow. The equation of motion must be damped to provide static or quasi-static (non-inertia) solutions. Local nonviscous damping similar to that described in Cundall (1987) is the damping algorithm for static analysis in *FLAC*^{3D}. Damping force $\mathbb{F}$ is expressed in terms of the generalized out-of-balance force $F_i^{<l>}$ and the generalized velocity $\upsilon_i^{<l>}$ and is given by:

$$\mathbb{F}_i^{<l>} = -\alpha \left| F_i^{<l>} \right| sign(\upsilon_{(i)}^{<l>}) \qquad sign(y) = \begin{cases} +1, & if\ y > 0; \\ -1, & if\ y < 0; \\ 0, & if\ y = 0 \end{cases} \qquad [4.13]$$

The damping force is controlled by the damping constant, α, whose default value is 0.8. This form of damping has the following advantages.

(a) Only accelerating motion is damped. Therefore, no erroneous damping forces arise from steady-state motion.

(b) The damping constant, α, is non-dimensional.

(c) Since damping is frequency-independent, regions of the assembly with different natural periods are damped equally, using the same damping constant.

The local nonviscous damping formulation in *FLAC*^{3D} is similar to hysteretic damping, in which the energy loss per cycle is independent of the rate at which the cycle is executed (Cundall, 1987).

4.2.4 Velocity, Displacement and Geometry Update Calculations

New nodal velocities are derived from known out-of-balance forces:

$$\upsilon_i^{<l>}(t+\frac{\Delta t}{2}) = \upsilon_i^{<l>}(t-\frac{\Delta t}{2}) + \frac{\Delta t}{M^{<l>}}(F_i^{<l>} + \mathbb{F}_i^{<l>}) \qquad [4.14]$$

In turn, nodal locations are similarly updated using the central finite difference approximation:

$$x_i^{<l>}(t+\Delta t) = x_i^{<l>}(t) + \Delta t \upsilon_i^{<l>}(t+\frac{\Delta t}{2}) \qquad [4.15]$$

The first-order error term vanishes with the finite difference scheme embodied in Equations 4.14 and 4.15. Nodal displacements are calculated in the code from the relation:

$$u_i^{<l>}(t+\Delta t) = u_i^{<l>}(t) + \Delta t \upsilon_i^{<l>}(t+\frac{\Delta t}{2}) \qquad [4.16]$$

with $u_i^{<l>}(0) = 0$.

4.3 Implementation Constitutive Model in *FLAC*^{3D}

The proposed constitutive model discussed in Chapter 3 was implemented in *FLAC*^{3D}, the incremental stress-strain relations that describe the model were written in C++ and compiled as a DLL file (dynamic link library). The equations that describe the proposed constitutive model are presented in this section. This is followed by the implementation procedure in *FLAC*^{3D}. The same sign convention adopted in *FLAC*^{3D} is used in the implementation of the proposed model. Thus, the three principal stresses are labeled such that $\sigma_1 \le \sigma_2 \le \sigma_3$ and compressive stress are negative.

4.3.1 Incremental Non-linear Elastic Stress-Strain Relationship

In the elastic range, the constitutive model is based on incremental form of Hooke's law which can be expressed in terms of the generalized stress and strain increments as follows:

$$\begin{aligned}
\Delta\sigma_1 &= \alpha_1 \Delta\varepsilon_1^e + \alpha_2(\Delta\varepsilon_2^e + \Delta\varepsilon_3^e) \\
\Delta\sigma_2 &= \alpha_1 \Delta\varepsilon_2^e + \alpha_2(\Delta\varepsilon_1^e + \Delta\varepsilon_3^e) \\
\Delta\sigma_3 &= \alpha_1 \Delta\varepsilon_3^e + \alpha_2(\Delta\varepsilon_1^e + \Delta\varepsilon_2^e)
\end{aligned} \qquad [4.17]$$

where α_1 and α_2 are material constants defined in terms of the elastic moduli. There are two options in the model. In the first one, Poisson's ratio ν is given and assumed to remain constant. Current values of tangent bulk and shear moduli are then evaluated from E_t and ν using the relation:

$$\begin{aligned}
K &= \frac{E_t}{3(1-2\nu)} \\
G &= \frac{E_t}{2(1+\nu)}
\end{aligned} \qquad [4.18]$$

and the material constants α_1 and α_2 are material constants are computed as follows

$$\begin{aligned}
\alpha_1 &= K_t + \frac{4}{3}G \\
\alpha_2 &= K_t - \frac{2}{3}G
\end{aligned} \qquad [4.19]$$

In the second option, the material constants are computed from the tangent bulk modulus K_t whose value varies with confining stress:

$$\alpha_1 = \frac{3K_t}{9K_t - E_t}(3K_t + E_t)$$
$$\alpha_2 = \frac{3K_t}{9K_t - E_t}(3K_t - E_t) \qquad [4.20]$$

Duncan, et al. (1980) placed the following limits on the value of bulk modulus, K_t to ensure that the value of the Poisson's ratio is restricted to between 0 and 0.49:

$$17E_t \geq K_t \geq \frac{E_t}{3} \qquad [4.21]$$

The elastic moduli are stress-dependent and are calculated using the procedure described in Section 4.3. The dependence of these moduli on confining stress produce the non-linearity behavior of soils.

4.3.2 Failure Criteria and Flow Rule

As mentioned previously, the proposed non-linear elastic plastic model yield function is based on Mohr-Coulomb failure criterion with tension cutoff. It is important to provide two separate *yield functions* to define the onset of shear and tensile failure. The initiation of shear failure is indicated by the shear yield function f^s obtained by rearranging Equation 4.13:

$$f^s = \sigma_1 - \sigma_3 N_\phi + 2c\sqrt{N_\phi} \qquad [4.22]$$

The tension failure is indicated by tensile yield function f^t defined by:

$$f^t = \sigma_3 - \sigma^t \qquad [4.23]$$

where the only undefined term σ^t is the tensile strength of the material. The maximum value of σ^t can be shown to be $\sigma^t_{\max} = c/\tan\phi$. These functions specify the limiting stress combination for which plastic flow takes place and they represent a surface in the generalized stress space. All stress points below the surface are characterized by elastic behaviour.

Similarly, the plastic potential function is described by means of two functions, g^s and g^t, which define shear plastic flow and tensile plastic flow respectively. The function g^s corresponds to a non-associated law as described in Section 4.2.3 and has the form:

$$g^s = \sigma_1 + \sigma_3 N_\psi \qquad [4.24]$$

The function g^t corresponds to an associated flow rule obtained in a manner similar to g^s and is written as:

$$g^t = -\sigma_3 \qquad [4.25]$$

The flow rule is given a unique definition by application of the following technique. A function $h(\sigma_1, \sigma_3) = 0$ is defined which is represented by the diagonal between the representation of $f^s = 0$ and $f^t = 0$ in the $\sigma_1 - \sigma_3$ plane as shown in Figure 4.4. The function is selected with its positive and negative domains, as indicated on the Figure, and has the form:

$$h = \sigma_3 - \sigma^t + a^p(\sigma_1 - \sigma^p) \qquad [4.26]$$

where constants a^p and σ^p are defined respectively as $a^p = \sqrt{1 + N_\phi^2} + N_\phi$ and $\sigma^p = \sigma^t N_\phi - 2c\sqrt{N_\phi}$.

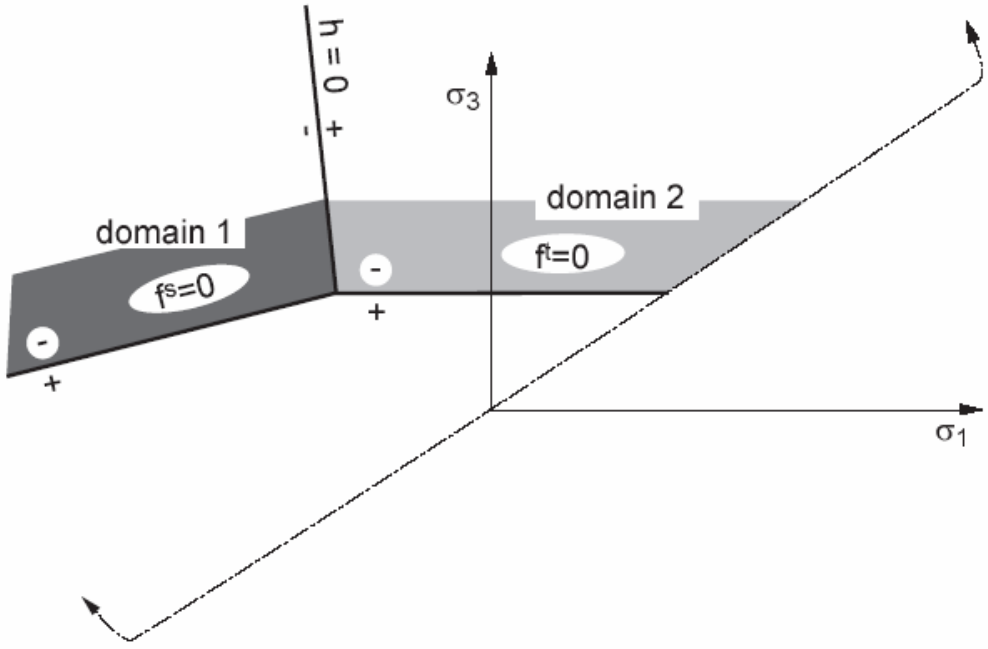

Figure 4.4: Mohr-Coulomb model- domains used in the definition of the flow rule

An elastic guess violating the composite yield function is represented by a point in the $\sigma_1 - \sigma_3$ plane located either in domain 1 or 2 -corresponding to negative or positive domains of h = 0, respectively as shown in Figure 4.4. If the stress point falls within domain 1, shear failure is declared, and the stress point is placed on the curve $f^s = 0$ using a flow rule derived from the potential function g^s. If the point falls within domain 2, tensile failure takes place, and the new stress point conforms to $f^t = 0$ using flow rule derived from g^t. By ordering the stresses such that $\sigma_1 \leq \sigma_2 \leq \sigma_3$, the case of a shear-shear edge is automatically handled by a variation on this technique (Itasca, 2005). The technique, applicable for small-strain increments, is simple to implement. At each step, only one flow rule and corresponding stress correction is involved in case of plastic flow. In particular, when a stress point follows an edge, it receives stress corrections alternating between two criteria. In this process, the two yield criteria are fulfilled to an accuracy that depends on the magnitude of the strain increment.

4.3.3 Numerical Implementation of the Proposed Model

The proposed non-linear elastic plastic constitutive model presented in the previous sections was implemented in *FLAC*^{3D} following the same numerical procedure used for *FLAC*^{3D} built-in models (Itasca, 2005). The constitutive model was written in C++, and compiled as a DLL file (dynamic link library) using Microsoft Visual Studio C++ 2005 (VC++). The source code for the model is provided in Appendix A. Detailed description of the numerical implementation of the proposed constitutive model is presented in this section.

The elastic moduli are stress dependent hence their *"initial"* values are computed during the initialization stage directly from the specified initial stress condition e.g. insitu overburden stresses. This initialization is completed prior the first calculation cycle i.e. cycle 0. The components of the total strain increment represented by vector $\Delta\varepsilon_i$ are considered equal to the sum of the elastic and plastic strain increment components ($\Delta\varepsilon_i = \Delta\varepsilon_i^e + \Delta\varepsilon_i^p$), the stress increment components represented by vector $\Delta\sigma_i$ are given by:

$$\{\Delta\sigma_i\} = [C]\{\Delta\varepsilon_i - \Delta\varepsilon_i^P\} \qquad [4.27]$$

The component of the plastic strain increment, $\Delta\varepsilon_i^P$ is unknown, it value is zero when the yield criteria is not violated i.e. $f < 0$ and deformation is totally elastic. When the yield criteria are violated $f = 0$, plastic flow occurs and $\Delta\varepsilon_i^P$ is determined from plasticity theory as $\Delta\varepsilon_i^P = \lambda \frac{\partial g}{\partial \sigma_i}$. Description of the plasticity theory is presented in Section 4.2.1.

The total strain increments $\Delta\varepsilon_i$ obtained from Equation 4.2 are used in incremental expression of Hooke's law (Equation 4.17) to derive the corresponding stress increments $\Delta\sigma_i^I$ assuming the deformation is totally elastic, i.e.

$$\{\Delta\sigma_i^I\} = [C]\{\Delta\varepsilon_i\} \qquad [4.28]$$

Equation 4.28 is a "guess" of the true value of $\Delta\sigma_i$. This guess will be the correct value only if $\Delta\varepsilon_i^P = 0$. The stress increments $\Delta\sigma_i^I$ are added to the current values of the stresses σ_i^{old}, thus:

$$\sigma_i^I = \sigma_i^{old} + \Delta\sigma_i^I \qquad [4.29]$$

The principal stresses $\sigma_1^I, \sigma_2^I, \sigma_3^I$ and the corresponding directions are then calculated. Stresses obtained at this stage are called the *elastic guesses* since they are derived on assumption that the material response is purely elastic and not elastic-plastic. They are distinguished with the superscript "I".

The elastic guesses are then used to evaluate the shear and tensile yield functions given Equations 4.22 and 4.23. If none of the criteria is violated, it implies that the state of stress lies within or on the boundaries of the elastic region defined by the current positions of the yield loci, and therefore, the response is purely elastic. In this case, the plastic strain increments $\Delta\varepsilon_i^P = 0$, thus $\Delta\sigma_i = \Delta\sigma_i^I$ and the new stresses σ_i^N are equal to the elastic guesses σ_i^I. If the stresses $\sigma_1^I, \sigma_2^I, \sigma_3^I$ violate either of the yield criteria, then the stresses must be corrected using the corresponding flow rule as follows:

$$\{\sigma_i^N\} = \{\sigma_i^I\} - [C]\left\{\lambda \frac{\partial g}{\partial \sigma_i}\right\} \qquad [4.30]$$

The non-zero scalar factor λ is calculated from the consistency condition for perfectly plastic material described in Section 4.2.1. The condition specifies that any state of stress that satisfies any of the yield criteria must lie on the yield surface. Hence σ_i^N must satisfy the yield function i.e. $f(\sigma_i^N) = 0$ during plastic flow. The scalar factor λ can be obtained by solving the systems of equations defined by:

$$f(\sigma_i^N) = f\left(\{\sigma_i^I\} - [C]\left\{\lambda \frac{\partial g}{\partial \sigma_i}\right\}\right) \qquad [4.31]$$

Violation of any of the yield criteria will result in the violations of the composite yield function described by Equation 4.26 such that either $h(\sigma_1^I, \sigma_3^I) \leq 0$ or $h(\sigma_1^I, \sigma_3^I) > 0$. In the first case, shear failure take place, and $\sigma_1^N, \sigma_2^N, \sigma_3^N$ are evaluated using the following equations:

$$\sigma_1^N = \sigma_1^N - \lambda^s(\alpha_1 - \alpha_2 N_\psi)$$

$$\sigma_2^N = \sigma_2^N - \lambda^s \alpha_2 (1 - N_\psi) \qquad [4.32]$$

$$\sigma_3^N = \sigma_3^N - \lambda^s(-\alpha_1 N_\psi + \alpha_2)$$

and

$$\lambda^s = \frac{f^s(\sigma_1^I, \sigma_3^I)}{(\alpha_1 - \alpha_2 N_\psi) + (\alpha_1 N_\psi - \alpha_2) N_\phi} \qquad [4.33]$$

In the second case, tensile failure occurs, and new principal stress components are evaluated from the following Equations:

$$\sigma_1^N = \sigma_1^N - \lambda^t \alpha_2$$

$$\sigma_2^N = \sigma_2^N - \lambda^t \alpha_2 \qquad [4.34]$$

$$\sigma_3^N = \sigma_3^N - \lambda^t \alpha_1$$

and

$$\lambda^t = \frac{\sigma_3^I - \sigma^t}{\alpha_1} \qquad [4.35]$$

The stress tensor components in the system of the reference axes are then calculated from the principal values by assuming that the principal directions have not been affected by the occurrence of a plastic correction. Finally, the elastic moduli are updated based on the new stresses. The numerical implementation procedure of the proposed constitutive model is illustrated in Figure 4.5.

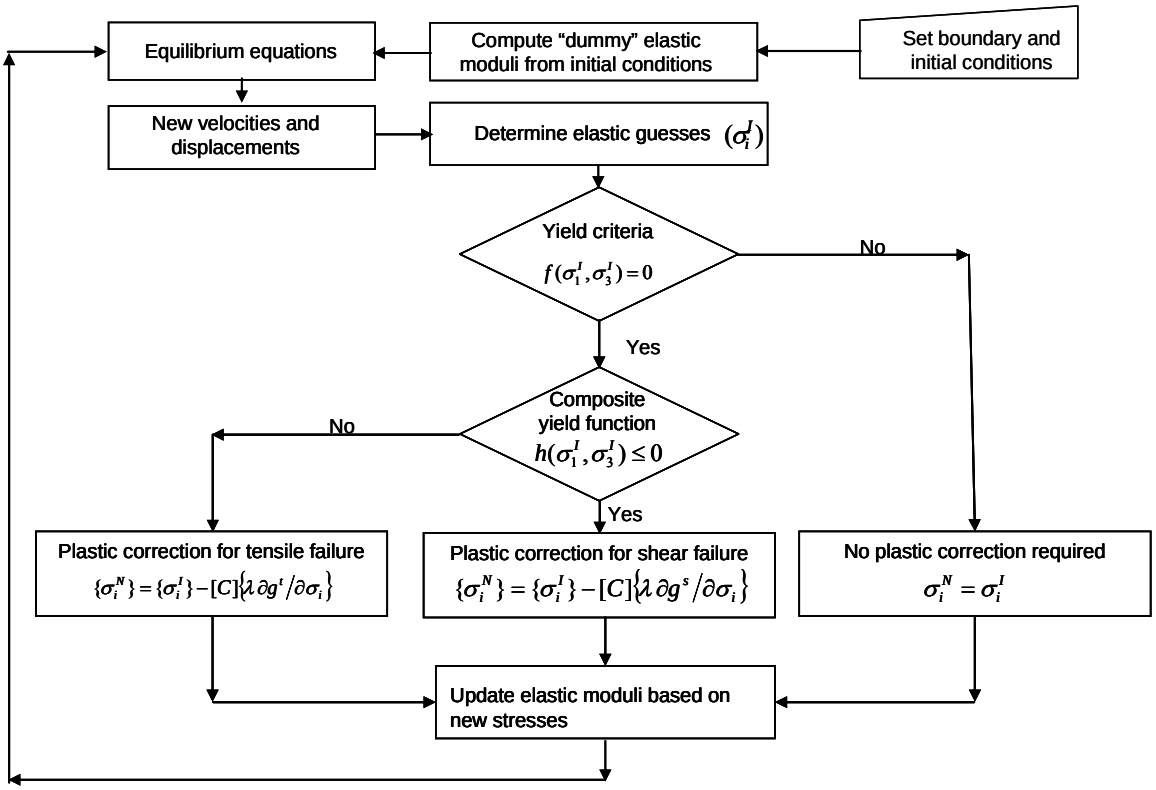

Figure 4.5: Schematic of proposed constitutive model numerical implementation

4.4 Validation of the Proposed Constitutive Model

The proposed constitutive model was validated to ascertain the capability of the model to capture the stress-strain behaviour of granular materials. The following problems were modeled using *FLAC*^{3D} with the proposed constitutive model to complete the model validation:

(a) Drained triaxial compression tests on density sand sample
(b) Rough strip footing on a cohesionless material
(c) Circular flexible pipe buried in silty sand soil

FLAC^{3D} outputs obtained from the analyses of the first two problems were compared with well documented experimental results while the model responses of the third problem was

compared with results obtained from an established finite element program. Detailed analyses of the problems are described in the following sections.

4.4.1 Drained Triaxial Compression Tests on a Density Sand Sample

Gomez et al. (2003) completed series of detailed laboratory tests on *Density Sand* including standard drained triaxial compression (CD) tests. Density sand is fine-to-medium silica sand with subrounded to rounded grains, available commercially for in situ density determinations. A more complete description of the properties of this soil is presented in the reference. Tests were conducted on sand specimens at 41% and 92% relative densities. The confining stress applied to the samples varied between 45kPa and 280kPa. Strength and hyperbolic model parameters were derived from the experiment results.

Model Response and Comparison with Experimental Data

The variations of deviatoric stress $(\sigma_1 - \sigma_3)$ with axial strain obtained from the laboratory tests are shown in Figures 4.6 and 4.7. The axial strains at failure were 4.5 to 5% for the medium dense sand and 2.5 to 3.5 % for the dense sand. The soil parameters determined from the test are presented in Table 4.1. These laboratory triaxial compression tests were modeled with *FLAC*^{3D} using the proposed constitutive model. The numerical tests were completed using one single zone with unit dimensions. The grid is fixed in the vertical direction, and a velocity boundary condition applied at the top of the model; and a constant lateral confining pressure is imposed. Sample of *FLAC*^{3D} input data used for the triaxial compression test simulation is provided in Appendix B.

Figures 4.8 and 4.9 compare *FLAC*^{3D}*'s* computed and experimentally determined stress-strain curves. Computed stress strain curves consist of two parts: the first part of each stress strain curve is a hyperbola extending up to the point where the strength of the sand is completely mobilized. At larger value of strain, where the hyperbola would indicate values of stiffness larger than the compressive strength, each stress-strain is represented by nearly horizontal straight lines corresponding to perfectly-plastic flow behavior. The results, presented in Table 4.2, indicate relative error between the measured and computed peak stress is less than 5.1%.

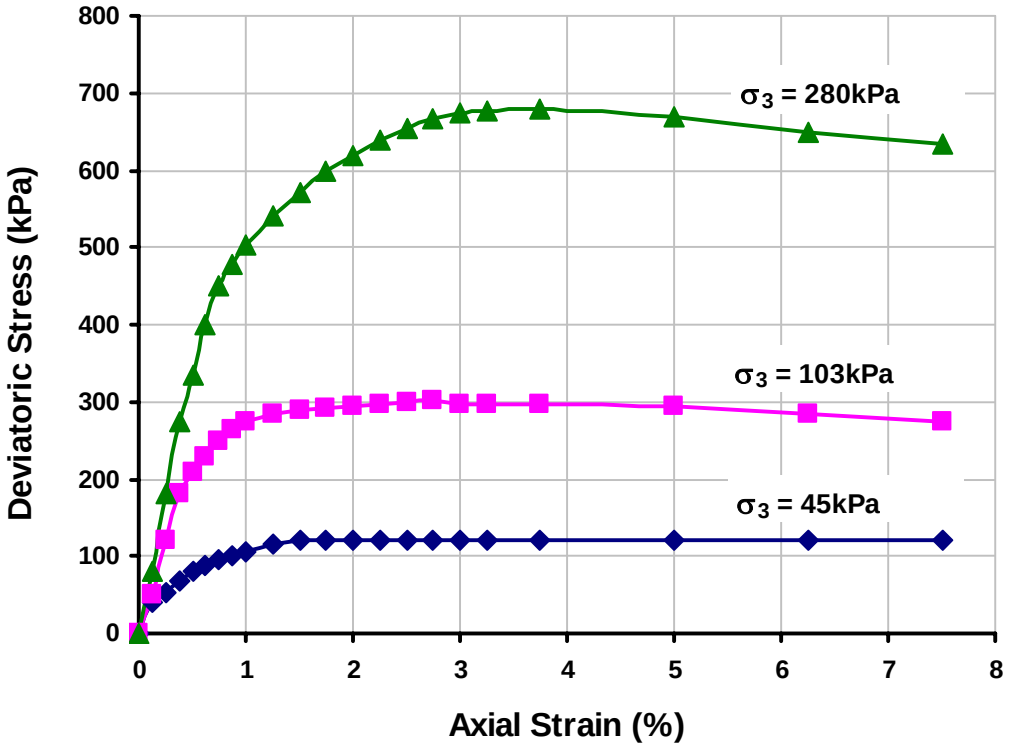

Figure 4.6: Laboratory test result on medium density sand specimen (Gomez et al., 2003)

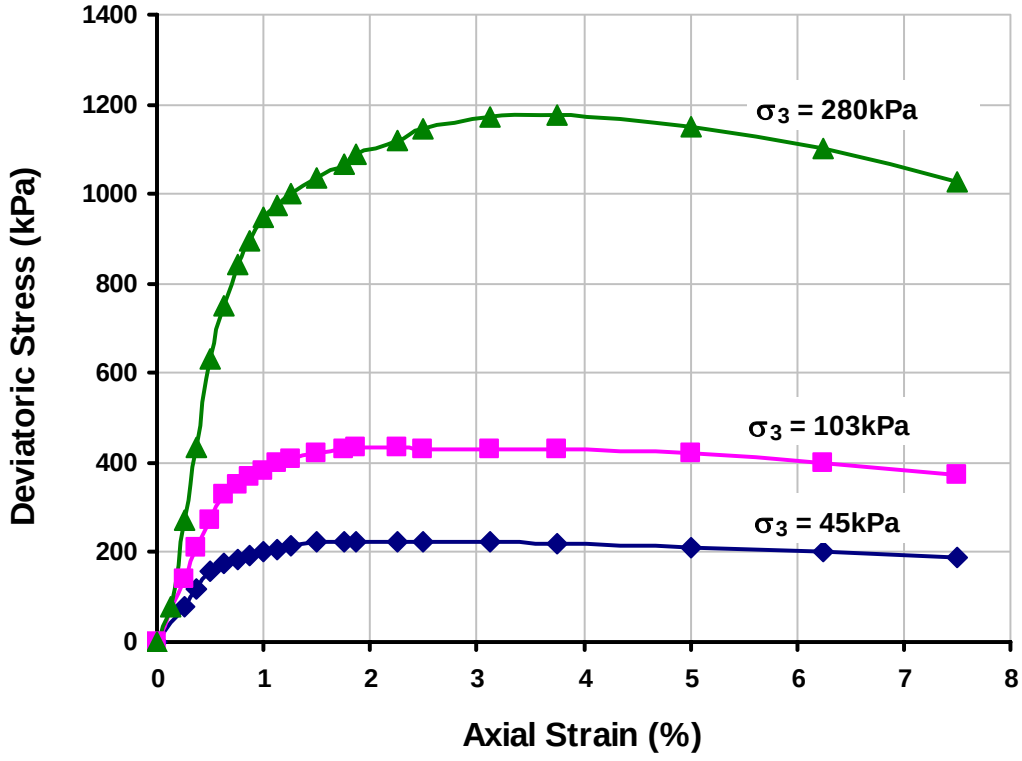

Figure 4.7: Laboratory test result on dense sand specimen from Gomez et al. (2003)

Table 4.1: Soil parameters obtained from triaxial tests

Properties		Medium dense sand	Dense sand
Relative density	D_r	41%	92%
Modulus number,	KL	780	1400
Modulus exponent	n	0.62	0.63
Failure ratio	Rf	0.91	0.9
Bulk modulus number	KB	530	915
Bulk modulus exponent	m	.42	.55
Unloading/reloading modulus number	KUL	1560	2800
Friction angle at a confining pressure of 101.4 kPa (1 atm)	ϕ_0	35°	43.8°
Friction angle reduction value for tenfold increase.	$\Delta\phi_0$	2.5°	3.2°

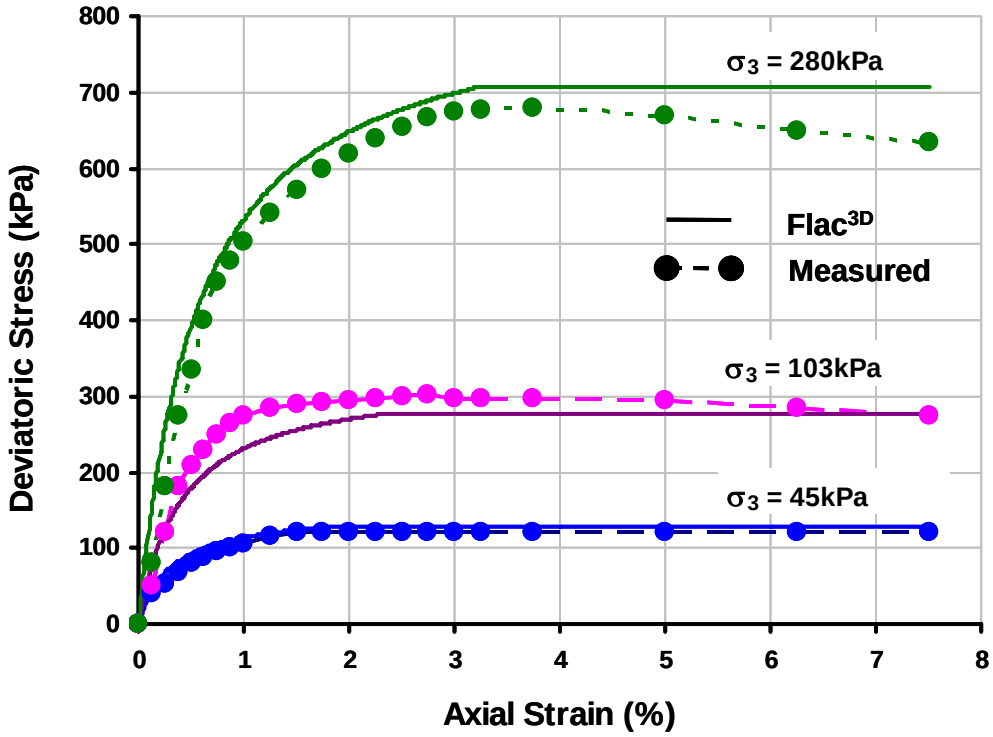

Figure 4.8: Comparison of *FLAC*^{3D} result and test result on medium density sand specimen

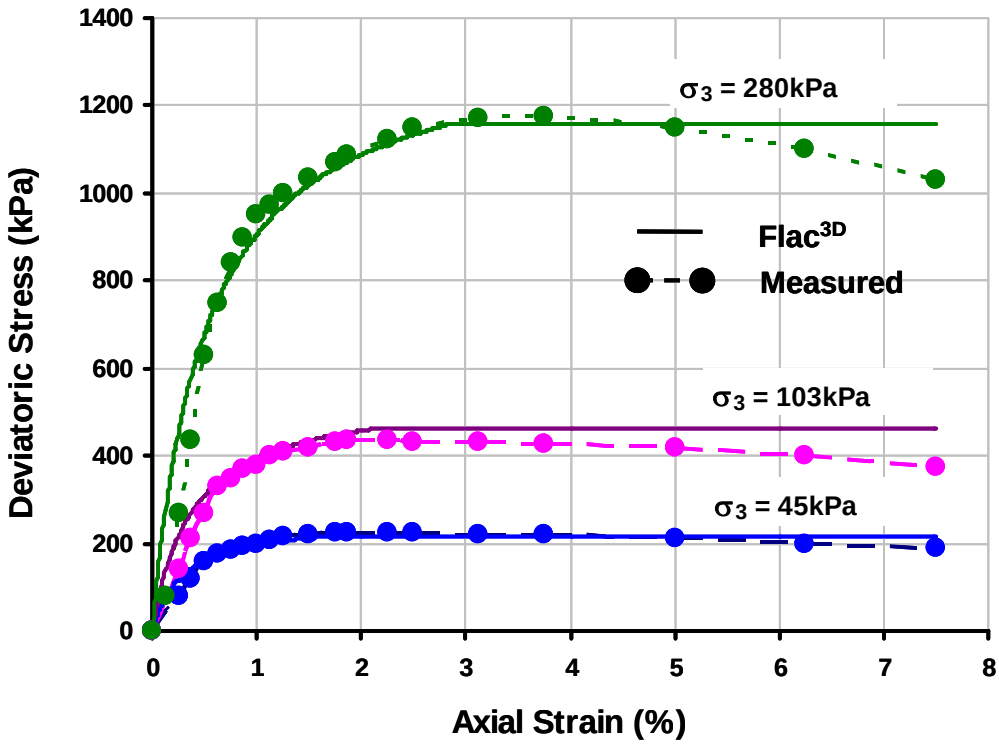

Figure 4.9: Comparison of *FLAC*^{3D} result and test result on dense sand specimen

Table 4.2: Comparison between measured and computed peak stress

Confining stress (kPa)	Stress at failure (kPa)			
	Medium dense specimens		Dense specimens	
	Measured	*Flac*^{3D}	Measured	*Flac*^{3D}
45	122	127	226	216
103	295	277	435	462
280	680	706	1175	1159

These comparisons show the accuracy with which the non-linear, stress dependent stress-strain behavior of granular material can be represented by the proposed non-linear constitutive model using the values of parameters listed in Table 4.1.

The difference observed between the computed and experimental stress-strain curves resulted from the following approximations: (1) representation of the actual primary loading stress-strain curves by hyperbolas; (2) representation of the actual variation of initial tangent modulus with confining pressure by the exponential equation, i.e. Equation 4.20 suggested Janbu (1963); (3) representation of the actual strength characteristics of the material by means of the Mohr-Coulomb criteria; and (4) assumption of perfect-plasticity after Mohr-Coulomb failure. The overall agreement, however, may be seen to be quite good and it may be concluded that the primary loading of the granular material can be accurately represented by the proposed constitutive model.

4.4.2 Rough strip footing on a cohesionless material

Duncan (1962) experimentally determined the load-displacement curve for a 60mm x 320 mm footing installed at a depth of 500mm in Chattahoochee River sand. The laboratory test was modeled in *FLAC*^{3D} using the proposed constitutive model. The domain used for the analysis is shown in Figure 4.10, half symmetry is assumed. The displacement of the rough footing is restricted in the lateral direction, and a velocity is applied to the model in the vertical direction to simulate the footing load. Sample of the *FLAC*^{3D} input data file for the footing is presented in Appendix B.

Model Response and Comparison with Experimental Data

The pressure-displacement curves obtained from the numerical simulation and the experimental data are shown in Figure 4.11. The calculated and the experimental curves are in excellent agreement -the two values of stress corresponding to the same displacement differing at most by about 5.2%. The ultimate bearing capacity for this footing, calculate using Terzaghi's bearing capacity factors, is 373kPa. A footing load of 373kPa would result in footing settlement of about 30mm.

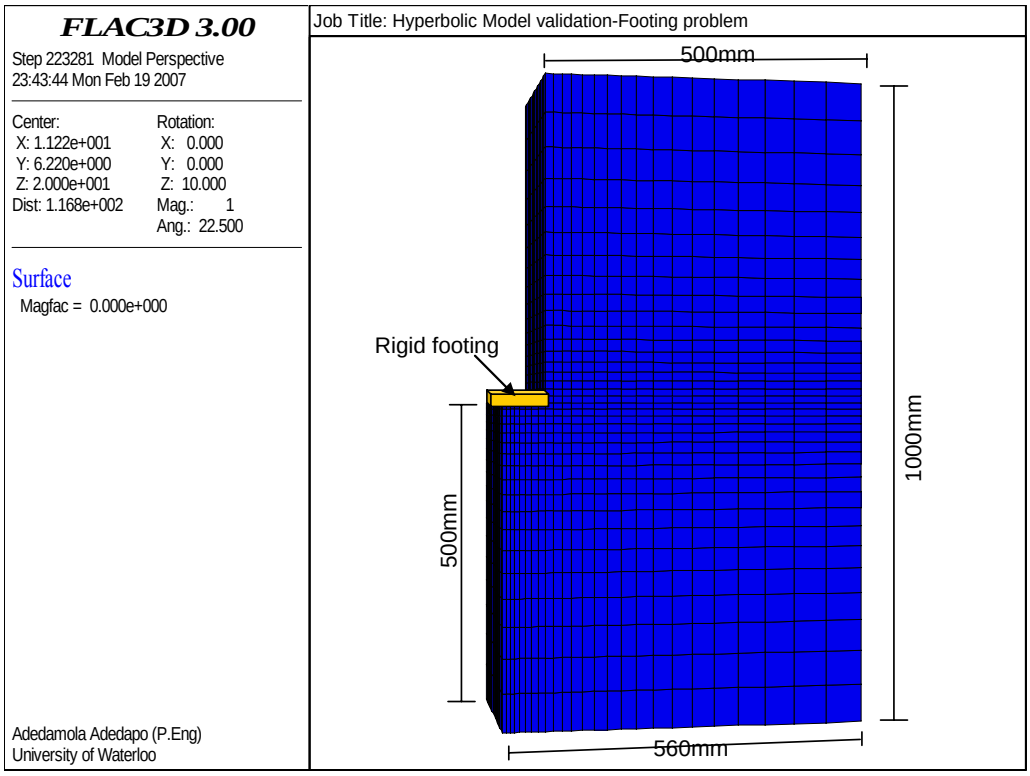

Figure 4.10: *FLAC*^{3D} geometry for footing on Rough foundation

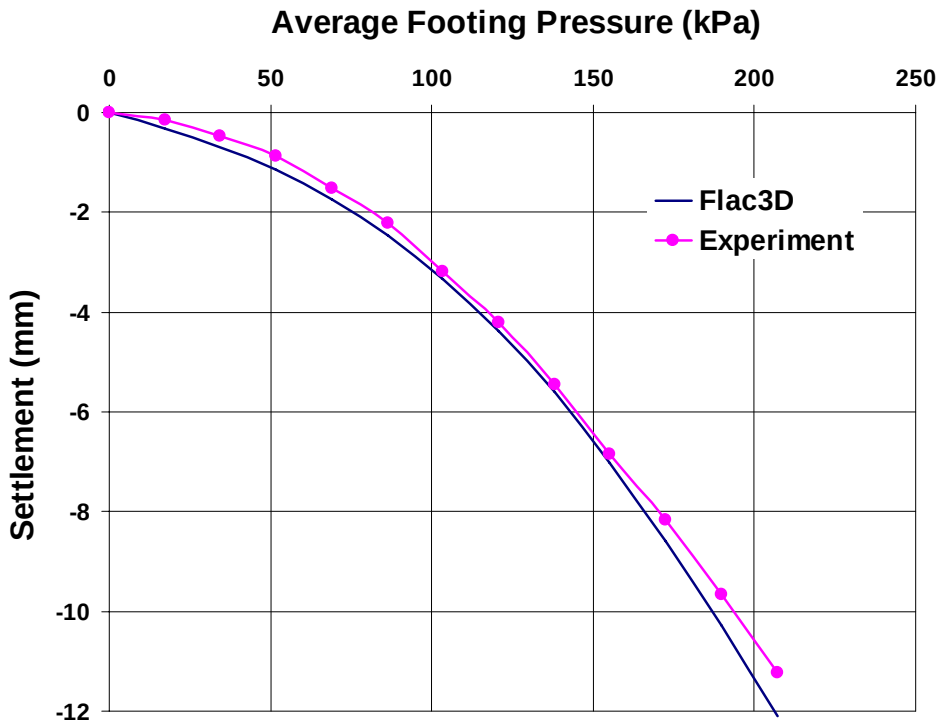

Figure 4.11: Pressure-displacement curves for rough strip footing on a cohesionless soil

4.4.3 Circular flexible pipe buried in silty-sand soil

A code-to-code comparison (benchmarking) was completed as part of the validation process. A 600mm circular HDPE pipe buried in silty-sand soil was analyzed with *FLAC*^{3D} using the proposed constitutive model and the same soil-structure system was analyzed with *CANDE'89.* The description of the simulation and model responses obtained from the two codes are discussed in this section.

***C**ulvert **An**alysis and **De**sign (CANDE'89)* is a 2-D plane-strain finite element program specifically developed for the analysis and design of buried conduits. It has been used extensively by many researcher and engineers since the development of its first version in 1976 (Musser, 1989). The main advantage CANDE'89 code is that its uses Duncan-Chang hyperbolic model to describe stress-strain behavior of soil. Its limitations include: (a) 2-D plane-strain assumption that neglects the out-of-plane effect, (b) use of small strain theory, and (c) quasi-static loading that neglect time dependent material response. Detail description of the software can be found in (Musser, 1989).

Since *CANDE'89* is based on plane-strain assumption, similar conditions were enforced in the *FLAC*^{3D} model by simulating a thin slice of material in the *y*-direction and imposing symmetry boundary conditions on these two surfaces. Symmetry boundary condition is also imposed on the planes at $x = 0$. The geometry of the *FLAC*^{3D} models is shown in Figure 4.12. The input data files for both *FLAC*^{3D} and *CANDE'89* are presented in Appendix B. The pipe was modeled in *FLAC*^{3D} with 3D structural shell elements and with beam-column elements in *CANDE'89.* The Young's modulus, Poisson's ratio and thickness of the plastic pipe are 758MPa, 0.45 and 30mm respectively. The soil properties used for the backfill material are shown in Table 4.3.

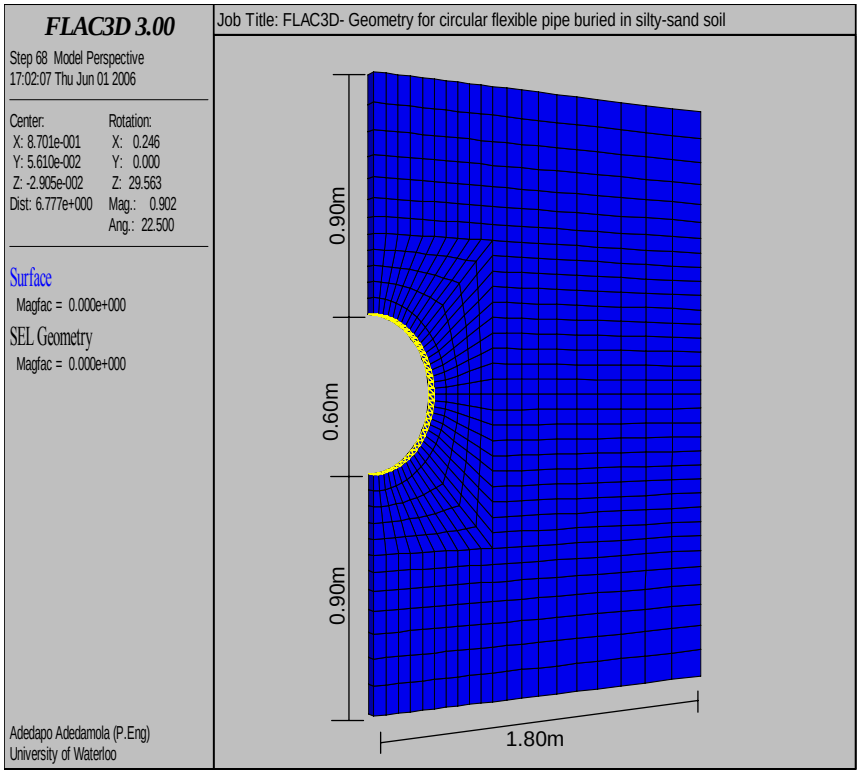

Figure 4.12: *FLAC*^{3D} geometry used for circular flexible pipe buried in silty-sand soil

Table 4.3: Properties of the silty-sand backfill material

Modulus number,	*KL*	480
Modulus exponent	*n*	0.44
Failure ratio	*Rf*	0.75
Bulk modulus number	*KB*	80
Bulk modulus exponent	*m*	0.38
Friction angle	ϕ	30°
Cohesion	*c*	57
Density	γ (kN/m^3)	18

Model Response and comparison with CANDE'89

Figure 4.13 shows the pipe's displacement at the crown and invert obtained from both numerical analyses codes and the corresponding change in vertical diameter of the pipe is shown in Figure 4.14. The results obtained from *FLAC*^{3D} show good agreement with values from *CANDE'89* with maximum percentage difference of 5.8%. The slight variation observed between *FLAC*^{3D} and *CANDE'89* output may have resulted from the difference in the behavior of the 3D shell elements used in *FLAC*^{3D} as compared to the beam-column used in *CANDE'89*. In addition, the plastic correction performed in *FLAC*^{3D} after plastic shear or tensile failure may also have contributed to the observed difference especially as the backfill height was increased.

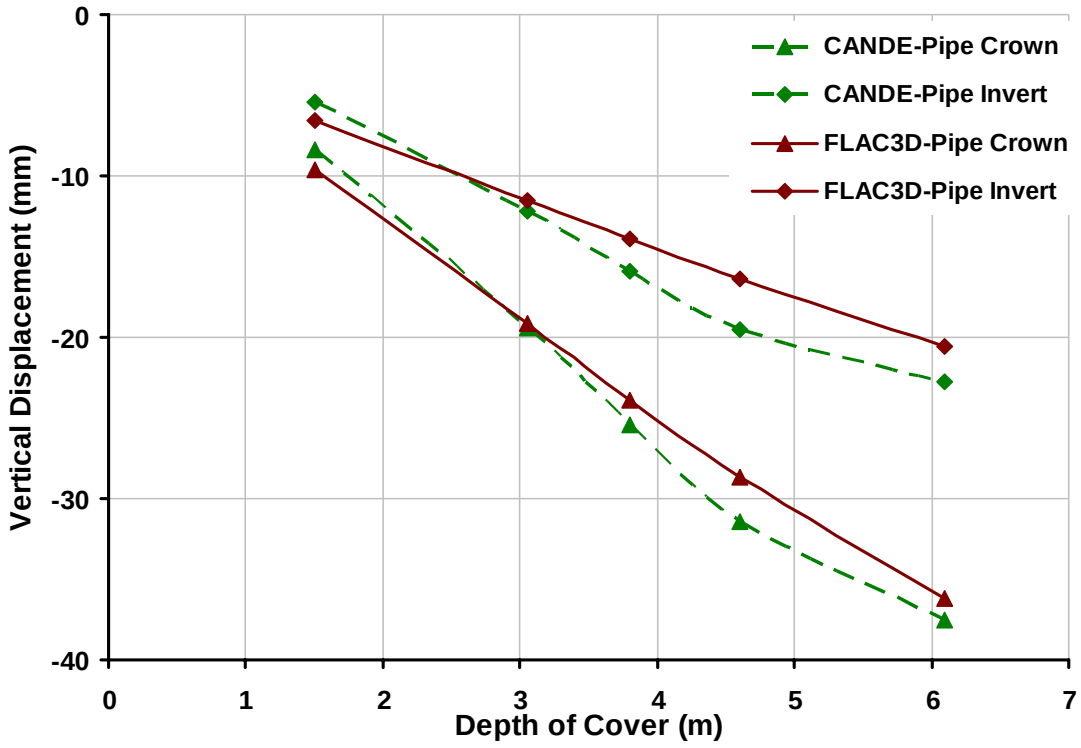

Figure 4.13: Comparison of pipe displacement obtained from *FLAC*^{3D} *and Cande'89*

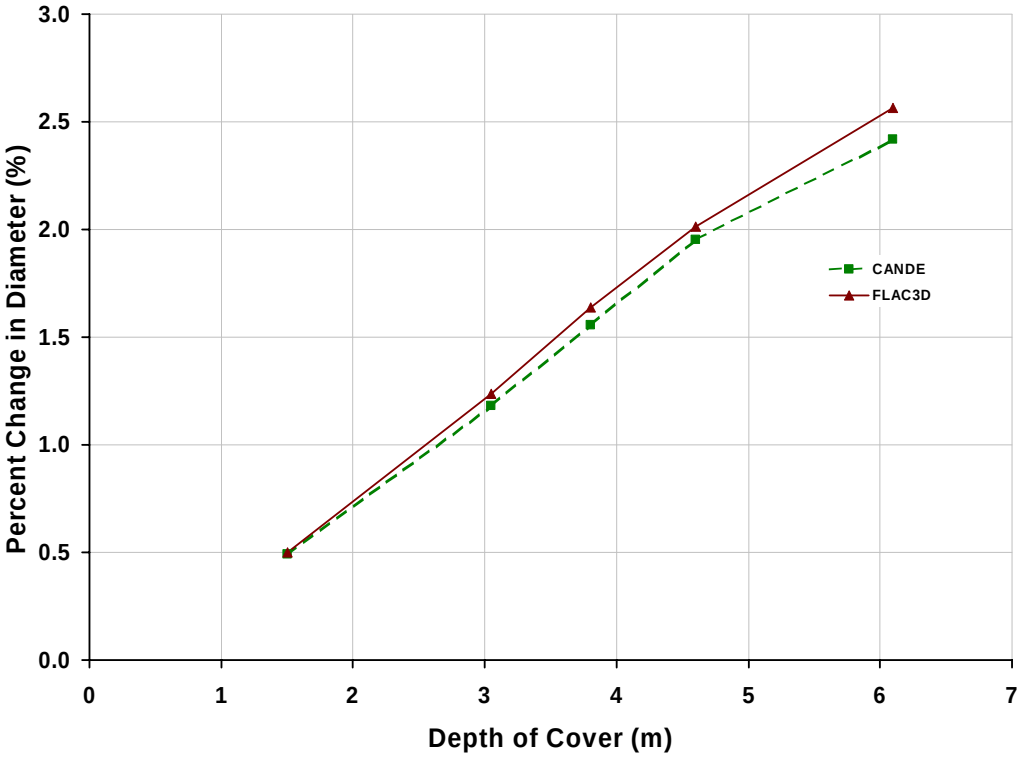

Figure 4.14: Comparison of percentage change in diameter obtained

4.4.3.1 Soil Arching

Soil arching is an important phenomenon in soil-pipe interaction and the capability of the proposed constitutive relation to model this phenomenon was verified. The flexible pipe used in the previous soil-pipe system described Section 4.4.3 was replaced with a rigid pipe and the model was re-analyzed. The rigid pipe has a Young's modulus of 227GPa, Poisson's ratio of 0.25 and a wall thickness of 75mm.

Model Response and Discussion

The distribution of the vertical stresses in the soil at the crown level of the flexible and rigid pipes are shown in Figures 4.15 and 4.16. The results clearly show that in case of the rigid pipe, vertical stress just above the crown of the pipe is about 149.1kPa and its decrease as we move away from the center of the pipe.

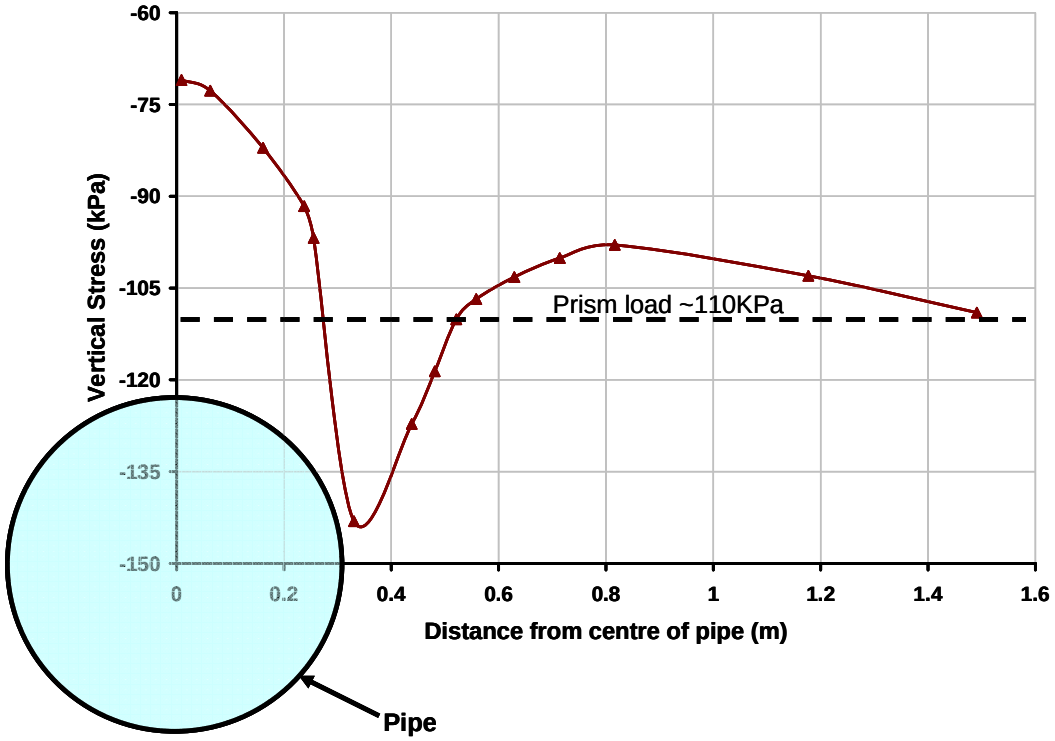

Figure 4.15: Vertical stresses distribution at the crown level of flexible pipe

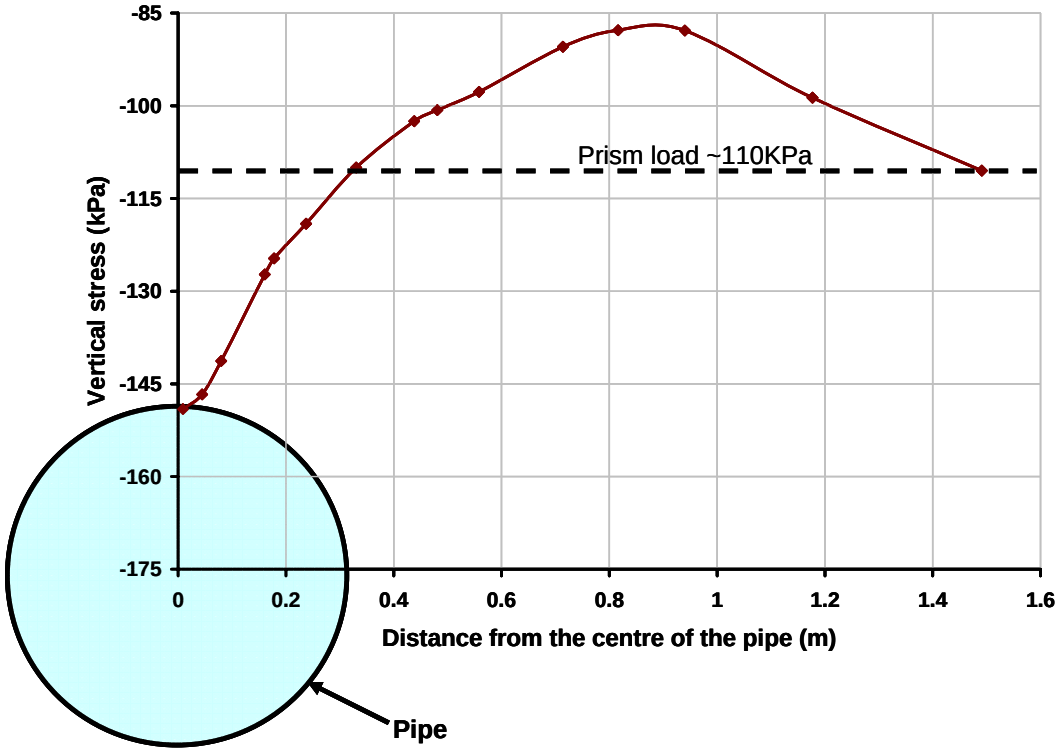

Figure 4.16: Vertical stresses distribution at the crown level of rigid pipe

This is a clear indication of the phenomenon of *negative arching* in which the load carried by the pipe is more than the sum of the overburden soil pressure (110 kPa). An opposite response is observed in the case of the flexible pipe, it can be seen from Figure 4.15 that the load at the crown of the pipe is much smaller (70.8kPa) than the overburden pressure (110kPa) and it increases as we move away from the pipe. The observed response of the flexible pipe is an indication of *positive arching*.

These observations show that the proposed model implemented in *FLAC*^{3D} is capable of modeling soil arching phenomenon in soil-structure interaction problems.

4.5 Summary

The numerical analysis procedure and implementation of the proposed constitutive model in *FLAC*^{3D} were discussed in this Chapter. The proposed constitutive model implemented *FLAC*^{3D} was validated by simulating laboratory tests and comparing the model response with measured experimental data.

Comparison of calculated and measured stresses and strains in specimens of medium dense and dense silica density sand showed that the proposed model is capable of accurately representing the behavior of the granular material under triaxial loading conditions. The maximum relative error between the measured and computed peak load is 5.1%. Additionally, analyses of the behavior of a strip footing in cohesionless soil indicate that the load-displacement curve obtained from *FLAC*^{3D} with the proposed non-linear constitutive relationship is in good agreement with data obtained from detailed experimental tests. The maximum difference in the two values of stresses, i.e. measured and calculated, corresponding to the same displacement is 5.2%.

To further verify the validity and accuracy of the proposed model, a code-to-code comparison (benchmarking) was completed. A pipe-soil interaction problem was analyzed with *FLAC*^{3D} and the predicted response was compared with *CANDE'89* - a widely used finite element program. The pipe responses obtained from the two codes showed good agreement. The maximum difference observed between the percentage vertical deflections is 5.8%. The

ability of the proposed model to simulate soil arching was investigated by computing the vertical stresses at the pipe crown level for a rigid and flexible pipe. The *FLAC*^{3D} model simulated the important phenomenon of soil arching correctly. Vertical stresses measured above the crown of the rigid pipe was 35.5% more than the overburden stress, this indicate *negative soil arching*. However, the vertical stress above the crown of the flexible pipe was 35.4% less than the overburden stress; this is an indication of positive soil arching.

Chapter 5: Field Investigation Program

5.1 Introduction

The technological challenges in roads and pavements are substantial and include not only the need for asset preservation but also the provision of adequate levels of service and safety and the need for continuing innovation and advancement in all areas. It is these challenges that have formed the basis for the ongoing research initiative in Canada – the University of Waterloo Centre for Pavement and Transportation Technology (CPATT) integrated laboratory and field-test facility. Support for the initiative came from a three-way partnership of the public sector (Federal, Provincial, Regional and Municipal), private sector (contractors, consultants, suppliers and manufacturers) and academia. The Canada Foundation for Innovation (CFI) and Ontario Innovation Trust (OIT) and private sector provided $6.0 million over four years for research infrastructure. An additional $3.0 million was provided by the Ontario Research Development and Challenge Fund (ORDCF), the Ministry of Transportation of Ontario, the University of Waterloo, and a group of private sector partners in terms of cash, material, equipment, and time donations. The research effort described in this dissertation is one of CPATT's sponsored projects.

The field investigation program described in this chapter was designed to monitor the actual field performance of utility pipes installed underneath flexible pavement using open cut-and-cover and horizontal directional drilling construction techniques. In addition, pavement deterioration resulting from these installation techniques is also monitored as part of the field program. The field-scale installations were completed at the CPATT's field test facility.

The following sections consist of detailed descriptions of CPATT's field test facility, HDPE pipe instrumentation and field-scale installations, pavement instrumentation and monitoring program. The results obtained from the field-scale investigations including those obtained from the long-term monitoring are also presented and discussed.

5.2 CPATT Field-test Facility

The CPATT field-test facility is located at the Regional Municipality of Waterloo's waste management site located in Waterloo, Ontario. The test facility consist of a torture test track that has truck monitoring and weighing capabilities, and buildings that house data acquisition system and other laboratory-scale testing equipment.

The 709m (2326ft) long and eight metres (26.2ft) wide torture test track was constructed in the summer of 2002 along the southeast boundary of the landfill site (Figure 5.1). The two lane test track is composed of a standard binder mix (Hot Laid 4 (HL4)) and four different surface mixes: namely Hot-Laid 3 (HL3), Polymer-Modified Asphalt (PMA), Stone Mastic Asphalt (SMA) and Superpave, as shown in Figure 5.2. The binder course consisted of a standard municipal mix which was HL4. Two control sections HL3-1 and HL3-2 were placed at each end of the test track. The test track pavement structure consists of 300mm of Granular B subbase, overlaid by 200mm Granular A base and 100mm of asphalt overlay (binder HL4 plus one type of surface mix). The three surface mixes that are being tested at this site will be examined using roughness characteristics, structural adequacy, skid properties, pavement resistance to fatigue cracking and rutting, thermal cracking and traffic noise reduction. Specific details of research work on the evaluation of the performance of the surface mixes can be found in Tighe et al, 2002. The test track has further been expanded to include recycled concrete aggregate sections and interlocking concrete pavement crosswalks.

The test track is an access road that connects the impermeable clay liner borrow pit to the solid waste storage cells. In the spring of 2004, a new waste storage cell was constructed and impermeable clay used was hauled along the test track using heavy duty off road hauling trucks shown in Figure 5.3. Unloaded and loaded hauling trucks contribute approximately 19 and 41 Equivalent Single Axle Loads (ESALs) respectively.

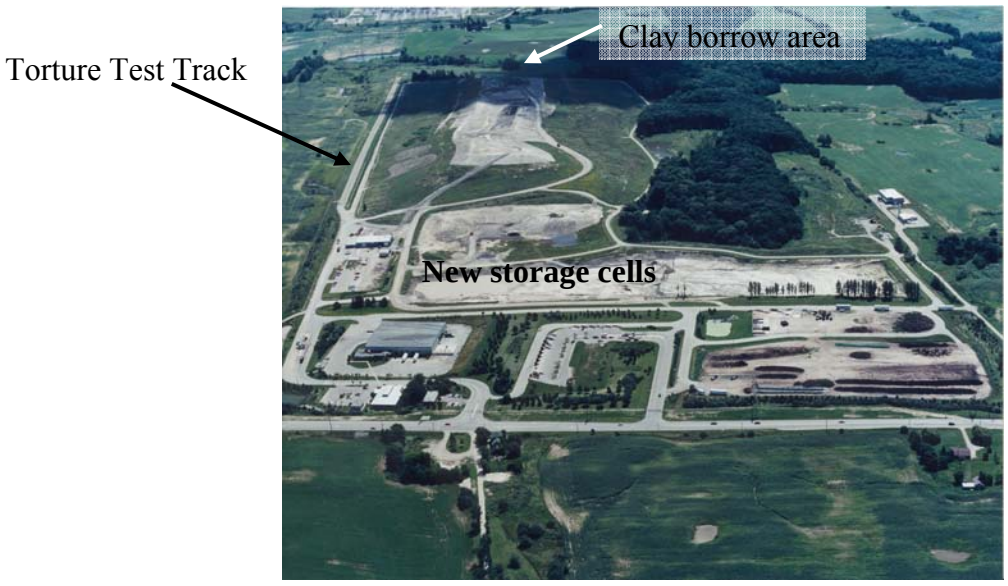

Figure 5.1: CPATT test track facility at the Region of Waterloo Municipal landfill site.

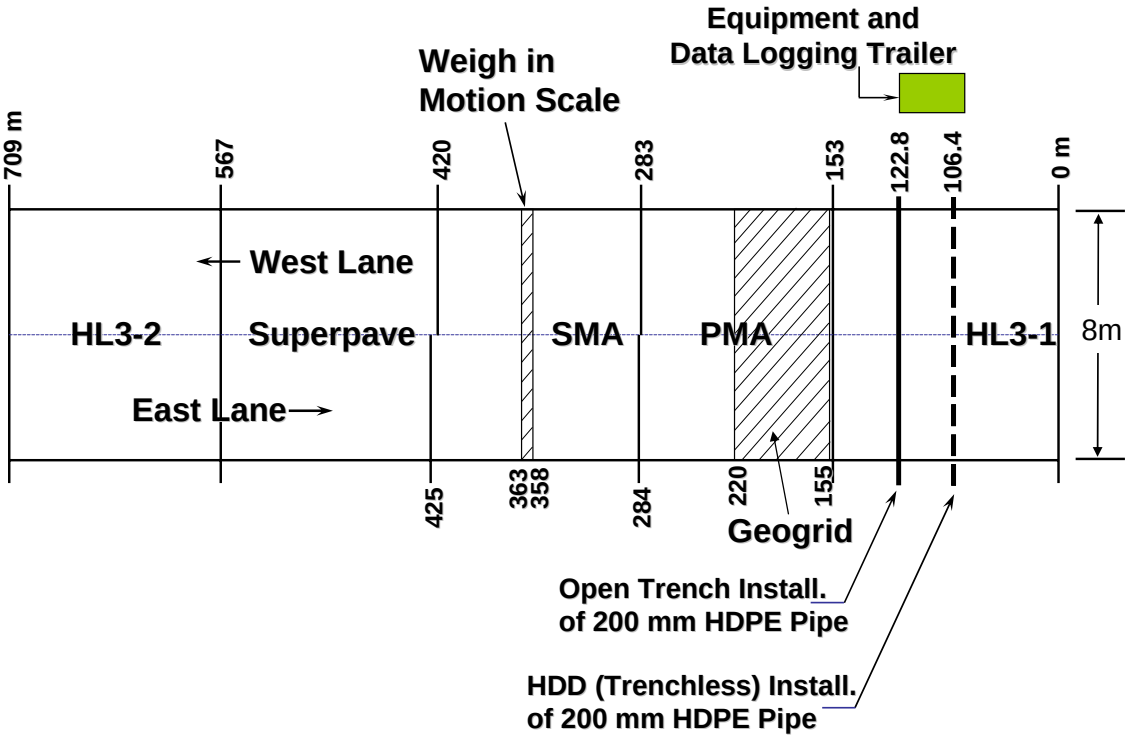

Figure 5.2: Layout of CPATT torture test track showing position of pipe installed pipes.

Figure 5.3: Typical off-road vehicle used for hauling clay along the test track.

During the summer of 2003 a weigh in motion was installed in the test track pavement to measure truck weights and traffic counts.

Falling Weight Deflectometer (FWD) pavement load/deflection testing, International Roughness Index (IRI) surveys and Distress surveys are completed regularly on the test track. Further details about the test track facility including report on its condition and performance of the pavement after construction can be found in Tighe et al. (2003).

5.3 Description of Pipe and Pavement Instrumentation

The pipe instrumentation was designed to evaluate both the short-term (installation induced) and long-term (post installation) performance of the HDPE pipe. Results from previous research work have shown that processes producing deformations in flexible PE pipes

installed using HDD construction practices differ from those associated with buried pipes (Knight and Duvestyn, 2003, Adedapo, 2002). Therefore, pipe instrumentation on the directionally drilled and buried pipes was designed to capture the actual behavior of each the pipe during and after installation.

5.3.1 HDD Installed HDPE Pipe Instrumentation

The HDD installed HDPE pipe instrumentation and installation was designed to assess: (a) HDPE pipe strains, ring deflection, pull-load and bore slurry pressure during installation using good HDD construction practices and properly formulated drilling fluids, (b) drill rig effort and HDPE response during installation, (c) time required for pipe strain relaxation after installation, (d) long-term pipe strain, ring-deflections and bore slurry pressure resulting from seasonal variability, and (e) ground deformation during and after installation.

A total of twenty one sensors were installed inside the HDPE pipe and on the drill rig to measure the pipe performance, bore annulus slurry pressure and drill rig response during and following pipe installation. The pipe sensors consisted of six pressure transducers, nine linear variable displacement transducers, four strain gauges, one thermistor, and a load cell.

Four 1.0m (3.28ft) long PE pipe test sections shown in Figure 5.4 were instrumented in the laboratory prior to butt fusion. The pull head test section (PH) contained a load cell, two pressure transducers and four strain gauges. The control test section (CO), contained three linear variable displacement transducers and it was placed beneath the pavement shoulder adjacent to the Southbound traffic lane away from the influence of traffic loading. The second and third test sections labeled as WL and EL test sections were placed directly beneath the right wheel path of the Southbound traffic lane and Northbound traffic Lane respectively. Each test section contained three linear variable displacement transducers and two pressure transducers. Detailed descriptions of the HDD installed HDPE pipe sensors are presented in the following sections.

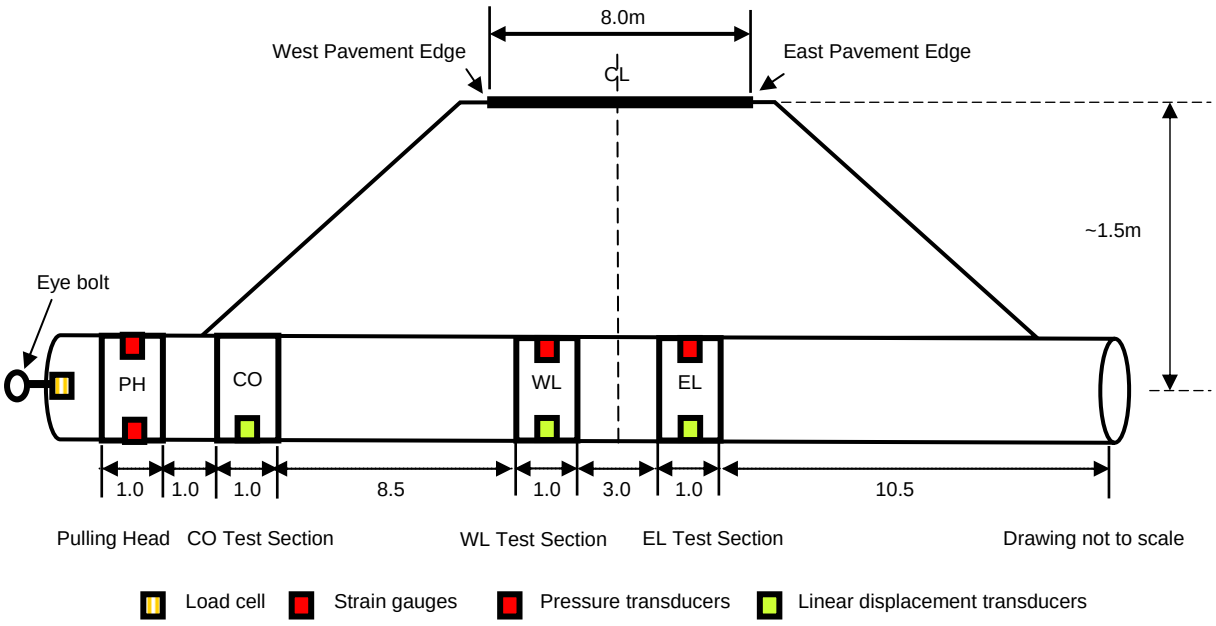

Figure 5.4: Layout of the sensors placed inside the HDD installed HDPE pipe.

Linear variable displacement transducers (LVDT)

The linear variable displacement transducers (LVDT) placed inside the test sections (CO, WL, and EL) are to measure changes in the diameter of the HDPE pipe. The arrangement of the displacement transducers is shown in Figure 5.5. One linear transducer was fixed between the pipe crown and invert (plane 0°-180°) to capture changes in the vertical diameter of the pipe. The second transducer connected the pipe springlines (plane 90°-270°) measures change in the horizontal diameter of pipe and the third transducer is positioned at an oblique angle along 45°-225° clockwise from the crown.

Temperature compensated strain gauges

Four strain gauges were placed inside the pull head test section (PH). They are oriented longitudinally along the pipe to capture axial and flexure strains near the pull-head during pipe installation. The gauges are positioned at the crown (12 o'clock), the springlines (3 and 9 o'clock) and invert (6 o'clock) of the pipe as shown in Figure 5.6. The pull-head was cut-off from the pipe after installation to access the data acquisition system placed inside the pipe.

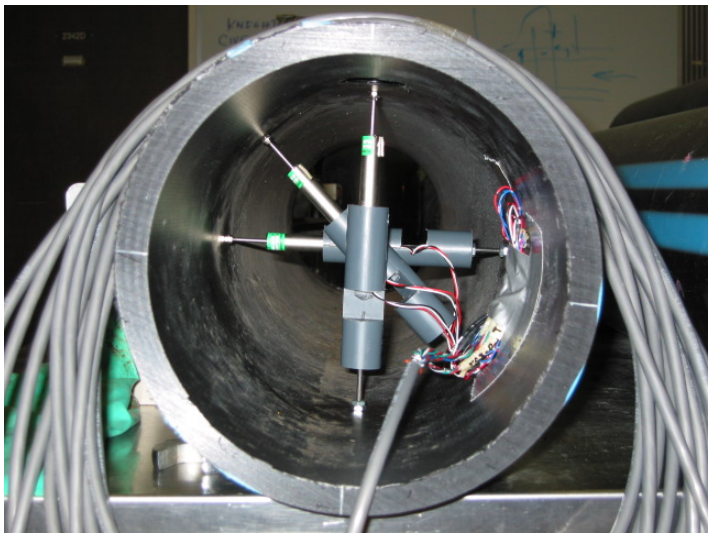

Figure 5.5: Arrangement of LVDTs inside each test section.

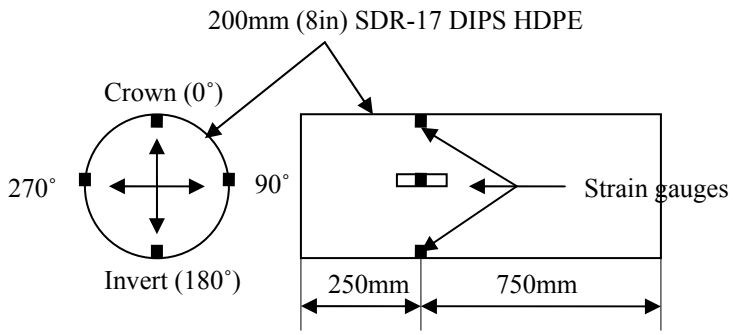

Figure 5.6: Arrangement of strain gauge inside the Pulling Head (PH) test section.

The strain gauges are temperature compensated GFLA-6-70-1L gauge manufactured by Sokki Kenkyujo Company and are designed for materials with low elastic modulus such as plastics. The operating temperature of the strain gauges specified by manufacturer is between -20 to 80°C. The gauges were glued to the wall of the pipe with bonding cement specially made for plastic materials.

Pressure Transducers

Two pressure transducers were placed in each test sections with the exception of the control test site to monitor change in pressure in the slurry (mixture of soil cutting and raw drilling fluid) within the annular space between the pipe and the native soil both during and after pipe installation. The 500kPa (75psi) pressure transducers Model A-105 manufactured by Sensotec Inc shown in Figure 5.7 were mounted flushed with the outside of the pipe wall at the crown (12 o'clock) and springline (3 o'clock).

Figure 5.7: 500kPa Pressure transducers Model A-105 manufactured by Sensotec Inc

Pull head load cell

A 222kN load cell was installed at the pulling head to record the axial load imparted to the pipe by the drill rig via an eyebolt with steel backing plates and bearing assembly installed inside the pull head. The eye bolt was connected to the drill string via a swivel, Figure 5.8, to minimize pipe rotation during pull back.

Drill Rig Instrumentation

The drill rig performance during pilot bore drilling and pipe installation was monitored with two pressure transducers installed on the drill rig, Figure 5.9. The transducers record the drill rig feed and return hydraulic pressures. A transducer installed in the drill fluid tank recorded the height of fluid in the drill fluid tank. The volume of drilling fluid expended during drilling and pipe installation is computed from this measurement and known tanks dimensions.

Figure 5.8: HDD installed HDPE pipe ready to be pulled through the pre-reamed bore

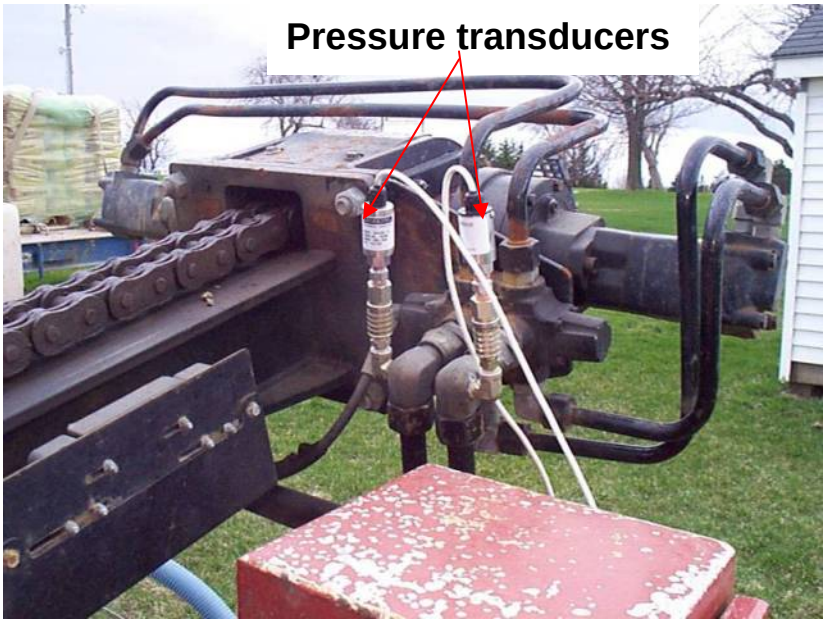

Figure 5.9: Transducers connected to drill rig feed and return hydraulic pressure lines

5.3.2 Open-cut Installation Instrumentation

The instrumentation requirements for the open-cut buried HDPE pipe are different from those of the HDD installed pipe and the instrumentation was design accordingly to capture the pipe response to installation and in-service loads. Also, because the pavement structure would be excavated to full-depth during open-cut pipe installation, there was opportunity to install sensors within the restored pavement sections. The pavement sensors installed within the trench backfill provide avenue for monitoring the response of backfill material to various loading which be correlated with the response, thereby enhancing the understanding of the pipe-soil interaction. The pavement structure instrumentation also provides data that would be use to evaluate the performance of the repaired section and validate numerical simulation models. Description of the open-cut buried pipe instrumentation is provided in this section while details of the pavement instrumentation are provided in the following sections.

Similar to HDD installed pipe, the open-cut buried pipe was instrumented to assess (a) HDPE pipe strains and ring deflection during open-cut installation using good construction practices, (b) Long-term pipe strain and ring-deflections caused by seasonal variability, and (c) Ground deformation during and after installation. Twenty one sensors were installed in the pipe to monitor pipe deflections, pipe strains and temperatures changes during and after installation. The sensors include nine linear variable displacement transducers, thirteen strain gauges and a thermistor; the relative locations of the sensors are shown in Figure 5.10.

Two 2.3m (7.5ft) long and one 1m (3.3ft) long PE pipe test sections were instrumented in the laboratory, Figure 5.10. The test sections were fused into the pipe length such that the sensors would be located directly underneath the wheel paths of the Northbound traffic lane (EL) and Southbound traffic lane (WL) and the control test section (CO) would be away from the influence of traffic loading. The CO test section was placed beneath the pavement shoulder adjacent to the Southbound traffic lane.

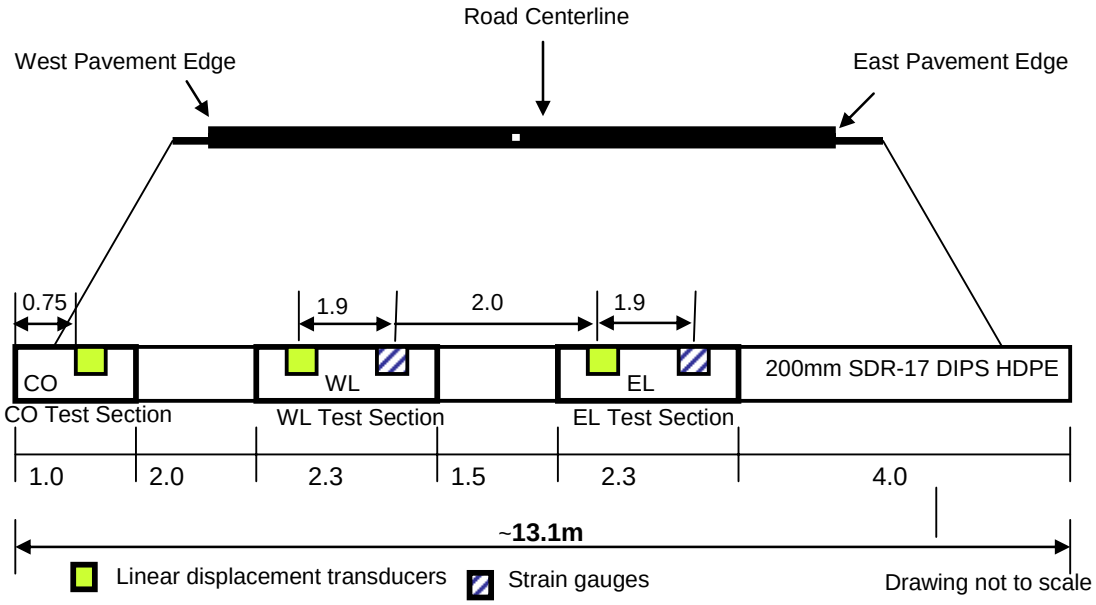

Figure 5.10: Layout of the sensors placed inside the Open cut installed HDPE pipe

Linear variable displacement transducers (LVDT)

The type and model of LVDTs installed in the open-cut installed HDPE pipe is the same as those placed inside the HDD installed pipe. The orientation of the transducers in both pipes was also the same. However, the sensitivity and resolution of the open-cut pipe LVDTs transducers was significantly improved by the use of passive filter that was designed as part of the instrumentation program by the author of this dissertation.

Signal noise problem was encountered during the HDD pipe instrumentation. Some low frequency noise interfered with the output signal which resulted in reduced resolution of the LVDT especially at low sampling rate. The primary sources of the noise was an electronic component in the circuit board of the multiplex through which input signal are transmitted from the sensors into SoMat 2100 DAS and the high voltage overhead power cable that runs parallel to the test tract at the landfill site. A passive filter that does not require an external power supply was designed to reduce the interferences. High-pass capacitor filters that pass high frequencies well and attenuate frequencies lower that the cut-off frequencies were designed and used. The original corrupted signals were analyzed to determine frequency-

components of the noise and an appropriate cut-off frequency for the filter. The capacitance of the filter was determined using the following equation:

$$f = \frac{1}{2\pi RC} \qquad [5.1]$$

where f is the cut-off frequency in hertz, R is the resistance in ohms and C is the capacitance in farads. The in-line high-pass filter that was designed resulted in an increased sensitivity of ±0.001mm for the linear variable displacement transducers.

Strain Gauges

The strain gauges installed on the buried pipe are same as those installed on HDD installed pipe. However, the orientation and location of the gauges were different. The HDD installed pipe strain gauges were placed near the pull-head to capture the tensile and flexural strains imposed on the pipe during pullback whereas the gauges on the open-cut installed pipe were placed and arranged in the three test sections to capture the pipe bending and circumferential strains. Each test section was equipped with four strain gauges fixed to the interior of the pipe, one each at the crown (12 o'clock), the springlines (3 and 9 o'clock) and invert (6 o'clock).

Although, the strain gauges used are temperature compensated i.e. the gauge produces only minimum thermal output (temperature-induced apparent strain) over the temperature range from about -45 to +200°C (-50 deg to +400 deg F). HDPE material behavior is temperature dependent. Therefore it is important to obtain strain-temperature relationship of the instrumented gauges under no stresses condition in order to obtain the real strain from the raw strain data. To accomplish this, a strain gauge was glued to a dummy HDPE pipe coupon (cut from the same HDPE pipe) and was placed inside the pipe. The dummy gauge was free from any external loading. The gauges were securely attached to the HDPE pipe using bonding cement specifically made for plastic materials.

5.3.3 Pavement Instrumentation

The structural responses of pavement system under various loading conditions are of primary interest to all involved with pavement design, management, and material selection. There are several significant benefits that can result from the use of field instrumentation. Perhaps the most important is better understanding of the response phenomenon of pavement system (White, 1985). In addition to this, pavement response data present an opportunity to validate analytical models, as well as, to calibrate model response variables. The conventional open-cut and cover pipe installation involves the excavation of the roadway to full-depth thereby giving the opportunity to install of sensors within the pavement structure during trench restoration. The research described in this dissertation attempts to monitor the impact of distresses caused by the presence of utility cut on the performance of the pavement section using pavement instrumentation. The information gathered from pavement sensors will also provide insight into the soils behavior around the installed PE pipe and useful data for numerical model validation.

A total of 19 sensors were installed in the restored pavement section to measure asphalt and soil strain, volumetric water content, ground temperature profile, and total vertical stress distribution within the pavement structure. Figure 5.11 shows the vertical and transverse distribution of the monitoring sensors installed under the Southbound and Northbound lanes. Detailed description of the pavement instrumentation including details of the gauges/sensors, calibration and installation procedure are presented in the following Sections.

5.3.3.1 Asphalt Strain Gauges

Various methods that have been employed for strain measurement in the bonded layer of asphalt concrete (AC) pavement include the use of strip gauges, H-type gauges, foil strain gauges cemented to or embedded in carrier block prepared in the laboratory or, foil strain gauges cemented to a core extracted from the pavement and inductive strain coil. The primary concern with the foil type strain gauge is the effectiveness of the bond between the instrumented core and the surrounding pavement, and if measured strain is representative of

the actually response. Inductive coils are influenced by the noise generated by the ignition system of vehicles, and therefore inaccurate measurements may result.

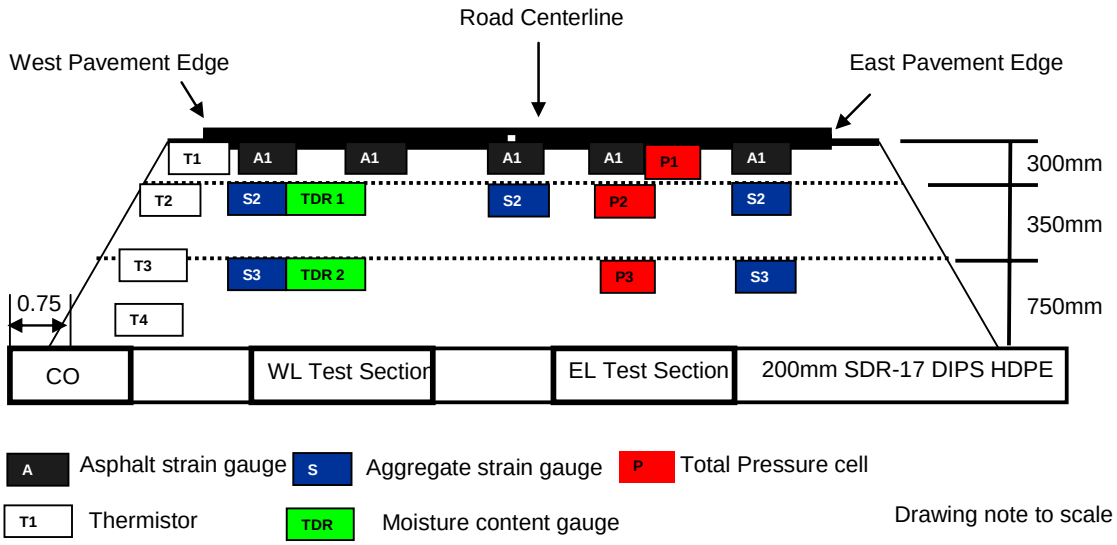

Figure 5.11: Distribution of pavement instrumentation within the backfill

H-type gauges are strain transducers that are currently widely used for pavement monitoring. The gauge consists of a strip of a given material onto which the strain gauges is connected. The ends of the strip are connected to a metal bar with the rectangular cross sections that act as anchors, thus forming the letter H, Figure 5.12.

Figure 5.12: H-Type Asphalt strain gauges

These transducers are embedded at the bottom of the asphalt concrete layer. As the pavement experience strain under the application of load, the anchor bars move with the pavement thus producing elongation (or compression) in the strip. The strain registered by the strain gauge attached to the strip will be the same as the true strain in the AC if the stiffness of the strip is the same as that of the AC layer (Tabatabaee et al., 1992). A large stiffness differential between the two materials will result in the separation of the anchor bars from the pavement materials and the failure of the instrumentation. Different materials (e.g. polyester, nylon 6/6) and dimensions for the strip and the anchor bar have been investigated to overcome this problem. The H-type strain gauges have been used extensively at several instrumented test sites that include Penn State Test Track, Mn Road, WesTrack, Ohio SPS, FHWA-PTF, RIOH-ALF in China, PRF-LA in Louisiana, DRTM in Denmark, TxMLS in Texas, and in Bedford, Virginia; and the performance of the gauges under dynamic loading have been reported to be satisfactory.

H-type asphalt strain gauge ASG-152, manufactured by Construction Technology Laboratories (CTL) Group Inc. was selected for this project because of its reliability, durability, low cost, short delivery time and satisfactory track-record. The CTL Group's asphalt strain gauges are also designed to withstand the high temperatures and compaction loads associated with asphalt pavement construction. The ASG-152 is a field proven design that uses durable materials to ensure accurate long-term data collection. The actual sensor within the instrument itself is a 350Ω Wheatstone bridge mounted on a nylon 6/6 bar. The approximate stiffness of the nylon is 2350 MPa (340,000 psi). There are four active strain gauges. Two aligned with the maximum longitudinal strain and the other two with the transverse strain. This full-bridge strain gauge configuration reduces cost by eliminating the need for expensive data-acquisition and signal-conditioning systems required for bridge completion. The maximum range on the gauges is ±1,500 με which is well within expected strain ranges for most flexible pavements. The gauge also has a braided shielding that protects the lead wire from electrical noise and an abrasion-resistant, Teflon polymer coating withstands temperatures up to 205°C (400°F). The general specification of the gauges is provided in Table 5.1

Table 5.1: General specification of CLTGroup's asphalt strain gage

Bridge Completion	Full bridge(no completion required)
Gage Resistance	350 Ohm
Excitation	up to 10 Volts
Output	≈ 2 mV/V @ 1500 micro strain
Calibration Factor	Individually provided
Grid Area	0133 cm^2
Gage Area	122 cm^2 overall
Fatigue Life	$<10^5$ repetitions @ +/- 1500 micro strain
Modulus	≈ 340,000 psi
Cell Material	Black 6/6 nylon
Coating	Two-part polysulfide liquid polymer encapsulated in silicone with butyl rubber outer core
Temperature	-34ºC (-30ºF) to 204ºC (400ºF)
Lead Wire	22 AWG braided shield four wire

Gauge Calibration

Individual calibration sheets were provided with each gauge by the manufacturer. Checking the strain gauge using a special clip-gauge produced result that differs from data generated using the gauge factor supplied by the manufacturer. Prior to the installation of the instrument, there were no facilities at the CPATT test Laboratories available to complete a detailed calibration on the asphalt strain gauges. However, each gauge was checked for proper functionality at the laboratory prior to installation. This was performed by connecting each gauge to a Vishay instruments digital strain indicator model P-3500, Figure 5.13, and pushing and pulling on the gauge to check that the response had the proper sign (i.e., correct polarity). A positive reading corresponded to tension while a negative response corresponded to compression. Also recorded was the "no load" strain box reading which were found comparable to the manufacturer's supplied strain box reading data for the gauges.

Installation Procedure

Once the granular base layer has been placed, 75mm (3") deep cable trenches were dug and granular base material (with the large aggregate removed) was placed to a depth of 25mm (1") in the trenches. The gauges were then placed in their predetermined locations and the

cables were laid in the trenches. The cable trenches were then backfilled with the sieved granular material and compacted using a Marshall hammer.

A sand-asphalt binder mixture consisting of sand and PG 64-22 binder was prepared to adhere the ASG to the base course. The ratio of sand to binder was 1:2 by weight. The gauges were properly oriented, gently pushed down into 5mm thick sand-binder mixture and leveled as shown in Figure 5.14. Samples of hot mixed asphalt (HMA) that had been hand raked to remove large particles was placed by hand on top of the gauges and compacted using a shovel and wooden compacting plate. The material was placed so that no part of the gauge was exposed, resulting in approximately 30mm (1.25”) of cover material as shown in Figure 5.15. The instrumented section was paved once the cover material had been placed on the ASG.

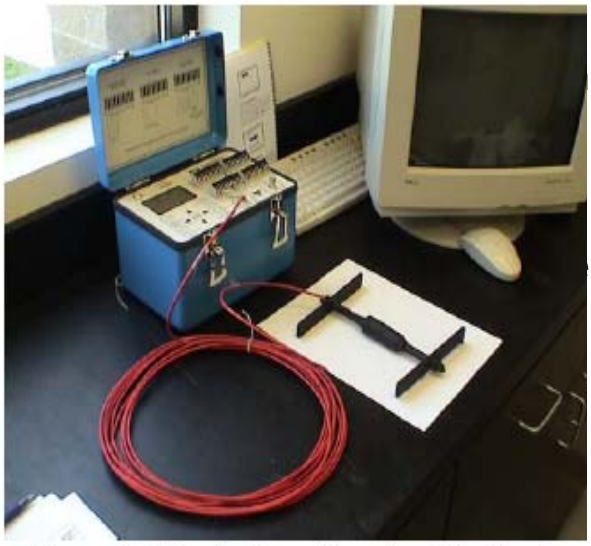

Figure 5.13: Vishay instruments digital strain indicator model P-3500

Figure 5.14: Asphalt strain gauge in sand-binder mixture

Figure 5.15: Asphalt strain gauge covered with HMA

5.3.3.2 Earth Pressure Cells

Total pressure cells were used to monitor the change in total vertical stress in the pavement structure with depth. These cells were placed approximately above the granular base course, subbase and subgrade. Campbell Scientific RST pressure cells were selected for this project based on the imprint size, cost, availability, measurement range, capability to withstand HMA temperature and previous use in pavement instrumentation. The gauges used in this research were RST TP-6-S, TP-9-S, and TP-12-S pressure cells with 690kPa, 345kPa and 172kPa stress capacity respectively. The capacities correspond to the expected full scale pressure ranges, the most sensitive cell TP-12-S with a 300mm (12”) diameter disc size was placed at near the top of the subgrade while TP-6-S with a 150mm (6”) diameter imprint was placed at the top of the base course. TP-9-S was placed in-between the other two cells. The output voltage of the pressure cell range from is 0-5V with excitation of 12V and the operating temperature ranged between -20 to 120°C.

The pressure cells, Figure 5.16, are hydraulic type pressure cells and consist of two circular steel plates welded together around their periphery to form a chamber or cavity. The chamber is filled with de-aired incompressible liquid. The total stress acting on the faceplate is balanced by equal pressure induced in the internal liquid. Changing earth pressure squeezes the two plates together causing a corresponding increase of fluid pressure inside the cell. A semi-conductor transducer converts this pressure into an electrical signal which is transmitted as a voltage change via cable to the DAS. These cells provide average pressure acting on the faceplate.

Calibration

The total pressure cells were also checked for functionality. Each was connected to the DAS and checked that there was a positive voltage change when pressure is applied to the surface on the surface of the cell. The calibration data supplied by Campbell Scientific for each pressure cell was used in converting the voltage output to pressure. It was not possible to complete a calibration check on the pressure cells due to lack of availability of sufficiently large pressurized chamber to conduct the calibration.

Installation Procedure

Circular holes were excavated at the location of each pressure cell. The diameter of the hole was roughly the same as that of the pressure cell. The bottom 25mm of the cavity was filled with fine sand to reduce any undesired concentrated stresses due to angular aggregates. The sensitive surface of the cell was then placed face-down in the hole. The pressure cell was leveled with the surface for each layer and additional fill material was placed by hand around the transducer and carefully compacted.

Figure 5.16: Installation of hydraulic total earth pressure cell

5.3.3.3 Granular Aggregate Strain Gauges

As part of the instrumentation program it is desirable to monitor the rarely measured strains at the interfaces between the base and subbase and subbase-subgrade. Geokon Model 3900 Embedment Strain Gauge was selected for the measurement. The Geokon gauge is designed for the measurement of dynamic strains in concrete structures, asphalt roadways and soils. It comprises a full bridge strain gauge proving ring coupled between two flanges with a spring

and shaft. When the flanges move relative to one another, the tension in the spring changes and hence the strain in the proving ring. A low modulus PVC tube serves as a protective housing and holds the gauge at the desired initial tension. The active gauge is 195mm-long and has a 26mm diameter. The diameter of its flange is 38mm which is larger than the maximum aggregate size used in the pavement. The gauge has a nominal output of 1.25 mV/V full scale with 10V excitation, hence it required some signal amplification. The full-scale strain is 5000 microstrain.

Calibration

The manufacturer Geokon™ Inc. provided calibration data for each of the gauges in compliance with ANSI Z540-1. The zero strain readings for the gauge were verified in the laboratory and were comparable to those provided by the manufacturer for each gauge.

Installation Procedure

At the sensor location a nominal cavity was dug for each gauge such that it is just adequate to fit the sensor in the pavement with least disturbance to the insitu soil. The gauge was then placed on a very thin layer of natural sand and then backfilled with the excavated material and carefully hand-compacted.

5.3.3.4 Time-Domain Reflectometry Probes (TDR)

The moisture content variation of the subgrade soil and unbounded material is an important parameter that influences their behavior. However, it is one of the most difficult to measure. For this project, the Campbell scientific CS616 TDR probed was selected based on performance, survivability, cost and ability to integrate with existing DAS. The probe consists of two parallel conducting rods that are 300mm in length, Figure 5.17. The epoxy head in the CS616 that holds the rods contains electronic components configured as a bistable multivibrator. The oscillation frequency of the multivibrator is dependent upon the dielectric constant of the material surrounding the conducting rods. Circuitry within the probe head scales the multivibrator output in terms of a frequency for measurement with a data acquisition system. The period of the square wave from the multivibrator ranged between 0.7 to 1.6 milliseconds. The relationship between the volumetric moisture content and the

dielectric constant is determined by using a regression equation programmed into the data acquisition system.

Figure 5.17: Time-Domain Reflectometry probe model CS616

Calibration

Calibration model for the TDR were completed in the laboratory, the soil used for the calibration was a sandy gravel granular material. The dried soil samples were moistened to predetermined moisture content that ranged from 3 to 32%. For each TDR probe, four readings were obtained at each moisture content with the probe rotated 90° between readings. The data were plotted and evaluated using best fit linear and quadratic functions. The resulting calibration coefficients for each gauge were programmed into the data acquisition system to obtain volumetric moisture contents from the TDR probes.

Installation Procedure

Holes were dug by hand approximately 200mm wide by 600mm long by 150mm in deep to accommodate the TDR probes. Cable trenches were then excavated by hand 75mm wide by 50mm deep running from the cavity to the edge of the pavement. Care was taken to ensure that the hole and the cable trenches were clean and free of sharp stones fragments that could

damage the probe or cables. The hole was partially filled with the pavement material (sieved to remove large aggregate). The probe was placed and then covered with soil. The soil was carefully compacted around and over the probe.

5.3.3.5 Temperature Probes

The variation of temperature in the pavement structure has significant influence on the response of the pavement as temperature affects the stiffness of the AC layers, which in turn affect the pavement response. Campbell Scientific T107B temperature probes, Figure 5.18, were selected for the project. The T107B temperature probe uses a thermistor to measure material temperature. A thermistor is a piece of semiconductor made from metal oxides, pressed into a small bead, disk, wafer, or other shape, sintered at high temperatures, and finally coated with epoxy or glass. The resulting device exhibits an electrical resistance that varies with temperature. The T107B thermistor is a negative temperature coefficient (NTC) thermistor, whose resistance decreases with increasing temperature. The main advantage of thermistors for temperature measurement is their extremely high sensitivity. For instance, a high resistance thermistor can exhibit temperature coefficients of -10 kΩ/°C or more; in comparison, a 100Ω platinum resistance temperature detector (RTD) has a sensitivity of only 0.4 Ω/°C (Potter, 1996). The large change in resistance with temperature makes them very accurate devices- ±0.1ºC compared to ±2.0ºC for a thermocouple. Another advantage of the thermistor is its relatively high resistance. The T107B has an internal resistance of 250kΩ. This high resistance diminishes the effect of inherent resistances in the lead wires, which can cause significant errors with low resistance devices such as RTDs.

The major tradeoff for the high resistance and sensitivity of the thermistor is its highly nonlinear output and relatively limited operating range. The T107B probe can measure temperature between -35° to 50°C. this temperature range is well within those expected for this study.

Figure 5.18: Thermistor temperature probe model 107B Campbell scientific

Calibration

The temperature probes were tested in both cold and hot water to determine their accuracy. Values obtained from the probes were very comparable with those measured with a highly sensitive specialized digital thermometer. The probes were also checked after construction to ensure that the thermistor bead was not damaged during installation

Installation Procedure

For the temperature probes, small cavities were dug at the pre-determined location. The sensing heads was placed horizontally while ensuring that a "dew-loop" is created by dropping the cable lower than the sensing head. This is done to prevent water from flowing down the cable and finding its way onto the sensing head.

5.3.4 Data Acquisition Systems

Some of the instrumentation described in the preceding sections of this Chapter required high sampling rate to effectively capture the pipe and/or pavement response under truck loading while other measured static responses that can be captured at relatively slow sampling rates. For instance, the moisture and temperature probes can be sampled effectively at a relatively slow frequency, say 0.01Hz (1 sample every 100sec), without missing any critical information. However, the sampling rate required for the asphalt strain gauges and pressure cells to capture truck load response is much higher due to the transient nature of the traffic loading and pavement response. The duration of loading could be in the order of milliseconds. In the absence of traffic loading, it is equally important that the acquisition system be capable of long-term monitoring of pipe and pavement response to seasonal variability such as temperature and moisture which are rather slow events.

With the above requirements as a guide, the Data Acquisition System (DAS) needs for the project was grouped into two (a) Slow-sampling data acquisition and (b) Fast-sampling data acquisition. The fast-sampling data acquisition system have triggering capabilities such that sensor data are stored at a preset slower sampling rate (0.01Hz) in the absence of truck loading. Detailed discussion on the DAS is presented in the following sub-sections.

5.3.4.1 Slow-Sampling Acquisition Systems

Campbell-Scientific® and Lakewood Systems dataloggers were acquired and used successfully on previous field-scale projects conducted at University of Waterloo and it was decided to use these existing acquisition systems to collect and record data for slow-sampling instruments. The Campbell-Scientific® CR10X datalogger, Lakewood CP-XA Data Recording Module and Lakewood Systems R-X Ultra-Logger shown in Figure 5.19 were selected for the task.

The Campbell Scientific CRX10 data logger was used to monitor the temperature probes and TDR moisture gauges installed in the pavement. The sampling rate on the CR10X logger was

set at 0.0033Hz (1 sample every 5 minutes). Two Lakewood CP-XA Data Recording modules were used during the HDD pipe installation to record the pull-head load cell reading and pipe temperature at a frequency of 0.1Hz (1 sample every 10 seconds). While the Lakewood R-X Ultra-Logger was used to collected data from the drill rig and drill-fluid tank pressure transducers also set at a frequency of 0.1Hz (1 sample every 10 seconds).

CP-XA Data Recording Module

R-X Ultra-Logger

CR10X datalogger

Figure 5.19: Slow-sampling data acquisition systems

The Campbell-Scientific CR10X logger has the following key features and capabilities: 12-bit resolution analog to digital converter, 12 single-ended or 6 differential individually configured multiplexed analog inputs channels with scanning rate programmable to a maximum of 64Hz, inbuilt 2 Megabytes memory for active and user-stored programs, 3 onboard switched excitation voltage sources (2.5, 5, 12V), a serial I/O port and direct connection to PC through parallel port and bidirectional data transfer.

The Lakewood CP-XA Data Recording Module is a basic logger with only two analog input channels with 1Hz maximum scanning frequency and 32 Kbytes internal memory. The Lakewood R-X Ultra-Logger can be expanded to handle a maximum of 10 analog input channels at a maximum scanning rate of 1Hz and it has 32 Kbytes internal memory for data storage. Sensors connected with the Lakewood loggers are excited with on onboard power supply from an internal 2A hour rechargeable battery. The slow sampling acquisition systems

have remote access capabilities and they can be equipped with radio modem to communicate and transfer data wirelessly to a remote PC. The wireless option was not used for this project.

5.3.4.2 Fast-Sampling Acquisition Systems

Pipe and pavement instrumentation have to be sampled at high frequencies to capture the traffic loading. Two different data acquisition systems (DAS) namely SoMat 2100® field computer and SoMat eDAQ-plus® DAS, both manufactured by SoMat™ Products Division UK, were selected as fast-sampling DAS SoMat 2100® field computers were used primarily to monitor sensors placed in the HDD installed pipe, during and after the construction. A total of 19 sensors that include six pressure transducers, nine linear variable displacement transducers, four strain gauges were wired to two SoMat 2100 field computers during pipe installation.

SoMat 2100 field computer, Figure 5.20, was selected because of its compactness and low cost per channel amongst other advantages. The system comes in modules and each module has a dimension is 76 x 108 x 16mm (3" x 4.25" x 0.6") and weighs only 260grams (0.6lb). The SoMat 2100 systems used for this research each has five modules namely processors, power, communications, memory and utility (network) modules. For the HDD installation instrumentation, it was important that the data acquisition system is small enough to be easily placed inside the installed pipeline during HDD pullback operation as this minimized the need for long sensor-to-DAS connection cables and eliminates the risk of damaging the cables during installation. The SoMat 2100 system also has inbuilt wireless remote monitoring capability that allows monitoring of test progress in real time.

Each SoMat 2100 field computer system has twelve multiplexed 12-bit analog input channels and can condition signals from voltage output transducers and full bridge devices. The channels provide excitation to transducers and allow them to be connected directly to the module without external signal conditioning. SoMat 2100 connects to a PC via the com port for a bi-directional data transfer speed up to 115Kbytes/s and has 4MB of RAM for onboard data storage. The two SoMat 2100 systems were connected and time-synchronized together via RS422 communications cable. The easy-to-use window based Test Control Software (WinTCS) that comes with the acquisition system makes the configuration and control of the

system quite convenient. Its also eliminates the need to write laborious ‘code’ required to configure some DAS.

Figure 5.20: Somat 2100 Field computer data acquisition system

(a) eDAQ –plus data acquisition system

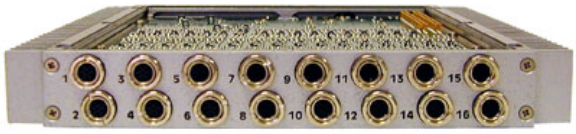

(b) High Level Simultaneous sampling board

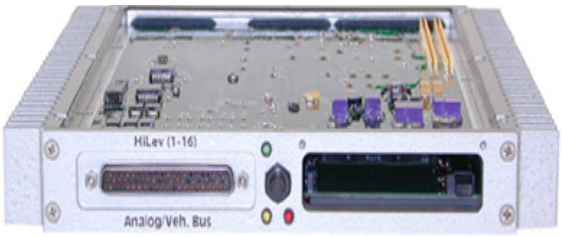

(d) High Level board

(c) Signal conditioning Smart modules

Figure 5.21: Somat eDAQ-plus Data acquisition system

Pipe and pavement instrumentation related to the open-cut HDPE pipe installation were monitored with SoMat eDAQ-plus® DAS, Figure 5.21. SoMat eDAQ system is a compact, rugged and modular DAS capable of collecting a wide range of signal types - including strain, analog to ±80V, digital, frequency and temperature directly from sensors. The eDAQ unit used for this research has the following modules: processor, high-level simultaneous sampling board and high level board. The speed of the processor is 266MHz with integrated floating point and 256MB on board DRAM for the operating system. The speed of the master sample clock is 100 kHz and it has a 2GB memory capacity for onboard data storage. The PC-to-eDAQ communication is via Ethernet 100BaseT and RS232 serial communication.

The high level simultaneous sampling board (HLS), Figure 5.21b, has 16 general-purpose analog inputs channels. Each input can be independently set to measure down to 3.8μV resolution or have a full-scale input range of ±80 volts. Each eDAQ system can accommodate multiple HLS boards and for very high channel count requirements, multiple eDAQ systems can be networked to obtain simultaneous sampling across all channels. Each channel has its own 16-bit *analog-to-digital converter* (ADC) running at a *frame check sequence* (FCS) master sample clock rate of 100kHz. The ADCs output is then down-sampled to the user-selected rate between 0.1 to 100,000 samples per second. The settings for full-scale range, sample rate, digital filtering, and transducer power voltage level are fully independent for each channel. That is, each of the 16 channels can collect data using 16 different sample rates, 16 different digital filters, and transducer power levels. Transducer power can be set from +3V to +28V in one volt increments with an accuracy of ±50mV. Each channel is power-limited to 400mW. Multiple transducer power outputs can be combined if more power is required to drive a transducer. Each channel has an input impedance of 10MΩ for ranges up to ±10V and 100kΩ for ranges greater then ±10V. Common mode input voltages of up to ±80V are allowable with the 100kΩ input impedance. Small conditioning modules called Smart Modules (Figure 5.21c) can be used to condition strain gauge and thermocouple inputs. The pavement sensors including asphalt strain gauges, granular aggregate strain gauges and earth pressure cells were connected to eDAQ-plus high level simultaneous board. This allowed for sampling up to 100 kHz and eliminated any form of data loss due to multiplexing for fast moving trucks.

The eDAQ High Level Board (HLB), Figure 5.21d, can be used to measure preconditioned signals in either ±10V or ±20V ranges. The HLB consists of 16 multiplexed, singled-ended channels. The 16 channels are multiplexed into a 16 bit A/D converter with a channel-to-channel skew of approximately 25μsec. There is an onboard excitation source of ±10V with 30mA output for sensor conditioning and the maximum sampling rate obtainable on the HLB is 2500Hz. Pipe instrumentation including strain gauges and linear variable displacement transducer attached to the open-cut buried pipe were wired to the eDAQ-plus high level board.

Test Control software (TCE) is the windows based software application used to set up and define test requirements in eDAQ DAS. TCE software was used to create the test setup files that defines and calibrates transducer channels; define DataModes and computed channels for online data calculations and analyses; specify triggering conditions for collection of test data; monitor test data using the TCE's run-time display; check test and memory status during data acquisition and initialize, start, stop and upload test data.

5.3.5 Power Supply and Management for Instrumentation

Power supply and management is an important aspect of field instrumentation and should be given careful attention during the planning stage especially for long-term monitoring in remote locations where electrical power supply is distributed. All the transducers/sensors and data acquisition systems employed for the research required some form of external power to operate effectively. The communication devices used for remote monitoring also need power to function. Power options that were evaluated for the project included commercial electrical power and solar power with batteries. Electrical power supply was judge to be the most reliable source requiring less maintenance. However, to physically connect to a direct dedicated electrical power source at the test site was found to be cost prohibitive. Hence solar power was selected as the viable and preferred power source for this project. Figure 5.22 show the solar panel used to charge the 12V deep cycle batteries.

Solar power can only support minimal loads and is typically not capable of sustaining heavy power consumption gauges and equipment. Hence, all the sensors and remote communication

devices used in this project have relatively low power consumption. Solar panels and the batteries are selected based on the following criteria a) average current drain of the system, b) the maximum time the battery must supply power to the system without being charged, and c) the location of the site. Solar panel specifications are presented in Table 5.2. The Solar panels continuously recharge two 12V deep cycle batteries.

Figure 5.22: Solar panel for recharging batteries at test site

Table 5.2: Specifications of the solar panels

Maximum Power output (Pp)	20W
Open Circuit voltage	18V
Voltage at load	12V
Current at load	1.17A
length	80cm
width	50cm
depth	5cm

There are other hardware components that are integrated into the power circuit to safely and effectively run the systems including charge regulator, safety disconnect switches, lighting arrestors and timer. The charge regulators prevent the batteries from overcharging or completely discharging. They also serve as low voltage disconnect and prevents voltage from flowing in the reverse direction from the batteries to the solar panel. Safety disconnect switches were installed as a means of shutting down power, during maintenance, without having to physically disconnect wires.

Power management and conservation becomes very important especially in the winter months when the duration of sunlight is limited. A programmable timer was installed to automatically turn the system off and on at predetermined time. The timer was programmed to turn the system ON continuously during daytime when the solar panel had adequate power to charge the batteries and then OFF when the sun set. To capture pavement behavior during night (or when the batteries are not being charged), the timer was programmed to turn the system ON for 10mins every hour and then shut down. Power was considerably conserved using this system.

5.3.6 Remote Communication and Real-time Monitoring System

A remote monitoring system was developed as part of the field instrumentation program with the following purposes. Firstly, to provide real time continuous monitoring and to automatically report any form of abnormalities within the instrumentation system. Secondly, to provide a real-time communication link between the University and the test site for easy data transfer.

The remote monitoring system shown in Figure 5.23 consisted of two parts: a) the host network system at the test site location and b) the client network located at the University. The host network consist of Ethernet enabled data acquisition systems and wireless communication devices. A Serial-to-Ethernet device was connected to the data acquisition systems with a RS-232 serial communication port to make them Ethernet ready. The conversion device used was the NPort-DE-311 serial-to-Ethernet device manufactured by

MOXA® and is shown in Figure 5.24. The NPort-DE-311 device provided seamless integration with serial device and Ethernet TCP/IP network.

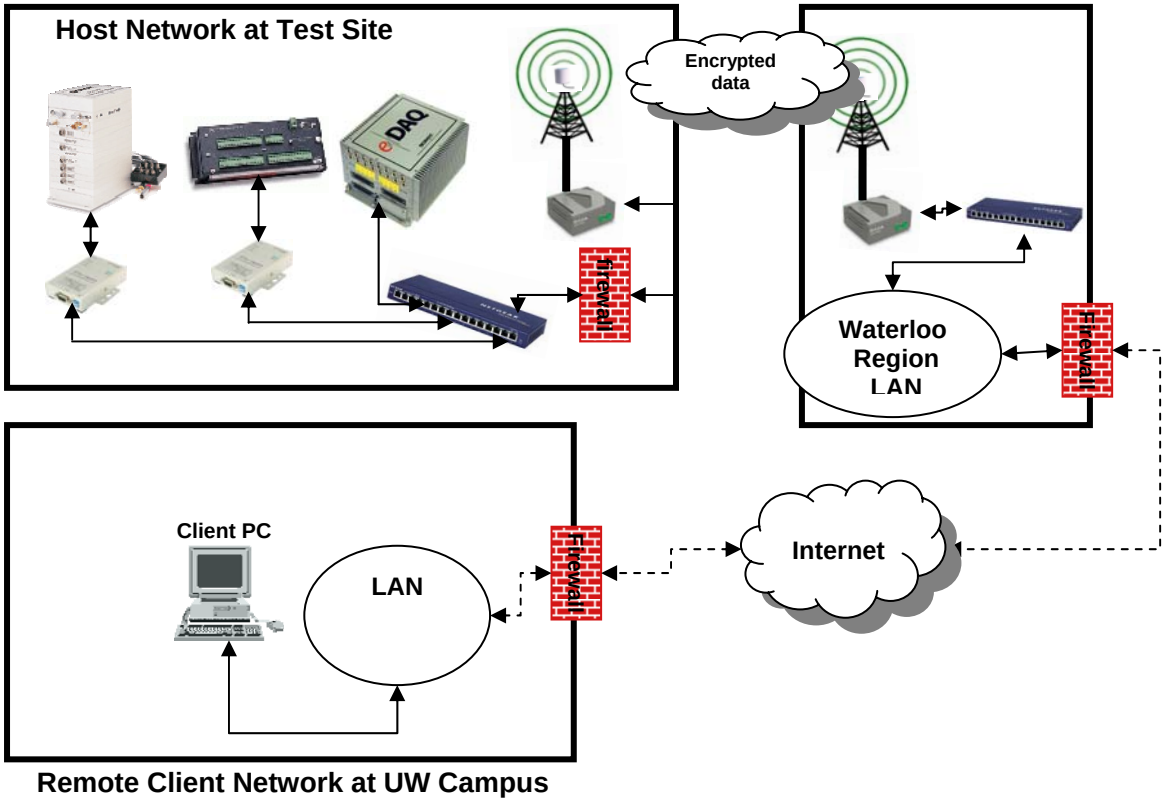

Figure 5.23: Schematic of developed secured remote monitoring system

Figure 5.24: Serial to Ethernet device model NPort-DE-311

The internet ready acquisition systems were each assigned an IP address and connected to a 10/100 Mbps Ethernet switch located inside the site trailer. The Ethernet switch was

connected to a D-Link DWL-G800AP wireless range extender device. The D-Link DWL-G800AP, shown in Figure 5.25, was a high-speed 802.11g wireless range extender capable of operating in two modes: Wireless Access Point or Wireless Repeater. Its wireless access point capability provides wireless communication access to the acquisition systems through the Ethernet switch. The DWL-G800AP features 128-bit WEP encryption, Wi-Fi Protected Access (WPA) and 802.1x user authentication to enhance the levels of data protection on the host network system. The high level of network security prevents unauthorized individuals from gaining access into the host network.

Figure 5.25: Wireless range extender device model DWL-G800AP

The strength and range of the wireless signal was enhanced by replacing the original antenna on DWL-G800AP wireless range extender device with D-Link ANT24-0801 antenna. The D-Link ANT24-0801 is a Pico Cell Patch Antenna for wireless data transmission and it provides 8.5dBi signal strength operating on 2.4~2.5 GHz ISM band (Industrial, Scientific and Medical). The Antenna provided wider range of wireless coverage and eliminated the cost of running standard cable lines to the closest internet access point. Another D-Link DWL-G800AP wireless range extender device also equipped with a Pico Cell Patch Antenna was connected to an Ethernet switch at the internet access point within the communication

network of the Regional Municipality of Waterloo located in a workshop about 500m away from the site trailer. Encrypted data was securely transmitted wirelessly between the site trailer and the receiving DWL-G800AP wireless at the workshop.

The client network mainly consist of dedicated computer with uniquely assigned IP address and privileges to tunnel through the firewall of the Municipality's communication network system. Each data acquisition system was assigned a specific external IP address that was mapped through the firewall to connect securely to the necessary communication port on the Host network.

The remote access considerably reduced the need for frequent site visit necessitated by the large quantity of data collected at the test site. Furthermore, problems at the test site such as low voltage output from the batteries, damaged sensor etc. were be promptly identified and fixed thereby minimizing instrumentation down-time and the loss of data. Other variations of this remote communication network, such as wireless phone modem could be used where internet access is not available.

5.4 Field-scale HDPE Pipe Installations

Two 200mm (8in) SDR-17 Ductile Iron Pipe Size (DIPS) high density polythene pipes were installed as part of the field-scale investigation. The basic geometric and material properties of the test pipes are presented in Table 5.3.

Table 5.3 Properties of HDPE pipe

Average wall thickness (mm)	13.5
Average outside diameter (mm)	230
Tensile strength at yield (MPa)	22
Modulus of elasticity Initial: short term (MPa) 50 years: long-term (MPa)	 758 200
Poisson's ratio	0.4

In April 2003, the first 200mm (8in) instrumented SDR-17 DIPS HDPE pipe was installed 1.52m (5ft) below the HL3-1 control test section using a horizontal directional drill. In October, 2003, a second 200 mm (8in) instrumented SDR-17 DIPS HDPE pipe was installed 1.67m (5.5ft) below the HL3-1 control test section using traditional open cut-and-cover construction technique. The locations of the two pipe installations are shown in Figure 5.2. The locations of the pipes were selected to have similar vehicle speed, drainage conditions and subsurface conditions.

5.4.1 HDD Pipe Installation

The directionally drilled installed pipe was pulled-in on April 30, 2003 by T.W. Johnston Ltd., London Ontario. The pipe length consist of four instrumented test sections, each approximately one metre (3.28ft) long, these test sections were fused together with other pipe sections to form a 22.9m (75ft) long continuous length of PE pipe. Pipe fusion and connection of sensor wires took approximately six hours to complete.

Using a Ditch Witch 2040 drill rig, a 125mm (5in) pilot bore was completed in 50 minutes. The drill was set back to ensure that the bore path under the test track was approximately horizontal and at the specified depth of 1.52m (5ft) and that the bore was above the landfill methane gas PE pipe collection conduit. The entire pilot bore was pre reamed using a 300mm OD Kodiak reamer shown in Figure 5.26. The instrumented 200mm (8in) DIPS HDPE pipe was installed behind the second pass of the 300mm (12in) Kodiak reamer. Drill fluid was pumped into the bore during the pilot bore, back-reaming and pipe installation. The water based drilling fluid mixture used consists of 225kg (500lbs) of BOREGEL™, 1.8 kg (4lbs) of No-Sag™ gel strength enhancer, and 5.4kg (12lbs) of QuikTrol™ mixed in 1400 litres (3700 gal) of water.

The design pumping rate and pullback rate were established to achieve a drilling-fluid to soil volume ratio of between 1.5 and 2.0 in accordance with good practice guidelines (Bennett et al, 2001). Depth, pitch and roll readings were recorded every 1.0m interval during the pilot bore. The HDPE pipe installation was completed in approximately 5 minutes. Greater detail

of the HDD pipe installed can be found in Knight et al (2004) and Adedapo and Knight (2005).

Figure 5.26: Kodiak reamer 300mm OD Diameter

5.4.2 Open-Cut Pipe Installation

On October 15 and 16, 2003, T.W. Johnston Ltd., London, Ontario installed the second 200mm (8in) DIPS HDPE pipe 13.1m (43ft) long, 1.68m (5.5ft) below the HL3-1 control test section. The centerline of the pipe is at station 122+8m which is 16.7m (54.7 feet) west of the HDD installation as shown Figure 5.2. The contractor was instructed to use "best construction practices" in accordance with the Ontario Provincial Standard Specifications for Pipe Sewer Construction by Open Cut Method (OPSS 410). The open-cut installed pipe has three 1m (3.28ft) long instrumented test sections. The sections were butt-fused together on October 15, 2003 and took approximately four hours to complete. Descriptions of the conventional HDPE pipe installation are presented hereunder.

Trench Excavation and Placement of Instrumented Pipe

The pavement was saw-cut 1.37m (4.5ft) on both sides of the proposed pipe centerline location using a gas powered circular saw (Figure 5.27) before excavating the asphalt concrete and granular layers to a depth of 1.82m (6ft) below the pavement surface (Figure 5.28). Samples of the granular layers were collected for soil classification and other laboratory tests. The excavation took approximately four hours to complete. A sketch of the trench geometry is provided in Figure 5.29.

Figure 5.27: Saw cutting of pavement with circular saw

Figure 5.28: Excavation of pavement with backhoe

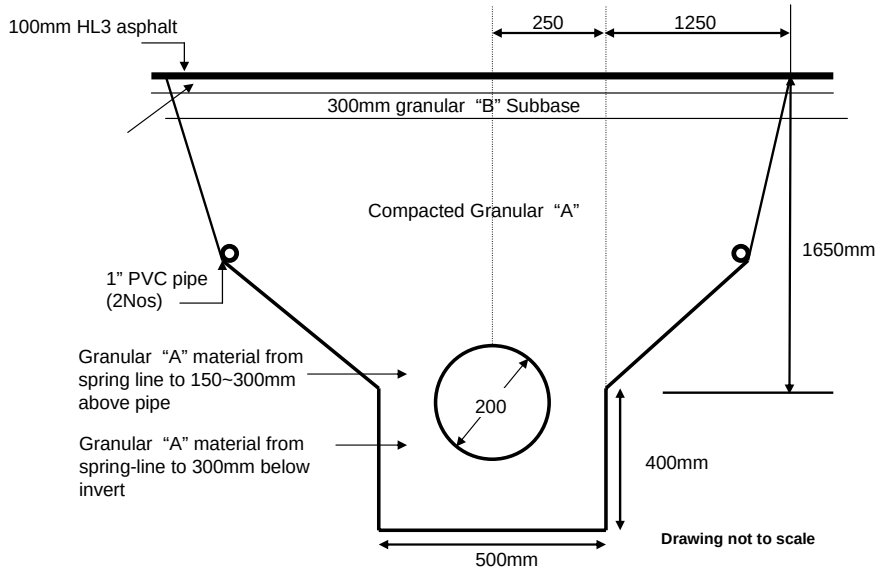

Figure 5.29: Open cut trench construction geometry and pipe location

The bedding for the HDPE pipe was prepared by placing two 150mm (6in) thick lifts of compacted granular "A" material on re-compacted and leveled subgrade. The subgrade was re-compacted using a hand operated tamping plate and the fused HDPE pipe was placed and set in position on the prepared bed within the trench with the backhoe.

During the late afternoon and evening of October 15, 42mm of rain was recorded at the test site. This heavy rainfall caused the walls of the unsupported open trench to slump onto the HDPE pipe and water to pond inside the trench. The trench was drained the following morning by opening the east end of the trench. Wet soil on the top of the pipe was removed and the pipe was taken out of the trench. All wet and soft soil was excavated until newly undisturbed subgrade was exposed. This additional excavation resulted in further widening and deepening of the trench. The pipe bedding was rebuilt on the newly exposed subgrade as described previously. The average insitu density and soil moisture of the bedding was determined to be 21.25 KN/m^3 and 9.3% respectively using Troxler Model 3440 nuclear soil moisture-density gauge.

Pavement Restoration

Granular A material was placed around and over the 200mm HDPE pipe. Additional care was taken to ensure that the soil material beneath at the haunch of the pipe was compacted well. The subbase and base material consist of 300mm and 200mm thick granular B and granular A respectively. The granular materials were placed in lifts 150 to 200mm (6 to 8in) thick and compacted mechanically using a portable engine driven pneumatic vibratory plate. The average insitu density of the soil immediately below the subbase and on top of the subbase was determined to be 20.5 and 21.75 KN/m^3 respectively and the insitu moisture content was 7.6 and 6.8% respectively.

The trench reconstruction took approximately five hours. Due to the small quantity of asphalt required for the pavement restoration and year end commitments by the contractor, the trench was not covered with asphalt concrete until November 12, 2003. The final trench restoration consisted of re-compacting and leveling granular A base course and laying approximately 100mm (4in) of HL3 asphalt in a single lift.

5.5 Pavement Monitoring

The condition of the pavement in the vicinity of the installed pipe was observed prior to and after pipe installations to identify any changes that may have resulted from the installations. The pavement was also examined throughout the long-term monitoring period to determine the influence of pipe installations on the pavement structure performance. Prior to pipe placement, the elevation survey grid 0.5 by 0.5m (1.5 by 1.5 feet) was setup on the asphalt surface. The survey baseline was set along centre line of the pipe installation and the grids were surveyed using a Total Station prior to, during, and following pipe installation.

Ground penetration radar surveys were completed prior to and following pipe installations to determine any change in the subsurface condition that may be attributed to the installation. CPATT regularly conduct IRI survey, Falling Weight Deflectometer (FWD) and Distress surveys on the test track as part of the on-going evaluation for the asphalt mixes used on the test track pavement. Field data collected near the vicinity of the pipeline were examined and

compared with those away from the influence of the installation to assess any change in pavement performance that may be attributed to the pipe installation.

5.6 Results of HDD Pipe Installation

The HDD pilot bore, reaming and pullback operations were completed successfully without any inadvertent returns observed. Results obtained during the HDD pipe installation included drilling fluid and bore slurry properties, drill-rig efforts, bore slurry pressures, installation induced pipe strains and deflections, and ground movements. Unfortunately, the pull load exerted on the pipe during installation was not captured by the Lakewood data acquisition placed inside the pulling head as the data logger was accidentally damaged during the pipe-fusion process and this was unknown until the pipe installation was completed. Drilling times for the HDD installation are provided in Table 5.4.

Table 5.4: Drilling times for HDD installation

Rod #	Time/rod min	Time/rod sec	Distance (ft)	Distance (m)
1	4	54	10	3.0
2	4	55	20	6.1
3	5	52	30	9.1
4	5	56	40	12.2
5	2	53	50	15.2
6	2	50	60	18.3
7	4	47	70	21.3
8	4	12	80	24.4
9	4	21	90	27.4
10	3	16	100	30.5
11	2	15	110	33.5

5.6.1 Drill Rig Efforts

The HDD drill rigs are typically equipped with hydraulic pressure gauges that provide that driller with an indication or measure of resistance being encountered by the drill rig. Driller traditionally use the feedback from the gauges to estimate the amount of force imposed on the

product pipeline being pulled into the bore. Although the actual amount of load imposed on the pipe is not explicitly indicated by the gauge, previous field investigations have shown that there is a good correlation between pull load exerted on the pipe and the thrust (or pullback) gauge reading (Knight and Duyvestyn, 2001 and Knight and Adedapo, 2002).

The drill rig used for the HDD installed was instrumented with pressure transducers installed on the drill rig thrust feed and return hydraulic pressure lines to capture the effort exerted by the rig during drilling and pipe pullback. The difference between the two pressure transducers readings, termed 'differential pressure', gives an indication of the net work done (or force exerted) by the drill rig on the product pipeline being installed. Differential drill rig thrust (and/or pullback) obtained from the feed and return hydraulic pressures are provided in Figure 5.30 through Figure 5.32 for the pilot bore, pre-reaming, and pipe pullback stages, respectively. Pressure spikes on the Figures are attributed to advancing/reversing of drill rig thrust carriage assembly, addition and removal of drill rods, application of torque to tighten/loosen drill rod connections, and steering corrections.

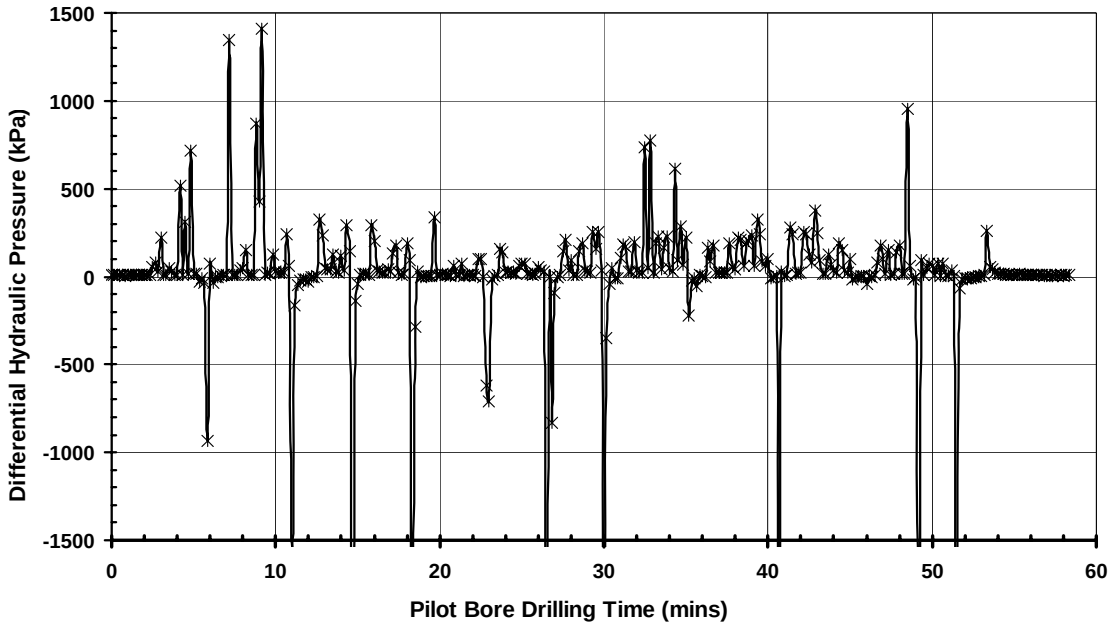

Figure 5.30: Differential drill rig thrust during HDD pilot bore

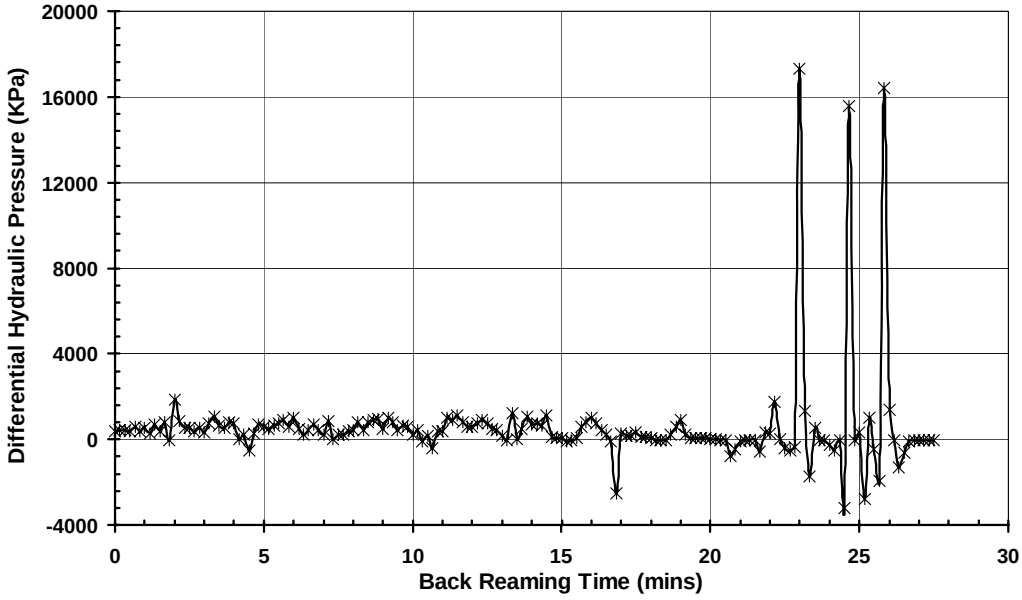

Figure 5.31: Differential drill rig effort during HDD back reaming

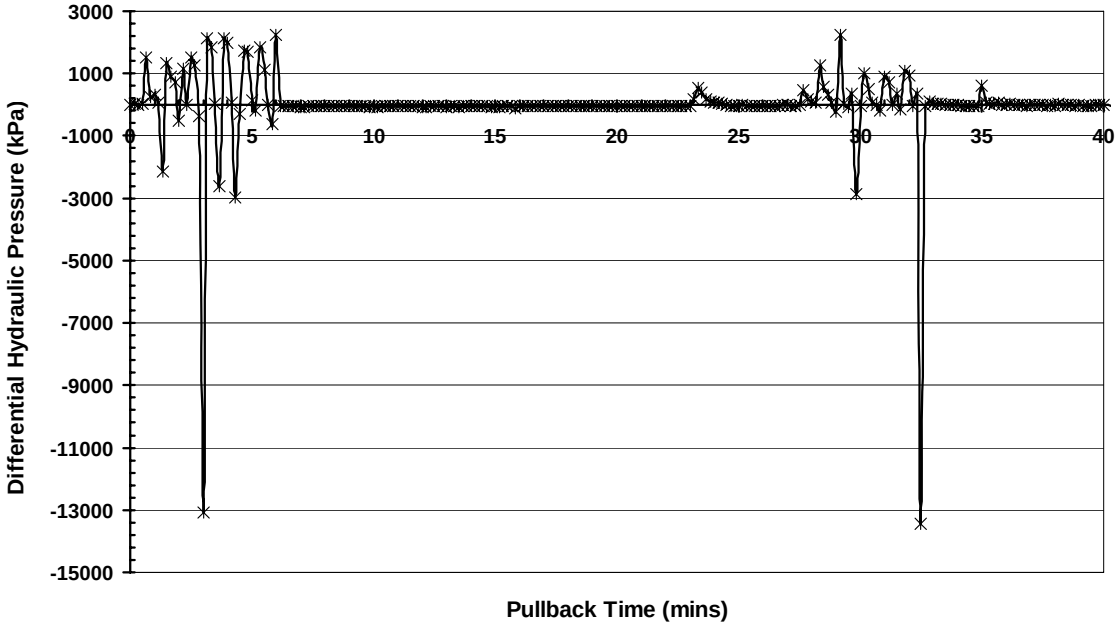

Figure 5.32: Differential drill rig effort during HDD pipe pullback

The drill rig effort required to advance the pilot bore from the entrance to the exit location varied approximately between 120 and 1410 kPa, Figure 5.30. The hydraulic pressure spikes recorded at approximately 7mins and 32mins into the pilot bore drilling are attributed to directional changes where the drill pipe and steering tool were thrust into the native soil without rotation. The drill rig effort required to ream (expand) the pilot bore from 125mm diameter to 300mm diameter was generally higher than effort exerted in creating the pilot bore owing to the additional volume of soil cutting. The differential hydraulic pressure recorded during the reaming process varied approximately between 500kPa and 17.3MPa, Figure 5.31. The high pressures recorded at approximately 23mins into the reaming were due to the presence of a vertical curve. The curve was negotiated to avoid an existing HDPE methane gas collection pipeline and additional thrust was required for directional changes to maintain bore alignment.

Compared to the effort required during the first reamer pass, a lower drill effort, generally below 2MPa, was required to pull the 300mm diameter reamer through the bore while concurrently pulling the 200mm diameter product pipe into the bore (Figure 5.32). There were no noticeable spikes in hydraulic pressure recorded during the pullback operation and the pipe was pulled into place with a maximum drill rig effort of approximately 2.2MPa. The pipeline pullback operation was stopped once the pipe was pulled through the roadway to the side slope of the Southbound traffic lane. A ditch was excavated to facilitate the cutting off of the pulling head and retrieval of the instrumentations (Figure 5.33). This stop time account for the drill rig inactivity period shown in Figure 5.32 between 6.5 and 27mins into the pullback operation. Figure 5.32 show that very little pull force was required to install the pipe.

5.6.2 HDD Installation Induced Deflections

Each test section consist of three linear variable displacement transducers (LVDT) oriented at plane 0°-180° between the crown and the invert to measure the diametric change between the pipe crown and invert, 90°- 270° between the springlines to measure the diametric change between the springlines and 45°-225° to measure the oblique plane diametric change as shown in Figure (5.5). The initial pipe diameters were measured in the laboratory prior to the

placement of the LVTD within the test sections and were taken as the initial pipe diameters for each test section and used as a basis for calculating HDD installation ring deflection.

Figure 5.33: Detachment of Pull head test section

The measured changes in pipe diameter during installation are provided in Figures 5.34 through 5.36; the resolution of the LVDT output signal as shown on the plots is approximately ± 0.15mm. Negative values indicate a reduction in the diameter of the pipe. The maximum observed diameter changes during installation and at various times following the installation are provided in Table 5.5. Test sections CO, WL and EL were located 3m, 12.5m and 16.5m behind the pulling head respectively, test sections WL and EL lagged test section CO by approximately 1.5 and 2.5 minutes respectively during installation.

The maximum change in diameter recorded during the installation occurred as the pipe was pulled into the bore through the entrance curve askew (sideways); the pipe experienced a reduction of -0.89mm in the horizontal diameter and a corresponding extension of +0.82mm in the vertical diameter (i.e. 0° - 180° plane).

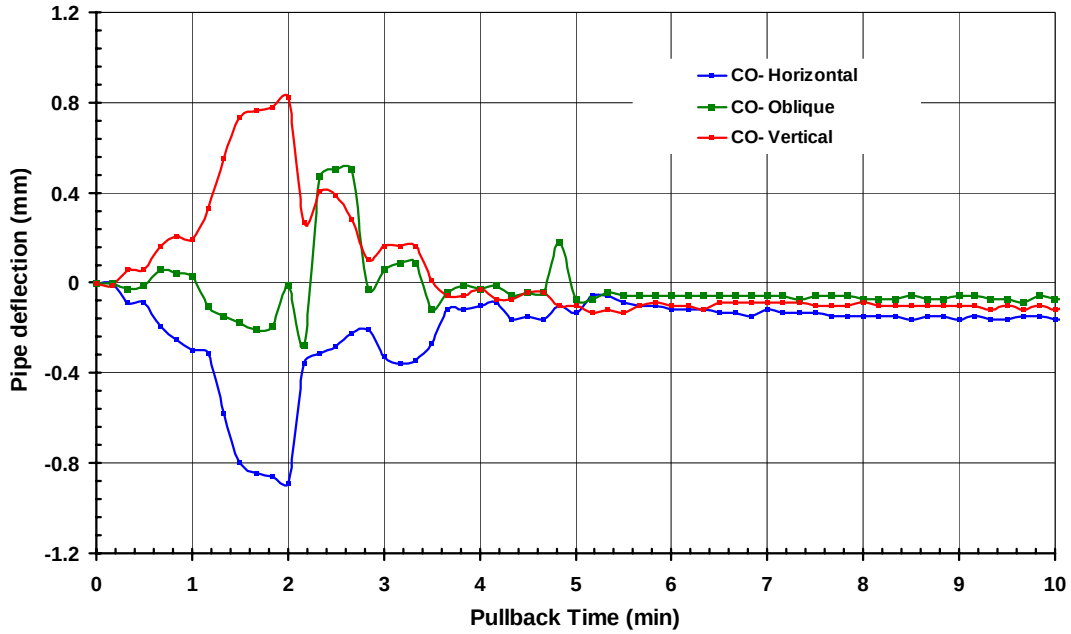

Figure 5.34: HDD installation induced deflection (CO Test Section)

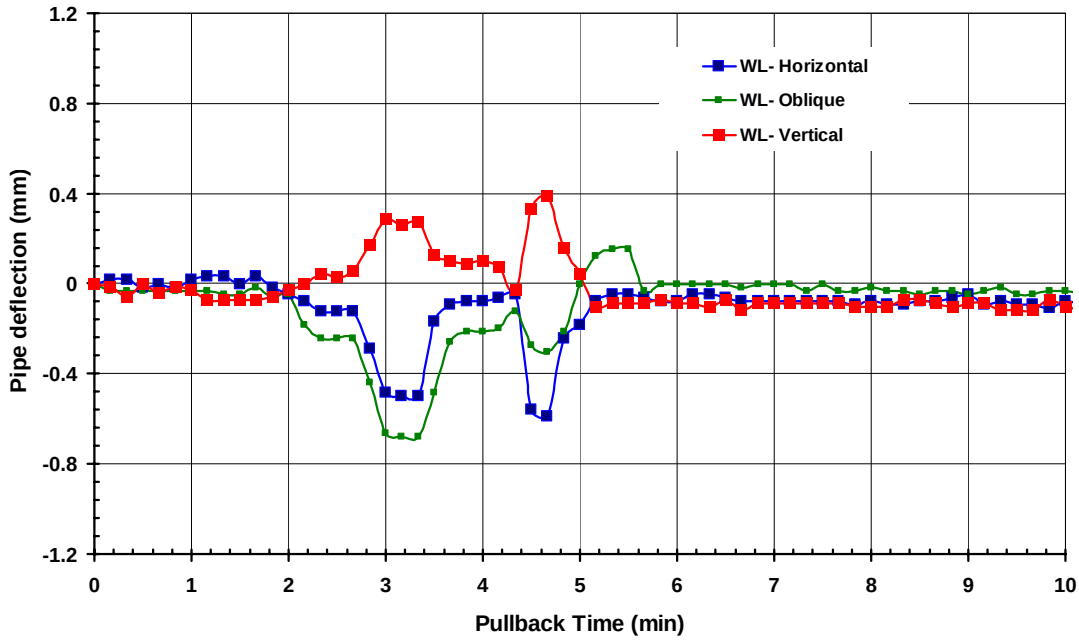

Figure 5.35: HDD installation induced deflection (WL Test Section)

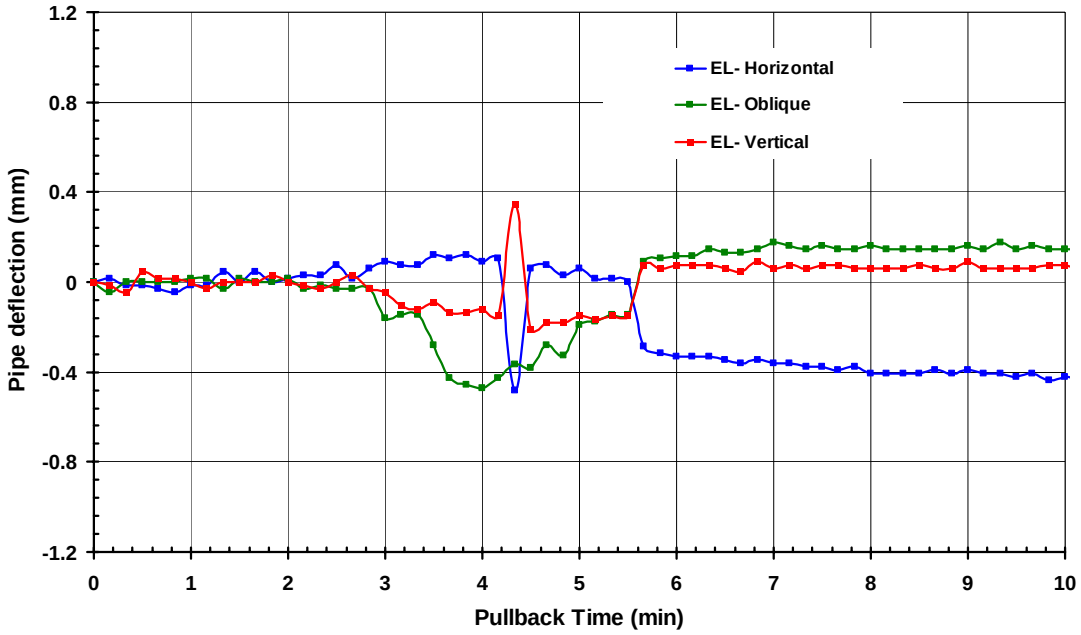

Figure 5.36: HDD installation induced deflection (EL Test Section)

The pipe strain data showed similar response during the same instance. The pipe diameter rebounded as the test section moved along the horizontal section of the bore. However, the recovery was not sufficient to restore the pipe to its pre-installation diameter. Similar trends were observed at the WL and EL test sections.

Table 5.5: Measured HDD installation induced ring deflections

		CO (mm)	WL (mm)	EL (mm)
Installation (entrance curve)	0°- 180°	+0.82	+0.39	+0.35
	45°- 225°	+0.50	-0.68	-0.47
	90°- 270°	-0.89	-0.59	-0.48
30 minutes after installation	0°- 180°	-0.13	-0.14	+0.03
	45°- 225°	-0.10	-0.09	+0.21
	90°- 270°	-0.19	-0.14	-0.44
60 minutes after installation	0°- 180°	+0.50	-0.14	-0.12
	45°- 225°	-0.18	-0.14	-0.15
	90°- 270°	-0.79	-0.20	-0.26
100 minutes after installation	0°- 180°	+0.52	-0.13	-0.12
	45°- 225°	-0.13	-0.16	-0.15
	90°- 270°	-0.79	-0.24	-0.26
10000 minutes after installation	0°- 180°	+0.65	-0.04	-0.12
	45°- 225°	+0.25	-0.21	-0.14
	90°- 270°	-0.85	-0.37	-0.25

However, due to short distance traveled through the bore, the EL test section was not able to recover from the ovalization induced at the entrance curve before the completion of the installation.

The change in pipe deflection data presented in Table 5.5 showed that the CO test section experience a significant change in deflection between 30 and 60 minute following pipe installation, Figure 5.37. The sudden change in pipe diameter around 38 minutes after the completion of the installation shown in Figure 5.37 was accidentally caused by the backhoe operation during restoration of the temporary ditch (shown in Figure 5.38) created along the drill to expose the methane gas pipes and facilitate retrieval of instrumentation placed inside at the pulling head. Generally, the deflections induced on the HDD installed pipe were very small and recoverable.

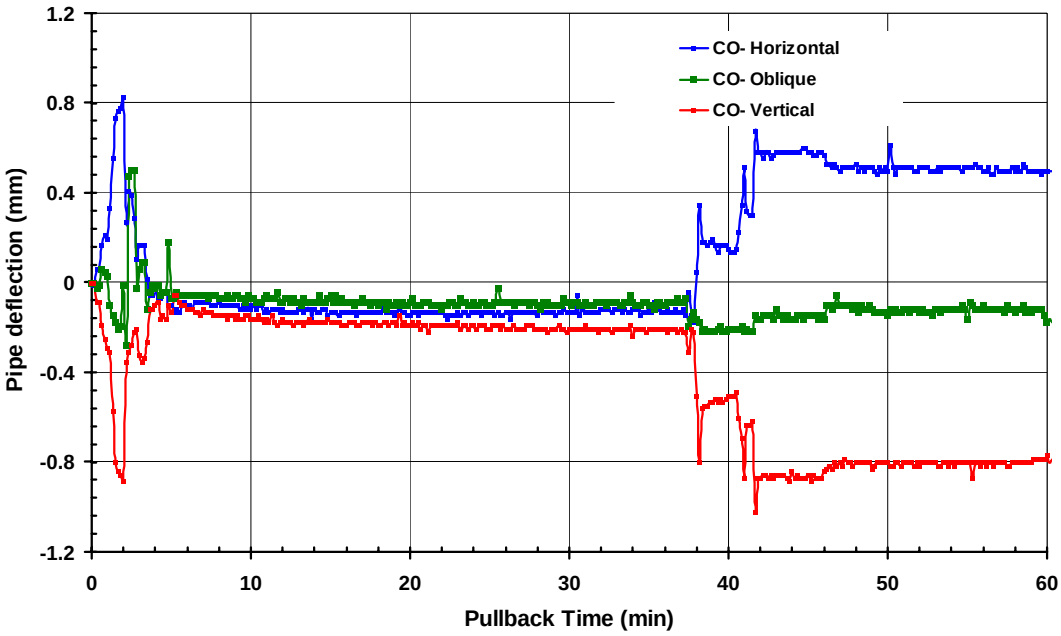

Figure 5.37: HDD pipe deflection 60min after installation (EL Test Section)

Figure 5.38: Backhoe inadvertently caused additional pipe deflection on CO test section

5.6.3 HDD Installation Induced Pipe strains

The product pipe is subjected to both axial and bending strains as the pipe is pulled into the bore during HDD installation. The axial strains develop in response to axial loading (pulling forces) imparted by the drill rig while bending strains develop as the pipe is forced to negotiate changes in bore trajectories. In addition, torsion strain may also develop if the pipe rotates unevenly throughout the bore. This type of strain is prevented or minimize with the use of a swivel.

The axial strain imposed on the pipe during pipe pullback was monitored and are shown in Figures 5.39 through 5.41. The following observations were made:

- The product pipe experienced the greatest strain when negotiating the entrance curve.
- The gauges placed at the crown and the invert showed similar trends but opposite signs when negotiating the curve.

- The crown of the pipe experienced tensile strain when negotiating the concave curves at the entrance and exit point and experienced compressive strains when the slight convex bore curve is negotiated.
- The invert of the pipe experienced compressive strains when concave bore curves are negotiated and tensile strains when convex bore curves are negotiated.
- The gauges placed along the springlines showed the highest strain when the pipe negotiated the entrance curve.

Review of the field record found that the product pipe went into the bore askew due to space limitation near the pipe entrance location as showed in Figure 5.8. This resulted in high bending strain on the sides of the product pipe. The bending strains were eliminated after the pipe completed the entrance curve leaving the pipe with mainly axial strain.

The tensile strain on the pipe reached a maximum value of about 5700 microstrain at the entry curve, and then decreased to around 710microstrain along the horizontal section and 830microstrain at the exit curve. The compressive strain on the pipe reached a maximum value of about 5100 microstrain at the entry curve, decreased to around 480microstrain along the horizontal section and approximately 650microstrain at the exit curve. The slight difference in the magnitude between the tensile and compressive strains may be attributed to a slight pipe rotation and the attached strain gauges so that they are not directly opposite each other. A summary of the maximum compressive and tensile strains observed during pipe installation at various locations along the bore are provided in Table 5.6. Substantial amount of the strains induced on the pipe during the installation were recovered following the installation as the pipe relaxed following the installation.

Table 5.6: Summary of strains observed during HDD installation at various locations

Location within bore	**Compressive Strain (με)**	**Tensile Strain (με)**
Entry Curve	5100	5700
Horizontal section	480	710
Exit curve	650	830

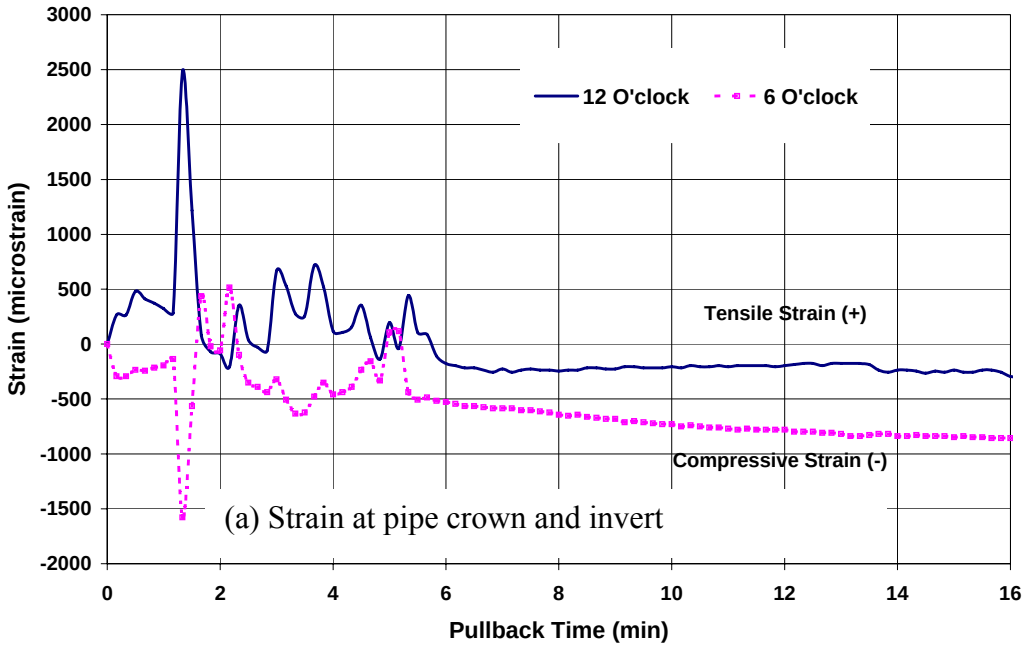

Figure 5.39: Installation induced pipe strain on HDD pipe at crown and invert location

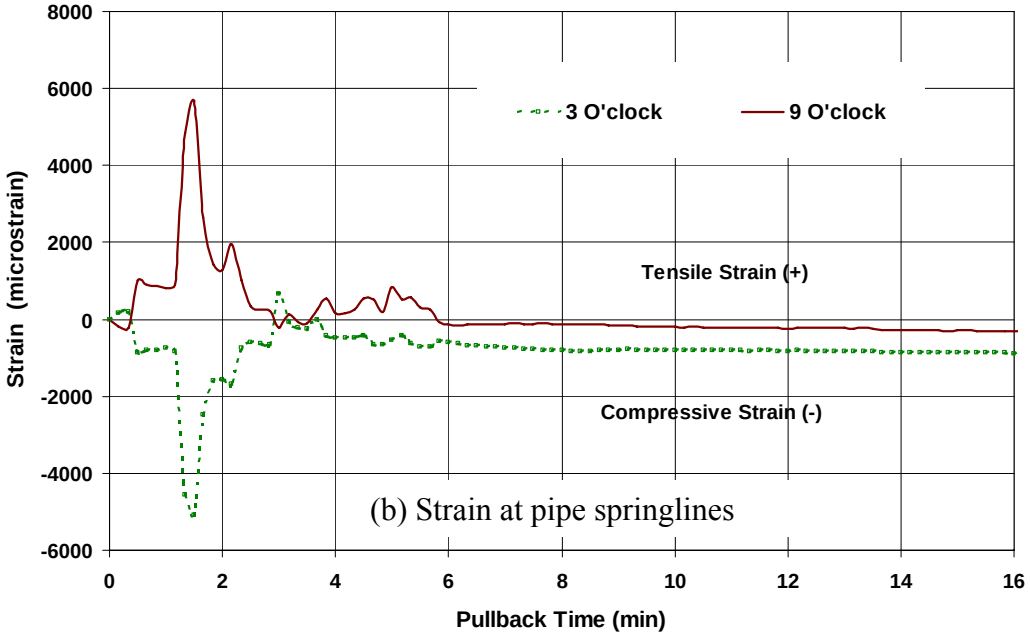

Figure 5.40: Installation induced pipe strain on HDD pipe at springline

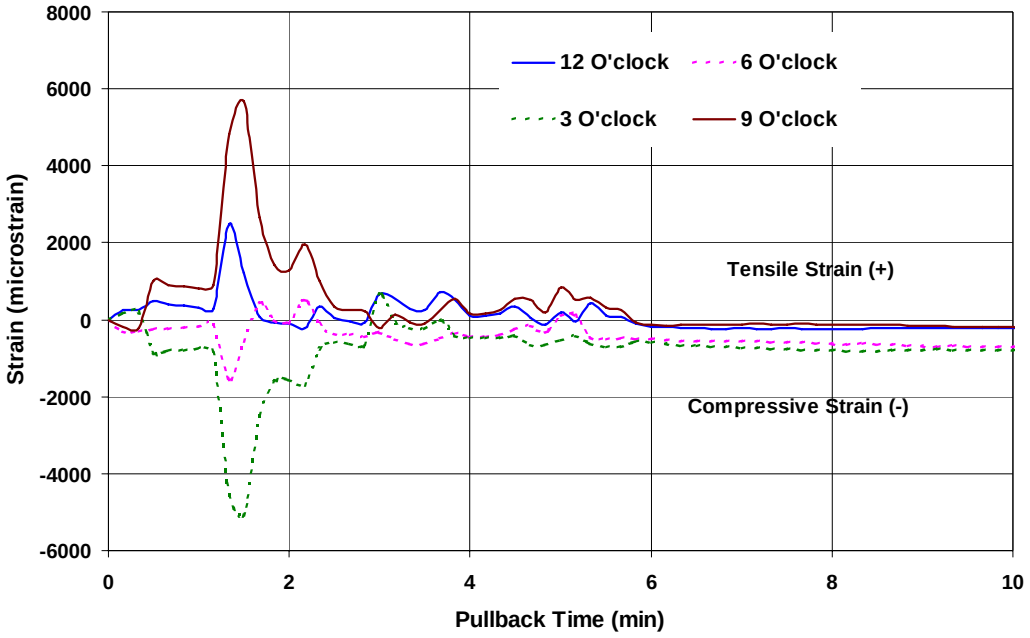

Figure 5.41: Installation induced pipe strain on HDD pipe (all sensors)

5.6.4 Bore Slurry Pressures

The bore slurry fluid pressures measured at the pipe pull head, WL and EL test sections during the pull back are shown in Figures 5.42, 5.43 and Figure 5.44 respectively. These fluid pressures represent pressure observed near the crown and the springlines of each test section. As stated earlier, the pipe installation consisted of installing a 200mm DIPS HDPE product pipe behind a 300mm (12 inch) reamer in an already pre-reamed 300mm (12 inch) bore. Hence no significant pressure build-up in the bore is expected during the pipe installation. The maximum pressure recorded was 21KPa (3 psi) at the crown of the pulling head during entry curve negotiation. Some of the factors that contributed to the significantly low slurry pressures observed during pipe pullback include completely pre-reaming the bore to its final diameter of 300mm (12 inch) prior to product pipe pull back, reduced solids contents within the bore slurry due to additional injection of drilling fluids into the bore through the reamer during pullback, and the relatively short distance between the entrance and exit points.

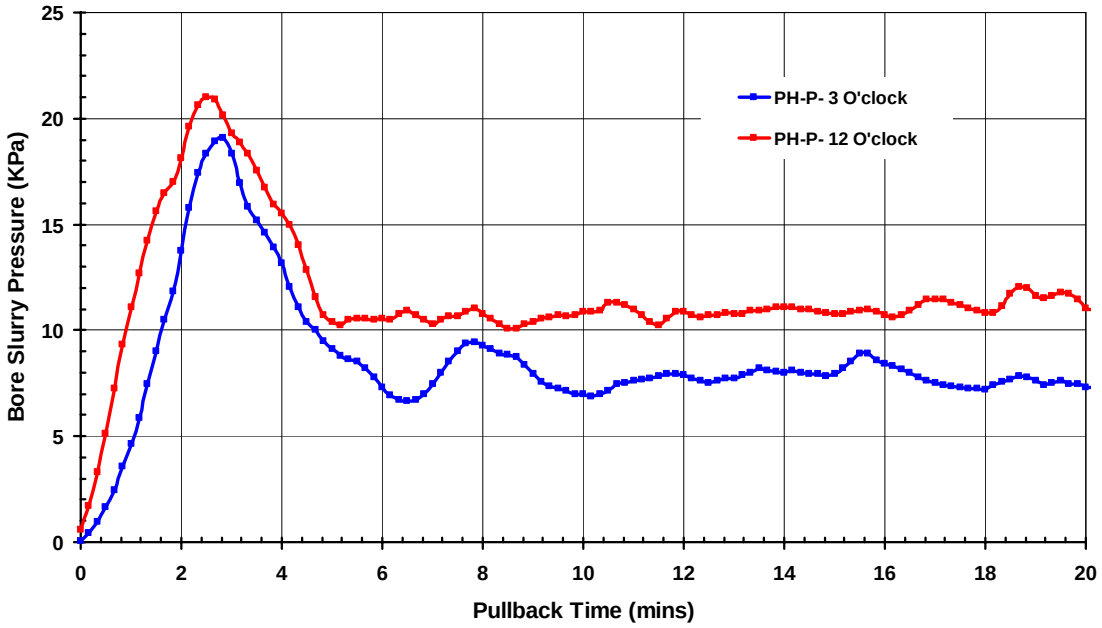

Figure 5.42: Bore slurry pressure during HDD installation (Pull-Head Test Section)

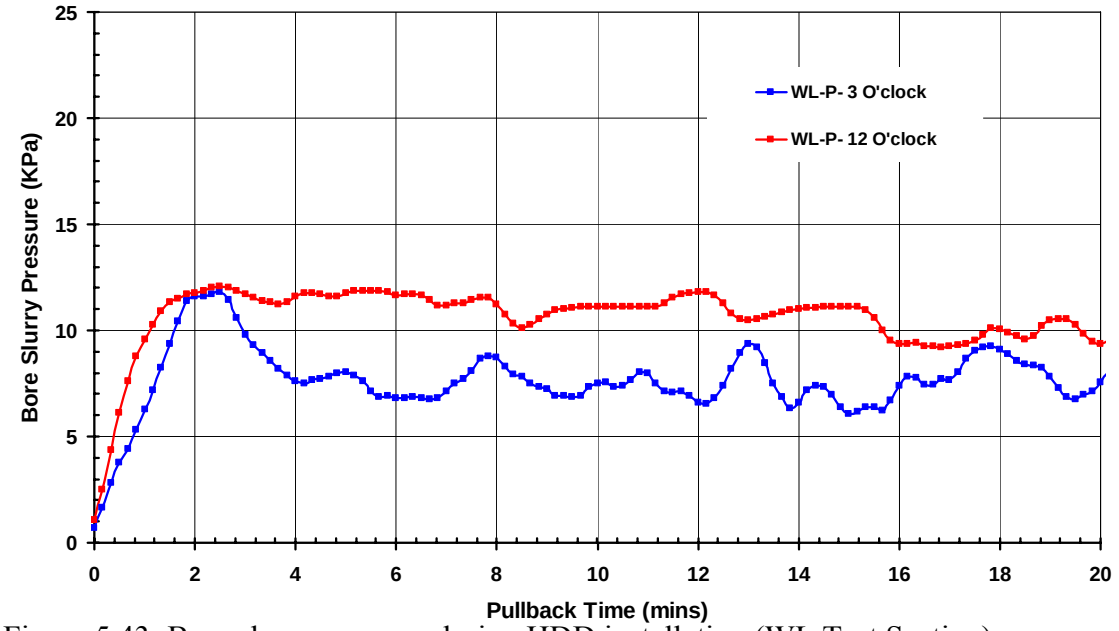

Figure 5.43: Bore slurry pressure during HDD installation (WL Test Section)

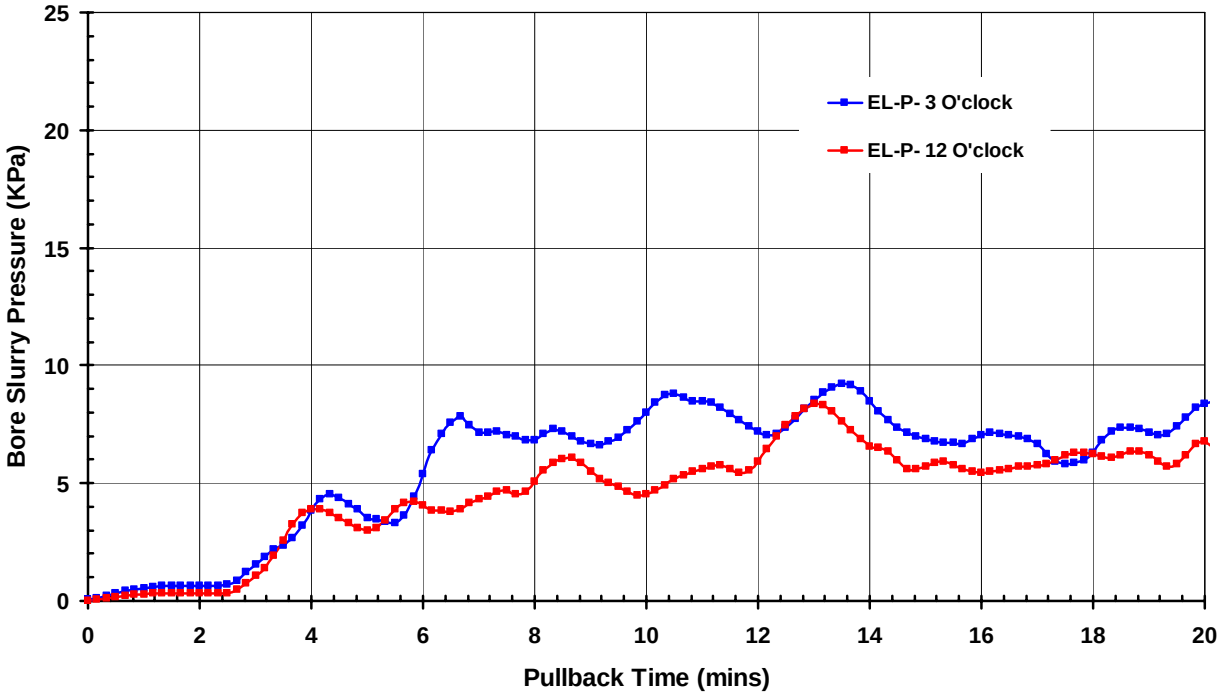

Figure 5.44: Bore slurry pressure during HDD installation (EL Test Section)

The introduction of additional drilling fluid into the pre-reamed bore during pipe insertion increased the proportion of the carrier fluid to soil cutting that significantly decreased the solid content of the bore slurry. This reduction in solid content resulted in a sharp decrease in density and viscosity of the slurry and aided slurry flow at low fluid pressure. The absence of slurry pressure build-up in the bore during pullback demonstrate the ability of reducing risk associated with inadvertent return/hydrofracture events by completely pre-reaming the entire bore path to its final diameter prior to installing the product pipe.

The pressure transducers placed at the crown and springline showed similar response. The bore slurry pressure data indicate there was a pressure gradient between the pulling head and the EL test section with the highest and lowest bore pressures shown at the pulling head and EL test section respectively.

5.6.5 Drilling Fluid and Bore Slurry Properties

Eight raw drilling fluid and bore slurry samples were collected during the HDD installation. Description of the samples including when and where they were collected are provided in Table 5.7. Samples A1 to A3 represent raw drilling fluids collected from the drill-fluid tank prior to pumping into the bore. Measured properties for the raw drilling fluid including density, pH, sand content, funnel viscosity, and gel strength are provided in Table 5.8. Samples B1 to B3 represent slurry returns collected at either bore entrance or exit locations during pre-ream operation and Samples C1 and C2 are slurry samples retrieved during product pipe pullback at bore entrance location. Measured properties of these slurry samples are provided in Table 5.9. A summary of typical drilling mud properties for cohesionless soils are summarized in Table 5.10.

Table 5.7: Description of Drilling fluid and Slurry Samples

Sample	**Drilling Phase**	**Description**
A-1	Pilot Bore	Mud tank
A-2	Pilot Bore	Mud tank
A-3	Pilot Bore	Mud tank (after adding QUIK-TROL®)
B-1	300mm Back Ream	Slurry returns at exit location
B-2	300mm Back Ream	Slurry returns at entrance location
B-3	300mm Back Ream	Slurry returns at exit location
C-1	PIPE PULLBACK	Slurry returns at entrance location
C-2	PIPE PULLBACK	Slurry returns at entrance location

Table 5.8: Raw Drilling fluid test results

Sample	Density (g/cm^3)	pH	Funnel Time (sec)	Sand Content (%)	Filter Cake thickness (inches)	Filtrate Volume (mL/15min)	Filtrate Volume (mL/30 min)
A-1	1.02	8.5	37	<1.0	<1 mm	12	17.5
A-2	1.03	9	39	<1.0	< 1mm	12.5	17
A-3	1.05	9	>60	<1.0	~1.5mm	9.5	13

Table 5.9: Bore slurry test results

Sample	Density (g/cm^3)	pH	Sand Content (%)
B-1	1.85	7.0	>25
B-2	1.75	7.5	>25
B-3	1.80	7.5	>25
C-1	1.32	7.0	12
C-2	1.29	7.0	10

Table 5.10: Typical raw drilling fluid properties (Bariod, 2002)

Mud Property	**Typical Value**
Density (g/cm^3)	1.01 to 1.08 (8.4 to 9.0 lb/gal)
Viscosity (Marsh Funnel) sec/quart	32 to 40
Filtrate Volume (cm^3)	10 to 15
Cake Thickness (inches)	Film to 2/32 inches (film to 1.6mm)
Sand Content (%)	< 2.0
pH	8.5 to 9.5
Plastic Viscosity (cP)	< 10.0
Yield Point ($lbs/100\ ft^2$)	< 10.0

As the reamer enlarges the bore, soil cuttings are produced and mixed with the raw drilling fluid pumped into the bore through the orifices on the reamer. Incorporation of the cuttings into the raw drilling fluid causes the density and viscosity of the slurry mixture to increase. The volume of cuttings mixed into the slurry (and hence the percent solids) is dependent on the reaming rate, drilling fluid pumping rate, and magnitude of the size of the reamer. The reamer size determines the quantity of solids that are produced as the bore advanced. The raw drilling fluid pumping rate dictates how much carrier fluid is made available for mixing by the reamer. The drilling rate is set such that there is a balance between the volume of drilling fluid pumped into the bore through the reamer and the volume of soil cuttings to ensure the percent solids within the slurry are less than 33% (i.e. ratio of volume of drilling fluid to soil is approximately 2:1). This balance must be made during all reaming passes and during the product pipe installation. Faster reaming rates require larger drilling fluid pumping rate and large reamer size require higher drilling fluid pumping rates or slower reaming rates to maintain desirable drilling fluid properties. During product pipe installation, higher slurry density and viscosity may lead to increased loads as the product pipe displaces the heavier/thicker bore slurry (Knight et al, 2002).

The density of the raw drilling fluid samples A-1 to A-3 (1.02 to 1.05 g/cm^3 or 8.51 to 8.76 lb/gal) are within the range of typical drilling fluid density (1.01 to 1.08 g/cm3 or 8.43 to 9.01 lb/gal) (Bariod, 2002). The higher densities measured in the slurry samples (1.29 and 1.85 g/cm^3 or 10.77 to 15.43 lb/gal) are attributed to the inclusion of soil cuttings into the drilling fluid. The variance in measured densities of the samples is attributed to variation in lithology, reaming rate, and fluid pumping rate. As anticipated the densities of the slurry samples collected during pipe pullback (C1 and C2) are lower than those collected during prereaming operation (B1 to B3). The same reamer size was used for the preream and the pullback hence there was no additional soil cuttings introduced into the bore. The additional drilling fluid pumped into the bore during pullback resulted in dilution of the existing slurry within the bore.

The raw drilling fluid used during the installation met the desirable sand content limits of less than two percent (Bariod, 2002). The values of pH for the raw drilling fluid samples (samples A) are also within desirable pH level of 8.5 to 9.5 for ideal drilling fluid (Bariod, 20021). The

sand content of the slurry returns reflect the lithology of the subsurface soils- sands contents of slurry samples exceed 10 percent. A total of three filter cake thickness and filtration test were completed on the raw drilling fluid samples. Samples A-1 and A-2 produced an identical filter cake thickness of <1.0mm (1/32 inch) while sample A-3 produced a slightly thicker filter cake of 1.5mm (2/32 inch). Sample A-3 also produced lower volume of filtrate 9.5ml per 30 minutes compared to 12 ml per 30 minutes produced by samples A-2. The variation in the mud properties is due to the addition of QUIK-TROL® to sample A-3. QUIK-TROL® is modified natural cellulosic polymer and it provides filtration control in most water-based drilling fluids. It was added to minimize the loss of fluid into the granular soil formation.

Funnel viscosity measurements are influenced by the gelation rate, density and the effective viscosity at the rate of shear prevailing in the funnel orifice (Darley and Gray, 1991). The addition of QUIK-TROL® increased the funnel viscosity of the drilling fluid by more than 20 seconds. In addition to providing filtration control, QUIK-TROL® also increased the gel strength of the drilling fluid which resulted in the observed longer Marsh Funnel time.

5.6.6 Ground Surface Movements during HDD Installation

Elevation survey grid 0.5 by 0.5m (1.5 by 1.5 feet) was established on the asphalt pavement surface over the pipe alignment to monitor the influence of each stage of the installation process. The survey baseline was set along centre line of the pipe installation. The grid was surveyed using a Total Station prior to, during, and following the completion of the drilling processes and pipe installation. Survey results showed that the ground surface elevations within the survey grid did not change during the installation. Recorded movements were in order of less than 1.0mm (0.04 inch). This was within the accuracy of the total station measurements.

5.7 Results of Open-Cut and Cover Installation

Similar to HDD pipe instrumentation, each test section of the open-cut HDPE pipe had three linear variable displacement transducers positioned in the pipe to measure the vertical, horizontal and oblique plane diametric changes as shown in Figure 5.5. The arrangement of the strain gauges differed from that of the HDD installed pipe oriented to measure the circumferential strain in the pipe. The rational for the location and orientation of the gauges can be found in Section 5.3.2. The results obtained from the open-cut and cover installation are presented and discussed in this section.

5.7.1 Cut and cover Installation Induced Pipe Deflection

The initial pipe diameters were measured in the laboratory prior to the placement of the LVDTs within the test sections. These pre-installation diameters were taken as the initial pipe diameters for each test section and used as a basis for calculating pipe ring deflection. The measured diameter changes during the pipe installation are provided in Figures 5.45 through 5.48. Positive values indicate a reduction in the diameter of the pipe. The pipe deflection time history is shown in Figure 5.45 while Figures 5.46 to 5.48 showed change in pipe deflection with height of backfill. The maximum observed diameter changes during installation are summarized Table 5.11. The resolution of the LVDT was ±0.001mm.

Table 5.11: Measured ring deflections during open-cut installation

	EL (mm)	**WL (mm)**	**CO (mm)**
0°- 180°	+1.2	+1.1	+0.29
45°- 225°	-0.12	-0.2	-
90°- 270°	-1.0	-1.0	-0.27

The change in pipe deflection, signified by the step-like pattern in Figure 5.45, clearly reflects the effect of backfill lift placement and compaction on the pipe. The first backfill lift, 0.15m from the pipe invert was placed around the haunch of the pipe. The compaction of this first lift resulted in a small extension of the pipe in the vertical direction and an inward deflection between the springlines. The maximum vertical and horizontal deflections measured after the compacted of the first lift were approximately -0.15mm and +0.1mm respectively.

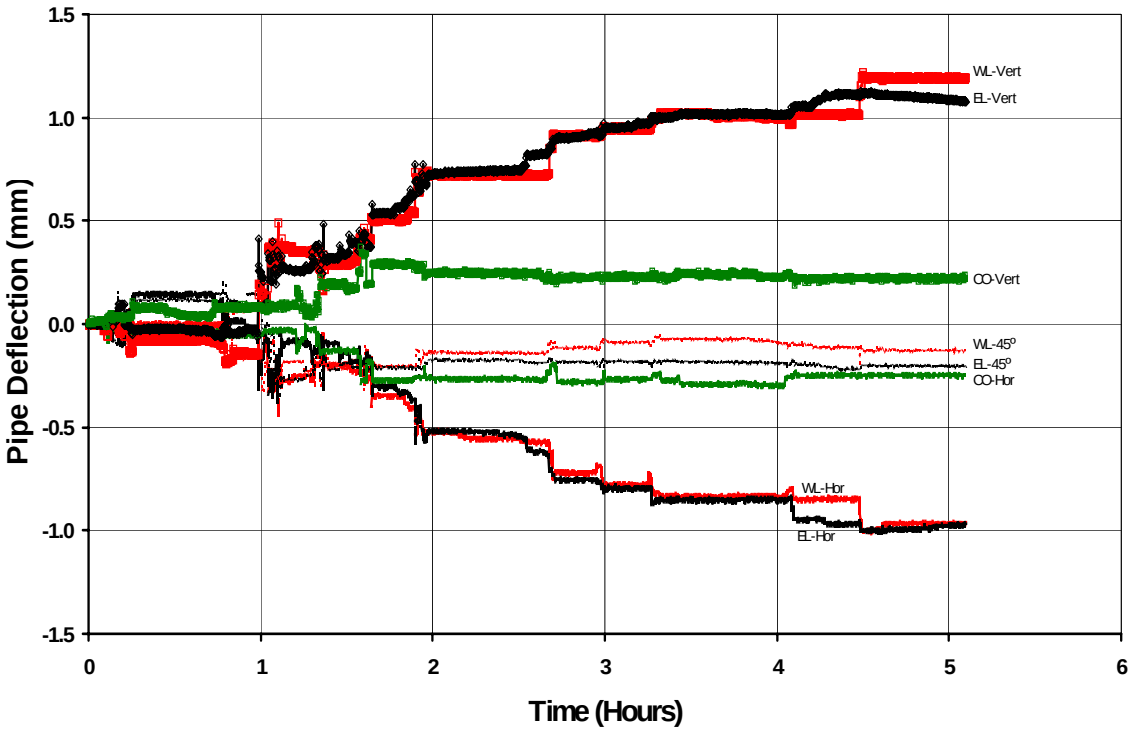

Figure 5.45: HDPE pipe deflection during open cut installation

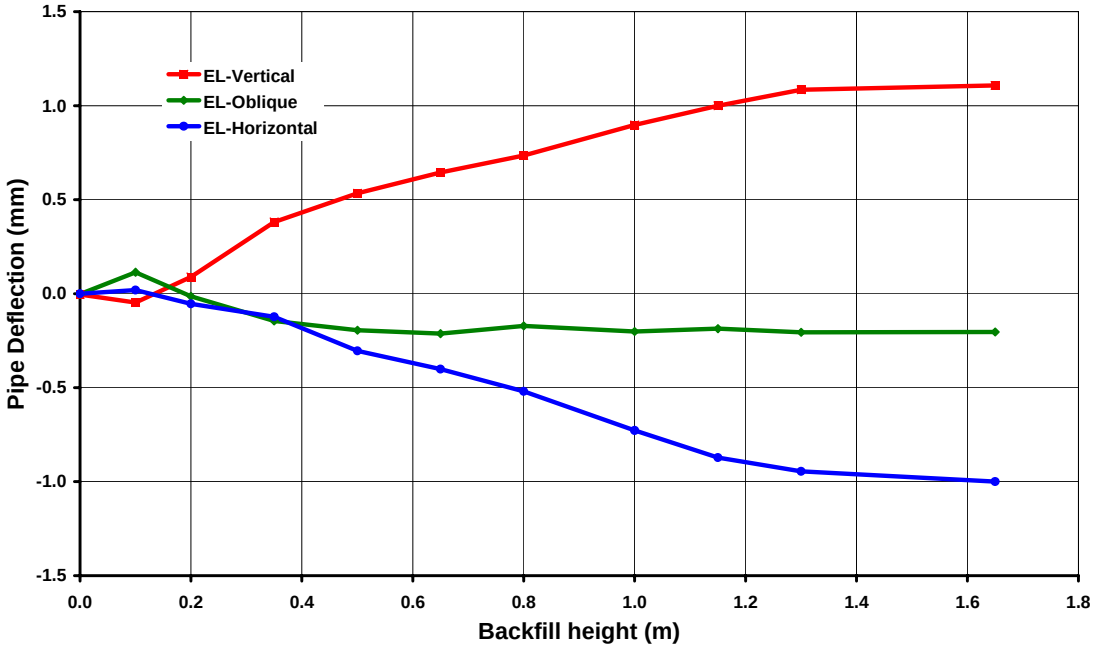

Figure 5.46: Pipe deflection versus height of backfill (EL-Test Section)

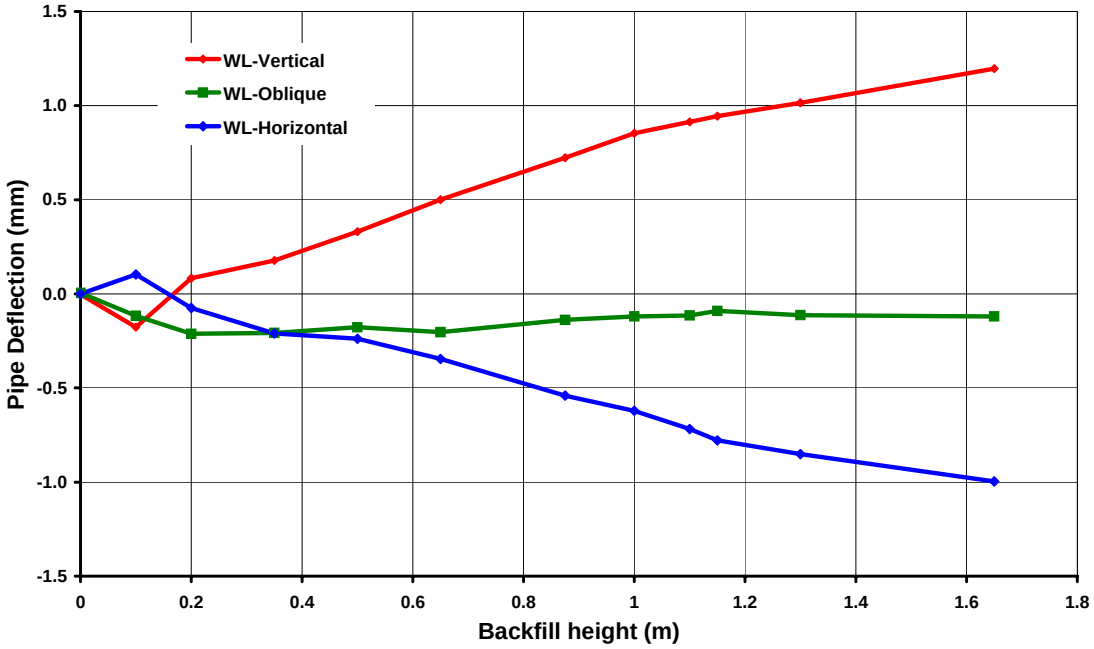

Figure 5.47: Pipe deflection versus height of backfill (WL-Test Section)

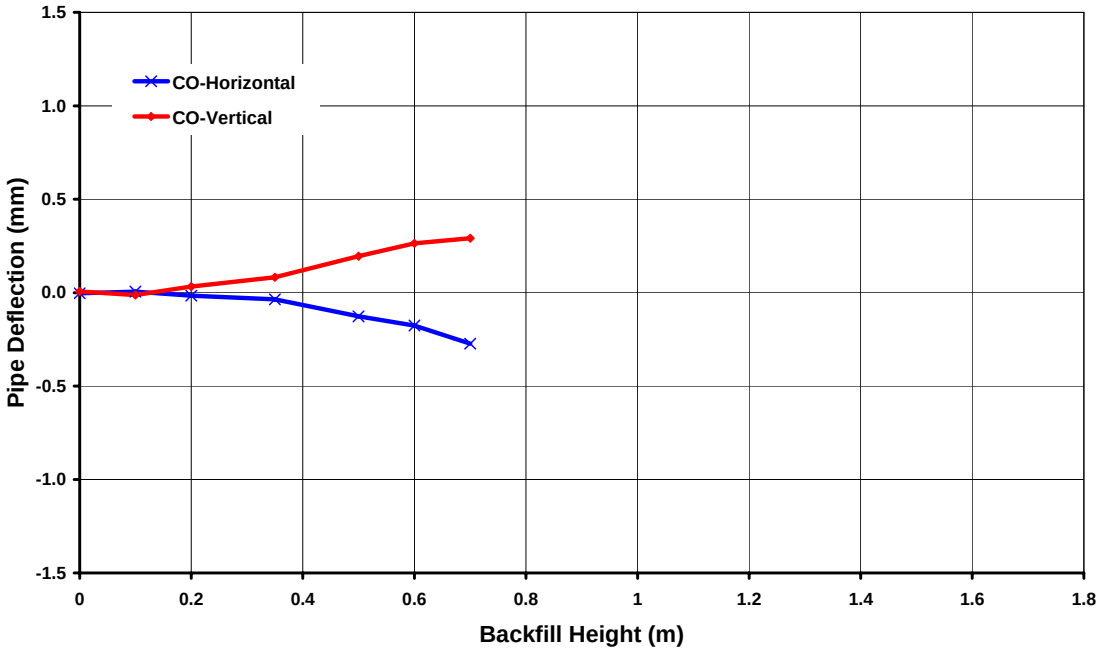

Figure 5.48: Pipe deflection versus height of backfill (CO-Test Section)

The placement and compaction of subsequent backfill lifts above the crown of the pipe generally resulted in compression of the pipe in the vertical direction and extension in the horizontal diameter of the pipe. Although the resulting pipe deflection is proportional to the height of backfill, the relationship is not entirely perfectly linear as shown in Figures 5.46 and 5.47. The slope of deflection versus height of backfill reduced gradually as additional backfill was placed. This may be explained by the reduction of the effect of compaction effort on the pipe. The magnitude of compactive effort that reaches the pipe is gradually reduced as the height of cover above the pipe increases. This observation suggests that compactive effort from the compactor has a significant effect on pipe deflection and that the effect is gradually reduced as additional height of fill is placed on the pipe.

Deflection measurements from the three test sections indicate that the final deflected shape of the pipe is slightly oval with the vertical deflection being 7.5% to 20% greater than the horizontal deflection. It can be inferred from this observation that the backfill material placement around the pipe near the springlines provided some side support to the pipe which resulted in the observed lower deflection measurements obtained for the horizontal diameter.

The maximum deflection measured at the end of construction indicate that the control test section (CO) had significantly less pipe deflection approximately +0.29mm and -0.27mm change in the vertical and horizontal diameters, respectively, compared to the other test sections placed beneath the West (WL) and East (EL) traffic lanes which have approximately +1.2mm and -1.0mm change in the vertical and horizontal diameters, respectively. The lower deflection in the CO test section can be attributed to the shallow height of fill placed above the pipe at this location and to the additional stiffness provided by a water tight plug/seal inserted at the pipe ends. The CO test section is located underneath the side slope of the pavement beyond the unpaved shoulder.

5.7.2 Cut and Cover Installation Induced Pipe Strains

Unlike the HDD installed pipe that was subjected to significant axial and bending strains during pipe pullback, the open-cut installed pipe was not subjected to any significant axial loading during installation. The results obtained strain measurement presented in Figures 5.49

through 5.52 suggest that the pipe was subjected mainly to bending and circumferential strains in its hoop direction during installation.

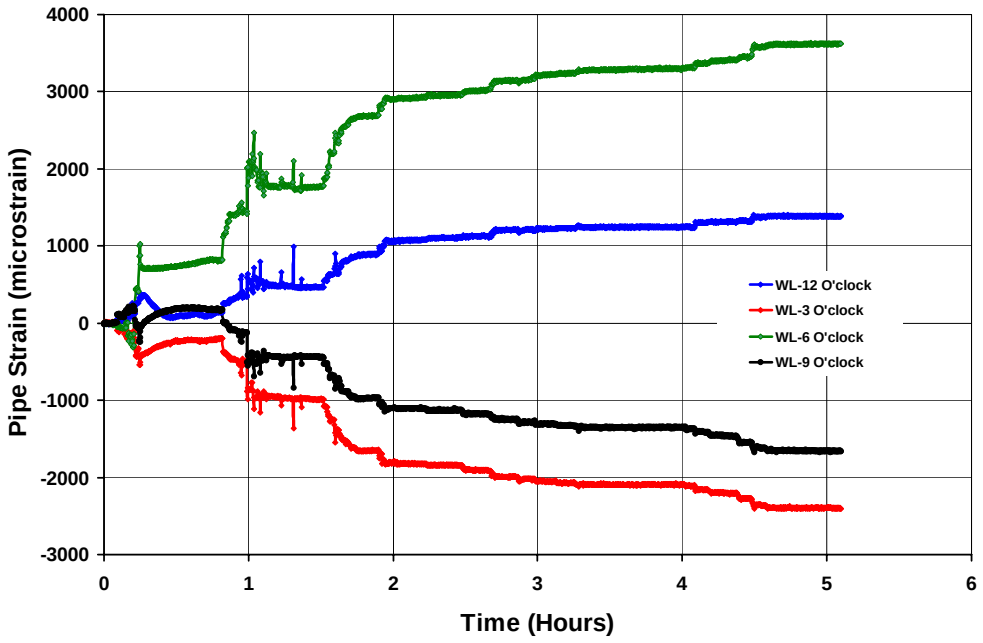

Figure 5.49: HDPE Pipe installation induced pipe strain (WL Test Section)

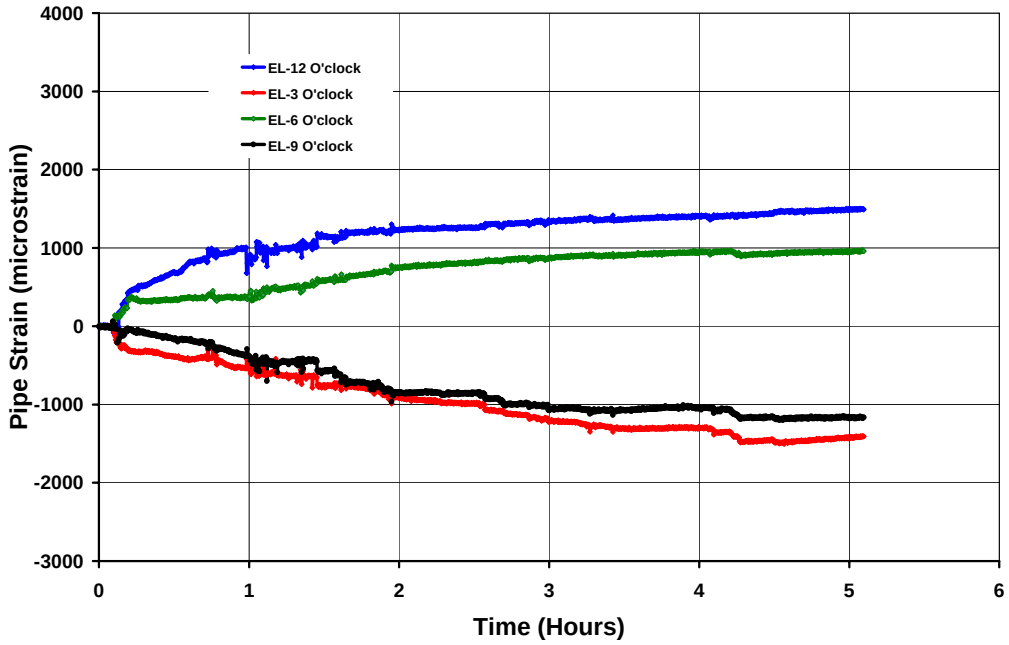

Figure 5.50: HDPE Pipe installation induced pipe strain (EL Test Section)

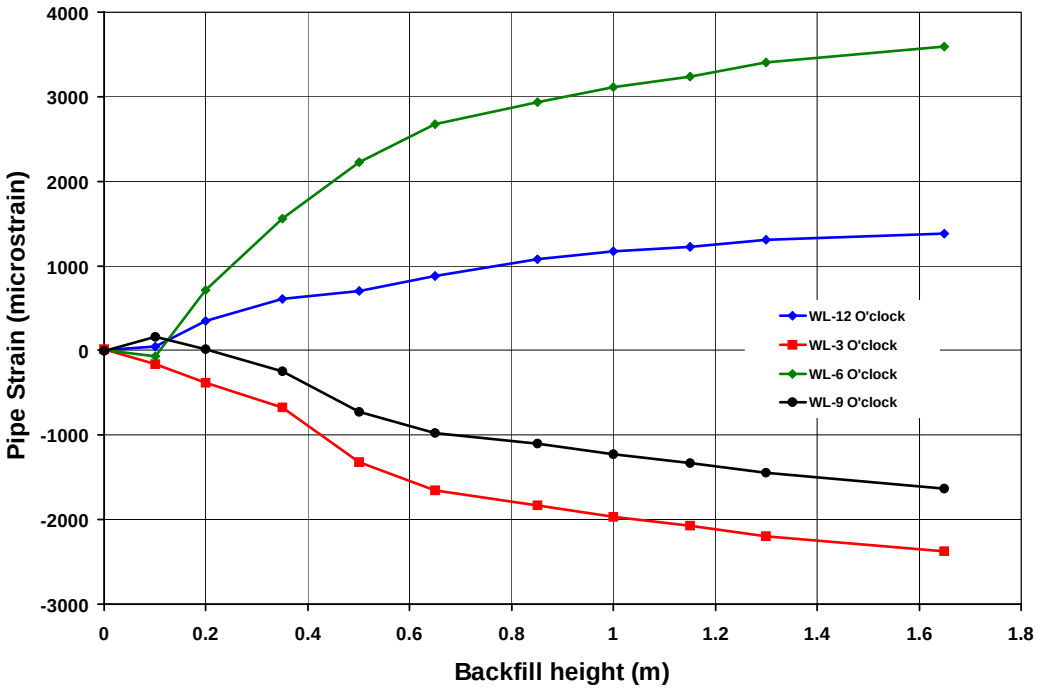

Figure 5.51: Pipe Strain versus height of backfill (WL-Test Section)

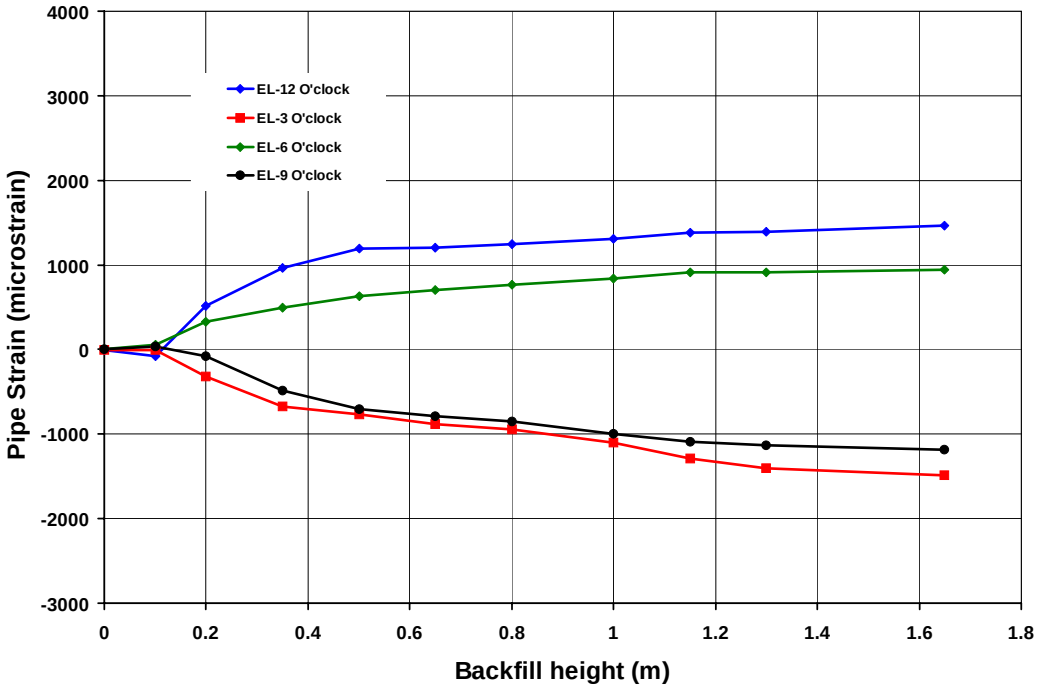

Figure 5.52: Pipe Strain versus height of backfill (EL-Test Section)

The strain gauges were located inside the pipe and oriented to capture these circumferential bending strains. A detailed description of the strain gauges can be found in Section 5.3.3.
The maximum installation induced pipe strains measured in the test sections are presented in Table 5.12. The placement and compaction of backfill material on the pipe resulted in compressive strain at the springlines that varied approximately between 1188 and 2375 microstrain and tensile strain at the crown and invert that ranged approximately between 960 and 3600 microstrain.

Table 5.12: Maximum Installation Induced Pipe strain during open-cut installation

Gauge Strain location	**EL (με)**	**WL (με)**	
12 o'clock	+1390	+1464	Tensile strain
6 o'clock	+3600	+960	
3 o'clock	-2375	-1482	Compressive strain
9 o'clock	-1635	-1188	

The strain induced on the pipe generally increased as additional backfill lifts were placed and compacted. The plots of pipe strain versus height of backfill, Figures 5.51 and 5.52, indicate that the relationship between height of backfill and induced strain is not perfectly linear over the entire range of backfill height due to soil arching. Over 60 percent of the maximum measured strain was induced on the pipe when less than 0.5m (about 30 percent) of the maximum height of backfill was placed on the pipe. The measured strain resulted from both the overburden stress from the backfill material and the compactive effort of the compactor. Additional backfill placed above the pipe resulted in increased overburden pressure. It also reduced the magnitude of the compactive effort that reached the pipe. This may explain the non-linearity in the pipe strain vs. height of backfill plot.

Generally, the test section located beneath the Northbound lane (EL) showed strains values significantly higher, as much as 275%, than those underneath the Southbound lane (WL). Whereas the deflection data obtained from the EL test section discussed in the previous Section is only approximately 9% higher than those measured in the WL test section. The difference observed in data obtained from the WL and EL test sections could result from the variability in stiffness of the trench bed material. Lower bed stiffness would result in lesser

pipe strain while stiffer bed will result in higher pipe strain. The quantity and thickness of adhesive glue used to secure the strain gauges to the wall of the pipe often produced some additional stiffness to the pipe at the location of the strain gauges. Variation in the quantity and the thickness of the glue used at each of the strain gauge location could also result in the variability shown in the strain test data.

The strain value of +3600 microstrain measured near the pipe invert at EL test section is significantly higher than the other strain measurement. The thickness of the glue used to secure the strain gauge to the pipe wall at this location might be considerable thinner than at other locations or the trench bedding might be stiffer.

5.7.3 Ground Surface Movement during Open-Cut Pipe Installation

Elevation survey grid 0.5 by 0.5m (~1.5 by 1.5 feet) was established on the asphalt concrete pavement surface adjacent to the trench excavation on both sides to monitor any surface movement that may occur during pipe installation. The grid was surveyed using a Total Station prior to, during, and following the completion of pipe installation. Development of sloughing of side slopes within the excavation was also monitored during installation. Survey results showed that there was no significant movement of the asphalt pavement surface within the survey grid during the installation. Recorded movements were less than 1.0mm (0.04 inch). It appears that the thickness of the asphalt concrete and the underlying materials provided adequate support for the machines and equipment that were used for the construction as there was no sloughing of the excavation side slope prior to the flooding of the trench due to rainfall at the test site after the first day of installation. The condition of the excavated trench before and after the rainfall is shown in Figures 5.53 and 5.54 respectively. The flooding of the trench by the rainfall resulted in substantial sloughing of the side slopes but there were no immediate noticeable movement or cracking of the asphalt concrete pavement surface due to the sloughing.

Figure 5.53: Excavated trench showing no sloughing prior to rainfall at test site

Figure 5.54: Condition of excavated trench following rainfall at test site

5.8 Long-Term Performance of Installed HDPE Pipes

The two 200mm HDPE pipes that were installed using HDD and open cut and cover construction techniques were continuously monitored over approximately three years after they were installed to evaluate how they perform over time and examine any variation in their performances that may have resulted from their method of installation.

The HDD installed HDPE pipe sensors were sampled continuously at a frequency of 100Hz over the entire period of monitoring and sampled data were stored on the data acquisition system onboard memory at a lower frequency of 0.01Hz (one sample every 100 sec). The HDD pipe sensors that were monitored are linear variable displacement transducers (LVDT) and pressure transducers. The sensors placed inside the open cut-and-cover installed pipe that were monitored after the installation are the linear variable displacement transducers and strain gauges. These sensors were sampled continuously at a frequency of 2000Hz over the study period and data were stored at a lower sampling rate of 0.01Hz (one sample every 100 sec).

The results obtained from the post-installation monitoring are presented and discussed in the following Sections. Preliminary analyses of measured field data showed that there is a close correlation between the measured pipe performance and seasonal temperature variation. This correlation was explored and discussed in the subsequent Sections. Investigation of the presence and influence of frost action on the observed behavior of the installed HDPE pipes is also presented.

5.8.1 Pipe Deflection Measurements of HDD Installed Pipe

Pipe deflection measurements provide an objective means of evaluating the performance of flexible pipes. Pipe ovality and overall deformation can be inferred from deflection measurements. Linear variable displacement transducers (LVDT) were placed inside three test sections positioned along the length of the HDD installed HDPE pipe to measure pipe deflection. Two of these test sections identified as EL and WL test sections were situated directly beneath the right wheel paths in the Northbound and Southbound traffic lanes respectively and the third control test section (CO) was placed underneath the side slope

adjacent to the Southbound traffic lane pavement shoulder. Detailed description of the LVDTs and the rational for their location and orientation inside the pipe are given in Section 5.3.1.

The long-term deflection time history data obtained from the EL, WL and CO test sections are presented graphically in Figures 5.55, 5.56 and 5.57, respectively. The plots show pipe deflection measurement versus number of days after May 15, 2003 when the long-term monitoring commenced. The actual calendar dates are also provided on the secondary x-axis at top of each plot. All the pipe sensors were reinitialized to zero value on May 15, 2003 hence; the long-term measurements do not include installation deflections. The resolution of the LVDT output signal as shown on the plot is approximately ± 0.15mm. Although this is somewhat low compared to the maximum value of deflection measured during the monitoring period, the performance of the pipe can still be substantially and objectively evaluated from the measured data.

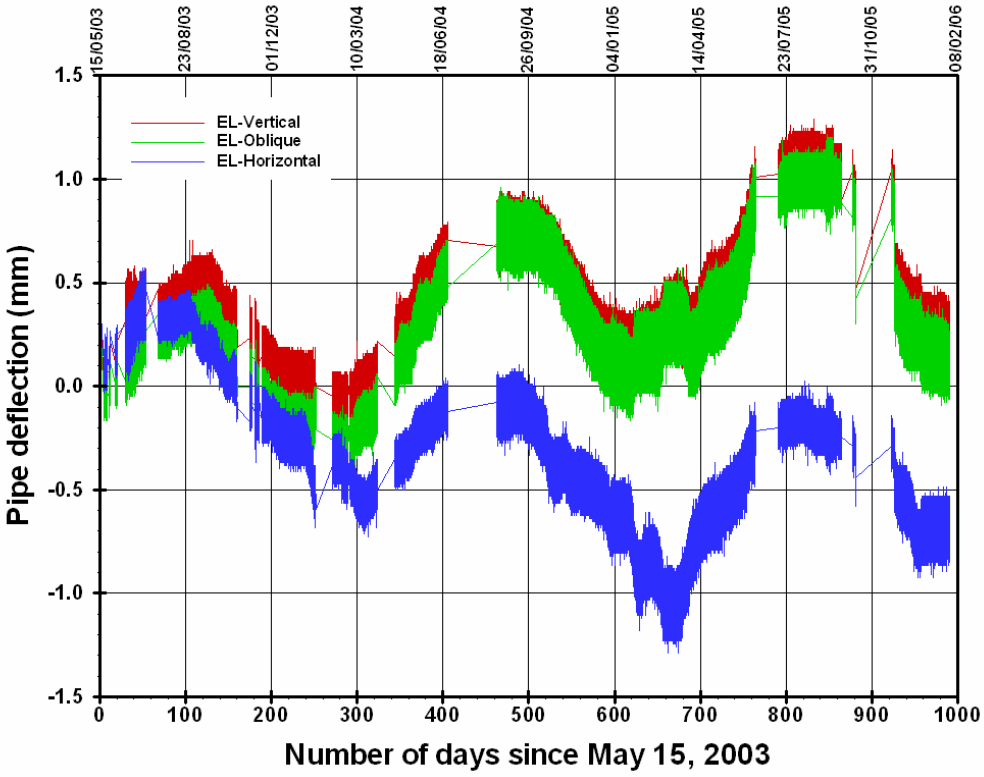

Figure 5.55: HDD installed HDPE pipe long-term deflection (EL Test Section)

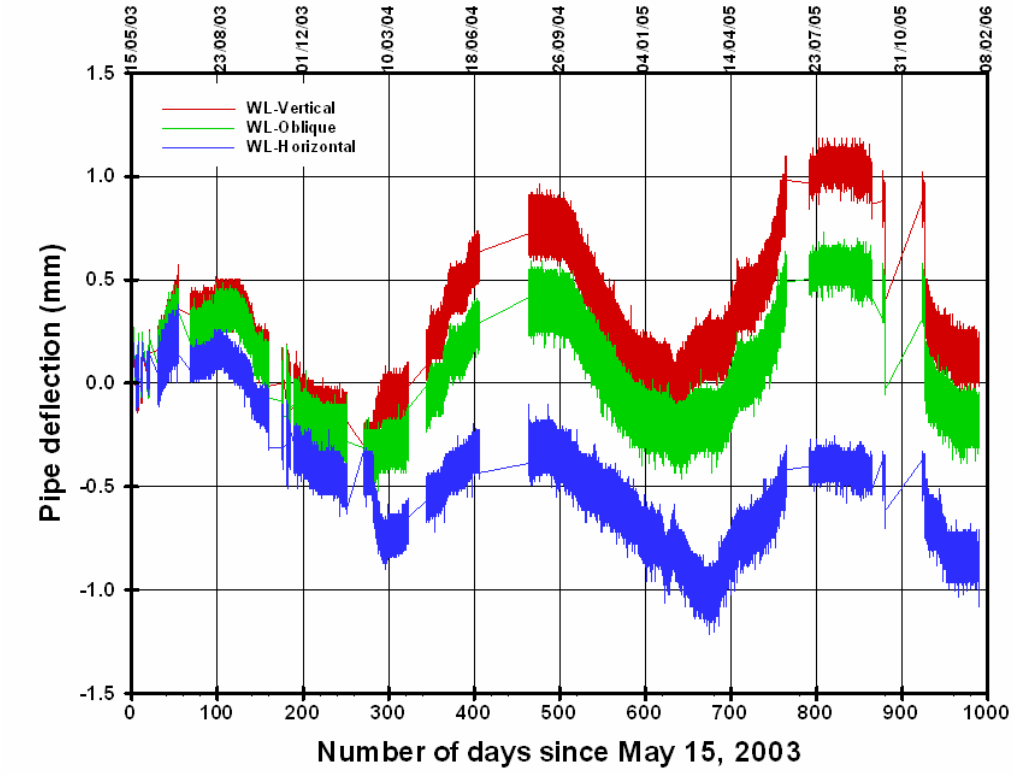

Figure 5.56: HDD installed HDPE pipe long-term deflection (WL Test Section)

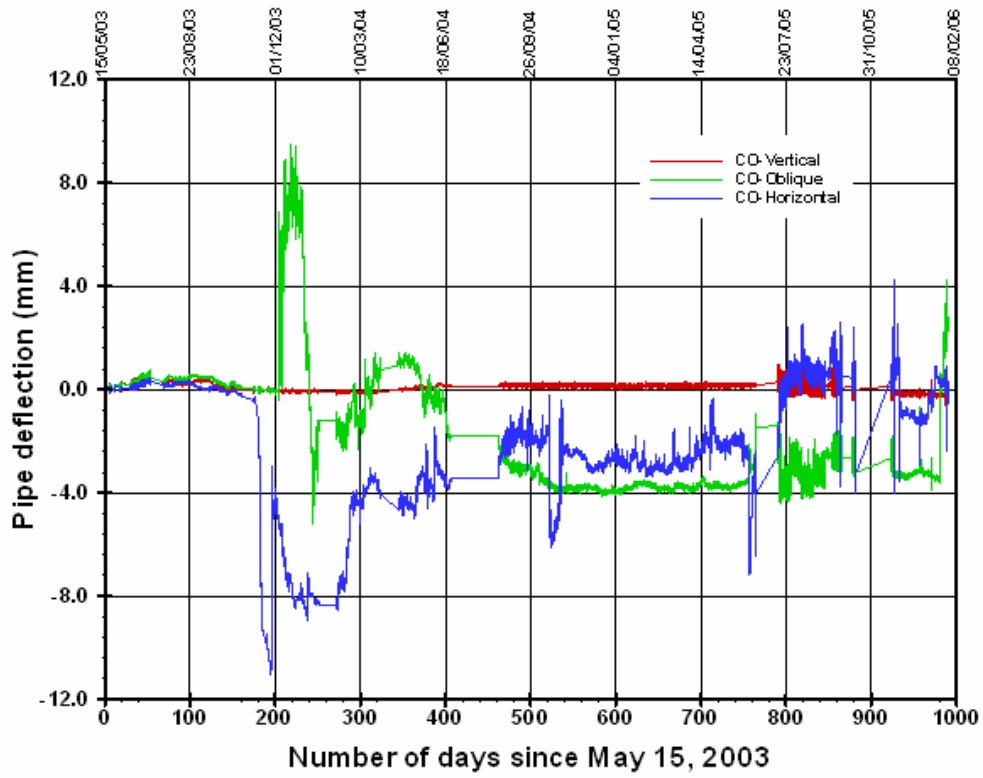

Figure 5.57: HDD installed HDPE pipe long-term deflection (CO Test Section)

The six LVDTs placed in test sections EL and WL underneath the Northbound and Southbound traffic lanes respectively showed very similar trends. The relationship between pipe deflection and time can be described by a sinusoidal wave with varying amplitudes. The maximum and minimum pipe deflection values measured throughout the monitoring period are provided in Table 5.13.

Table 5.13: Long-term maximum pipe deflection for HDD installed PE pipe

Day	Date	EL			WL		
		Vertical (mm)	Oblique (mm)	Horizontal (mm)	Vertical (mm)	Oblique (mm)	Horizontal (mm)
114	6-Sep-2003	0.50	0.35	0.30	0.40	0.35	0.15
298	8-Mar-2004	-0.10	-0.20	-0.55	-0.25	-0.30	-0.70
490	16-Sep-2004	0.80	0.70	-0.15	0.75	0.40	-0.30
669	14-Mar-2005	0.20	0.10	-0.95	0.05	-0.20	-1.05
818	10-Aug-2005	1.10	0.90	-0.25	1.05	0.60	-0.35
980	19-Jan-2006	0.25	0.15	-0.70	0.15	-0.15	-0.85

These values correspond to the crest and valley of the sinusoidal wave-like curves. The difference between consecutive maximum and minimum deflections measurements are provided in Table 5.14. It should be noted that the displacement transducers were wired such that pipe extension is positive.

Table 5.14: Change in pipe deflection measurements for HDD installed PE pipe

Date		EL			WL		
Start	End	Vertical (mm)	Oblique (mm)	Horizontal (mm)	Vertical (mm)	Oblique (mm)	Horizontal (mm)
15-May-03	6-Sep-03	0.50	0.35	0.30	0.40	0.35	0.15
7-Sep-03	8-Mar-04	-0.60	-0.55	-0.85	-0.65	-0.65	-0.85
9-Mar-04	16-Sep-04	0.90	0.90	0.45	1.00	0.70	0.40
17-Sep-04	14-Mar-05	-0.60	-0.60	-0.85	-0.70	-0.60	-0.75
15-Mar-05	10-Aug-05	0.90	0.80	0.70	1.00	0.80	0.70
11-Aug-05	19-Jan-06	-0.85	-0.75	-0.45	-0.90	-0.75	-0.50

The data obtained from EL and WL test sections indicate that the pipe gradually expanded within the bore after installation until around day 114 (i.e. September 6, 2003) as showed in Figures 5.55 and 5.56. The average maximum vertical and horizontal deflections measured

near day 114 was approximately +0.45mm and +0.25mm respectively indicating that the pipe expanded about 100% more in the vertical direction than in the horizontal direction. The pipe's response was similar between days 298 - 490 (March 9 and September 16, 2004) and 669 - 818 (March 15 and August 10, 2005). The average change in vertical and horizontal diameter of the pipe during these two periods are approximately +0.95 and +0.60mm respectively. This suggests that the vertical diameter of the pipe extended approximately 70% more than the horizontal diameter. The expansion periods coincide with the spring and summer seasons when the ambient temperature warms up at the test site location. The influence of changes due to seasonal variability on performance of HDPE pipe is explored in later sections of this Chapter.

Following each of the outward expansion periods described in the preceding paragraphs are pipe deflections that indicated gradual inward contraction of the pipe. The deflection of pipe inwardly were observed between the following days after pipe installation 115 - 297 (September 6, 2003 and March 7, 2004), 491 - 669 (September 16, 2004 and March 13, 2005) and 819 - 980 (August 10, 2005 and January 19, 2006). The deflection measurement obtained during the first two pipe contraction periods between days 115 - 297 and 491 - 669 were similar with the measured average change in vertical and horizontal diameter of the pipe being approximately -0.65mm and -0.80mm respectively. The pipe appears to have contracted slightly unevenly resulting in a greater deflection, approximately 0.15mm (or ~23%) higher in the horizontal diameter. The last pipe contraction phase during the monitoring period was between days 819 – 980. The average change in vertical and horizontal pipe diameter measured during the time period was -0.88mm and -0.48mm respectively. It is clear from the plot that the end of this particular contraction phase, between days 819 - 980 has not been reached.

The pipe deflection data obtained at CO test section, Figure 5.57, are similar to those obtained from EL and WL test sections until around 178 (November 9, 2003). Around November 9, 2003 the displacement transducer oriented along the 90°- 270° plane in the CO test section showed a sudden change in pipe deflection while the LVDT oriented along plane 0°- 180° seized to show any significant change in pipe diameter after day 178. Review of field record indicated that November 9, 2003 coincides with the period when the heavy

machines used for restoration of asphalt concrete on the patched surface of the restored open-cut trench. The heavy equipment and machinery used during the pavement restoration could have caused substantial disturbance in the shallow granular fill material placed above the CO test section which resulted in the spike in deflection measurement indicated by the LVDT. The construction equipments could also have permanently damaged the displacement transducer oriented along plane 0°- 180° meant to measure the pipe's vertical deflection. There were no substantial changes in the deflection data obtained from the EL and WL test section around day 178 suggesting that the EL and WL test sections were shielded from the adverse influence of construction equipment. This is probably due to the relatively stiff asphalt concrete and thicker pavement materials above these test sections.

Both ends of the HDD installed HDPE pipe were sealed with water tight rubber end plugs that are removed periodically to access the data acquisitions systems placed inside the HDD installed pipe. The loosening and tightening of the rubber end plug placed at the end of the pipe could cause accidental change in pipe that could considerable impact deflection measurements at the CO test section situated only approximately 300mm (~1ft) away from the end of the pipe.

Overall, the long-term deflection data showed that the HDD installed HDPE pipe experienced continuous steady change in pipe diameter that consist of alternating extension and contraction of the pipe diameter throughout almost three years monitoring period. The pipe deflection time history plots showed sinusoidal wave-like pattern with varying amplitude. Although each period of pipe contraction is followed by a period of pipe extension, it appears that some of the reduction experienced by the pipe between its springlines (change in horizontal diameter) during the contraction phase is not fully recovered during the following extension phase.

Lack of uniformity of soil stiffness around the pipe and the expansive behavior of the bore slurry produced during drilling could have resulted in the variation observed between change in vertical and horizontal diameter of the pipe. Uneven distribution of the bore slurry in the annular space surrounding the pipe after pipe insertion could result in higher side stiffness around the pipe springline compare to the crown of the pipe. This is particularly plausible if

the pipe is located at the bottom of the bore rather than being concentrically located within it. Stiffer side stiffness could prevent outward horizontal expansion of the pipe. The expansive behavior of the bentonitic clay and other additives used as drilling fluid during pipe installation could also result in higher horizontal inward deflection experienced by the pipe. The bore slurry material has ample access to water needed for swelling from the side drain adjacent to the CO test section. Availability of water to the fine grained bentonitic bore slurry could also promote influence of frost on the pipe.

At the end of the monitoring period, the measured field deflection data indicate the pipe had experienced gradual cumulative decrease, approximately -0.75mm, in the horizontal diameter over the monitoring period. Consequently, the average measured cumulative change in vertical diameter at the end of the monitoring period was approximately +0.2mm indicating that the pipe deflection outwardly in the vertical direction.

It can be inferred from the difference observed in the measured average cumulative change in vertical and horizontal diameter that there are some side resistance provided by the slurry immediately surrounding the pipe that resulted in reduced outward deflection of the pipe in the horizontal direction.

5.8.2 Pipe Deflection Measurements of Open-cut Installed Pipe

Similar to the HDD installed HDPE pipe, linear variable displacement transducers (LVDT) were placed within three test sections located along the length of the open-cut installed HDPE pipe to monitor the change in pipe deflection. Two test sections identified as EL and WL test sections were positioned beneath the wheel paths in the Northbound and Southbound traffic lanes respectively and the third control test section (CO) was placed underneath the side slope adjacent to the Southbound traffic lane pavement shoulder.

Plots of measured long-term deflection data obtained from the open-cut and cover installed HDPE pipe is given in Figures 5.58 through 5.60. The plots show pipe deflection measurement versus number of days since November 6, 2003. Actual calendar dates are placed on the secondary x-axis at the top of the plot for easy reference.

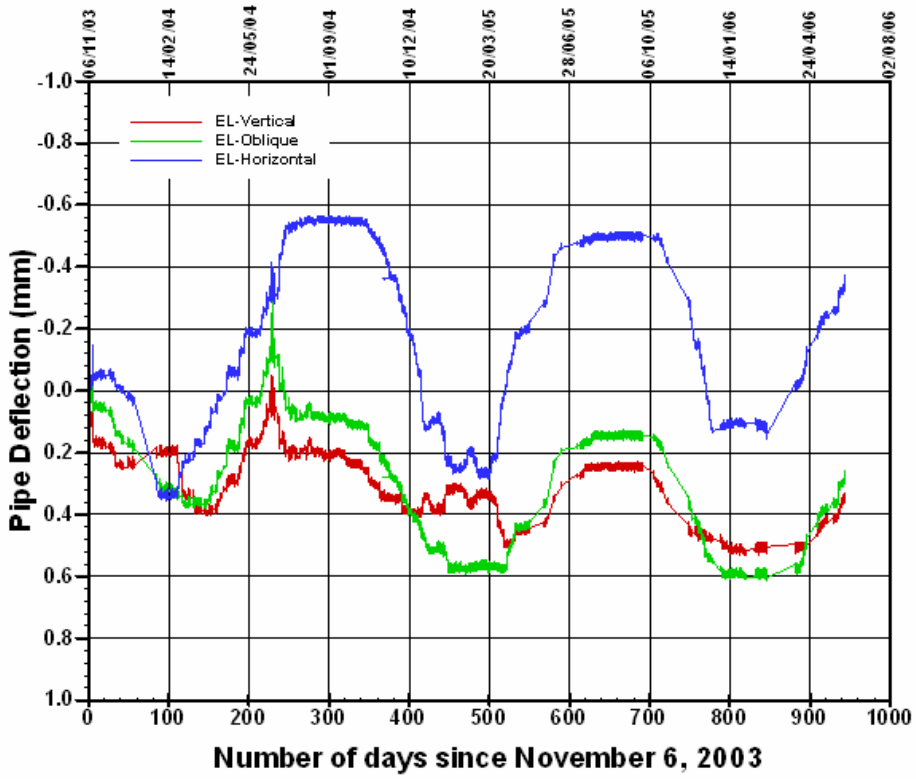

Figure 5.58: Open-Cut installed HDPE pipe long-term deflection (EL Test Section)

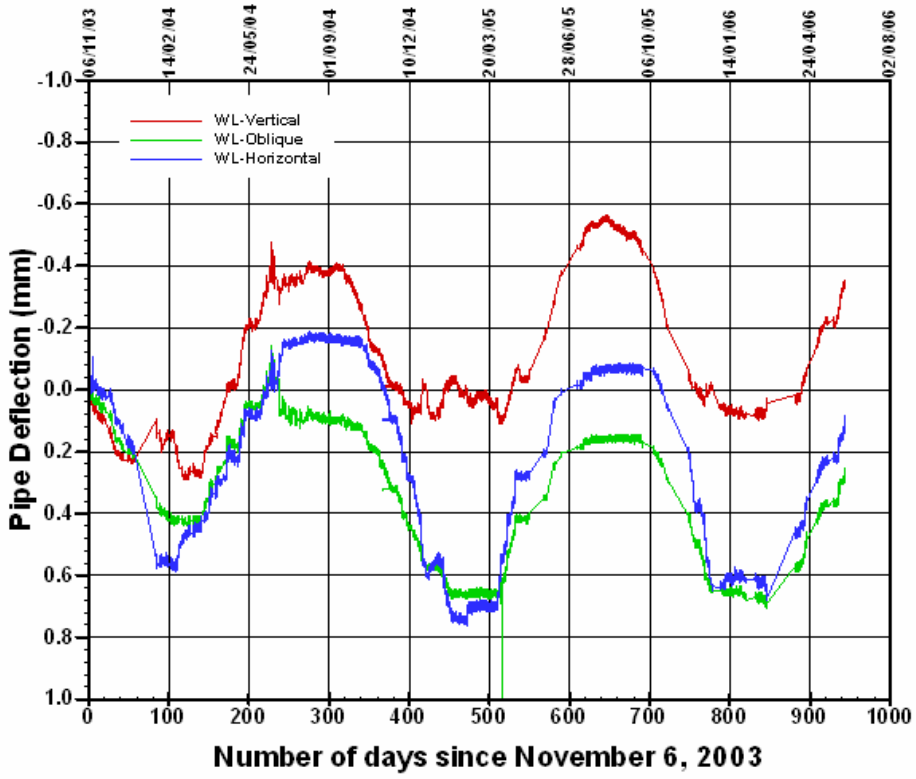

Figure 5.59: Open-Cut installed HDPE pipe long-term deflection (WL Test Section)

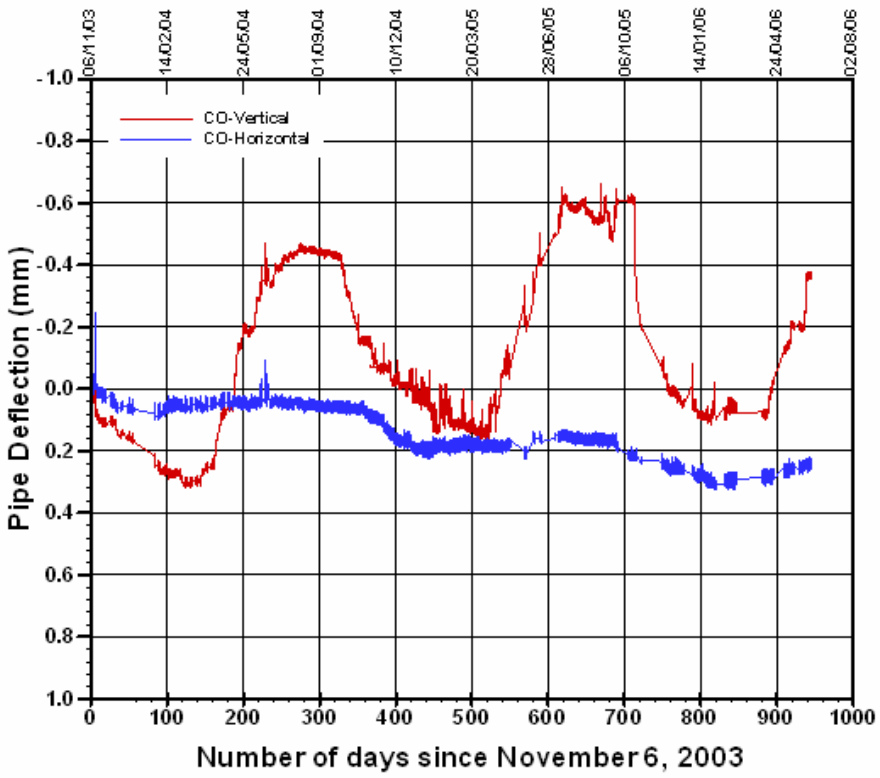

Figure 5.60: Open-Cut installed HDPE pipe long-term deflection (CO Test Section)

As shown in Figures 5.58 through 5.60 the resolution of the output signal was significantly improved by the filtering and conditioning that were applied to the signals. The output signal resolution obtained was in order of ± 0.001mm after conditioning compared to ± 0.15mm obtained from the HDD installation with similar LVDTs.

The deflection data obtained from the three test sections showed similar trends and varied sinusoidally with time like the HDD pipe deflection data. The maximum pipe deflection values denoted by the maximum and minimum points on the sinusoidal-like plots are provided in Table 5.15 and the change in pipe deflection between consecutive maximum and minimum point on the deflection plots are provided in Table 5.16. It should be noted that the LVDTs placed in the open-cut installed pipe were wired differently from the HDD pipe as positive deflection indicates pipe reduction in pipe diameter.

Table 5.15: Long-term maximum pipe deflection for open-cut installed PE pipe

Day	Date	EL			WL			CO	
		0°- 180° (mm)	45°- 225° (mm)	90°- 270° (mm)	0°- 180° (mm)	45°- 225° (mm)	90°- 270° (mm)	0°- 180° (mm)	90°- 270° (mm)
125	10-Mar-04	0.396	0.373	0.341	0.279	0.43	0.57	0.304	0.067
316	17-Sep-04	0.198	0.084	-0.546	-0.401	0.07	-0.176	-0.447	0.058
495	15-Mar-05	0.334	0.568	0.270	0.098	0.665	0.71	0.143	0.203
657	24-Aug-05	0.247	0.144	-0.497	-0.556	0.162	-0.069	-0.61	0.155
830	13-Feb-06	0.505	0.586	0.111	0.082	0.687	0.634	0.103	0.31
945	8-Jun-06	0.357	0.230	-0.320	-0.332	0.289	0.128	-0.364	0.258

Table 5.16: Change in pipe deflection measurements for open-cut installed PE pipe

Day	Date	EL			WL			CO	
		0°- 180° (mm)	45°- 225° (mm)	90°- 270° (mm)	0°- 180° (mm)	45°- 225° (mm)	90°- 270° (mm)	0°- 180° (mm)	90°- 270° (mm)
125	10-Mar-04	0.396	0.373	0.341	0.279	0.43	0.57	0.304	0.067
316	17-Sep-04	-0.198	-0.289	-0.887	-0.680	-0.360	-0.746	-0.751	-0.009
495	15-Mar-05	0.136	0.484	0.816	0.499	0.595	0.886	0.590	0.145
657	24-Aug-05	-0.087	-0.424	-0.767	-0.654	-0.503	-0.779	-0.753	-0.048
830	13-Feb-06	0.258	0.442	0.608	0.638	0.525	0.703	0.713	0.155

The deflection data suggest that the pipe slowly contracts and deflects inward from November 6, 2003 until around day 125 (March 10, 2004) as showed in Figures 5.58 through 5.60. The average inward vertical and horizontal deflections measured at the EL and WL test sections near day 125 was approximately +0.338mm and +0.456mm respectively. The pipe's response was similar between days 317 - 495 (September 18, 2004 and March 15, 2005) and 658 - 830 (August 25, 2005 and February 13, 2006). The average reduction in the vertical and horizontal diameter of the pipe between September 18, 2004 and March 15, 2005 was +0.318mm and +0.851mm respectively. Between August 25, 2005 and February 13, 2006, the vertical and horizontal diameter of the pipe reduced by approximately +0.448mm and +0.655mm respectively. The change in vertical diameter of the pipe was approximately 26 to 62 percent lower than the reduction experienced by the pipe in the horizontally.

Following each of the contraction (reduction in pipe diameter) the pipe showed a gradual outward expansion. An increase in pipe diameter was observed between the following days 126 - 316 (March 11, 2004 and September 17, 2004), 496 - 657 (March 15, 2005 and August 24, 2005) and 831 - 945 (February 13, 2006 and June 8, 2006). Measured average change in vertical and horizontal diameter of the pipe between March 11, 2004 and September 17, 2004 was approximately -0.439mm and -0.816mm respectively. This indicates that the change in vertical diameter was 46% lower than those measured between the springline of the pipe.

The average change in vertical diameter of the pipe at the end of the other two outward expansion periods March 15, 2005 to August 24, 2005 and February 13, 2006 to June 8, 2006 were -0.371mm and -0.281mm respectively. The average change in horizontal diameter during these periods was -0.773mm and -0.469mm respectively. The increase in vertical diameter of the pipe is noticeable lower than the change in the horizontal diameter as the vertical deflection was 52 and 40 percent lower than the horizontal deflection at the end of the second and third expansion periods.

The LVDT that monitored change vertical deflection in the control (CO) showed trends that are very comparable to the LVDT placed in the WL test section. The vertical deflections measured at the CO test section are 10 to 12% higher than those of WL test section.

Unfortunately, the deflection gauge that monitor change in the horizontal deflection in the CO test section did not function properly over the long-term monitoring period.

Although the deflection measurements in test section EL and WL showed similar trends, there is a significant difference in the magnitude of deflections obtained from the two test sections. Examination of the test data showed that an event occurred between days 56 and 118 (January 2 and March 3, 2004) that caused a noticeable change in the pipe deflection. The LVDTs that measured pipe's vertical deflection along 0°- 180° plane within the two test sections showed a significant increase in pipe's diameter (extension) while the ones that measured change in horizontal diameter of the pipe showed higher inward deflection (reduction in diameter). The EL and WL test sections showed 0.05mm and 0.13mm increase in vertical diameter respectively and 0.25mm and 0.38mm reduction (compression) in horizontal diameter of the pipe respectively within a relatively short period of time. Similar occurrence was observed in the pipe deflection data between day 403 to 495 (December 13, 2004 to March 15, 2005) following pipe installation. The period of time when the observed abrupt change in pipe deflection trends occurred coincide with the time when the lowest air temperature was reached during the 2003-2004 and 2004-2005 winter season. The average daily air temperature above the pavement surface fell and stayed below -20°C around these periods and the temperature of backfill material above the pipe was below 0°C during these periods.

It is worthwhile to mention that the observed trend described in preceding paragraphs was also observed during the 2005-2006 winter season but the magnitude of the changes in pipe deflection was very minimal. The minimum temperature recorded above the surface of the pavement was -15°C, higher than temperature recorded during previous winter season. The change in pipe behavior identified in the preceding Sections could result from frost action within the backfill. This will be discussed further in Section 5.9.

5.8.3 Pipe Strain Measurement of Open-cut Installed Pipe

Temperature compensated strain gauges were fixed to the pipe interior to capture the changes in pipe strain. The EL and WL test sections were each equipped with four strain gauges

placed at the crown (12 O'clock), springlines (3 and 9 O'clock), and invert (6 O'clock). The strain gauges were oriented to capture the circumferential strain in the pipe's hoop direction. Detailed description of the strain gauges can be found Section 5.3.2.

The change in circumferential pipe strain measured during the long-term monitoring period are presented in Figures 5.61 and 5.62. The location of the strain gauges inside the test section is referenced with the clock referencing scheme. The gauges placed at the crown and invert are referenced as 12 O'clock and 6 O'clock respectively and the springline gauges are referred to 3 O'clock and 9 O'clock. The Figures, 5.61 and 5.62, show pipe strain measurement versus number of days after November 6, 2003 with the actual calendar dates on the secondary x-axis at top of each plot. The gauges were reinitialized to zero to exclude pipe installation strains. Compressive circumferential strain is negative.

Strain data from both test sections showed similar trends. The variation of pipe strain with time is sinusoidally and similar to the trends observed from the deflection data. The maximum pipe strain measurements given by the maximum and minimum points on the sinusoidal-like curve are provided in Table 5.17 and the change in pipe strain between consecutive maximum and minimum points are presented in Table 5.18.

The strain gauges all indicated that the pipe slowly contracted inwardly from November 6, 2003 till around day 125 (i.e. March 10, 2004). The average compressive strain measured at the crown and invert of the pipe at the EL and WL test section was approximately -1825 and -1565 microstrain respectively while the springlines strained approximately -1715 and -1445 microstrain respectively. The pipe showed similar strain response between days 317 - 505 (September 18, 2004 and March 25, 2005) and 658 - 871 (August 25, 2005 and March 26, 2006). The average strain measured by gauges placed directly opposite each other are given in Table 5.19.

Pipe strain measurements indicate that the pipe gradually expand circumferentially as the ground temperature increases at the test site. The strain gauges showed tensile strain between the following days 126 - 316 (March 11, 2004 and September 17, 2004), 505 - 657 (March 25, 2005 and August 24, 2005) and 871 - 945 (March 26, 2006 and June 8, 2006).

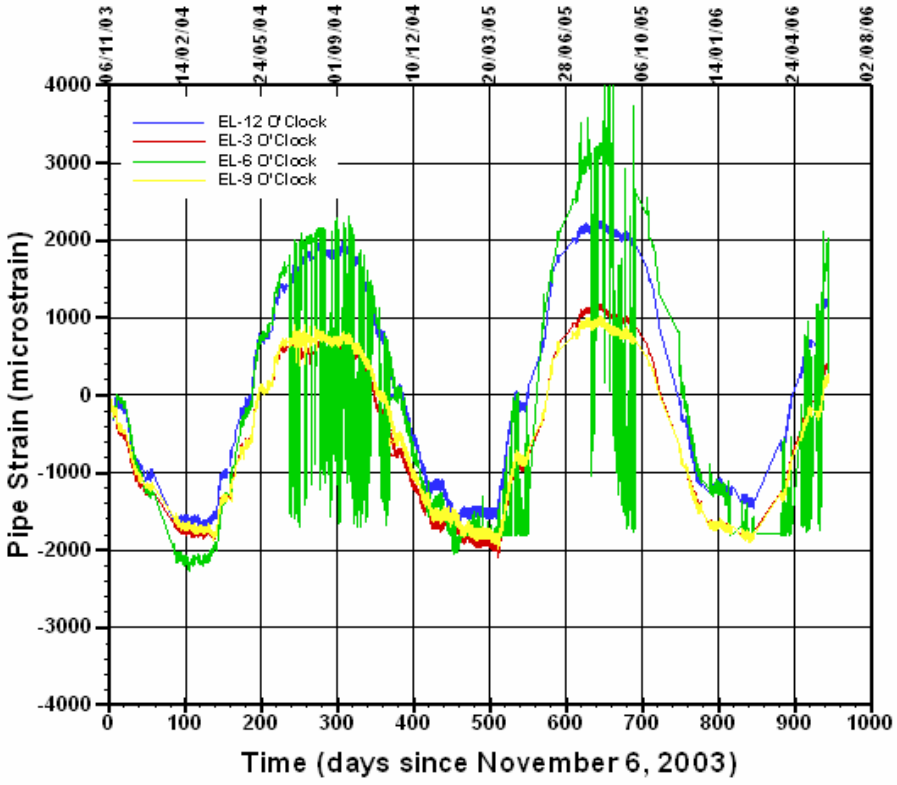

(a) Plot showing all sensors

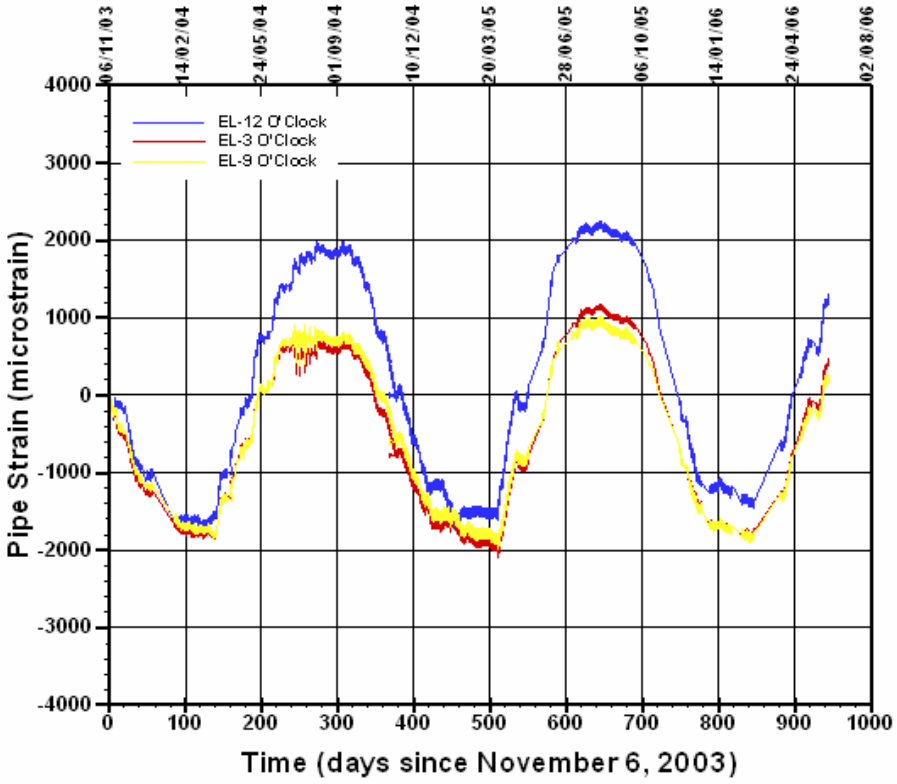

(b)- Plot without sensor placed at 6 o'clock

Figure 5.61: Open-Cut installed HDPE pipe long-term Strain (EL Test Section)

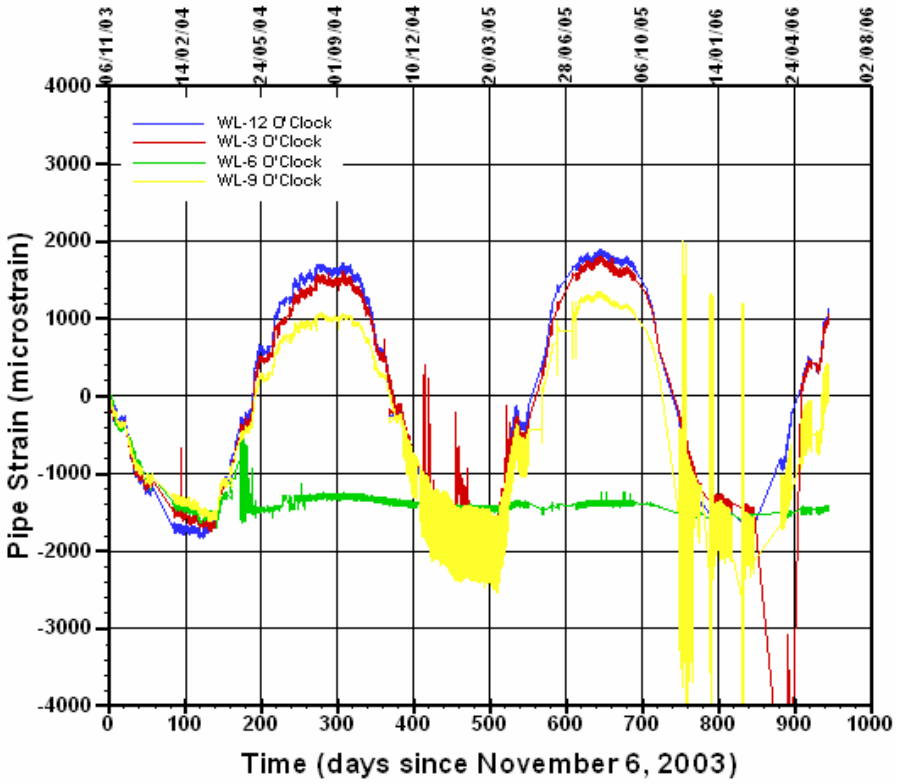

(a) Plot showing all sensors

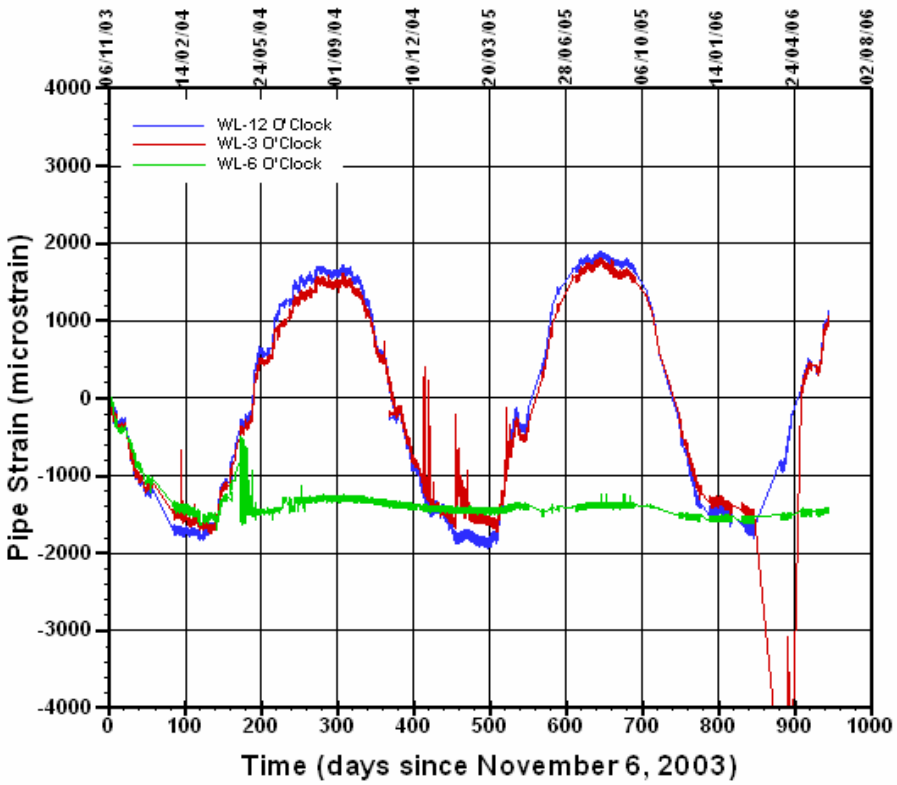

(b) Plot without sensor placed at 9 o'clock

Figure 5.62: Open-Cut installed HDPE pipe long-term Strain (WL Test Section)

Table 5.17: Long-term maximum strain measurements for open-cut installed PE pipe

Day	Date	EL				WL			
		0° (μm/m)	180° (μm/m)	90° (μm/m)	270° (μm/m)	0° (μm/m)	180° (μm/m)	90° (μm/m)	270° (μm/m)
125	10-Mar-04	-1570	-2080	-1750	-1680	-1720	-1410	-1570	-1320
316	17-Sep-04	1930	2140	680	810	1710	-	1610	1050
505	25-Mar-05	-1720	-1860	-1680	-1610	-1770	-	-1610	-1620
657	24-Aug-05	2230	3250	1150	990	1870	-	1770	1290
830	13-Feb-06	-1320	-1820	-1780	-1800	-1640	-	-1460	-2160
945	8-Jun-06	1300	1810	450	260	1080	-	1040	70

Table 5.18: Change in strain measurements for open-cut installed PE pipe

Day	Date	EL				WL			
		0° (μm/m)	180° (μm/m)	90° (μm/m)	270° (μm/m)	0° (μm/m)	180° (μm/m)	90° (μm/m)	270° (μm/m)
125	10-Mar-04	-1570	-2080	-1750	-1680	-1720	-1410	-1570	-1320
316	17-Sep-04	3500	4220	2430	2490	3430	-	3180	2370
505	25-Mar-05	-3650	-4000	-2360	-2420	-3480	-	-3220	-2670
657	24-Aug-05	3950	5110	2830	2600	3640	-	3380	2910
830	13-Feb-06	-3550	-5070	-2930	-2790	-3510	-	-3230	-3450
945	8-Jun-06	2620	3630	2230	2060	2720	-	2500	2230

Table 5.19: Average strain measured by gauges placed directly opposite each other

Day	Date	EL		WL	
		0°- 180° (μm/m)	90°- 270° (μm/m)	0°- 180° (μm/m)	90°- 270° (μm/m)
125	10-Mar-04	-1825	-1715	-1565	-1445
316	17-Sep-04	3860	2460	3430	2775
505	25-Mar-05	-3825	-2390	-3480	-2945
657	24-Aug-05	4530	2715	3640	3145
830	13-Feb-06	-4310	-2860	-3510	-3340
945	8-Jun-06	3125	2145	2720	2365

The average tensile strain measured during the first expansion season between March 11, 2004 and September 17, 2004 at the crown and invert of the pipe at the EL and WL test section was approximately 3860 and 3430 microstrain respectively while the gauges at 3 and 9 O'clock indicated that the pipe strained approximately 2460 and 2775 microstrain respectively. The average strains recorded by the gauges placed directly opposite each other are given in Table 5.20.

Table 5.20: Input parameter used for estimation of ring deflection of HDPE pipe

Parameters	
Pipe Diameter, D (mm)	200
Standard dimension ratio, SDR	17
Bedding factor, K	0.1
Lag factor, L	1.0
Long-term apparent modulus of elasticity of the pipe, E (MPa)	757.9
Short-term apparent modulus of elasticity of the pipe, E MPa)	200
Modulus of soil reaction, E' (MPa)	6.89
Height of Backfill, H (m)	1.55
Unit weight of soil, γ (kN/m^3)	20
Effective friction angle of backfill material, ϕ'	30°

The average circumferential strain measured at the crown and invert of the pipe was 6 to 40% higher than those measured at the springlines. The observed difference is more pronounced on pipe strain data obtained from the EL test section in which relatively large strains were

measured at the invert of the pipe. This same strain gauge showed relatively large strains during the pipe installation (see Table 5.12). It is likely that the local stiffening effect created by the glue used to secure the strain gauge to the wall of the pipe played some role in the variation observed in the magnitude of the strain. The local stiffening effects of glue with which strain gauges are fixed to plastic pipes have also been identified by Mwanangonze et al (2003).

The strain gauge placed at 6 O'clock at the WL test section malfunctioned after day 175. The cause of failure is not known but it should be note that the same strain gauge showed somewhat low strain during pipe the installation (see Table 5.12).

5.8.4 HDD installed PE Bore Slurry Pressures

The change in bore slurry pressure within the annular space around the HDD installed pipe was monitored as part of the long-term monitoring program. Two pressure transducers were placed inside each test sections, one at the crown (12 O'clock) and the other one at the springline (3 O'clock). The measured change in bore pressure at the EL and WL test section location are presented in Figures 5.63 and 5.64 respectively. The resolution of the output signal from the pressure transducers as shown on the plots is approximately ± 10 kPa (± 1.5psi) which correlates to about 2% at full-scale for the 500kPa (75psi) capacity transducer. This resolution is low when compared to the maximum pressure value obtained during monitoring period.

The bore slurry pressure history does not appear to have obvious correlation with the change in ambient temperature like those shown by pipe strain and deflection data. The pressure data does suggest that there were minor changes in bore pressure during the monitoring period. The magnitudes of these changes are barely greater than 14kPa (2.0psi) which is close to the resolution of the pressure transducer. It is difficult to conclude if the observed changes are signal noise or actual change in the bore pressure. Pressure transducers placed at the crown of the pipe showed an observable increase of approximately 28 kPa (4.0psi) and 17kPa (2.5psi) in the bore pressure between September 2003 to March 2004 and September 2004 to March 2005 respectively.

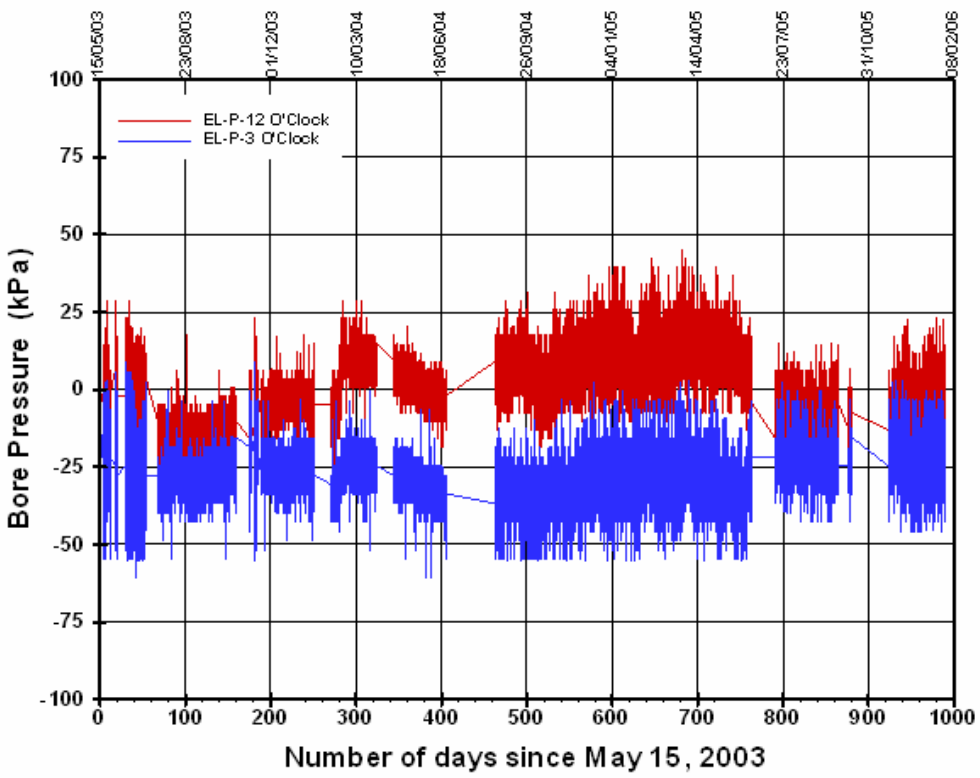

Figure 5.63: Bore slurry pressure around HDD installed pipe (EL Test Section)

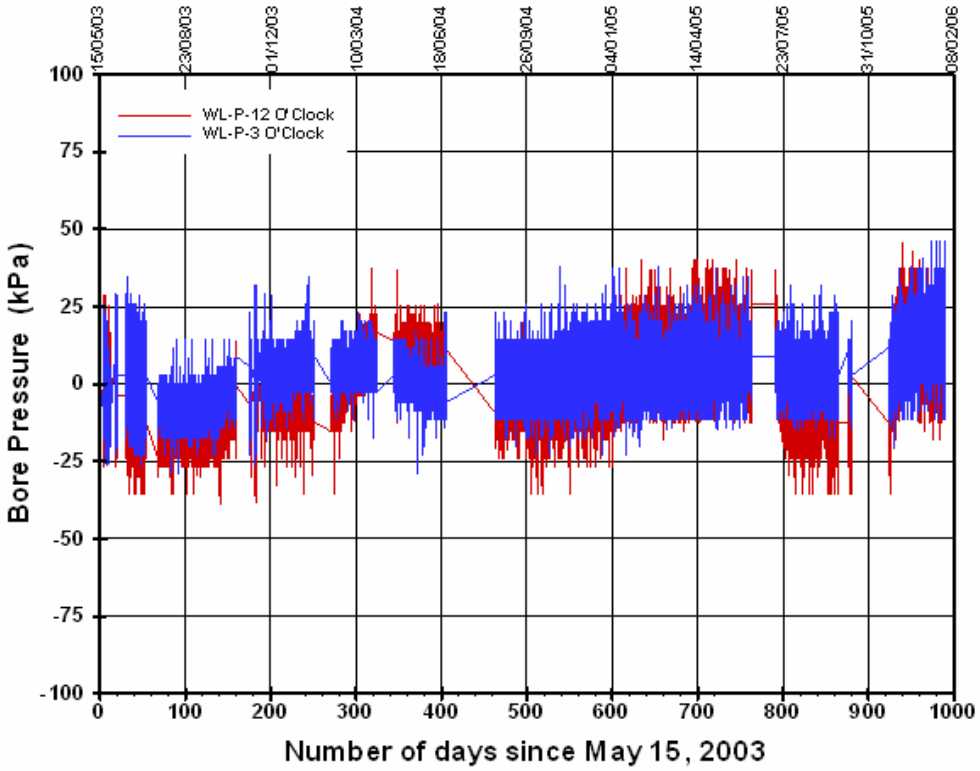

Figure 5.64: Bore slurry pressure around HDD installed pipe (WL Test Section)

5.9 Influence of Seasonal Temperature Variation on HDPE Pipe Performance

The influence of seasonal temperature variation on the performance of HDPE pipes was examined by evaluating the correlation between measured pipe deflections, circumferential strains and changes in temperature observed over the monitoring period. Pipe deflections and strain measurements along with observed temperature obtained from the EL test sections are shown in Figures 5.65 through 5.67. Figures 5.65 and 5.66 show long-term pipe deflection and temperature measurements obtained from the EL test section of the HDD and open-cut installed HDPE pipes respectively while the circumferential strains and temperature data obtained from the traditional open-cut and cover installed HDPE pipe are shown in Figure 5.67. Data obtained from the WL test sections of both pipes are similar to those from the EL test section. Thus, the plots are not presented.

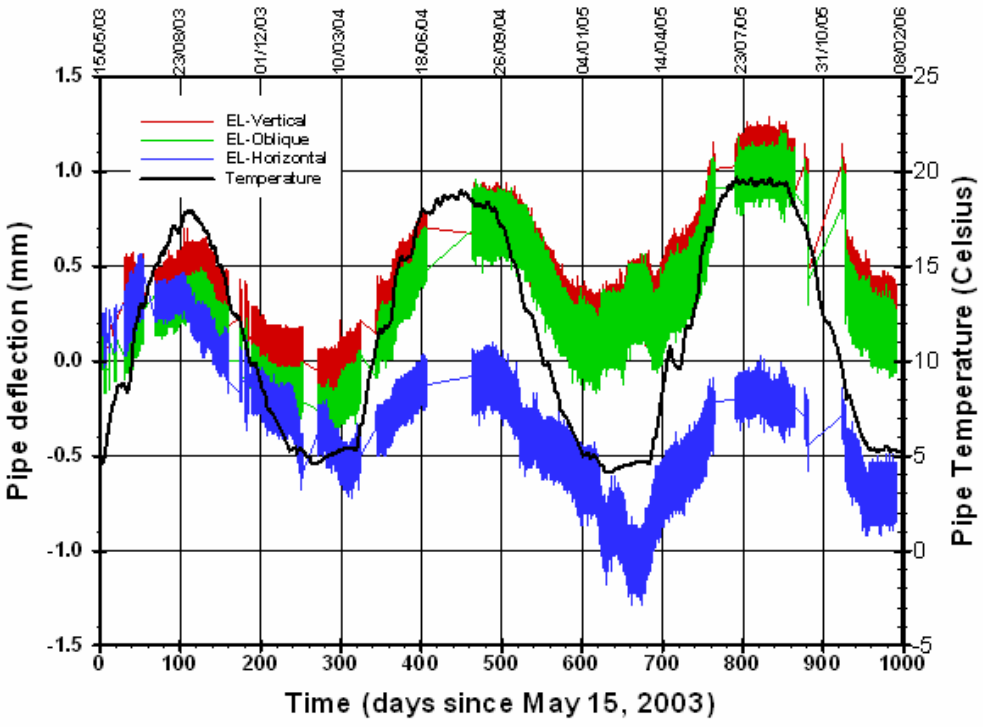

Figure 5.65: HDD pipe deflection and temperature variation (EL Test Section)

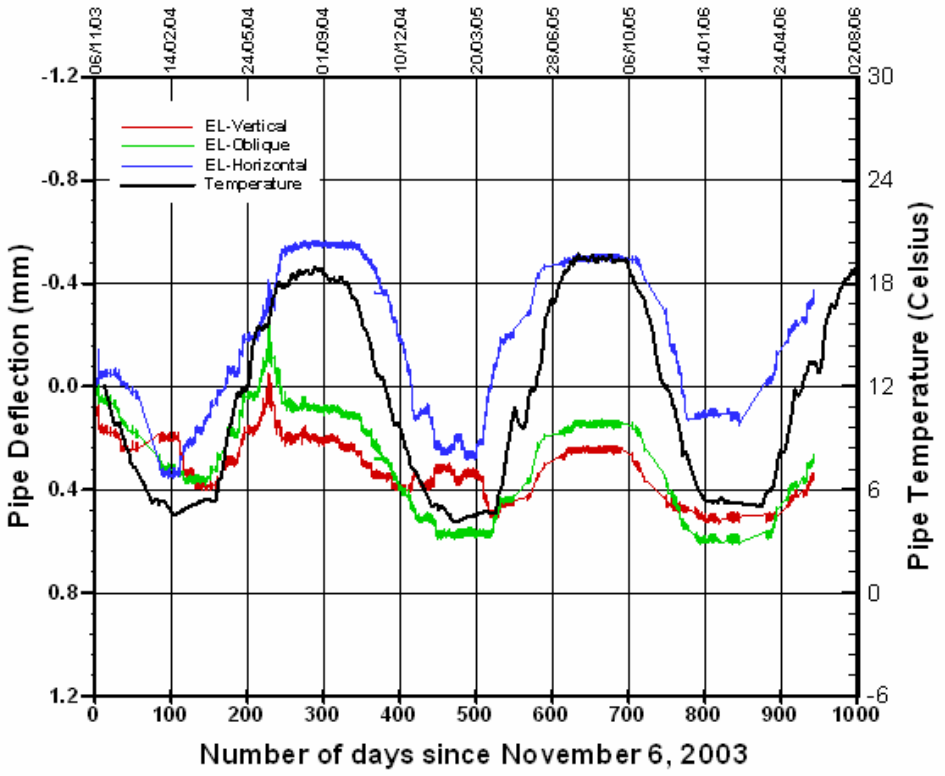

Figure 5.66: Open-cut pipe deflection and temperature variation (EL Test Section)

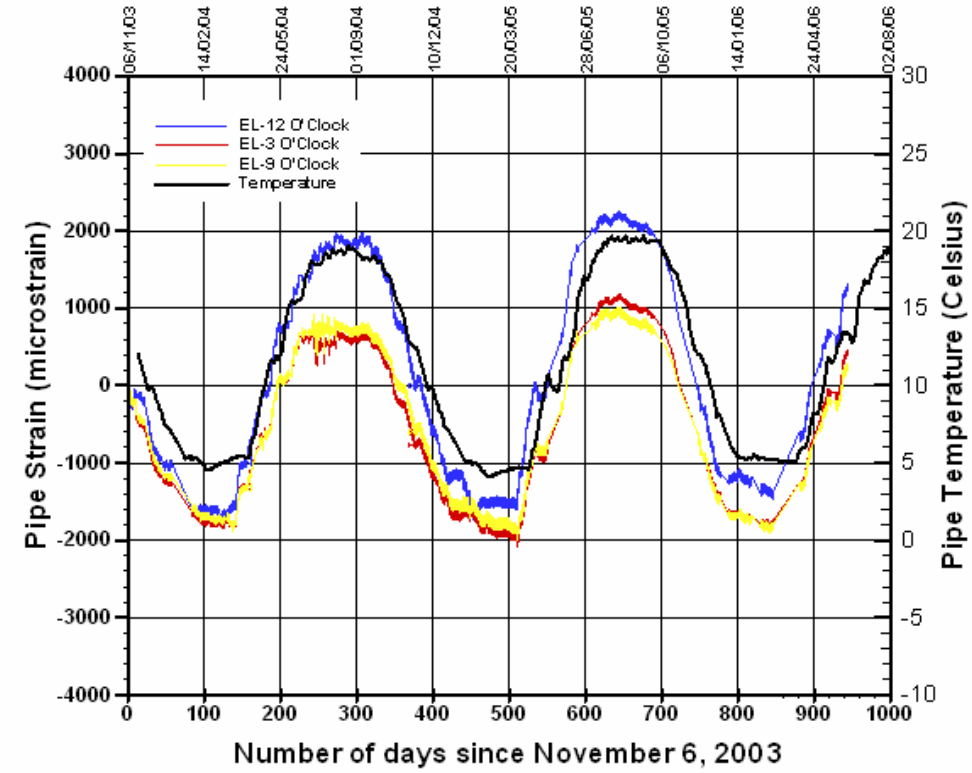

Figure 5.67: Open-cut pipe strain and temperature variation (EL Test Section)

Figures 5.65 through 5.66 indicate that there is a good correlation between HDPE pipe behavior and seasonal temperature variation over the monitoring period. The pipes contracted and expanded gradually as the temperature decreases and increases respectively. These observed relationships suggest that the sinusoidal-like trends seen in both deflections and strains measurements are mainly due to seasonal temperature variation. Although changes in earth pressure, backfill consolidation/settlement, soils moisture content and annual freeze-thaw cycle could significantly impact the performance of the installed pipes, it is improbable that these sources of influence will create sinusoidal variation in pipe deflection and strains that will closely resemble temperature sinusoidal variation.

During the HDD pipe installation, the native soil surrounding the pipe provided very minimal to no restraint to the moving HDPE pipeline since the bore was oversized (1.5 times outside diameter of the pipe). However, it is expected that once the installation velocity and mud flow into the bore were stopped that the bore-slurry (bore-slurry is the mixture of native soil and raw drilling fluid) in the annular space around the pipe would slowly consolidate and embed the pipeline. Thus, allowing the soil to grip the pipeline and provide some restraint to the pipe. There is evidence from field measurements that the bore-slurry did provide some restraint to the pipe after installation as shown in Figure 5.65. During the warm seasons, the increase in horizontal diameter of the pipe is approximately 16 to 52% smaller than the amount of inward contraction experienced by the pipe during the cold seasons even though the magnitude of temperature changes with respect to the initial temperature were similar. Thus, the pipe appears to be relatively free to contract as the temperature drops, but is restrained from expanding outward by the side support provided by bore-slurry as the temperature increases.

The magnitude of observed changes in the horizontal diameter of the open-cut installed pipeline is significantly greater, about 46 to 167 percent, than changes observed in the vertical diameter of the pipe. This observation suggests that there is less restraint provided by the backfill material close to the springline of the pipe compared to those at the crown and invert of the pipe. Inconsistent backfill compaction during trench restoration and additional overburden pressure from prism load acting at the crown of the pipe are some of the probable causes of anisotropy in the stiffness. Thus, the level of restraint provided to the pipe.

Although, the open-cut installed HDPE pipe deflection history can generally be related to variation in temperature, there is evidence that suggests there are other factors, in addition to change in temperature, contributes to the behaviour of the pipe. For instance, the changes observed in the HDPE pipe deflection during the winter months particularly when air temperature fell below -15°C (e.g. days 60 to 125 and 400 to 500) indicated that the vertical diameter of the pipe increased noticeably and the pipe experienced a rapid reduction in horizontal diameter during the same time (unlike the gradual reduction shown prior to and after this occurrence). Typically, gradual continuous decrease in temperature such as that indicated by the temperature measurements is expected to result in corresponding gradually contraction of the pipe in the absence of other factors. Change in earth pressure, backfill consolidation/ settlement, soils moisture content and freeze-thaw in the backfill could result in the observed variation in the pipe performance. Frost action in and/or around the restored trench can result in the observed behavior and will be explored in the following sections.

5.10 Influence of Frost Load on HDPE Pipe Performance

Statistical analyses have shown that failure of water and gas distribution pipes during winter months is significantly higher than during warm summer months (Lochbaum, 1993 and Habibian, 1994). Rajani and Zhan (1996) identified increase in the earth pressure associated with freezing soil as a possible cause of pipe failure during winter as they observed an increase in earth pressure within a utility trench for PVC water mains during a field trial. Other researchers including Monie and Clark (1974) and Smith (1976) have also observed an increase in earth pressure due to freezing soil. The presence of frost action at the test site and its influence (if present) on the observed behavior of the installed HDPE pipes are investigated in this section This is accomplished by examining measurements obtained from different sensors (instrumentation) installed within the backfill above the installed HDPE pipe. The field measurements that are examined include temperature profile within the pavement, change in volumetric water content at different depth and variation in earth pressure within the trench. Detailed description of the field instrumentation embedded within the restored pavement can be found in Section 5.3.3.

5.10.1 Temperature Profile

The variation of temperature with depth was monitored by an array of thermistors placed at approximately 250, 550, 1000 and 1150mm below the surface of the asphalt concrete roadway. The temperature time history obtained from the thermistors are shown in Figures 5.68 through 5.71. The gaps in the data represent time when the data acquisition system was temporarily removed for another research project. The average daily air temperature measured at the test site is also shown on each plot. The temperature profile measurement within the trench covered the 2004-2005 and 2005-2006 winter seasons.

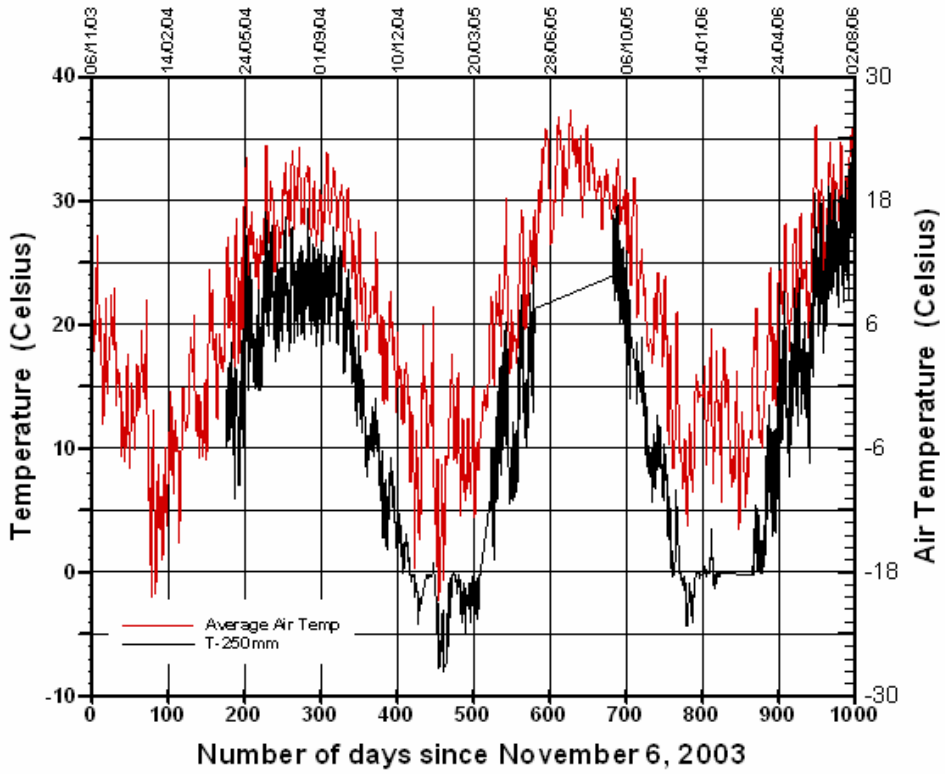

Figure 5.68: Variation of temperature near 250mm below asphalt pavement surface

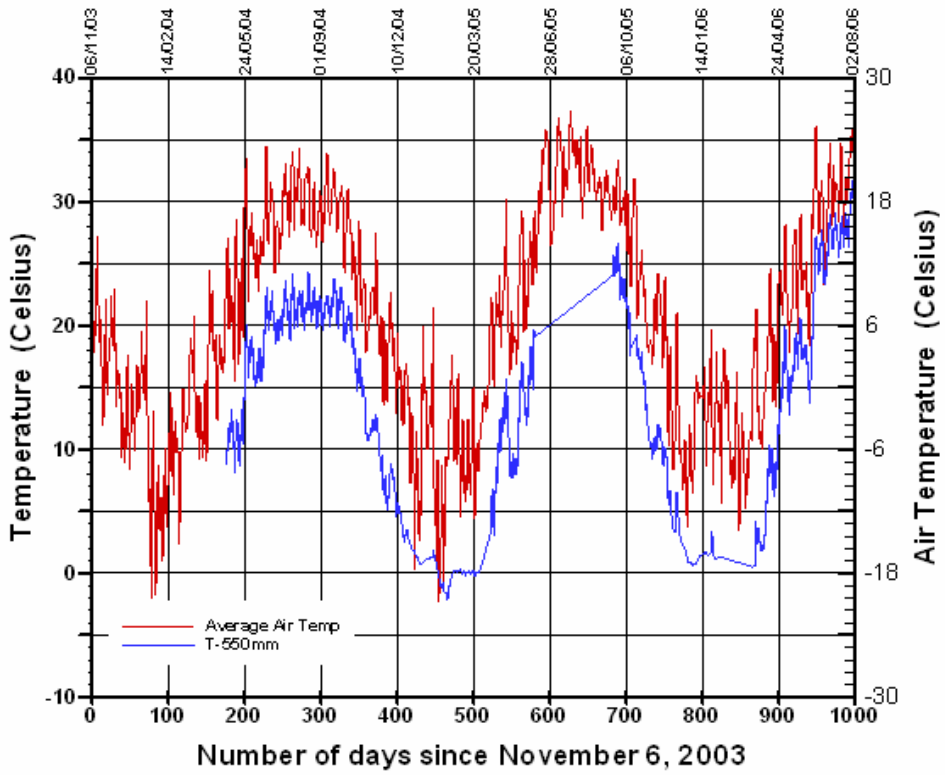

Figure 5.69: Variation of temperature near 550mm below asphalt pavement surface

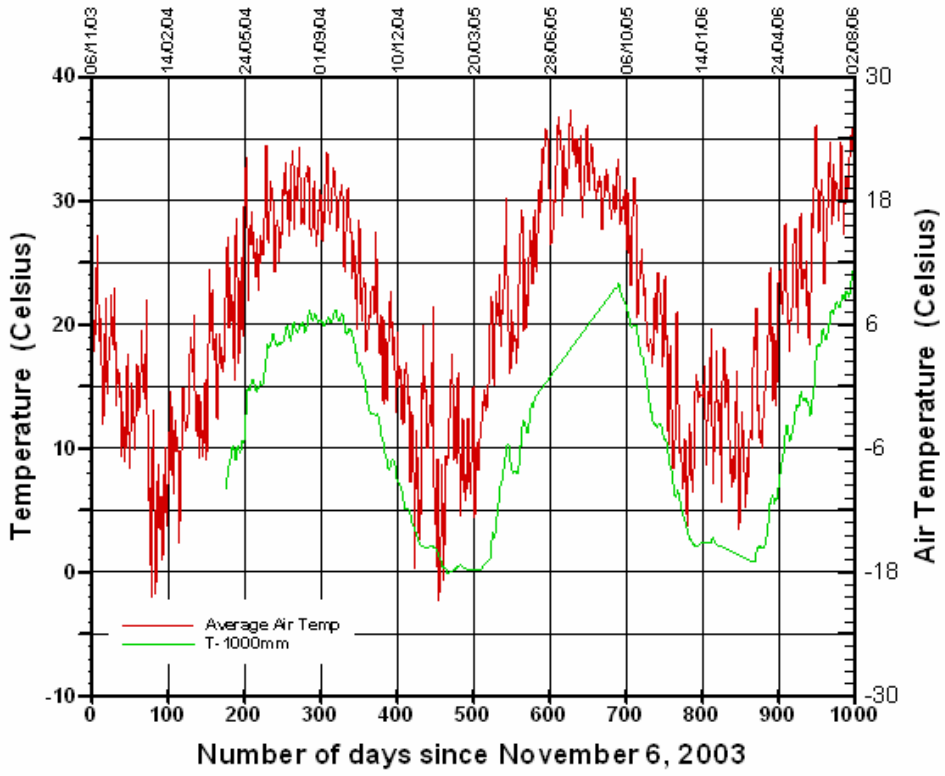

Figure 5.70: Variation of temperature near 1000 mm below asphalt pavement surface

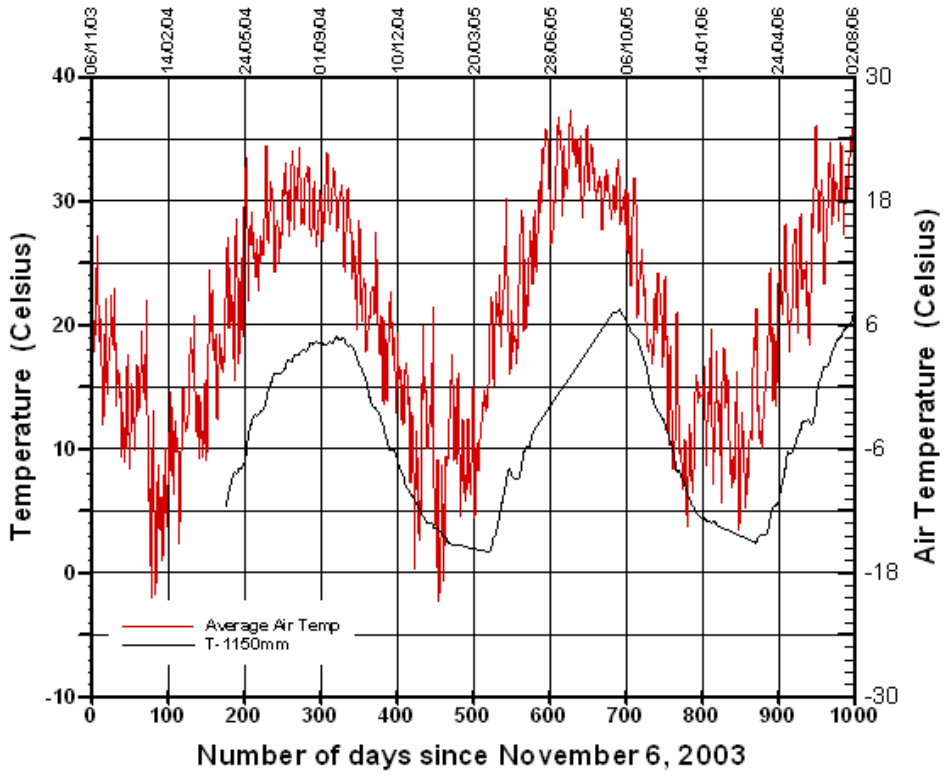

Figure 5.71: Variation of temperature near 1150mm below asphalt pavement surface

There is evidence from the temperature measurements shown in Figures 5.68 through 5.71 that there was significant frost penetration into the trench between days 404 and 496 (December 13, 2004 and March 16, 2005). The deepest frost penetration occurred near day 452 (January 31, 2005) when all the thermistors installed up to a depth of 1000mm below pavement surface recorded temperatures below 0°C indicating frost action. Relatively cold ambient temperature was recorded at the test site during the same period of time. For instance, on January 27 and 28, 2005 air temperatures as low as -32°C were measured. The freezing index during the 2004-2005 winter season was approximately 719°C-days. This value was computed from air temperature measurements obtained at the test site. The freezing index is defined as the number of degree days (above and below 0°C) between the highest point in the autumn and the lowest point in the spring on the cumulative degree-day time curve for one winter season. The winter of 2005-2006 was generally mild compare to the previous year when the freezing index computed from the air temperature was about 406 °C-days. Consequently the depth of frost penetration was generally less than 550mm.

Analyses of the data collected during the winter of 2004-2005 and 2005-2006 suggests that the temperature gradient measured at 0°C isotherm within the trench backfill was in the range of 0.02 to 0.025°C/mm between December and March. The value of the temperature gradient is comparable with the value of 0.02°C/mm reported by Zhan and Rajani (1996) for similar soils. The relatively high thermal conductivity and lower moisture content of the backfill material (Granular A) promote deep frost penetration during winter and quick thaw during spring -as observed from field data obtained from the test site. The thermal conductivity of Granular A material at 11% moisture content is 1.72 when it is unfrozen and increases to 2.32 when frozen (Zhao et al, 2001).

Although, the temperature profile within the backfill was not monitored during 2003-2004 winter season, the depth of frost can be estimated from average daily air temperature values measured at the test site. The air temperature measured at the test site during the 2003-2004 winter season reached values that were below -20°C. Based on the estimated temperature gradient at the site and data obtained during 2004-2005 and 2005-2006 winter months, it can be inferred from the winter 2003-2004 daily air temperature that the depth of frost was approximately between 750 and 1000mm during the 2003-2004 winter months. The air freezing index computed from the air temperature data for 2003-2004 winter season was approximately 595° C-days.

It is worthwhile to mention that the measured air freezing index and depth of frost observed at the test site during the monitoring period are comparable with historical data obtained near the test site location between 1931 and 1975. In 1970, the then Ontario Ministry of Transportation and Communications (now Ontario Ministry of Transportation) initiated a five year program aimed at measuring frost penetration in different subgrade soils throughout Ontario. The depth of frost and temperature data between 1970 and 1975 were collected from over 60 stations spread throughout the Province (Chisholm and Phang, 1983). Data collected during the study period and climatological data obtained from 224 locations across the Province between 1931 and 1970 were used to develop frost penetration and freezing index maps for the Province. The maps are shown in Figure 5.72 and Figure 5.73. The depth of frost measured on Highway 7 in Guelph, ON (station closest to Waterloo) between 1970 and 1975 ranged between 1.22m and 1.57m and the freezing index was between 650 and 705 °C-

days. The pavement structure consisted of 100mm of asphalt concrete underlain by 460mm of granular material and a sandy gravel subgrade soil.

The depth of frost and freezing index for Waterloo, ON estimated from maps shown in Figures 5.72 and 5.73 are approximately 1200mm and 600°C-days respectively. The maximum depth of frost measured at the test site was about 1050mm and the freezing index ranged between 406 and 719 °C-days. These values are comparable with values estimated from the historical maps.

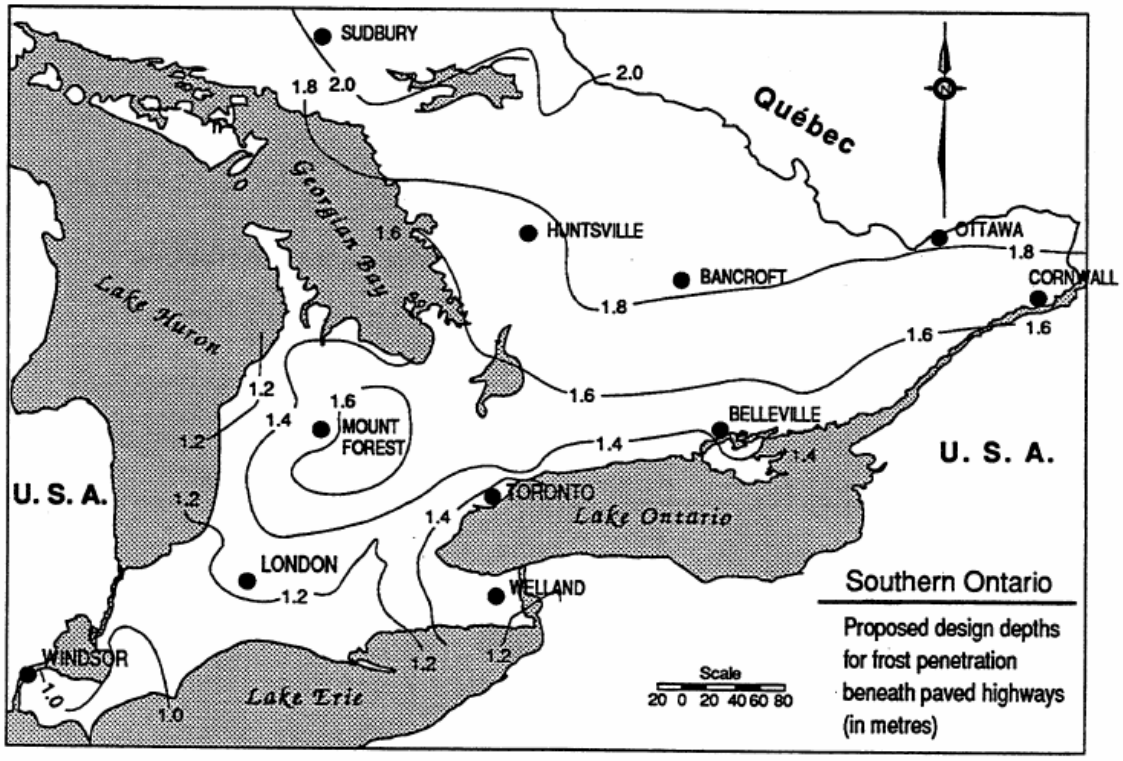

Figure 5.72: Frost penetration depths map for Southern Ontario (Chisholm, 1983)

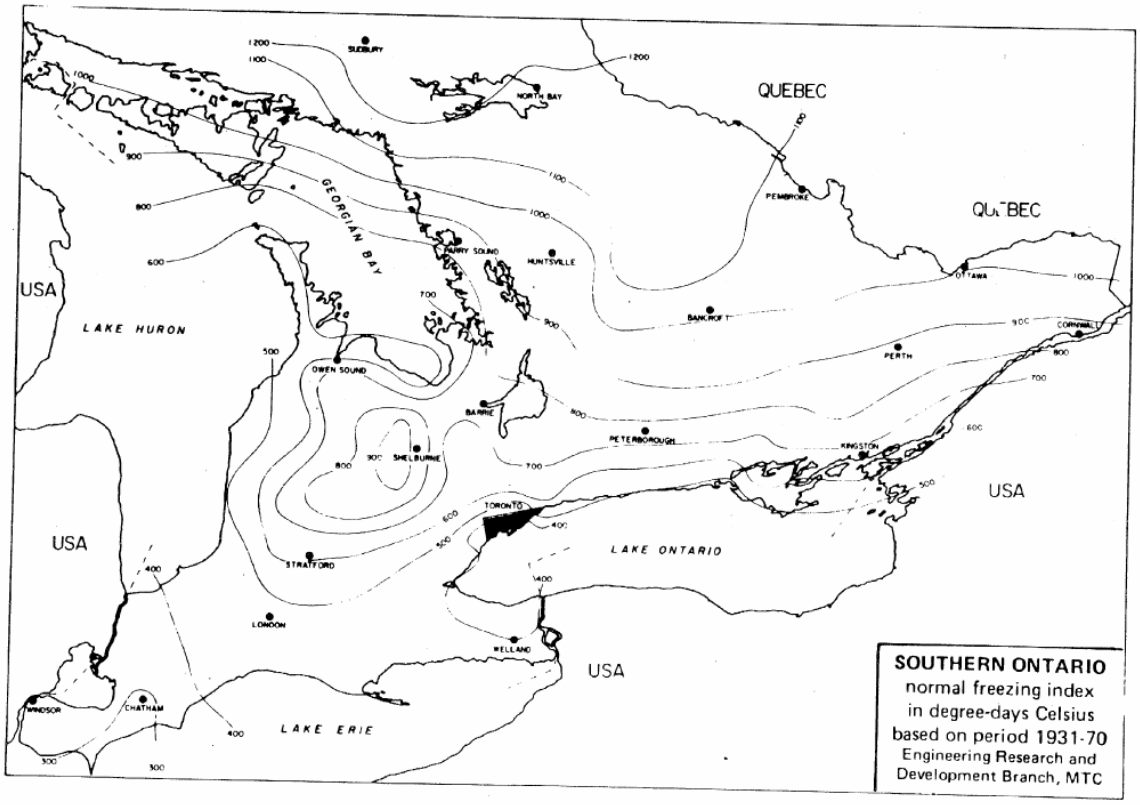

Figure 5.73: Freezing Index map for Southern Ontario (Chisholm, 1983)

5.10.2 Volumetric Moisture Content Variation

Water migration and phase change in water during freezing can be deduced from changes in soil volumetric moisture content measured by the TDR probe. Patterson and Smith (1981) showed through laboratory testing that the volumetric water content of a frozen soil measured by TDR probes provide an indication of unfrozen volumetric water content of the soil because the dielectric constant of ice (3.2) is nearly same as that of dry soils (2.5-3.5) relative to the large dielectric constant of unfrozen water (87.7) at 0°C.

The data obtained from the two TDR probes placed in the restored trench above the open-cut installed HDPE pipe are evaluated for presence and extent of frost within the backfill. The variation of unfrozen volumetric water content with time measured by the TDR probes installed approximately 600mm and 1000mm below the pavement surface labeled are shown in Figure 5.74. The magnitudes of volumetric moisture content shown in Figure 5.74 are somewhat high. The moisture content of the soil measured during the compaction of backfill

material over the HDPE pipe ranged from 6.4 to 8.1%. The TDR probes were not calibrated with the actual samples of Granular-A material used by the contractor for trench backfill and this could be the reason for higher then expected moisture content values shown in the Figure. Although, the exact magnitude of change in volumetric moisture content obtained from the TDR probes cannot be determine, nevertheless, the measurements presented in Figure 5.74 permits qualitative observation of the effects of freezing on the moisture content variation within the backfill soil.

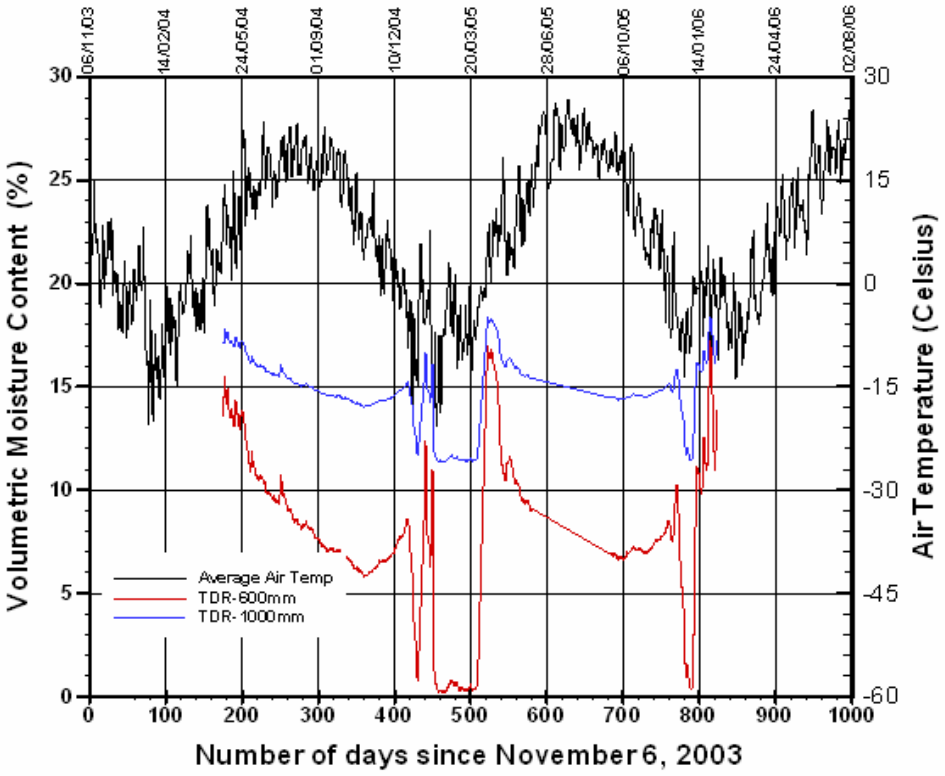

Figure 5.74: Pavement volumetric moisture content variation with time

The TDR measurements suggest that the volumetric moisture content of soil gradually decreased immediately following the spring season. The spike observed in the data during the summer months signifies an increase in moisture content due to precipitation at the test site. For instance, 50mm of rain was recorded at the test site between July 12 and 17, 2004 and the change in backfill soil moisture due to the rainfall is clearly shown on Figure 5.74 by the increase in moisture content during days 249 and 254.

Both TDR probes showed drastic change in unfrozen volumetric water content measured near day 416 (December 26, 2004) when the probes showed a significant reduction in volumetric moisture content. Between day 416 and 430 (December 26, 2004 to January 9, 2005) the TDR placed at 600mm and 1000mm showed changes from approximately 8.6 to 0.8% and 15.2 to 11.7% respectively. Examination of the temperature data revealed that the observed rapid decline in volumetric moisture content within the backfill was preceded by a significant drop in air temperature from approximately -7.5 to -22°C during the same period. The temperature increased momentarily afterward and rose above the freezing point to about +7.5°C leading to a sharp increase in soil moisture between day 432 and 450 (January 11 to 29, 2005).

The measured average daily temperature at the test site indicate that temperature decreased to about -17°C near day 452 (January 31, 2005) and remained well below freezing until near day 501 (March 20, 2005) when the temperature begin to gradually increase. The average daily temperature between January 31 and March 20, 2005 was approximately -13°C with the coldest measured average daily air temperature being -22°C. The upper TDR probes near depth 600mm below pavement surface suggest that the unfrozen volumetric moisture content of soil around the probe was nearly 0% over the sustained freezing period between January 31 and March 20, 2005. The relatively low unfrozen moisture content indicates that the water within the soil in the vicinity of the TDR probe is frozen or near freezing. The lower TDR near depth of 1000mm below pavement surface showed a similar drastic reduction in moisture content during the same period of time. Similar trends were observed in change in volumetric water content during the 2005-2006 winter season.

An examination of the field data in Figure 5.74 showed that prior to complete freezing of the soil water, the TDRs showed that there was a gradual steady increase in unfrozen volumetric water content of the soil followed by a decrease in unfrozen volumetric water content of the soil. These variations can be attributed to water migration towards the frost front and also partially due to freezing of water in the soil above the TDR probes. The upper TDR probe placed 600mm below pavement surface showed a higher increase in water content due to being closer to the frost front.

5.10.3 Change in Earth Pressure

Three total earth pressure cells were installed in the restored trench to monitor the change in total vertical stress with time above the open-cut installed HDPE pipeline. The pressure cells TPC1, TPC2 and TPC3 were embedded in fine sand at approximately 200mm, 600mm and 950mm beneath the surface of the asphalt concrete roadway respectively. Figure 5.75 shows the variation in total vertical stress with time measured at the various elevations above the HDPE pipe. The pressure cells were reinitialized after installation. Thus values shown in Figure 5.75 do not include change in earth pressure in the backfill due to construction and pipe installation. The middle and lower pressure cells, TPC2 and TPC3, showed similar trends throughout the monitoring period while the upper pressure cell installed at depth of about 200mm showed a different trend.

The total pressure cells response to changes in earth pressure due to frost penetration during 2003-2004 winter season started near day 60 (January 1, 2004) and lasted till around day 126 (March 11, 2004) when a short warm break in mid February from day 105 to 114 (February 19 to 28, 2004) occurred. Similar responses to change in earth pressure were observed between days 403 and 495 (December 13, 2004 to March 15, 2005) and from 757 to 865 (December 2, 2005 to March 20, 2006). These days corresponds to the 2004-2005 and 2005-2006 winter seasons respectively. The middle and lower total pressure cells indicated a steady decrease in total earth pressure during the three winter seasons. The maximum change in earth pressure, measured near the location of the middle and lower pressure cells, was 16 and 9kPa (2.3 and 1.3psi) respectively during the three winter seasons. There were also short respites during 2004-2005 and 2005-2006 winter seasons when the temperature increased and resulted in some thawing, this led to a brief jump in earth pressure.

Thawing of frozen soil at the onset of spring season due to an increase in air temperature corresponded to a substantial increase in vertical earth pressure within the trench. This is evident by a spike in earth pressure at the onset of spring season. The earth pressure becomes steady once all the frozen soil is thawed.

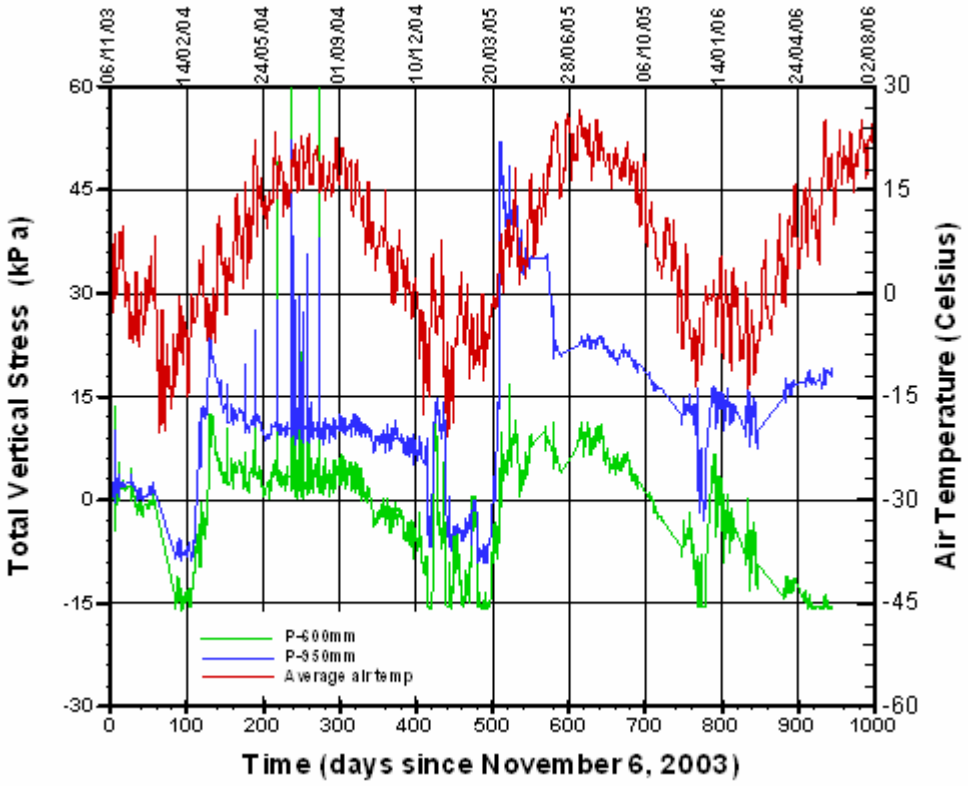

(a) Middle and lower total pressure cell

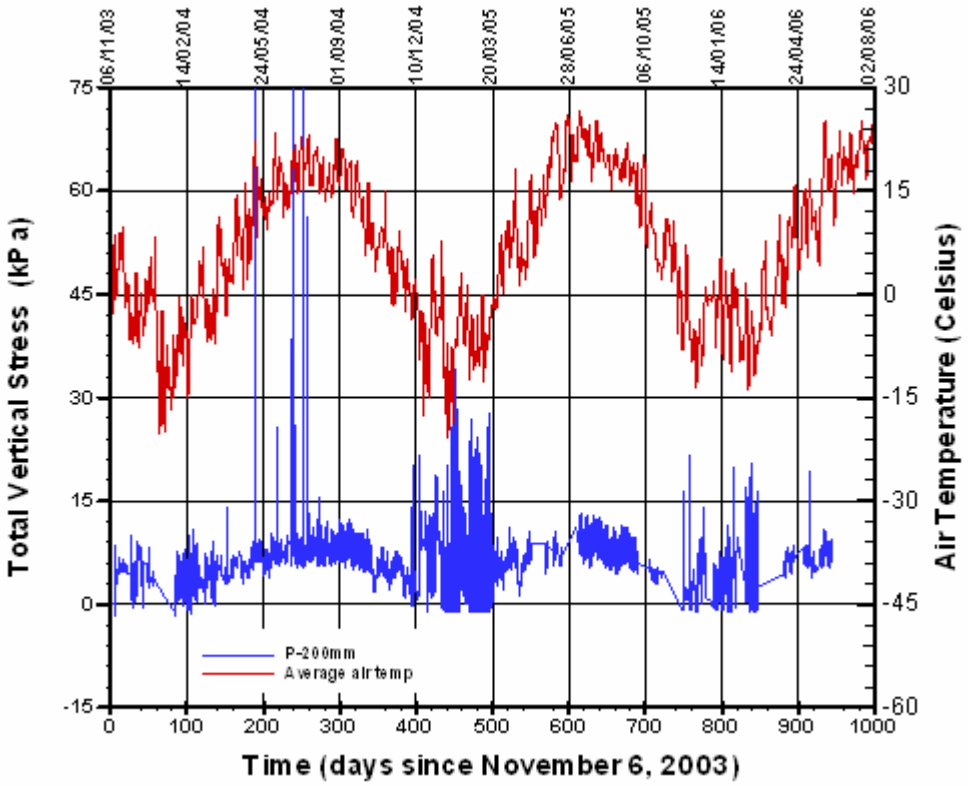

(a) Upper total pressure cell

Figure 5.75: Total vertical stress variation within pavement

Unlike the other pressure cells, the upper load cell placed directly beneath the asphalt concrete showed an increase in earth pressure during the winter months. The vertical earth pressure measured at the depth reverted back to initial pre-winter values after at the onset of the spring season. The increase in vertical earth pressures, shown by the spike in the data between April and August 2004, are due to traffic load from heavy duty 80-tonnes off road trucks that hauled clay along the test track in the summer of 2004.

Frost load is typically associated with an increase in the earth pressure as a result of frost penetration. The reduction in earth pressure measured within the backfill suggest that the backfill material (Granular A) used in restoring the trench has a lower frost susceptibility and heave potential than the native soil material. An increase in earth pressure is expected if the backfill material has a higher frost heave potential than the native material. This observation is in agreement with the findings of Zhan and Rajani (1996) from field test conducted on buried jointed metallic pipe at Gatineau, Quebec were they showed that the change in earth pressure is proportional to the difference in the frost heave potential between the native and backfill material.

5.10.4 HDPE Pipe Response to Frost Load

The presence of frost action beneath the roadway at the test site is evident as there are convincing evidence from temperature profile, changes in volumetric water content and vertical earth pressure observed within the pavement that indicate the existence of frost during the winter seasons. The performance of the HDPE pipes during winter seasons are evaluated to identify any behavior that may be related directly with the observed frost action at the test site.

Pipe deflections measurements obtained from the EL test section of the open-cut installed HDPE pipe and the variation of vertical earth pressure observed above the pipe are shown in Figure 5.76. The correlation between measured pipe response and frost action during freezing is clearly shown on this plot. The pipe deflection measurement during freezing, for instance between days 60 to 125 and 400 to 500 indicated that the vertical diameter of the pipe increased noticeably while the pipe experienced a rapid reduction in horizontal diameter during the same time. The total pressure cells showed that the vertical earth pressure above

the pipe reduced causing the top of the pipe to rebound upward. This load relaxation at the crown of the pipe resulted in the observed increased in the vertical diameter of the pipe and a corresponding decrease in the horizontal diameter of the pipe.

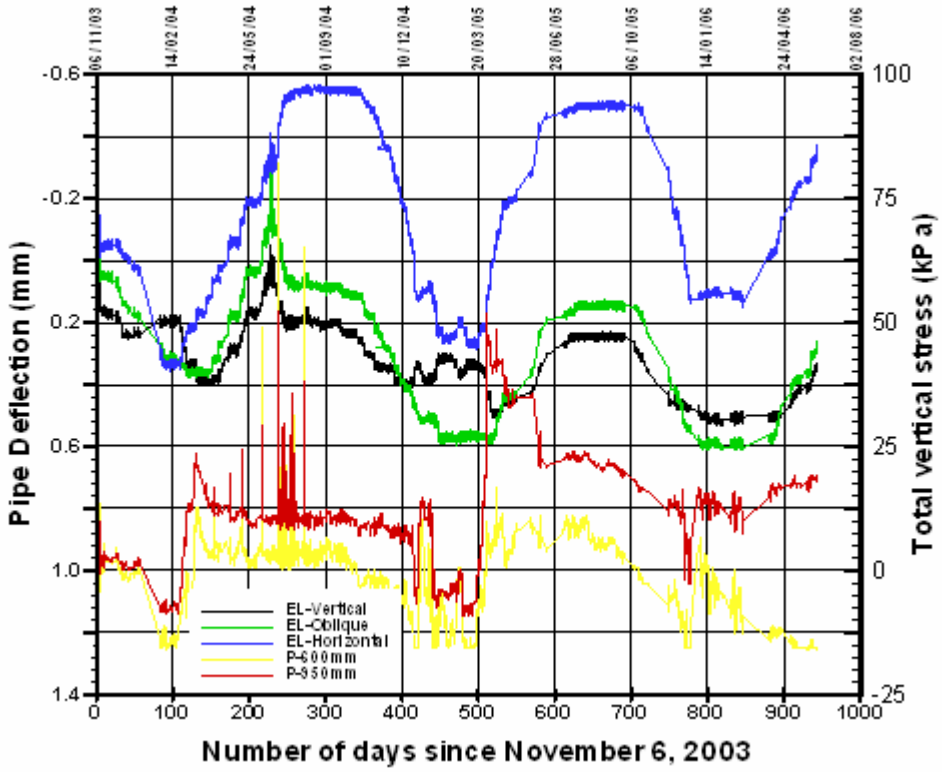

Figure 5.76: Open-cut installed HDPE Pipe deflection response to frost load

The change in earth pressure above the HDD installed pipe was not monitored and it is expected to be different from those observed above the open-cut installation due to the difference in soil material properties and lack of discontinuity (no-cut) in the pavement. Zhan and Rajani (1997) suggested that frost load is generated primarily as a consequence of difference in the frost heave potential between the native and backfill material and that no earth pressure change should be expected if both the native and backfill materials have the same frost heave potential. If their proposition is valid, no change in earth load due to frost action should be expected on the HDD installed pipe.

Nevertheless, the change in earth pressure observed above the open-cut installed pipe and the pipe deflection measurement obtained from the EL test section of HDD installed HDPE are

shown in Figure 5.77 for qualitative evaluation. The objective of the qualitative evaluation is to identify any response shown by the HDD installed HDPE pipe that may signify action of frost similar to those observed in the open-cut installed pipe. There is no obvious indication of frost load on the HDD pipe deflection obtained during the 2003-2004 winter season as shown in Figure 5.76. However, the data recorded during the 2004-2005 showed some trends similar to those observed in the open-cut installed pipe between days 600 and 700. For instance near day 660 (March 5, 2005) in Figure 5.76, the vertical diameter of the pipe showed a noticeable increase while the horizontal diameter of the pipe contracted significantly. Although, this observation suggest the presence of frost action on the HDD installed pipe, no conclusion can be drawn on the action of frost on HDD installed pipe based on this single observation. Addition information is required to investigate the presence and effect of frost on HDD installed HDPE pipe.

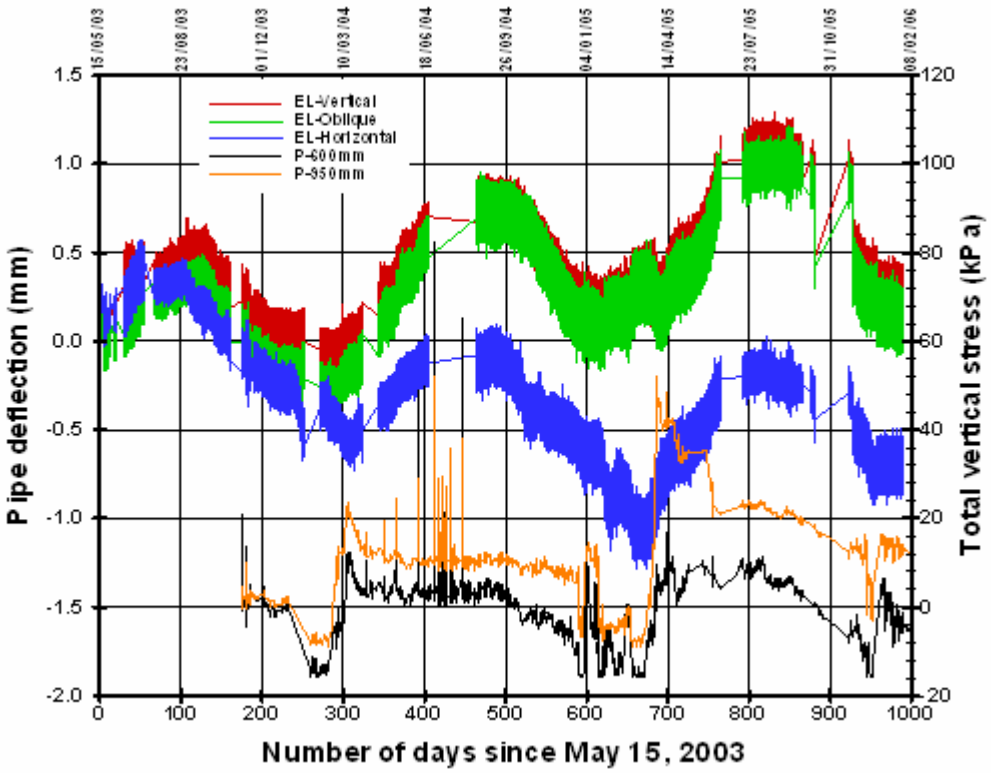

Figure 5.77: HDD installed HDPE Pipe deflection response to frost load

5.11 Evaluation of Existing Design Equations for Flexible Pipes

The applicability of the current design equations use for the design of buried and HDD installed flexible pipes discussed and presented in Chapter 2 was investigated. Change in pipe diameter measured immediately following the field-scale pipe installations and those obtained during the long-term monitoring were compared with deflection predicted by the current design equations, and the results of the comparison are presented herein. Input parameters used in estimating the ring deflection of the HDPE pipe are presented in Table 5.21.

Table 5.21: Estimated pipe deflection obtained from design equations

	Open-cut Installation			HDD Installation		
	Measured	Estimated	% Diff	Measured	Estimated	% Diff
Short-term (construction)	1.2 mm	1.2 mm	0	0.4 mm	0.8mm	100

The change in diameter of the buried (open-cut installed) pipe was estimated with modified Iowa equations given in Equation 2.8. The modified Iowa equation is considered as the state-of-the-art design equation for flexible pipe (Uni-Bell, 2001). Detail description and underlying assumptions inherent in this design equation are discussed and presented in Section 2.3.3. The magnitude of the short-term (construction induced) ring deflection estimated by the modified Iowa equation using the input parameters shown, in Table 5.21, was 1.2mm. The estimated short-term (end-of-construction) pipe deflection is very comparable to maximum change in pipe diameter, 1.2mm measured at the end of pipe installation. The long-term ring deflection estimated for the buried pipe using the modified Iowa's equation is 1.5mm. The predicted long-term ring-deflection is significantly higher than the maximum change in pipe diameter of about 0.7mm measured during the long-term monitoring period.

The ring deflection for the HDD installed pipe was estimated using equations suggested by Plastic Pipe Institute (PPI, 2000). Detail of the equations are given in Section 2.3.3. The magnitude of the short-term (construction induced) ring deflection estimated for the HDD

installed pipe following the procedure outlined by the Plastic Pipe Institute was about 0.8mm. The measured change in pipe diameter immediately after pipe installation was approximately 0.4mm which is about 50 percent lower than estimated change in pipe diameter. The long-term change in pipe diameter estimated for the HDD installed HDPE pipe using the PPI equation was 1.8mm while the maximum change in pipe diameter that was measured during the long-term monitoring was about 1.2mm. The long-term change in pipe diameter was overestimated by approximately 50 percent using the PPI equation.

The results obtained from the analysis are summarized in Table 5.22. The long-term change in pipe diameter estimated with the modified Iowa's equation is very conservative when compared to actual measurements obtained from the field test. The reasons for the deviation are the simplifying assumptions inherent in the derivation of the equation that was originally developed for thin wall corrugated metal pipe using elastic theory. Uniform pressure distribution is assumed around the pipe and pipe-soil interaction considerations were excluded in the formulation of the equations. These factors play an important role in determining the magnitude of pipe deflection and could have contributed to the difference between the estimated and measured deflection.

The fundamental assumption made in the derivation of the PPI equation for estimating ring deflection of HDD installed pipe is that the slurry occupying the annular space between the bore and the installed pipe provides no side-support along the springline to restrain vertical deflection and that the primary resistance to deflection is provided by the long-term ring-stiffness of the pipe. The large disparity between the predicted and measured change in pipe diameter suggest that the assumption of 'no-side support' is excessively over-conservative.

5.12 Evaluation of Pavement Structure Performance

The Centre for Pavement and Transportation Technology (CPATT) regularly conduct IRI surveys, Falling Weight Deflectometer (FWD) and Distress surveys on the test track as part of the on-going evaluation for the asphalt mixes used on the test track pavement. Detailed description of the survey program is given in Tighe et al. (2003). The condition of the

pavement in the vicinity of the installed pipe was observed prior to and after pipe installations to assess the impact of pipe installation on the pavement performance. The results obtained from the Ground Penetration Radar (GPR) surveys, Falling Weight Deflectometer (FWD), surface distress surveys and ground surface elevation survey are presented in the following sections.

5.12.1 Ground Penetration Radar (GPR) Images

Ground penetration radar survey was conducted prior to pipe installation and subsequently after the installation by Sensor and Software, Inc. The information obtained from the GPR was used to identify the presence and extent of subsurface disturbance within the pavement structure resulting from pipe installation. The GPR data was acquired with the SmartCart profiling system, which comprises of a Noggin 1000 and a Noggin 250 production control unit equipped with a Digital Video Logger (DVL-IIG) shown in Figure 5.78. All GPR surveys were completed by Sensor software Ltd.

Figure 5.78: SmartCart ground penetration radar profiling system

GPR grid surveys performed over the location of the HDD installed pipe are presented in Figure 5.79. The hyperbolic responses shown in Figure 5.79 (b) near 1.5m depth are signal reflections from the HDD installed pipe.

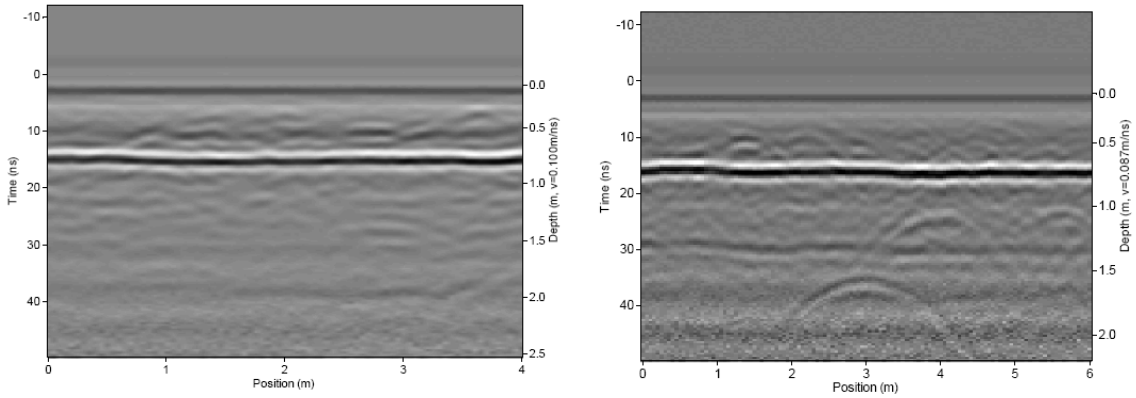

(a) Before installation (b) After installation

Figure 5.79: GPR section at the location of the HDD installed pipe

A close-up view of the subsurface condition after pipe installation in the vicinity of the HDD installed pipe along the longitudinal direction is shown in Figure 5.80. There is no evidence of subsurface disturbance visible from the GPR survey images obtained before and after the HDD pipe installation.

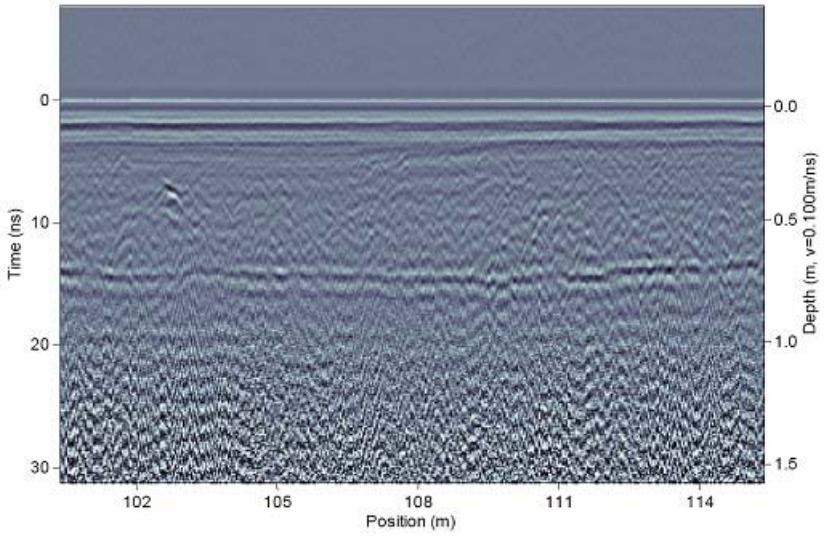

Figure 5.80: GPR longitudinal section over HDD installed pipe near position 108 m

GPR grid surveys completed above the traditional open cut installed HDPE pipe are presented in Figure 5.81. A close-up view of the subsurface condition after pipe installation in the vicinity of the open-cut installed pipe along the longitudinal direction of the roadway is shown in Figure 5.82. Data acquired after the pipe was installed using traditional open-cut installation revealed a clear disturbance within the pavement structure. The post installation GPR data also showed that the asphalt layer over the patched section is substantially thicker than the adjacent intact sections.

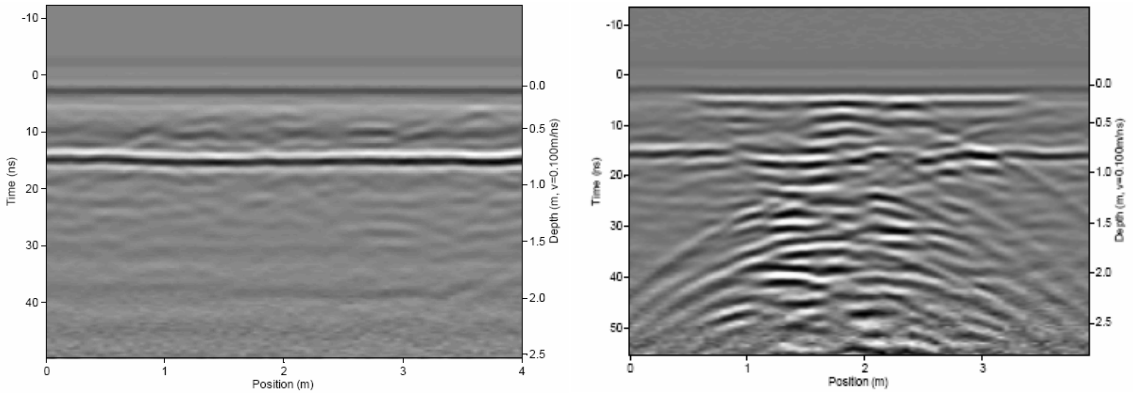

(a) Before installation (b) After installation

Figure 5.81: GPR section at the location of the open-cut buried pipe

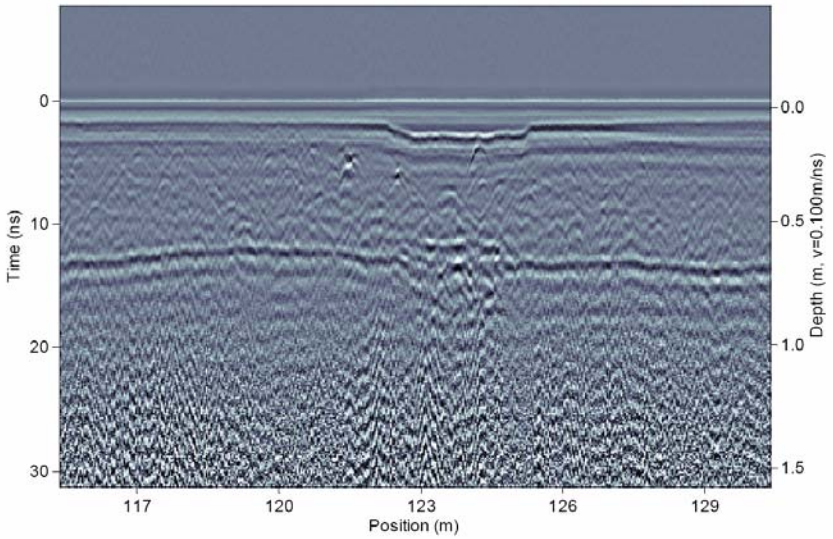

Figure 5.82: GPR longitudinal section over open-cut installed pipe near position 124 m

5.12.2 Falling Weight Deflectometer (FWD) Tests

The Falling Weight Deflectometer (FWD) is a device used to determine the structural capacity and properties of pavement structure. Pavement deflections responses to FWD loading obtained prior and after pipe installation in the vicinity of the installed pipe were evaluated to determine the impact of pipe installation to the structural capacity and performance of the pavement section. Small deflection is an indication of a stiffer material with higher elastic moduli and therefore increasing pavement structural adequacy and life. A Dynatest model 8002-952 series FWD shown in Figure 5.83 was used to measure the impact of a force exerted on the pavement surface. The loading sequence include application of different measured weights of magnitude 29, 40 and 53kN, while deflection response of the pavement were measured with several geophones placed at different distances from the load. The deflection basins (maximum point of deflection) at each geophone location are used to generate deflection profiles under the loads stated above. The data obtained was normalized to a standard load level of 40kN.

Figure 5.83: Dynatest model 8002-952 Falling Weight Deflectometer

Figure 5.84 shows the normalized deflection profile obtained from FWD tests conducted at various times before and after pipe installation at different stations along the pavement section. It is evident from the deflection profile that the pavement section in the vicinity of the open-cut pipe installation buried near station 124m has been weakened due to pipe installation activities and has resulted in a noticeable deflection. Assuming the deflection measured in the far field of the utility cut area represents the response of undisturbed pavement (i.e., utility cut has negligible influence on the pavement system). The increased in pavement deflection observed around the utility cut section at the buried pipe location is an indication of premature pavement deterioration resulting from a strength reduction of pavement material within this zone. In contrast, the pavement section in the vicinity of the HDD installed pipe placed near station 108m did not show any change deflection when compared to values obtained away from the pipe location. Hence the FWD data did not revealed deterioration or reduction in structural capacity of the pavement due to the HDD construction technique.

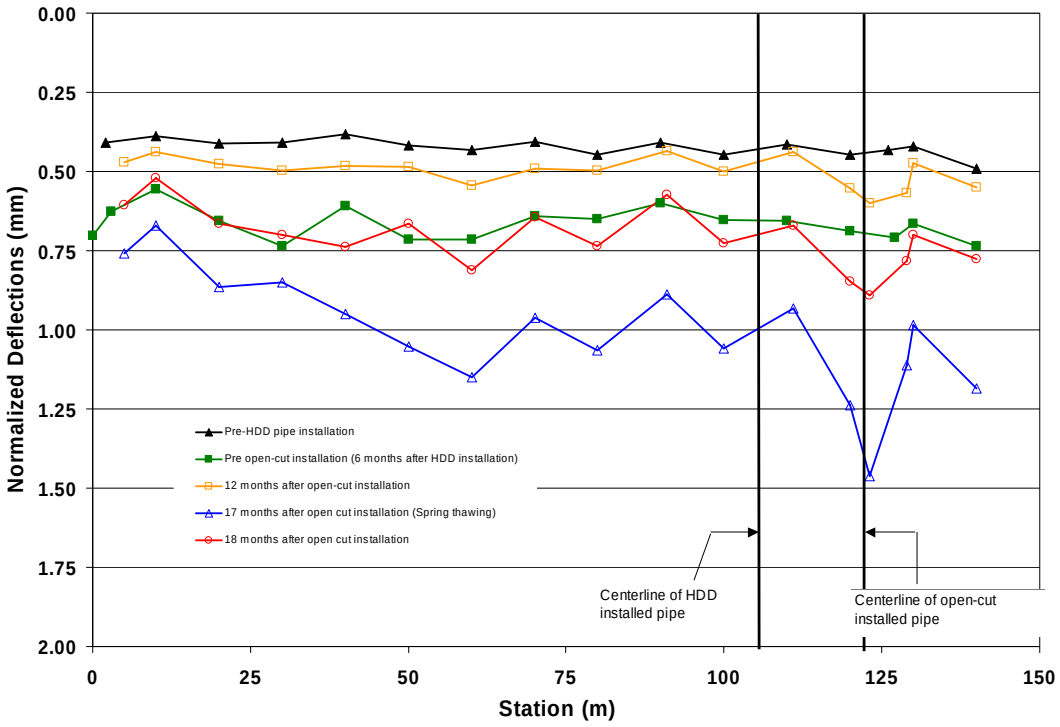

Figure 5.84: FWD Normalized deflection along pavement section

It is important to note that the magnitude of deflections obtained from FWD test is significantly influence by the effect of seasonal variability (freeze and thaw) and moisture content in the base and subgrade layers of pavement. These seasonal and moisture content effects are visible in the deflections data presented in Figure 5.84. For example the FWD test completed 17 months after open-cut installation were conducted on April 1, 2005 coinciding with the spring thaw period. The variation in temperature and moisture content of the base and subgrade layers of the pavement presented in Figure 5.74 showed significant increase in pavement moisture content due to spring thaw on April 1, 2005 which correspond to day 512 on the Figure. The increased moisture weakened and reduced the stiffness of the pavement structure resulting in greater deflection all along the pavement and more significantly in the vicinity of the repaired section.

5.12.3 Surface Distress Survey

Visual examination of pavement surface distress or cracks at the vicinity of the pipe installations are conducted periodically. Till date, there has been no crack or other visible pavement distress at the vicinity of the HDD installed pipe following pipe installation. The pavement surface condition remained virtually unchanged since after the installation. On the other hand, the repaired section at the open-cut pipe location started to show signs of surface distress following the second winter season. As shown in Figure 5.85, the edge of the patch area has permanently detached from the intact pavement section allowing infiltration of water into the pavement through the crack could subsequently leads to other pavement distress such as alligator cracks that cause structural damage.

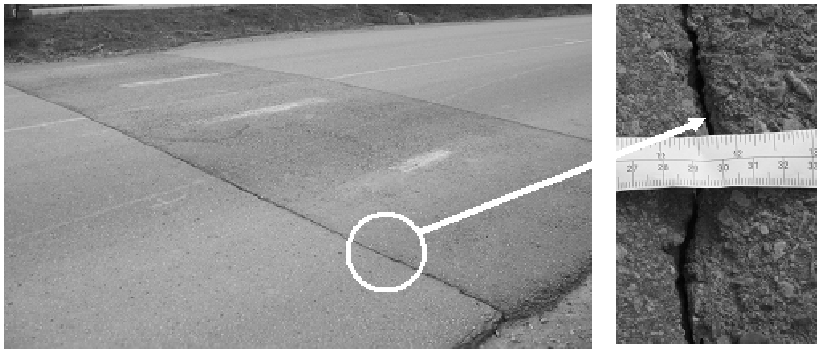

Figure 5.85: Distress at the location of the open-cut installed pipe installed

5.12.4 Ground Surface Elevation Survey

Elevation surveys were conducted prior and after the pipe installations to identify any pavement movement or deformation resulting from pipe installations. Prior to pipe placement, elevation survey grid 0.5 x 0.5m was setup on the asphalt surface. The survey baseline was set along centre line of the pipe installation and the grids were surveyed using a Total Station prior to, during, and following pipe installation. Pavement elevations surveys were also conducted periodically to monitor any long-term pavement deformation that may occur over time.

There was no significant change in the pavement surface elevation at the vicinity of the HDD installed pipe immediately after pipe installation. Similarly, the pavement surface elevation of pavement sections adjacent to the repair section were not affected by the utility cut excavation and trench restoration process but a hump, about 24mm, developed at the patched section after trench restoration. The serviceability and riding comfort of the roadway is impacted by the presence of the hump along the roadway.

Elevation survey conducted over the long-term monitoring period showed that the change in ground elevation (frost heave) during the winter season within the pavement in the vicinity of open-cut installed pipe was significantly from those observed at the vicinity of the HDD installed pipe and the rest of the pavement section. Evidence of frost heave was observed from the survey data obtained between the months of November 2004 and March 2005. Figure 5.86 shows the change in ground surface elevation of survey grid points along the center of the open-cut and the HDD installed pipes. It is clear from the Figure that the change in pavement elevation due to frost heave on the patched section above the open-cut installed pipe is substantially lower than that along the HDD installed pipe. The magnitude of frost heave in the pavement above the HDD installed pipeline is comparable to those measured on the pavement section unaffected by the pipeline installations.

The lower frost heave observed at the vicinity of the open-cut installation is directly related to the lower segregation potential of the granular material (with no fines) used to backfill the trench. Segregation potential defined as the ratio of frost heave rate to temperature gradient in

the frozen soil, increases with increasing fines content and also depends on the mineralogy of the soil (Konrad and Morgenstern, 1981). Although the frost heave in the patched pavement section is lower, the stress induced by the differential heave developed between the patched area and the adjacent pavement sections could be considerable and may have contributed to the distress pavement distress discussed in the preceding sections.

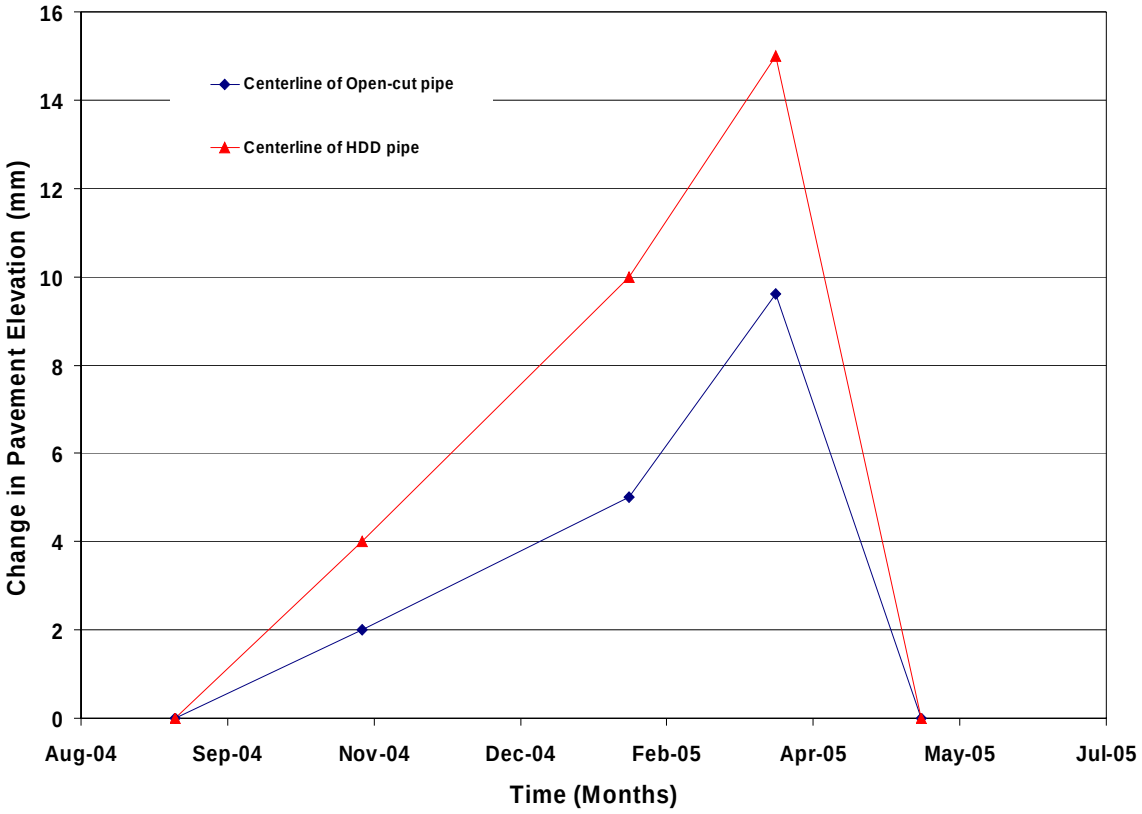

Figure 5.86: Change in surface elevation due to frost heave

Chapter 6: Numerical Simulations of HDD Installation

6.1 Introduction

The research work presented in this chapter is an extension of the ongoing HDD - polyethylene pipe research at the University of Waterloo that was initiated in 1996. A detailed description of the research program has been published in Knight et al (2002). The use of numerical simulation has been an integral part of the HDD research program at Waterloo due to limited published field case studies. A part of the HDD program, Marshall (2003) developed a 3D numerical model to simulate HDD bore pressurization and used the results obtained from series of laboratory tests to validate the model. Duyvestyn (2004) built on the frame work laid by Marshall (2003) and completed a series of numerical simulations to study the displacement response of dry sand soil due to HDD bore pressurization. The present research work uses numerical modeling to simulate bore pressurization during HDD installations beneath flexible pavement with the goal of understanding ground deformation mechanism. The charts, tables, findings, discussions and conclusions from numerical simulations presented in this Chapter are those completed by the author of this dissertation.

The objectives of the numerical simulations presented in this chapter are to:

1). Develop and validate a numerical model that simulates HDD installation process beneath flexible pavement structure using *FLAC*^{3D}. The numerical model is validated using analytical solution of cylindrical cavity expansion in Mohr-Coulomb medium (Yu and Houlsby, 1991) and measured field data (Duyvestyn, 2004).

2). Characterize ground deformation-bore pressure relation during HDD installation beneath flexible pavement using *FLAC*^{3D}. The numerical simulations are used to develop bore pressure-displacement relationship that can be use to estimate limiting bore pressure during HDD roadway crossings.
3). Generate a series of HDD simulations to identify and characterize relationship between key parameters that influence bore pressure-displacement response during HDD installation beneath flexible pavement. These relationships include the influence of depth of cover; bore diameter, thickness of filter cake, thickness of asphalt concrete, and strength properties of subgrade on bore pressures require to initiate and propagate displacement fields outwards away from the bore.
4). Develop design charts and tables that provide a first order approximation that can be used to limit allowable bore pressures during HDD installation beneath flexible pavement.

This chapter includes description and verification of *FLAC*^{3D} numerical model, modeling procedure, results of the HDD simulations and discussions on limitations, validity and practical significance of the simulation results.

6.2 Simulation of Cylindrical Cavity Expansion with *FLAC*^{3D}

As mentioned earlier in Chapter 2, the removal of bore slurry (i.e. mixture of soil cutting and raw drilling fluid) out of the bore is accomplished by inducing fluidic pressure gradient within the bore. In addition, the fluidic pressure exerted against the bore wall also assists in keeping the bore wall stable during the drilling processes. However, ground deformations can result from bore slurry pressure when its magnitude exceeds the resistance provided by the native soil surrounding the bore. Especially in shallow HDD bores such as those generally installed beneath urban roadways.

The action of fluid pressure against HDD bore wall can be approximated to that of a cylindrical cavity expansion. Cavity expansion theory has several applications in soils mechanics, principally in the areas of interpretation of in-situ tests (both cone penetrometer

and pressuremeter tests) and also in the prediction of the behavior of driven piles. Expansion of a cylindrical cavity was simulated with *FLAC*^{3D} and the results of the simulation are compared with an analytic solution to verify the code's ability to simulated HDD processes.

A number of analytical solutions have been derived for cavity expansion problem with the complexity generally dependent on the type of constitutive model used to represent the material and whether they are applicable to large strain problems. For example, a linear elastic material has a simpler analytical solution than that of a viscous elastic plastic material. The study presented in this section uses analytical solution for a linear elastic perfectly plastic constitutive model. Since the aim of the work presented in this section is to compare *FLAC*^{3D} output to a well establish analytical solution it seemed reasonable to use relatively simple and general constitutive soil models such as the chosen linear elastic perfectly plastic model. The use of more complex constitutive such as the strain hardening/softening models would not produce any additional advantage.

Yu and Houlsby (1991) presented a unified closed form solution for the expansion of both cylindrical and spherical cavities in dilatant elastic-plastic soils using the Mohr-Coulomb yield criterion with a non-associated flow rule. The closed form solution by Yu and Houlsby (1991) is also applicable to large strain analysis. In deriving the closed form solution for the cylindrical cavity expansion, axial stress is assumed to be the intermediate stress and plane strain conditions in the axial direction are assumed.

In the following section, expansion of a cylindrical cavity in a frictional soil was simulated with *FLAC*^{3D} and the computed stresses and displacement were compared to those obtained from closed form solution by Yu and Houlsby (1991) for the same problem.

6.2.1 Closed-form Solutions of Yu and Houlsby (1991)

The closed-form solution for cavity expansion problems derived by Yu and Houlsby (1991) was based on the assumption that stress-dilatancy theory is valid and that the soil fails at a constant ratio of principal stress. Yu and Houlsby (1991) closed form solution is an extension

of the original method proposed by Chadwick (1959) for solving spherical cavity expansion problems in Tresca and associated Mohr-Coulomb material using the total strain approach. In this approach, the incremental form of the plastic flow rule is integrated directly to result in a relationship between total stresses and total strains. To use the stress-strain relation in its total form, Chadwick's definitions of finite strain was adopted. Chadwick (1959) suggests the use of natural (or logarithmic or Hencky) strains, which are simply the time integral of the deformation rates for the cavity problems in which no rotation of the principal strain occurs. The constitutive models used in the total strain approach are as follows: once yielding occurs, stress-strain relationships are expressed between the Eulerian stresses and the logarithmic (Hencky) strains. Since the total strain approach assumes the strain (and stresses) depends on current positions (i.e., radius) of the soil particles and their initial positions, it may be termed as the Lagrangian method.

The Mohr-Coulomb yield criterion for a purely frictional material at the cavity interface is given by:

$$\alpha = \frac{\sigma_1}{\sigma_3} = \frac{\sigma_r}{\sigma_\theta} = \frac{1+\sin\phi}{1-\sin\phi} \qquad [6.1]$$

where σ_1 and σ_3, σ_r and σ_θ are the stress in the major and minor principal direction, σ_r and σ_θ are the radial and tangential stresses and ϕ is the angle of friction.

A non-associated flow rule is used for the problem described and analyzed in this section to minimize volumetric strain (dilation) of the soil on yielding. The flow rule is governed by the angle of dilation ψ, proposed by Davis (1968):

$$-\beta = \frac{\varepsilon_3^p}{\varepsilon_1^p} = \frac{\varepsilon_\theta^p}{\varepsilon_r^p} = -\frac{1+\sin\psi}{1-\sin\psi} \qquad [6.2]$$

where ε_1^p and ε_3^p are the plastic strains in the major and minor principal direction, ε_r^p and ε_θ^p are the plastic strains in the radial and tangential stresses. Davis (1969) assumed that the soil dilates plastically at a constant rate.

After several mathematical operations Yu and Houlsby (1991) obtained the following relationships for a cavity expanded from an initial radius a to a current radius r.

The *yield zone radius* b which represents the elastic-plastic interface is expressed in terms of the initial cavity radius a as follows:

$$\frac{b}{a} = \left[\frac{(1+\alpha)[Y + (\alpha - 1)P]}{2\alpha[Y + (\alpha - 1)P_0]} \right]^{\frac{\alpha}{\alpha - 1}} \qquad [6.3]$$

where P is the pressure inside the cavity, P_0 is the absolute value of the in-situ isotropic stress and $Y = 2c\cos\theta / 1 - \sin\theta$. α is as previously defined in equation 6.2. The *stress components in the elastic zone* are given by:

$$\begin{aligned} \sigma_r &= -P_o - Br^{-2} \\ \sigma_\theta &= -P_o + Br^{-2} \end{aligned} \qquad [6.4]$$

Where $B = [Y + (\alpha - 1)P_0]b^2 / 1 + \alpha$. The *stress components in the plastic zone* given by:

$$\begin{aligned} \sigma_r &= \frac{Y}{\alpha - 1} - Ar^{\frac{1-\alpha}{\alpha}} \\ \sigma_\theta &= \frac{Y}{\alpha - 1} - \frac{A}{\alpha} r^{\frac{1-\alpha}{\alpha}} \end{aligned} \qquad [6.5]$$

where $A = 2\alpha[Y + (\alpha - 1)P_0]b^{\frac{\alpha-1}{\alpha}} / (1+\alpha)(\alpha - 1)$. The *displacements in the elastic region* is given as:

$$u = \frac{Y + (\alpha - 1)P_0}{2G(1+\alpha)} \left(\frac{b}{r} \right)^2 r \qquad [6.6]$$

where G is the shear modulus.

The relationship between the current cavity radius r_c due to application cavity pressure P and the initial radius of the cavity r in the plastic region is given by the following:

$$\frac{r_c}{r} = \left\{ \frac{R^{\frac{\alpha(1+\beta)}{\beta(1-\alpha)}}}{\left(1 - \frac{Y + (\alpha-1)P_0}{2G(1+\alpha)}\right)^{(1+\beta)/\beta} + \frac{\alpha(1+\beta)}{\beta(1-\alpha)\chi} \sum_{n=0}^{\infty} A_n(R,\mu)} \right\}^{\frac{\beta}{\beta+1}} \qquad [6.7]$$

where

$$\chi = \exp\left[\frac{(1+\beta)(1-2\nu)(1+\nu)[Y + (\alpha-1)P_0}{E(\alpha-1)\beta} \right]$$

$$\mu = \left\{ 2P_o \frac{Y + (\alpha-1)(1-\nu^2)}{2G(1+\alpha)(1+\nu)(\alpha-1)\beta} \right\} \left\{ 1 + \alpha\beta - \frac{\nu(\alpha+\beta)}{1-\nu} \right\} \qquad [6.8]$$

$$R = \frac{(1+\alpha)[Y + (\alpha-1)P]}{2\alpha[Y + (\alpha-1)P_0]}$$

$$A_n(R,\mu) = \begin{cases} \dfrac{\mu^n}{n!} InR & \text{if } n = \gamma \\ \dfrac{\mu^n}{n!(n-\gamma)}(R^{n-\gamma} - 1) & \text{otherwise} \end{cases}$$

The displacement in the plastic region can be found from:

$$u = r_c - r \qquad [6.9]$$

6.2.2 FLAC^{3D} Model for Cavity Expansion

Stresses and displacements are determined numerically for a series of cylindrical cavities expanded in an infinite elasto-plastic material subjected to in-situ stresses. The material is assumed to be linearly elastic perfectly plastic and the failure surface is defined by the Mohr-Coulomb criterion and a non-associated flow rule.

The grid of the *FLAC*^{3D} model used for the simulation is shown in Figure 6.1. The far x- and z- boundaries are situated at a distance of 100 bore-diameters from the axis of the cavity. The thickness of the domain is selected as one-tenth of the cavity diameter. The initial radius of the cavity is 0.0125m. The radius of the cavity is assumed to be small compared to the length of the cylinder, so that plane-strain condition is applicable.

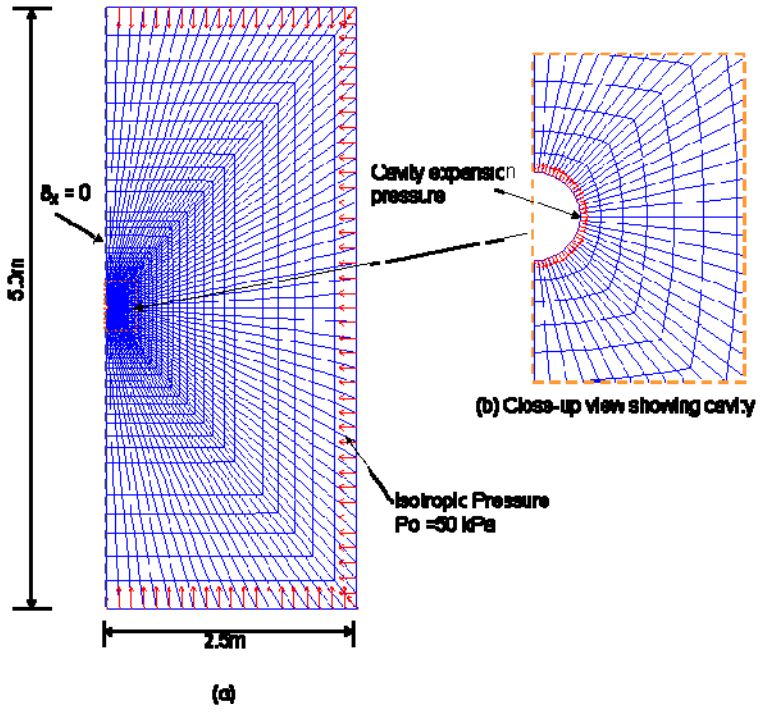

Figure 6.1: *FLAC*^{3D} grid used for simulation of cavity expansion

For the purpose of comparison with the closed-form solution, the model was assigned a zero gravity component with no boundary fixity apart from the line of symmetry, where movement is fixed in the horizontal direction.

An isotropic pressure P_o = 50 kPa was applied to the periphery of the grid to simulate far field stresses. The in-situ pressure P_o = 50kPa was also applied to the wall of the cavity as shown in the close-up of the cavity in Figure 6.1b. The properties assigned to the Mohr-Coulomb material are shown in Table 6.1.

Table 6.1: Properties Mohr-Coulomb material for cavity expansion

Property	
Shear modulus (G)	3.5 MPa
Bulk modulus (K)	7.5 MPa
Friction angle (ϕ)	25°, 30°, 35°
Dilation angle (ψ)	0°, 10°, 15°

To simulate cavity expansion, the boundary pressure acting against the wall of the cavity was gradually increased in a stepwise manner to simulate the application of expansion pressure. The model was run after each load step until the point of equilibrium, where no further cavity expansion occurred. The displacement was noted at this point and the next increment of expansion pressure applied.

6.2.3 Results Obtained from Simulations Cavity Expansion

Figure 6.2 shows the pressure–cavity expansion relationship predicted by the finite-difference model (numerical solution) and the analytical solutions obtained for the soil material described in Table 6.1. Close agreement between the numerical prediction and the analytical solution was obtained as shown in Figure 6.2. The responses of the model indicate considerable dependence on the magnitude of the friction angle and dilatancy of the medium. Increasing the dilatancy and friction angle of the soil resulted in an increased stiffness of the response.

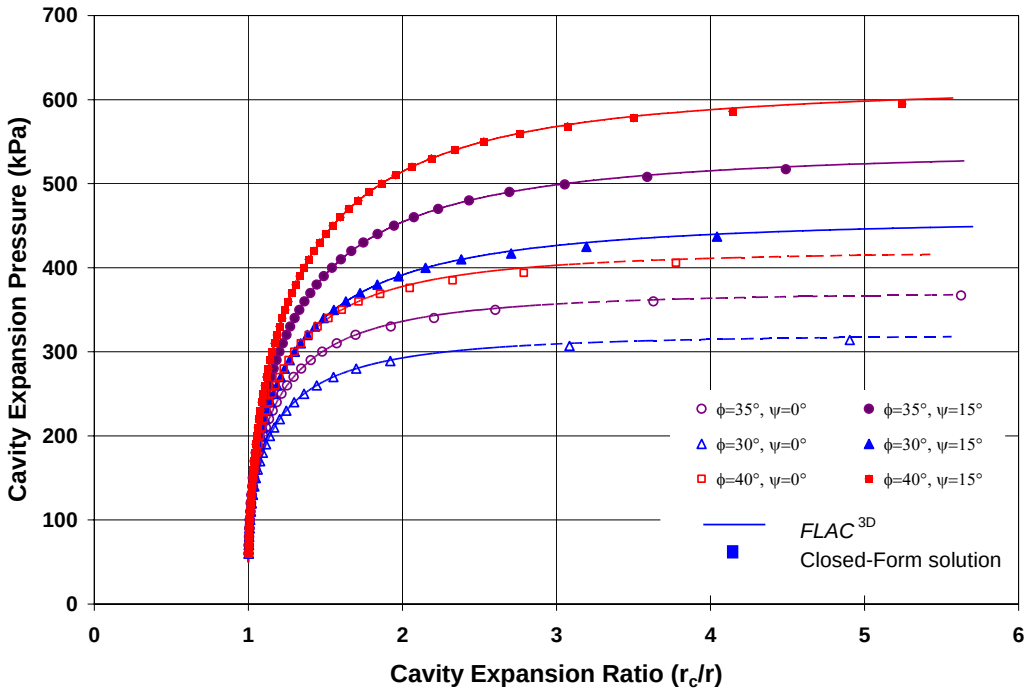

Figure 6.2: *FLAC*^{3D} vs. closed-form solutions for cylindrical cavity expansion in infinite Mohr- Coulomb material

Both the numerical simulations and the closed form solution suggest the existence of a *limiting pressure* represented by the asymptotic line shown at large strains during which the radius of the cavity increases indefinitely as the cavity pressure approaches this finite limiting value. The limiting pressure is highly dependent on the angle of dilation, as the plastic zone around the cavity increases with the angle of dilation. Figure 6.3 shows the variation of *limit pressure* with angle of dilation and friction angle, it can be seen from Figure 6.3 that the angle of dilation has a very important effect, increasing the limit pressures considerably.

It should be noted that some of the numerical simulations shown in Figure 6.2 were terminated after the zones in the periphery of the cavity experienced significant distortion that resulted in zero (or negative) volume of the tetrahedra in the overlay that are used in the zones, a phenomenon similar to getting a *negative Jacobian* with a finite element code. The results obtained from the simulations at these extremely large strains are compromised due to excessive distortion of the grid.

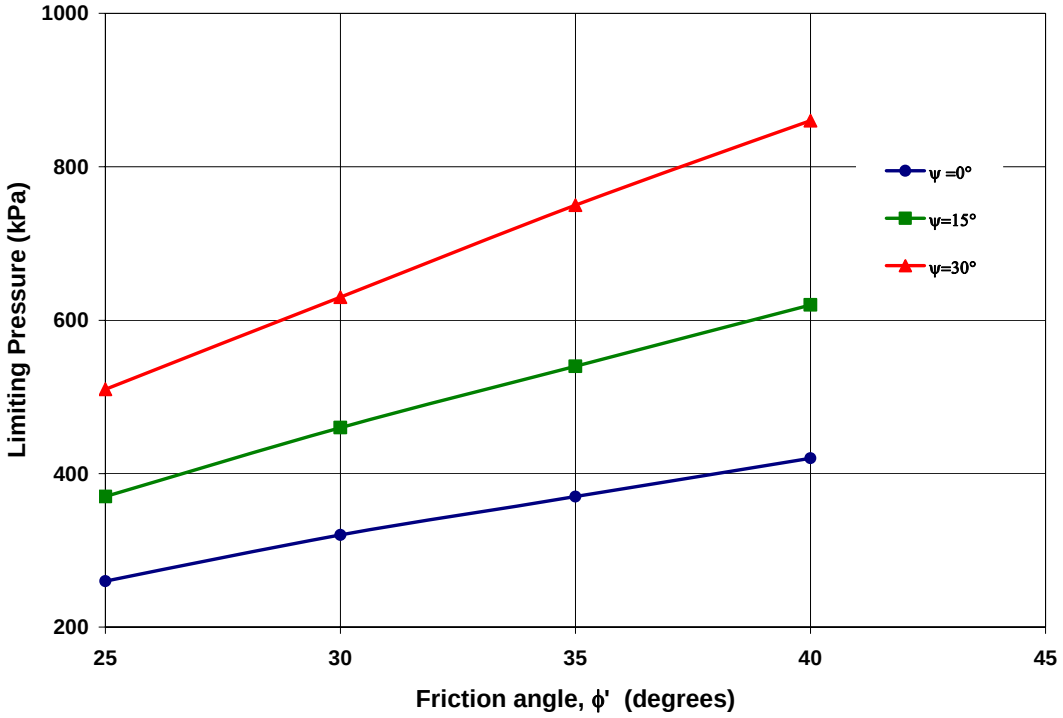

Figure 6.3: Variation of limiting pressure with friction angle and angle of dilation

The model can be re-grid before the zone geometry becomes too distorted. Regridding involve moving the old zone stresses into the new zones but the current version of *FLAC*^{3D} does not have regridding capabilities.

Contour plots of the radial and tangential stresses obtained from *FLAC*^{3D} simulation of an expanding cylindrical cavity at a cavity expansion ratio, $\frac{r_c}{r} = 1.25$ for material with $\psi = 0^{\circ}$ and $\phi = 35^{\circ}$ are shown in Figures 6.4 and 6.5, respectively. It is important to evaluate the dissipation of cavity pressure and displacement at distances away from the cavity when considering the effect of bore pressure on existing structure around the bore. Comparison between *FLAC*^{3D} and the analytical solution along a radial line are shown in Figures 6.6 and 6.7. The radial and tangential stresses are plotted versus radius in Figure 6.6 and the displacements are represented in Figure 6.7. The stresses and displacements obtained from results of *FLAC*^{3D} simulations and analytical solution are very comparable. The average relative error between the stresses is less than 1.2% throughout the grid while those of the displacements are 6.5%.

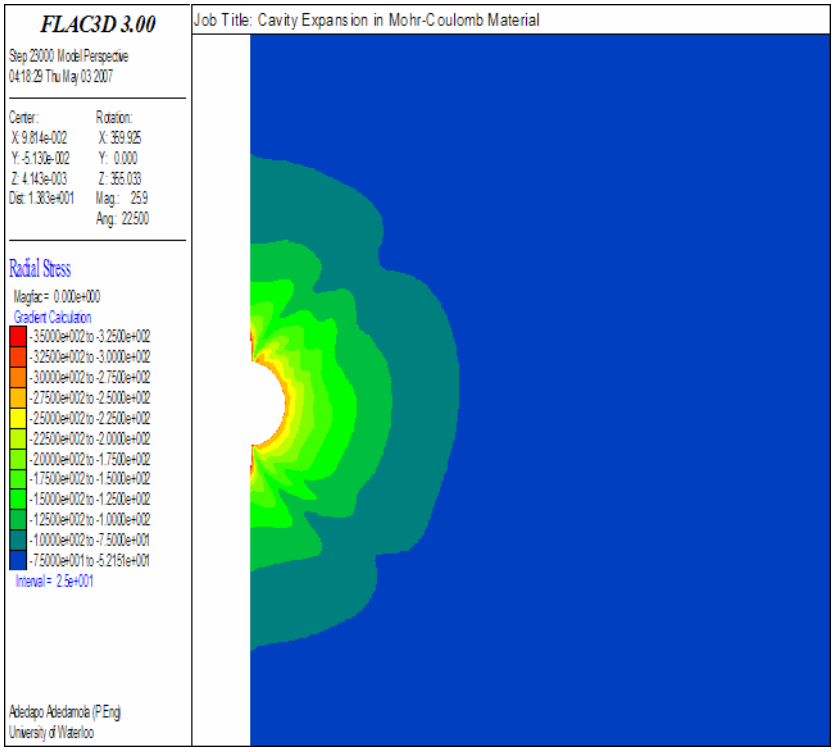

Figure 6.4: Radial stress contour of an expanding cavity

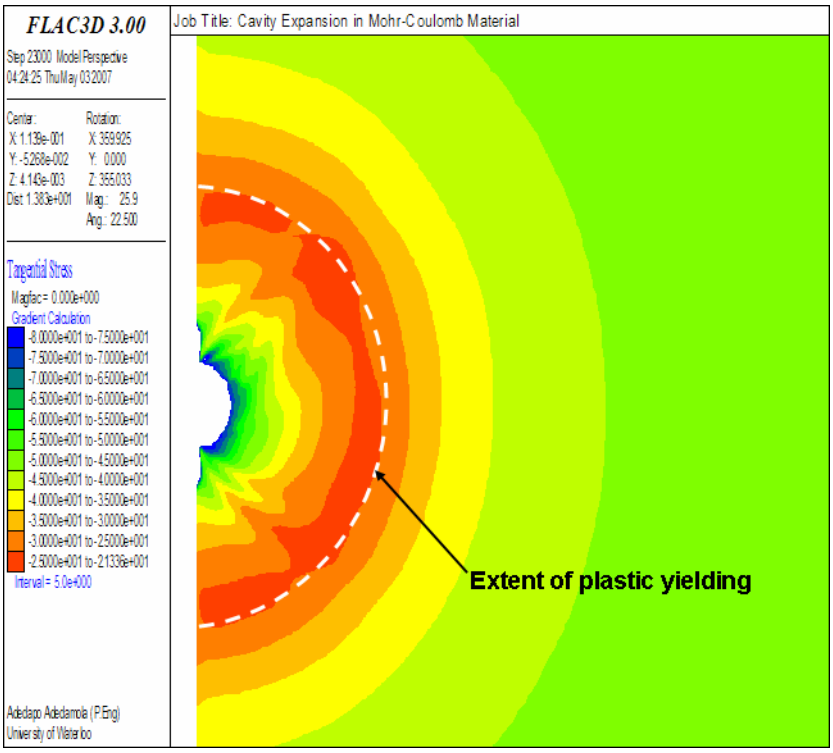

Figure 6.5: Tangential stress contour of an expanding cavity

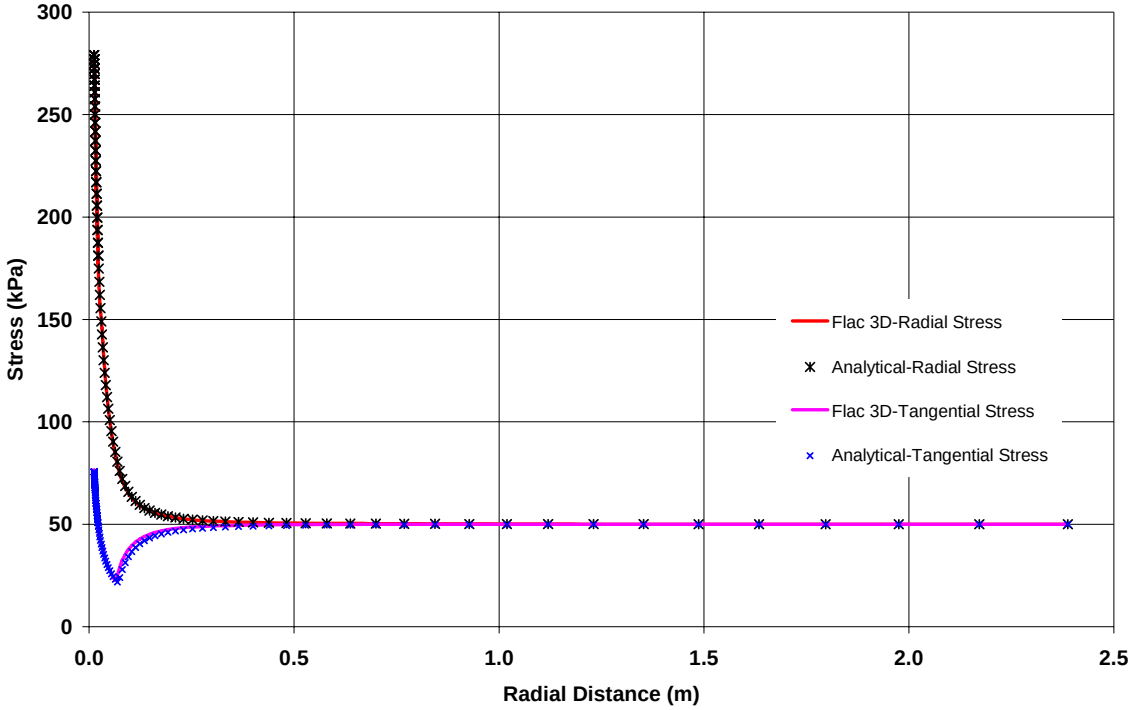

Figure 6.6: Comparison of Radial and Tangential Stress Variation

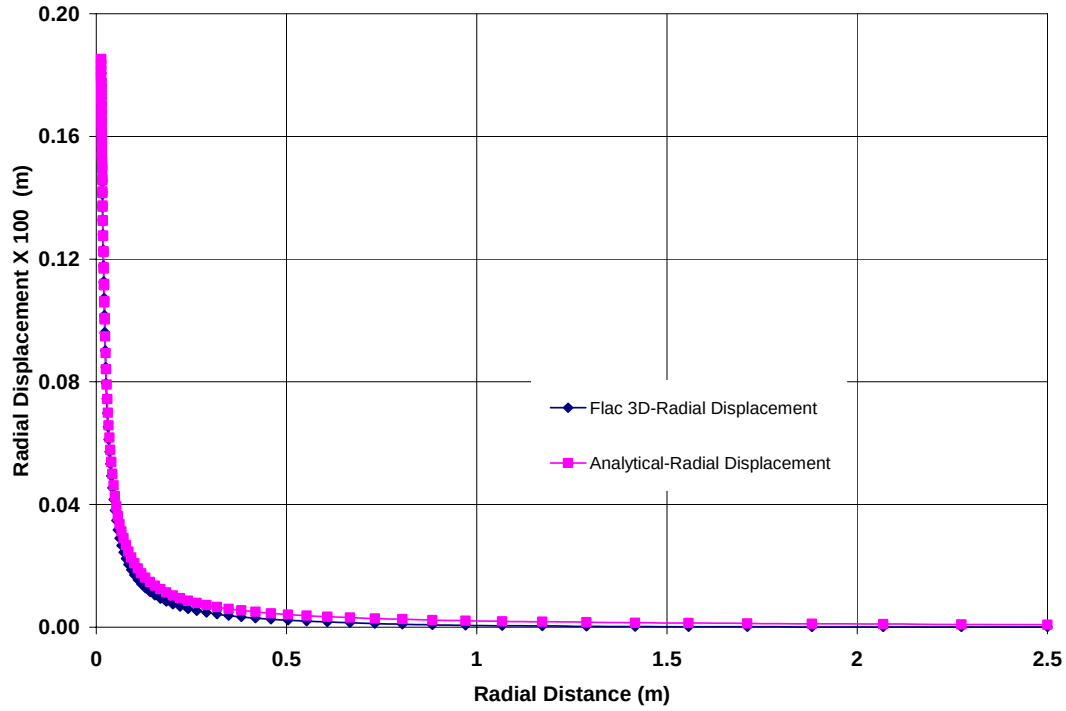

Figure 6.7: Comparison of Radial Displacement Solutions

The radial extent of the plastic zone was found to be approximately 0.068m in *FLAC*^{3D} simulations. This value compares well with the plastic yield zone radius of about 0.07m estimated using Equation 6.3. The displacement contours and vectors are presented in Figure 6.8.

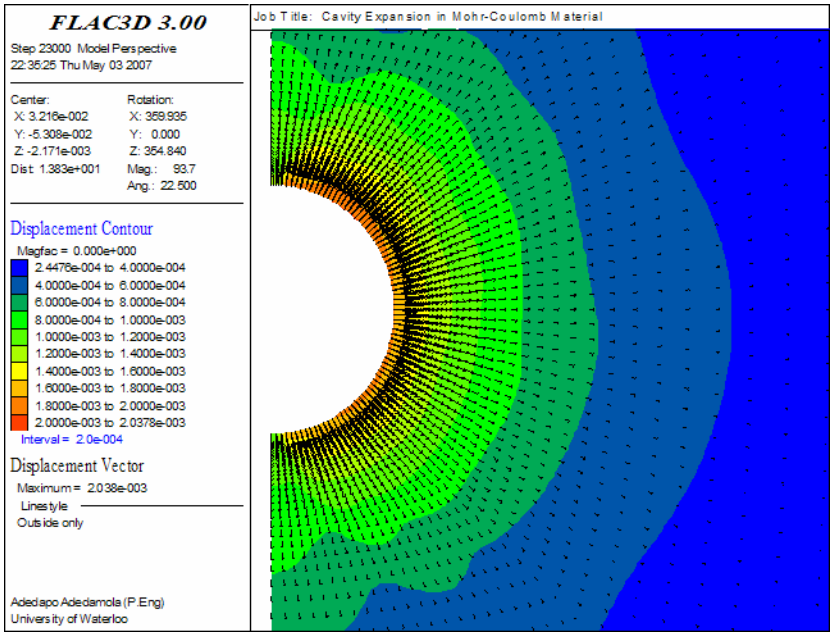

Figure 6.8: Displacement contour of an expanding cavity

$$(\frac{r_c}{r} = 1.25\ ,\ \psi = 0^\circ \text{ and } \phi = 35^\circ)$$

6.3 *FLAC*^{3D} Simulation of Field Scale HDD Installation

Three field scale HDD installations were completed in 2001 as part of the HDD research program at the University of Waterloo. The installations were conducted at the North Campus of the University. The first two installations consisted of installing 180m long 150mm nominal diameter SDR-11 MDPE pipes approximately 2.0m below ground surface. The third installation consisted of installing a 180m long 200mm nominal diameter SDR-17 HDPE pipe also at approximately 2.0m depth below ground surface. The soil found at the test site include clayey silt with some sand, silt with varying sand content and traces of gravel, and

sand with traces of silt and clay. Complete details of the field installation can be found in Knight et al. (2002) and Duyvestyn (2004).

The bore slurry pressures and ground deformations were continuously monitored during the 2001 HDD installations process. Ground movements (surface heave) were observed during the third installation at approximately 35m from the pipe exit location, the magnitude of the surface heave at this location was determined to be about 115mm. The maximum bore slurry pressure observed at the same location was 210 kPa. These well documented HDD field installations provide an exceptional case study for the validation of the HDD numerical simulations presented in this thesis.

6.3.1 *FLAC*^{3D} Numerical Model

The HDD field installation was modeled as a plane-strain problem, it is recognized that the plane strain condition is an approximation of the real 3D process encountered in HDD. During HDD the soil is subjected to rapid rotational local shearing by the rotating head while cutting through the soil (Hunter, 2005). However the end result is a *'cylinder'* bore filled with bore slurry that exerts fluid pressure against the wall of the bore, and so the method of stress analysis employed is a reasonable approximation.

The diameter of the bore was assumed to be equal to the reamer diameter of 300mm and the soil was modeled as a uniform frictional Mohr-Coulomb material. The domain is discretized into one layer of 1800 zones with the zones organized in a radial pattern around the bore as shown in Figure 6.9 where advantage has been taken of the half-symmetry of the geometry. The boundary conditions applied to the domain are shown on Figure 6.10. The far x- and z-boundaries are situated at a distance of 10 bore-diameters and the thickness of the domain is selected as one-tenth of the bore diameter.

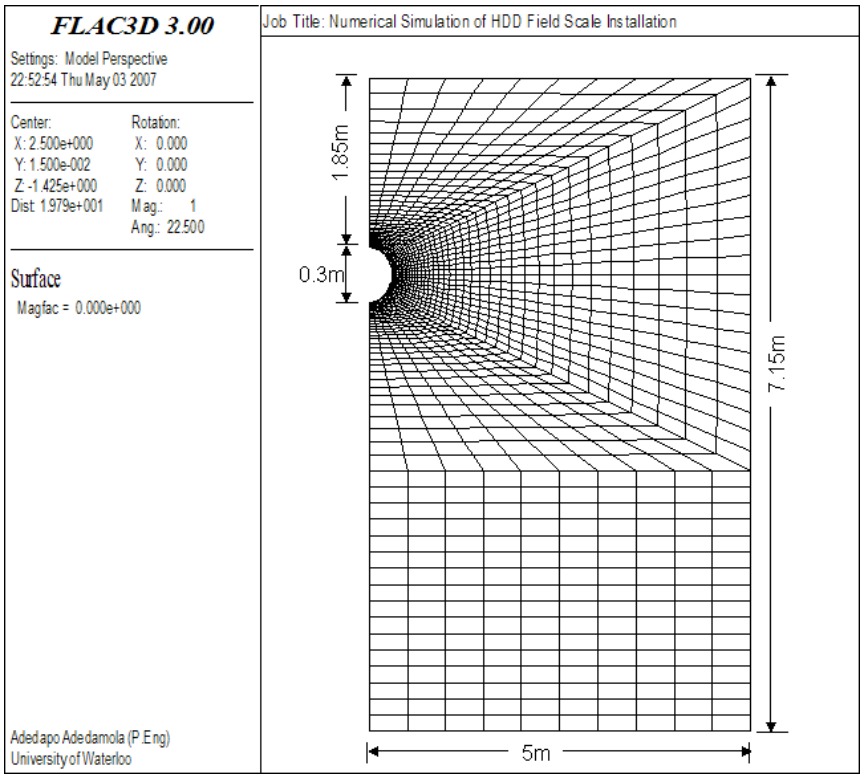

Figure 6.9: FLAC^{3D} grid used for simulation of field-Scale HDD Installation

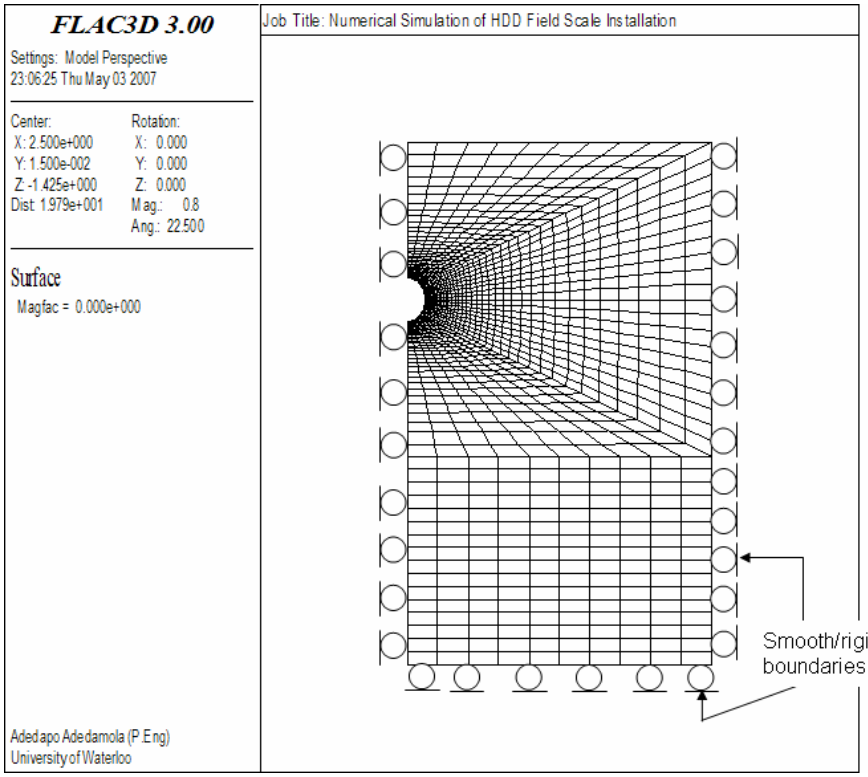

Figure 6.10: Boundary Conditions for *FLAC*^{3D} simulation of field-Scale HDD Installation

6.3.2 Simulation of HDD Bore Pressurization Process

Appropriate boundary and initial conditions were imposed on the *FLAC*^{3D} model following grid generation including the initialization of in-situ stresses within the model. Initialization of in-situ stresses within the model was completed to simulate the geostatic stresses. The soil properties shown in Table 6.2 were then assigned to the model and the *solve-elastic* command was activated in *FLAC*^{3D} to bring the model to initial state of equilibrium. The *solve-elastic* command performs a mechanical calculation in two steps: during the first step it treats the model as linearly elastic before assigning the actual material property and strength to the model. The cohesion and tensile strength for all materials in the model are set to high values for the first step. For the second step, the cohesion and tensile strength are reset to their original values. These steps ensure that equilibrium is reached faster by preventing model failure while transient forces are damped.

Table 6.2: Soil properties for the HDD field installation simulation (Duyvestyn, 2004)

Property	
Shear modulus (G)	14.8 MPa
Bulk modulus (K)	44.4 MPa
Friction angle (ϕ)	35°
Dilation angle (ψ)	3.75°
Density	1800 kg/m^3

The influence of fluidic pressure against the wall of the bore pressurization during HDD installation was simulated by assigning uniform radial stress to the grid zones along the periphery of the bore. The radial stresses were increased gradually to minimize shock to the model and to observe model response to change in applied bore pressure. The model is run to equilibrium after each bore pressure increment. The maximum nodal force vector also called the unbalanced or out-of-balance force is monitored to know when a mechanical equilibrium state has been reached. A model is in exact equilibrium if the net nodal-force vector at each grid-point is zero. However, the maximum unbalanced force will never exactly reach zero for a numerical analysis. In this simulation, the model is considered to be in equilibrium when

the maximum unbalanced force is considerably small (1.0e-05) compared to the total applied forces in the problem.

Once equilibrium was reached, the bore pressure was increased and the simulation was continued until equilibrium was again reached. The stepwise bore pressurization was continued until the maximum surface vertical displacement of 115mm (total measured surface heave) was attained.

6.3.3 Results obtained from Simulation of Field-scale HDD Installation

The bore pressure–displacement relationship predicted by the *FLAC*^{3D} is shown in Figure 6.11. The results of the simulation indicate that a bore pressure of approximately 208kPa was required to generate a surface heave of 115mm. The estimated bore pressure is similar to those observed during the actual installation. The vertical displacement of the vector at this bore pressure is shown in Figure 6.12. The predicted bore pressure of 208 kPa is very comparable to the maximum observed bore pressure of 210 kPa during the field scale installation reported in Duyvestyn (2004). The close agreement between the estimated and measured bore pressure and the corresponding surface heave demonstrates the ability of *FLAC*^{3D} to simulate HDD bore pressurization reasonably well for this scenario.

6.4 Numerical Modeling of HDD beneath Flexible Pavement

A number of Horizontal Directional Drilling (HDD) installations beneath flexible pavement were simulated with *FLAC*^{3D}. The purpose of the simulations was to study the response of flexible pavement structure during HDD bore pressurization installation and to develop allowable bore pressure charts and tables to aid in the design of HDD installation of utility pipelines beneath flexible pavements. The description of the pavement structure modeled, the numerical approach used, characteristics of the numerical model including assumptions and simplifications, and the results obtained from the simulations are presented in the following sections. The section is concluded with discussion on the limitations, applicability and practical significance of the simulation results.

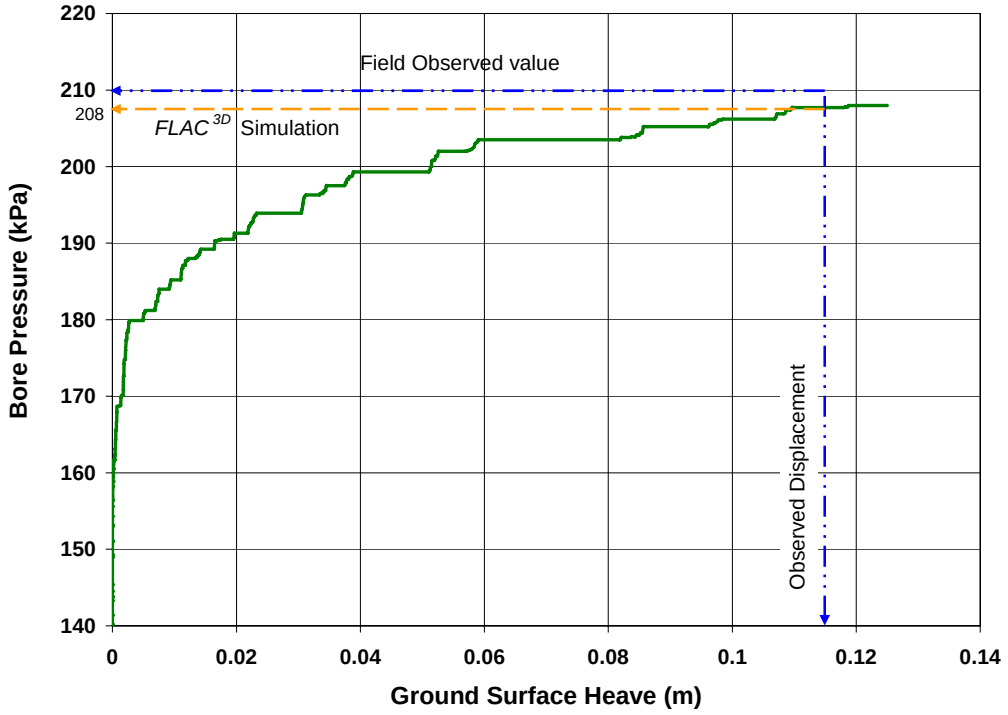

Figure 6.11: Estimate pressure–displacement relationship for HDD field-scale installation

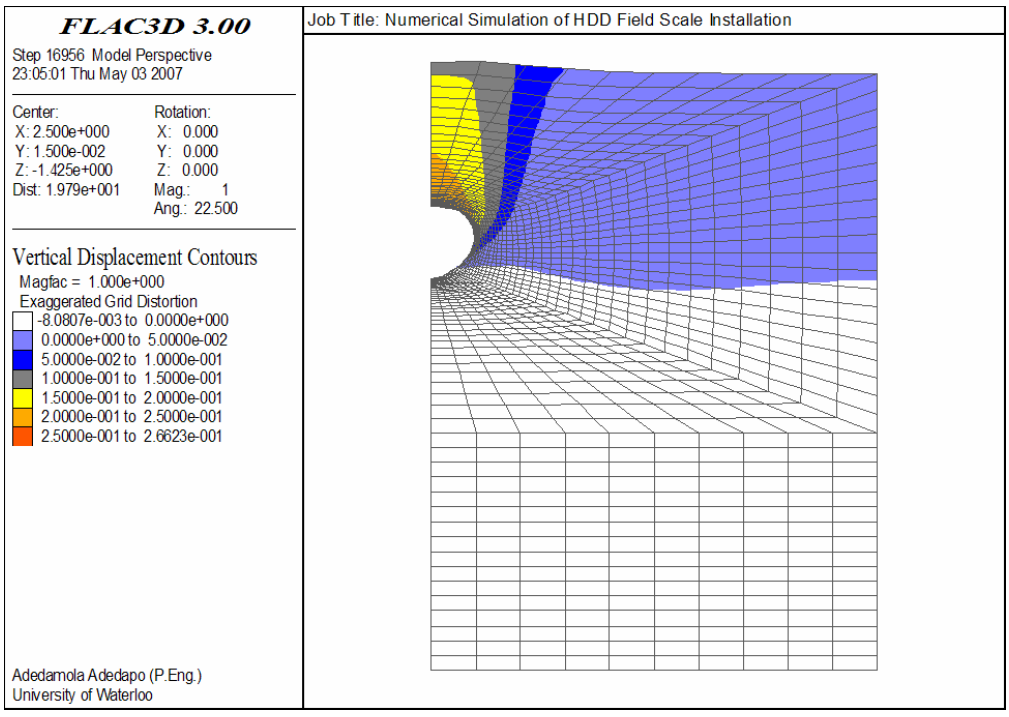

Figure 6.12: Contours of vertical displacement at bore pressure of 208 kPa

6.4.1 Description of the Pavement Structure Modeled

The research work presented herein examines the impact of HDD installation processes on typical flexible pavement structure found on urban roadways. The flexible pavement was idealized as a three-layer structure comprising an asphalt layer, a granular base and a soil subgrade as shown in Figure 6.13. All the layers were assumed to be fully bonded and to have homogenous isotropic material properties. The asphalt concrete was modeled as a linear elastic material while the sub-base and sub-grade materials were modeled as Mohr-Coulomb material with non-associated flow rule. The material properties assigned to the granular sub-base and the subgrade soil, shown in Table 6.3, were obtained from the results of extensive laboratory tests published by Titus-Glover (1995). Although it is recognized there are some differences in asphalt concrete mixes, for simplicity, the properties of the asphalt concrete used for the analyses were those published in by Lytton et al (1993). These material properties are representative of those found for typical urban flexible pavement structure.

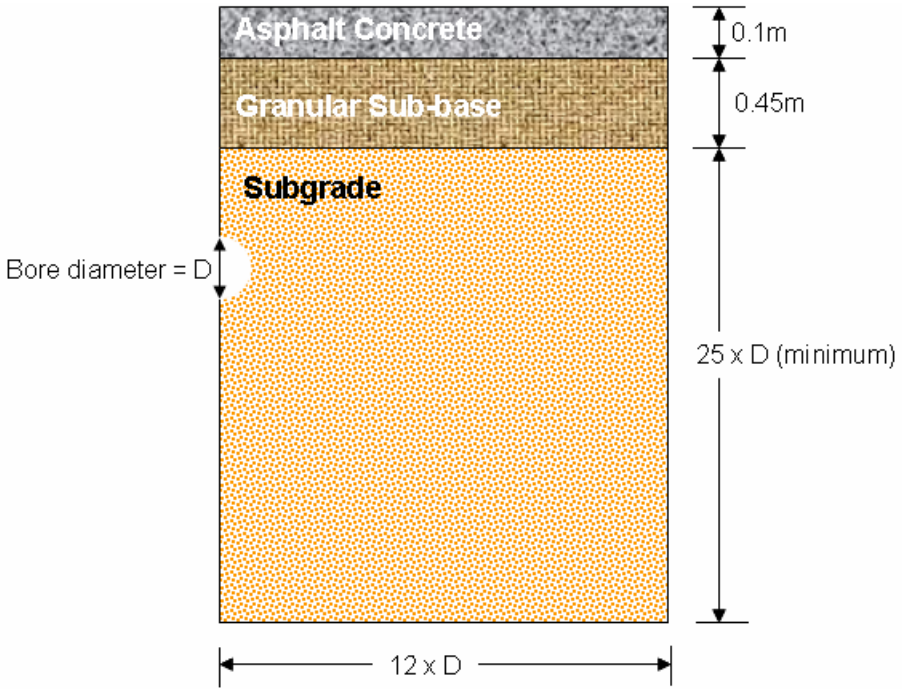

Figure 6.13: Typical pavement structure used for numerical simulations

Table 6.3: Properties of pavement material

Properties	Asphalt Concrete	Granular Sub-base	Sandy Subgrade	Clayey Subgrade
Bulk Modulus (kPa)	7.55×10^6	4.2×10^5	4.0×10^4	2.5×10^4
Shear Modulus (kPa)	2.52×10^6	1.9×10^5	1.3×10^4	7.5×10^3
Friction angle (°)	20	40	35	25
Angle of dilation (°)	0	10	6.25	0
Cohesion (kPa)	2.0×10^3	0	0	10
Density (Kg/m^3)	2400	2200	1800	1650

Details of the HDD simulations completed as part of the numerical investigation are presented in Table 6.4. The bore diameter and depth of installation were selected to reflect HDD installation parameters typically encountered when installing utility pipe underneath flexible pavement structure in urban area. Numerical simulations were limited to bore diameters of 200 mm, 300 mm and 450mm and depth of cover of 2.0m, 3.0m and 4.0m. Depth of cover refers to the height of soil above the crown of the bore. Both cohesionless and cohesive subgrade materials were evaluated. The numerical analyses also examined the influence of filter-cake on pavement structure response to bore-pressurization in cohesionless subgrade.

6.4.2 Description of FLAC^{3D} Model used for HDD Simulations

The *FLAC*^{3D} model used the simulations and the simplifications made to the numerical model were similar to those described in Section 6.5. The HDD installations were modeled as a plane strain problem. The plane-strain approximation was deemed applicable since the size of the bore is considerably smaller than the length of the installation. Smooth, rigid boundaries were placed along the bottom and sides of the model while symmetry was assumed along the longitudinal bore axis. The far x- and z- boundaries are situated at a distance of 12 bore-diameters from the bore axis. This distance ensures that stresses along the boundaries remain close to geostatic stress conditions throughout the simulation. The thickness of the domain is selected as one-tenth of the cavity diameter.

Table 6. 4: Summary of HDD Installation numerical simulations

Test ID	Bore diameter (mm)	Depth of cover	Thickness of Asphalt Concrete (mm)	Friction angle (°)	Density (kg/m^3)	Comment
1	300	2.0	100	35	1800	Sandy subgrade
2	300	2.0	100	40	1800	
3	300	2.0	100	25	1650	Clayey subgrade
4	300	2.0	100	30	1650	
5	300	3.0	100	35	1800	Sandy subgrade
6	300	3.0	100	40	1800	
7	300	3.0	100	25	1650	Clayey subgrade
8	300	3.0	100	30	1650	
9	300	4.0	100	35	1800	Sandy subgrade
10	300	4.0	100	40	1800	
11	300	4.0	100	25	1650	Clayey subgrade
12	300	4.0	100	30	1650	
13	200	2.0	100	35	1800	Sandy subgrade
14	200	2.0	100	40	1800	
15	200	2.0	100	25	1650	Clayey subgrade
16	200	2.0	100	30	1650	
17	200	3.0	100	35	1800	Sandy subgrade
18	200	3.0	100	40	1800	
19	200	3.0	100	25	1650	Clayey subgrade
20	200	3.0	100	30	1650	
21	200	4.0	100	35	1800	Sandy subgrade
22	200	4.0	100	40	1800	
23	200	4.0	100	25	1650	Clayey subgrade
24	200	4.0	100	30	1650	
25	450	2.0	100	35	1800	Sandy subgrade
26	450	2.0	100	40	1800	
27	450	2.0	100	25	1650	Clayey subgrade
28	450	2.0	100	30	1650	
29	450	3.0	100	35	1800	Sandy subgrade
30	450	3.0	100	40	1800	
31	450	3.0	100	25	1650	Clayey subgrade
32	450	3.0	100	30	1650	
33	450	4.0	100	35	1800	Sandy subgrade
34	450	4.0	100	40	1800	
35	450	4.0	100	25	1650	Clayey subgrade
36	450	4.0	100	30	1650	
37	300	2.0	125	35	1800	Influence of asphalt concrete thickness
38	300	2.0	150	35	1800	

The final bore diameter was assumed to be fully formed at the beginning of bore pressurization and no attempt was made to simulate the bore enlargement processes during the pilot bore and pre-reaming stages. It is sometimes possible for bore pressure to dissipate during HDD installation but no such pressure relief was simulated in this study. The bore pressure is assumed to be uniform, steadily increasing and occurring simultaneously throughout the entire bore. In reality, the loss of drilling fluid to the surrounding soils (especially in porous granular subgrade) and changes in drilling rates will lead to oscillating fluid pressures within the bore, when the rate of fluid flow into the surrounding native soil is greater than the rate at which drilling fluids are being introduced into the bore, the pressure gradient decreases, and hence the bore pressures causing the outward bore expansion dissipate.

6.4.3 Bore Pressurization Process for HDD Simulations

The methods used to simulate HDD bore pressurization process are similar to those described in Section 6.5. Once the grid was created, appropriate boundary conditions are imposed on the model followed by initialization of insitu stresses to simulate the geostatic stresses. The soil properties shown in Table 6.3 were then assigned to the model.

The model is brought to initial state of equilibrium with the s*olve-elastic* command in *FLAC*^{3D}. Bore pressurization was initiated once equilibrium was reached. Pressurization was accomplished by assigning uniform radial stress to the grid zones along the wall of the bore. The bore pressure was increased gradually to minimize shock on the model and to obtain the bore pressure-displacement relationship from the simulation. The model is run to equilibrium after each bore pressure increment. The model is considered to be in equilibrium when the maximum unbalanced force is small (1e-05) compared to the total applied forces in the problem. The bore pressured was increased after attaining equilibrium and the simulation continued until the system equilibrate again.

The stepwise bore pressurization was continued until the maximum ground surface vertical displacement of 12.5mm (surface heave) was attained or until equilibrium could not be

reached indicating occurrence steady plastic flow within the model. An arbitrary value of 12.5mm was chosen as the maximum allowable heave that can be tolerated on the pavement. The author of this thesis is not aware of any establish criteria for allowable pavement heave currently being used by the HDD industry.

The results of the HDD bore pressurization simulations in the cohesionless and cohesive subgrade materials are presented and discussed in the following sections.

6.4.4 Flexible Pavement response to HDD Bore Pressurization in Cohesionless Subgrade

A total of twenty-two (22) simulations were completed in cohesionless subgrade. The response of the pavement structure founded on cohesionless granular subgrade to HDD bore pressurization is presented in this section. Pavement response during Test #1 (see Table 6.4) will be discussed in detail. Test #1 simulates a 300mm diameter bore installed at a depth of 2.0m beneath a flexible pavement in a cohesionless subgrade with a friction angle of 35°. The pavement response during Test #1 is typical and representative of the response observed during the other bore pressurization in cohesionless subgrade that will be presented afterwards.

6.4.4.1 Variation of principal stresses during HDD installation in cohesionless subgrade

The contour plots of the minimum (σ_1) and maximum (σ_3) principal stresses prior to bore pressurization are presented in Figures 6.14 and 6.15 respectively. Note that because compressive stresses are negative in *FLAC*^{3D}, the minimum (σ_1) principal stress is the most negative (major) principal stress and conversely the maximum (σ_3) principal stress is the least negative (minor) principal stress. The values of minimum and maximum principal stresses shown in Figures 6.14 and 6.15 coincide exactly with the values of vertical and horizontal stresses, respectively prior to bore pressurization.

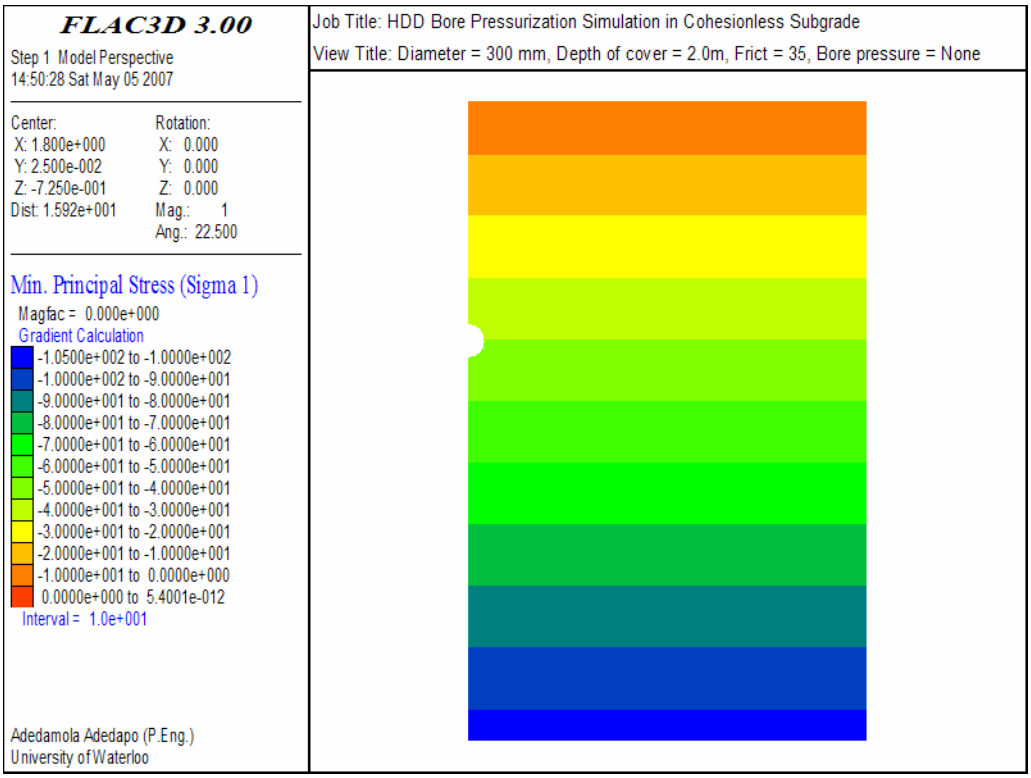

Figure 6.14: Minimum principal stress (σ_1) contours prior to bore pressurization

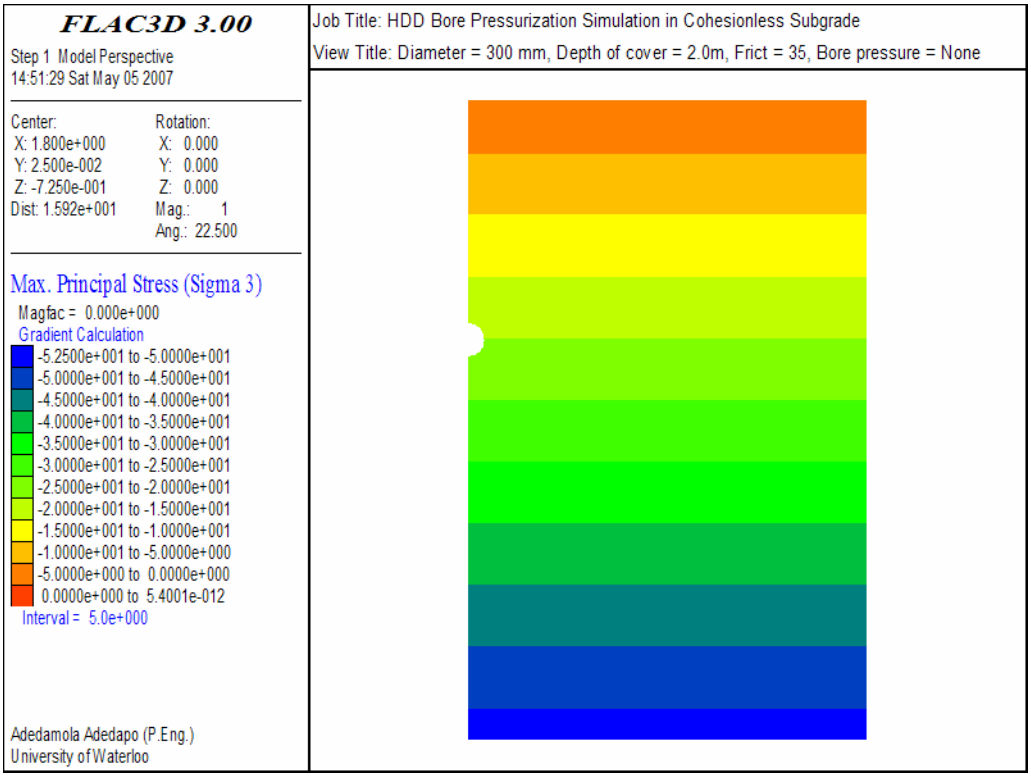

Figure 6.15: Maximum principal stress (σ_3) contours prior to bore pressurization

As the bore is pressurized, an induced stress field develops in the subgrade soil surrounding the HDD bore. The contours plots of the minimum principal stress (σ_1) around the HDD bore at applied bore pressure of 25, 45, 105, 205 and 225 kPa are presented in Figures 6.16 through 6.20. Similarly, the contour plots showing the maximum principal stress (σ_3) in the soil surrounding the bore during pressurization at applied bore pressures of 25, 45, 105, 205 and 225 kPa are shown in Figures 6.21 through 6.25.

The change in annular radial and tangential (hoop) stresses with applied bore pressure at the crown, springline and invert of the bore are shown graphically in Figures 6.26 and 6.27, respectively. The magnitude of the radial stresses at the bore crown, springline and invert are very similar and equal in magnitude to the applied bore pressure (P_i). It was observed that the magnitudes of the minimum and maximum principal stresses are equal to the radial or tangential stress depending on the level of stress applied in the bore. When the applied bore pressure is lower than 20 kPa, the magnitudes of the minimum (σ_1) and maximum (σ_3) principal stresses at the bore wall are equal to the tangential and radial stresses, respectively. However at greater bore pressures, the principal axes rotated such that the minimum (σ_1) and maximum (σ_3) principal stresses at the bore wall are equal to the radial and tangential stresses, respectively.

The variation of tangential stresses at the bore wall with applied bore pressure shown in Figure 6.27 shows that the tangential stress at the crown and invert have lower magnitude compare to those observed at the springline. The tangential stresses at the invert are also slightly higher than those at the crown due to difference in geostatic stress over the diameter of the bore.

Figures 6.28 through 6.32 show the plasticity state in the vicinity of the bore at applied pressures of 25, 45, 105, 205 and 225 kPa, respectively. These Figures exhibit zones that were yielding plastically (extent of the plastic zone) after pressurization. At lower bore pressures (P_i < 20 kPa), the bore wall showed an elastic response to the applied pressure loading. Increased bore pressure resulted in a corresponding reduction in the tangential stress at the bore wall, while the response was elastic, until the tensile strength of the subgrade soil was reached, Figure 6.28.

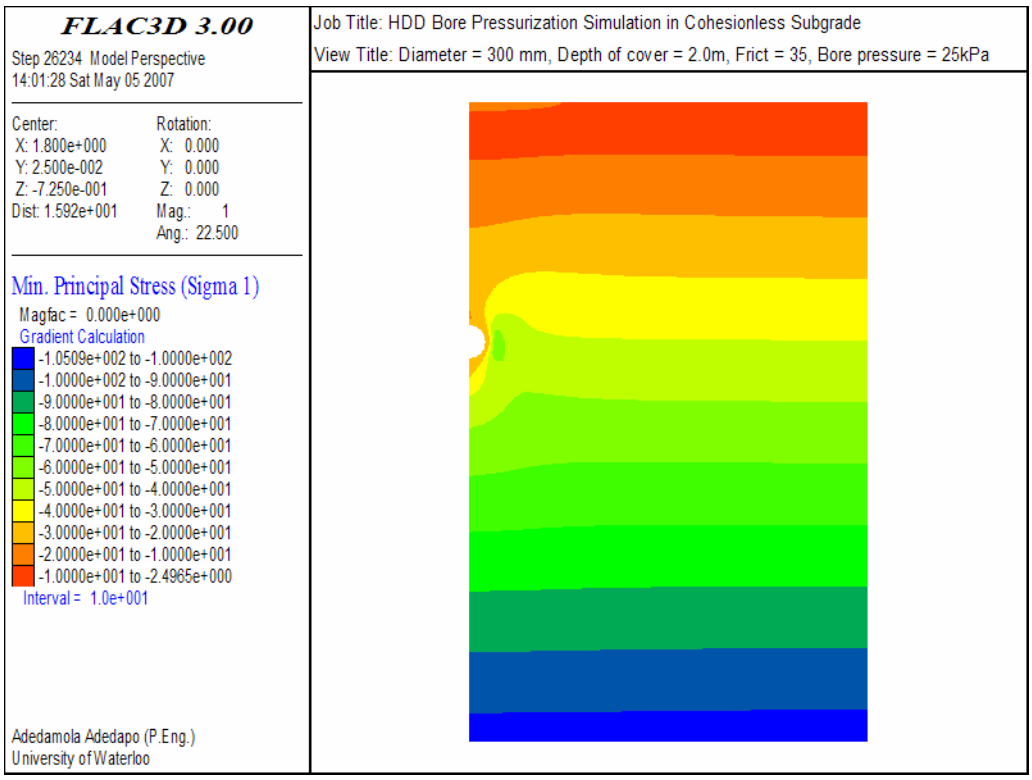

Figure 6.16: Minimum principal stress (σ_1) contours at 25 kPa in cohesionless subgrade

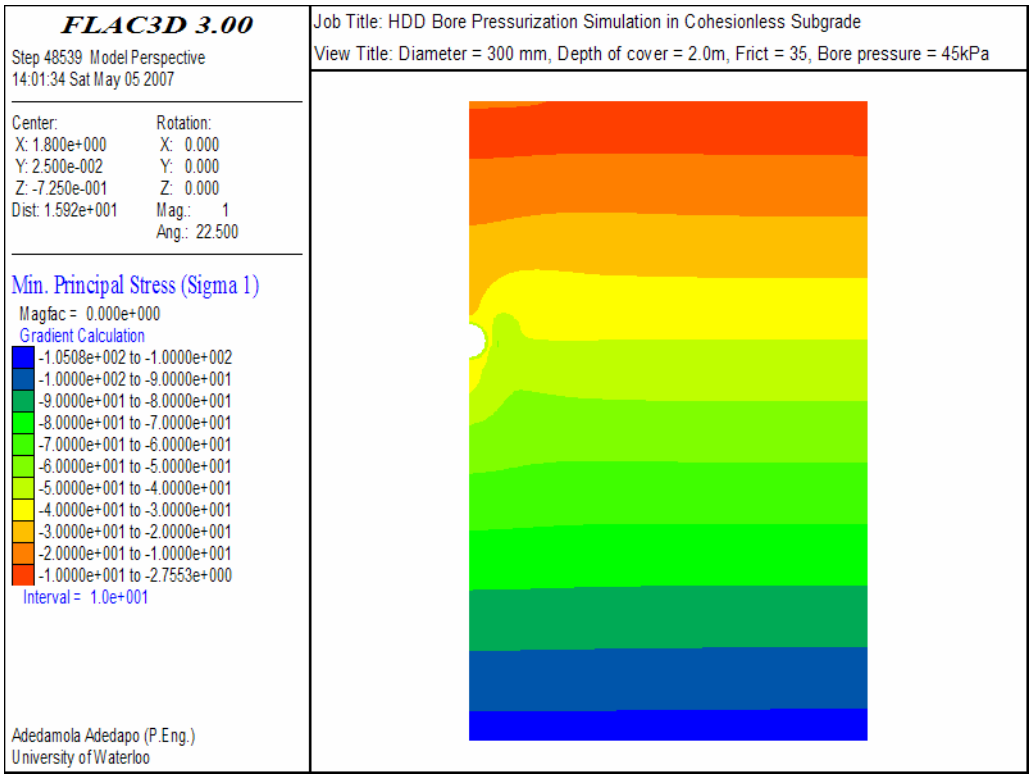

Figure 6.17: Minimum principal stress (σ_1) contours at 45 kPa in cohesionless subgrade

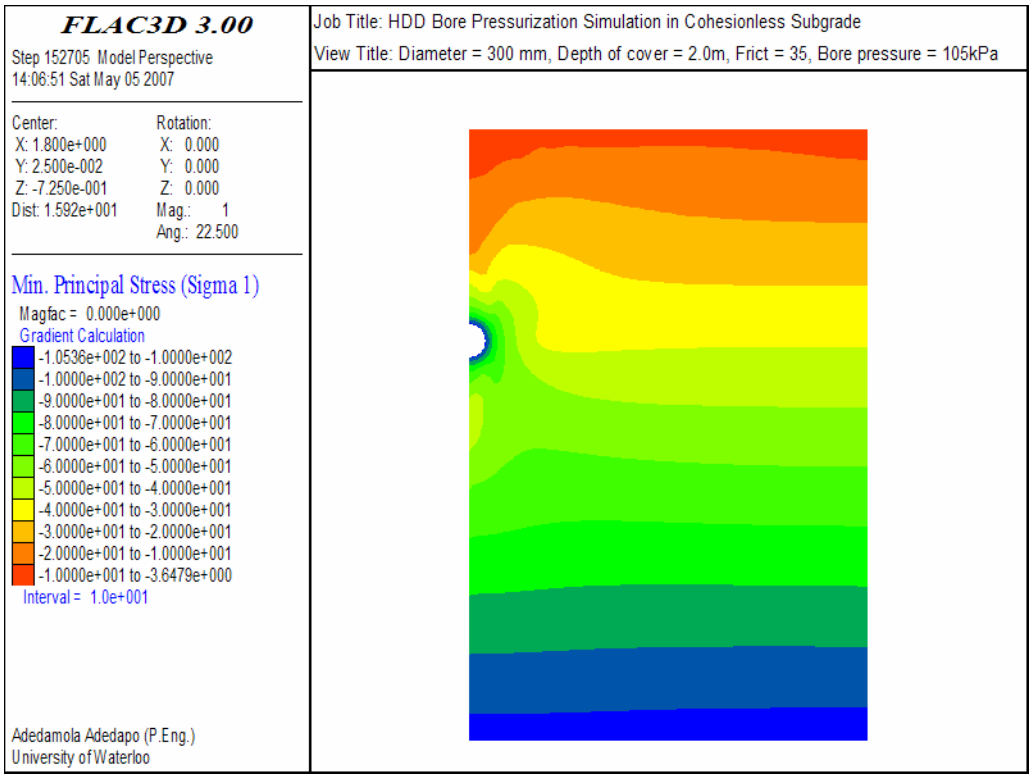

Figure 6.18: Minimum principal stress (σ_1) contours at 105 kPa in cohesionless subgrade

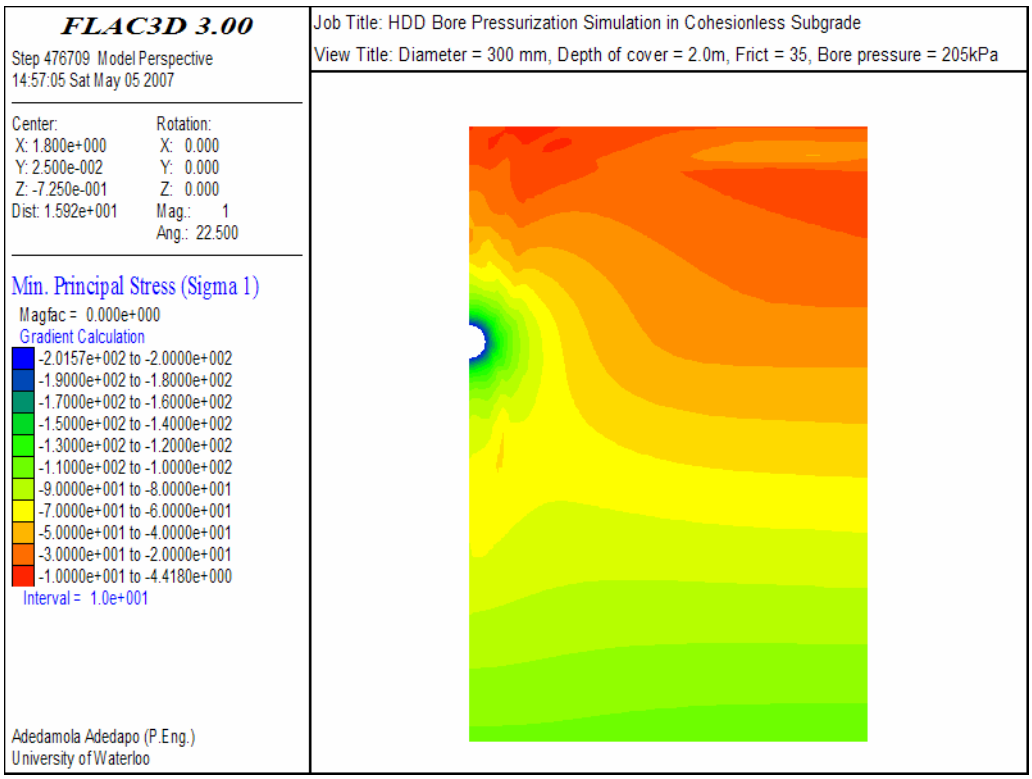

Figure 6.19: Minimum principal stress (σ_1) contours at 205 kPa in cohesionless subgrade

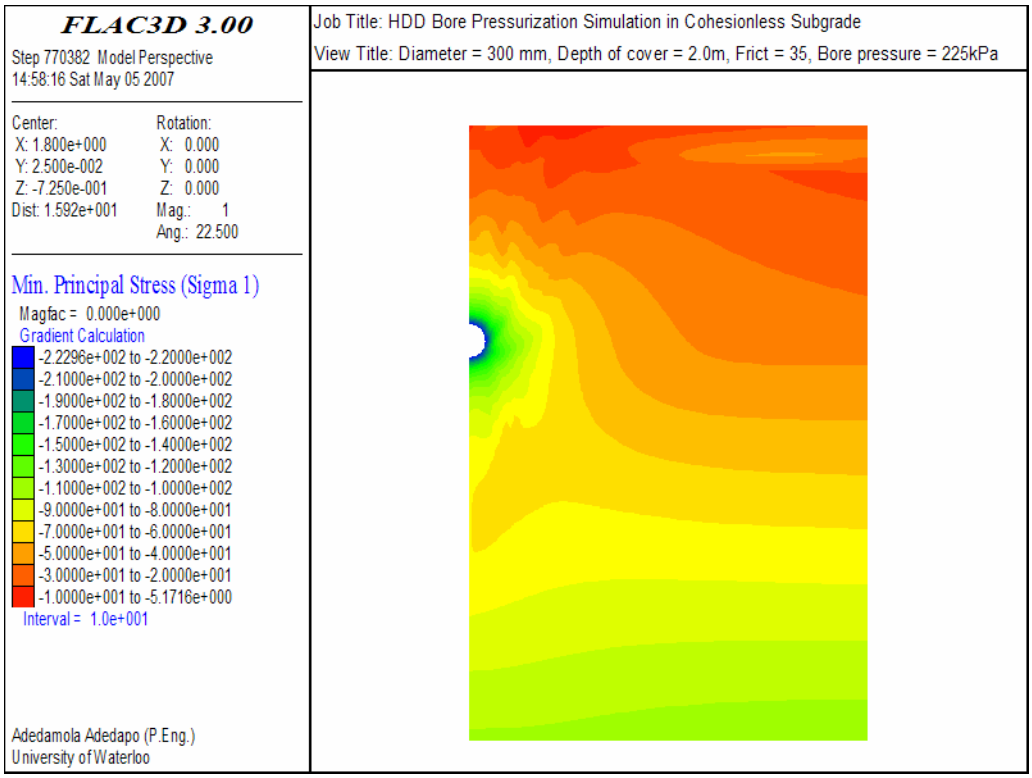

Figure 6.20: Minimum principal stress (σ_1) contours at 225 kPa in cohesionless subgrade

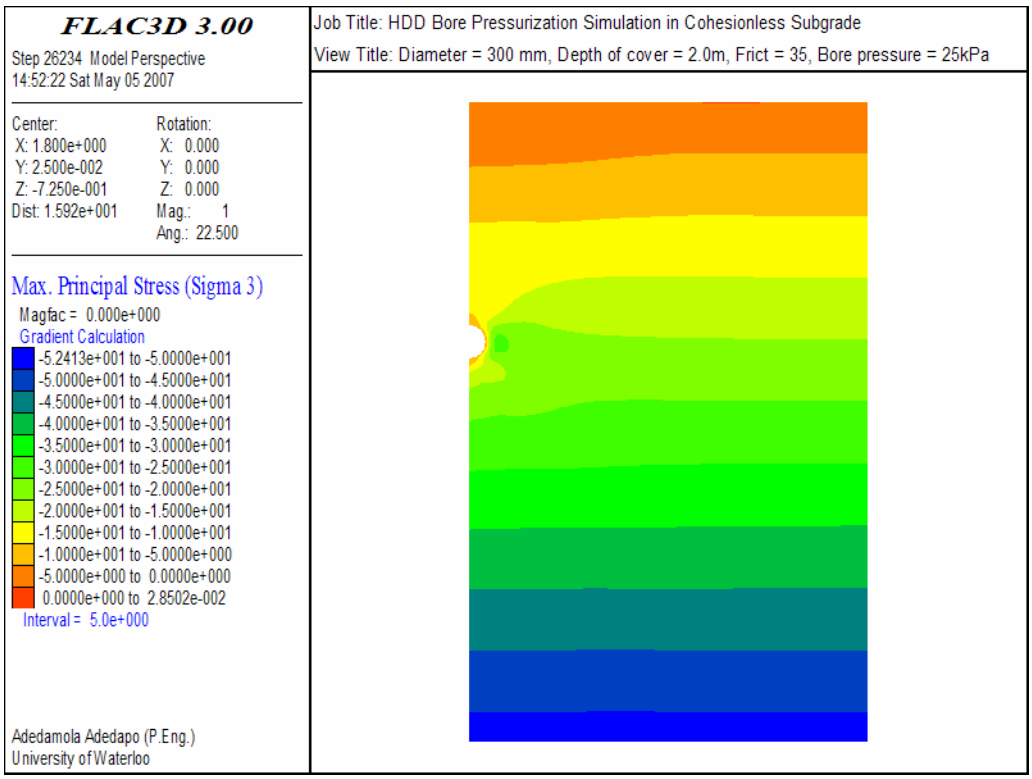

Figure 6.21: Maximum principal stress (σ_3) contours at 25kPa in cohesionless subgrade

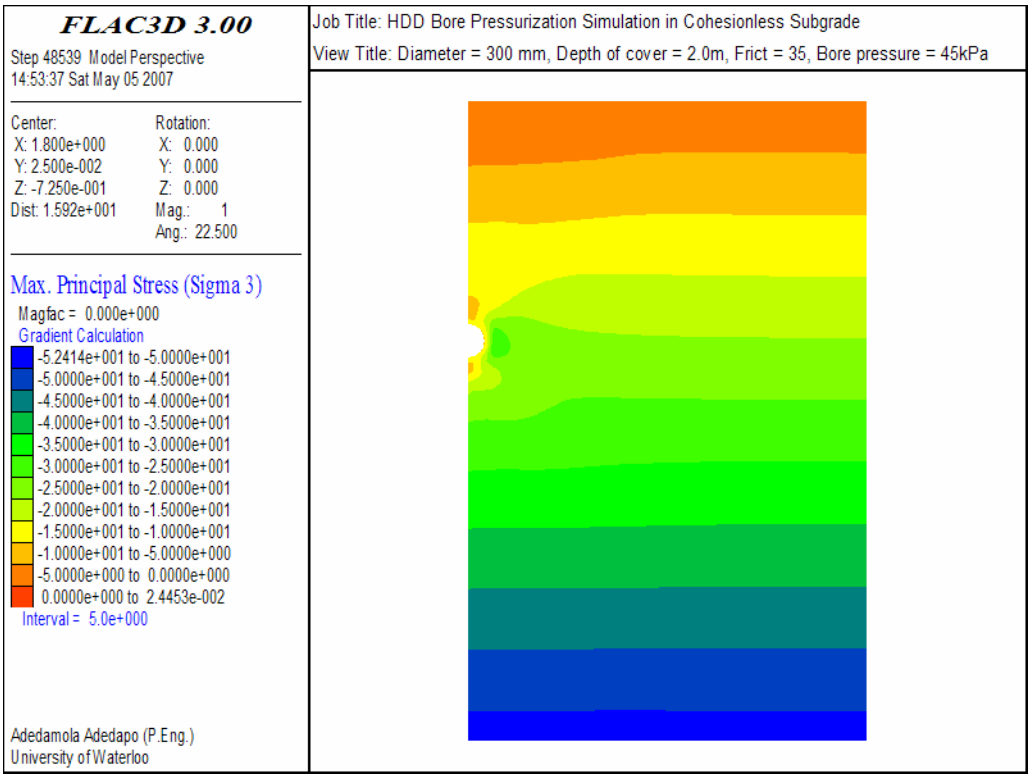

Figure 6.22: Maximum principal stress (σ_3) contours at 45 kPa in cohesionless subgrade

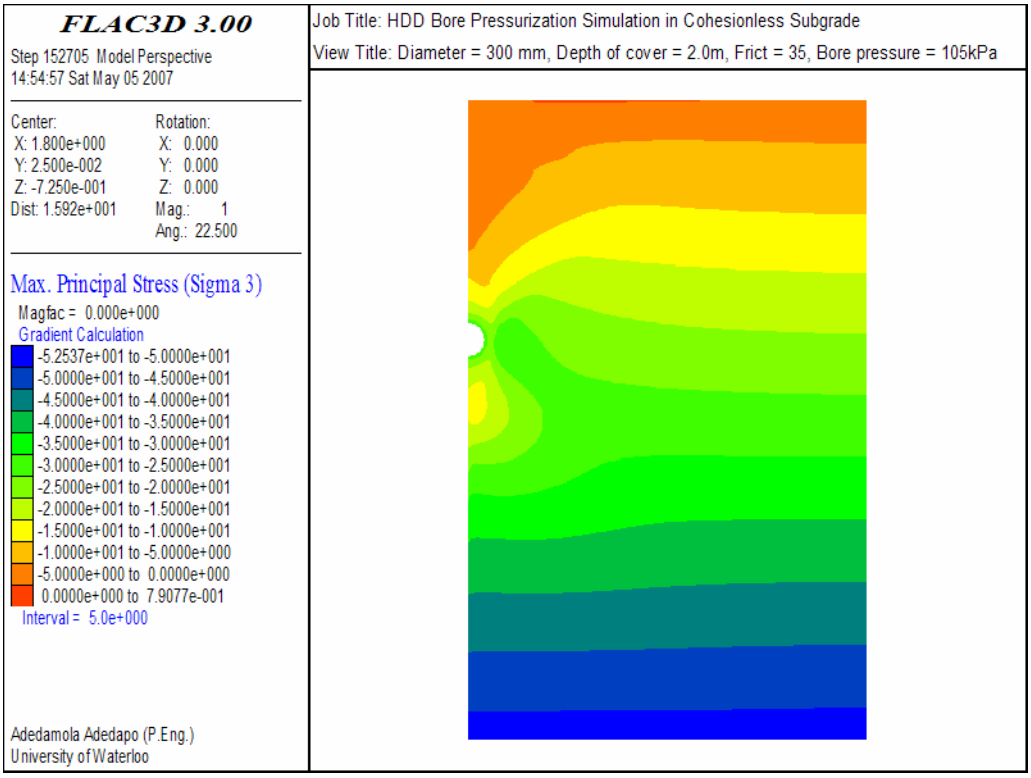

Figure 6.23: Maximum principal stress (σ_3) contours at 105 kPa in cohesionless subgrade

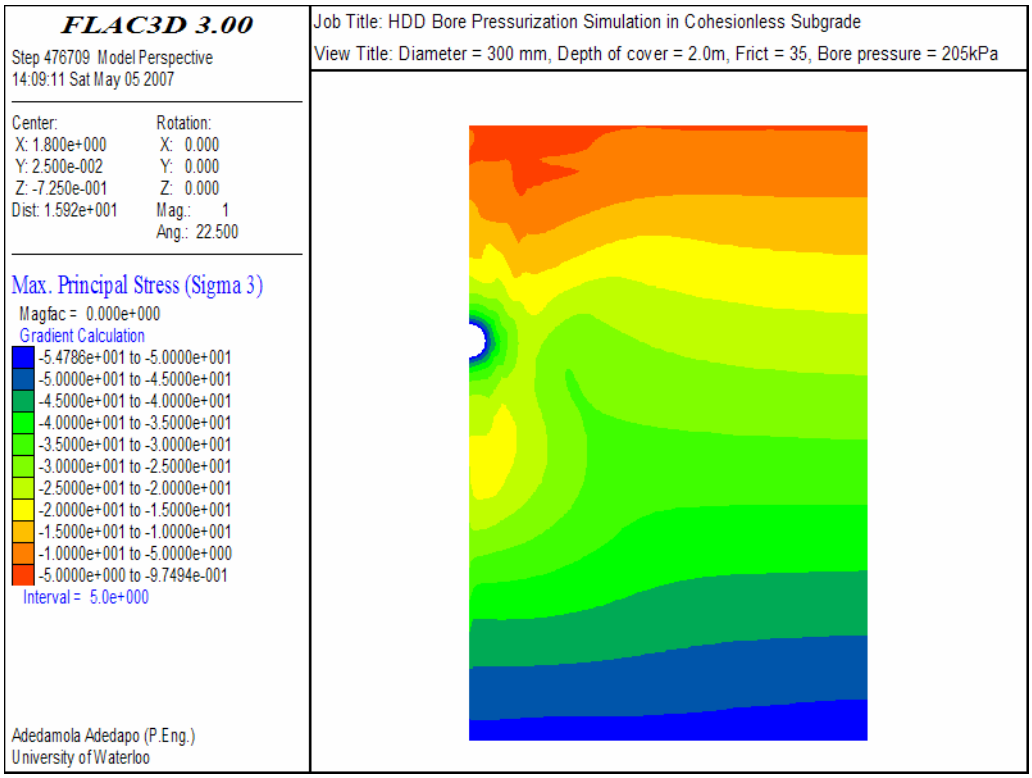

Figure 6.24: Maximum principal stress (σ_3) contours at 205 kPa in cohesionless subgrade

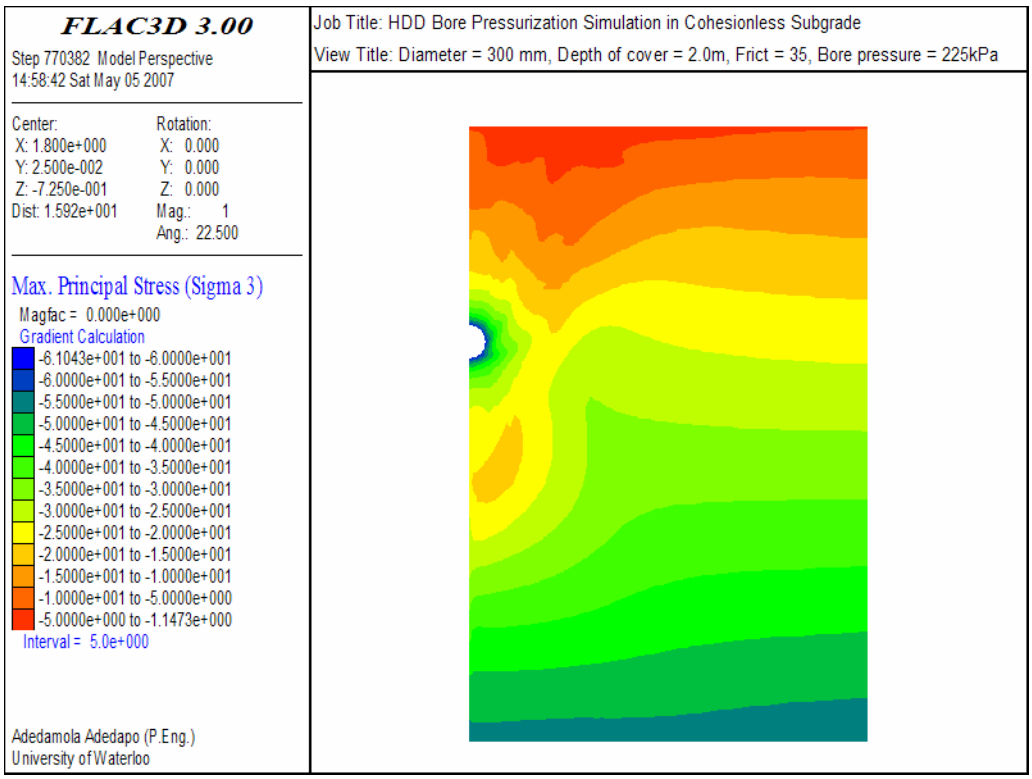

Figure 6.25: Maximum principal stress (σ_3) contours at 225 kPa in cohesionless subgrade

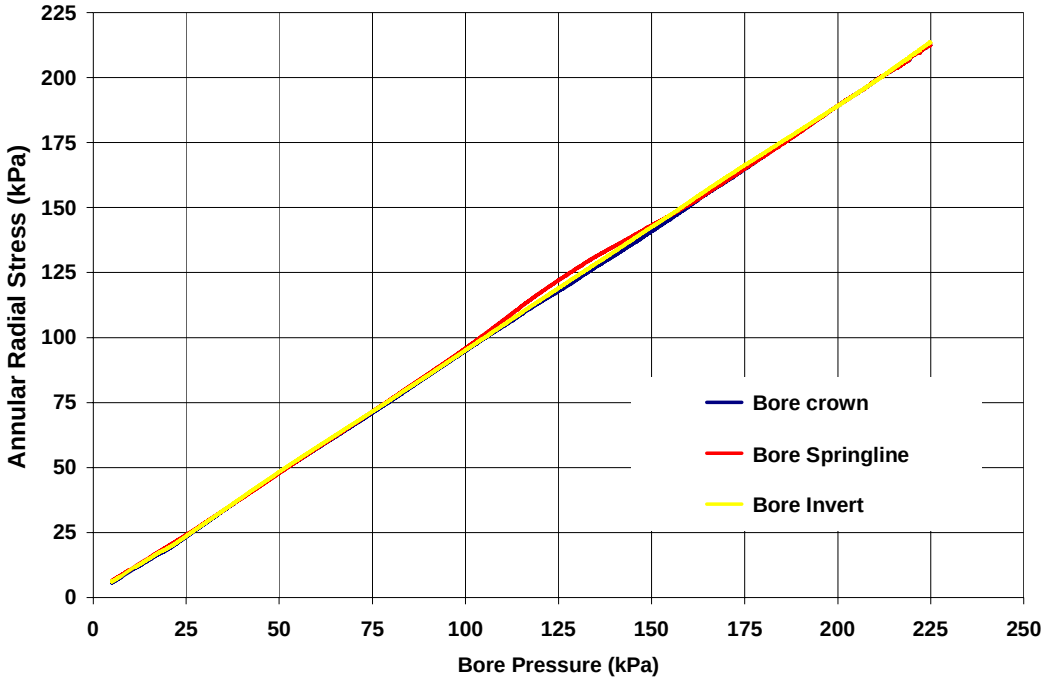

Figure 6.26: Annular Radial Stress vs. bore pressure in cohesionless subgrade (Bore diameter 300mm, depth of cover = 2.0m, friction =35°)

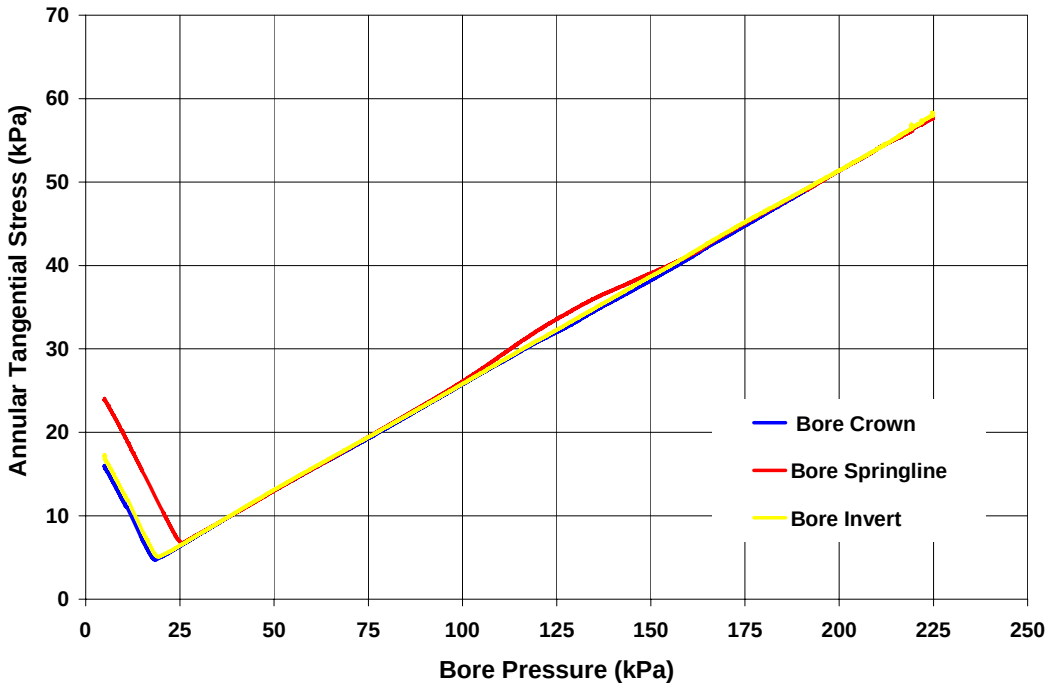

Figure 6.27: Annular tangential stress vs. bore pressure in cohesionless subgrade (Bore diameter 300mm, depth of cover = 2.0m, friction =35°)

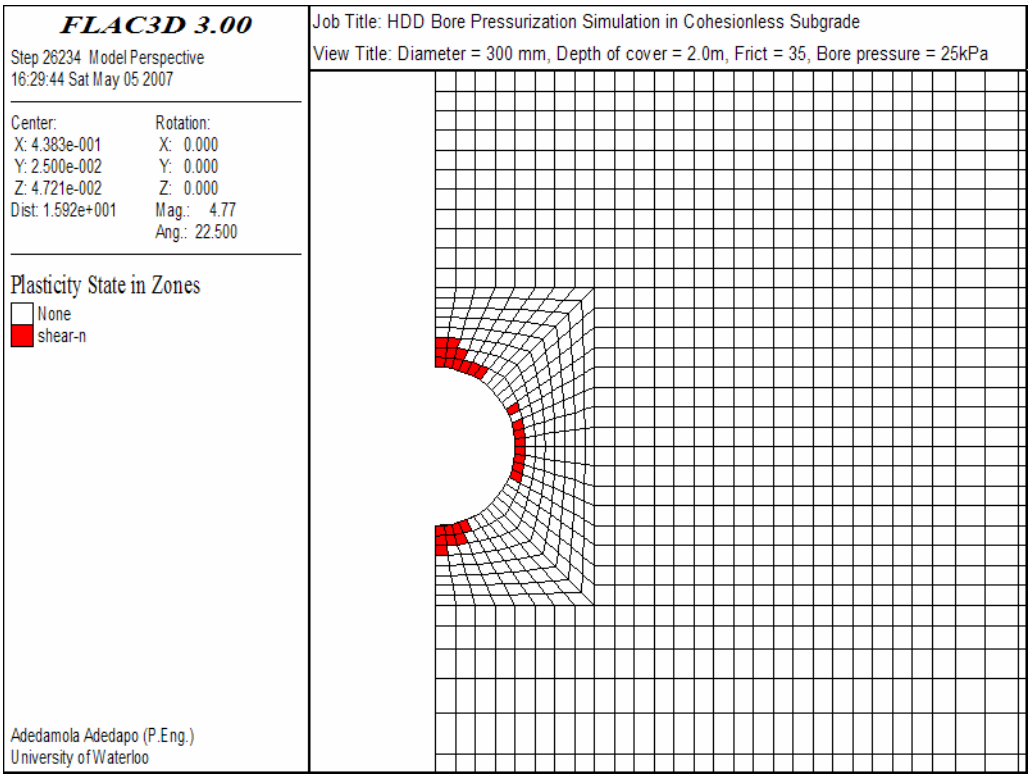

Figure 6.28: Plasticity state around the bore at 25 kPa in cohesionless subgrade

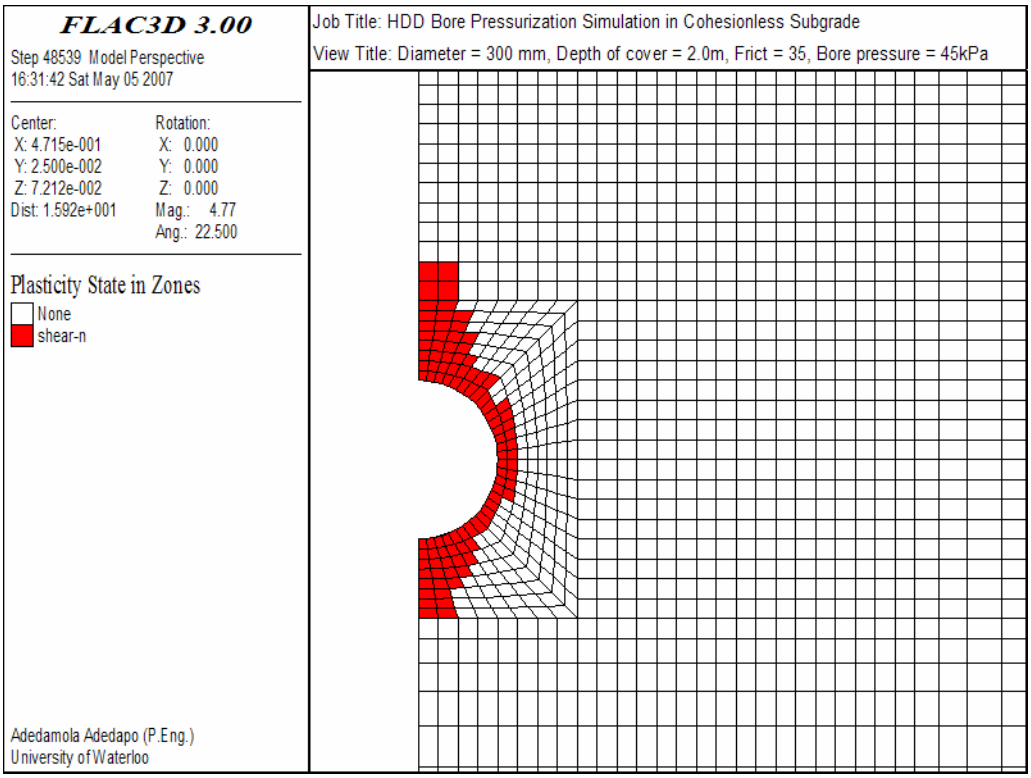

Figure 6.29: Plasticity state around the bore at 45 kPa in cohesionless subgrade

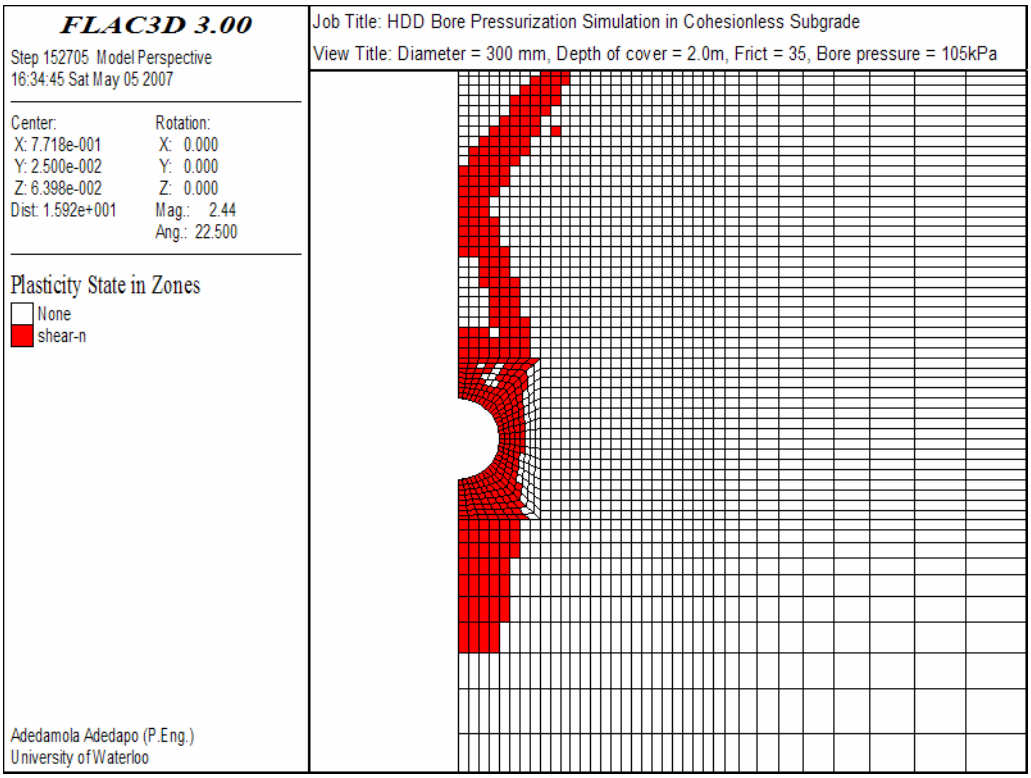

Figure 6.30: Plasticity state around the bore at 105 kPa in cohesionless subgrade

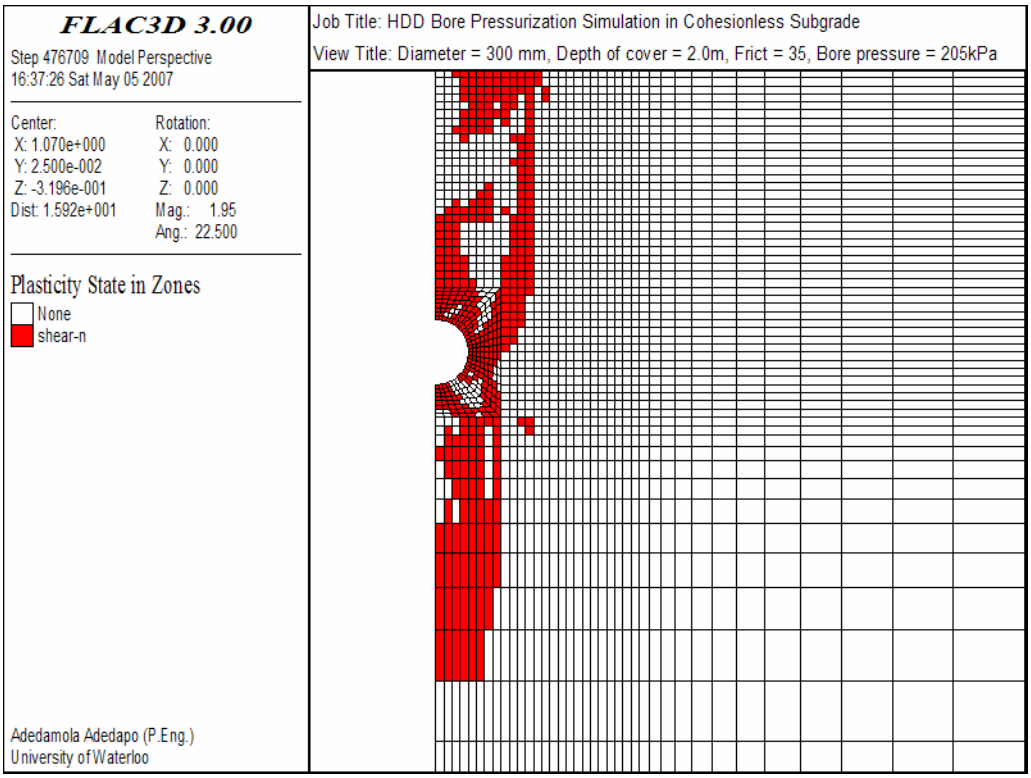

Figure 6.31: Plasticity state around the bore at 205 kPa in cohesionless subgrade

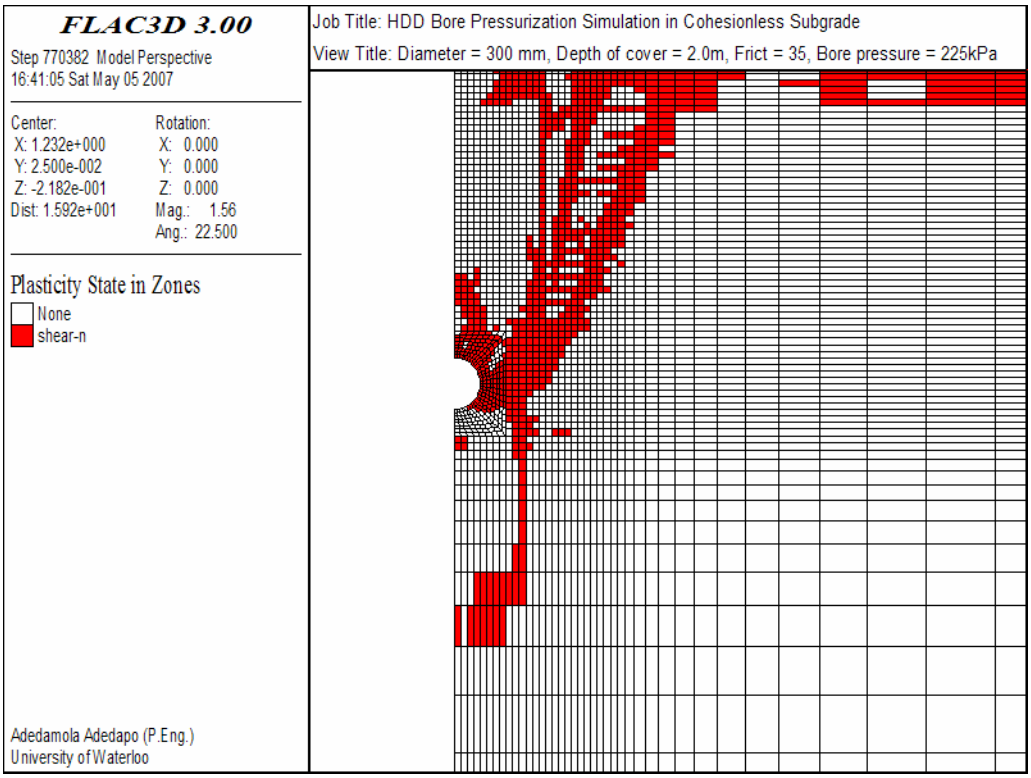

Figure 6.32: Plasticity state around the bore at 225 kPa in cohesionless subgrade

This observation is consistent with results of Kirsch's solution for stress distribution around a circular hole in isotropic linearly elastic medium presented by Obert and Duvall (1967). The minimum tangential stresses observed at the crown, springline and invert were 4.7, 6.6 and 5kPa, respectively.

Further increase in bore pressure beyond the elastic limit of the subgrade soil resulted in yielding in the periphery of bore due to '*plastic expansion'* of the bore. Figure 6.29 shows the plasticity state at applied bore pressure of 45 kPa. Once yielding is initiated at the bore periphery, additional increase in bore pressure resulted in the increase of the tangential stresses and extent (spread) of the *plastic zones* as shown in Figures 6.30 through 6.32. This caused the location of minimum circumferential stress to moves further away from the bore wall into the subgrade soil towards the pavement surface as shown in Figures 6.21 through 6.25.

6.4.4.2 Ground displacements observed during HDD installation in cohesionless subgrade

The radial displacement at the crown and the springline of the bore due to increased bore pressure is presented in Figure 6.33. The plots indicate that there is a significant non-linearity in the bore pressure-displacement curve beyond bore pressures (20 kPa) where elastic response was observed as discussed in the previous section. The bore pressure-displacement curve can be described with a hyperbolic or logarithmic function approaching an asymptotic value (limit pressure) at higher bore pressure.

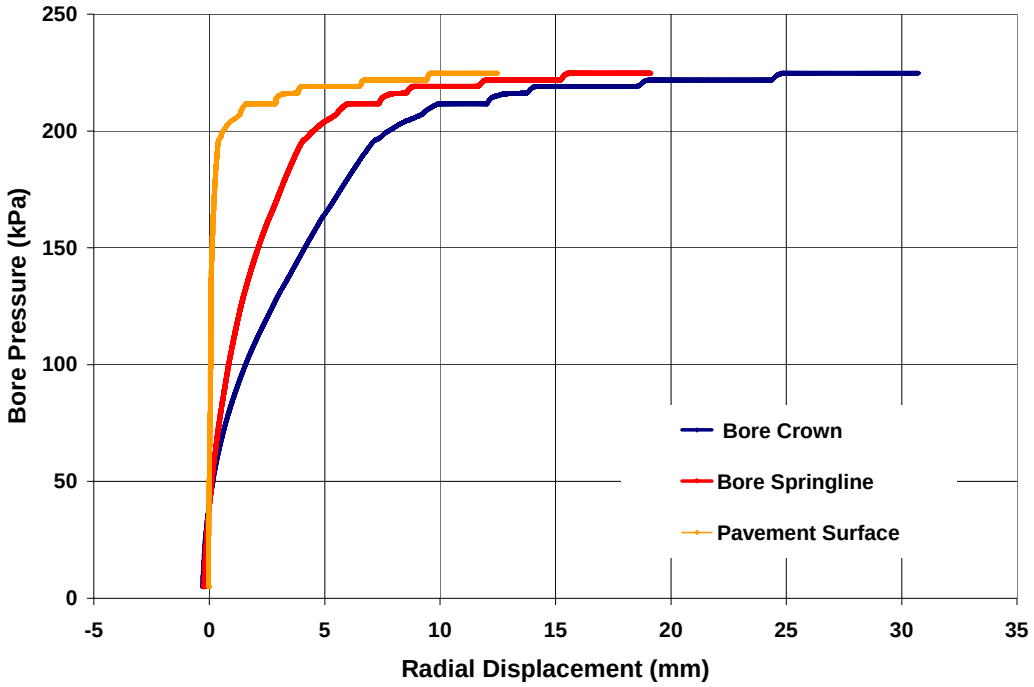

Figure 6.33: Bore pressure-displacement relationship in cohesionless subgrade
(Bore diameter 300mm, depth of cover = 2.0m, friction =35°)

Although uniform radial pressure was applied to the bore to simulate bore pressurization during HDD installation, the resulting outward radial displacement at the periphery of the bore wall was non-uniform. Figure 6.33 indicates that there is a noticeable difference in the magnitude of the outward radial displacement at the crown and the springline, the bore expanded outwardly more at the crown more than at the springline. The difference between the displacement at the crown and springline progressively increased with bore pressure. The

variation in the displacement response around the bore may be attributed to the difference in the geostatic stress and lateral resistance provided by the native soil adjacent to the springline. The pressure required to propagate displacement laterally at the springline is significantly higher than those required to propagate displacement vertically at the bore crown.

Figures 6.34 through 6.38 show contour plots of the displacement around the HDD bore at various applied bore pressures (25, 45, 105, 205 and 225 kPa). As the bore pressure is increased, the displacement field is pushed further outward away from the bore until it finally reached the pavement surface at around 200 kPa bore pressure.

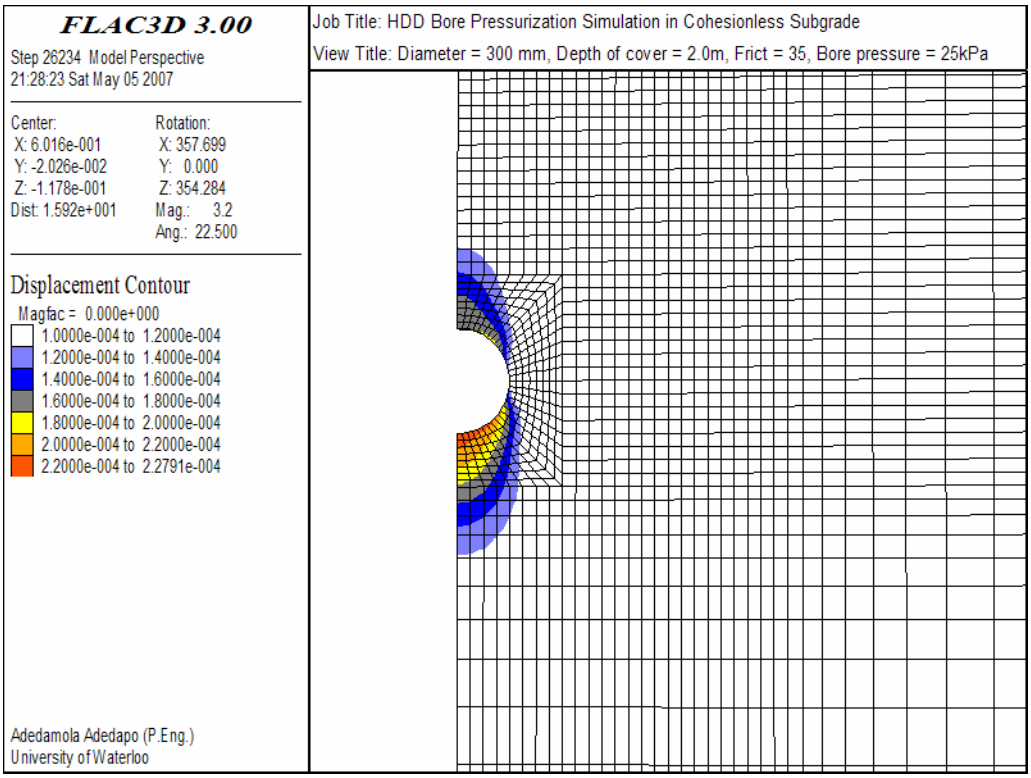

Figure 6.34: Displacement contour at 25 kPa in cohesionless subgrade

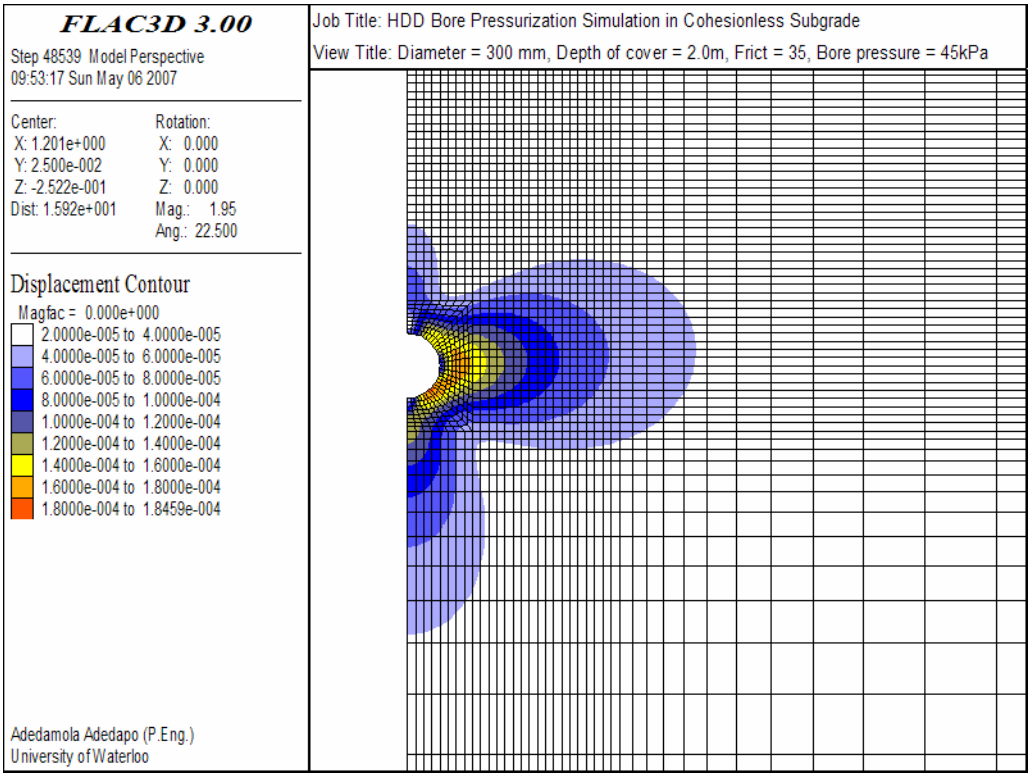

Figure 6.35: Displacement contour at 45 kPa in cohesionless subgrade

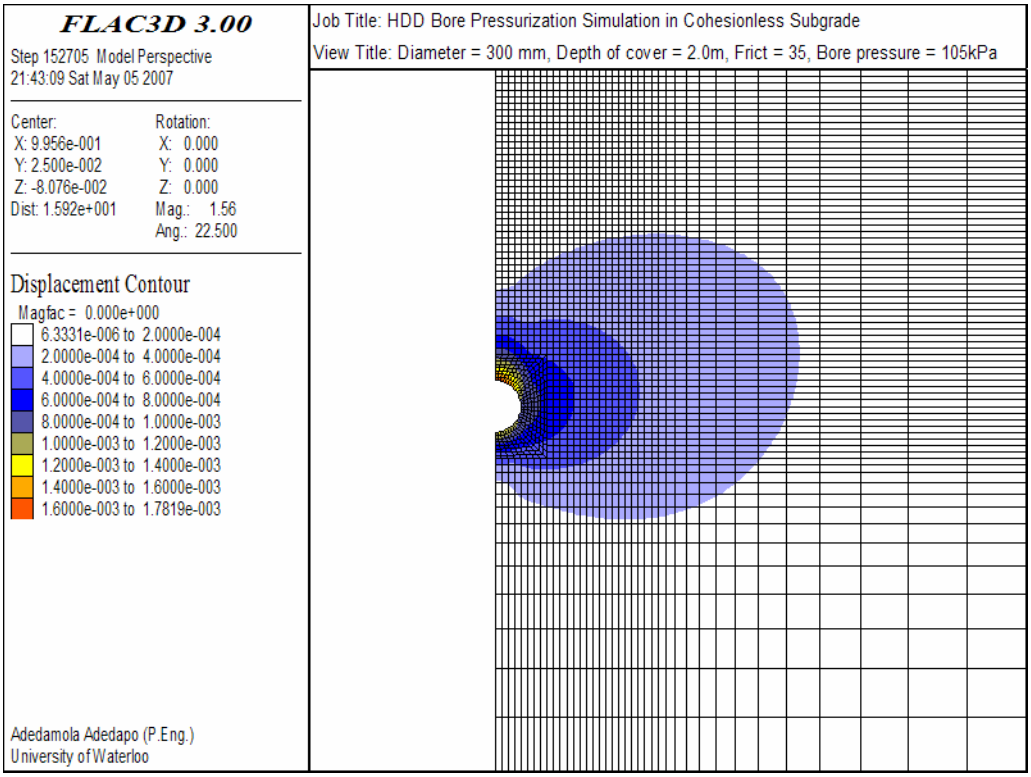

Figure 6.36: Displacement contour at 105 kPa in cohesionless subgrade

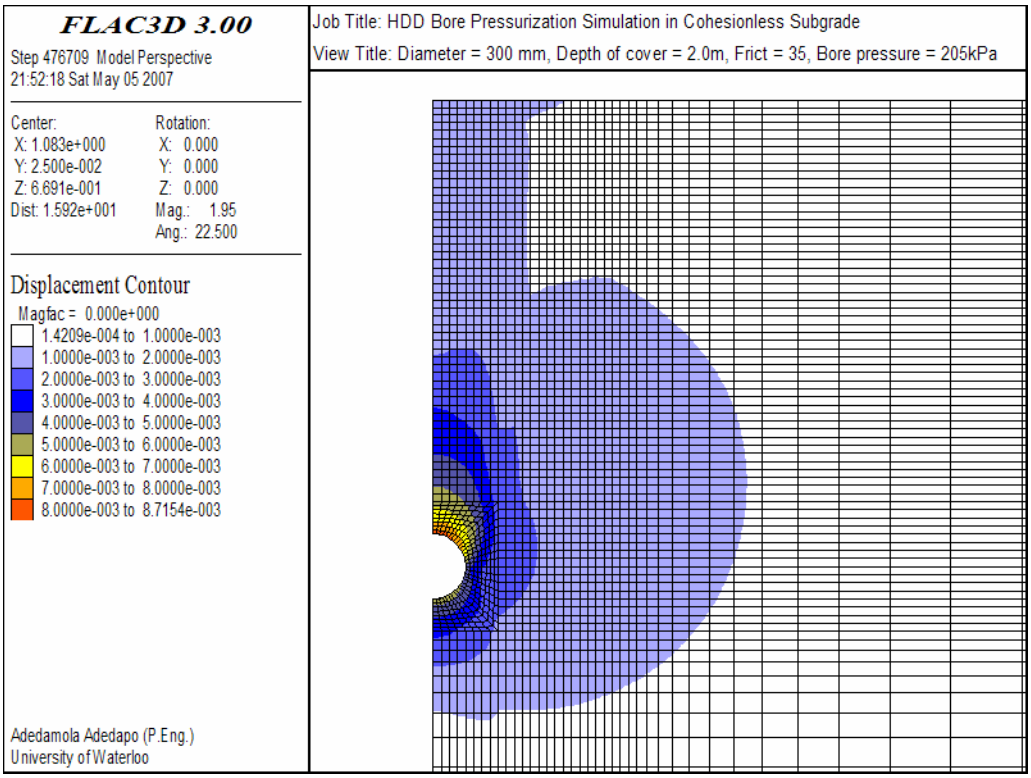

Figure 6.37: Displacement contour at 205 kPa in cohesionless subgrade

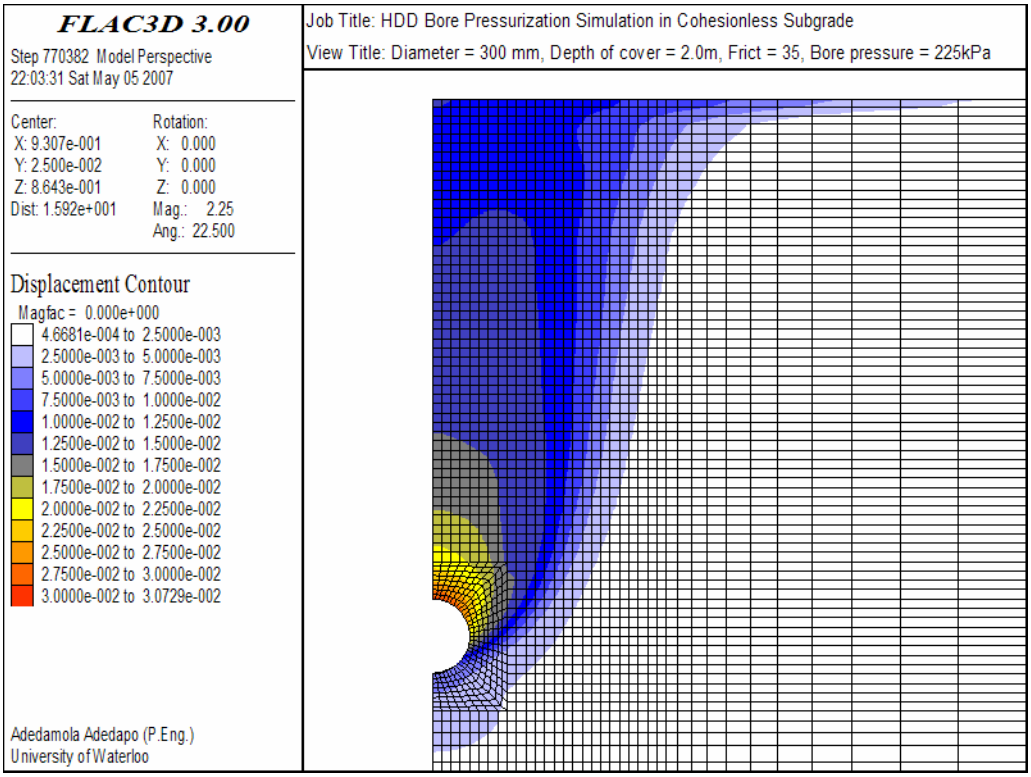

Figure 6.38: Displacement contour at 225 kPa in cohesionless subgrade

Figure 6.39 shows the bore pressure-displacement response at different elevations above the bore crown. Bore pressure of about 120 kPa was required to initiate an upward vertical displacement of 0.5mm at a height of about 0.5m above the bore crown in the cohesionless subgrade soil. Higher bore pressures, 165kPa, 195 kPa and 198 kPa were required to initiate similar magnitude of vertical displacement at 1.0m, 1.3m, and 2.0m above the bore crown, respectively. It should be noted that once the ground movements was initiated at about 1.3m above the crown of the bore , a distance that correlate to 75% of the height of cover only minimal additional bore pressure (about 3 kPa) was required to initiate ground movement at the pavement surface.

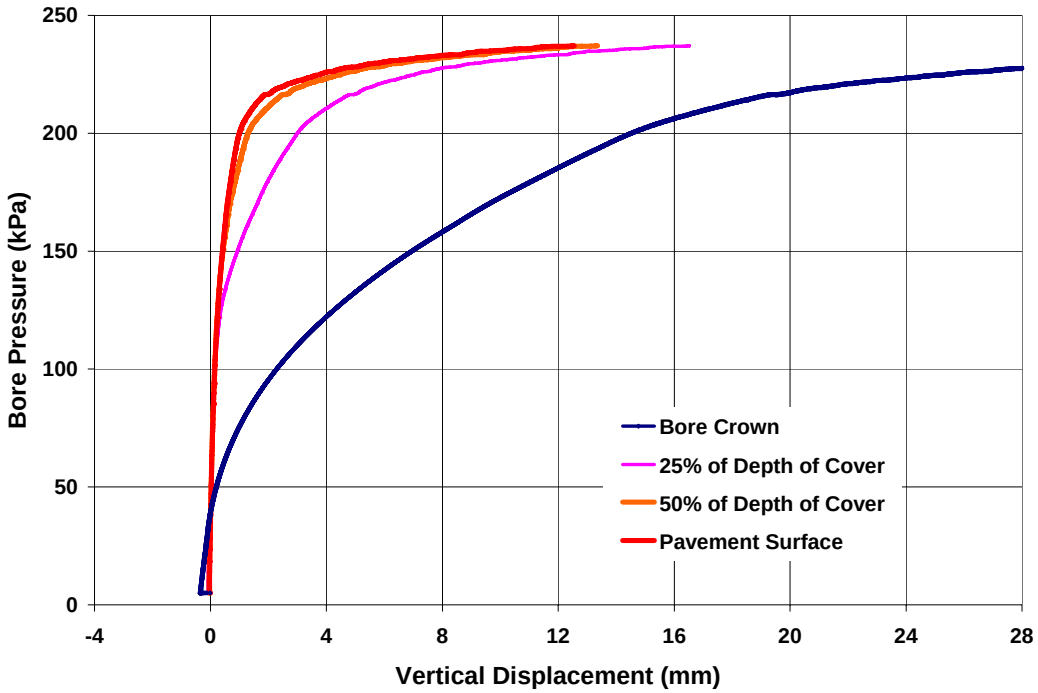

Figure 6.39: Bore pressure-displacement response in cohesionless subgrade
(Bore diameter 300mm, depth of cover = 2.0m, friction =35°)

Further increases in the bore pressure extended the plastic yield zones vertically outward towards the pavement surface (Figure 6.32) and once the yield surface reached the pavement surface at a bore pressure of about 200kPa, the rate of surface deformation increased exponentially with minimal increase in bore pressure. For example, vertical movements in the order of 9.6 and 1.45mm were observed at the bore crown and pavement surface, respectively, for a bore pressure of 210 kPa compared to vertical displacements of about 30.7 and 12.5mm, respectively observed at bore a pressure of 225 kPa. Displacements near the

bore springline showed similar exponential increase. The asymptotic nature of the bore pressure-displacement curve at high bore pressure clearly indicates the presence *limiting pressure* in pure frictional subgrade material. It has been shown in Sections 6.4 that the limit pressure is strongly dependent on the angle of dilation, as higher angles of dilation increases the extent of plastically deforming zones.

6.4.4.3 Shear and volumetric strains during HDD installation in cohesionless subgrade

The mechanism, magnitude, and extent of deformation within the pavement structure due to HDD bore pressurization can be better understood from information derived from the shear and volumetric strains measurements. The variation of these strains during bore pressurization process are presented and discussed herein.

Shear Strains

Shear strain contours around the HDD bore at applied bore pressures 25 kPa, 45 kPa, 105 kPa, 205kPa and 225 kPa are presented in Figures 6.40 through 6.44. The change in shear strains around the bore due to the applied pressure were negligible for bore pressures that were below the overburden pressure (approx 40 kPa). However, as the bore pressure increased and exceeded the overburden stress, the soil adjacent to the periphery of the bore developed shear strain. Figure 6.41 shows the shear strain contours for applied bore pressure of 45 kPa, pressure just slightly above the overburden pressure, the plot suggests that shear strain developed all along the bore wall with maximum strain of about 2e-03 occurring at the crown, springline and invert of the bore.

As the bore pressure was increased further, the magnitude and the extent of the shear strain also increased. At bore pressure of 105 kPa, Figure 6.42, the shear strain contours extended non-uniformly to 0.8, 0.6 and 0.15 m away from the crown, invert and springline of the bore, respectively. The magnitude of the maximum shear strain which occurred at crown and invert of the pipe was about 1e-02, the magnitude of the shear strains at the springline was about half of those observed at the crown.

Increasing the bore pressure from 105kPa to 205 kPa, Figure 6.43, resulted in considerable increase in both the intensity (magnitude) and the spread of the shear strain contour; there was also a noticeable increase in the lateral extent and magnitude of the shear strain contour adjacent to the springline in particular. At this bore pressure, significant plastic deformation and formation of shear bands (or planes) have developed. The shear bands originate from the springline and extend outward and upward at angle to the horizontal (Figure 6.32). The maximum shear strain near the springline was about 5e-02 and approximately 10% less at the crown and invert at bore pressure of 205kPa.

It is of particular interest to note that at as the bore pressure approached the limit pressure around 225kPa, there were significant shearing along the shear-bands/plane, Figure 6.44, resulting in significant vertical upward movement of a '*wedge*' of soil above the crown, this eventually led to excessive '*surface heave*' on the pavement.

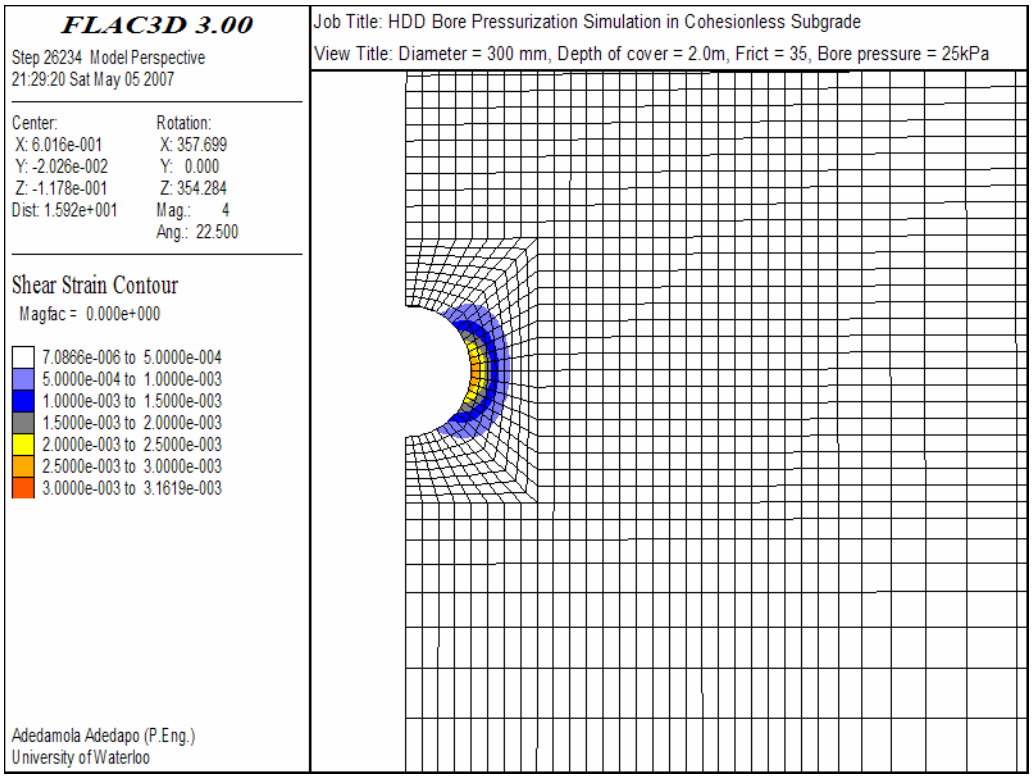

Figure 6.40: Shear strain contour at 25 kPa in cohesionless subgrade

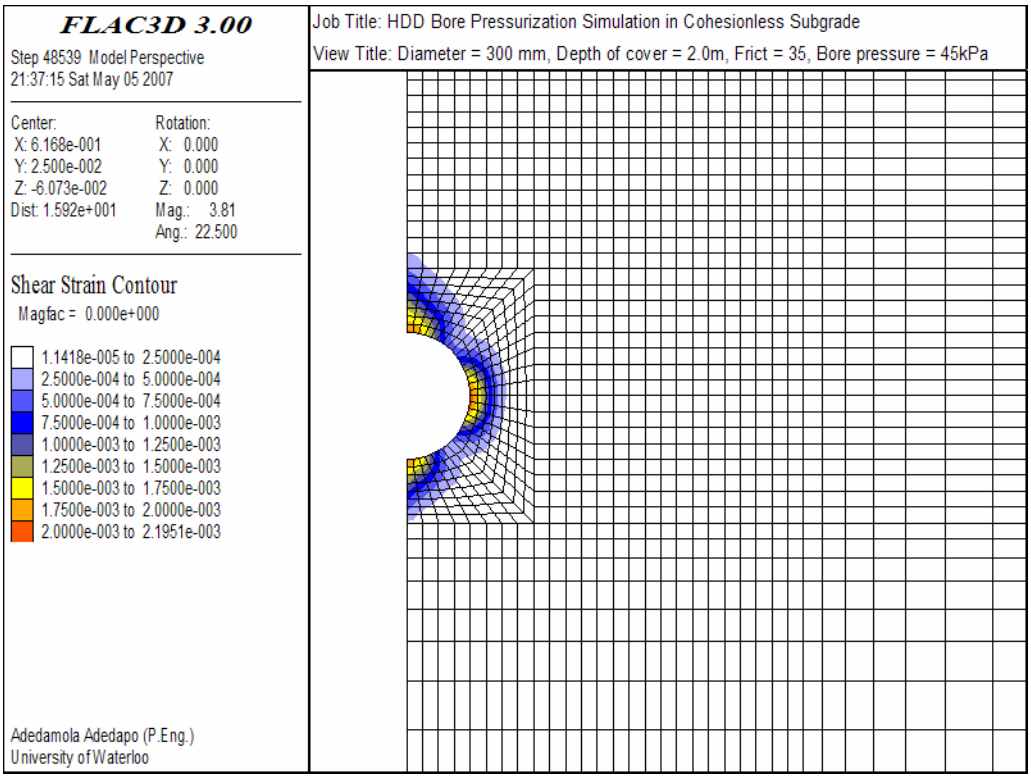

Figure 6.41: Shear strain contour at 45 kPa in cohesionless subgrade

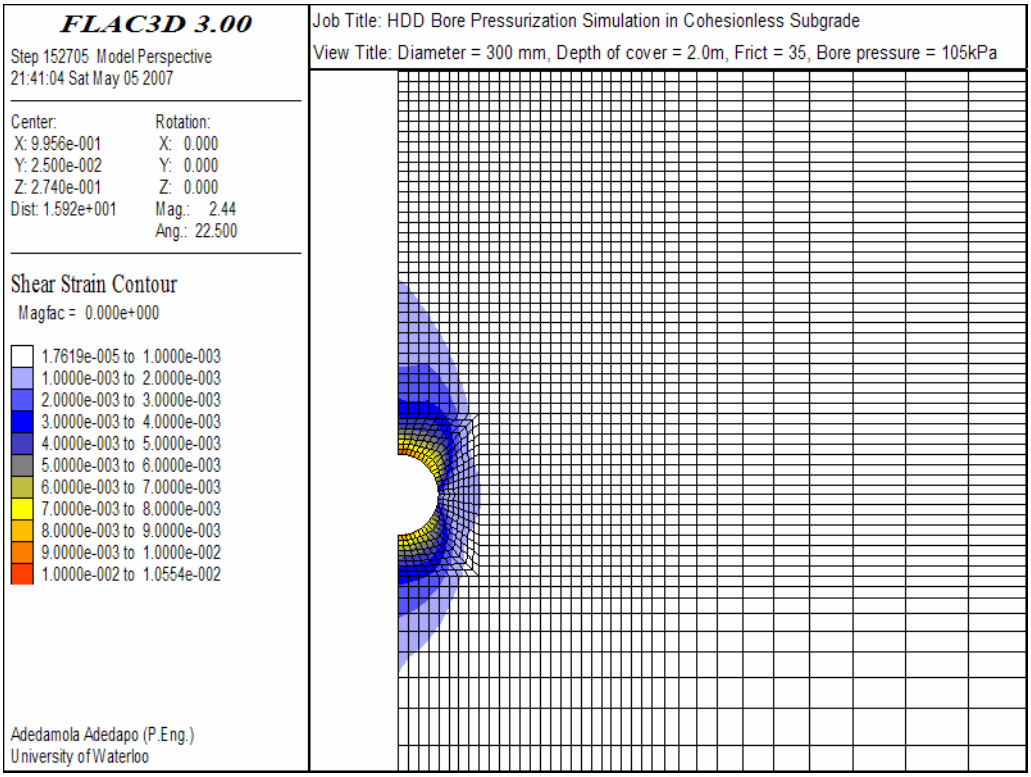

Figure 6.42: Shear strain contour at 105 kPa in cohesionless subgrade

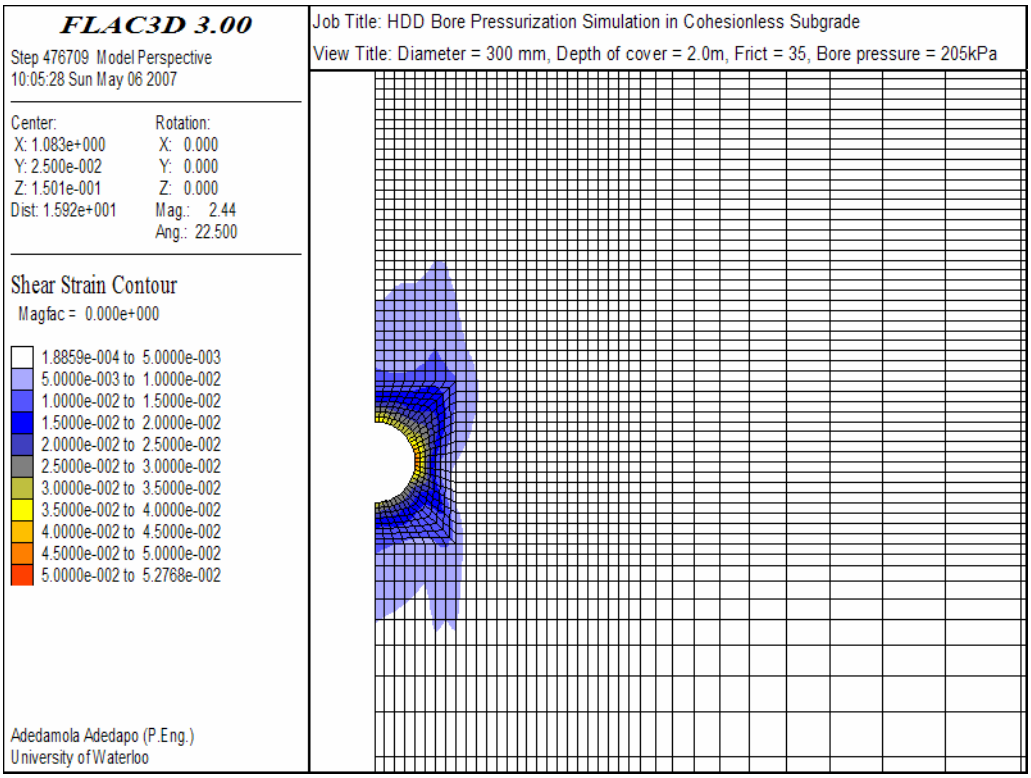

Figure 6.43: Shear strain contour at 205 kPa in cohesionless subgrade

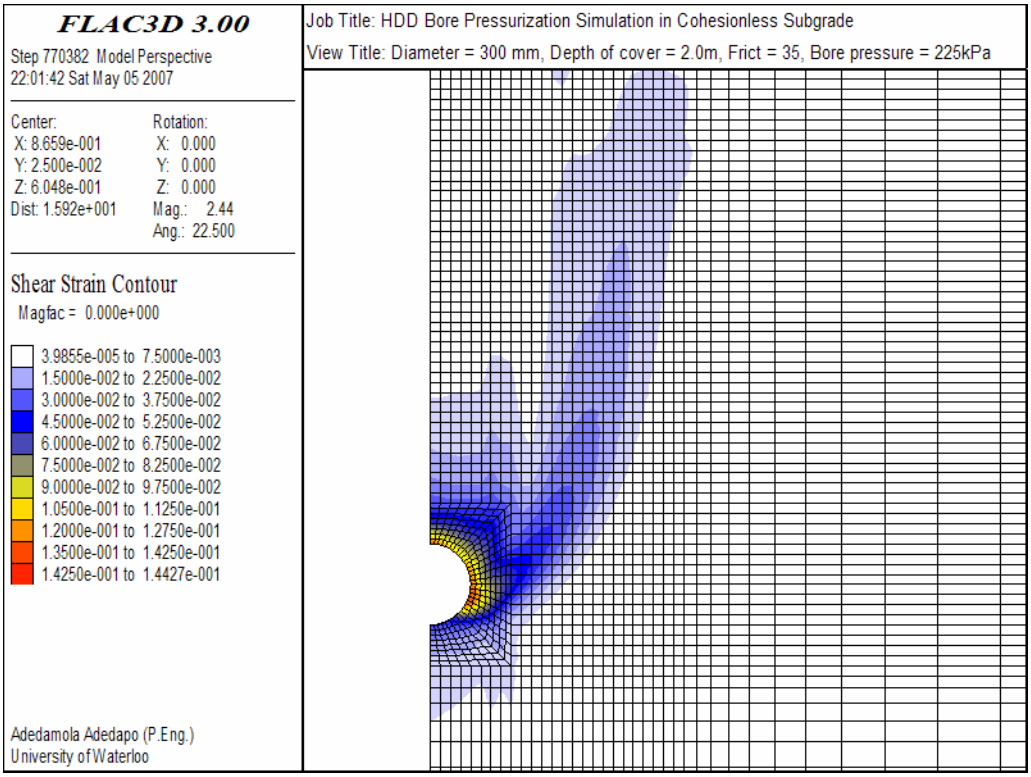

Figure 6.44: Shear strain contour at 225 kPa in cohesionless subgrade

Volumetric Strains

Contour plots of the volumetric strain around the HDD bore at bore pressures 25, 45, 105, 200 and 225 kPa are presented in Figures 6.45 through 6.49, respectively. The sign convention for volumetric strains in *FLAC*^{3D} follows those of direct stresses, positive volumetric strain indicates extension and negative strain indicates compression. The magnitude of volumetric strain is strongly influence by shear dilatancy property of the soil. Shear dilatancy, or simply dilatancy, is the change in volume that occurs with shear distortion of a material. Dilatancy is characterized by a dilation angle, ψ, which is related to the ratio of plastic volume change to plastic shear strain. Hence, there is a good correlation between volumetric strain and shear strain contours in zones that have experienced plastic yielding.

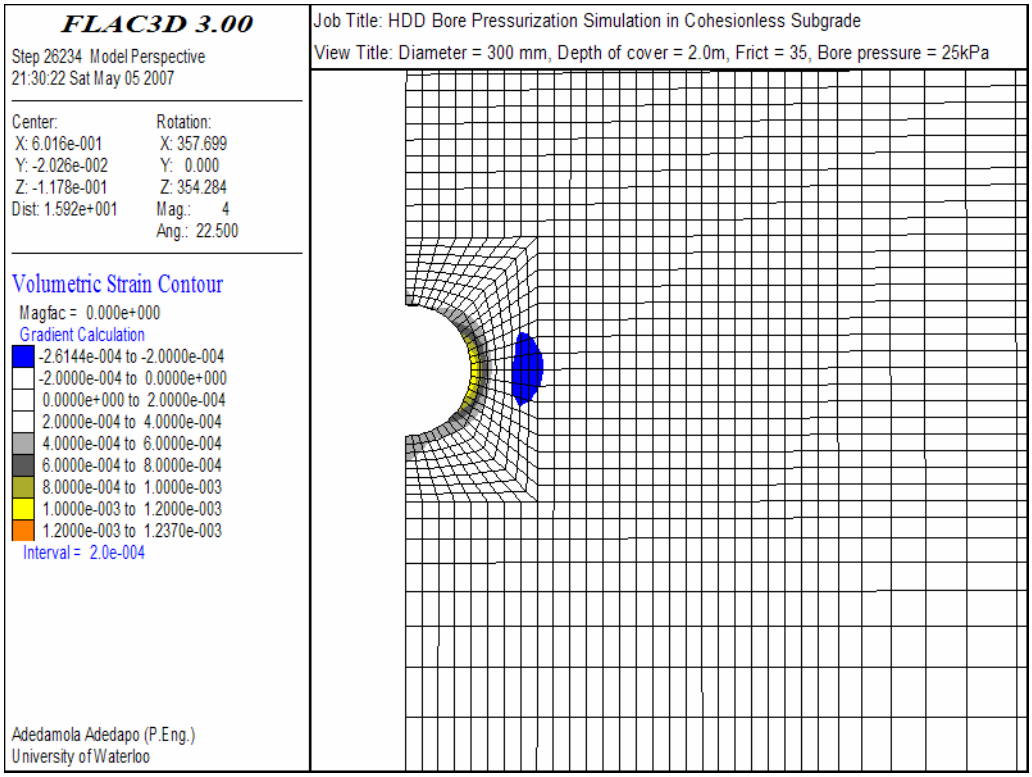

Figure 6.45: Volumetric strain contour at 25 kPa in cohesionless subgrade

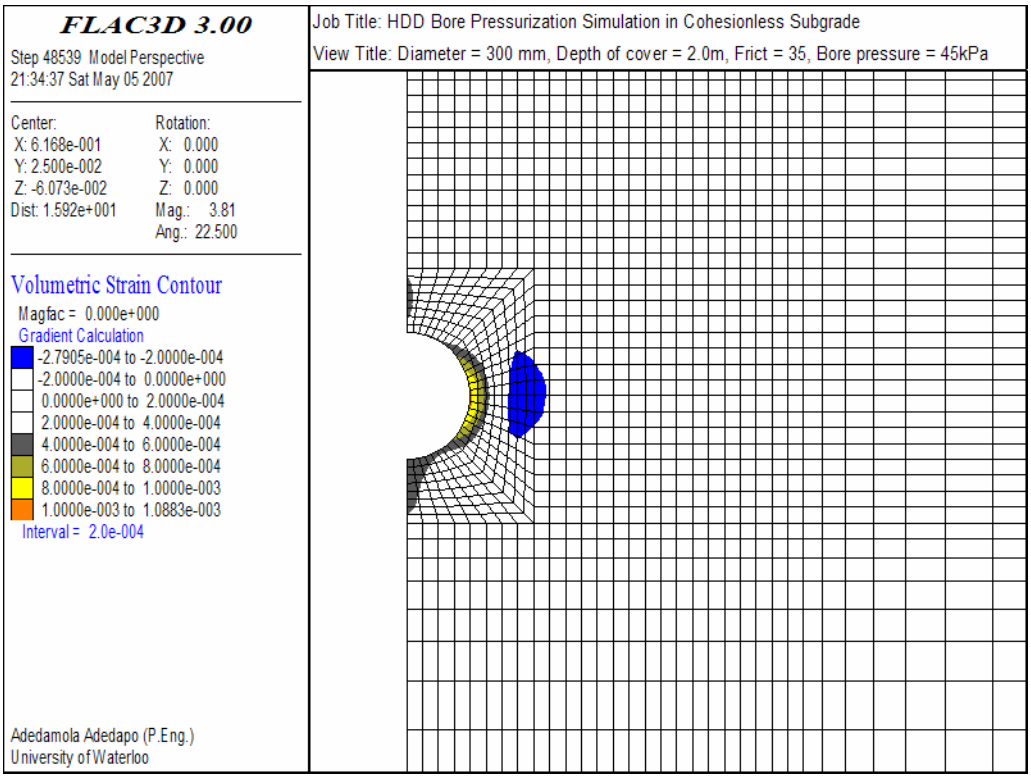

Figure 6.46: Volumetric strain contour at 45 kPa in cohesionless subgrade

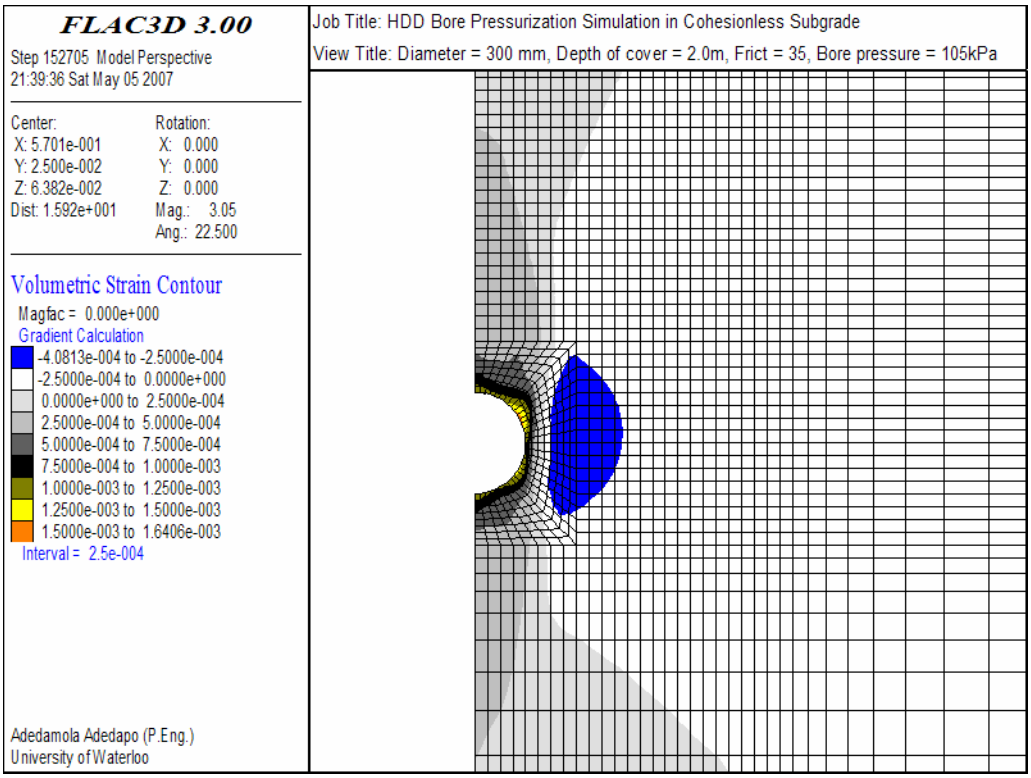

Figure 6.47: Volumetric strain contour at 105 kPa in cohesionless subgrade

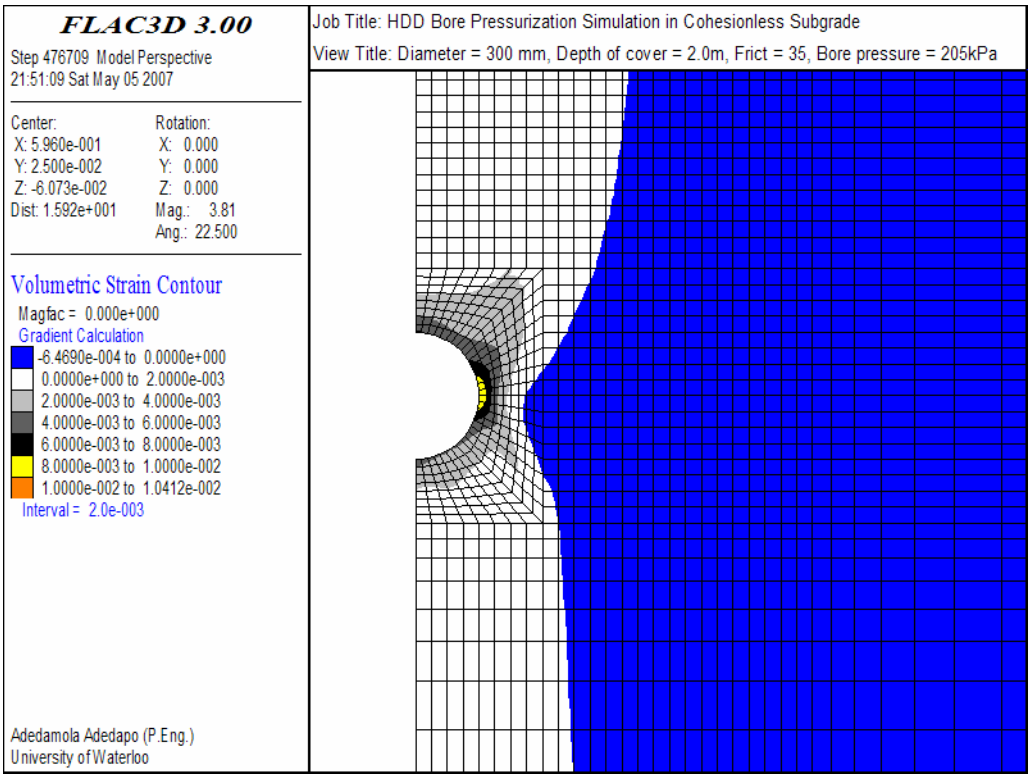

Figure 6.48: Volumetric strain contour at 205 kPa in cohesionless subgrade

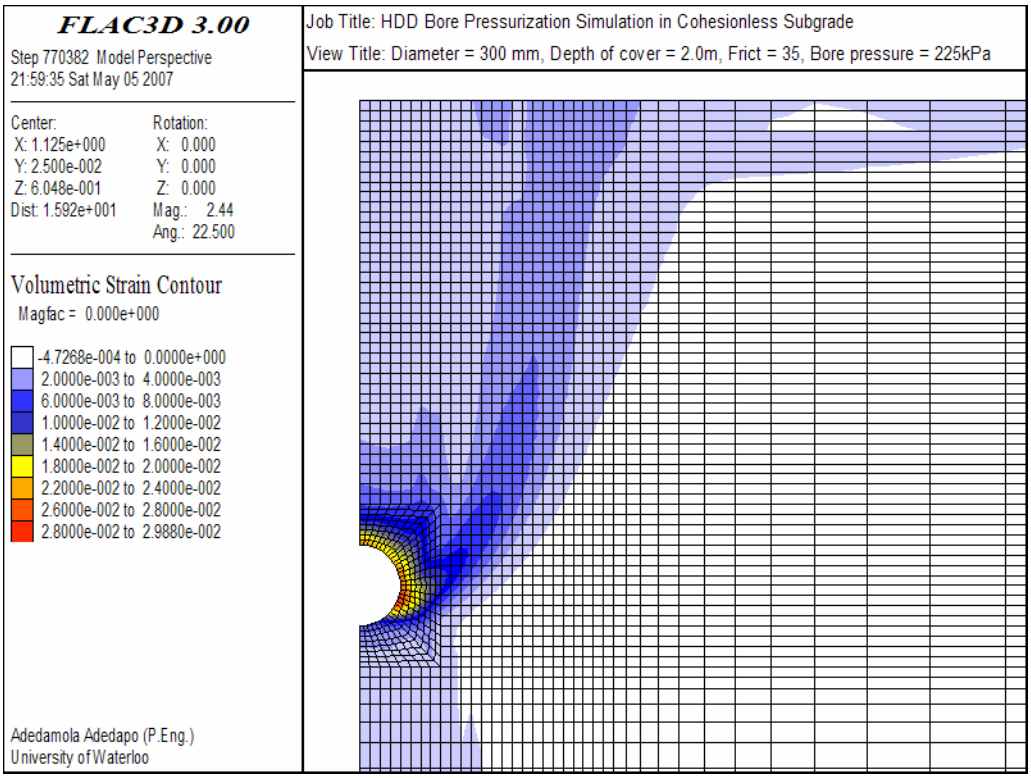

Figure 6.49: Volumetric strain contour at 225 kPa in cohesionless subgrade

At bore pressures lower than the overburden stresses (about 40 kPa), the zones around the bore wall experienced negligible volumetric strain. The maximum volumetric strain of about 1e-03 occurred near the springline where the soil experienced some expansion due to plastic yield, the extent of the yielding was only about 50mm from the edge of the bore. There was compression in the soil zones about 100mm away from the springline, Figure 6.46, the increased bore pressure resulted in elastic compression of about -2.7e-04 in the soil at this location.

As the bore pressure was increased, zones of plastic yielding expanded outwardly away from the bore and the extent as well as magnitude of the volumetric strain also increased. At bore pressures of 105kPa; all the soils around the periphery of the bore have dilated and experienced volumetric strain of about 1.25e-03. The volumetric strain contours, Figure 6.47, have extended to a distance about the size of the bore diameter (0.3m) above the crown and below the invert of the bore. However there was no significant change in the lateral extent of volumetric strain near the springline. The magnitude of volumetric strain of the zones near the springline experiencing elastic compression was about -4e-04.

Further pressurization of the HDD bore shifted the volumetric strain contour away from the bore towards the pavement surface; at bore pressure of 205 kPa, most of the soils above the crown of the bore have yielded plastically and have experienced volumetric strain. Similarly, the soils extending to about 5 bore diameter (1.5m) below the invert of the bore have also yielded plastically and dilated. The dilatation only extended to about a bore diameter (0.3m) laterally away from the springline; the magnitude of volumetric strain in soil zones undergoing elastic compression away from the springline increased to about -6.5e-04.

As the bore pressure approached the limit pressure around 225kPa, the failure bands/plane originating from the invert and extending vertical upward became more conspicuous and are similar in extent to those of shear strains. Once the failure bands extend to the pavement surface, addition of small bore pressure resulted in substantial vertical displacement (*heave*) of the soil within the shear plane. The excessive change in volume of the subsoil due to dilation in addition to the change in volume caused by rigid upward movement and/or displacement of the soil ultimately resulted in heave that is visible on the pavement structure.

6.4.4.4 Bore Pressure-displacement Response in Cohesionless Subgrade

The results obtained from numerical simulations of HDD installation in cohesionless subgrade beneath flexible pavement roadway are compiled, presented and discussed in this section. The description and key parameters of the numerical simulations completed are summarized in Table 6.4. Generally, the mechanism of ground deformations observed during the simulations are similar to those described in the preceding sections and will not be repeated. The primary results that are presented and discussed in this section are bore pressure-displacement response observed during the simulations.

Bore pressure-displacement relationship

The limiting displacement (or heave) was arbitrarily assumed to be 12.5mm for discussion purpose. The amount of pavement heave that would be deemed acceptable will (or may) be specified in a HDD contract. The *allowable heave* would vary from one project to the other depending on the acceptable level of risk and the consequence of potential heave. Two new terms are introduced and defined. These terms will be referred to extensively in discussions that follow:

"Initiation pressure" refers to the least bore pressure require to generate a vertical displacement of 12.5mm at the crown of HDD bore

"Critical pressure" refers to least bore pressures require to propagate a vertical displacement of 12.5mm to the pavement surface i.e. full height of cover, D, above the bore.

The magnitude of bore pressures required to initiate vertical displacements of 12.5mm at the bore periphery specifically at the crown and to propagate the same amount of displacement to distances $\frac{1}{4}D$, $\frac{1}{2}D$, $\frac{2}{3}D$ and D above the crown of the bore are summarized in Table 6.5. D is the depth of cover and is taken as the height of soil above the crown of the bore. The bore pressures required to limit 12.5mm vertical displacement to a distance of $\frac{1}{4}D$, $\frac{1}{2}D$, $\frac{2}{3}D$ and D above the crown for 200mm, 300mm and 450mm diameter HDD bores in cohesionless subgrade are presented graphically in Figures 6.50 through 6.52, respectively.

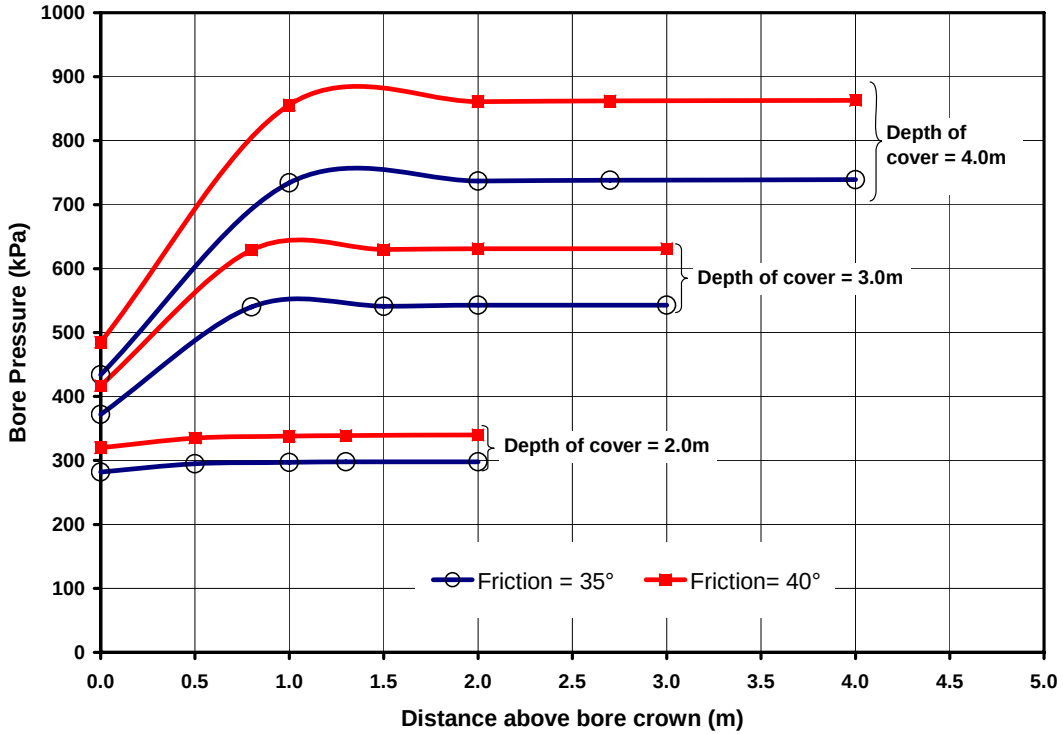

Figure 6.50: Estimated bore pressure required to initiate and propagate 12.5mm vertical displacement above a 200mm HDD bore installed in a cohesionless subgrade

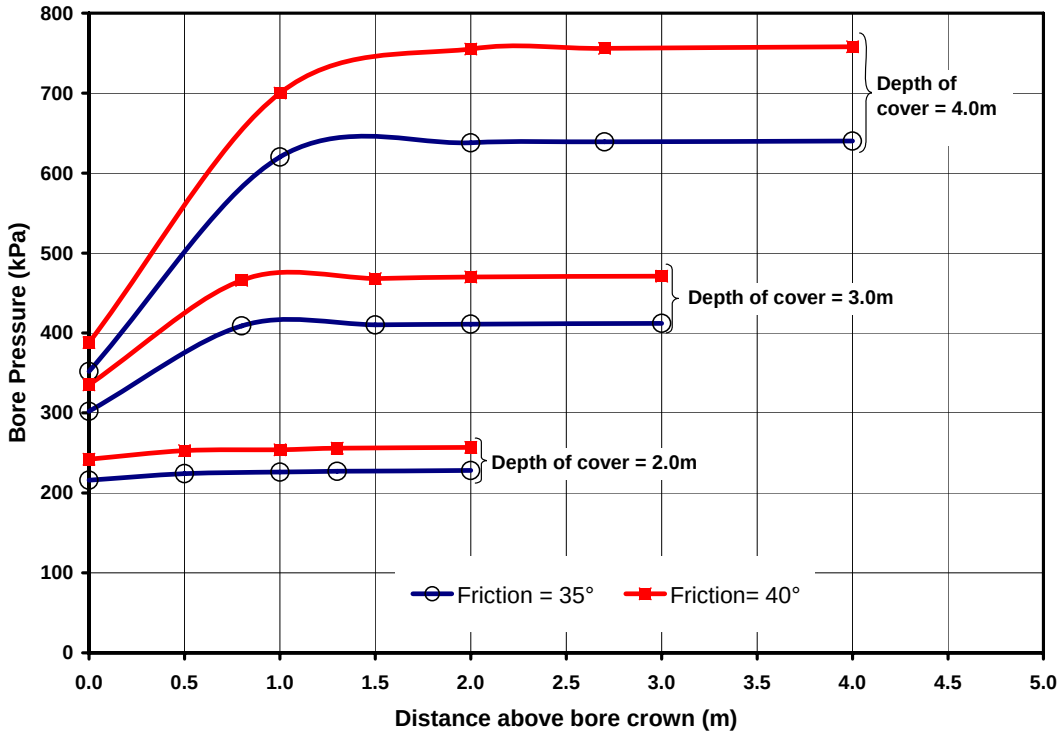

Figure 6.51: Estimated bore pressure required to initiate and propagate 12.5mm vertical displacement above a 300mm HDD bore installed in a cohesionless subgrade

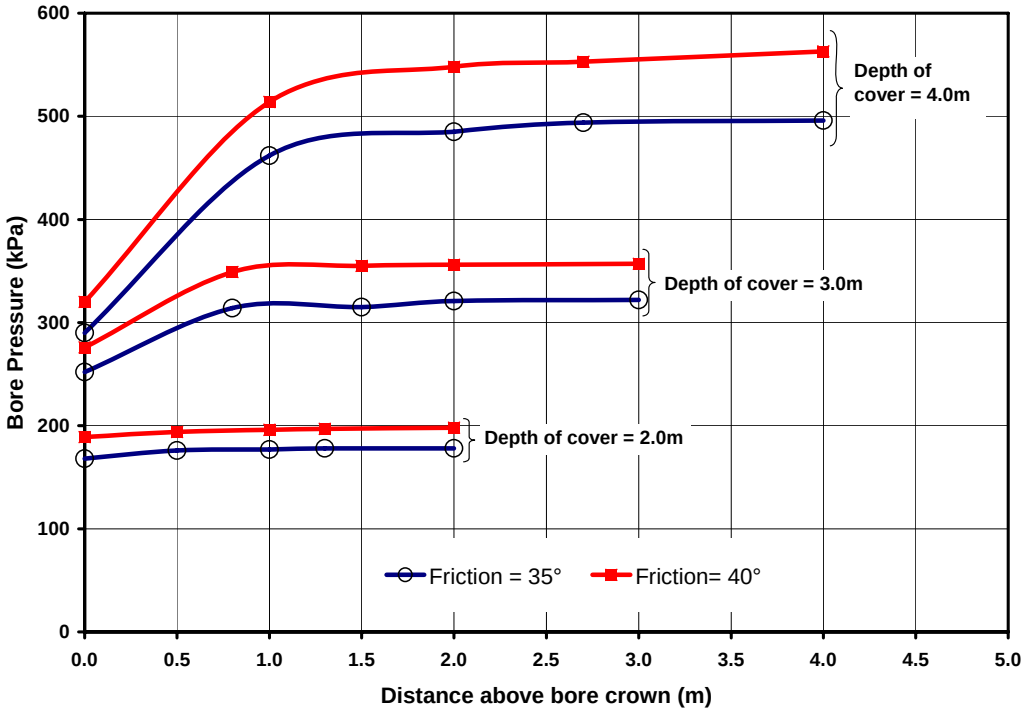

Figure 6.52: Estimated bore pressure required to initiate and propagate 12.5mm vertical displacement above a 450mm HDD bore installed in a cohesionless subgrade

Although lateral displacement away from the springline of the bore may not have the same direct impact on pavement with respect to surface heave as would vertical deformation, excessive horizontal displacement due to HDD bore pressurization may adversely impact existing buried utilities such as brittle asbestos and clay pipes that can only resists minimal deflection. The magnitude and extent of lateral deflections in the subgrade soil away from the springline of the bore were monitored during HDD bore pressurization simulation. The bore pressure required to initiate horizontal displacement of 12.5mm at the springline of the bore are presented in Table 6.6. Bore pressures required to propagate the same magnitude of horizontal displacement to a distance of $\frac{1}{4}D$ or more away from the springline were in all cases greater than pressures required to cause vertical displacement of 12.5mm at the pavement surface. Excessive deformations of *FLAC*^{3D} zones adjacent to the bore occurred in an attempt to propagate the lateral displacements from the springline further into the subgrade soil and these led to instability of the numerical model.

Influence of angle of friction on bore pressure-displacement relationship

The HDD installations that were simulated all showed greater outward displacements with increased bore pressure. The *initiation* and *critical pressures* are directly proportional to the friction angle. Higher friction angle provided greater resistance to deformation and hence, requiring greater bore pressure to initiate and propagate deformation outwardly from the bore. For example, the *critical pressure* for a 200mm diameter bore installed at a depth of 3m below the pavement surface in a cohesionless subgrade with a friction angle of 35° was about 543kPa compared to about 631 kPa required for the same bore geometry in a cohesionless soil with friction angle of 40°. This correlates to an increase of approximately 16.2% in *critical pressure*.

Table 6.5: Bore pressures required for vertical displacement in cohesionless subgrade

Bore Diameter (mm)	Depth of cover (m)	Depth of cover to bore diameter ratio	Friction angle of subgrade soil (°)	Bore Wall (KPa)	Height above bore crown expressed as fraction of depth of cover, D						Pavement Surface (KPa)
					$\frac{1}{4}D$		$\frac{1}{2}D$		$\frac{2}{3}D$		
					Depth (m)	Pressure (KPa)	Depth (m)	Pressure (KPa)	Depth (m)	Pressure (KPa)	
200	2	10	35	282	0.5	295	1.00	297	1.3	298	298
	3	15	35	372	0.8	540	1.50	541	2.0	543	543
	4	20	35	434	1.0	734	2.00	737	2.7	738	739
	2	10	40	320	0.5	335	1.00	338	1.3	339	340
	3	15	40	417	0.8	629	1.50	630	2.0	631	631
	4	20	40	485	1.0	856	2.00	861	2.7	862	863
300	2	6.7	35	218	0.5	224	1.00	226	1.3	227	227
	3	10	35	302	0.8	409	1.50	410	2.0	411	412
	4	13.4	35	352	1.0	620	2.00	638	2.7	639	640
	2	6.7	40	242	0.5	253	1.00	254	1.3	256	257
	3	10	40	335	0.8	466	1.50	468	2.0	470	471
	4	13.4	40	388	1.0	700	2.00	755	2.7	756	758
450	2	4.4	35	168	0.5	176	1.00	177	1.3	178	178
	3	6.7	35	252	0.8	314	1.50	315	2.0	321	322
	4	8.9	35	290	1.0	462	2.00	485	2.7	494	496

Table 6. 6: Bore pressures required for lateral displacement in cohesionless subgrade

Bore Diameter (mm)	Depth of cover (m)	Depth of cover to bore diameter ratio	Friction angle of subgrade soil (°)	Bore wall (springline) (KPa)
200	2	10	35	286
	3	15	35	423
	4	20	35	500
	2	10	40	327
	3	15	40	491
	4	20	40	582
300	2	6.7	35	221
	3	10	35	366
	4	13.4	35	422
	2	6.7	40	254
	3	10	40	421
	4	13.4	40	500
450	2	4.4	35	175
	3	6.7	35	302
	4	8.9	35	378
	2	4.4	40	195
	3	6.7	40	333
	4	8.9	40	418

Influence of depth of cover on bore pressure-displacement relationship

The *initiation* and *critical pressures* are directly proportional to the depth of cover, as increased height of cover provided significant resistance to ground deformations. Contours of vertical displacements were rapidly transmitted upward once the *initiation pressure* is attained and plastic deformation develops above the bore especially for shallower HDD bores. For shallower HDD bores the *critical pressures* are only marginally higher than the *initiation pressures*; whereas, deeper HDD bores required pressure significantly above the *initiation pressures* to transmit the same magnitude of deformation upward to the pavement surface. For example, only about 10kPa additional bore pressure was required above the *initiation pressure* before the *critical pressure* was attained for a 300mm HDD bore installed at a shallow depth of 2.0m in a cohesionless subgrade soil with friction angle of 35° compare to about 288 kPa additional pressure required for a deeper bore at 4.0m below pavement

surface with the same bore diameter. This observation suggests that bore pressures need to be maintained well below those of the *initiation pressures* to prevent excessive heave of the pavement for shallow HDD installation since there is very small margin between *initiation* and *critical pressures*.

Once the *critical pressure* is attained, additional increase in pressure produced significant ground deformation above the bore. For example, the *critical pressure* for a 300mm diameter HDD bore drilled at a depth of 3.0m below the pavement surface in a cohesionless subgrade with a friction angle of 35 was about 412 kPa. Increasing the bore pressure slightly to 414 kPa resulted in approximately 56mm heave on the pavement surface compared to 12.5mm heave observed at a *critical pressure* of 412 kPa. Similarly, the additional 2 kPa increase in bore pressure increased the vertical deflection at the bore crown significantly from 44 to 110mm. These observations indicate that once the limiting pressure is reached and shear bands/planes are fully developed within the soil, further pressurization of the HDD bore could cause excessive pavement deformations if the drilling contractor does not promptly address and relieve the increased bore pressure.

The *initiation pressures* increased between 30 to 50 percent for a 50 percent increase in depth of cover; and between 50 to 72 percent when the depths of cover were doubled. Whereas, the *critical pressures* increased between 80 to 85 percent for 50 percent increase in depth of cover and between 150 to 200 percent when the depths of cover were doubled. The magnitude of increase in *initiation and critical pressures* due to additional depth of cover are proportional to bore diameter and slightly inversely proportional to friction angle.

The lateral deformation observed near the springline increased with bore pressure and generally did not extend beyond a distance equivalent to one bore diameter from the springline for bore pressures less than the *critical pressures* for the simulations completed for this thesis. The magnitude and extent of lateral deformation near the bore springline increased with depth of cover. The *critical pressures* are significantly higher for deeper installation allowing lateral deformation to develop while the vertical deformation is being propagated upwardly to the pavement surface.

The vertical downward displacement at the invert of the bore increased in magnitude and extent with greater depth of cover. The rate of deformations at the invert of the bore were significant retarded once vertical movement developed in the soil above the crown of the bore and the extent of plastic yielded zone at the crown of the pipe increased. The magnitude and extent of vertical downward deformation at the invert of the bore increased with depth of cover. This is because the *critical pressures* are significantly higher for deeper installation which allows downward deformation to develop and expand while the vertical deformation is being propagated upwardly to the pavement surface.

Influence of bore diameter on bore pressure- displacement relationship

Smaller bore diameter required greater *initiation* and *critical pressures*. For example, the *initiation* and *critical pressures* for a 300mm HDD bore installed at depth of 3.0m below the pavement surface in cohesionless subgrade with friction angle of 35° are about 302 and 412kPa, respectively. Whereas, for a smaller 200mm diameter bore installed at the same depth of cover and in the same subgrade material, the *initiation* and *critical pressures* are about 372 and 543 kPa, respectively. An increase of about 23 and 32 percent in the *initiation* and *critical pressures,* respectively over those of 300mm diameter bore. The percentage increase is slightly higher (by 2%) in subgrade soil with friction angle of 40°.

The increase in bore pressures with smaller bore diameter can be attributed to a smaller circumferential surface over which the applied bore pressures acts on smaller bore diameters. Smaller bore would require greater bore pressure to achieve a similar driving force needed to initiate and propagate deformation outwardly from the bore compare to larger diameter bore.

6.4.4.5 Influence of Asphalt Concrete on Estimated Bore Pressures

Sensitivity analysis was completed to examine the influence of asphalt concrete thickness on the magnitude of both *initiation* and *critical pressures*. For the analysis, bore pressure-deformation response of 300mm diameter HDD bore installed 2.0m below the pavement surface in a cohesionless subgrade with friction angle of 35° and asphalt concrete thicknesses of 100, 125 and 150mm was evaluated. The bore diameter, depth of cover, thickness of

granular subbase and material properties assigned to each pavement layer were keep constant for the three analyses.

The *initiation* and *critical pressures* obtained for each asphalt concrete thickness are presented graphically in Figure 6.53. The sensitivity analyses revealed that the thickness of asphalt have some effect on the magnitudes of the limiting bore pressures. Increasing the thickness of asphalt concrete from 100mm to 125mm, a 25% increase, resulted in approximately 3% and 4.8% in the *initiation* and *critical pressures*, respectively. The *initiation* and *critical pressures* for a 150mm thick asphalt concrete (a 50% increase) increased by 6% and 9.6%, respectively over those obtained for 100mm thick asphalt concrete pavement. There appears to be a direct linear correlation between the thickness of asphalt concrete and the percentage change in limiting bore pressures for the installation configuration that was examined. The influence of asphalt concrete thickness is more significant on the *critical pressures* compared to the *initiation pressures* at the bore wall.

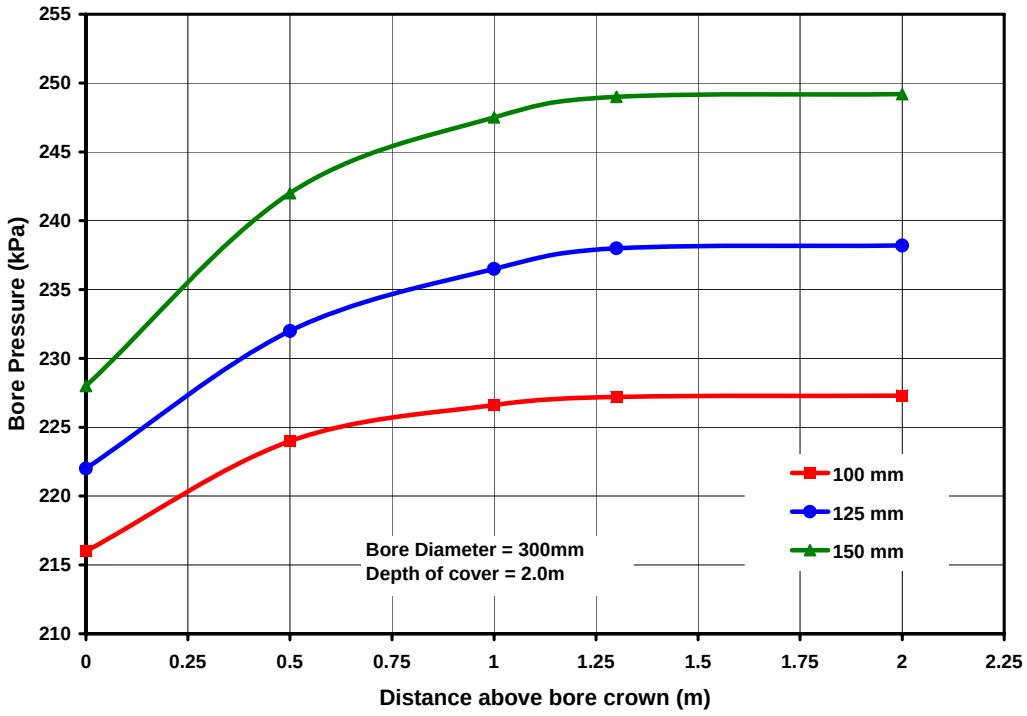

Figure 6.53: Estimated bore pressure required to initiate and propagate 12.5mm vertical displacement for different asphalt concrete thicknesses

6.4.4.6 Influence of Filter-cake on Estimated Bore Pressures

It is important to prevent loss of fluid into the native soil during HDD. This ensures that the drilling fluid pumped into the bore is available to make flowable slurry (i.e. soil cutting and drilling fluid) that remains in the bore path. This is accomplished by the formation of a thin low permeability '*filter-cake*' around the circumference of the bore. The *filter-cake* is developed as the suspended colloidal bentonite platelets and/or polymers e.g. QUIK-TROL^{TM} migrates into the native soil immediately surrounding the bore. The clay platelets "pack-off" the pore structure as they become blocked with successive layers forming a band of a low permeability-high shear strength soil around the bore, referred to as '*filter-cake*'.

In addition to preventing loss of fluid into the native formation, the filter-cake also alter the strength characteristics and behavior of the soil surrounding the bore especially in highly permeable cohesionless soils. The purpose of the investigation presented in this section is to quantify influence of *filter-cake* on the magnitude of the *initiation* and *critical limit pressures*. The thickness and the strength of the *filter-cake* will affect the magnitude of estimates limiting pressures. It is difficult to determine the thickness of filter-cake formed around the bore during drilling. Filter-cake is formed under dynamic condition and its thickness depends on rate of deposition versus erosion caused by fluid circulation and mechanical abrasion by the rotating drill string. However, the thickness of filter cake measured in the laboratory is formed under static conditions with no erosion. The thickness of filter cake formed during laboratory test is very small and is reported in 32nd's of an inch.

The 'filter cake' referred in the remainder of this section includes not only the thin layer of clay platelet deposit directly on the face of the bore but also the saturated band of soil at the periphery of the bore that has been infiltrated by the drilling fluid. Arends (2003) suggested a thickness 25.4mm for '*filter-cake'* in sandy soil. For the analysis, bore pressure-deformation response of 300mm diameter HDD bore installed 2.0m below the pavement surface in a cohesionless subgrade with friction angle of 35° and filter-cake thicknesses of 0, 25 and 50mm were evaluated. While the thickness of *filter cake* was varied; the bore diameter, depth of cover, thickness of granular subbase and asphalt concrete and material properties assigned to each pavement layer were keep constant for the three simulations. The material properties

assigned to the *filter-cake* shown in Table 6.7 were those proposed by Wang and Sterling (2004). The *initiation* and *critical pressures* obtained from numerical simulations for different filter-cake thickness are presented graphically in Figure 6.54.

Table 6. 7: Material properties assigned to filter-cake (after Wang and Sterling, 2004)

Properties	**Clayey Subgrade**
Bulk Modulus (kPa)	1.5e5
Shear Modulus (kPa)	5.1e4
Friction angle (°)	25
Angle of dilation (°)	0
Cohesion (kPa)	138

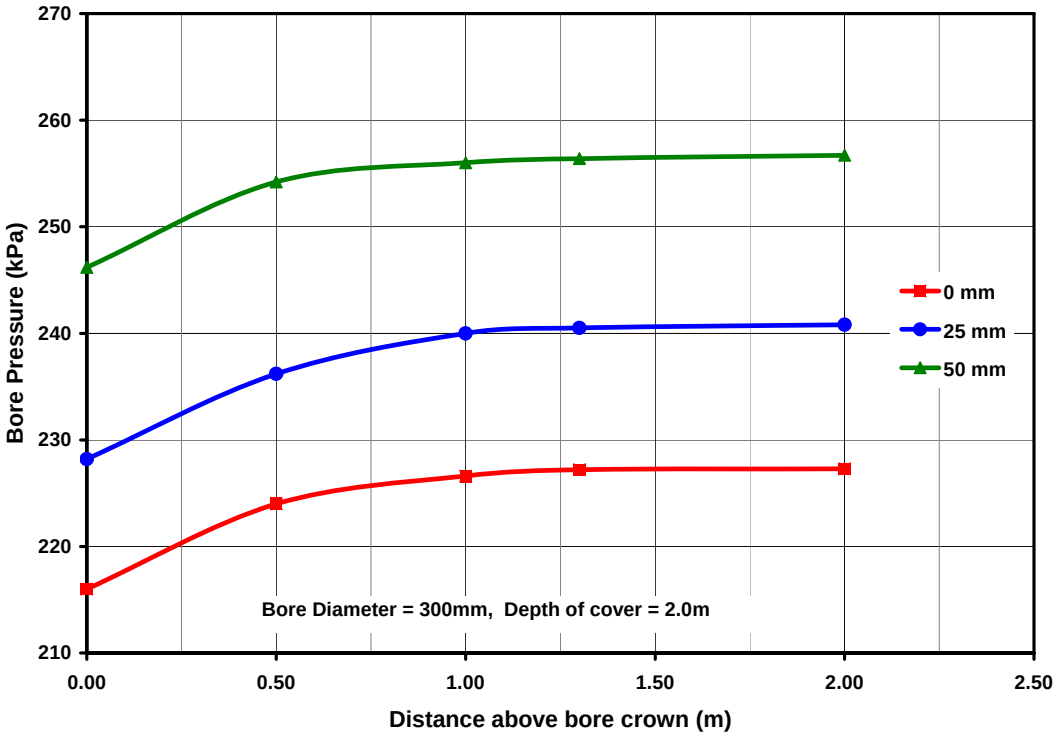

Figure 6.54: Estimated bore pressure required to initiate and propagate 12.5mm vertical displacement for different filter-cake thicknesses

The sensitivity analyses revealed that the formation of *filter-cake* around the HDD bore during drilling contributes positively to the bore resistance to deformation. The *initiation* and *critical pressures* estimated for a 300mm diameter bore with 25mm thick filter-cake around it was approximately 228 and 240 kPa, respectively; an increase of about 6% over values obtained for bore without filter cake. The same bore diameter surrounded by 50mm thick filter cake yielded an *initiation* and *critical pressures* of 246 and 257 kPa, respectively, an increase of about 13.5% over values obtained for bore without filter cake. There is almost a direct linear correlation between the thickness of filter-cake and the percentage increase in limiting bore pressures for the installation configuration that was examined.

The analysis suggests that addition resistance to ground deformation can be achieved during HDD installation by using drilling-fluid and/or polymers that would create excellent filter-cake around the bore. However, the additional resistance provided by the filter-cake should only be considered as a bonus and should not be rely upon since the actual thickness of filter-cake can not be measured and may vary considerably during HDD installations.

6.4.4.7 Comparison of limiting Bore Pressure Estimate from Delft Geotechnics Equations and *FLAC*^{3D} for HDD bores in Cohesionless Subgrade

The *yield zone radius* which defines the elastic-plastic interface for a cylindrical cavity expanded in an infinite Mohr-Coulomb medium can be obtained from Equation 6.3. Equation 6.3 can be re-arranged to obtain the pressure inside the bore (denoted as P in Equation 6.3) that would limit the yield zone radius, b to a pre-determined value. Re-arranging Equation 6.3 and replacing P and b with $P_{\max}$ and $R_{P\max}$, respectively would yield:

$$\left.\begin{aligned} P_{\max} &= u + (p'_f + c.\cot\phi)\left[\left(\frac{R_o}{R_{P\max}}\right)^2 + Q\right]^{\frac{-\sin\phi}{1+\sin\phi}} - c.\cot\phi \\ p'_f &= \sigma'_o.(1+\sin\phi) + c.\cos\phi \\ Q &= (\sigma'_o.\sin\phi + c.\cos\phi)/G \end{aligned}\right\} \quad [6.10]$$

where u is the initial pore pressure, p'_f is the slurry pressure at which plastic deformation first occurs, ϕ is the angle of internal friction, σ' is the effective stress at the bore crown, c is the cohesion of the soil, R_o is the initial radius of the plastic zone (i.e. radius of HDD bore), $R_{P\max}$ = is the maximum allowable radius of the plastic zone, and G is the shear modulus of the soil.

Equation 6.10 is the design equation used by HDD practitioners to estimate maximum allowable bore slurry pressure (P_{max}) that would limit plastic deformation. The use of the equation for HDD application was first suggested by research at Delft University of Technology (Delft Geotechnics 1997). The recommended allowable safe radius $R_{P\max}$ when drilling in sand is two third of the height of cover and one half of the height of cover is recommended in clay to prevent hydraulic fracture (Delft Geotechnics 1997). Equations 6.10 are solely derived from cavity expansion theory and the soil is assumed to be an infinite medium and homogenous. The stress field is also assumed to be uniform and isotropic. In so doing it neglects the effects geostatic stress distribution and lateral earth pressure coefficient Ko at rest. There are little data available to assess the magnitude of ground movements associated with the allowable bore pressure predicted using this equation. The purpose of the work presented in this section is to examine the applicability of the Delft Geotechnics equations by compare the limiting bore pressures estimated with the equation to those from *FLAC*^{3D} simulations.

The allowable bore pressures that would limit the plastic yield zone radius to two-third of the depth of cover were estimated with Delft Geotechnics equations for the HDD installations simulated with *FLAC*^{3D}. The maximum allowable bore pressures estimated using the Delft Geotechnics equations are presented in Table 6.8 and are compared to the *critical limiting* pressures obtained from numerical simulation with *FLAC*^{3D} shown on the same Table. *Critical limiting* pressure is defined as the least bore pressures required to propagate a vertical displacement of 12.5mm to the pavement surface i.e. full height of cover above the bore.

The Delft Geotechnics equations were formulated for uniform isotropic single layered soil. Therefore, in applying the equations to the multilayer pavement structure, the influence of the strength and properties of the asphalt concrete and the granular sub base layer on allowable bore pressure were ignored in the analysis. In essence, the pavement was assumed to be a single layered structure with the strength and properties of the cohesionless subgrade soil. It is has been shown in Section 6.6.4.5 that the strength of asphalt concrete provides some additional resistance to the ground deformation due to pressurization. Hence ignoring the additional resistance should yield a conservative estimate. Moreover, Equation 6.10 limits plastic yielding to two-third of the height of cover and does not extent beyond the subgrade soils.

The maximum bore pressures that would limit the extent of plastic yield zone to a radius of two-third of the height of cover from the center of the bore estimated with the Delft Geotechnics equations are consistently higher, between 9 and 27%, than *critical* bore pressures obtained from numerical simulations. Despite replacing the strength and properties of the asphalt concrete and granular subgrade with those of weaker cohesionless subgrade material, the maximum allowable bore pressures predicted by the Delft Geotechnics equations are noticeably higher than those required to limit the extent of plastic yield zone around HDD pressurized bore. Considerable ground and pavement surface deformations would have occurred before reaching the allowable bore pressure predicted by Delft

Table 6.8: Comparison of *FLAC*^{3D} and Delft Equations estimated bore pressures in cohesionless subgrade

Bore Diameter (mm)	Depth of cover (m)	Depth of cover to bore diameter ratio	Friction angle of subgrade soil (°)	FLAC3D	Delft Geotechnics Equations		Percent Difference (%)
				Critical Pressure (kPa)	Height above bore crown (m)	Allowable bore Pressure (kPa)	
200	2	10	35	298	1.23	342	14.7
	3	15	35	543	1.90	591	8.9
	4	20	35	739	2.57	807	9.2
	2	10	40	340	1.23	403	18.6
	3	15	40	631	1.90	696	10.3
	4	20	40	863	2.57	943	9.2
300	2	6.7	35	227	1.18	267	17.5
	3	10	35	412	1.85	494	19.8
	4	13.4	35	640	2.52	717	12.0
	2	6.7	40	257	1.18	310	20.8
	3	10	40	471	1.85	578	22.8
	4	13.4	40	758	2.52	837	10.5
450	2	4.4	35	178	1.11	203	14.2
	3	6.7	35	322	1.77	392	21.9

equations. Generally, the difference between limiting bore pressures obtained using the Delft Geotechnics equations and *FLAC*^{3D} increased with greater friction angle and bore diameters.

There are several inherent assumptions in the formulation of the Delft Geotechnics equations that could have resulted in the disparity observed between bore pressures estimated using the equations and those obtained from numerical simulations with *FLAC*^{3D}. The Delft equations are based in cavity expansion theory and assume a uniform and isotropic stress field, an infinite soil medium, and homogenous soil properties. The influence of lateral earth pressure, tensile strength of material, shear dilatancy and spatial boundary were not included in the formulation of the equations. All these ignored factors play important roles in numerical modeling and the actual stress-deformation.

6.4.5 Flexible Pavement response to HDD Bore Pressurization in Clayey Subgrade

The response of flexible pavement structure founded on clayey subgrade to HDD bore pressurization is presented in the following section. The bore pressurization process and corresponding pavement structure response during Test #3 (see Table 6.4) is discussed in details in the following paragraphs. Test #3 simulates the bore pressurization of 300mm diameter HDD bore installed 2.0m beneath flexible pavement in a cohesive subgrade soil. The subgrade material was assigned a friction angle of 25°, cohesion of 10 kPa and no dilation. The material properties assigned to the clayey subgrade soil are included in Table 6.3. Pavement response during Test #3 discussed in the following Sections is representative of the response observed during the other HDD installation simulations in clayey subgrade.

6.4.5.1 Annular Tangential and Radial Stresses

The contour plots of the minimum (σ_1) and maximum (σ_3) principal stresses prior to bore pressurization are presented in Figures 6.55 and 6.56 respectively. Note that because compressive stresses are negative in *FLAC*^{3D}, the minimum (σ_1) principal stress is the most negative (major) principal stress and conversely the maximum (σ_3) principal stress is the least negative (minor) principal stress. The values of minimum and maximum principal stresses shown in Figures 6.55 and 6.56 coincide with those of the vertical and horizontal stresses, respectively prior to bore pressurization.

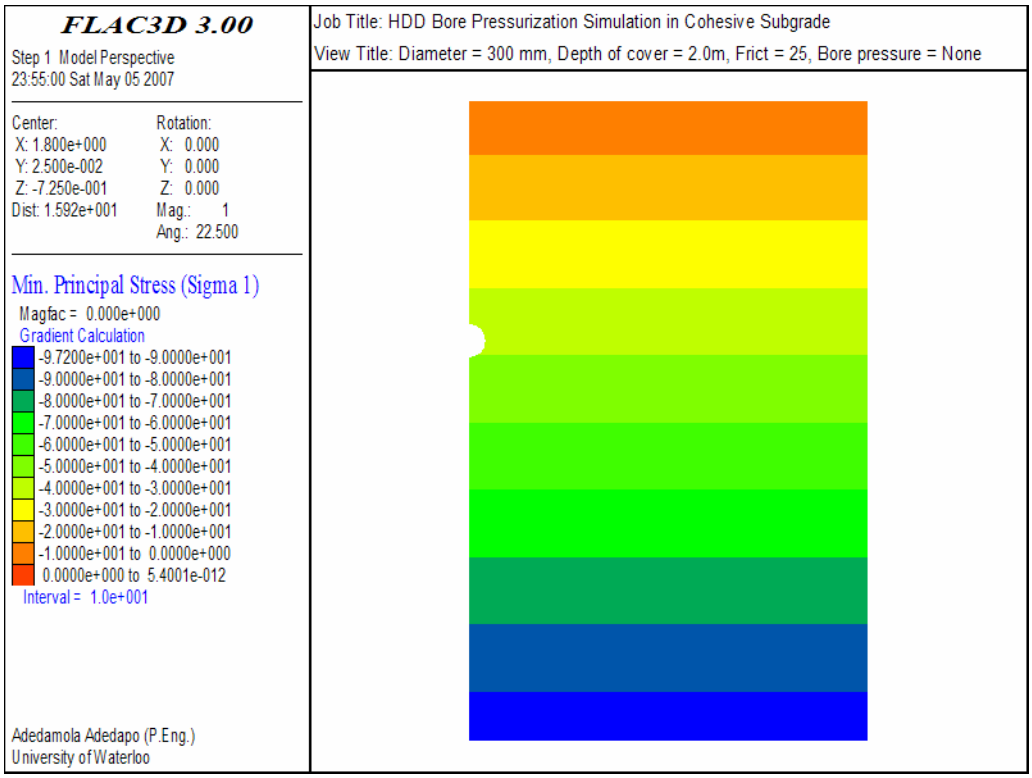

Figure 6.55: Minimum principal stress (σ_1) contours prior to bore pressurization

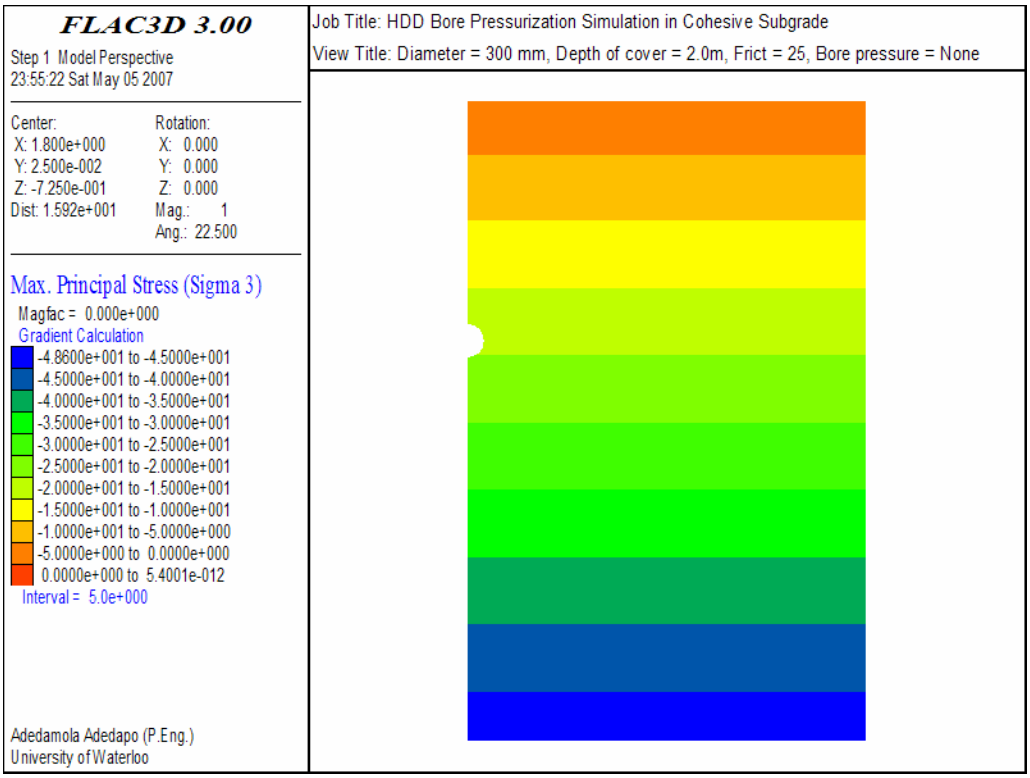

Figure 6.56: Maximum principal stress (σ_3) contours prior to bore pressurization

As the bore pressure is increased, an induced stress field develops in the clayey subgrade soil around the HDD bore. The contours plots of the minimum principal stress (σ_1) around the HDD bore at applied bore pressure of 35, 55, 105, 215 and 235 kPa are presented in Figures 6.57 through 6.61. The contour plots showing changes in maximum principal stress (σ_3) with bore pressurization in the clayey subgrade are presented in Figures 6.62 through 6.66 for bore pressures of 35, 55, 105, 215 and 235 kPa.

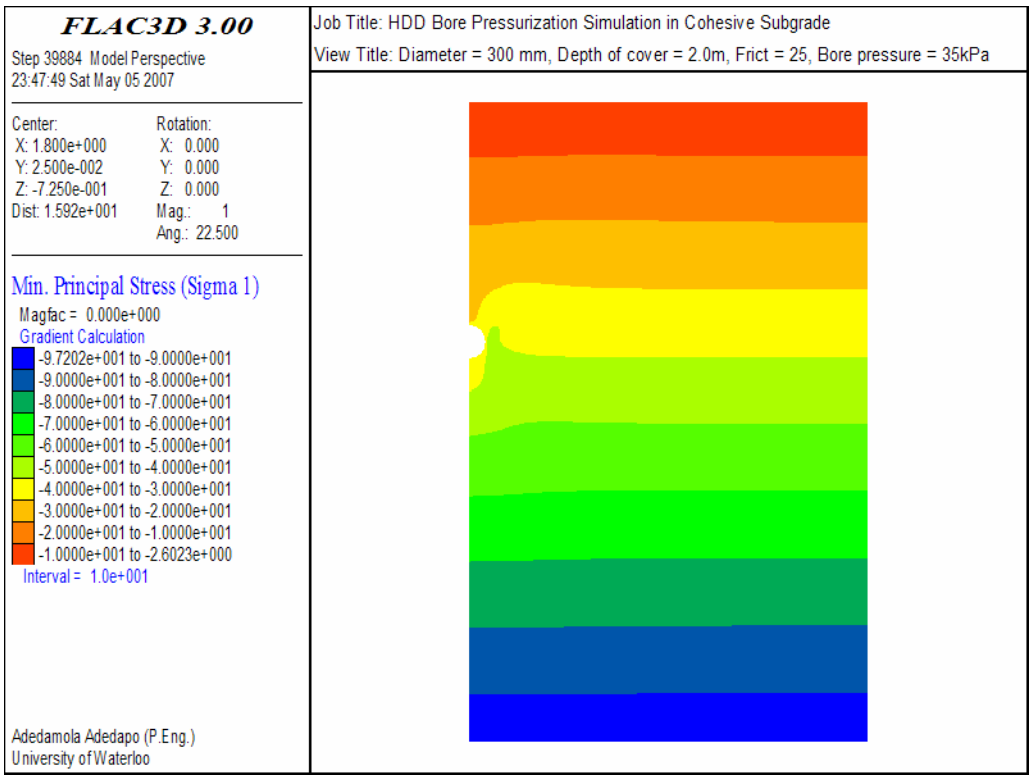

Figure 6.57: Minimum principal stress (σ_1) contours at 35 kPa in cohesive subgrade

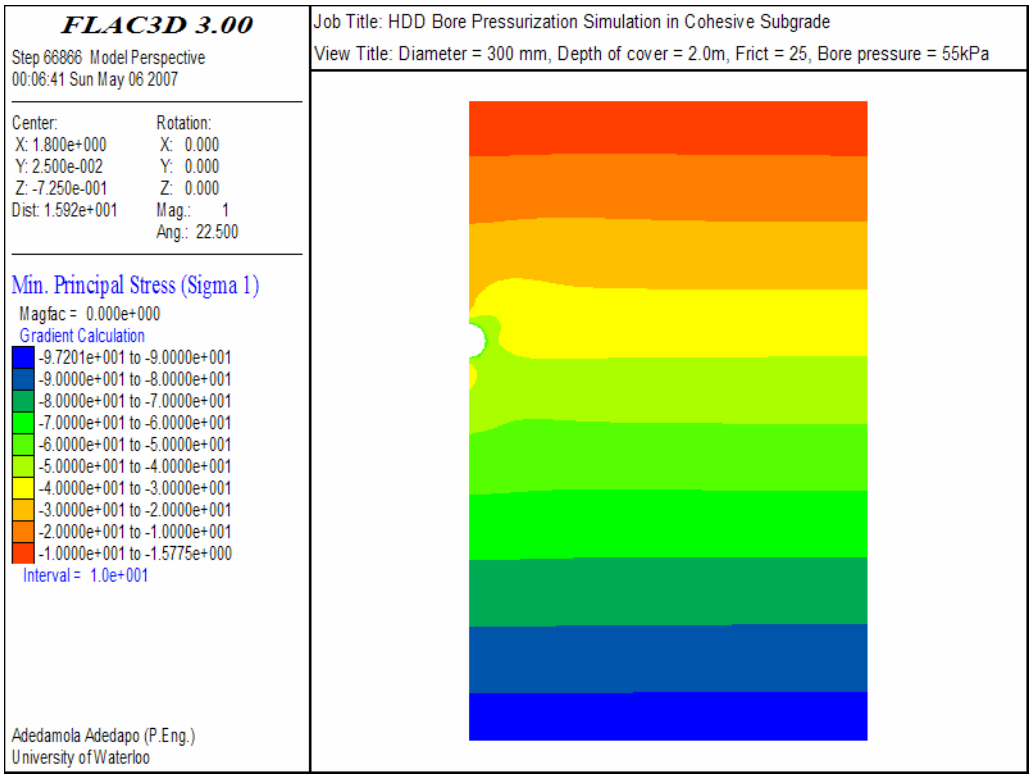

Figure 6.58: Minimum principal stress (σ_1) contours at 55 kPa in cohesive subgrade

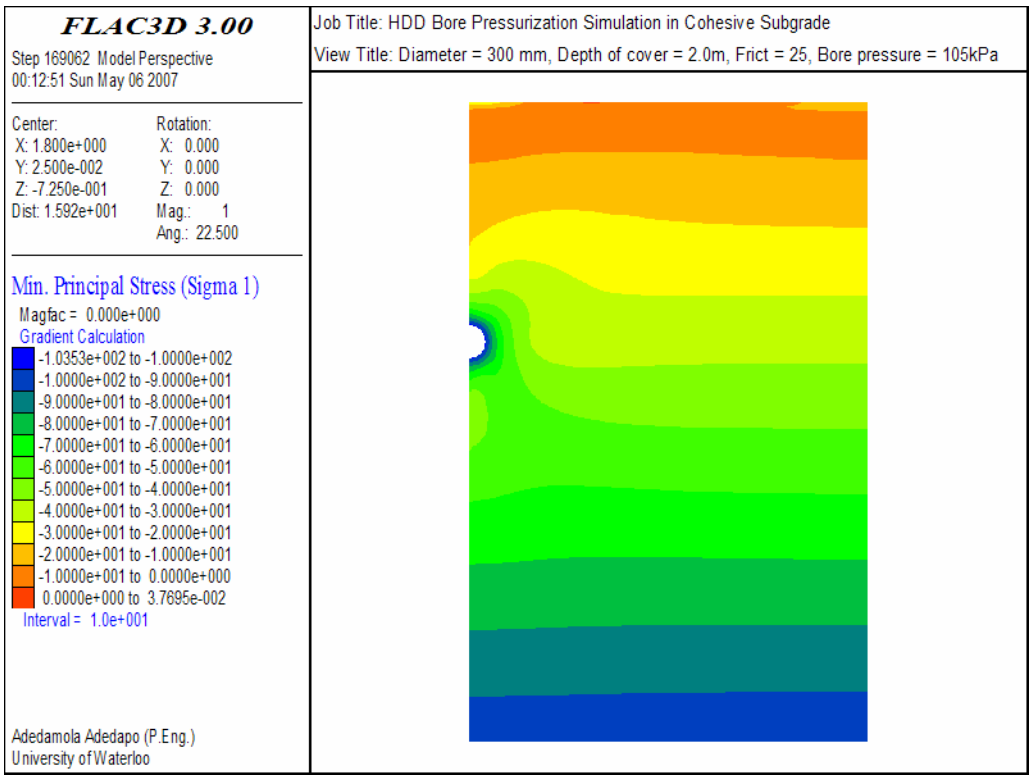

Figure 6.59: Minimum principal stress (σ_1) contours at 105 kPa in cohesive subgrade

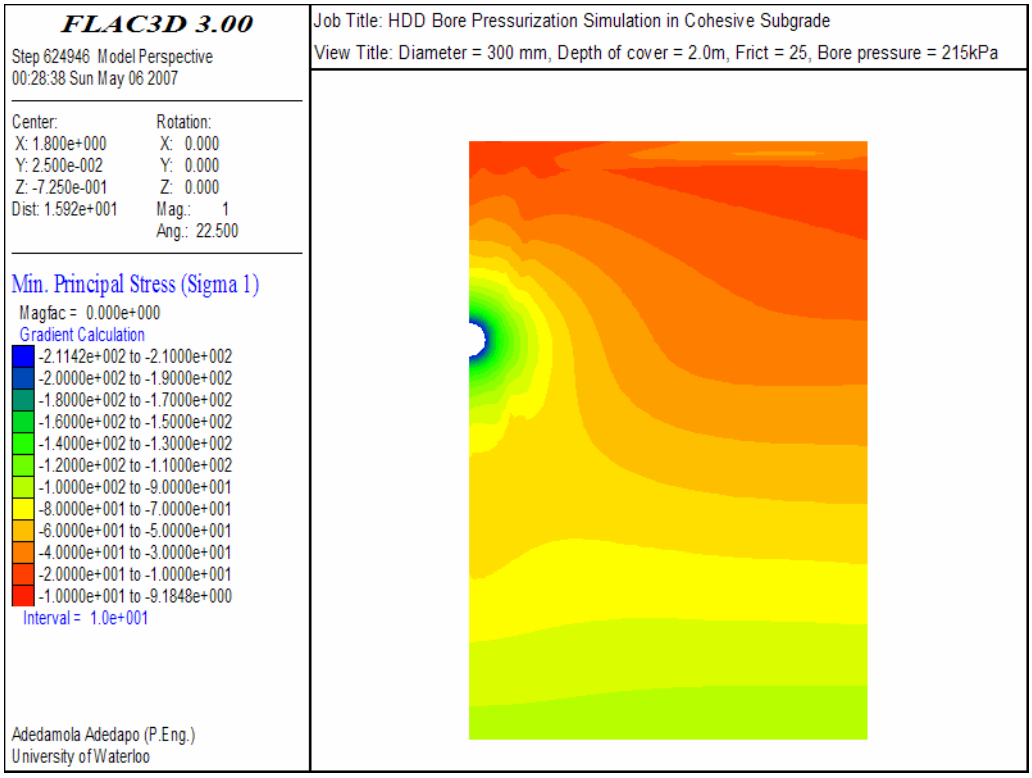

Figure 6.60: Minimum principal stress (σ_1) contours at 215 kPa in cohesive subgrade

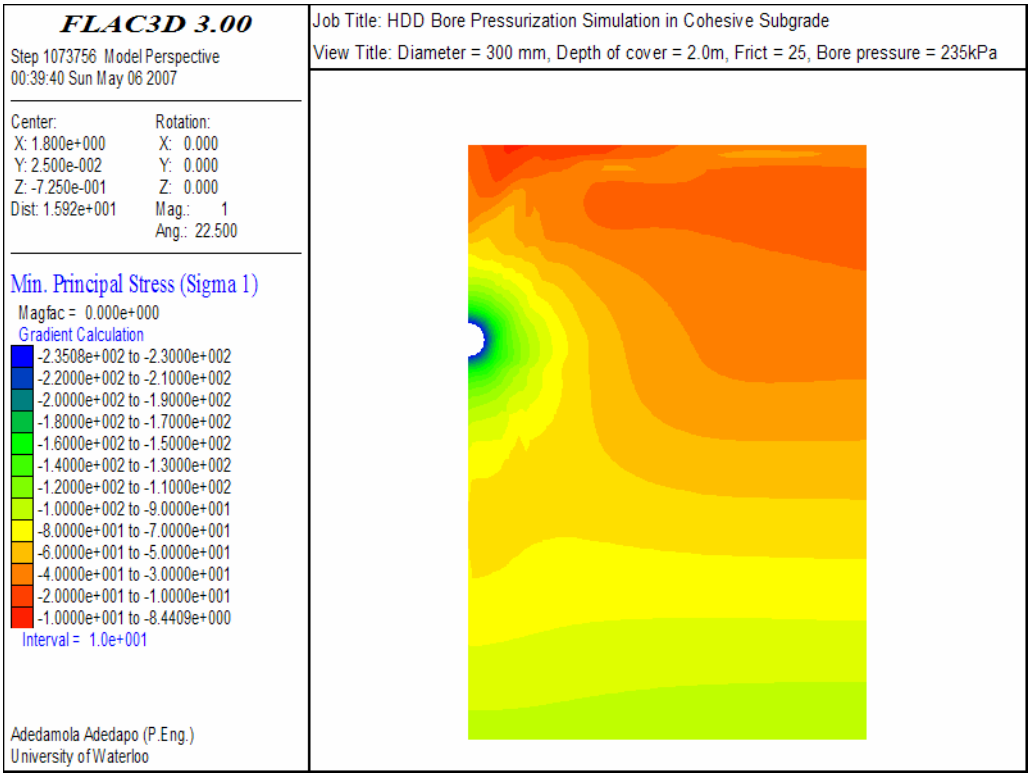

Figure 6.61: Minimum principal stress (σ_1) contours at 235 kPa in cohesive subgrade

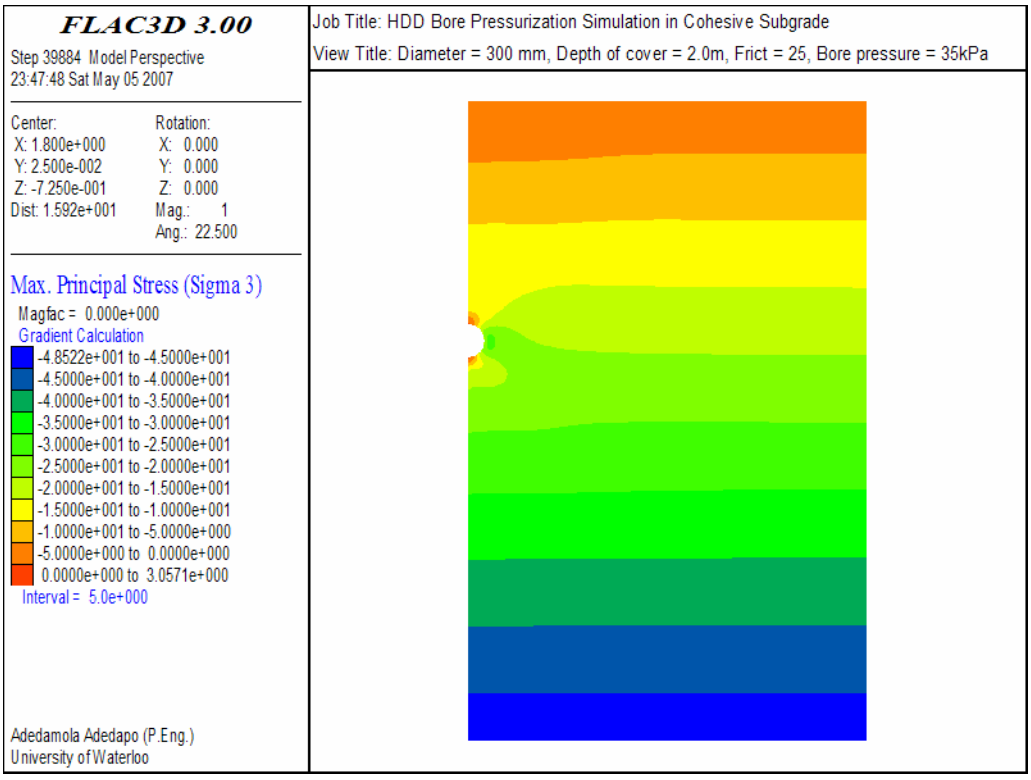

Figure 6.62: Maximum principal stress (σ_3) contours at 35kPa in cohesive subgrade

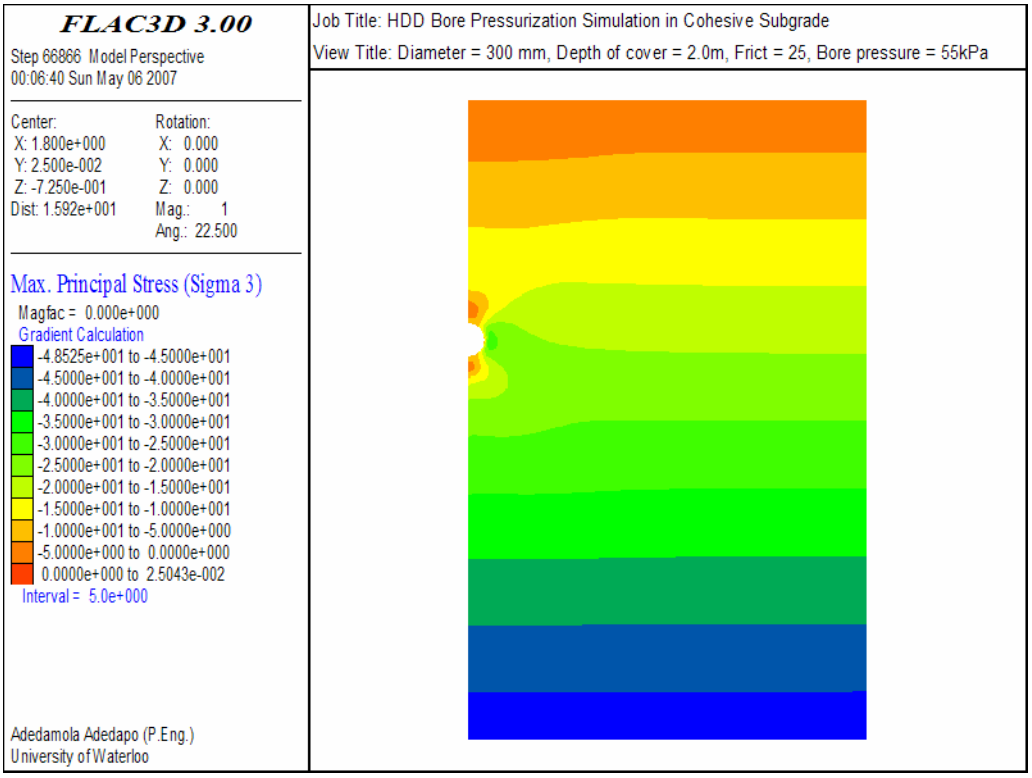

Figure 6.63: Maximum principal stress (σ_3) contours at 55 kPa in cohesive subgrade

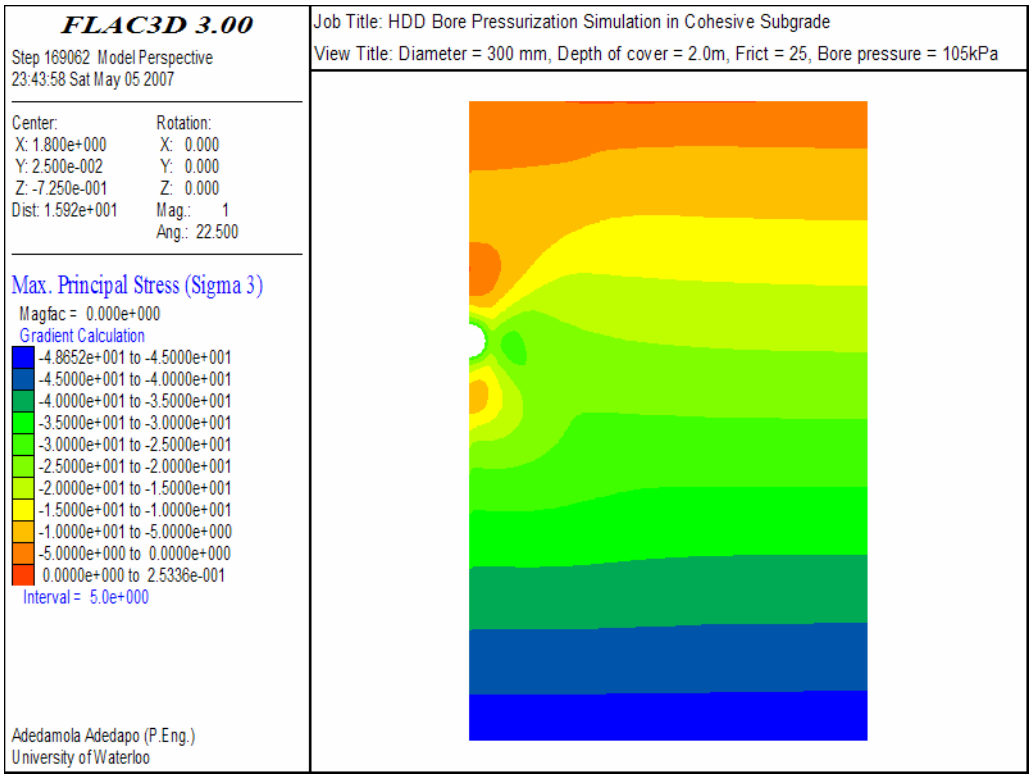

Figure 6.64: Maximum principal stress (σ_3) contours at 105 kPa in cohesive subgrade

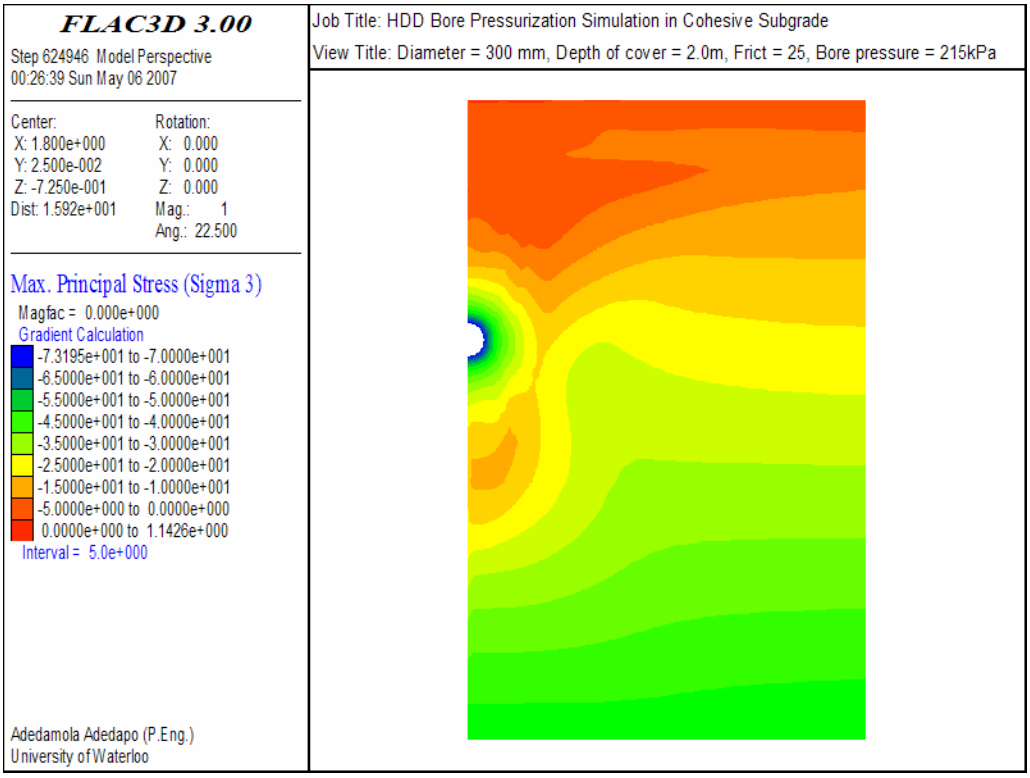

Figure 6.65: Maximum principal stress (σ_3) contours at 215 kPa in cohesive subgrade

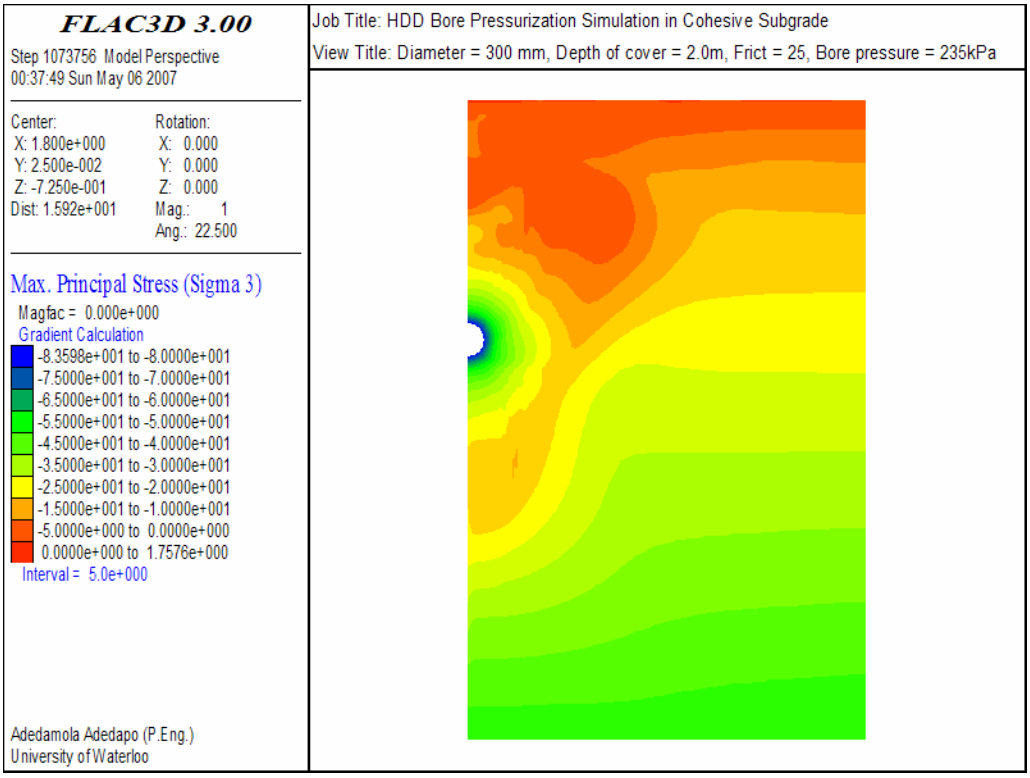

Figure 6.66: Maximum principal stress (σ_3) contours at 235 kPa in cohesive subgrade

The change in annular radial and tangential stresses with applied bore pressure at the crown, springline and invert of the bore are presented graphically in Figures 6.67 and 6.68, respectively. The magnitude of the radial stresses at the bore crown, springline and invert were very similar and equal in magnitude to the applied bore pressure (P_i). The magnitudes of the minimum (σ_1) and maximum (σ_3) principal stresses are equal to the radial or tangential stress depending on the level of stress applied in the bore. When the applied bore pressure was lower than 15 kPa, the tangential (hoop) stresses at bore wall were higher than radial stresses signifying that the minimum (σ_1) and maximum (σ_3) principal stresses at the bore wall correlate to the tangential and radial stresses, respectively at lower bore pressures. The orientation of the principal stresses changed at the crown and invert of the bore as the bore pressure exceeded 15 kPa. The principal axes rotated such that the minimum (σ_1) and maximum (σ_3) principal stresses at the bore wall correspond to the radial and tangential stresses, respectively. The rotation of principal stresses occurred at the springline when the bore pressure was about 35 kPa, a pressure similar to the vertical overburden pressure.

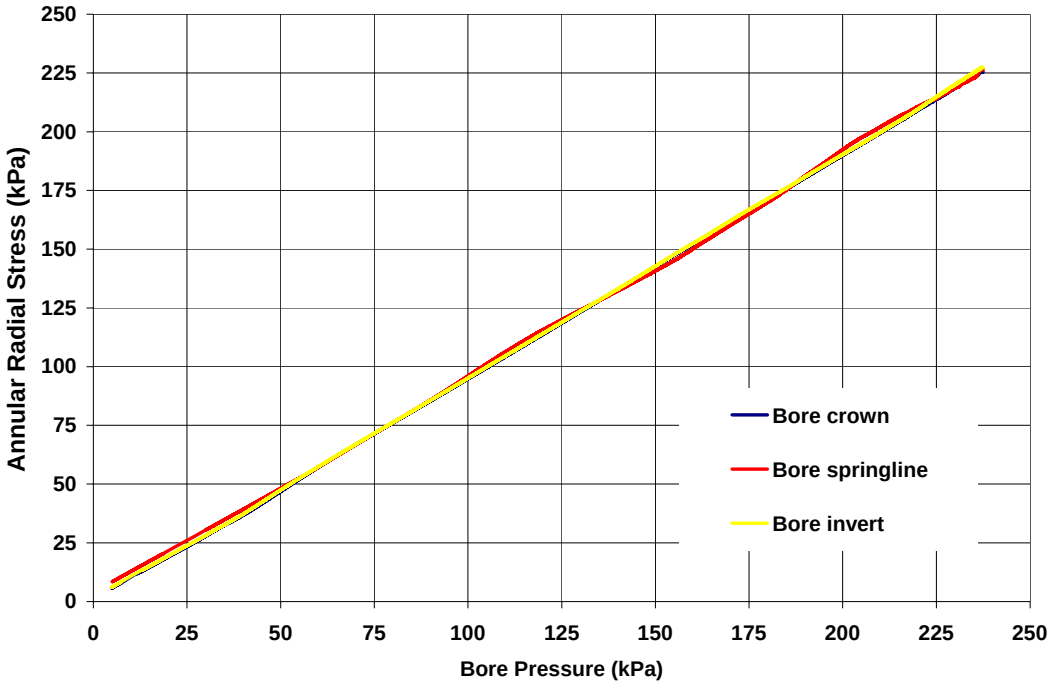

Figure 6.67: Annular radial stress vs. bore pressure in cohesive subgrade
(Bore diameter 300mm, depth of cover = 2.0m, friction =25°)

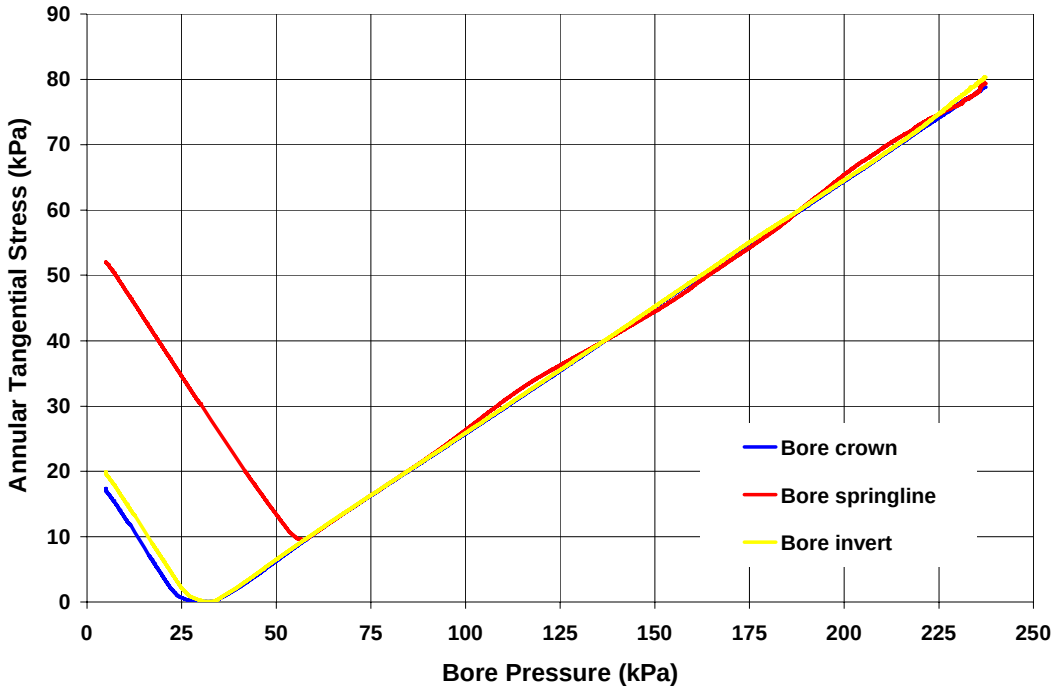

Figure 6.68: Annular tangential stress vs. bore pressure in cohesive subgrade
(Bore diameter 300mm, depth of cover = 2.0m, friction =25°)

The variation of tangential stresses with applied bore pressure at the periphery of the wall as shown in Figure 6.68 indicate that the tangential stress at the crown and invert have lower magnitude compare to those observed at the springline for bore pressures lower than 58 kPa. The tangential stresses at the invert are also slightly higher than those at the crown due to difference in geostatic stress over the diameter of the borehole. The plasticity state (i.e. extent of the plastic zone) in the soil at applied bore pressures of 35, 55, 105, 215 and 235 kPa are presented in Figures 6.69 through 6.73. These Figures show zones that were yielding plastically.

At bore pressures lower than the vertical overburden pressure (P_i < 35 kPa), the response of the soil along the periphery of the bore to the applied pressure was mainly elastic. Increased bore pressure resulted in a corresponding reduction in the tangential stress at the bore crown and invert until the strength of the clayey soil was exceeded and plastic yielding was initiated, Figure 6.69. The reduction in tangential stress with increased bore pressure at the springline of the bore continued until the bore pressured exceeded 58 kPa. The minimum tangential

stresses observed at the crown and invert was about 0 kPa and approximately 9.6 kPa at the springline.

Further increase in bore pressure beyond the elastic range resulted in the *initiation* of plastic yielding around the circumference of the bore due to '*plastic expansion'* of the bore as shown in Figure 6.70. Once yielding occurred in the native clayey soil at the bore wall, the tangential stresses seized to decrease and begin to increase. It is interesting to note that the cohesive soil behaved somewhat "ductile" while transitioning from the elastic behavior to plastic yielding as shown in Figure 6.68 unlike the sharp shift observed in the cohesionless subgrade (Figure 6.27).

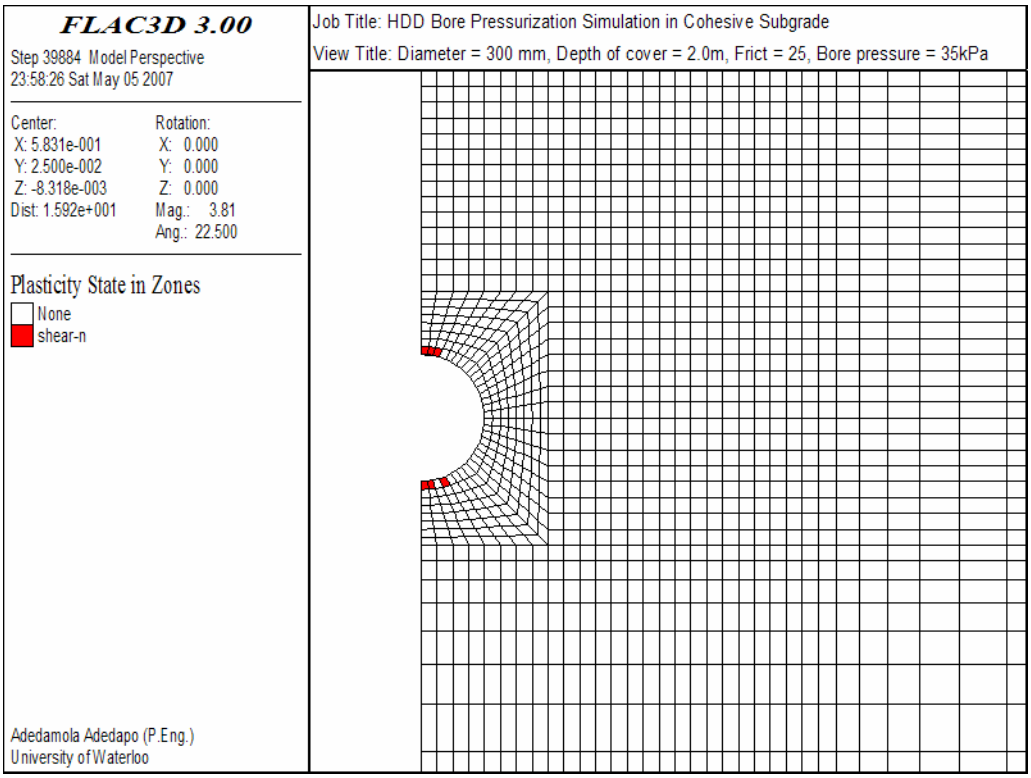

Figure 6.69: Plasticity state around the bore at 35 kPa in cohesive subgrade

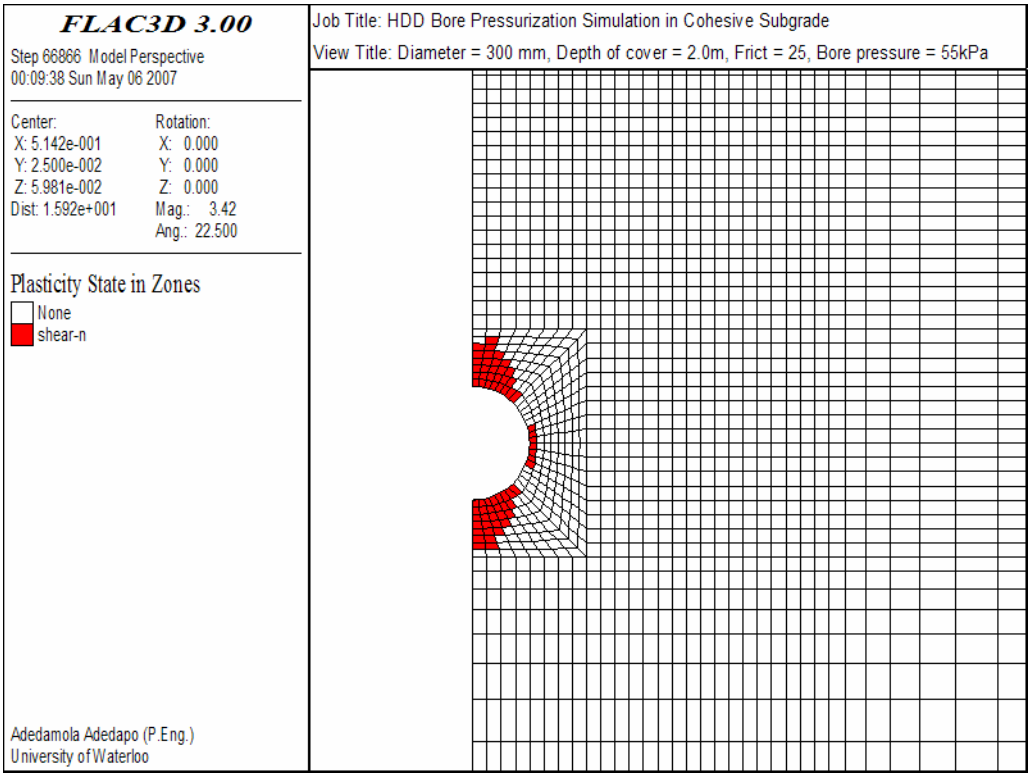

Figure 6.70: Plasticity state around the bore at 55 kPa in cohesive subgrade

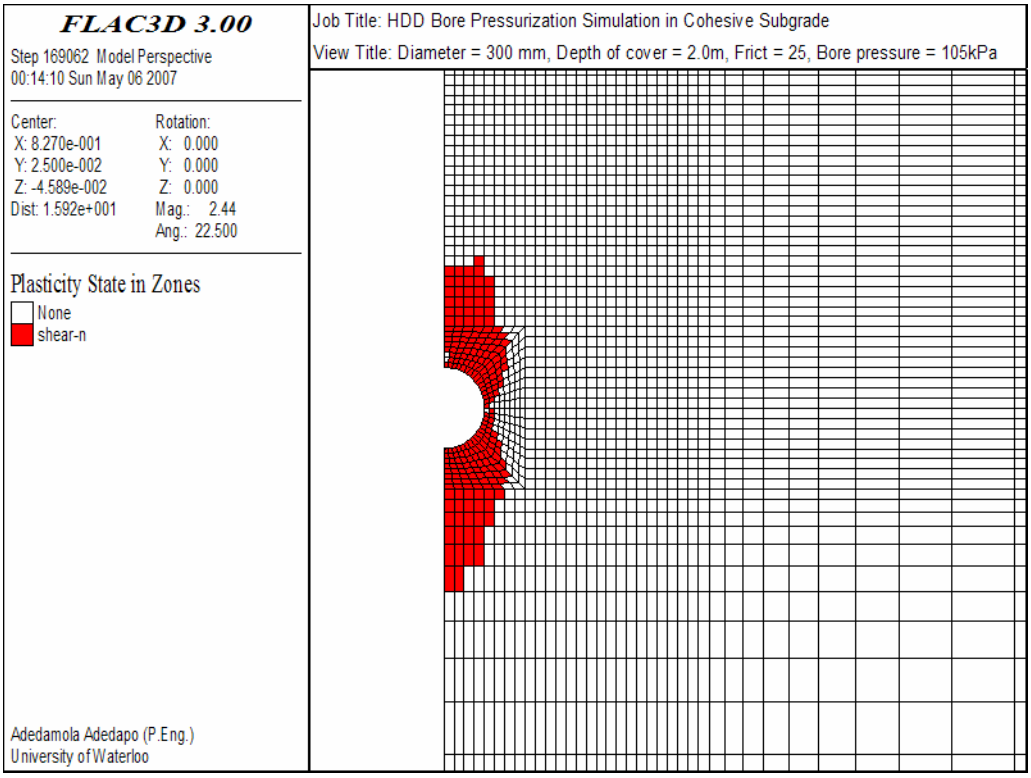

Figure 6.71: Plasticity state around the bore at 105 kPa in cohesive subgrade

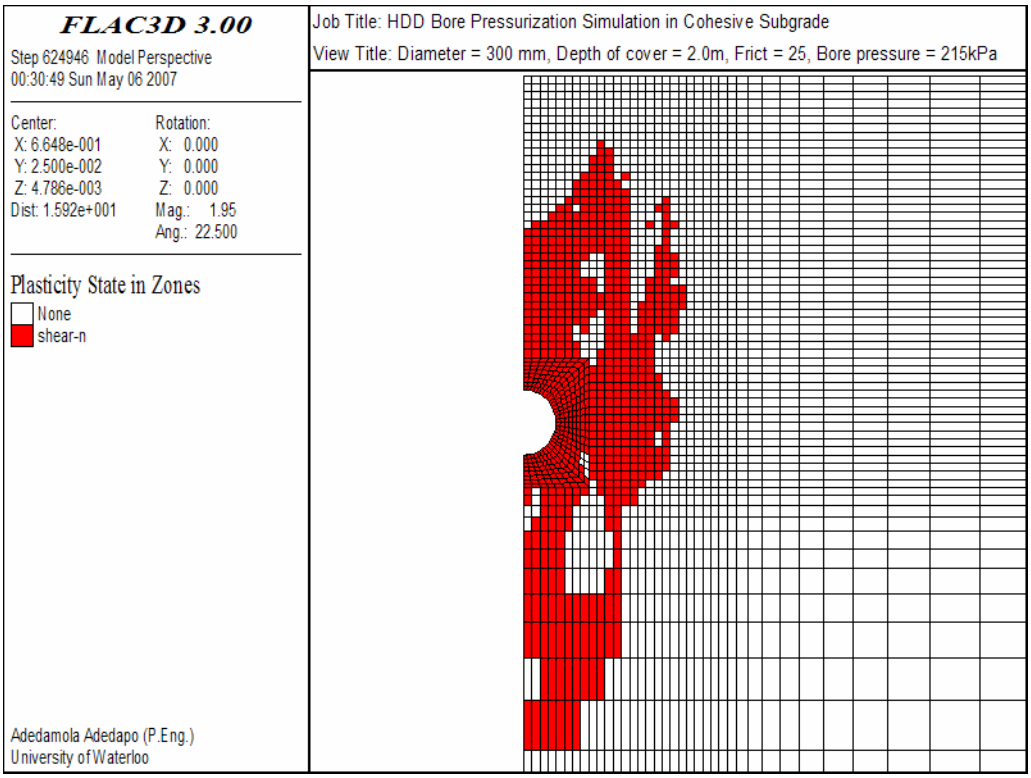

Figure 6.72: Plasticity state around the bore at 215 kPa in cohesive subgrade

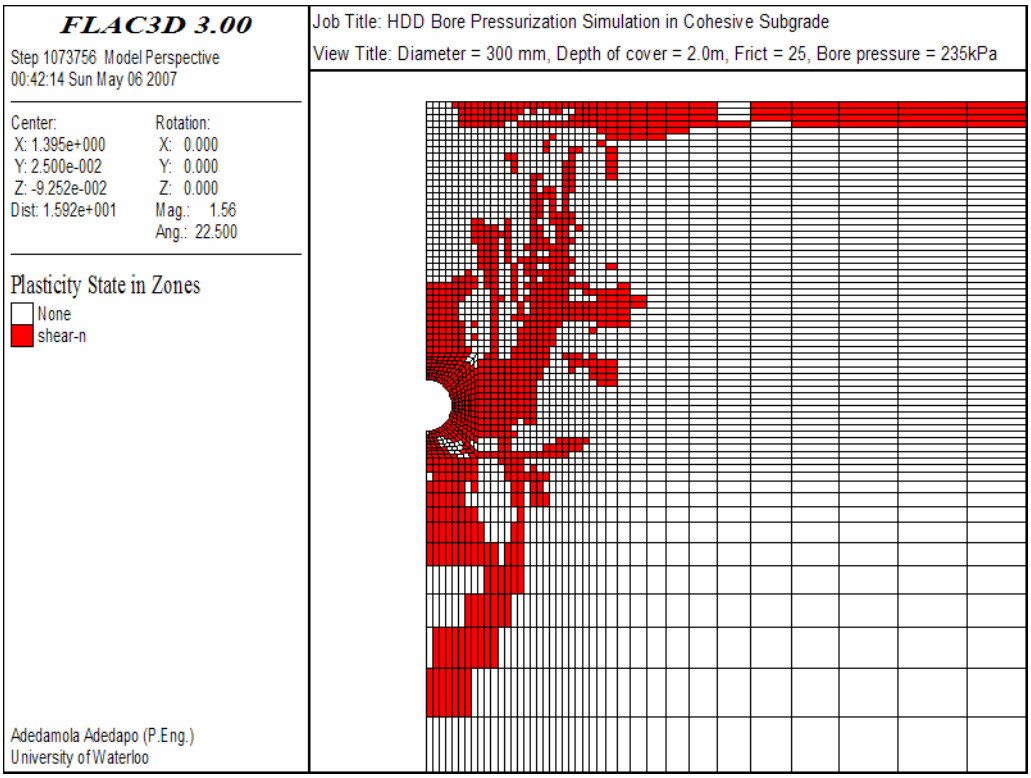

Figure 6.73: Plasticity state around the bore at 235 kPa in cohesive subgrade

Additional increase in bore pressure increased the extent of the plastic zone significantly (Figures 6.71 through 6.73) such that the contour of minimum circumferential stress moves further away from the bore wall into the subgrade soil towards the pavement surface and the tangential stresses at the bore wall increases. Figures 6.62 through 6.66 demonstrate these observations more clearly.

6.4.5.2 Vertical, Horizontal and Radial Displacements

The change in radial displacements at the crown and springline of the bore due to increased bore pressure are presented in Figure 6.74. There is a significant non-linearity in the bore pressure-displacement curve beyond bore pressures where the elastic response was observed as discussed in the previous section. The bore pressure-displacement relationship can be represented with a hyperbolic or a logarithmic curve approaching an asymptotic value (limiting value) at higher bore pressure.

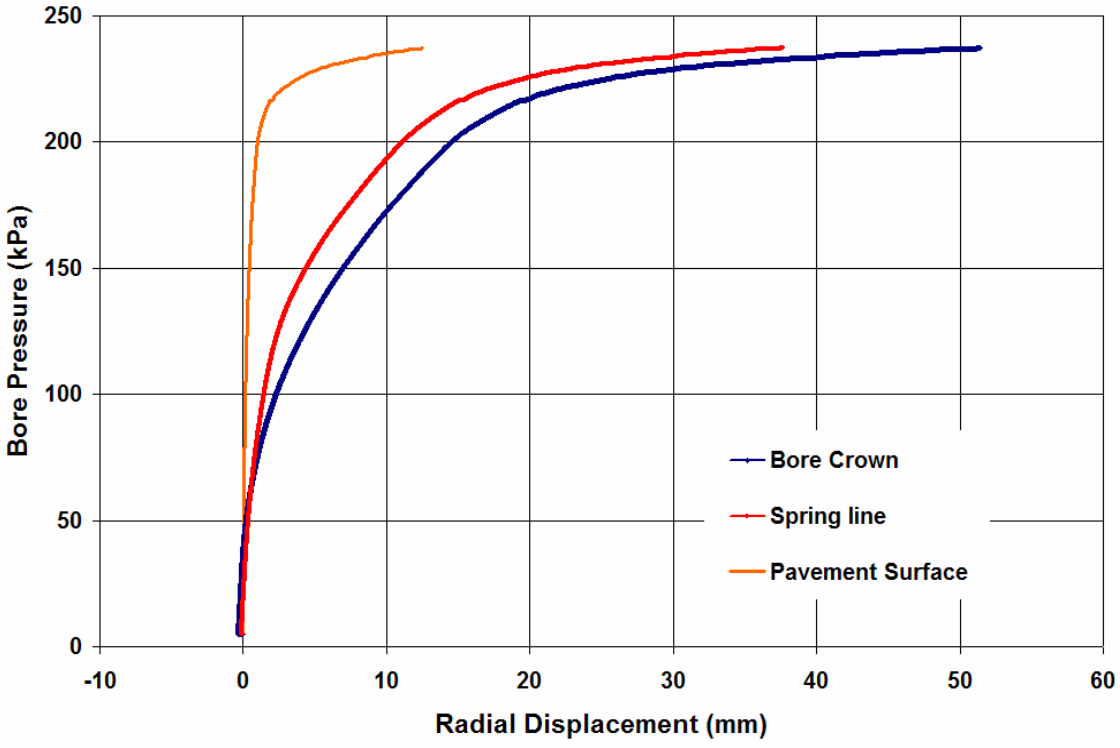

Figure 6.74: Bore pressure-displacement response in cohesive subgrade
(Bore diameter 300mm, depth of cover = 2.0m, friction =25°)

Although most of the soils above the crown of the bore have yielded and bore pressure is approaching an asymptotic value, it does not appear that the *limit pressure* has been reached when the simulation terminated. This is evident by the fact that the bore pressure-displacement curve has not completely flattened when the *critical pressure* was attained and the simulation terminated. The *critical pressure* as defined earlier, is the bore pressure required to propagate a vertical displacement of 12.5mm to the pavement surface i.e. full height of cover, D above the bore while the *limit pressure* is defined as the bore pressure at which plastic flow is initiated at the bore i.e. the bore deforms infinitely with no additional increase in bore pressure.

The uniform radial pressure applied to the periphery of the bore to simulate bore pressurization during HDD installation resulted in a non-uniform outward radial displacement. Figure 6.74 suggests that there is a noticeable difference in the magnitude of the outward radial displacement at the crown and the springline as the bore expanded outwardly more at the crown more than at the springline. The difference between the displacement at the crown and springline progressively increased with bore pressure. The variation in the displacement response around the bore may be attributed to the difference in the geostatic stress and lateral resistance provided by the soil adjacent to the side wall. The pressure required to propagate displacement laterally at the springline is significantly higher than those required to propagate displacement vertically at the bore crown due to lateral confinement (passive pressure) at the springline.

Figures 6.75 through 6.79 show contour plots of the displacement around the HDD bore at applied bore pressure of 35, 55, 105, 215 and 235 kPa. The Figures indicate that as the bore pressure is increased, the displacement field is pushed further outward away from the bore until it finally reached the pavement surface at approximately 220 kPa bore pressure. Figure 6.80 shows the bore pressure-displacement response at different elevations above the bore crown. Bore pressure of about 132 kPa was required to initiate an upward vertical displacement of 0.5mm at approximately 0.5m above the crown in the cohesive subgrade soil. Higher bore pressures, 156kPa, 160 kPa and 161 kPa were required to initiate similar magnitude of vertical displacement at 1.0m, 1.3m, and 2.0m above the bore crown, respectively.

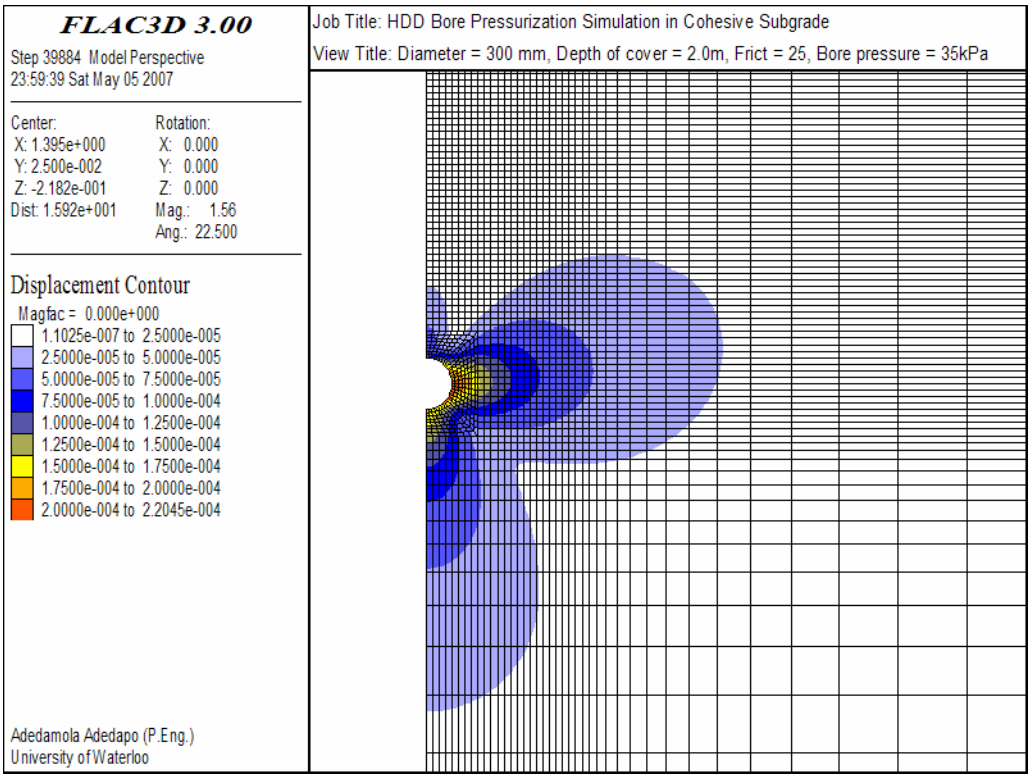

Figure 6.75: Displacement contour at 35 kPa in cohesive subgrade

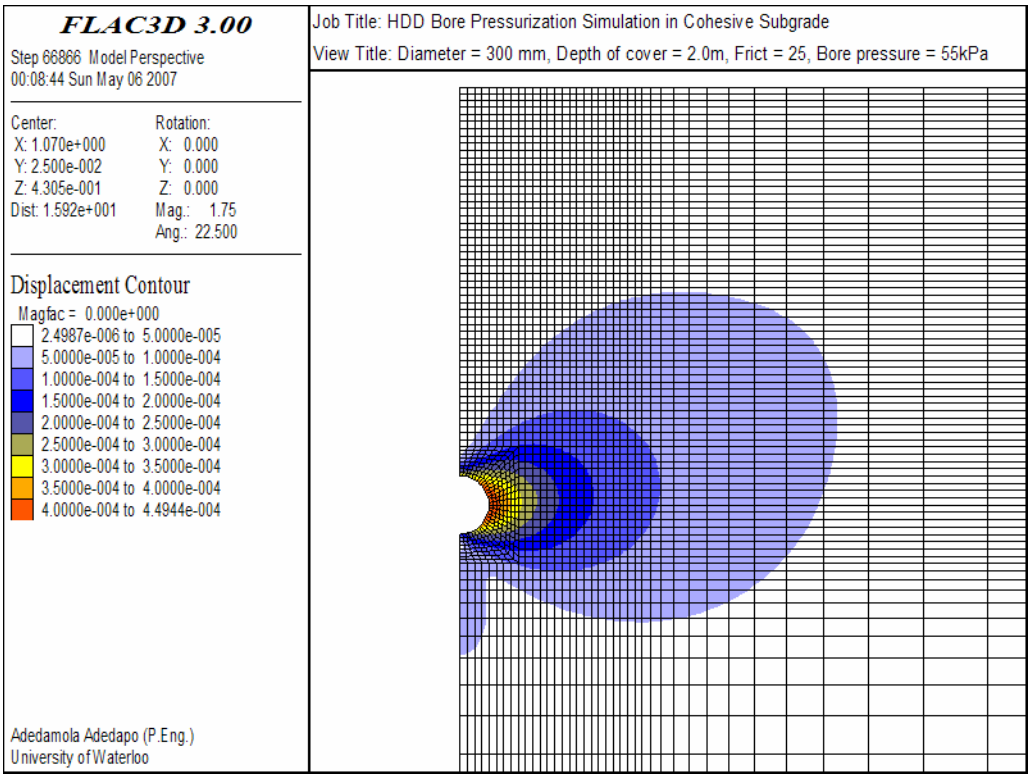

Figure 6.76: Displacement contour at 55 kPa in cohesive subgrade

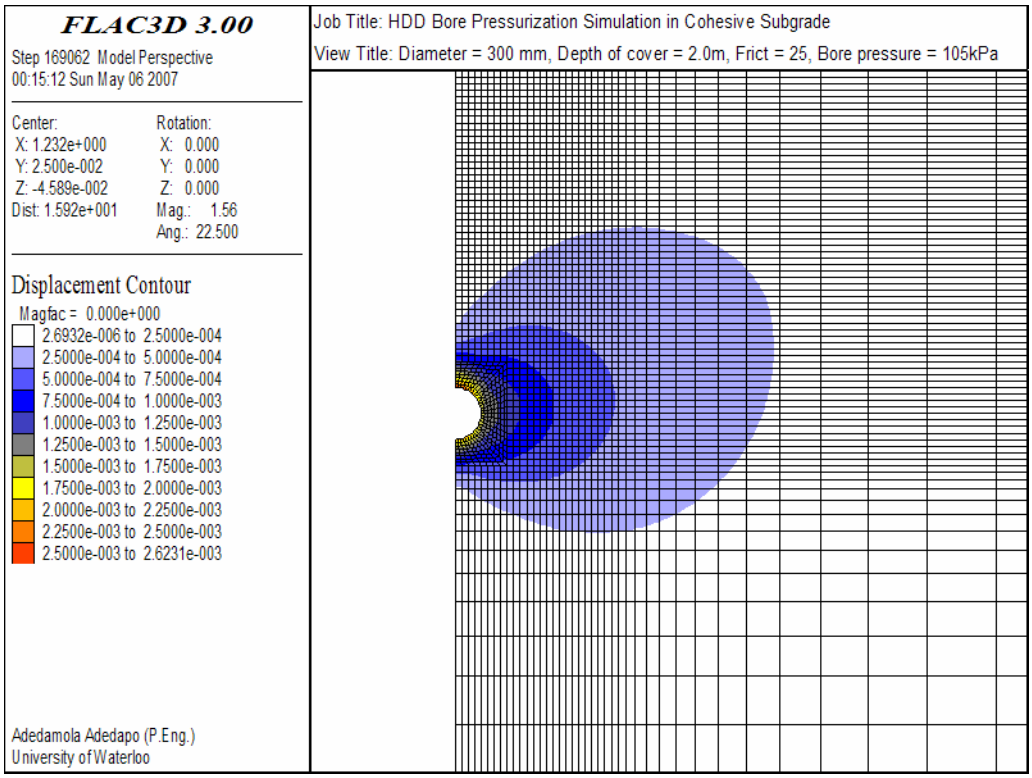

Figure 6.77: Displacement contour at 105 kPa in cohesive subgrade

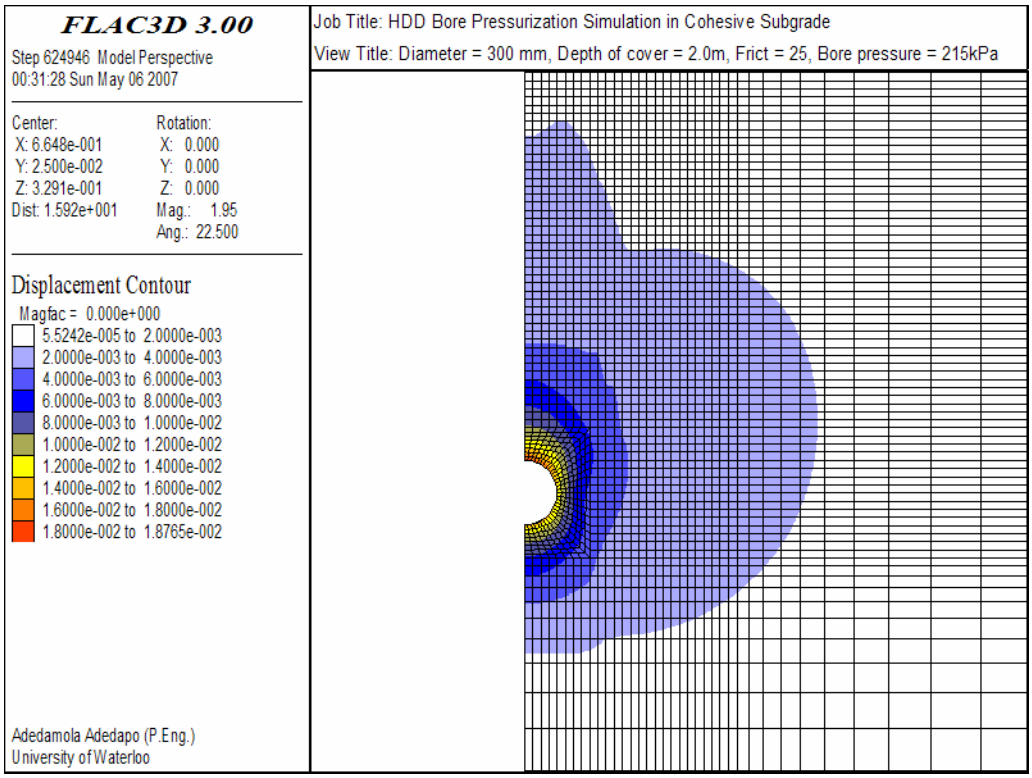

Figure 6.78: Displacement contour at 215 kPa in cohesive subgrade

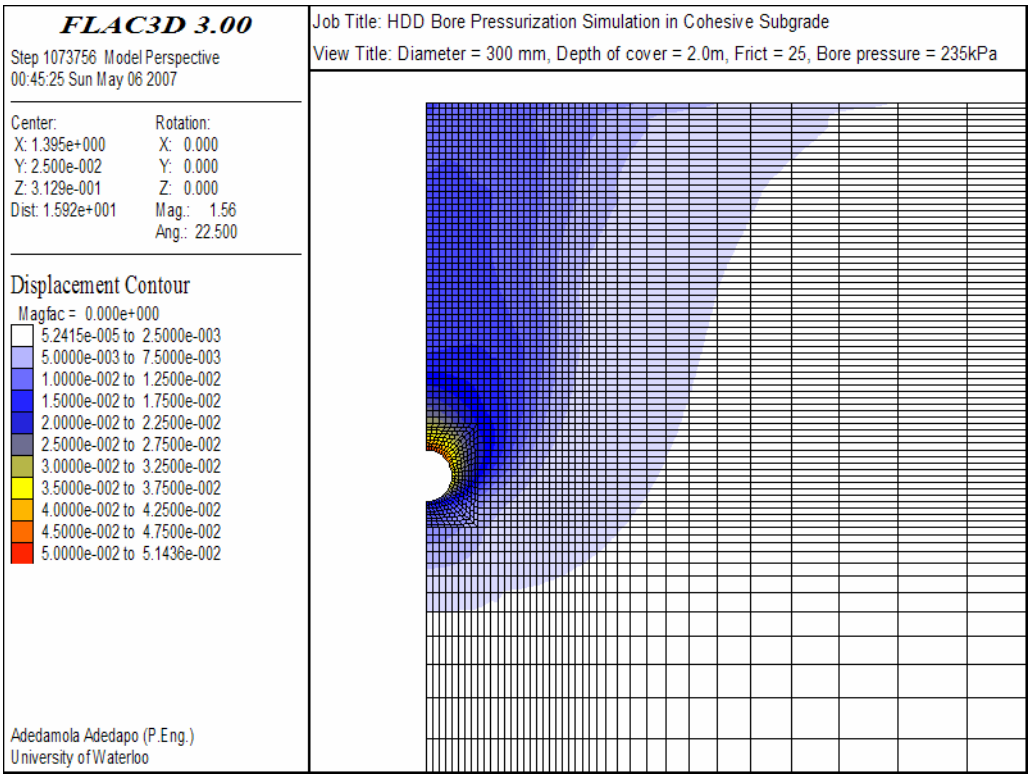

Figure 6.79: Displacement contour at 235 kPa in cohesive subgrade

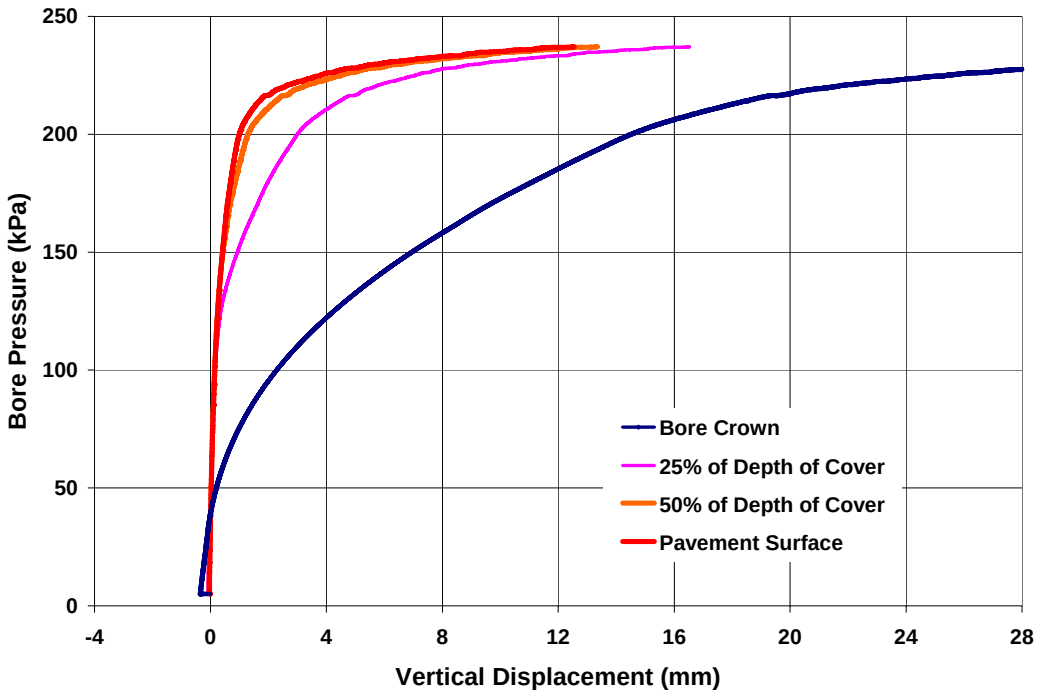

Figure 6.80: Bore pressure-displacement response above bore crown in cohesive subgrade (Bore diameter 300mm, depth of cover = 2.0m, friction =25°)

It should be noted that once the ground movements was initiated at about 1.3m above the crown of the bore , a distance that correlate to 75% of the height of cover only minimal additional bore pressure (about 1 kPa) was required to initiate the same magnitude of ground movement at the pavement surface. The rate of heave at the pavement surface was however minimal until the bore pressure of 220 kPa was exceeded.

Further increase in bore pressure extended the plastic yield zones vertically outward towards the pavement surface (Figure 6.78) and once the yield surface reached the pavement surface at a bore pressure of about 220kPa, the rate of surface deformation increased considerably with additional bore pressure. For example, vertical movements of 21.4 and 2.5mm were observed at the bore crown and pavement surface, respectively, for a bore pressure of 220 kPa compared to upward movements of 51.4 and 12.5mm, respectively observed at bore a pressure of 237 kPa. Displacements near the bore springline showed similar exponential increase.

6.4.5.3 Shear and Volumetric Strains

Shear Strains

Figures 6.81 through 6.85 show contour plots of the shear strain around the HDD bore at applied bore pressures of 35, 55, 105, 215 and 235 kPa. The shear strains at the crown and invert of the bore due to the applied bore pressure were negligible for bore pressures that were below the overburden pressure (approx 35 kPa). The shear strains in the subgrade soil near the springline were also small for bore pressure below overburden pressure. However, as the bore pressure increased and exceeded the overburden pressure, shear strain developed in the soil adjacent to the periphery of the bore. Figure 6.81 shows the shear strain contours for applied bore pressure of 35 kPa. The plot suggests that shear strain has developed along the periphery of the bore with maximum strain of about 1.4e-03 occurring at the crown, springline and invert of the bore. As the bore pressure increased, the magnitude and the extent of the shear strain also increased. At bore pressure of 105 kPa, Figure 6.83, shear strain contours have increased outwardly away from the bore and the extent of straining around the bore was not uniform. The shear strain contour extended to 0.6, 0.55 and 0.25 m way from the crown, invert and springline of the bore, respectively. The magnitude of the maximum

shear strain at the crown and invert of the pipe was about 2.25e-02. The magnitude of the shear strains at the springline was about half of those at the crown.

The intensity (magnitude) and extent of the shear strain contours continued to increase with additional increase in bore pressure. At bore pressure of 235 kPa there was a noticeable increase in the lateral extent and magnitude of the shear strain contour adjacent to the springline in particular. The increased bore pressure resulted in plastic deformation and formation of shear bands/plane originating from the springline extending outward and upward at angle to the horizontal (Figure 6.85). The maximum shear strain near the springline was about 2.5e-01 and 2.7e-01 at the crown and invert at *critical pressure* of 237kPa.

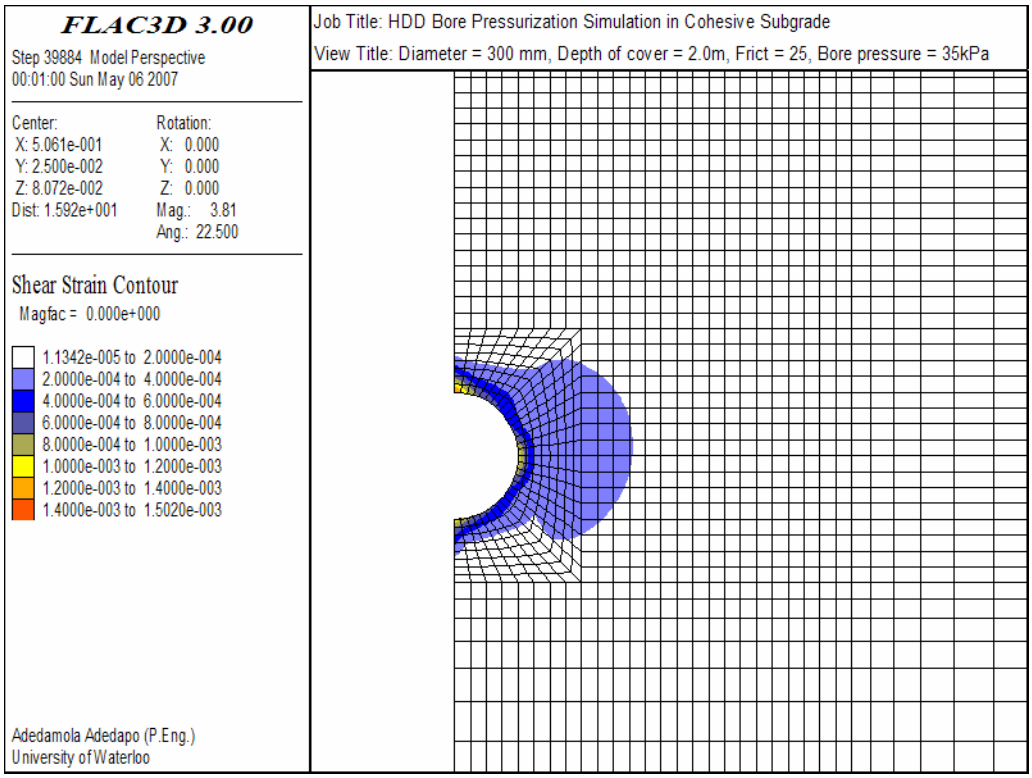

Figure 6.81: Shear strain contour at 35 kPa in cohesive subgrade

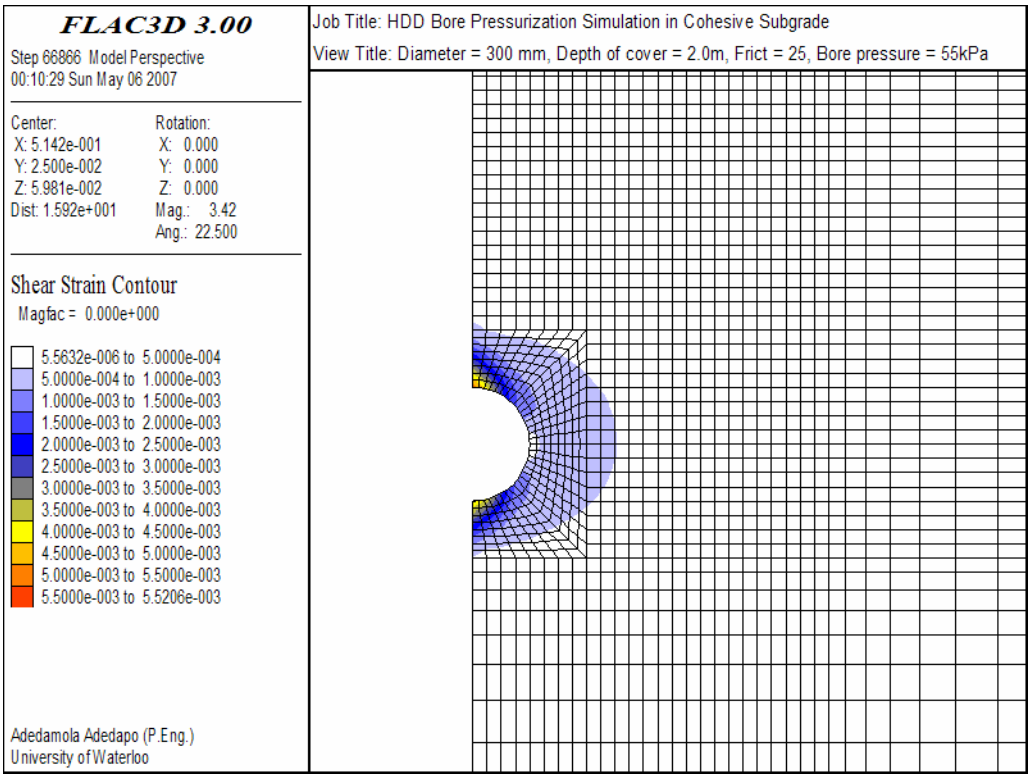

Figure 6.82: Shear strain contour at 55 kPa in cohesive subgrade

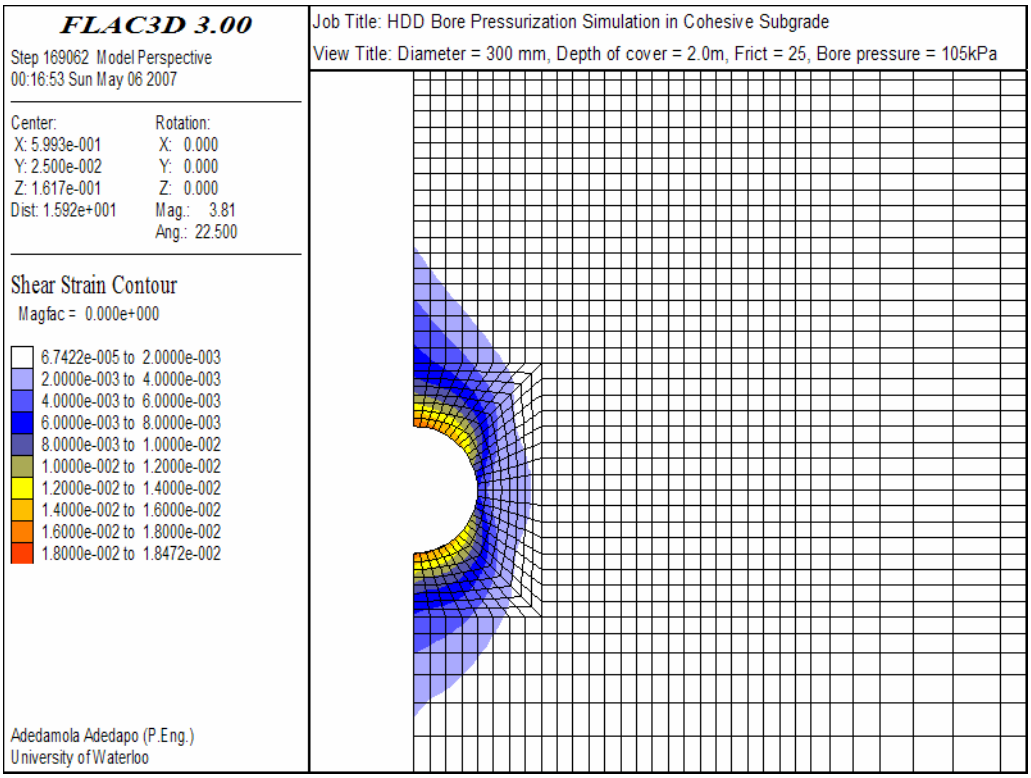

Figure 6.83: Shear strain contour at 105 kPa in cohesive subgrade

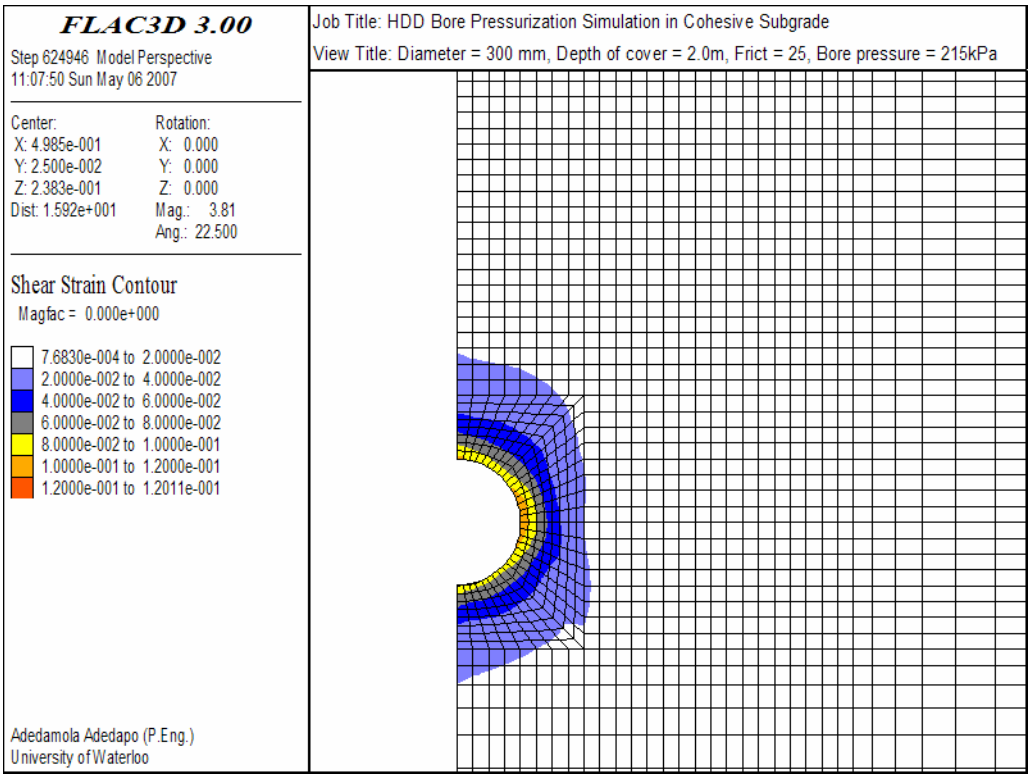

Figure 6.84: Shear strain contour at 215 kPa in cohesive subgrade

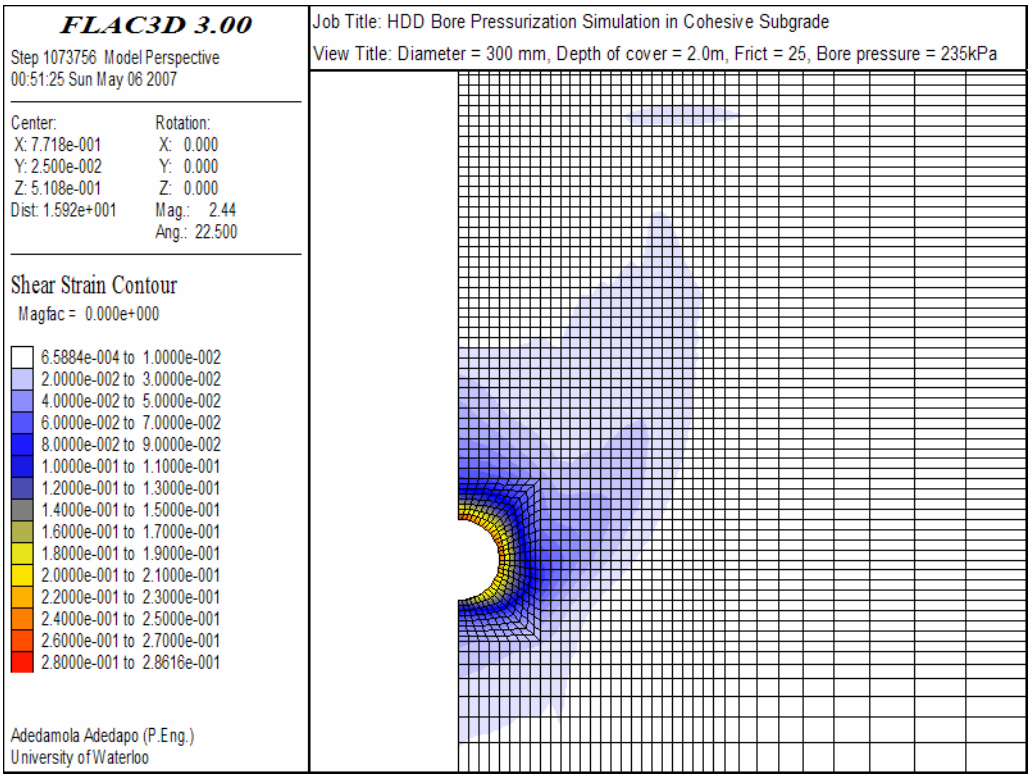

Figure 6.85: Shear strain contour at 235 kPa in cohesive subgrade

Volumetric Strains

Contour plots of the volumetric strain around the HDD bore for different bore pressures are presented in Figures 6.86 through 6.90. Positive volumetric strain indicates extension and negative strain indicates compression. A dilation angle of zero was assigned to the clayey subgrade. Hence, there was no effect of shear dilatancy on the volumetric strain discussed herein.

At bore pressure below the overburden stresses, the zones around the bore wall experienced only minimal volumetric strain. At bore pressure of 35kPa, the maximum volumetric strain of 1.6e-03 occurred at the crown and invert of the bore (Figure 6.86) where the soil has experienced some plastic yielding as indicated in Figure 6.69. Figure 6.86 indicates that a small zone of soil about 50mm away from the springline experienced elastic compression due to loading; the compressive volumetric strain in the soil at this location was about -4.4e-04.

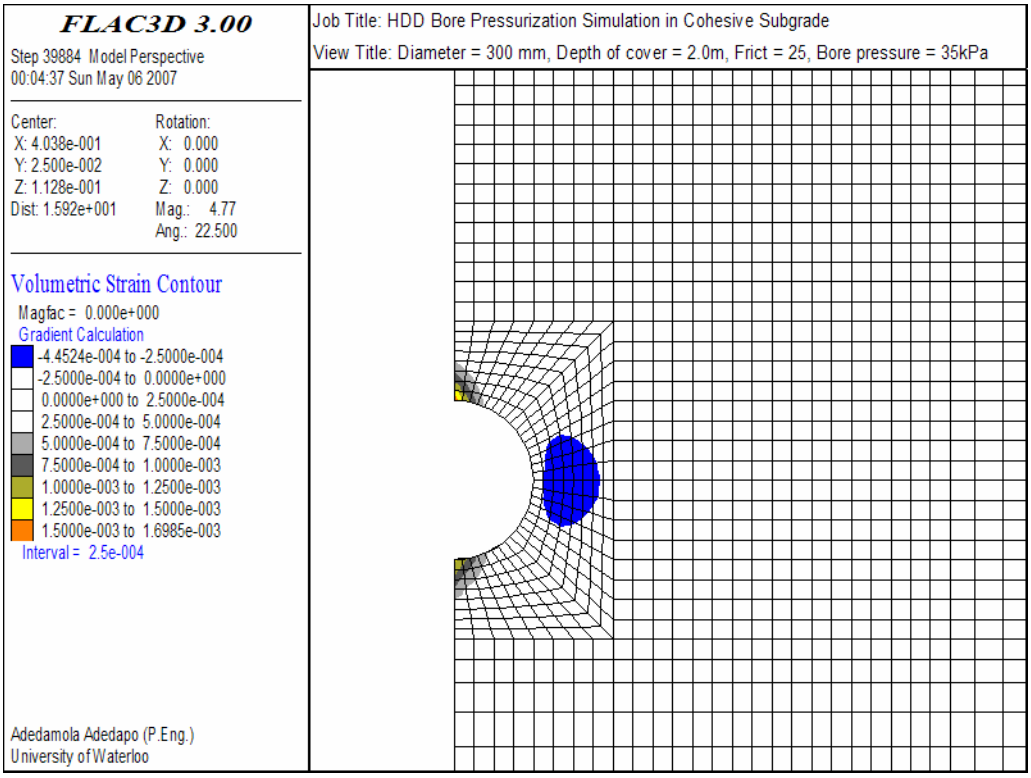

Figure 6.86: Volumetric strain contour at 35 kPa in cohesive subgrade

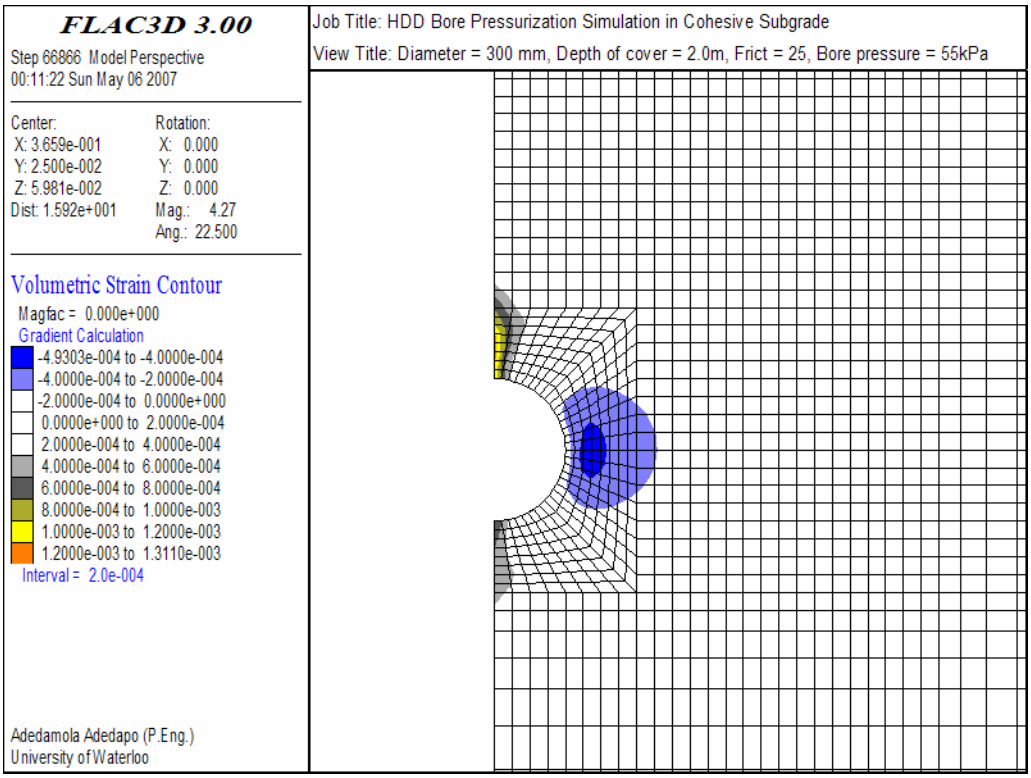

Figure 6.87: Volumetric strain contour at 55 kPa in cohesive subgrade

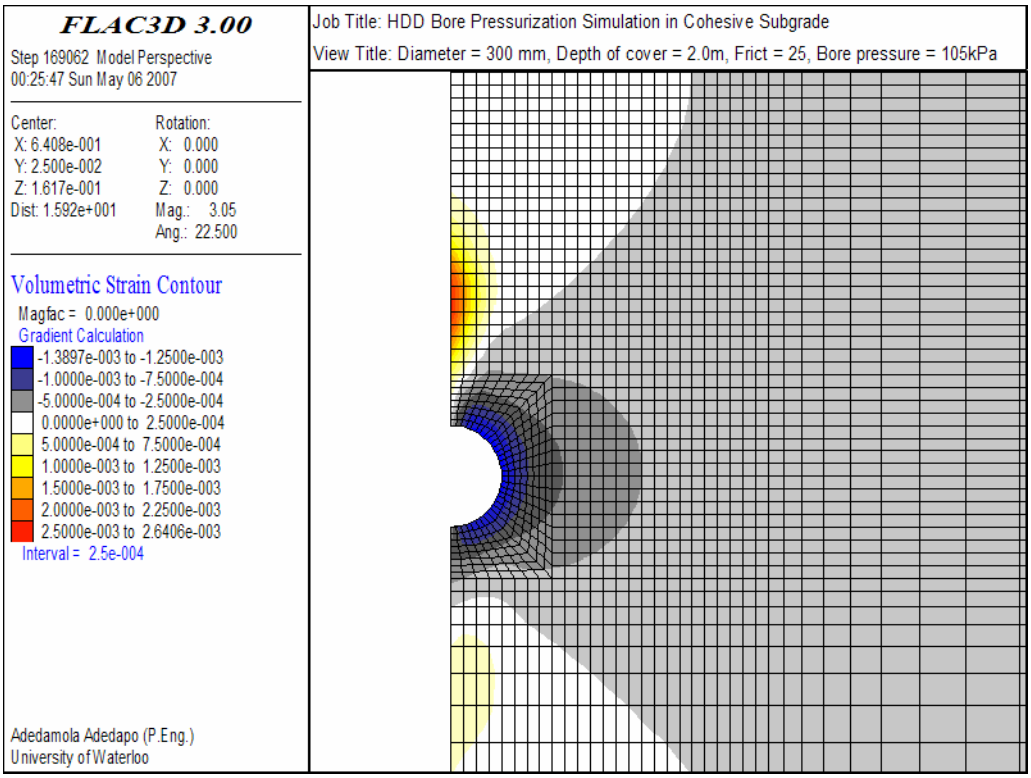

Figure 6.88: Volumetric strain contour at 105 kPa in cohesive subgrade

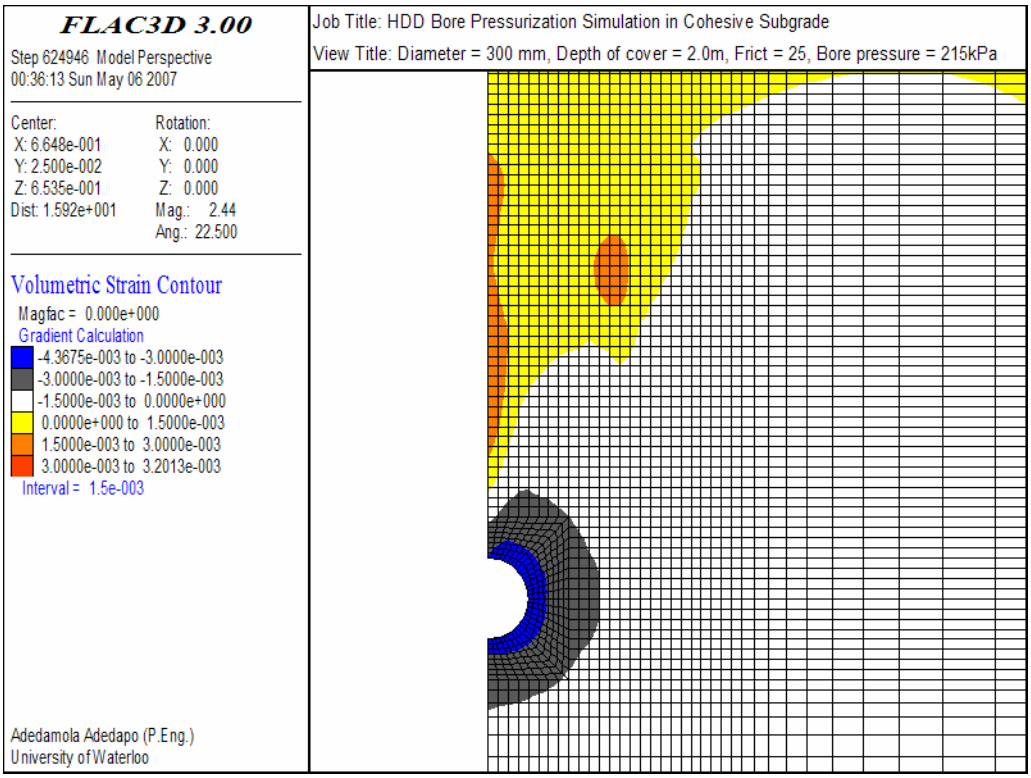

Figure 6.89: Volumetric strain contour at 215 kPa in cohesive subgrade

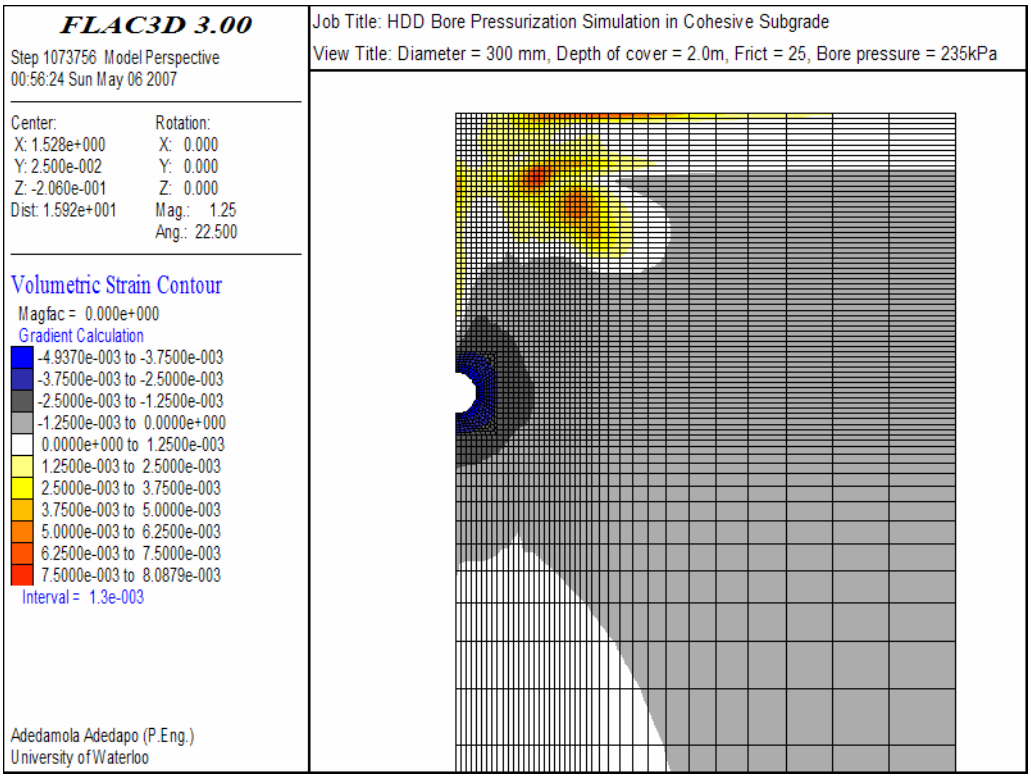

Figure 6.90: Volumetric strain contour at 235 kPa in cohesive subgrade

As the bore pressure was increased, the soil magnitude and extent of volumetric strain increased. At bore pressure of 105kPa the majority of the soils around the periphery of the bore experienced significant compression resulting in volumetric strain of up to 1.35e-03. The compressive volumetric strain contours, Figure 6.88, have extended beyond the bore diameter (0.3m) at the springline of the bore and about 0.15m above the crown and below the invert of the bore. There is a noticeable development of tensile strain about 200mm above the above the crown, this zones correspond to the location where the tangential stress contour is least and approaching zero (see Figure 6.64). Once tensile failure was initiated at this location above the crown of the bore, subsequent increase in the bore pressure causes the extent of the yielding to increase and forces the zones of minimum circumferential stress outwardly towards the pavement surface as shown in Figures 6.65 and 6.66. The tangential stress along the bore wall is increased resulting in additional compressive volumetric strain within the soil at the immediate vicinity of the bore.

As the bore pressure approached the *critical pressure* of 237kPa, the magnitude of the volumetric strain in the soil immediately around the bore increased. Unlike the volumetric strain response in the pure frictional subgrade, there was no evidence of rigid upward movement and/or displacement of the soil wedge above the crown of the bore shown in Figure 6.49.

6.4.5.4 Bore Pressure-displacement Response in Clayey Subgrade

The results obtained from HDD bore pressurization simulations in clayey subgrade beneath flexible pavement roadway are compiled and presented in this section. The mechanism ground deformation during the pressurization process in clayey subgrade are similar to those described in the preceding sections and will not be repeated; the primary result of the numerical modeling that are presented in this section is the bore pressure-displacement response.

Bore pressure-displacement relationships

The limiting displacement (or heave) is assumed to be 12.5mm, similar to the value used for simulations in cohesionless subgrade, and as previously stated, this is an arbitrary value assumed to be reasonable for discussion. The magnitude of bore pressures required to initiate

vertical displacements of 12.5mm at the crown of the bore and to propagate the same amount of displacement to a vertical height of $\frac{1}{4}D$, $\frac{1}{2}D$, $\frac{2}{3}D$ and D towards the pavement surface are summarized in Table 6.9; where D is the depth of cover taken as the height of soil between the pavement surface and the crown of the bore. The bore pressures required to propagate the limiting vertical displacement to height $\frac{1}{4}D$, $\frac{1}{2}D$, $\frac{2}{3}D$ and D above the crown are presented graphically in Figures 6.91 through 6.93.

The magnitude and extent of lateral deflections in the subgrade soil away from the springline of the bore were also monitored during HDD bore pressurization simulation and bore pressures required to initiate horizontal displacement of 12.5mm at the springline of the bore are summarized in Table 6.10. Bore pressures required to propagate the same magnitude of horizontal displacement (i.e. 12.5mm) to a lateral distance of $\frac{1}{4}D$ or more away from the springline were greater than pressures required to cause vertical displacement of 12.5mm at the pavement surface.

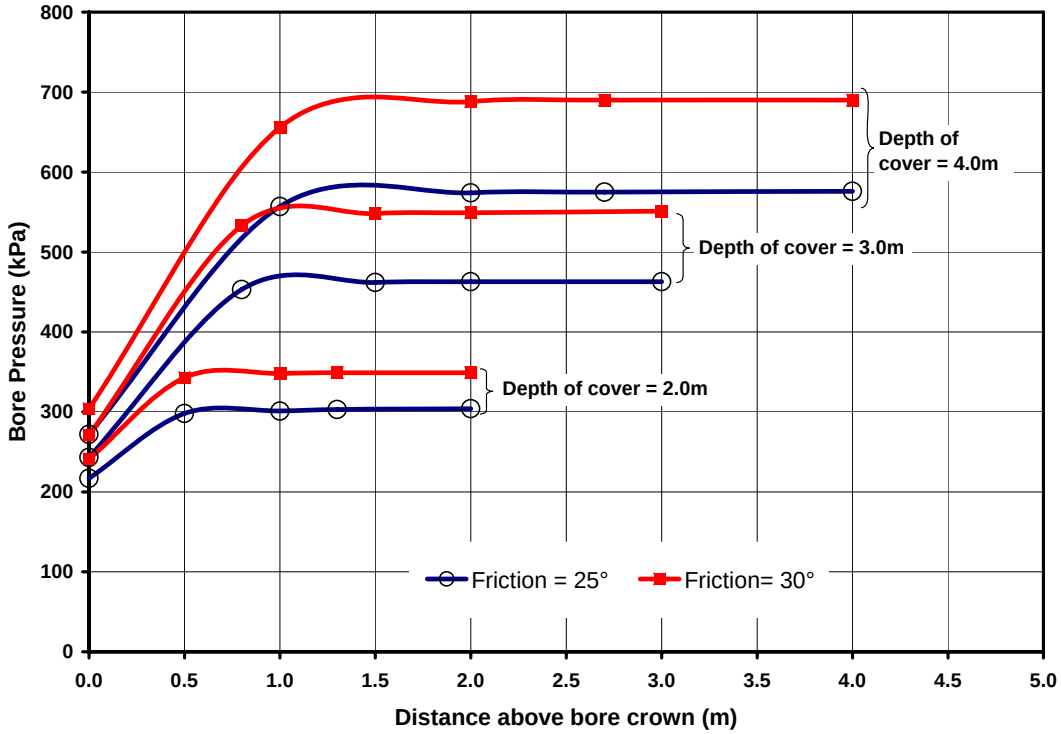

Figure 6.91: Estimated bore pressure required to initiate and propagate 12.5mm vertical displacement above a 200mm HDD bore installed in a cohesive subgrade

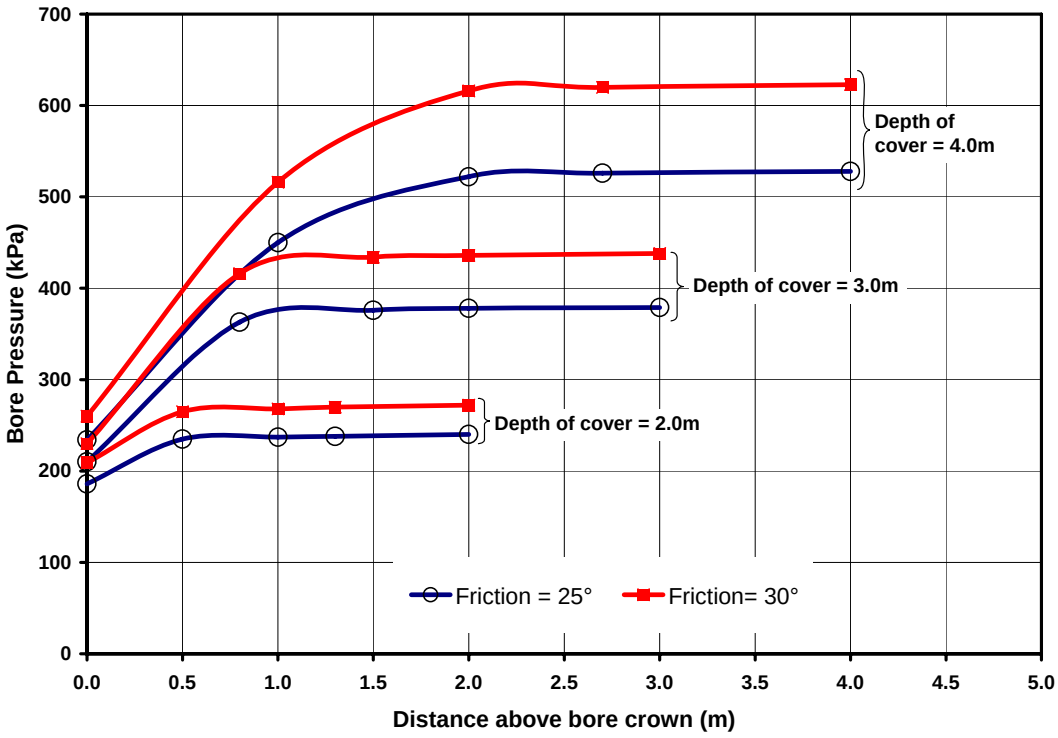

Figure 6.92: Estimated bore pressure required to initiate and propagate 12.5mm vertical displacement above a 300mm HDD bore installed in a cohesive subgrade

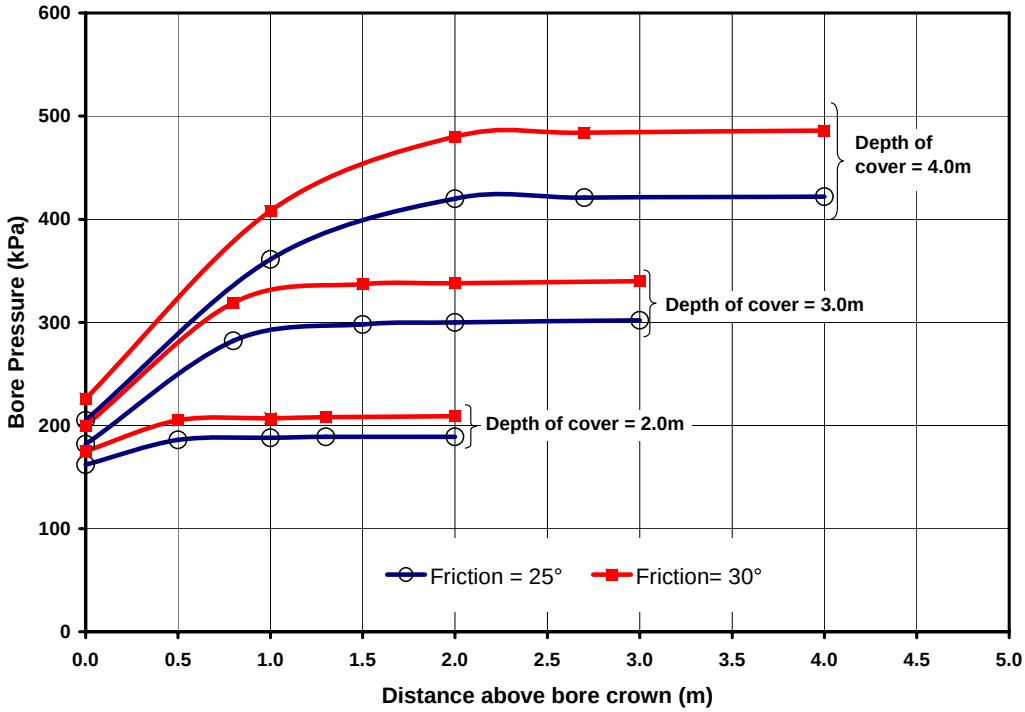

Figure 6.93: Estimated bore pressure required to initiate and propagate 12.5mm vertical displacement above a 450mm HDD bore installed in a cohesionless subgrade

Influence of angle of friction on bore pressure-displacement relationship

The HDD installations that were simulated all showed greater outward displacements with increased bore pressure. The *initiation* and *critical* bore pressures are directly proportional to the friction angle and depth of cover and inversely proportional to the bore diameter. Higher friction angle provided greater resistance to deformation requiring greater bore pressure to initiate and propagate deformation outwardly from the bore. For example, the *critical pressure* for a 300mm diameter bore in a clayey soil with a friction angle of 25° at 3m below pavement surface was about 379kPa compared to a *critical pressure* of about 438 kPa required for the same bore geometry in a clay subgrade material friction angle of 30°.

Influence of depth of cover on bore pressure-displacement relationship

Increased height of cover provided significant resistance to ground deformations. For shallower bore, the difference between *initiation pressures* and pressures required to propagate 12.5mm displacement vertically above the bore to a height of about $\frac{1}{4}D$ (25% of the depth of cover) were noticeably higher than those observed for simulations in cohesionless subgrade. Nevertheless, contours of vertical displacements are rapidly transmitted upward once plastic deformation develops above the crown of the bore and extend to a height of about $\frac{1}{4}D$ (25% of the depth of cover) particularly for small diameter and shallower bores. For example, only about 5 kPa additional pressure was required once the vertical displacement has reached a height of about 0.5m or $\frac{1}{4}D$ (25% of the depth of cover) above the crown of the bore before the *critical pressure* were attained for a 300mm HDD bore at a depth of 2.0m in a clayey subgrade soil with friction angle of 25° compare to about 78 kPa additional pressure required for a deeper bore at 4.0m below pavement surface. This observation suggests that bore pressures need to be maintained well below those required to propagate vertical displacement of 12.5mm to a height of about $\frac{1}{4}D$ (25% of the depth of cover) above the bore crown for shallow HDD installation in cohesive subgrade.

Table 6.9: Bore pressures required for vertical displacement in cohesive subgrade

Bore Diameter (mm)	Depth of cover (m)	Depth of cover to bore diameter ratio	Friction angle of subgrade soil (°)	Bore Wall (kPa)	Height above bore crown expressed as fraction of depth of cover, D						Pavement Surface (kPa)
					$\frac{1}{4}D$		$\frac{1}{2}D$		$\frac{2}{3}D$		
					Depth (m)	Pressure (kPa)	Depth (m)	Pressure (kPa)	Depth (m)	Pressure (kPa)	
200	2	10	25	217	0.5	298	1.00	301	1.3	303	304
	3	15	25	243	0.8	453	1.50	462	2.0	463	463
	4	20	25	272	1.0	557	2.00	574	2.7	575	576
	2	10	30	241	0.5	343	1.00	348	1.3	349	349
	3	15	30	271	0.8	533	1.50	548	2.0	549	551
	4	20	30	304	1.0	656	2.00	688	2.7	690	690
300	2	6.7	25	186	0.5	235	1.00	237	1.3	238	240
	3	10	25	210	0.8	363	1.50	376	2.0	378	379
	4	13.4	25	234	1.0	450	2.00	522	2.7	526	528
	2	6.7	30	209	0.5	265	1.00	268	1.3	270	272
	3	10	30	230	0.8	416	1.50	434	2.0	436	438
	4	13.4	30	260	1.0	516	2.00	616	2.7	620	623
450	2	4.4	25	162	0.5	186	1.00	188	1.3	189	189
	3	6.7	25	182	0.8	282	1.50	298	2.0	300	302
	4	8.9	25	205	1.0	361	2.00	420	2.7	421	422
	2	4.4	30	175	0.5	205	1.00	207	1.3	208	209
	3	6.7	30	200	0.8	319	1.50	337	2.0	338	340
	4	8.9	30	226	1.0	408	2.00	480	2.7	484	486

Table 6. 10: Bore pressures required for lateral displacement in cohesive subgrade

Bore Diameter (mm)	Depth of cover (m)	Depth of cover to bore diameter ratio	Friction angle of subgrade soil (°)	Bore wall (springline) (KPa)
200	2	10	25	231
	3	15	25	268
	4	20	25	300
	2	10	30	262
	3	15	30	302
	4	20	30	346
300	2	6.7	25	207
	3	10	25	236
	4	13.4	25	268
	2	6.7	30	231
	3	10	30	270
	4	13.4	30	306
450	2	4.4	25	175
	3	6.7	25	215
	4	8.9	25	243
	2	4.4	30	192
	3	6.7	30	240
	4	8.9	30	270

The *initiation pressures* increased between 10 to 14 percent for a 50 percent increase in depth of cover, and increased by between 24 to 29 percent when the depths of cover were doubled. Whereas, the *critical pressures* increased between 52 to 63 percent for a 50 percent increase in depth of cover; and increased by between 90 to 132 percent when the depths of cover were doubled. The magnitude of increase in *initiation* and *critical pressures* due to additional depth of cover were proportional to bore diameter and to friction angle.

The lateral deformation observed near the springline increased with bore pressure and generally did not extend beyond one bore diameter from the bore for bore pressures less than the *critical* limit pressures for the numerical simulations presented in this Section. The magnitude and extent of lateral deformation near the bore springline increased with depth of cover. Probably because the *critical pressures* are significantly higher for deeper installations

which allow lateral deformations to develop while the vertical deformation is being propagated upwardly towards the pavement surface.

The vertical downward displacement at the invert of the bore increased in magnitude and extent with greater depth of cover. The rate of deformations at the invert of the bore were significant retarded once vertical movement developed in the soil above the crown of the bore and the extent of plastic yielded zone at the crown of the pipe increased. The magnitude and extent of vertical downward deformation at the invert of the bore also increased with depth of cover. Probably because the *critical pressures* are significantly higher for deeper installations allowing downward deformation to develop and expand while the vertical deformation is being propagated upwardly to the pavement surface.

Influence of bore diameter on bore pressure- displacement relationship

Smaller bore diameter required greater *initiation* and *critical pressures*. For example, the *initiation* and *critical pressures* for a 450mm HDD bore installed in clayey subgrade with friction angle of 25° at depth of 3.0m below the pavement surface are about 182 and 302 kPa, respectively; whereas, the *initiation* and *critical pressures* for a smaller 200mm diameter bore installed in same subgrade material and depth of cover are about 243 and 463 kPa, respectively an increase of about 33 and 53 percent, respectively over those of 450mm diameter bore. The percentage increase is about 9% higher in cohesive subgrade soil with friction angle of 30° and c = 10 kPa. The higher bore pressures required for smaller bore is attributed to a smaller circumferential surface over which the applied bore pressures acts on smaller bore diameters. Smaller bore would require greater bore pressure to achieve a similar driving force required to initiate and propagate deformation outwardly from the bore compare to larger diameter bore.

6.4.5.5 Influence of Cohesion on Estimated Bore Pressures

Sensitivity analysis was completed to examine the influence of the cohesion of both *initiation* and *critical* bore pressures. The sensitivity analysis was completed by varying the effective cohesion of the clayey subgrade soil for a 300mm diameter HDD bore drilled 2.0m below the

pavement surface in a clayey subgrade with an effective friction angle of 25°. The limiting bore pressures obtained for different cohesion are presented graphically in Figure 6.94. The bore diameter, depth of cover, thickness of granular subbase and material properties each pavement layer were keep constant for the three analyses.

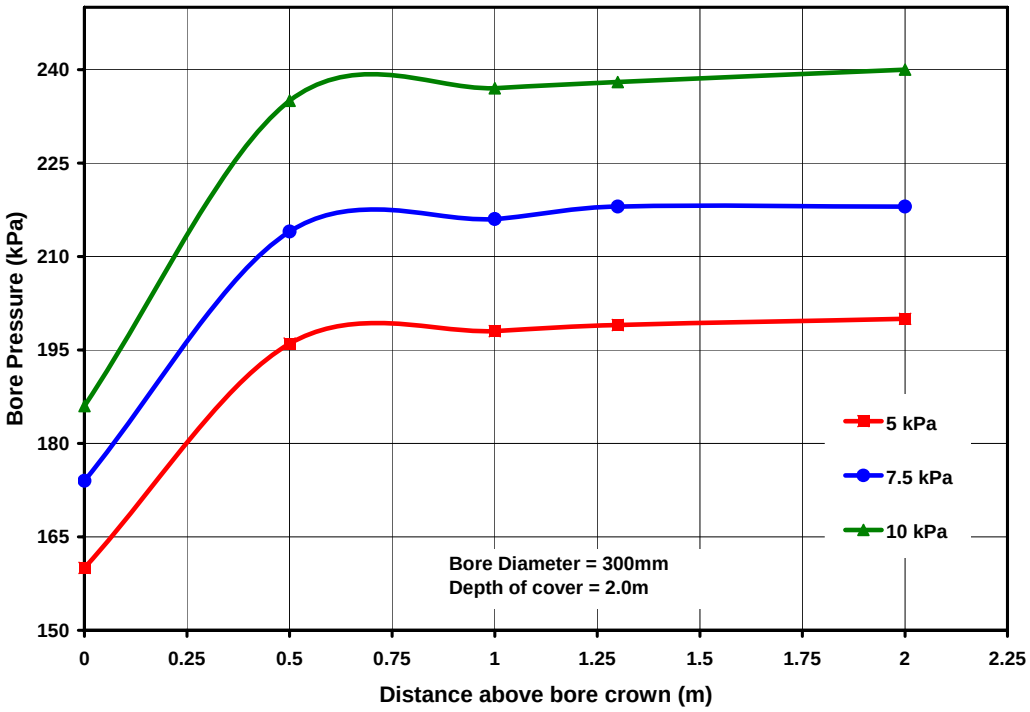

Figure 6.94: Estimated bore pressure required to initiate and propagate 12.5mm vertical displacement above a 300mm bore installed in a cohesive subgrade for different magnitude of cohesion

The sensitivity analyses revealed that the value of effective cohesion assigned to the subgrade has a considerable influence on the magnitudes of the limiting bore pressures. Increasing the value of effective cohesion from 5 kPa to 7.5 kPa, a 50% increase, resulted in approximately 9% increase in the *initiation* and *critical* limiting bore pressures. The *initiation* and *critical* limiting bore pressures for installations in cohesive subgrade soil with an effective cohesion of 10 kPa increased by about 20% over those obtained for clayey subgrade with 5 kPa cohesion. There appears to be a linear correlation between the effective cohesion assigned to the clayey subgrade soil and the percentage change in limiting bore pressures for the installation configuration that was examined.

6.4.5.6 Comparison of limiting Bore Pressure Estimate from Delft Geotechnics Equations and *FLAC*^{3D} for HDD bores in Clayey Subgrade

The allowable bore pressures that would limit the plastic yield zone radius to one half of the depth of cover were estimated with Delft Geotechnics equations (Equation 6.10) for the HDD installations that were simulated with *FLAC*^{3D}. The maximum allowable bore pressures estimated using the Delft Geotechnics equations are presented in Table 6.11 and are compared to the *critical pressures* (also shown on Table 6.10) obtained from numerical simulation with *FLAC*^{3D}.

The maximum bore pressures that would limit the extent of plastic yield zone to a radius of one-half of the height of cover from the center of the bore estimated with the Delft Geotechnics equations were in some instances very close to *critical pressures* obtained from numerical simulations. The allowable bore pressures computed using the Delft Geotechnics equations were between -7.2 to 16.6 % higher than the *critical pressure* numerically estimated with *FLAC*^{3D}. The depth of the cover to bore diameter ratio appears to have played a significant role in the difference observed between the values estimated with the Delft's equation and *FLAC*^{3D}. Figure 6.95 shows the plot of the computed difference between the two values against depth of the cover to bore diameter ratio. It can be inferred from Fig. 6.95 that the difference between limiting bore pressures obtained using the Delft Geotechnics equations and *FLAC*^{3D} increased with greater friction angle and bore diameters and that for a particular bore diameter, the difference between values estimated from the two methods reduces with depth of cover. Further more, the estimated allowable bore pressure obtained from the Delft's equations were lower than critical pressures estimated by *FLAC*^{3D} for installations for which the depth of cover to bore diameter ratio is greater than 12.5.

Table 6. 11: Comparison of *FLAC*^{3D} and Delft Equations estimated bore pressures in cohesive subgrade

Bore Diameter (mm)	Depth of cover (m)	Depth of cover to bore diameter ratio	Friction angle of subgrade soil (°)	FLAC3D	Delft Geotechnics Equations		Percent Difference (%)
				Critical Pressure (kPa)	Height above bore crown (m)	Allowable bore Pressure (KPa)	
200	2	10	25	304	0.90	304	0.1
	3	15	25	463	1.40	434	-6.3
	4	20	25	576	1.90	541	-6.1
	2	10	30	349	0.90	357	2.2
	3	15	30	551	1.40	514	-6.8
	4	20	30	690	1.90	640	-7.2
300	2	6.7	25	240	0.85	258	7.5
	3	10	25	379	1.35	389	2.7
	4	13.4	25	528	1.85	505	-4.3
	2	6.7	30	272	0.85	299	9.9
	3	10	30	438	1.35	459	4.8
	4	13.4	30	623	1.85	598	-4.1
450	2	4.4	25	189	0.78	213	12.9
	3	6.7	25	302	1.28	336	11.1
	4	8.9	25	422	1.78	454	7.5
	2	4.4	30	209	0.78	244	16.6
	3	6.7	30	340	1.28	392	15.3
	4	8.9	30	486	1.78	535	10.0

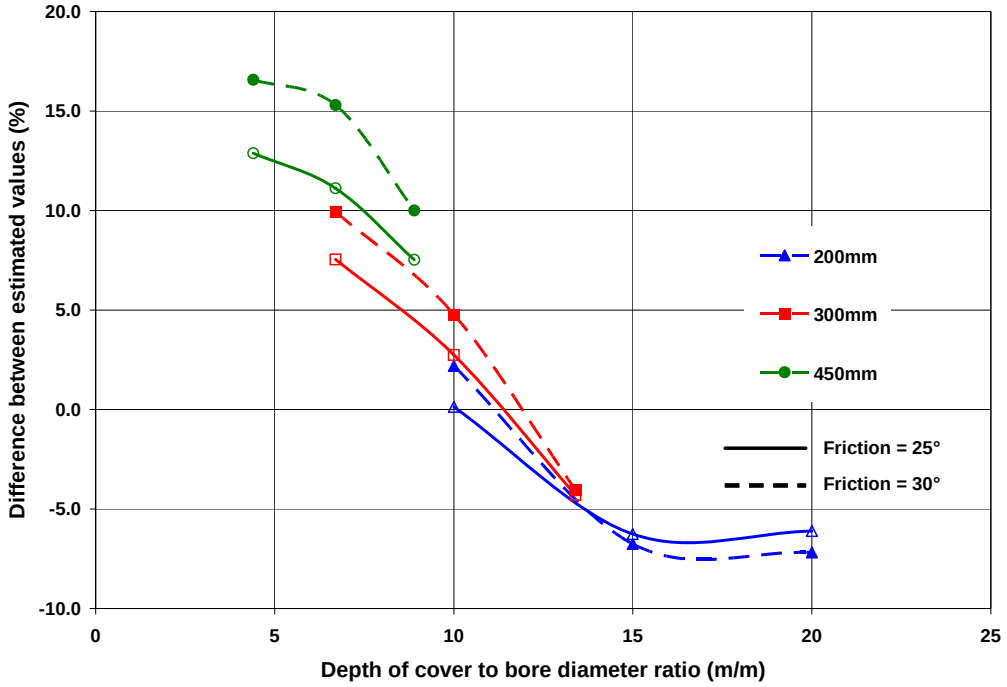

Figure 6.95: Difference between allowable bore pressures obtained with Delft Geotechnics equations and critical pressures obtained from *FLAC*^{3D} versus depth of cover-to-bore diameter ratio

It is not surprising that the allowable bore pressures estimated by the Delft Geotechnics equations are slightly lower, in some instance, than the *critical* bore pressures since greater bore pressures (*critical pressures*) are required to propagate the plastic zones to the pavement surface compared to Delft's allowable pressure that limits the plastic zone to a distance of one-half the depth of cover. Although, the allowable bore pressures estimated with the Delft Equations were in some cases lower than the critical pressure estimated with *FLAC*^{3D}, pavement surface would still have heaved at those "lower" bore pressures. This indicates that the Delft Geotechnics equations do not limit the ground deformation (or the extent of plastic zone) to the desired one-half of the depth of cover.

The difference observed between the bore pressure obtained from the numerical simulation and those estimated with Delft Geotechnics equations is largely due to the assumptions made

in the derivation of the equation which was based on cavity expansion theory. The assumptions include a uniform and isotropic stress field, an infinite soil medium, and homogenous soil properties. The influence of lateral earth pressure, tensile strength of material, shear dilatancy, spatial boundary and boundary conditions were not included in the formulation of the equations. All these ignored factors play important roles in numerical modeling and the actual stress-deformation behavior of pavement structure.

6.5 Design Charts and Tables for HDD Installations beneath Flexible Pavement

The results of the numerical simulation presented and discussed in the preceding Sections indicated that the *critical pressure* (i.e. bore pressure required to propagate a vertical displacement of 12.5mm above the bore crown to the pavement surface) were significantly less than the bore pressures required to propagate a lateral displacement of 12.5mm from the springline of the bore to a distance equivalent to twice diameter of the bore. Hence, the bore pressures associated with vertical displacements above the HDD bore represent the *limiting pressures* (i.e. maximum allowable) for all the HDD bore pressurization simulation completed for this thesis.

The design charts and tables presented herein are based on limiting bore pressures for vertical displacements above HDD bores and the approach used in developing the charts is similar to those proposed by Duyvestyn (2004) for HDD installation in uniformly graded sand. The bore pressures that would propagate vertical displacement of 12.5mm to the bore crown and to distances, $\frac{1}{4}D$, $\frac{1}{2}D$ and D above the bore beneath a flexible pavement are presented in the form of charts and can be used as first approximation by HDD designers as a preliminary design tool. D is the depth of cover above the crown.

Design charts that relate various limiting bore pressures to depth of cover are provided in Appendix C for HDD installations in cohesionless and clayey subgrade beneath flexible pavement. An example of design chart that relates the bore pressures to depth of cover is

provided in Figure 6.96. The Figure shows bore pressures that would initiate a vertical displacement of 12.5mm at the crown of HDD bores of various diameters at different depths in cohesionless subgrade underneath flexible pavement.

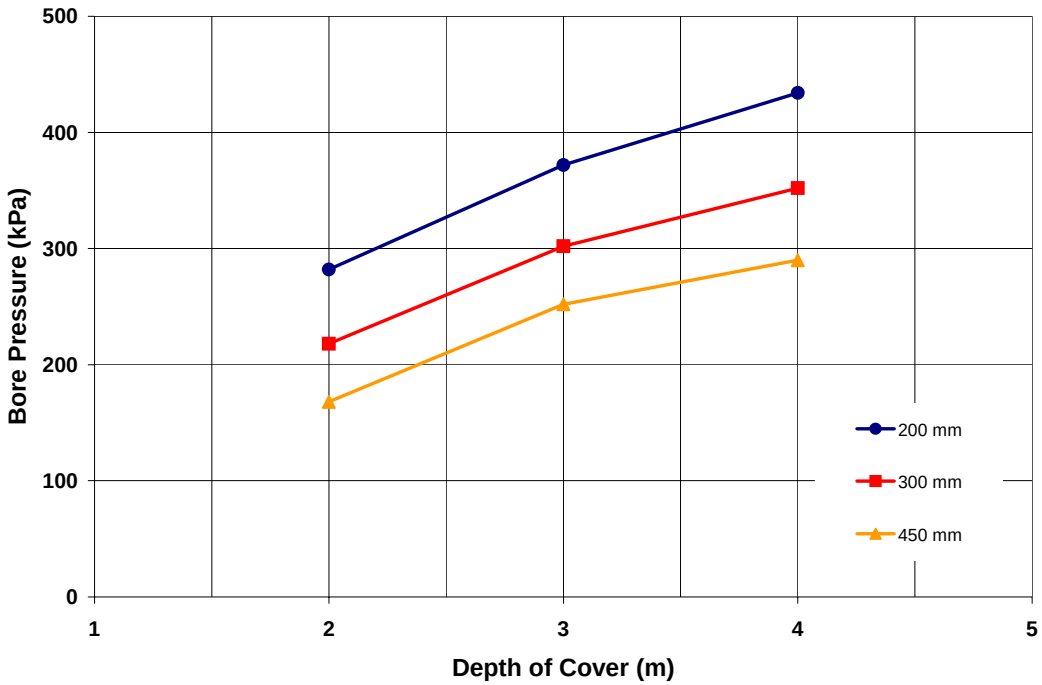

Figure 6.96: Bore pressure-depth of cover relationship for initiating 12.5mm displacement at the bore wall in cohesionless subgrade with friction of 35°

6.5.1.1 Validity and Limitations of the Design Charts and Tables

The accuracy of the limiting bore pressures deduced from the proposed design charts were examined by comparing values obtained from the chart (by interpolation and extrapolation between curves) with estimated values from numerical simulations. For the comparison, limiting bore pressures were numerically estimated using *FLAC*^{3D} for a 250mm diameter HDD bore installed cohesionless subgrade with effective friction angle of 35°. Depth of cover of 2.0m, 3.5m and 4.5m were examined. The estimated bore pressures that would propagate vertical displacement of 12.5mm to the bore crown and to distances $\frac{1}{4}D$, $\frac{1}{2}D$ and D above

the 250mm diameter HDD bore installed in cohesionless subgrade beneath flexible pavement are presented in Table 6.12. D is the depth of cover above the crown.

The values estimated from the design chart are also shown on Table 6.12 for comparison. There is excellent agreement between the bore pressures estimated by *FLAC*^{3D} and those obtained from design charts. The percentage maximum difference between the values obtained from the charts and *FLAC*^{3D} was less than 2.0%.

The bore pressures-displacement relationships obtained from the numerical analysis are dependent on the HDD installation parameters (bore diameter, depth of cover) and material properties assigned to the model. There were several simplifying assumptions made in the numerical simulations of HDD bore pressurization presented herein. Clearly, the use of a constant friction and dilation angles for the simulations are obvious simplifications. As a soil dilates it approaches the critical state, the angle of dilation gradually approaches zero and the angle of friction approaches its critical state value. The angles of friction and dilation can be estimated with some accuracy if the stress level and the current density are known. It would be more realistic to complete the simulation with using variable angles of dilation and friction.

Furthermore, the material properties assigned to the pavement layers were assumed to be uniform and homogenous The influence of initial porosity and stress history of the materials were not considered; the influence of construction sequence/bore-enlargement were also ignored as the bore was assumed to have been reamed to the final diameter; pre-existing discontinuities and potential path for pressure relief were not considered; the subgrade material was considered to be in drained condition and the influence of bonding on dilation was not considered. Due to these simplifying assumptions, the magnitude and extent of pavement structure displacements/movements due to bore pressurization estimated from numerical simulations may differ from actual ground movements that would be observed in the field. The proposed design charts and tables presented are therefore meant to be used with engineering discretion as a guide for first order approximation during the preliminary design stage.

Table 6. 12: Comparison of bore pressures estimated with FLAC3D and proposed design charts for a 250mm diameter bore installed in cohesionless subgrade with friction angle of 35°

Bore Diameter (mm)	Depth of cover (m)	Bore Wall		Height above bore crown expressed as fraction of depth of cover, D				Pavement Surface	
				$\frac{1}{4}D$		$\frac{1}{2}D$			
		FLAC^{3D} (kPa)	Chart (kPa)	*FLAC*^{3D} (kPa)	Chart (kPa)	*FLAC*^{3D} (kPa)	Chart (KPa)	*FLAC*^{3D} (kPa)	Chart (kPa)
250	2.0	250	250	264	262	266	265	266	265
	3.5	373	370	607	600	615	605	615	605
	4.5	427	425	831	825	839	830	839	830

6.6 Practical Significance of the Results obtained from Numerical Simulations of HDD Bore Pressurization.

Despite the limitations inherent in the results obtained from the numerical analysis due to the simplifying assumptions identified in the previous Section, the method of analysis presented herein is a step forward from the existing guidelines for limiting HDD ground movements and the results of the simulations provide better (more conservative) estimate of limiting bore-pressures than the existing design equations. In addition, the simulations also provide very useful information and insight that helps in understanding the mechanism of ground movements due to HDD bore pressurizations. The bore pressure-displacement relationships obtained are useful as first approximation with potential to reduce the risk associated with ground movements during HDD installation beneath pavement structure, if applied within the bounds of validity of the model.

Many of the existing HDD guidelines employed in limiting ground movement (e.g. Caltrans 2002; DCA 2001) are based solely on bore diameter-depth of cover ratio and do not consider the allowable slurry pressure, factors that contribute to fluid pressure build-up during installation bore or clearance to existing underground utility. Factors that directly influence HDD slurry fluidic pressure build-up include characteristics of drilling fluid, reaming sequence, reaming and pullback rates, length of installation, annular space, and bore geometry. Greater bore pressures are required to promote slurry flow within the bore with higher slurry solid contents, faster reaming/pullback rates, increased installation length, smaller bore annular space and poor bore geometry with greater elevation differences between the deepest position along the bore and the entry or exit location.

The allowable bore pressures estimated with Delft Geotechnics equations (cavity expansion theory) may result in excessive vertical displacement/heave at the pavement surface based on the magnitude of displacement produced by similar bore pressures in the numerical simulations. The risk of excessive heaving is particularly significant in shallow bores where the overburden pressure provides limited resistance against bore slurry bore.

Based on the results from the numerical simulations, limiting bore pressures for HDD bores with shallow depth of cover should be limited to magnitudes well below the *initiation* pressures, an allowable bore pressure below 50% of the *initiation pressure* is suggested for depth of cover below 2.0m. This is because once *initiation pressure* is reached and the subgrade material above crown of the bore yield plastically, very minimal additional bore pressure is required to propagate the displacement from the bore wall to pavement surface.

With greater depth of cover, the magnitude of the bore pressures can be increased due to increased confinement and resistance provided by the overburden pressure. For HDD bore with 3.0m and 4.0m depths of cover, the allowable bore pressures should be limited to magnitude below those required to propagate displacement of 12.5mm to a distance of $\frac{1}{4}D$ (25 percent of the depth of cover) above the bore crown. This again is due to small additional bore pressure required to propagate the displacement field to the pavement surface once it reached a height of $\frac{1}{4}D$ (25 percent of the depth of cover) above the bore crown. The use of additional factor of safety should be considered to account for different variability encountered during construction especially for high risk installations.

The numerical simulations assume that the bore slurry is confined to the bore, but there could be situations when the slurry will find its way into the overlying material. In cohesive soils for instance, loss of slurry into the subgrade can occur as a result of hydraulic fracturing. Hydraulic fracturing is a tensile failure in the tangential (hoop) direction along the bore wall due to increased bore pressurization. As the bore pressure in the bore is increased the annular tangential stress will decrease. Once the tangential stress reduces below the tensile strength of the soil, the soil will experience tensile failure and a crack will be initiated at the bore wall. The crack can grow outwardly with additional bore pressure. The theory of hydraulic fracturing is not applicable to cohesionless soils due to their lack of tensile strength in general. However, inadvertent returns can occur through pre-existing discontinuities and fissures in the subgrade layer. The bore slurry may find its way into the surrounding soils and migrate toward the surface due to lower resistance along these preexisting flow paths.

Slurry flow will continue along the preferential flow path (along the discontinuity) until the fluid pressure is relieved or until stronger soil layer or structure (e.g. asphalt concrete, concrete side-walks) is encountered above the bore. If a more resistance feature such as asphalt concrete is encountered, the pressurized slurry may collect beneath it and could cause significant heave or crack to the pavement if the fluidic pressure continues to build-up. The consequence of risk associated with intersecting preexisting discontinuity/ preferential slurry flow path is significantly reduced when the bore pressure is below the specified allowable. Avoiding slurry pressure build-up and the corresponding outward displacement around the bore will also lower the risk and consequence of HDD induced deflections on existing utilities and or underground structure beneath roadways.

Additional instrumented HDD field-scale installations and monitoring is necessary to substantiate findings from the numerical simulations.

Chapter 7: Numerical Simulations of Open-cut Pipe Installation

7.1 Introduction

Presented in this Chapter is the numerical simulation of the installation of small diameter utility pipes underneath flexible pavement using traditional open-cut installation techniques. The objective of the numerical simulations presented in the following Sections are to analytically investigate the behavior of flexible pavement structure during excavation of utility cut/trench and the influence of backfill compaction on performance of the installed HDPE pipe.

The following Sections include description of the modeling procedure, assumptions and simplifications used for the analyses, analytical modeling of the HDPE pipe installed beneath flexible pavement at CPATT field test facility, and comparison of the analytical results with measured field data. Results from the simulations and discussion of the key findings including the impact of trench excavation on pavement structure response are then presented.

7.2 Pipe Installation Simulations

7.2.1 Numerical Approach

FLAC^{3D} was used to develop a numerical model with the goal to examines the impact of utility pipes installed using open-cut methods across flexible pavements and the performance of the installed pipe. The components of the pavement structure were modeled with continuum zones and the pipe was model with structural (shell) elements. The soil-pipe interaction problem is idealized as a two-dimensional plane strain problem.

The fact that the observed pipe response during the field-scale installation presented in Chapter 6 did not vary significantly along the length of the buried pipe justifies the two-dimensional plane strain approximation.

Figure 7.1 shows the numerical grid used to simulate the field-scale pipe installation approximately 1.5m beneath the CPATT Test Tract Facilities. For illustrative purpose, the zones representing the pipe have been removed from the Figure using FLAC3D built-in null model command. The symmetry of the idealization allows the modeling of only one-half of the problem domain. The size of the grid was selected after a series of parametric analyses, to concurrently optimize accuracy and computational speed.

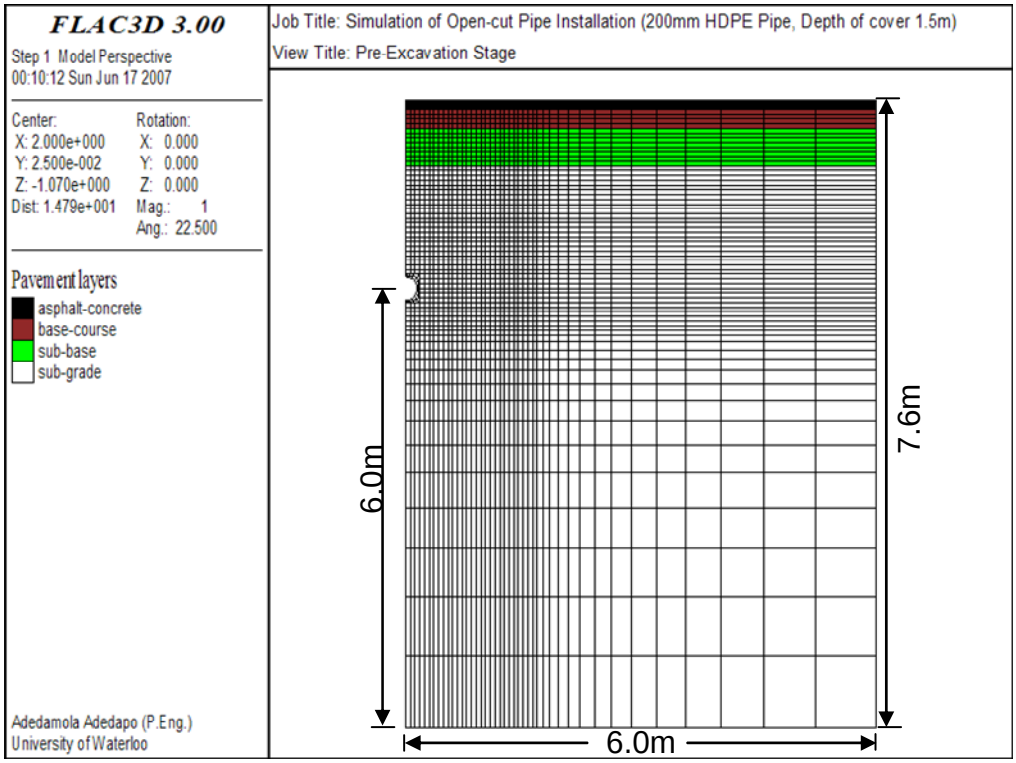

Figure 7.1: *FLAC*^{3D} grid used for simulation of open-cut pipe installation

The flexible pavement was idealized as a layered structure comprising of asphalt layer, granular base and subbase layers and soil subgrade as shown in Figure 7.1. All the layers were assumed to be fully bonded and to have homogenous isotropic material properties. The thickness of the asphalt concrete layer, road base and subbase layer are 100mm, 150mm, and

300mm respectively while the subgrade was assumed to be infinite. The HDPE pipe has a nominal diameter of 200mm and a wall thickness of approximately 12.5mm. The right hand boundary is placed 6.0m away from the center of the pipe with a restricted horizontal displacement and free vertical displacement. The bottom boundary is located 6.0m below the center of the pipe with a restricted vertical displacement and free horizontal displacements.

The stages of construction including trench excavation, preparation of the bedding, pipe placement and trench backfilling with compacted soil in small lifts were simulated in the numerical analyses. The numerical computation was completed in large-strain deformation mode to ensure that the large strain response of the trench walls are captured during trench excavation and restoration.

7.2.2 Material Properties

The asphalt concrete was modeled as a linear elastic material. The granular base, subbase and soil subgrade materials were modeled as non-linear elastic plastic material with Mohr-Coulomb failure criterion and non-associated flow rule. The proposed constitutive model described in Chapter 3 was implemented in *FLAC*^{3D} and used to model the soil non-linearity with confining pressure. The material properties assigned to the granular base, subbase and subgrade soil, shown in Table 7.1, were obtained from the results of extensive laboratory tests on compacted soils published by Selig (1988). Properties of the asphalt concrete used for the analyses were those published in by Lytton et al (1993). The material properties assigned to the base and subbase were those of well-graded sandy gravel (Granular 'A') and well-graded gravel (Granular 'B'), respectively compacted to 90-95% standard proctor maximum dry density and the subgrade material was assumed to be a sandy silt. The backfill material used for trench restoration is assumed to be Granular 'A'. The HDPE pipe was modeled as an elastic material with short-term apparent modulus of elasticity 758MPa and Poisson's ratio of 0.35. The HDPE material properties assigned to model were those recommended by Plastic Pipe Institute (PPI, 2000).

Table 7.1: Summary of pavement material properties used for open cut pipe installation simulation

Properties		Asphalt Concrete	Granular Base	Granular Sub-base	Subgrade
Elastic bulk modulus (kPa)		1.75×10^6			
Elastic shear modulus (kPa)		8.08×10^6			
Modulus number,	KL		950	640	440
Modulus exponent	n		0.6	0.43	0.4
Failure ratio	Rf		0.7	0.75	0.95
Initial bulk modulus ratio	B_i		187	102	120.8
Volumetric coefficient	ε_u		0.014	0.036	0.043
Unloading/reloading modulus number	KUL		1140	768	528
Friction angle at a confining pressure of 101.4 kPa (1 atm)	ϕ_0		48°	42°	34°
Friction angle reduction value for tenfold increase.	$\Delta\phi_0$		8°	4°	0°
Density (kg/m^3)		2400	2200	1800	1800

7.3 FLAC^{3D} Simulation of Field Scale Open-cut Pipe Installation

1n October 2003, a 200 mm (8in) instrumented SDR-17 high density polythene (HDPE) was installed 1.67m below the CPATT Test track HL3-1 control test section using traditional open cut-and-cover construction method. Ontario Provincial Standard Specifications for Pipe Sewer Construction by Open Cut Method (OPSS 410) were followed. Complete details description of the field installation process can be found in Section 6.4 and also in Knight et al (2004). The pavement structure layers and materials properties are similar to those described in the preceding Sections.

The changes in pipe deflections were continuously monitored throughout the pipe installation and trench restoration stages. Details of the installation induced pipe deflections are presented in Section 6.7.1. The deflection measurements at the end of construction indicate that the pipe

experienced a change in vertical and horizontal diameters approximately +1.2 and -1.0mm, respectively. These well documented field installations provide an exceptional case study for the validation of the numerical simulations presented in this Chapter.

Numerical modeling of the field-scale open- cut pipe installation is presented in the following Sections. The installation stages simulated numerically included trench excavation, preparation of the bedding, pipe placement, and trench backfilling with compacted soil in small lifts.

7.3.1 Trench Excavation Simulation

The schematic of the unsupported trench excavation is shown in Figure 7.2. The overall depth of excavation is 2.0m and the width is 1.0m given a clearance of 0.4m on either side of the pipe. Excavation was simulated in stages so that it will be similar to actual excavation in the field. Each time approximately 0.25 to 0.3m excavation was completed by removing the affected zones with *FLAC*^{3D} inbuilt 'null model' command before running the pavement model to equilibrium. This process was continued until the required depth of excavation was achieved. The change in stresses and deformations were monitored throughout the excavation simulations to determine the impact of excavation on the pavement structure.

A small cohesion value (c = 5kPa) was introduced in the pavement model to prevent premature soil yielding in locally low confinement pressure zones and to account for possible additional apparent cohesion due to small amount of moisture in the soils. The magnitude of the cohesion did not introduce any significant increase to the strength of the pavement material. Detailed discussions on the impact of excavation on the pavement structure are presented in subsequent Sections.

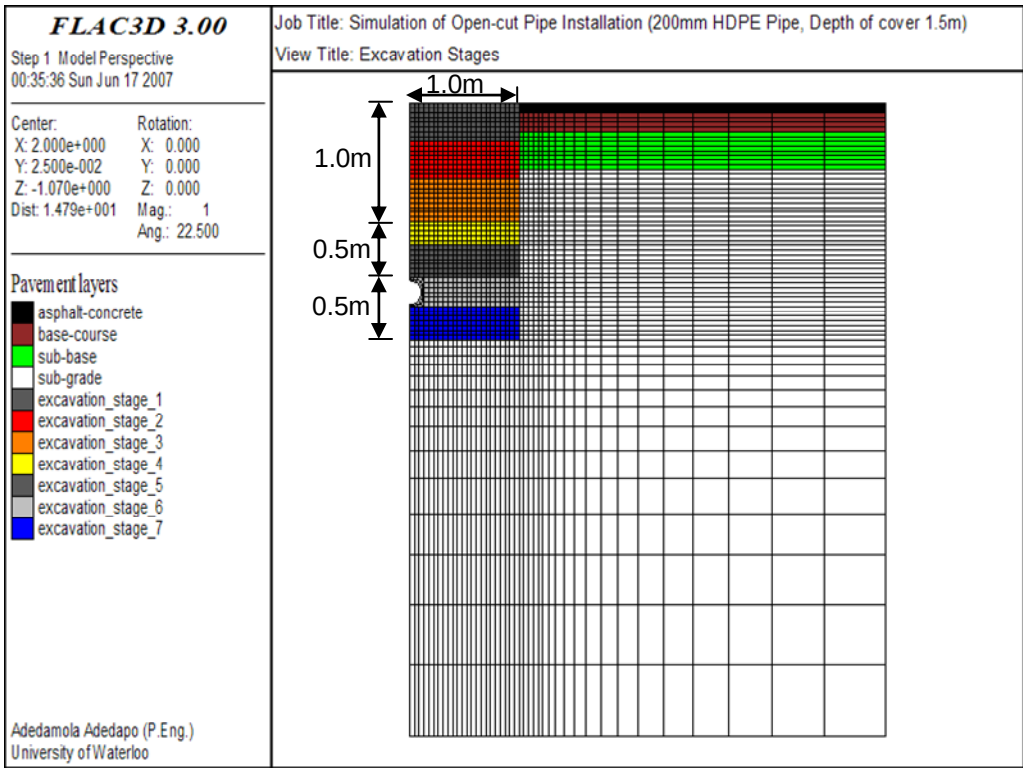

Figure 7.2: Excavation sequence for open-cut pipe installation simulation

7.3.2 Trench Restoration Simulation

Trench restoration activities simulated include the preparation of the bedding, placement of HDPE pipe, and trench backfilling with compacted soil. Approximately 0.3m of bedding material (Granular 'A') was placed at the bottom of the excavation and compacted, followed by the placement of pipe and backfill placement and compaction in small lift from pipe invert up to the elevation of the pavement surface. The backfill from the invert to the crown of the pipe was placed in two lifts of approximately 0.1m while the thickness of subsequent lifts placed above the crown was about 0.3m. Granular 'A' was used as the backfill materials as well.

Observations from the field-scale investigations indicate that the performance of the pipe and the restored trench are significantly influenced by the compaction of the backfill soil. Compaction of backfill soil has two different effects on the backfill material. First, it increases the lateral earth pressure in the backfill (Duncan et al, 1991). Secondly, it reduces

the Poisson's ratio of the backfill. Both effects were simulated by applying a uniform surcharge pressure to the surface of each 'new' soil layer before solving the model to equilibrium. The surcharge pressure applied during the numerical placement of the backfill lift was removed prior to the placement the next lift. This vertical stress increment was applied only to the top of the soil backfill zones at each lift as the trench was being restored from bottom up.

7.3.3 Pipe Deflections obtained from Simulation of Field-scale Open-cut Pipe Installation

A plot showing change in pipe deflection versus computational steps for surcharge pressure of 10kPa is presented in Figure 7.3, the plot shows a step-like pattern that resembles pipe-deflection time history plots obtained from the field scale installation presented shown in Figures 5.45. Positive values indicate a reduction in the diameter of the pipe. The step-like pattern shown in Figure 7.3 clearly reflects the significant effect of backfill lift placement and compaction on the pipe.

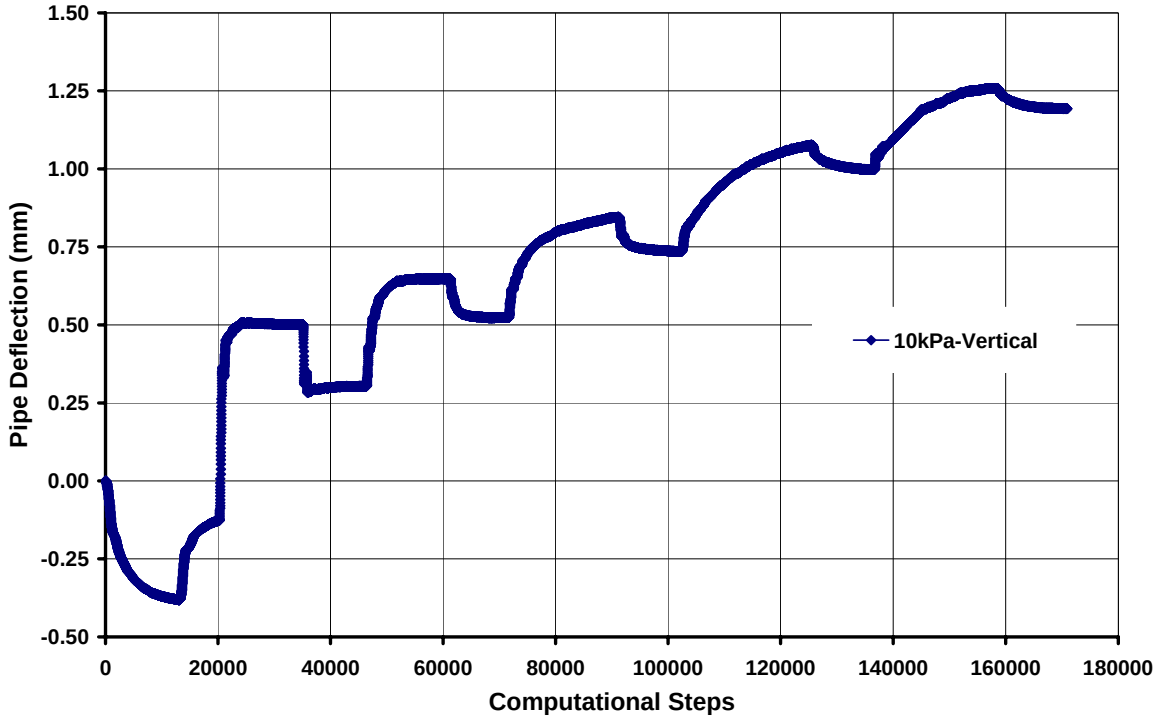

Figure 7.3: Typical pipe deflection versus *FLAC*^{3D} computational steps curve

Simulation of backfill compaction was completed with vertical stresses of 5, 10 and 20 kPa. Figure 7.4 shows the change in pipe deflection with height of backfill for the various compaction surcharge pressures i.e. 5, 10 and 20 kPa. The first backfill lift placed on the side of the pipe up to the springline, resulted in an upward deflection of the pipe in the vertical direction and an inward deflection between the springlines. The placement and compaction of subsequent backfill lifts above the crown of the pipe resulted in compression of the pipe in the vertical direction and extension in the horizontal diameter of the pipe. Although the resulting pipe deflection is proportional to height of backfill, the relationship is not linear for the entire backfill height. The slope of deflection versus height of backfill reduces as additional backfill is placed. This is consistent with the field observations. The impact of the backfill compaction diminishes with increased backfill height. This resulted in the piecewise linear nature of the plots.

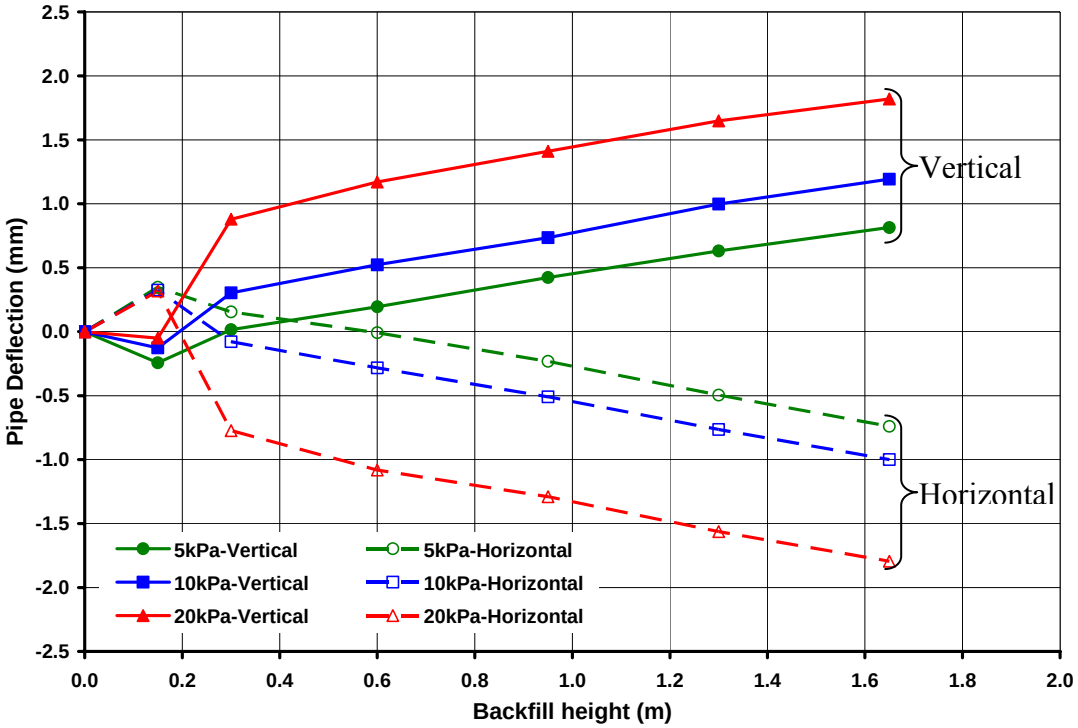

Figure 7.4: Pipe deflection versus height of backfill for different compaction pressure

As shown in Figure 7.5, compaction surcharge pressure of 10kPa produced the most satisfactory agreement between predicted and measured pipe responses during field installation. Specifications matching the reversible plate compactor used during the actual field installation recommend a dynamic contact pressure of approximately 115 kPa.

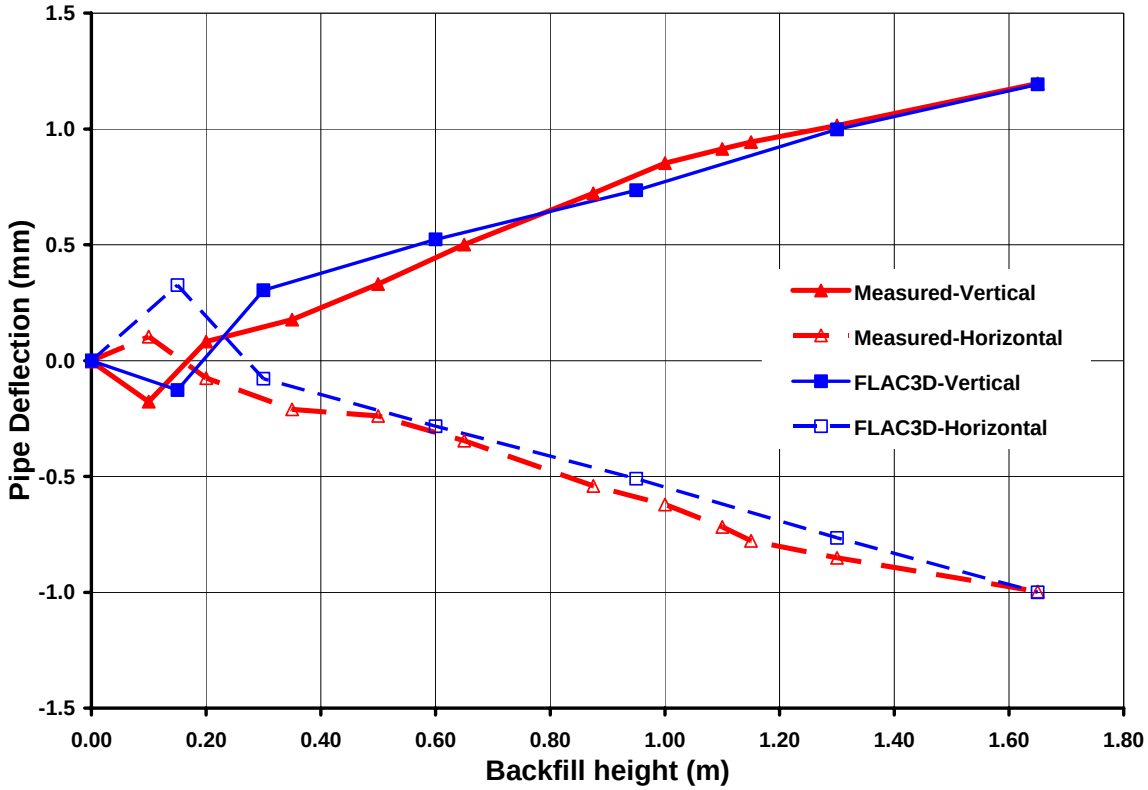

Figure 7.5: Comparison of measured and *FLAC*^{3D} estimated pipe deflection

This value resulted in excessive pipe deformation when used as uniform surcharge pressure across the entire soil surface. The change in pipe diameter at the end of trench restoration and the percent difference between measured deflection and those obtained from *FLAC*^{3D} simulations with 10kPa surcharge load are summarized in Table 7.2. The estimated pipe deflections at the end of trench restoration are very comparable to the observed deflections during the field scale installation. The maximum difference between the observed and *FLAC*^{3D} estimated deflections were less than 1.0%. The close agreement between the estimated and measured pipe deflection demonstrates the ability of *FLAC*^{3D} to simulate the open-cut pipe installation process.

Table 7.2: Comparison of pipe deflection estimated by *FLAC*^{3D} and measured values

Properties	**Field Measurement**	***FLAC*^{3D}**
Vertical Deflection (mm)	1.2	1.19
Horizontal Deflection (mm)	-1.0	-0.99

7.3.4 Impact of Trench Excavation on Pavement Structure

The mechanism, magnitude, and extent of deformation within the pavement structure due to open-cut pipe installation was investigated by monitoring changes in principal stresses, strains, and displacements within the pavement structure throughout the numerical simulation. The variation of these parameters during the simulation and their implication on the performance of the pavement structure are presented and discussed herein.

Principal stresses

Contour plots of the minimum (σ_1) and maximum (σ_3) principal stresses prior to trench excavation are presented in Figures 7.6 and 7.7 respectively. Note that because compressive stresses are negative in *FLAC*^{3D}, the minimum (σ_1) principal stress is the most negative (major) principal stress and conversely the maximum (σ_3) principal stress is the least negative (minor) principal stress.

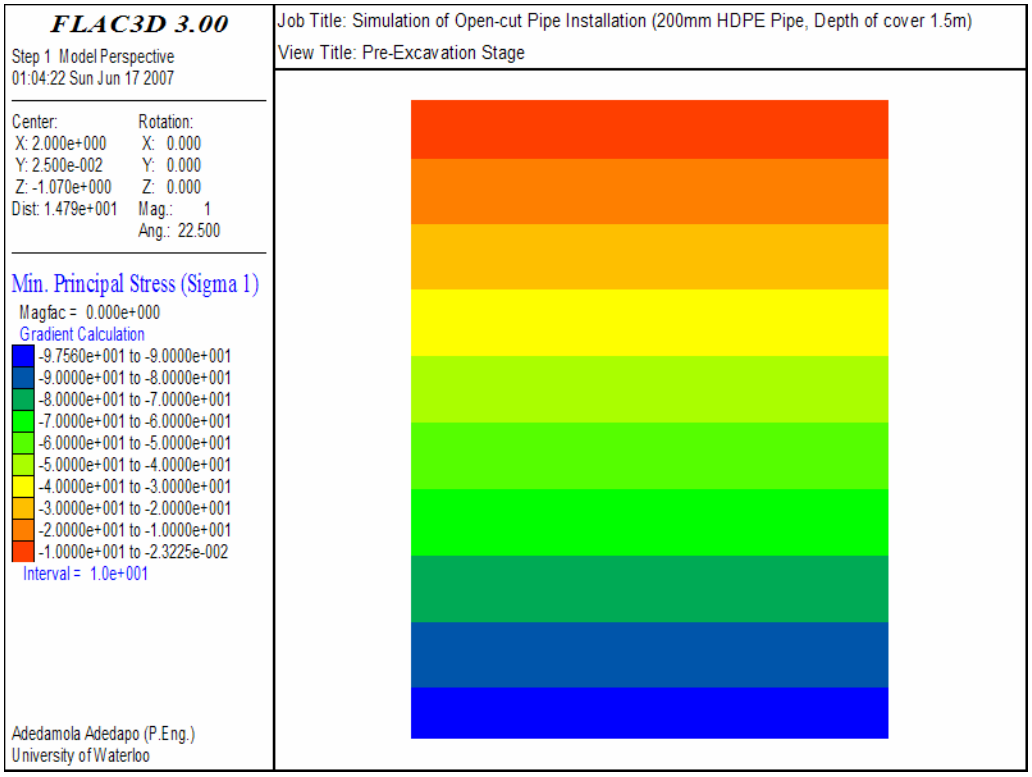

Figure 7.6: Minimum principal stress (σ_1) contours prior to trench excavation

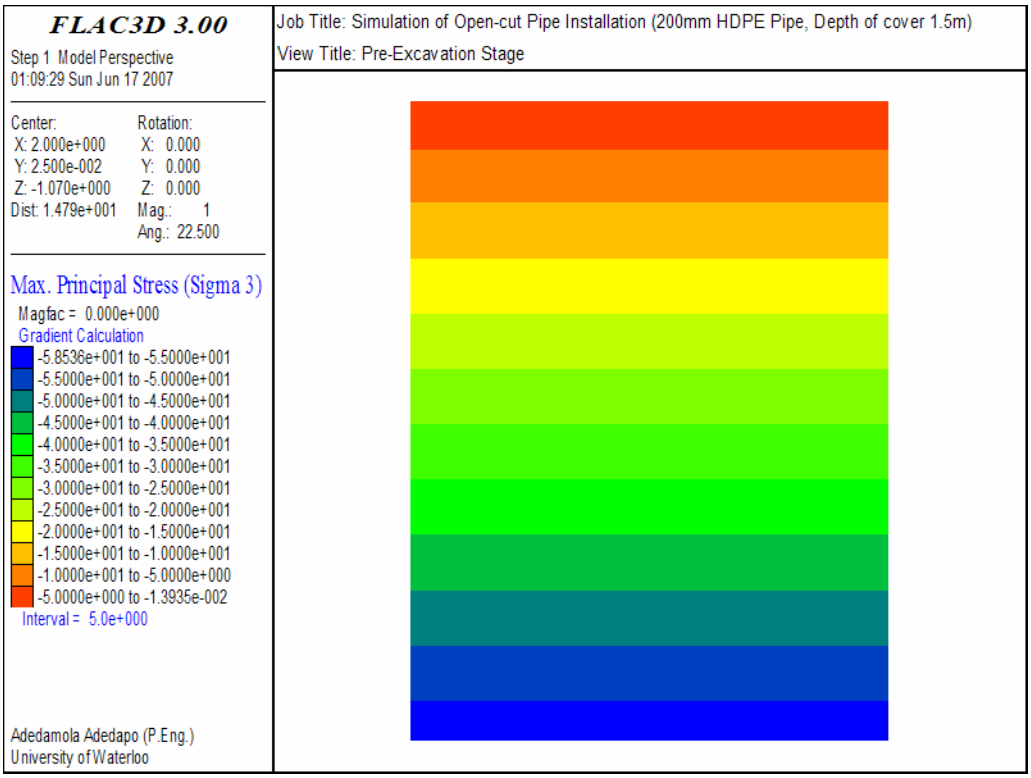

Figure 7.7: Maximum principal stress (σ_3) contours prior to trench excavation

As the trench excavation progressed, an induced stress field developed in the pavement structure adjacent to the excavation. The contours plots of the maximum principal stress (σ_3) around the trench at excavation depth of 1.0, 1.5 and 2.0m are presented in Figures 7.8 through 7.10, respectively. Similarly, the contour plots showing the minimum principal stress (σ_1) in the soil surrounding the trench at excavation depth of 1.0, 1.5 and 2.0m are presented in Figures 7.11 through 7.13, respectively. Figures 7.8 to 7.10 indicate that confining stresses or maximum principal stresses (σ_3) are considerably reduced in the soils adjacent to the face of the trench due to the excavation and unloading resulting in lateral deformation, which releases the horizontal stress. The change in minimum principal stresses (σ_1) or vertical stresses were less severe than the change in horizontal stresses near the face of the trench excavation due to the influence of overburden stress. However, the variation of principal stresses at the base of the excavation due to the unloading was more significant compared to the variation in horizontal stresses.

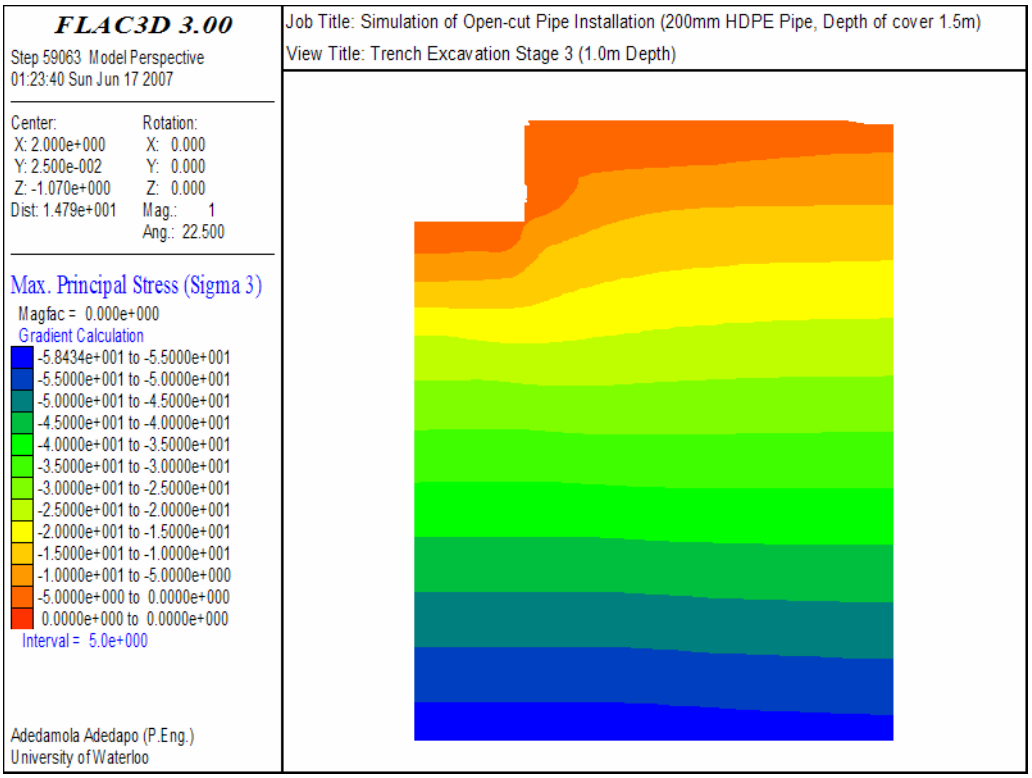

Figure 7.8: Maximum principal stress (σ_3) contours at excavation depth of 1.0m

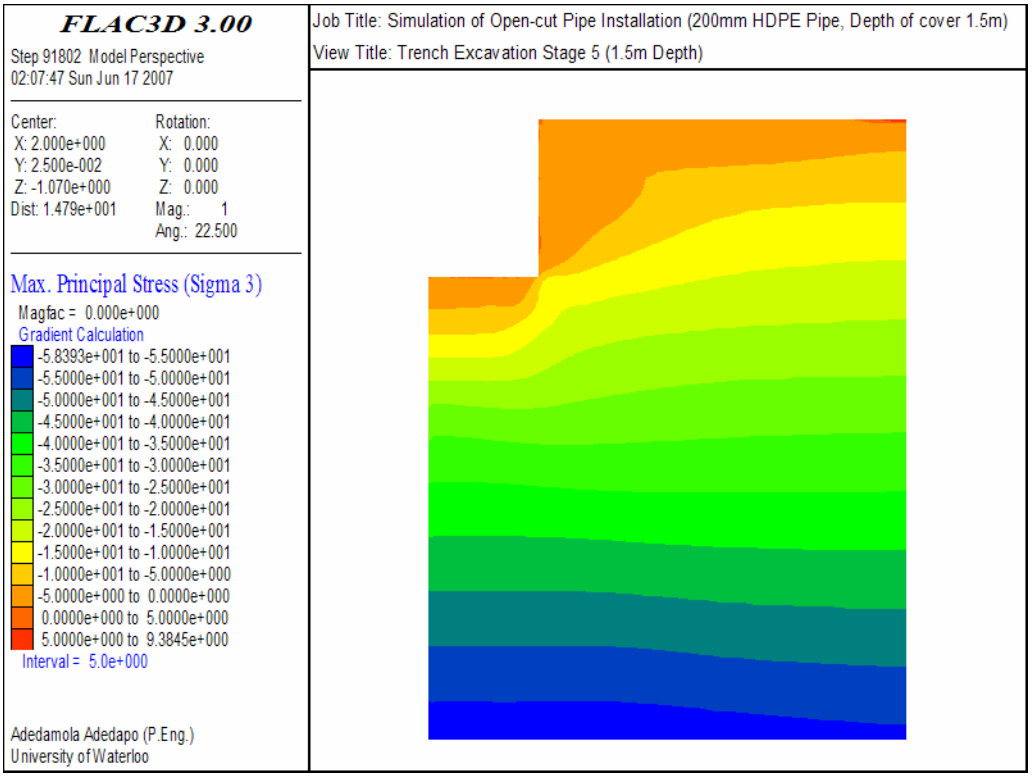

Figure 7.9: Maximum principal stress (σ_3) contours at excavation depth of 1.5m

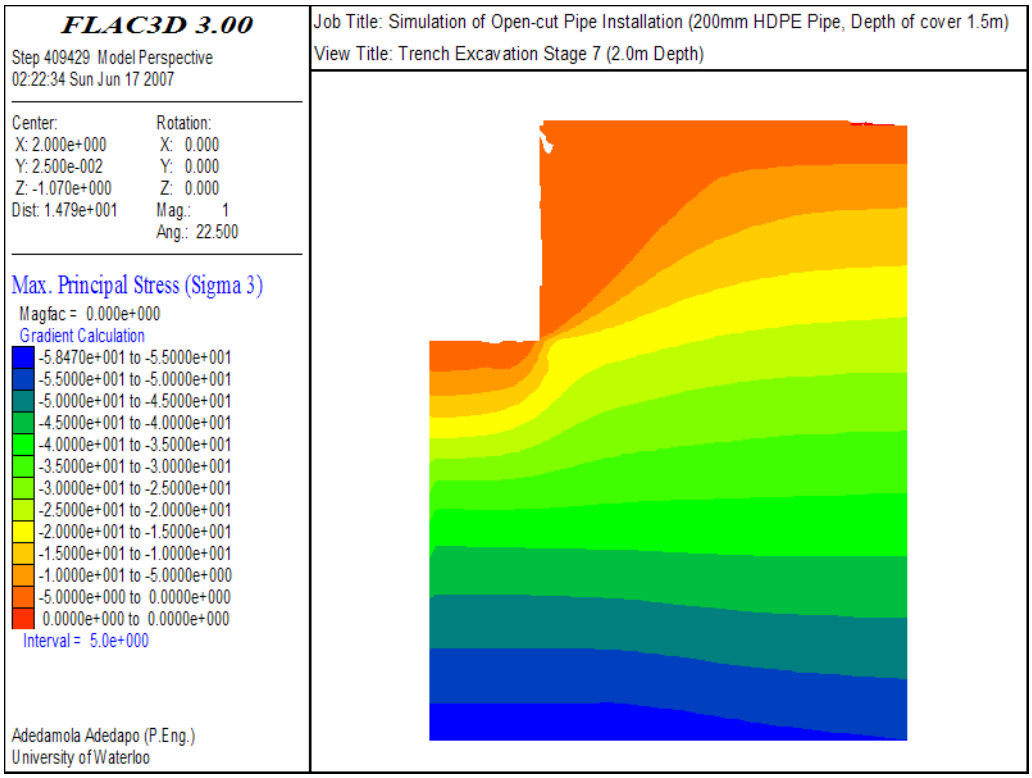

Figure 7.10: Maximum principal stress (σ_3) contours at excavation depth of 2.0m

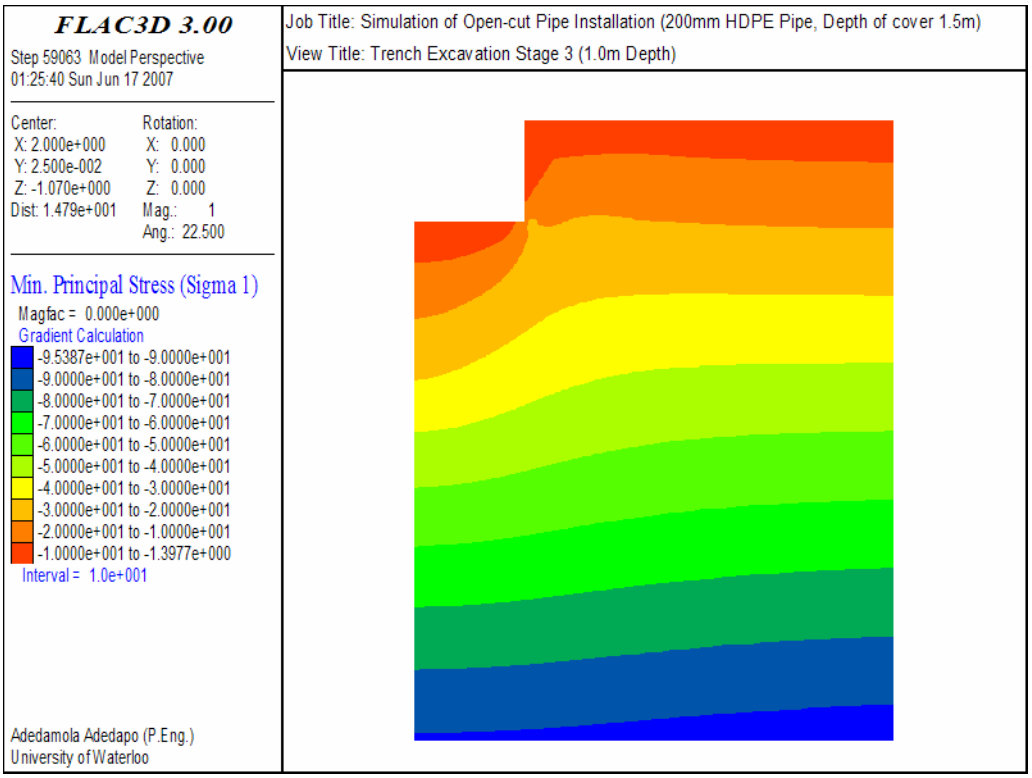

Figure 7.11: Minimum principal stress (σ_1) contours at excavation depth 1.0m

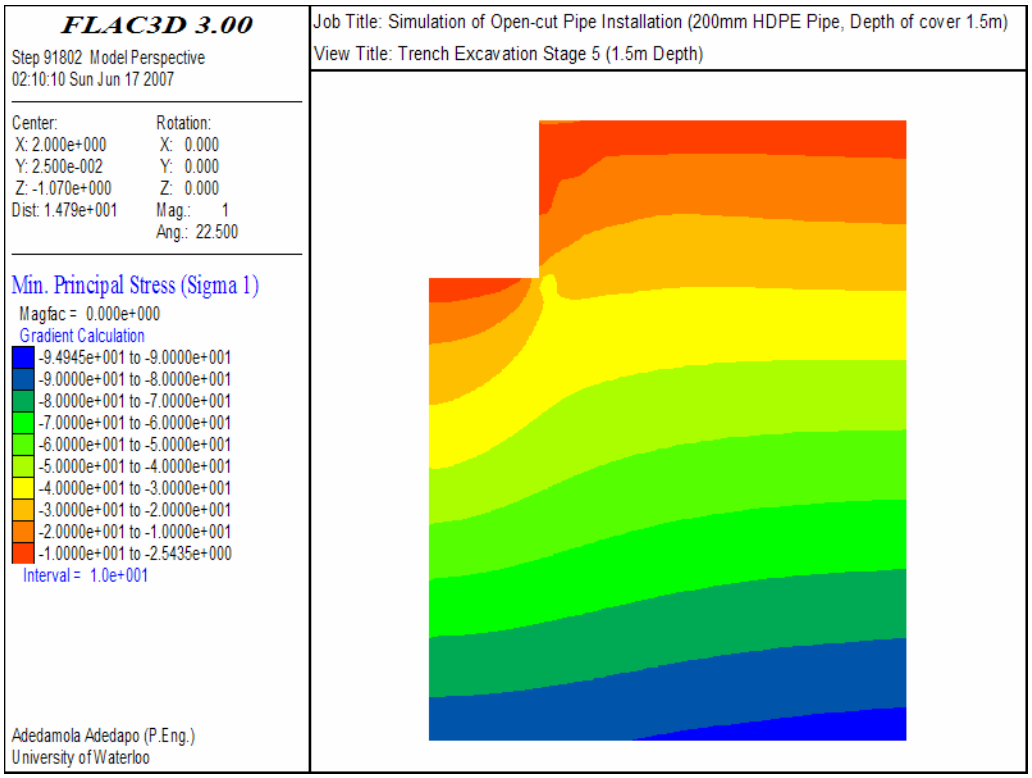

Figure 7.12: Minimum principal stress (σ_1) contours at excavation depth 1.5m

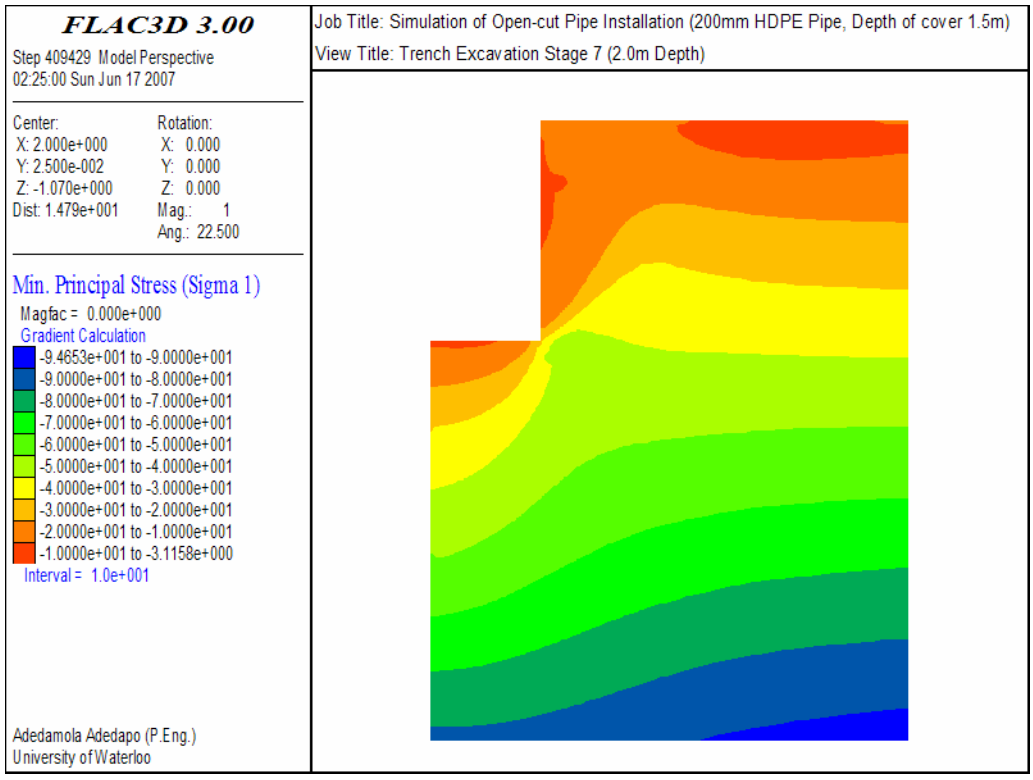

Figure 7.13: Minimum principal stress (σ_1) contours at excavation depth 2.0m

The observed reduction in the principal stresses near the face of the excavation has a significant impact on the shear strength, as well as, the stiffness of the pavement structure material at that location. Figures 7.14 and 7.15 show the contour plots of bulk modulus in the granular layers prior to and after trench excavation, respectively. It is clear from the contour plots that the stress relief near the face of the excavation resulted in reduced stiffness within the affected zones. The stress reduction also resulted in decreased shear strength within soil zones adjacent to the face of the trench due to loss of confinement.

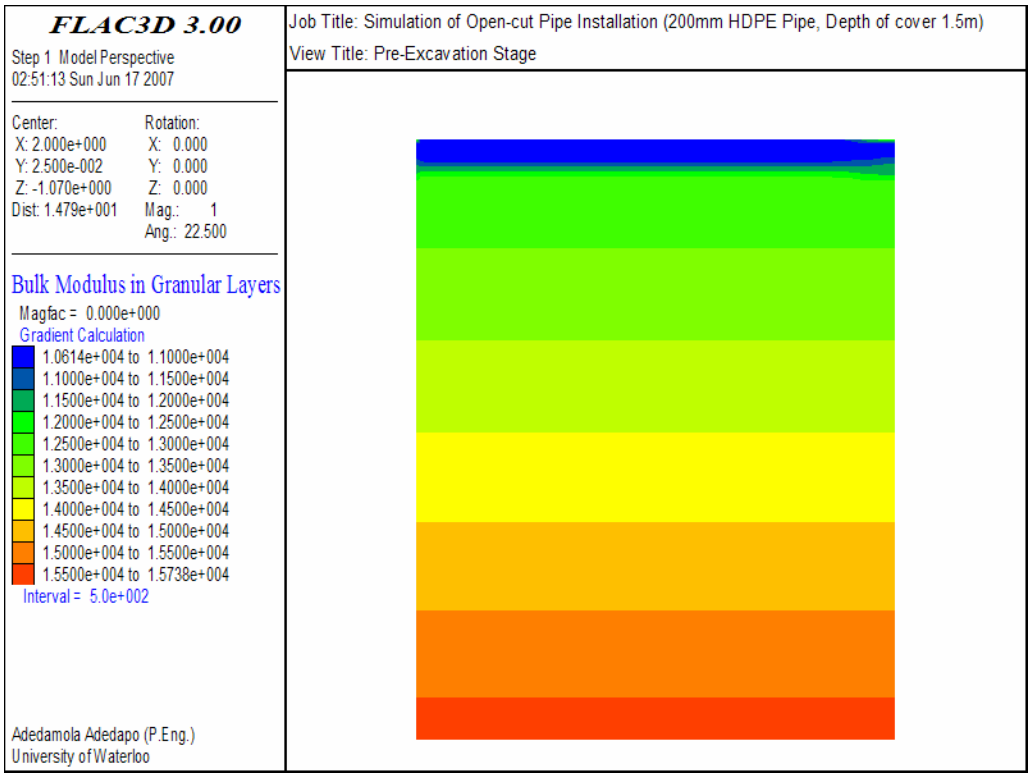

Figure 7.14: Bulk modulus contours in granular layers prior to trench excavation

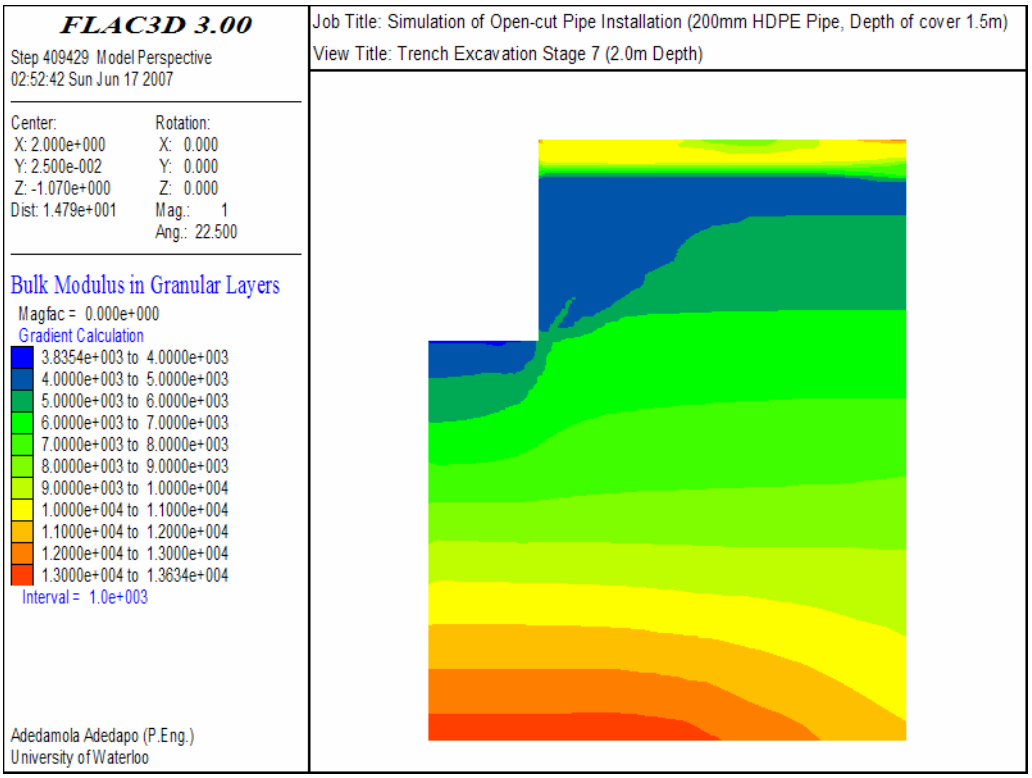

Figure 7.15: Bulk modulus contours in granular layers at excavation depth 2.0m

Shear and Volumetric Strains

The contour plots of the shear strains near the trench at excavation depth of 1.0, 1.5 and 2.0m are presented in Figures 7.16 through 7.18, respectively. Similarly, the contour plots showing the volumetric strains in the soil surrounding the trench at excavation depth of 1.0, 1.5 and 2.0m are presented in Figures 7.19 through 7.21, respectively. The sign convention for volumetric strains in *FLAC*^{3D} follows those of direct stresses such that positive volumetric strain indicates extension and negative strain indicates compression.

The shear and volumetric strain plots suggest evidence of progressive deformation within the soil near the face of the excavation as the excavation progressed and confining stress is reduced. At an excavation depth of 1.0m, deformation within the pavement structure extended to about 0.54m away from the face of the excavation into the soil. At this excavation depth, the maximum shear and volumetric strain of 1.16e-02 and 1.63e-02, respectively, occurred within the soil immediately adjacent to the excavation face and gradually dissipate further away from the face of the trench.

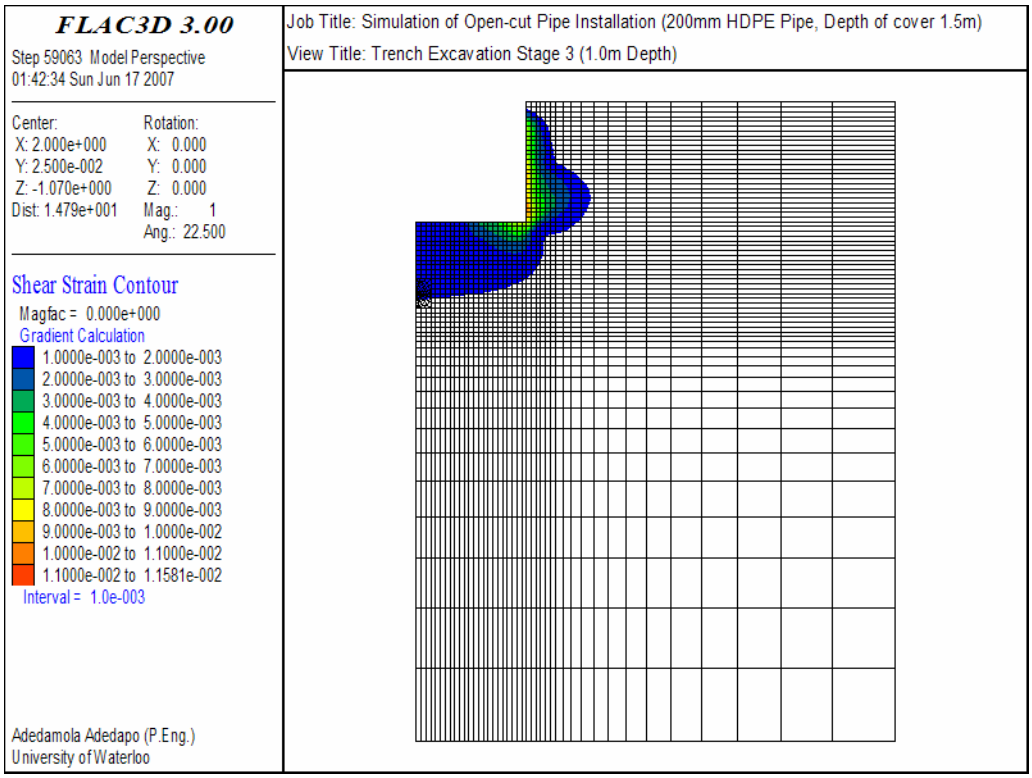

Figure 7.16: Shear strain contours at excavation depth 1.0m

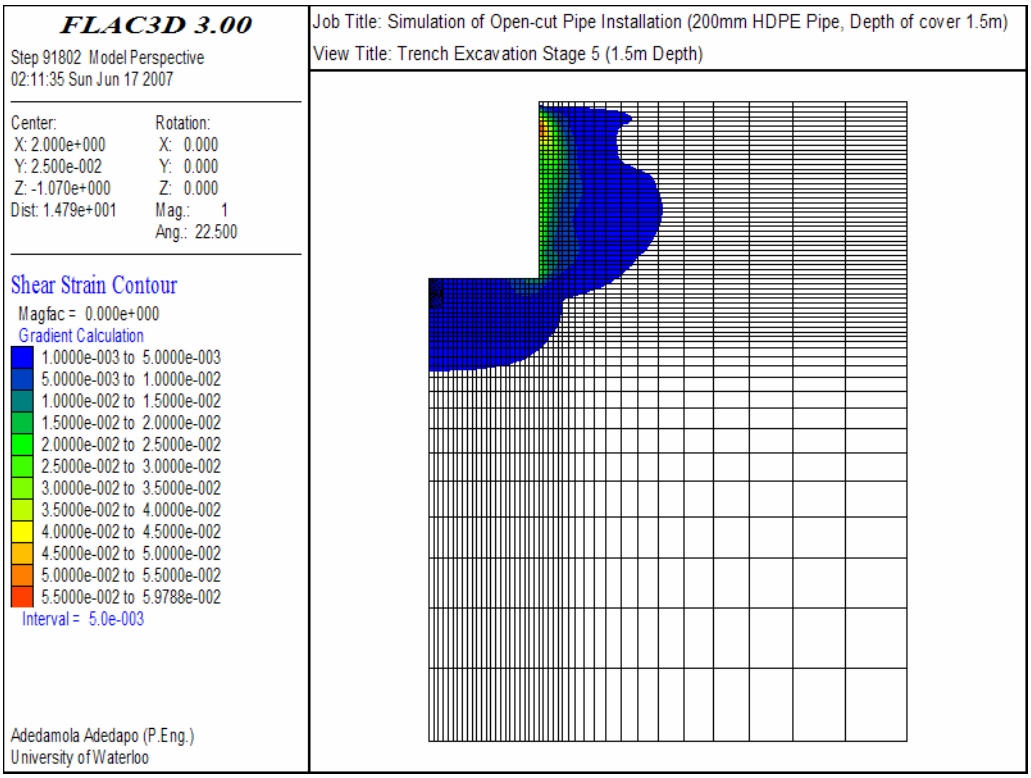

Figure 7.17: Shear strain contours at excavation depth 1.5m

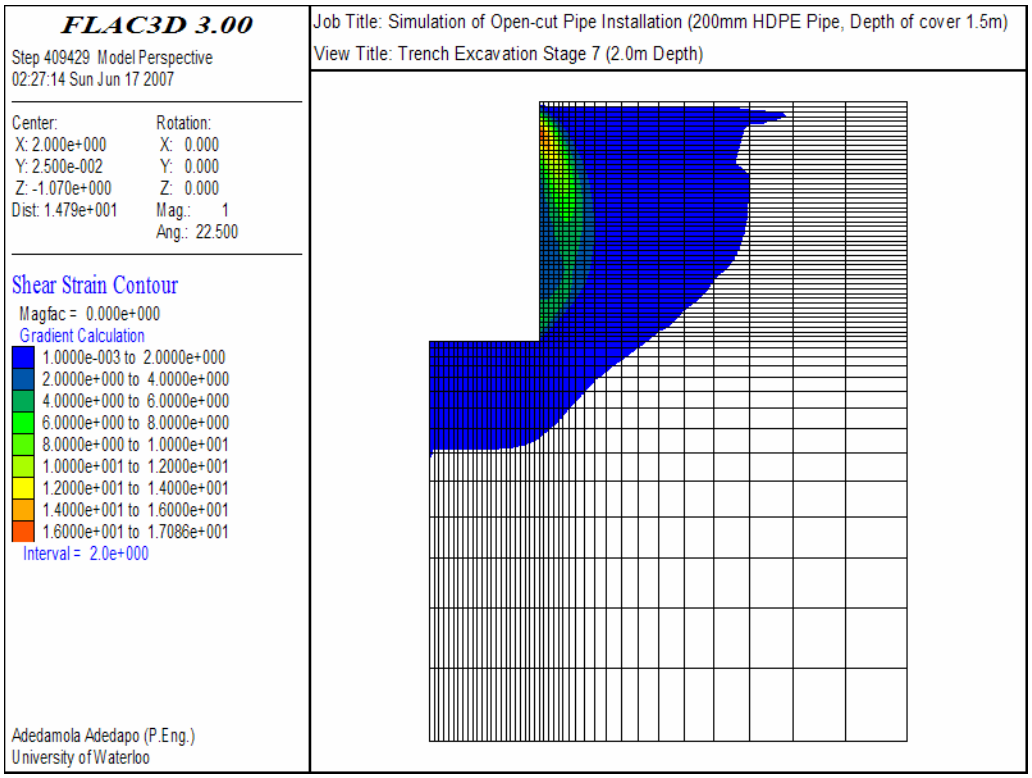

Figure 7.18: Shear strain contours at excavation depth 2.0m

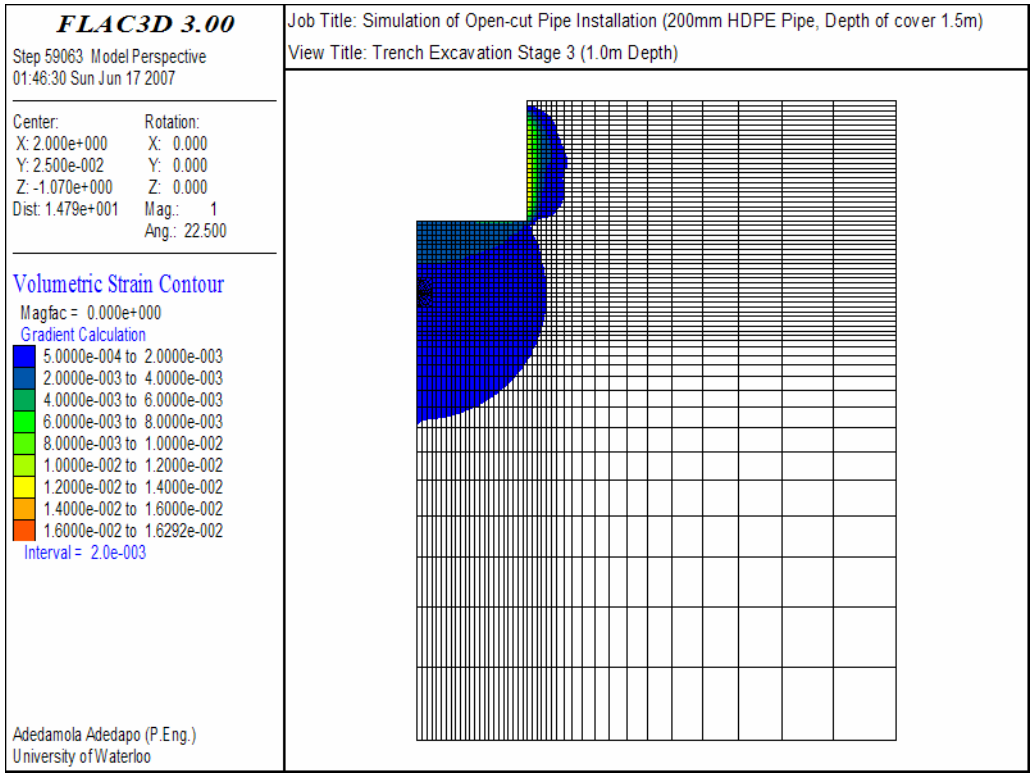

Figure 7.19: Volumetric strain contours at excavation depth 1.0m

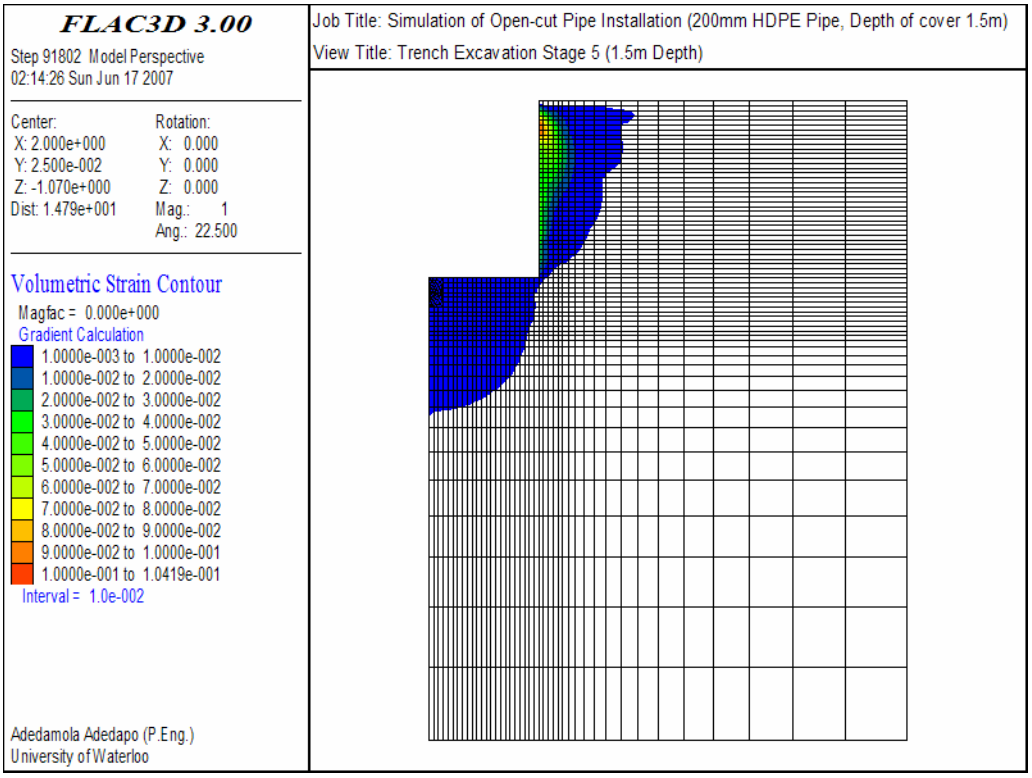

Figure 7.20: Volumetric strain contours at excavation depth 1.5m

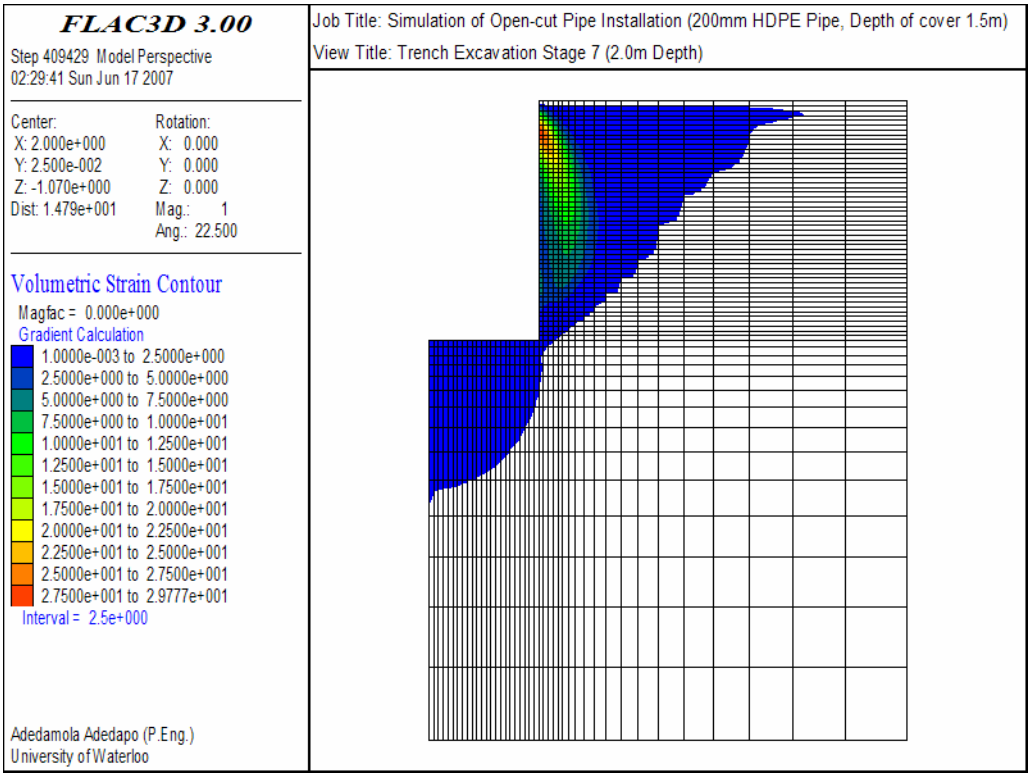

Figure 7.21: Volumetric strain contours at excavation depth 2.0m

As the trench was excavated to a depth of 1.5m, the zone of deformation extended to about 1.03m away from the face of the excavation; while the magnitude of shear and volumetric strain near the face of the trench increased to 6.0e-02 and 1.0e-01, respectively. The maximum shear and volumetric strain at the face of the excavation increased to 1.7e-01 and 3.0e-01, respectively, as the depth of excavation reached 2.0m. The zone of distress within the pavement structure now extended to about 1.65m from the face of the trench. If x is the extent of the distress zone from the face of the excavation and H is the depth of excavation, then the ratio $\frac{x}{H}$ for trench depths 1.0, 1.5 and 2.0m are 0.54, 0.67 and 0.82, respectively.

The stiffness of the asphalt concrete layer appeared to provide some resistance to lateral straining and movement of granular base material towards the trench. Examination of the plasticity state at the end of 2.0m depth of excavation, Figure 7.22, indicates that a failure plane (active Rankine state) has developed within the model -especially in the subgrade soil. It appears that the asphalt concrete layer at the above the *'active zone'* provided some stability to the model by preventing the development of a tension crack.

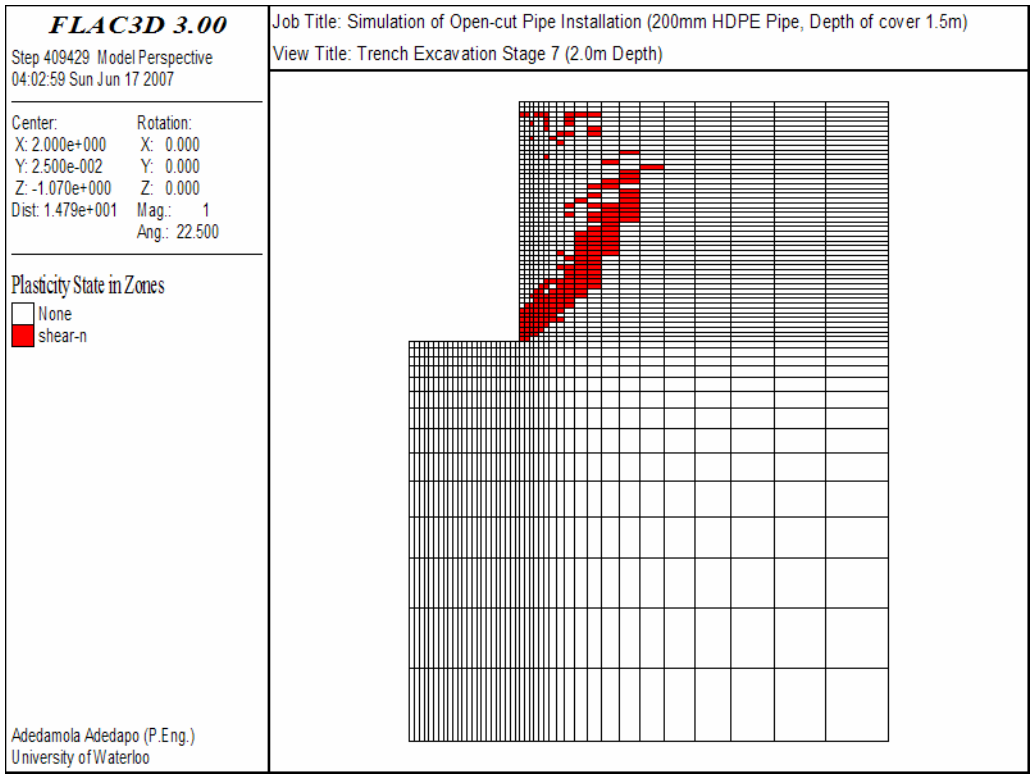

Figure 7.22: Plasticity state within the pavement at excavation depth 2.0m

The mode of deformation predicted by the numerical model is consistent with field observations as minor sloughing was observed near the face of the trench during the actual field installation. The shear and volumetric strain contour plots suggest that the magnitude and the extent of disturbance created within the pavement surface increase as the depth of excavation increases.

Ground Displacements

Ground displacements in the vicinity of the trench at excavation depths of 1.0, 1.5 and 2.0m are presented in Figures 7.23 through 7.25, respectively. The maximum displacement within the pavement structure occurred at the face of the cut with displacement magnitude decreasing away from the face of the trench. The maximum displacement observed at excavation depth of 1.0, 1.5 and 2.0m were 3.2, 14.1 and 50.0 mm, respectively and the extents of ground movement are similar to those of shear and volumetric strains.

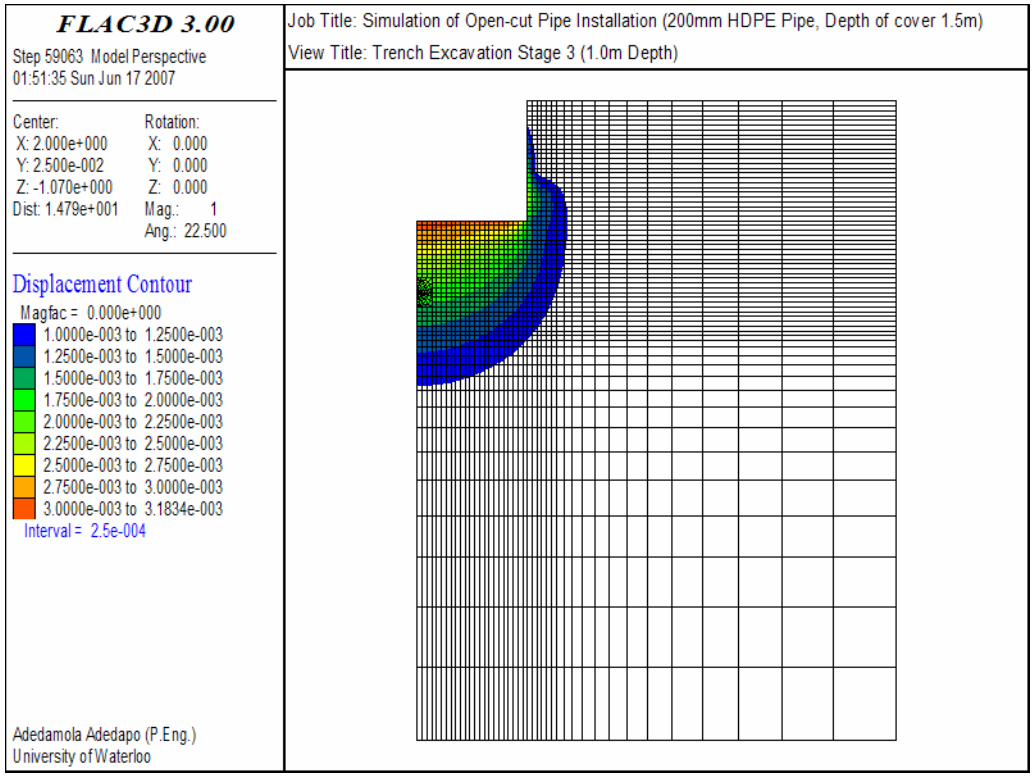

Figure 7.23: Displacement contours within the pavement at excavation depth 1.0m

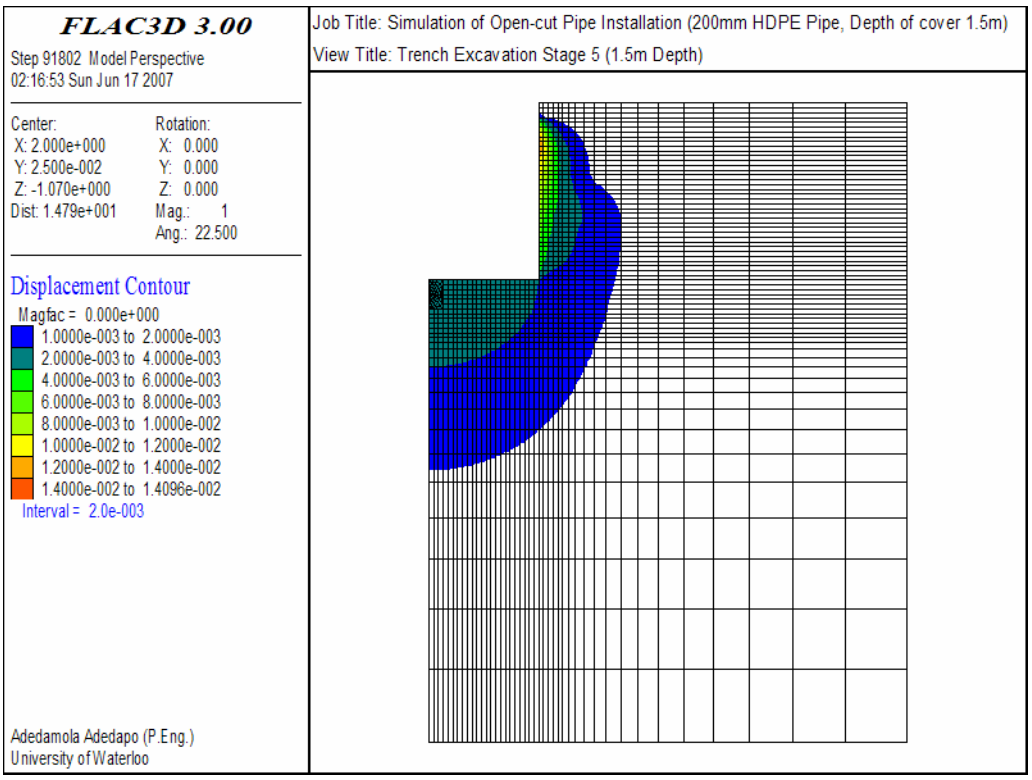

Figure 7.24: Displacement contours within the pavement at excavation depth 1.5m

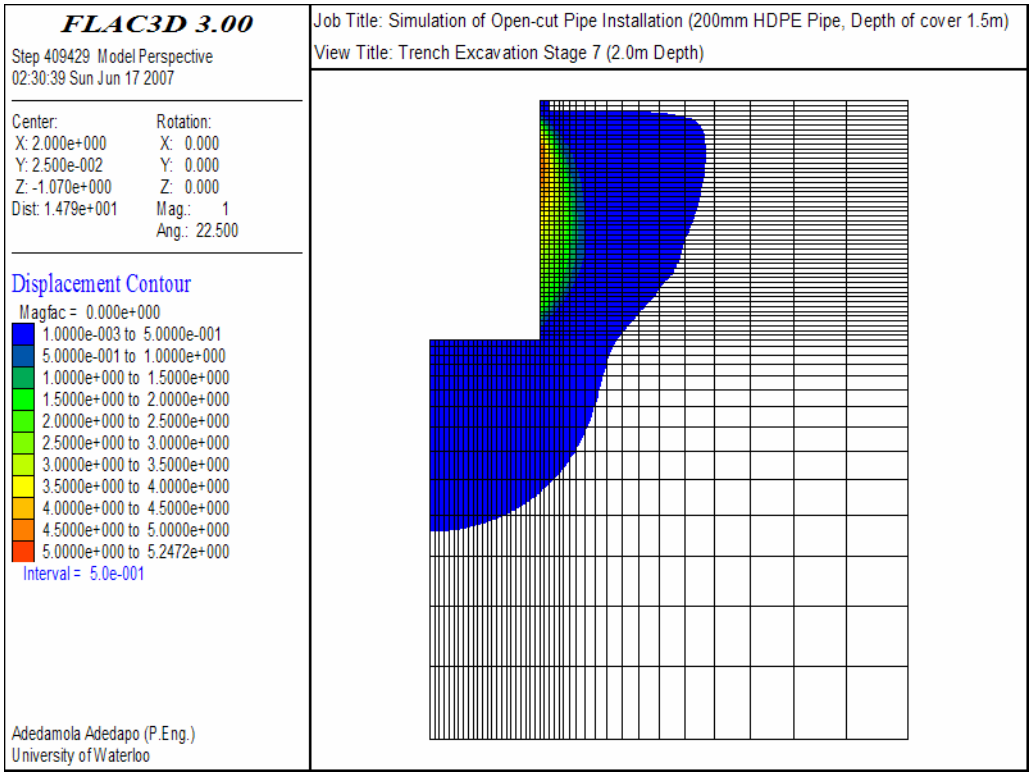

Figure 7.25: Displacement contours within the pavement at excavation depth 2.0m

The pattern of deformation depicted by the strains and displacements plots suggest the development of a localized distress zone within the pavement structure adjacent to the face of the trench probably caused by the reduction of confining stress due to the excavation. The magnitude and extent of distress appears to be proportional to the depth of excavation. The existence of a localized distress zone within the pavement structure depicted by the numerical modeling are consistent with observed distress pattern shown in the Ground Penetration Radar (GPR) Survey Data obtained at the location of the open-cut installed pipe described in Chapter 6.

Previous investigations by Shahin and Crovetti (1987) also suggested the presence of distress zone in subsurface in the vicinity of utility cuts. They conducted an extensive field evaluation of several utility cuts within the City of Burlington, Vermont by visual inspection and the use of non-destructive evaluation technique i.e. Fall Weight Deflectometer (FWD). It was determined that within the utility cut patch area and for some distance up to 1.0m beyond the boundary of the utility cut, there were observable pavement weaknesses and surface distresses. Similar observations around utility cuts were reported by Bodocsi et al (1995) and Lee and Lauter (1999).

7.4 Summary and Practical Significance of Open-cut Installation Simulations

The goal of the numerical analysis presented in this Chapter is to examine pavement structure response to the utility cut and the mechanism that resulted in the observed surface distresses in the vicinity of utility cut on flexible pavement. The influence of backfill compaction on the performance of buried pipes was also investigated.

It was determined from the numerical analysis that when an unsupported excavation is created within a flexible pavement structure, distress zone that extends laterally to a distance of about 0.54, 1.03 and 1.65m for an excavated depth of 1.0, 1.5 and 2.0m, respectively, from the face of the trench are developed within the pavement. The vertical pressure applied on the

backfill material via compaction during trench restoration does not provide sufficient lateral pressure against the face of the trench to re-compact the 'distress zone' around the utility trench. Figure 7.26 shows the presence of distress zone indicated by the positive shear strain within the pavement after trench restoration. The results of the analyses suggest that a more efficient restoration technique is required to eliminate the adverse effect caused by the stress relief within the pavement structure during utility cut excavation. Furthermore, the area of potential pavement deterioration should be extended beyond the edge of the utility cut to encompass the 'distress zones' when determining fees to cover pavement damage and restoration costs.

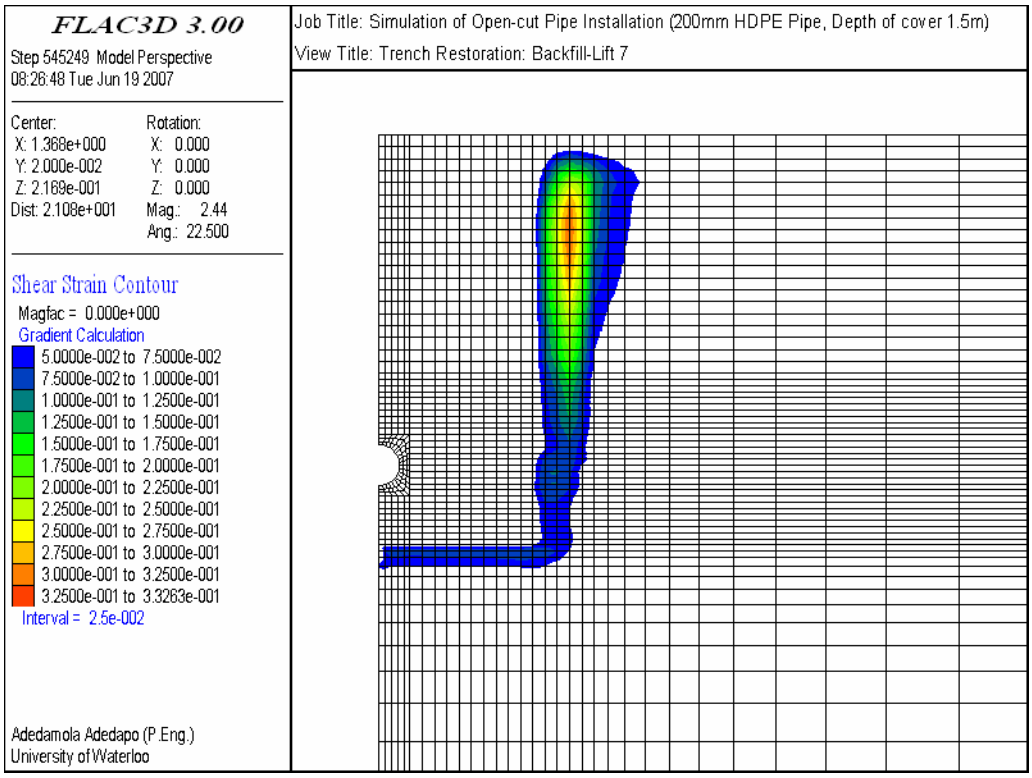

Figure 7.26: Shear strain contours after completion of trench restoration

Accurate prediction of buried pipe response required a technique to account for compaction-induced stresses in the backfill material. A transient 10 kPa vertical surcharge load was applied to the backfill surface at each stage during simulation of backfill placement, and that, together with a combination of appropriate constitutive model and representative soil

parameters produced satisfactory agreement between predicted and field measured pipe responses during field installation.

Backfill compaction has a considerable influence on the magnitude pipe deflection. When the compaction effort was doubled from 5 to 10kPa the resulting deflection increased by about 40%. Increasing the compaction effort from 5 to 20 kPa resulted in 130% increase in the pipe deflection. Appropriate bedding and side support are required should be provided for flexible pipes (such as HDPE) to prevent excessive pipe deformations during installation.

Numerical simulations have shown that a distressed zone will exist outside the excavated trench. This distress zone will occur on both sides of the trench up to a distance equivalent to 80 percent of the depth of excavation even when good construction practices are used. It will also results in deterioration of the pavement and loss of pavement life. HDD simulations have shown that the soil above the installed pipe will have no such distress zone if good construction practices are used to install the pipe i.e. when bore pressure are kept below the initiation pressures. Thus, the chance of HDD pipeline installation resulting in any pavement deterioration or loss of pavement life is low compared to open-cut pipeline installations when best construction practices are used.

Chapter 8: Conclusions and Recommendations

8.1 Conclusions

Pavement deterioration resulting from the installation of utility pipes beneath flexible pavement using traditional open-cut and horizontal directional drilling (HDD) construction techniques and the performance of the installed HDPE pipes were presented in this dissertation. The research work presented in this dissertation was formulated to address the need to (*i*) objectively study issues related to utility pipeline installations using HDD and open-cut excavation and restoration, and its impact of pavement performance; and (*ii*) understand field performance of HDPE when installed using different installation techniques. The research approach devised for the work described in this thesis involved detailed field-scale studies and numerical investigations using *FLAC*^{3D}.

A number of contributions to the understanding of the influence of pipe installation techniques on the performance of flexible pavement and HDPE pipe have been presented in this dissertation. Key findings and contributions from the various investigations conducted for this thesis are summarized and presented in this Chapter. Suggestions for further work are also provided.

8.1.1 Field Scale Investigations Program

The field investigation consisted of installing two 200mm SDR 17 DIPS HDPE pipes beneath flexible pavement using HDD and open-cut construction methods and the development of instrumentation to monitor the performance of the pipes during and after the installation.

A state-of-the-art pavement instrumentation and data acquisition system that captures pavement response in real-time with full remote access capabilities was also developed as part of the field investigation program. The impact of the pipe installation technique on the pavement was objectively evaluated as part of the research effort described in this thesis.

The important findings and contributions from the various aspects of the field investigation program are presented in the following sections.

8.1.1.1 Instrumentation and Data Acquisition System

An important aspect of the field investigation program was the development and refinement of instrumentation and data acquisition installed within the HDPE pipes to evaluate both the short-term (installation induced) and long-term (post installation) performance of HDPE pipe. Pipe parameters monitored include pipe strains, ring deflections and temperature. Additional parameters monitored during HDD installations included bore slurry pressures, drill rig parameters hydraulic pressures, drilling times, and raw drilling fluid pumping rates.

The data acquisition systems used for this study have significant improvement over those used in previous investigations. These include the ability to provide real time feedback and full remote access and control capabilities. The sensitivity and resolution of the LVDTs transducers (±0.001mm) and strain gauges (±10με) for the open-cut installed HDPE pipe was significantly improved by the use of passive filters.

A state-of-the-art pavement instrumentation and data acquisition system was developed and implemented to measure strain in the asphalt concrete and granular materials, total vertical stress distribution, volumetric water content and ground temperature profile within the pavement structure. A monitoring system with complete remote access and control capabilities was designed as part of the field instrumentation program to provide real time continuous monitoring and to automatically report any form of abnormalities within the instrumentation system. The internet based monitoring system provides real-time access and efficient communication link to the test site for fast and easy data transfer. The remote access capabilities considerably reduced the need for frequent site visit necessitated by the large

quantity of data collected during the long-term monitoring period. Furthermore, problems at the test site such as low voltage output from the batteries, damaged sensor etc. were promptly detected and rectified thereby minimizing instrumentation down-time and the loss of data.

8.1.1.2 HDPE Pipe Performance during Installation

The performance of two 200mm SDR 17 DIPS HDPE pipes installed beneath flexible pavement using HDD and open-cut construction methods are well documented in this thesis. This is the first known study that investigates the comparative effect of horizontal directional drilling and traditional open-cut pipeline installation techniques on HDPE pipe performance. The HDD and open-cut installed pipes were installed beneath the pavement section with similar subsurface conditions, vehicle speed and drainage conditions.

Pipe strain and ring deflection measured during pipe installation showed that the HDD installed HDPE pipe experienced the greatest deformation when negotiating the bore curvature and the magnitude of the construction induced deformation decreased with time as the HDPE pipe relaxed following installation. The mechanism that produced deformation in open cut is very different from that of HDD. There is no axial load imposed on open-cut installed pipe and the pipe does not negotiate any bore trajectories. Open cut installed pipe construction induced deformation and bending strain that progressively increased during the installation and compaction of backfill lifts. The maximum strains measured within the HDD and open-cut installed pipe at the end of installation was approximately 850 and 3600 microstrain, respectively. The maximum change in pipe diameter measured at the end of installation in the HDD and open-cut installed HDPE pipe was 0.4 and 1.2 mm respectively. The results obtained from the field-scale monitoring showed that construction induced deformations on HDD installed pipe can be significantly minimized when good drilling practices are employed and properly formulated drilling fluids are used.

The maximum change in pipe diameter measured after the open-cut pipe installation was comparable with values estimated using the modified Iowa's equation. The change in diameter of the HDD installed HDPE pipe immediately after installation using Plastic Pipe Institute design equations was about 100 percent higher than the field measured deflections.

8.1.1.3 Long-term Performance of HDPE pipes

The performance of the HDPE pipes was continuously monitored for a period of about three years following installation and the observed HDPE pipe response to seasonal variations are well documented in this dissertation. The quality and the uniqueness of the data collected over the long-term monitoring period is a significant contribution to the understanding of the performance and design of HDPE pipes, as the data can be used to qualitatively assess the performance of HDPE under shallow depth cover beneath flexible pavement.

The long-term deflection data showed that both the HDD and open-cut installed HDPE pipes experienced continuous steady change in pipe diameter that consist of alternating extension and contraction of the pipe throughout the monitoring period. The pipe deflection time history plots showed sinusoidal wave-like pattern with varying amplitude that is generally related to seasonal variation in temperature. In addition, there are significant evidence from the temperature profile, volumetric moisture content variation measurement and change in magnitude of earth pressure within the backfill that suggest that the behaviour of the shallow buried open-cut installed pipe is also influenced by frost action.

Although each period of pipe contraction is followed by a period of pipe extension, it appears that some of the reduction experienced by the HDD installed pipe between its springlines (change in horizontal diameter) during the contraction phase is not fully recovered during the following extension phase. At the end of the monitoring period, the measured field deflection data indicate the HDD installed pipe had experience gradual cumulative decrease, approximately -0.75mm, in the horizontal diameter and approximately +0.2mm change in vertical diameter at the end of the monitoring period which indicating that the pipe deflected outwardly in the vertical direction. It can be inferred from the difference observed in the measured average cumulative change in vertical and horizontal diameter that side resistance is provided by the soil immediately surrounding the pipe. This side resistance resulted in reduced outward deflection of the pipe in the horizontal direction. Current HDD design methods assume the pipe has no side support.

The magnitude of observed changes in the horizontal diameter of the open-cut installed pipeline is significantly greater, about 46 to 167 percent, than changes observed in the vertical diameter of the pipe. This observation suggests that there is less restraint provided by the backfill material close to the springline of the pipe compared to those at the crown and invert of the pipe. Inconsistent backfill compaction during trench restoration and additional overburden pressure from the prism load acting at the crown of the pipe are some of the probable causes of anisotropy in the stiffness. Thus, the level of restraint provided to the pipe.

The maximum change in pipe diameter of the HDD and open-cut installed pipe measured during the long-term monitoring period were approximately 1.2 and 0.75 mm, respectively. The maximum change in pipe strain measured on the buried pipe during the long-term monitoring period was approximately 4530 microstrain. Overall, the HDPE pipe performed very well over the monitoring period. The deflections and strain levels recorded were very small and well below acceptable levels, and there was no apparent deterioration of the pipe. The results obtained from this research indicate that thermal effects are very significant and are greater than other deflection such as those due to creep. The thermal strains induced on the HDPE pipe are mostly recoverable. Thermal effect on HDPE pipe should be given careful consideration when determining the minimum depth of cover for HDD and open-cut installed PE pipes.

Furthermore, current analytical methods used to predict long-term change in pipe diameter overestimated the measured pipe deflection of HDD and open-cut installed pipes by about 50 and 114 percent, respectively.

8.1.1.4 Flexible Pavement Performance

The research work described in this thesis is the first known study that objectively investigates the comparative effect of directional drilled and conventional open cut and cover pipeline installations on pavement integrity and performance. Obtaining such comparisons under the same levels of subgrade type, pavement structure, traffic, and environmental conditions is unique and the data obtained from the field investigation is of significant importance to the trenchless and pavement industries, as well as public agencies.

The condition of the pavement in the vicinity of the installed pipe was observed prior to and after pipe installations to identify any changes in pavement condition that may have resulted from the pipe installations. The pavement was also examined throughout the long-term monitoring period to determine the influence of pipe installations on the pavement structure performance. Surface elevation survey data, ground penetration radar (GPR) surveys, Falling Weight Deflectometer (FWD) and distress surveys were conducted to evaluate pavement performance.

There was no observable change in the condition of the pavement structure performance in the vicinity of the HDD installed pipe following pipe installation. The elevation survey and pavement surface distress data indicated that there has been no change in elevation, no crack or other visible pavement distress at the HDD installed pipe location. FWD and GPR survey data also showed that the pavement structure integrity was not altered by the HDD pipe installation. The effect of frost at the HDD installed pipe location was similar to the rest of the pavement. Therefore no discontinuity was created in the pavement as the result of the HDD installation.

Despite the use of best construction practices, the traditional buried pipe installation technique resulted in a noticeable hump more than 25mm in the pavement section in the vicinity of the buried pipe. The hump will result in the change of the International Roughness Index (IRI) which is a measure of the serviceability and riding comfort of the pavement. The patch pavement section started to show signs of surface distress after the first year following pipe installation. The construction joint between the repair section and the existing pavement has widened considerable allowing infiltration of water into the pavement. Infiltration if not addresses could subsequently leads to alligator cracking and may cause structural damage. GPR survey revealed that the pavement section was significantly altered by open-cut installation. The deflection data from the FWD test also showed that the repair section is not as structurally sound as the undisturbed pavement sections. Frost action was also enhanced at the location of the trench. The result found that the trench resulted in a significant discontinuity that will result in pavement deterioration, increased cost of maintenance and loss of life.

8.1.2 Numerical Investigations

The ability of *FLAC*^{3D} finite difference program to replicate field-scale HDD and open-cut installations was demonstrated in this dissertation. A number of numerical simulations were generated for HDD installations in cohesionless and clayey subgrade material at various depths beneath flexible pavement using *FLAC*^{3D}. The results of these simulations were complied into charts and tables, and provide a first order approximation that can be used to set the maximum allowable bore pressures for new HDD installations beneath flexible pavements.

The installation of small diameter utility pipes underneath flexible pavement using traditional open-cut installation technique was also simulated with *FLAC*^{3D}. Flexible pavement structure response to utility cut and the mechanism that resulted in the observed surface distresses in the vicinity of utility cut on flexible pavement was determined analytically from the results of the simulations. The influence of backfill compaction on the performance of buried pipes was also determined from the series of simulations.

The following sections summarize conclusions and contributions from the numerical investigations conducted for this thesis.

8.1.2.1 Implementation of Constitutive Model in FLAC^{3D}

A modification to the conventional Mohr-Coulomb linear elastic-plastic model was presented in this dissertation. The constitutive model is a hybrid of the traditional Duncan-Chang hyperbolic model and Mohr-Coulomb perfectly plastic model. The model combines the good aspect of both models by using the hyperbolic stress-strain relationship to model the soil's behavior before failure, and the conventional Mohr-Coulomb plastic model to determine the behaviour at and after failure. The constitutive model is based on elastic-plastic theory and it addresses most of the characteristics of granular material behavior relevant to ground movements around the excavation and the pressurized bore –non linearity, stress dependency of the stress-strain relationship and path dependence.

The proposed constitutive model was implemented in *FLAC*^{3D}. The incremental stress-strain relations that describe the model were written in C++, and compiled as a DLL file (dynamic link library). The numerical analysis procedure and equations that describe the proposed constitutive model are presented in this dissertation. The proposed constitutive model implemented in *FLAC*^{3D} was validated by simulating triaxial laboratory tests and comparing the model response with measured experimental data. Good agreement was obtained between simulated and measured stress-strain response. To further verify the validity and accuracy of the proposed model, a code-to-code comparison (benchmarking) was completed. A pipe-soil interaction problem was analyzed with *FLAC*^{3D} and the predicted response was compared with *CANDE'89* - a widely used 2D finite element program. The pipe responses obtained from the two codes showed good agreement.

8.1.2.2 Results of Horizontal Directional Drilling Simulations

The response of flexible pavement structure to HDD bore pressurization was numerically simulated to characterize bore pressure-ground deformation relationship during HDD installation beneath flexible pavement. The mechanism, magnitude, and extent of deformation within the flexible pavement structure due to HDD bore pressurization in cohesionless and clayey subgrade was examined in detail in this thesis. The influence of depth of cover, bore diameter, thickness of filter cake, thickness of asphalt concrete, and strength properties of the subgrade on bore pressures require to initiate and propagate displacement fields outwards away from the bore were also evaluated and presented.

It was determined from the numerical simulations that the *initiation* and *critical pressures* are directly proportional to the depth of cover, as increased height of cover provided significant resistance to ground deformations. In this dissertation, "***initiation pressure***" refers to the least bore pressure require to generate a vertical displacement of 12.5mm at the crown of HDD bore while "***critical pressure***" refers to least bore pressures require to propagate a vertical displacement of 12.5mm to the pavement surface i.e. full height of cover, D, above the bore.

The contours of vertical displacements were rapidly transmitted upward once the *initiation pressure* was attained and plastic deformations develop above shallow HDD bores drilled 2.0m beneath the flexible pavement. The *critical pressures* are only marginally higher than the *initiation pressures* for bores with shallow depth of cover. The HDD bores with depth of cover 3m or more required pressure significantly above the *initiation pressures* to transmit the same magnitude of deformation upward to the pavement surface. These observations suggest that bore pressures need to be maintained well below those of the *initiation pressures* to prevent excessive heave of the pavement for shallow HDD installation since there is a very small difference between the *initiation* and *critical pressures*.

Once the *critical pressure* is achieved, additional increase in pressure produced significant ground deformation above the bore. For example, the *critical pressure* for a 300mm diameter HDD bore drilled at a depth of 3.0m below the pavement surface in a cohesionless subgrade with a friction angle of 35 was about 412 kPa. Increasing the bore pressure slightly to 414 kPa resulted in approximately 56mm heave on the pavement surface compared to 12.5mm heave observed at a *critical pressure* of 412 kPa. These observations indicate that once the limiting pressure is reached and shear bands/planes are fully developed within the soil, further pressurization of the HDD bore could cause excessive pavement deformations if the drilling contractor does not promptly address and relieve the increased bore pressure.

Smaller bore diameter required greater *initiation* and *critical pressures*. For example, the *initiation* and *critical pressures* for a 300mm HDD bore installed at depth of 3.0m below the pavement surface in cohesionless subgrade with friction angle of 35° are about 302 and 412kPa, respectively; whereas, for a smaller 200mm diameter bore installed at the same depth of cover and in the same subgrade material, the *initiation* and *critical pressures* were about 372 and 543 kPa, respectively. An increase of about 23 and 32 percent in the *initiation* and *critical pressures,* respectively over those of 300mm diameter bore. The higher bore pressures required for smaller bore may be attributed to a smaller circumferential surface area over which the applied bore pressures acts on smaller bore diameters. Smaller bore would require greater bore pressure to achieve a similar driving force required to initiate and propagate deformation outwardly from the bore compare to the larger diameter bore.

Sensitivity analyses conducted to determine the influence of effective friction angle and cohesion in the subgrade on the magnitudes of the limiting bore pressures revealed that *initiation* and *critical pressures* are directly proportional to the strength parameters assigned to the subgrade. Increasing the value of effective cohesion by 50 and 100 percent resulted in an increase of about 9 and 20 percent, respectively, in the *initiation* and *critical* limiting bore pressures for installation in a clayey subgrade with 5 kPa effective cohesion. The *initiation* and *critical pressures* are directly proportional to the friction angle. For example, the *critical pressure* for a 200mm diameter bore installed at a depth of 3m below the pavement surface in a cohesionless subgrade with a friction angle of 35° was about 543kPa compared to about 631 kPa required for the same bore geometry in a cohesionless soil with friction angle of 40°.

Results of the numerical simulations showed that the *filter-cake* formed around the HDD bore during drilling contributes to the bore resistance to deformation. The *initiation* and *critical pressures* estimated for a 300mm diameter bore with 25mm thick filter-cake around it was approximately 228 and 240 kPa, respectively -an increase of about 6% over values obtained for bore without filter cake. The same bore diameter surrounded by 50mm thick filter cake yielded an *initiation* and *critical pressures* of 246 and 257 kPa, respectively -an increase of about 13.5% over values obtained for bore without filter cake. There is almost a direct linear correlation between the thickness of filter-cake and the percentage increase in limiting bore pressures for the installation configuration that was examined. The analysis suggests that addition resistance to ground deformation can be achieved during HDD installation by using drilling-fluid and/or polymers that would create excellent filter-cake around the bore. However, the additional resistance provided by the filter-cake should only be considered as a bonus and should not be rely upon since the actual thickness of filter-cake can not be measured , controlled and may vary considerably during HDD installation.

Sensitivity analysis completed to examine the influence of asphalt concrete thickness on the magnitude of both *initiation* and *critical pressures* revealed that the thickness of the asphalt concrete does have some effect on the magnitudes of the limiting bore pressures. For example, increasing the thickness of asphalt concrete from 100 to 125mm resulted in approximately 3 and 5 percent increase in the *initiation* and *critical pressures*, respectively. The *initiation* and *critical pressures* increased by about 6 and 10 percent respectively for a

150mm thick asphalt concrete. There appears to be a direct linear correlation between the thickness of asphalt concrete and the percentage change in limiting bore pressures for the installation configuration that was examined. The influence of asphalt concrete thickness is more significant on the *critical pressures* compared to the *initiation pressures* at the bore wall.

Bore pressure-displacement charts and tables have been produced to estimate the allowable bore pressures for a given installation depth and bore diameter beneath flexible pavement. These estimates could be used to evaluate potential ground deformations and the impact an HDD installation could have on existing underground structures. Care should be taken when using these design tools especially where the subsurface condition differs from those assigned to the numerical model. A factor of safety of at least 1.5 is recommended under such circumstances.

There was poor correlation observed between the bore pressure obtained from the numerical simulation and those estimated with Delft Geotechnics equations. The Delft Geotechnics equation which was solely derived from cavity expansion theory tends to overestimate allowable bore pressure especially for HDD installation in purely frictional subgrade. There are several inherent assumptions in the formulation of the Delft Geotechnics equation that could have resulted in the disparity observed between bore pressures estimated using the equations and those obtained from numerical simulations with *FLAC*^{3D}. The Delft Geotechnics equations was based in cavity expansion theory and assume a uniform and isotropic stress field, an infinite soil medium, and homogenous soil properties. The influence of lateral earth pressure, tensile strength of material, shear dilatancy and spatial boundary were not included in the formulation of the equations. All these ignored factors played an important role in the numerical modeling and the actual stress-deformation behavior of a pavement structure.

If good drilling practices are used to keep bore pressures below the initiation pressure, no ground disturbance will occur. Thus there will be no loss of pavement life. Should excessive bore pressurization occur during HDD installation, leading to ground deformation, the repair will consist mainly of replacing the asphalt concrete layer (where no underground utilities are

damaged). The other structural material (base and subbase) will not require replacement; thus, minimizing pavement deterioration and potential loss of pavement life.

8.1.2.3 Results of Open-cut Pipe Installation Simulations

The response of flexible pavement structure to utility cut and the mechanism that resulted in observed surface distresses in the vicinity of restored pavement section was presented in this dissertation. The construction stages involved in traditional open cut pipe installation including trench excavation, preparation of the bedding, pipe placement and trench backfilling with compacted soil in small lifts were simulated using FLAC^{3D}. The numerical computation was completed in large-strain deformation mode to ensure that large strain response of the trench walls were captured during trench excavation and restoration.

It was determined from the numerical analysis that when an unsupported excavation is created within a typical flexible pavement structure, distress zones that extend laterally to a distance of about 0.54, 1.03 and 1.65m for an excavated depth of 1.0, 1.5 and 2.0m, respectively, from the face of the trench. This equates to $\frac{x}{H}$ of 0.54, 0.67 and 0.82 for depth of excavation of 1.0, 1.5 and 2.0m, respectively; where x is the extent of the distress zone from the face of the excavation and H is the depth of excavation. The vertical pressure applied on the backfill material via compaction during trench restoration does not provide sufficient lateral pressure against the face of the trench to re-compact the 'distress zone' around the utility trench. The results of the analyses suggests that a more efficient restoration technique is required to eliminate the adverse effect caused by the stress relief within the pavement structure during a utility cut excavation. Furthermore, the area of potential pavement deterioration should be extended beyond the edge of the utility cut (up to 0.8H) to encompass the 'distress zones' when determining fees to cover pavement damage and restoration costs.

Accurate prediction of buried pipe response required a technique to account for compaction-induced stresses in the backfill material. A transient 10 kPa vertical surcharge load was applied to the backfill surface at each stage during simulation of backfill placement, and that,

together with a combination of appropriate constitutive model, and representative soil parameters produced satisfactory agreement between predicted and field measured pipe responses.

It was concluded from the numerical simulation that the compaction of backfill material has a considerable influence on the magnitude pipe deflection. For example, increasing the compaction effort from 5 to 10kPa resulted in an increase of about 40 percent in pipe deflection. While increasing the compaction effort from 5 to 20 kPa resulted in approximately 130 percent increase in the pipe deflection. The numerical simulation also showed that the stiffness of the bedding and side support significantly impacts the performance of the flexible pipe. Excessive deformation resulted from poorly placed bedding material.

8.2 Recommendations for Future work

The following are recommendations for future work:

(i) A continuation of this research should be conducted to monitor the performance of the field-scale installation and the performance of the pavement. According to previous studies, a restored trench will progressively deteriorate over time. Therefore, to determine the performance of the restored trench with time, monitoring should continue for as long as possible, at least another two years.

(ii) The scope of the research described in this thesis was limited to flexible pavement structure. The study should be extended to rigid and composite pavement structures.

(iii) The impact of the installation technique on pavement and HDPE pipe response to traffic loading should be investigated.

(iv) The field scale investigation showed that the variation of temperature has a considerable effect on the response of the HDPE pipe. Therefore future numerical simulations of HDPE pipe should include thermal analysis.

(v) The high quality data set of pavement response obtained from pavement instrumentation and data acquisition system that was developed as part of this dissertation provides a unique opportunity to calibrate and validate existing pavement design methodology. Research effort in the areas of insitu pavement response monitoring should be pursued to expand the use of the pavement sensors and data acquisition system.

(vi) Use numerical simulation results to determine if a simple analytical model can be developed to predict the initiation bore pressure for HDD installed pipelines.

(vii) Use *FLAC*^{3D} to determine construction methods for open-cut installations to reduce the size of the distress zone.

References

Abdel-Sayed, G., Bakht, B., and Jaeger, L. G. (1994). Soil-Steel bridges: design & construction. McGraw-Hill, Inc.

Allouche, E.N., Ariaratnam, S.T. and Lueke, J.S. (2000). Horizontal Directional Drilling: Profile of an Emerging Industry. Journal of Construction Engineering and Management, Vol. 126, Issue 1, Pp. 68-76.

Al-Suhaibani, A., Alani, B. A., and Al-Kharashi, I. A. (1992). Effects of utility cut patching on pavement deterioration. Journal of King Saud University; Engineering Sc. Vol. 4, no2, Pp. 171-192.

AMEC (2002) Evaluation of Pavement Cut Impacts, prepared for League of Arizona Cities by AMEC Earth & Environmental, Inc. Phoenix, Arizona.

APWA (1991) Recovering Cost of Pavement Cuts, Proc., Project Sponsors 1991 Annual Meeting, American Public Works Association, Sept 1991.

APWA (1997) Managing Utility Cuts, Special Report American Public Works Association

Arends, G. (2003), Need and Possibilities for a Quality Push within the Techniques of Horizontal Directional Drilling (HDD), Proc. ISTT/NASTT No-Dig 2003 Conference, Las-Vegas, Nevada, March 2003. North American Society for Trenchless Technology, Arlington VA.

Ariaratnam, S. T., Lueke, J. S., Beljan, I. J., and Colwell, D. A. F. (2000). Insitu Monitoring and Evaluation of Horizontal Directional Drilling Installations. Proc., 4th CSCE Construction Specialty Conf., Victoria, B.C., Canada

Ariaratnam, S.T., and Beljan, I.J. (2005), Post-Construction Evaluation of HDD Installations, Practice Periodical on Structural Design and Construction, ASCE, Vol 10, No 2, Pp. 115-126

Baumert, M.E., Allouche E.N. and Moore, I.D. (2004). Experimental Investigation of Pull Loads and Bore Pressures During HDD Installations. Canadian Geotechnical Journal, Vol. 41, Pp. 672-685.

Bennett, D., Ariaratnam, S., and Como, C. (2001). Horizontal Directional Drilling Good Practices Guidelines, HDD Consortium.

Bodocsi, A., Pant, P. D., Aktan, A. E., and R. S. Arudi, (1995). Final Report: Impact of Utility Cuts on Performance of Street Cuts, report prepared by The Cincinnati Infrastructure Institute, Department of Civil & Environmental Engineering, University of Cincinnati, Cincinnati, OH, and sponsored by the City of Cincinnati and the American Public Works Association.

Boscardin, M.D., Selig, E.T., Lin, R., and Yang, G. (1990) Hyperbolic parameters for compacted soils. Journal of Geotechnical Engineering, ASCE, 116(1), Pp. 88-104.

Brinkgreve, R. B.J. (2005) Selection of soil models and parameters for geotechnical engineering aPplication. Geotechnical Special Publication, No. 128, Soil Constitutive Models - Evaluation, Selection, and Calibration, Pp. 69-98.

Burland, J.B. (1989) Ninth Laurits Bjerrum Memorial Lecture. 'Small is beautiful'. The stiffness of soils at small strains. Canadian Geotechnical Journal, Vol. 26, No. 4, Nov, 1989, Pp. 499-516.

CalTrans Encroachment Permit (2002). Guidelines and Specifications for Horizontal Directional Drilling Installations. California Department of Transportation, Sacramento California, August 12, 2002.

Chadwick, P. (1959). The Quasi-Static Expansion of a Spherical Cavity in Metals and Ideal Soils, Quarterly Journal of Mechanics and APplied Mathematics, Vol. 12, Pp. 52-71

Chen, W.F., and Baladi, G.Y (1985). Soil Plasticity: Theory and Implementation, Elsevier press, New York.

Chen, W.F., and Han, D.J (1988). Plasticity for Structural Engineers. Springer-Verlag press, New York.

Chen, W.F and Mizuno, E. (1990) Nonlinear Analysis in Soil Mechanics: Theory & Implementation. Developments in Geotechnical Engineering Series #53. Elsevier press, Amsterdam, Netherlands. 672Pp

Chen, W. F. and Saleeb, A. F. (1994) Constitutive Equations for Engineering Materials Vol.1: Elasticity and Modeling. Elsevier press, Amsterdam, 580 Pp.

Chisholm, R. A., and Phang, W. A. (1983). Measurement and Prediction of Frost Penetration in Highway. Transportation Research Record No 918, Transportation Research Board, Washington D.C., Pp. 1-10

Chow, C., and Troyan, V. (1999). Quantifying Damages from Utility Cuts in Asphalt Pavement by Using San Francisco's Pavement Management Data. Journal of the Transportation Research Board, No 1655, Pp. 1-7.

Cowan, H. J. (1953) The strength of plain, reinforced and prestressed concrete under the action of combined stresses with particular reference to combined bending and torsion of rectangular sections.. Magazine of Concrete Research, Vol. 5, No. 14, Pp. 75-86.

CSA (1987). CAN/CSA-b182.7-87: Plastic Drains and Sewer Pipe and Fittings. 4th edition December

Cundall, P. A. (1987) Distinct Element Models of Rock and Soil Structure. Analytical and Computational Methods in Engineering Rock Mechanics, E. T. Brown, Ed. London: Allen & Unwin., Ch. 4, Pp. 129-163.

Darley, H.C., and Gray, G.R. (1991) Composition and properties of drilling and completion fluids. Fifth Edition. Gulf Publishing Company, Houston, Texas, 643p

Davis, E.H. (1969). Theories of Plasticity and the Failure of Soil Masses, Soil Mechanics (Ed I.K. Lee). London; Butterworth

DCA (2001). Horizontal Directional Drilling DCA Technical Guidelines, 2nd Edition, February 2001, Drilling Contractors Association - Europe.

Desai, C. S., and Christian, J. T. (1977). Numerical Methods in Geomechanics. New York, McGraw-Hill.

Desai, C.S. and Siriwardane, H. J. (1984) Constitutive laws for engineering materials, with emphasis on geologic materials. Prentice-hall, Englewood Cliffs, New Jersey.

Deresciewicz, H. (1958). Mechanics of Granular Matters. Advances in APplied Mechanics, vol. 4. Academics Press, New York, Pp. 233-306.

Directional Drilling Contractors Association (1998). Guidelines to Successful Mid-sized Directional Drilling Projects. International Register of Directional Drilling, Directional Drilling Contractors Association.

Duncan, J.M. (1962) The influence of depth on the bearing capacity of strip footings in sand. Georgia Institute of Technology, Atlanta, Georgia.

Duncan, J.M. and C.Y. Chang. (1970) Nonlinear analysis of stress and strain in soils. Journal of Soil Mechanics and Foundation Division, ASCE, 96(SM5), Pp. 1629-1653.

Duncan, J. M., Byrne, P., Wong, K. S., and Mabry, P. (1980). Strength, stress-strain and bulk modulus parameters for finite element analysis of stress and movements in soil masses. UCB/GT/80-01, College of California, Berkeley, California.

Duncan, J.M., Seed, R.B., Wong, K.S., and Ozawa, Y. (1984) FEADAM 84: A computer program for finite element analysis of dams. Department of Civil Engineering, Stanford University, Report No. SU/GT/84-03.

Duncan, J. M., Williams, G. W., Sehn, A. L., and Seed, R. B. (1991). Estimation Earth Pressures due to Compaction, Journal of Geotechnical Engineering Division, ASCE, Vol. 117, No. 12.

Duyvestyn, G., Knight, M.A., and Polak, M.A. (2001a) Excavation and analysis of two HDPE pipes installed using HDD techniques. Proc., 2001 No-Dig Conference, North American Society for Trenchless Technology, Nashville. TN.

Duyvestyn, G.M., Knight M.A., Polak, M.A., (2001b). Measurement of HDPE pipeline axial load during horizontal directional drilling installation. Proceedings of Underground Construction Conference. Houston, Texas

Duyvestyn, G.M. (2004). Field and Numerical Investigation into Pipe Bursting and Horizontal Directional Drilling Pipeline Installation Ground Movements, Ph.D. Thesis, Department of Civil Engineering, University of Waterloo, Waterloo, Ontario, Canada

Emery, J. J, and Johnston, T. (1986). Unshrinkable fill for utility cut restorations. Publication SP - American Concrete Institute, 1986, Pp. 187-212

Emery, J. J., and Johnson, T. H. (1987). Influence of Utility Cut on Urban pavement Performance, 2nd North American conference on managing pavements, proceedings Vol. 1, Toronto, Canada.

Filz, G., Clough,G.W.; and Duncan, J.M (1990) User's Manual for SOLISTRUCT. Virginia Polytechnic Institute and State University, Blacksburg, Virginia.

Gelinas, M., and Mathy, D.C. (2001). Horizontal Directional Drilling: Lessons Learned In Telecommunications Conduit Installations, Proceedings of The 2001 No-Dig Conference and Exhibition, North American Society For Trenchless Technology, Nashville, Tennessee.

Gokhale, S., Hamm, R., and Sterling, R. (1999). A Comprehensive Survey on the State of Horizontal Directional Drilling in North America Provides an Inside Look at this Increasing Growing Industry. Directional Drilling, Vol. 7, No.1, Pp.20-23.

Gómez, J.E., Filz, G.M. and Ebeling, R.M. (2003) Extended Hyperbolic Model for Sand-to-Concrete Interfaces. Journal of Geotechical and Geoenvironmetal Engineering, Vol. 129, Issue 11, Pp. 993-1000.

Habibian, A. (1994). Effects of temperature changes on water mains breaks. Journal of Transportation Engineering, ASCE, Vol. 120, No 2, Pp. 312–321.

Hill, R. (1950) The Mathematical Theory of plasticity. Clarendon Press, Oxford, U.K.

Howard, A.K. (1977) Modulus of Soil reaction Values for Buried Flexible Pipe. Journal of the Geotechnical Engineering Division, ASCE, Vol. 103, No 1, Pp. 33-43

Humphrey, M.H., and Parker, N.A. (1998). Mechanics of small utility cuts in urban street pavements: implications for restoration. Journal of the Transportation Research Record, No. 1629, Pp. 226-234

Hunter, A. (2005). Effect of Trenchless Technologies on Existing Iron Pipelines. Proceedings of The Institution of Civil Engineers- Geotechnical Engineering, Vol. 158, No. 3, Pp. 159-167.

Iseley, T., and Tanwani, R. (1990) Social cost of traditional methods of utility installation. Proceeding of first Trenchless Excavation Symposium, Houston, Taxas. AA1-AA7.

Itasca. (2005). Flac 3D: Fast Lagrangian Analysis of Continua, Version 2.1, User's Guide, Itasca Consulting Group, Inc. Minneapolis.

Janbu, N. (1963) Soil compressibility as determined by oedometer and triaxial tests. Proceedings of the 3rd European Conference on Soil Mechanics and Foundation Engineering,Wiesbaden, Germany. Vol. 1, Pp. 19–24.

Jardine, R.J., Potts, D.M., Fourie, A.B. and Burland, J.B. (1986) Studies of the influence of non-linear stress strain characteristics in soil structure interaction. Géotechnique 36, No. 3, Pp. 377-396.

Jones, C.J.F.P (1999). Policy, Incentives and Barriers to the use of Trenchless Technology, in Life Extension of Technologies Workshop, New York, August 25-26, USA.

Khogali, W.E.I., and Mohammed, E. (1999). Managing Utility Cuts: Issues and Considerations in Innovations in Urban Infrastructures. APWA International Public Works Congress and Exhibition, Las Vegas, Nevada, September 14-17, sponsored by the National Research Council Canada and the Canadian Public Works Association.

Knight, M., Duyvestyn, G., and Gelinas, M. (2001). Excavation of surface installed pipeline. Journal of Infrastructure Systems, Vol.7, No3.

Knight, M., and Duyvestyn, G.M (2001). Excavation and Analysis of HDPE Pipelines Installed Using a Horizontal Directional Drill. Proceedings of Underground Construction Technology Educational Program, January 23-25, 2001, 16Pp.

Knight, M.A., Duyvestyn, G.M., and Polak, M.A. (2002). Behavior of Polyethylene Pipes Installed Using Midi Horizontal Directional Drill, Proceeding of International No-Dig 2002, May 23-27, Copenhagen, Denmark

Knight M.A., Tighe, S.T., and Adedapo, A. (2004). Trenchless Installations Preserve Pavement Integrity. Proceedings Annual Conference of the Transportation Association of Canada, Quebec City, September 2004.

Kolymbas, D. (1985). A generalized hypoplastic constitutive law. Proceeding of 11th international conference on soil mechanics and foundation division. Balkema, Rotterdam.

Kondner, R.L. (1963), Hyperbolic stress-strain response: Cohesive soils. Journal of soil Mechanics and Foundation. Division, ASCE, 89(SM1):Pp. 115-143.

Konrad, J.M., and Morgenstern, N.R. (1981) The segregation potential of a freezing soil. Canadian Geotechnical Journal, Vol 18: 482–491

Lade, P. V. (2005) Overview of constitutive models for soils. Geotechnical Special Publication, No. 128, Soil Constitutive Models - Evaluation, Selection, and Calibration, Pp. 1-34

Lee, S.Q.S., and Lauter, K.A. (1999) Impact of Utility Trenching and APpurtenances on Pavement Performance in Ottawa-Carleton, report prepared by Trow Consulting Engineers, Ltd for Environment and Transportation Department, Regional Municipality of Ottawa-Carleton, Ottawa, Ontario, Canada, July 29, revised August 13.

Lee, S.Q.S., and Lauter, K.A. (2000) Using pavement management system concepts to determine the cost and impact of utility trenching on an urban road network Transportation Research Record, no. 1699, Pp. 33-41

Lefebvre, G., Laliberte, M.,Lafebvre, L.M., Lafleur, J. and Fisher, C.L., (1976) Measurement of soil arching above a large diameter flexible culvert, Canadian Geotechnical Journal, Vol. 13, No 1, Pp. 58-71.

Lin, R.D (1987) Direct determination of Bulk Modulus of partially saturated soils. Project ACP87-341P, University of Massachusetts, Amherst, MA.

Lochbaum, B. S. (1993). PSE&G develops models to predict main breaks. Pipeline and Gas Journal, Vol. 20, No. 9, Pp. 20-27.

Lueke, J.S., and Ariaratnam, S.T. (2003) Experimental Procedure For Evaluating Ground Displacements Factors in Directional Drilling. Canadian Journal of Civil Engineering. Vol. 30, Pp. 830-840.

Lytton, R.L., Uzan,J., Fernando, E. G., Roque, R., Hiltunten, D., and Stoffels, S.M. (1993). Development and Validation of Performance Prediction Models and Specifications for Asphalt Binders and Paving Mixes. Report SHRP-A-357. Strategic Highway Research Program. National Research Council, Washington, DC

Mangolds, A., and J. Carapezza, (1991). Assessment of Pavement Cutback Requirements, Foster-Miller, Inc., Final Report, RD & D Project D.28.3, report BUG-D283-FM-9081-429 prepared for Brooklyn Union Gas Company, Research Development and Demonstration Department, Brooklyn, NY and Consolidated Edison Co. of New York, Inc., Research and Development, New York, NY.

Marshall, A. (2003). A Laboratory and Numerical Modeling of Soil Deformation Caused By Near-Surface Pressurized Bores. MASc. Thesis, Department of Civil Engineering, University of Waterloo, Waterloo, Ontario, Canada.

Marti, J., and Cundal,l P. A. (1982). "Mixed Discretization Procedure for Accurate Solution of Plasticity Problems," Int. J. Num. Methods and Anal. Methods in Geomech., Vol. 6, Pp. 129-139

Masada, T. (2000) Modified Iowa formula for vertical deflection of buried flexible pipe. Journal of Transportation Engineering, ASCE, Vol. 126, No. 5.

Massicotte, D. (2000) Finite Element calculations of Stress and Strain Deformations in Buried Pipes. MSc Thesis, Department of Civil Engineering, University of Ottawa

Monie, W.D., and Clark, C.M. (1974). Loads on underground pipe due to frost penetration. Journal of the American Water Works Association, Vol. 66, No. 6, Pp.353–358.

Musser, S.C (1989) CANDE'89 Culvert analysis and design computer program user manual. FHWA-RD-89-169, US Department of Transportation, Federal Highway Administration, Washington, D. C.

Nichols-Vallerga & Associates, 2000, Final Report: Impact of Utility Cuts on Performance of Seattle Streets, report submitted to City of Seattle, Seattle Transportation, project 178.01.30, January 31.

Obert, L., and Duvall, W.I. (1967). Rock Mechanics and the Design of Structures in Rock. John Wiley and Sons, Inc, N.Y. Pp. 98-108

Ohde, J. (1939). Zur theorie der Druckverteilung im Baugrund. Der Bauingenieur, Vol. 20, Pp. 451-459

Patterson, D.E., and Smith, M. W. (1981). The measurement of unfrozen water content by the time domain Reflectometry: results from laboratory tests. Canadian Geotechnical Journal. Vol. 18, Pp. 131-144

Performance Pipe (2003). The performance pipe engineering manual. Chevron Phillips Chemical Company, Plano, TX.

Petroff, L.J. (1990) Stress relaxation characteristics of the HDPE pipe-soil system Pipeline Des Install Proc Int. Conf, 1990, Pp. 280-294

Polak, M. A., Duyvestyn, G. and Knight, M. A. (2004). Experimental Strain Analysis for Polyethylene Pipes Installed by Horizontal Directional Drilling. Tunneling and Underground Space Technology, Vol.19, Pp. 205-216.

Potter, D. (1996) Measuring Temperature with Thermocouples APplication Note 043, National Instruments Corporation. Austin, TX

PPI (2000) Polythylene Pipe for Horizontal Directional Drilling published by Plastic Pipe Institute

Radenkovic, D. (1961) Thèorèmes limites pour un matériau de Coulomb à dilatation non standardisée, C.R.Ac.Sc. 252, Paris, Pp. 4103-4104

Rajani, B., and Zhan, C. 1996. On the estimation of frost loads. Canadian Geotechnical Journal, Vol. 33, No. 4, Pp. 629–641.

Rajani, B., and Zhan, C. (1997) Estimation of frost load in a trench: theory and experiment. Canadian Geotechnical Journal, Vol. 34, No. 4, Pp. 568-579

Schaefer, V., Suleiman, M., White, D., Swan, C. and Jensen, K. (2005) Utility cut repair techniques—investigation of improved cut repair techniques to reduce settlement in repaired areas. Iowa Highway Research Board. Iowa Department of Transportation, 800 Lincoln Way Ames, IA 50010. Report # IHRB Project TR-503

Selig, E.T. (1988). Soil Parameters for Design of Buried Pipelines, Pipeline Infrastructure. Proceedings of the Conference, American Society of Civil Engineers, New York, NY, Pp. 99-116.

Shahin, M. Y. and Kohn, S. D. (1981). Pavement maintenance management for roads and parking Lots. US Army Corps of Engineers, Construction Engineering Research Laboratory (CERL), Technical Report M-294

Shahin, M. Y., Crovetti, J. A., and J. L. Franco, (1986), Effects of Utility Cut Patching on Pavement Performance and Rehabilitation Costs, Annual Meeting of the Transportation Research Board, Washington, D. C., December 23.

Shahin, M.Y., and Crovetti J A. (1987) Determining the effect of Utility Cut patching on service life prediction of Asphalt concrete pavement, 2nd North American conference on managing pavements, proceedings Vol. 1, Toronto, Canada. Pp. 225-236.

Shield, R.T., (1955) On Coulomb's law of failure in soils. Journal of the mechanics and physics of solids, Vol. 4, Issue 1: Pp. 10-16.

Smith,W.H. 1976. Frost loadings on underground pipe. Journal of the American Water Works Association, Vol. 68, No. 12, Pp. 673–674.

Smith, I. M. (1994) Validation of finite element solutions. Proceedings of the 13th International conference on Soil Mechanics and Foundation Engineering, New Delhi, 5, Pp. 229-231

Spangler, M.G (1938) The structural design of flexible culverts. Public Roads, Vol. 18, No. 12.

Spangler, M.G. (1941). The Structural Design of Pipe Culverts. The Iowa state college bulletin, No 30, Vol XL, Iowa Engineering Experimental Station, Iowa State College of Agriculture and Mechanic Arts. Ames, Iowa.

Spangler, M.G., and Handy, R.L. (1982) Soil Engineering, 4th Edition, Hamper and Row Publications, New York.

Tabatabaee, N., Al-Qadi, I. L. and Sebaaly, P.E. (1992) Field evaluation of pavement Instrumentation Methods. Journal of testing and evaluation, Vol. 20, No. 2, Pp.144-151.

Tarakji, G. (1995) Effect of Utility Cuts on the Service Life of Pavements in San Francisco, Study Procedure and Findings, Final report by Engineering Design Center, San Francisco State University for the Department of Public Works, City and County of San Francisco, San Francisco, CA.

Tighe. S., Lee, T., McKim, R., and Hass, R. (1999). Traffic delay cost savings associated with trenchless technology. Journal of Infrastructure Systems. Vol. 5, No. 2, Pp.45-51.

Tighe. S., Knight, M., Papoutsis, D., Rodriguez, V., and Walker, C. (2002). User Cost Savings in eliminating pavement excavation through employing trenchless technology. Canadian Journal of Civil Engineering Vol. 29, Pp.751-761.

Tighe, S., Jeffray, A., Kennepohl, G., Haas, R., and and Matheson, M. (2003) Field experiments in CPATT's long-term program of pavement research. Proceedings Transportation Association of Canada Annual Conference, St. John's, NF.

Titus-Glover, L. (1995). Evaluation of Pavement Base and Subgrade Material Properties and Test Procedures. MSc. Thesis. Texas A &M University, College Station, Texas.

Todres, H. A., and C. L. Wu, (1990), Theoretical Analysis of Utility Cut Restoration in Asphaltic Pavement, Vol.ume I, report by Construction Technologies Laboratories, Inc. submitted to Institute of Gas Technology, Chicago, IL, October.

Todres, H.A., and P.E. Baker (1996), Utility Research in Pavement Restoration, Presented at APWA International Public Works Congress and Exposition, Washington, D.C.,

Todres, H., and Saha N. (1996) Asphalt Paving repairs Study – Theoretical Modeling, APWA Reporter November 1996.

Todres, H.A., (1999), Utility Cuts in Asphalt Pavements: Best Engineering Practices, in Innovations in Urban Infrastructure, APWA International Public Works Congress and Exhibition, Las Vegas, Nevada, September 14-17

Uni-Bell (1993) Handbook of PVC Pipes, 3rd Edition published by Uni-Bell PVC Pipe Association, Dallas, TX.

Wang, J.X., and Sterling, R.L. (2004) Stability Analysis of A Borehole Wall In HDD. Proceeding of 2004 North American No-Dig Conference, New-Orleans, Louisiana, Paper E-1-02.

Watkins, R. K., (1966) Structural Design of Buried Circular Conduits. Highway Research Board. No 145, Pp. 1-17.

Watkins, R.K., and Anderson, L.R (2000) Structural mechanics of buried pipes. CRC. Press, New York.

White, T. D. (1985) Pavement Instrumentation: guide to instrumentation plan for flexible and rigid pavements. FHWA/EP-621-01, Demonstrations Projects Division, FHWA Washington, DC.

Yang, G.R (1987) Hyperbolic Young's Modulus parameters for compacted soils. Project ACP87-342P, University of Massachusetts, Amherst, MA.

Yu, H.S., and Houlsby, G.T. (1991) Finite Cavity Expansion in Dilatant Soils: Loading Analysis. Geotechnique, Vol. 41, 173-183.

APPENDIX A:

C++ SOURCE CODE FOR NEW CONSTITUTIVE MODEL IMPLEMENTED IN FLAC^{3D}

```
//hyperDuncanSelig.CPP C++ SOURCE FILES

#include "hyper.h"
#include <math.h>

//variables used by all model objects. Hence only one copy is
maintained for all objects
static const double d2d3    = 2.0 / 3.0;
static const double dPi     =
3.14159265358979323846264338327950288419716939 9;
static const double dDegRad = dPi / 180.0;

// Plasticity Indicators
static const unsigned long mShearNow    = 0x01;
      /* state logic */
static const unsigned long mTensionNow  = 0x02;
static const unsigned long mShearPast   = 0x04;
static const unsigned long mTensionPast = 0x08;



// One static instance is neccessary as a part of internal registration
process of the model with FLAC/FLAC3D
static HyperModel hypermodel(true);


HyperModel::HyperModel(bool bRegister)
          :ConstitutiveModel(mnHyperModel,bRegister),
               dBulk(0.0),dShear(0.0), dCohesion(0.0),
dFriction(0.0),dDilation(0.0),
               dTension(0.0),
dYoung(0.0),dPoisson(0.0),dMypoisson(0.0),dKload(0.0),dKunload(0.0),
               dKbulk(0.0),
dMexp(0.0),dKmexp(0.0),dFratio(0.0),dPa(0.0),

dSSmax(0.0),dCmodulus(0.0),dKmax(0.0),dGmax(0.0),dSig3max(0.0),
               dSL(0.0),dSS(0.0),dS1S3(0.0),dBulkmin(0.0),
dVolumax(0.0), dElastmin(0.0),dFrictmin(0.0),dFrictDelta(0.0),
               dNPH(0.0),dCSN(0.0),dRnps(0.0),dApex(0.0) {
}

const char **HyperModel::Properties(void) const {
  static const char *strKey[] = {
    "Bulk",
"Shear","Cohesion","Friction","Dilation","Tension","Young","Poisson","M
ypoisson","KL","KUL",
      "KB","Lmod","ULmod","Rf","Pa",
"SSMax","CMod","KMax","GMax","S3max","SL","SS","S1-S3max","Kmin",
      "VolMax", "Emin","PhiMin","DeltaPhi", 0
  };
  return(strKey);
}


const char **HyperModel::States(void) const {
  static const char *strKey[] = {
    "shear-n","tension-n","shear-p","tension-p",0
```

```
  };
  return(strKey);
}

/*  * Note: Maintain order of property input/output
*/
double HyperModel::GetProperty(unsigned ul) const {
  switch (ul) {
    case 1:  return(dBulk);
    case 2:  return(dShear);
    case 3:  return(dCohesion);
    case 4:  return(dFriction);
    case 5:  return(dDilation);
    case 6:  return(dTension);
    case 7:  return(dYoung);
    case 8:  return(dPoisson);
      case 9:  return(dMypoisson);
      case 10: return(dKload);
      case 11: return(dKunload);
      case 12: return(dKbulk);
      case 13: return(dMexp);
      case 14: return(dKmexp);
      case 15: return(dFratio);
      case 16: return(dPa);
      case 17: return(dSSmax);
      case 18: return(dCmodulus);
      case 19: return(dKmax);
      case 20: return(dGmax);
      case 21: return(dSig3max);
      case 22: return(dSL);
      case 23: return(dSS);
      case 24: return(dS1S3);
      case 25: return(dBulkmin);
      case 26: return(dVolumax);
      case 27: return(dElastmin);
      case 28: return(dFrictmin);
      case 29: return(dFrictDelta);
      ;

  }
  return(0.0);
}


void HyperModel::SetProperty(unsigned ul,const double &dVal) {
  switch (ul) {
    case 1: {
      dBulk = dVal;
      YoungPoissonFromBulkShear(&dYoung,&dPoisson,dBulk,dShear);
      break;
    }
    case 2: {
      dShear = dVal;
      YoungPoissonFromBulkShear(&dYoung,&dPoisson,dBulk,dShear);
      break;
    }
    case 3: dCohesion = dVal;  break;
```

```
    case 4: dFriction = dVal;  break;
    case 5: dDilation = dVal;  break;
    case 6: dTension  = dVal;  break;
    case 7: {
      dYoung = dVal;
      BulkShearFromYoungPoisson(&dBulk,&dShear,dYoung,dPoisson);
      break;
    }
    case 8: {
      if ((dVal==0.5)||(dVal==-1.0)) return;
      dPoisson = dVal;
      BulkShearFromYoungPoisson(&dBulk,&dShear,dYoung,dPoisson);
      break;
    }
      case 9:  dMypoisson     = dVal;  break;
      case 10: dKload       = dVal;  break;
      case 11: dKunload = dVal;  break;
      case 12: dKbulk         = dVal;  break;
      case 13: dMexp          = dVal;  break;
      case 14: dKmexp         = dVal;  break;
      case 15: dFratio  = dVal;  break;
      case 16: dPa            = dVal;  break;
      case 17: dSSmax         = dVal;  break;
      case 18: dCmodulus      = dVal;  break;
      case 19: dKmax          = dVal;  break;
      case 20: dGmax          = dVal;  break;
      case 21: dSig3max = dVal;  break;
      case 22: dSL            = dVal;  break;
      case 23: dSS            = dVal;  break;
      case 24: dS1S3          = dVal;  break;
      case 25: dBulkmin = dVal;  break;
      case 26: dVolumax = dVal;  break;
      case 27: dElastmin      = dVal;  break;
      case 28: dFrictmin      = dVal;  break;
      case 29: dFrictDelta= dVal;  break;

    }
}


const char *HyperModel::Copy(const ConstitutiveModel *cm) {
  //Detects type mismatch error and returns error string. otherwise
returns 0
  const char *str = ConstitutiveModel::Copy(cm);
  if (str) return(str);
  HyperModel *mm = (HyperModel *)cm;
  dBulk     = mm->dBulk;
  dShear    = mm->dShear;
  dCohesion = mm->dCohesion;
  dFriction = mm->dFriction;
  dDilation = mm->dDilation;
  dTension  = mm->dTension;
  dYoung    = mm->dYoung;
  dPoisson  = mm->dPoisson;
  dMypoisson = mm->dMypoisson;
  dKload    = mm->dKload;
  dKunload  = mm->dKunload;
```

```
  dKbulk    = mm->dKbulk;
  dMexp     = mm->dMexp;
  dKmexp    = mm->dKmexp;
  dFratio   = mm->dFratio;
  dPa       = mm->dPa;
  dSSmax    = mm->dSSmax;
  dCmodulus = mm->dCmodulus;
  dKmax           = mm->dKmax;
  dGmax     = mm->dGmax;
  dSig3max  = mm->dSig3max;
  dSL     = mm->dSL;
  dSS       = mm->dSS;
  dS1S3           = mm->dS1S3;
  dBulkmin  = mm->dBulkmin;
  dVolumax  = mm->dVolumax;
  dElastmin = mm->dElastmin;
  dFrictmin = mm->dFrictmin;
  dFrictDelta= mm->dFrictDelta;

  return(0);
}

const char *HyperModel::Initialize(unsigned uDim,State *) {

      if ((uDim!=2)&&(uDim!=3)) return("Illegal dimension in Hyper
constitutive model");

      double dPsin      = sin(dDilation * dDegRad);
               dRnps    = (1.0 + dPsin) / (1.0 - dPsin);

    return(0);
}

const char *HyperModel::Run(unsigned uDim,State *ps) {
  if ((uDim!=3)&&(uDim!=2)) return("Illegal dimension in Hyper
constitutive model");

  if(ps->dHystDampMult > 0.0) HDampInit(ps->dHystDampMult);

  /* --- plasticity indicator: store 'now' info. as 'past' and turn
'now' info off --- */

  if (ps->mState & mShearNow)
      ps->mState = (unsigned long)(ps->mState | mShearPast);
  ps->mState = (unsigned long)(ps->mState & ~mShearNow);
  if (ps->mState & mTensionNow)
      ps->mState = (unsigned long)(ps->mState | mTensionPast);
  ps->mState = (unsigned long)(ps->mState & ~mTensionNow);

  int iPlas = 0;

// The following are utility members for ease of calculation

  double dE1          = dBulk + d4d3 * dShear;
  double dE2          = dBulk - d2d3 * dShear;
  double dE21         = dE2 / dE1;
  double dG2          = 2.0 * dShear;
```

```
  double dRsin = sin(dFriction * dDegRad);
  dNPH         = (1.0 + dRsin) / (1.0 - dRsin);
  dCSN         = 2.0 * dCohesion * sqrt(dNPH);
  if (dFriction)
  {
   double dApex = dCohesion * cos(dFriction * dDegRad) / dRsin;
   dTension     = dTension < dApex ? dTension : dApex;
  }

  double dRa   = dE1 - dRnps * dE2;
  double dRb   = dE2 - dRnps * dE1;
  double dRd   = dRa - dRb * dNPH;
  double dSC1  = dRa / dRd;
  double dSC3  = dRb / dRd;
  double dSC2  = dE2 * (1.0 - dRnps) / dRd;
  double dBISC = sqrt(1.0 + dNPH * dNPH) + dNPH;

 /* --- trial elastic stresses --- */


  double dE11 = ps->stnE.d11;
  double dE22 = ps->stnE.d22;
  double dE33 = ps->stnE.d33;

  ps->stnS.d11 += dE11 * dE1 + (dE22 + dE33) * dE2;
  ps->stnS.d22 += (dE11 + dE33) * dE2 + dE22 * dE1;
  ps->stnS.d33 += (dE11 + dE22) * dE2 + dE33 * dE1;
  ps->stnS.d12 += ps->stnE.d12 * dG2;
  ps->stnS.d13 += ps->stnE.d13 * dG2;
  ps->stnS.d23 += ps->stnE.d23 * dG2;

  /* --- calculate and sort ps->incips->l stresses and ps->incips->l
directions --- */
  Axes aDir;
  double dPrinMin,dPrinMid,dPrinMax,sdif=0.0,psdif=0.0;
  int icase=0;

  bool bFast=ps-
>stnS.Resoltopris(&dPrinMin,&dPrinMid,&dPrinMax,&aDir,uDim, &icase,
&sdif, &psdif);

  double dPrinMinCopy = dPrinMin;
  double dPrinMidCopy = dPrinMid;
  double dPrinMaxCopy = dPrinMax;
  /* --- Mohr-Coulomb failure criterion --- */
  double dFsurf = dPrinMin - dNPH * dPrinMax + dCSN;
  /* --- Tensile failure criteria --- */
  double dTsurf = dTension - dPrinMax;
  double dPdiv = -dTsurf + (dPrinMin - dNPH * dTension + dCSN) * dBISC;
  /* --- tests for failure */
  if (dFsurf < 0.0 && dPdiv < 0.0) {
    iPlas = 1;
    /* --- shear failure: correction to ps->incips->l stresses ---*/
    ps->mState = (unsigned long)(ps->mState | 0x01);
    dPrinMin -= dFsurf * dSC1;
    dPrinMid -= dFsurf * dSC2;
```

```
    dPrinMax -= dFsurf * dSC3;
  } else if (dTsurf < 0.0 && dPdiv > 0.0) {
    iPlas = 2;
    /* --- tension failure: correction to ps->incips->l stresses ---*/
    ps->mState = (unsigned long)(ps->mState | 0x02);
    double dTco = dE21 * dTsurf;
    dPrinMin += dTco;
    dPrinMid += dTco;
    dPrinMax  = dTension;
  }
  if (iPlas) {
    ps->stnS.Resoltoglob(dPrinMin,dPrinMid, dPrinMax, aDir,
dPrinMinCopy,dPrinMidCopy,dPrinMaxCopy, uDim, icase, sdif,  psdif,
bFast);
    ps->bViscous = false; // Inhibit stiffness-damping terms
  } else {
    ps->bViscous = true;  // Allow stiffness-damping terms
  }


// Update the Hyperbolic Model Parameters

static double dSigm1, dSigm2,dSigm3,dSigma1,dSigma2,dSigma3,dSigma1max;
// use in computation
double
dSS_SS(0.0),dS1_S3(0.0),dSL_sl(0.0),dElastini(0.0),dElast(0.0),dbulkmax
i (0.0),dbulkmini (0.0), _Sigm(0.0);


// --- Hyperbolic: initialize stacks to calculate hyperbolic parameters
for zone

  if (!ps->bySubZone)
      {
        dSigm1 = 0.0;
        dSigm2 = 0.0;
        dSigm3 = 0.0;
      }

/* Something to consider in the future, what happens if after the mohr
correction, the axes changes? */


  double sd1 = -dPrinMin;        // Use positive compression
  double sd2 = -dPrinMid;
  double sd3 = -dPrinMax;

  sd1 = sd1 > 0 ? sd1 : 0;
  sd2 = sd2 > 0 ? sd2 : 0;
  sd3 = sd3 > 0 ? sd3 : 0.1*dPa;

  dSigm1 += sd1;                    // Accumulate stress for each tetra
  dSigm2 += sd2;
  dSigm3 += sd3;


if (ps->bySubZone==ps->byTotSubZones-1) {
```

```
      double Aux = 1.0/ps->byTotSubZones;
      dSigma1 = dSigm1*Aux;
      dSigma2 = dSigm2*Aux;
      dSigma3 = dSigm3*Aux;

      dS1_S3 = dSigma3*(dNPH - 1) + dCSN;   // --- Shear Stress
difference at failure sigma 1 minus sigma 3 --- ---

      if (dS1_S3) {

            dSL = (dSigma1-dSigma3)> 0.0 ? ((dSigma1-dSigma3)/dS1_S3) :
0.0;  // ---  Stress level  --- ------ ---
            dSS = dSL*(sqrt(sqrt((dSigma3 + dApex)/dPa))) ;
            dS1S3 = dS1_S3;
            dSL_sl = dSL;
            dSS_SS = dSS;

            if (dKunload) {
                  if (dSS_SS >= dSSmax * 0.999){
                        dElastini = dKload*dPa*pow(dSigma3/dPa,dMexp);
                              // ---Calculating initial Modulus
                        dElast = (1.0 - dFratio*dSL_sl)*(1.0 -
dFratio*dSL_sl)*dElastini;    //--- Modulus is being computed for
loading
                        }
                  else {dElast = dKunload*dPa*pow(dSigma3/dPa,dMexp);}
                        /*--- Modulus is being computed for unloading
ONLY if Kunload is specify*/
                              }
            else {
                        dElastini = dKload*dPa*pow(dSigma3/dPa,dMexp);

                        dElast = (1.0 - dFratio*dSL_sl)*(1.0 -
dFratio*dSL_sl)*dElastini;
                        }
      }
      else
      {   dSL_sl  = 0.0;
            dSS         = 0.0;
            dElast      = 0.0;
      }

      if (!dElastmin) { dElastmin = 0.1*dPa;}                     // --
-Default minimum value of Elast to avoid Invalid Modulus

      dElast   = dElast > dElastmin ? dElast : dElastmin ;
      dYoung = dElast;                                    // Update
Young modulus
      dbulkmini = (dElast/2.900) ;                          // minimum
Bulk to limit poisson's ratio value
    dbulkmaxi = (8.0*dElast) ;                                  //
maximum Bulk to limit poisson's ratio value

      if (dFrictDelta)    { dFriction = dFrictmin - dFrictDelta *
log10(dSigma3/dPa);}  // Update friction
```

```
      if (dKbulk)
                  {
                        double dChkbulk =
dKbulk*dPa*pow(dSigma3/dPa,dKmexp);    /*--- For varying poisson's
ratio  0 - 0.49 ---*/

                dChkbulk = dChkbulk > dbulkmini ? dChkbulk : dbulkmini;
                        dChkbulk = dChkbulk < dbulkmaxi ? dChkbulk :
dbulkmaxi;
                     dBulk = dChkbulk;
                                 // Update Bulk
                        dShear = 3.0* dElast* dChkbulk /((9.0*dChkbulk)
- dElast);      // Update Shear
                        dMypoisson = (0.5 - (dElast/(6.0*dChkbulk)));
      }              // Update Poisson

      else {            if (dVolumax){
                                  _Sigm = (dSigma1 + dSigma2 +
dSigma3 )/3;

                                  double dChkbulk = dBulkmin*(1 +
_Sigm/(dBulkmin*dVolumax))*(1 + _Sigm/(dBulkmin*dVolumax));

                                  dChkbulk = dChkbulk > dbulkmini ?
dChkbulk : dbulkmini;
                                  dChkbulk = dChkbulk < dbulkmaxi ?
dChkbulk : dbulkmaxi;
                                  dBulk = dChkbulk;
                                          // Update Bulk
                                  dShear = 3.0* dElast* dChkbulk
/((9.0*dChkbulk) - dElast);     // Update Shear
                                  dMypoisson = (0.5 -
(dElast/(6.0*dChkbulk)));           }             // Update Poisson

                        else {
                                  dBulk  = dElast/(3.0*(1.0 -
2.0*dPoisson));               // Update bulk for constant poisson's
ratio --- */
                                  dShear = dElast/(2.0*(1.0 +
dPoisson));                   // Update shear for constant poisson's
ratio
                                  dMypoisson = (0.5 -
(dElast/(6.0*dBulk)));  }     // Update Poisson
            }
}
dSSmax = dSSmax > dSS_SS ? dSSmax : dSS_SS;

dKmax = dKmax > dBulk ? dKmax : dBulk;

dGmax = dGmax > dShear ? dGmax : dShear;

return(0);
}

/* *
Save all properties for the model
```

```
   * Note: It is not necessary to save and restore member variables
that would be
     initialized. This reduces the size of save file.
*/

const char *HyperModel::SaveRestore(ModelSaveObject *mso) {
 // Checks for type mismatch and returns error string. Otherwise 0.
  const char *str = ConstitutiveModel::SaveRestore(mso);
  if (str) return(str);
  // 28 represents 28 properties that are doubles
  // and 0 represents 0 properties that are integers
  mso->Initialize(29,0);
  mso->Save(0,dBulk);
  mso->Save(1,dShear);
  mso->Save(2,dCohesion);
  mso->Save(3,dFriction);
  mso->Save(4,dDilation);
  mso->Save(5,dTension);
  mso->Save(6,dYoung);
  mso->Save(7,dPoisson);
  mso->Save(8,dMypoisson);
  mso->Save(9,dKload);
  mso->Save(10,dKunload);
  mso->Save(11,dKbulk);
  mso->Save(12,dMexp);
  mso->Save(13,dKmexp);
  mso->Save(14,dFratio);
  mso->Save(15,dPa);
  mso->Save(16,dSSmax);
  mso->Save(17,dCmodulus);
  mso->Save(18,dKmax);
  mso->Save(19,dGmax);
  mso->Save(20,dSig3max);
  mso->Save(21,dSL);
  mso->Save(22,dSS);
  mso->Save(23,dS1S3);
  mso->Save(24,dBulkmin);
  mso->Save(25,dVolumax);
  mso->Save(26,dElastmin);
  mso->Save(27,dFrictmin);
  mso->Save(28,dFrictDelta);

  return(0);
}

// EOF
```

```
// MOHRHYPER.H FILE

#ifndef __HYPER_H
#define __HYPER_H


#ifndef __CONMODEL_H
#include "conmodel.h"
#endif


class HyperModel : public ConstitutiveModel {
  public:

      // User must give a number greater than 100 to avoid conflict
with inbuilt models.
    enum ModelNum { mnHyperModel=121 };
    // Creators
    EXPORT HyperModel(bool bRegister=true);
    // Use keyword to load model into FLAC/FLAC3D
    virtual const char *Keyword(void) const { return("hyper"); }
      // Expanded name for printing purposes
    virtual const char *Name(void) const { return("Hyperbolic"); }

    virtual const char **Properties(void) const;
    virtual const char **States(void) const;
    virtual double GetProperty(unsigned ul) const;

    virtual ConstitutiveModel *Clone(void) const { return(new
HyperModel()); }


//  check to see where to place confined modulus since rgis is not
constant//

    virtual double ConfinedModulus(void) const { return(dKmax +
d4d3*dGmax); }
    virtual double ShearModulus(void) const { return(dShear); }
    virtual double BulkModulus(void) const { return(dBulk); }
    virtual double SafetyFactor(void) const { return(10.0); }

       //version control..
    virtual unsigned Version(void) const { return(2); }

    // Manipulators
    virtual void SetProperty(unsigned ul,const double &dVal);
      //Explicit Copy instead of Copy Constructor
    virtual const char *Copy(const ConstitutiveModel *m);

      //Initialize and Run
    virtual const char *Initialize(unsigned uDim,State *ps);
    virtual const char *Run(unsigned uDim,State *ps);

      //Save Restore
    virtual const char *SaveRestore(ModelSaveObject *mso);
  private:
      //properties
```

```
    double
dBulk,dShear,dCohesion,dFriction,dDilation,dTension,dYoung,dPoisson,dMy
poisson;
      double
dKload,dKunload,dKbulk,dMexp,dKmexp,dFratio,dPa,dSSmax,dCmodulus,dKmax,
dGmax,dSig3max,dSL,dSS,dS1S3;
      double dBulkmin, dVolumax, dElastmin,dFrictmin,dFrictDelta;

      ////utility members for ease of calculation
    double dNPH,dCSN,dRnps,dApex;
      };


#endif
// EOF
```

APPENDIX B:

B1: INPUT DATA FILE FOR NUMERICAL SIMULATIONS

```
;Triaxial Test for verification of Hyperbolic model
title
   Triaxial Test Simulation of Medium Density sand Gomez (2000)
gen zone brick p0 0 0 0 p1 1 0 0 p2 0 1 0 p3 0 0 1 size 1 1 1
; assign model properties ;density Sand ( Dr 41% Medium : 280, 103, 45
kpa)
model hyper
prop Pa=101.3 KL=780 lmod=0.62 Rf=0.852
prop KB=530 ULmod=0.42
prop Phimin = 35, DeltaPhi = 2.5,  Dilation = 5
prop S3max = 280  Emin = 10.13
; --- initialisation ---
ini sxx -280 syy -280 szz -280
hyper_ini
; --- boundary conditions ---
apply sxx -280
apply szz -280
apply yvel 5e-7 range y -0.1 0.1
apply yvel -5e-7 range  y 0.9 1.1
;---fish function
Def Ax_strain
;
_zp1 = zone_head
_gp11 = gp_near(0, 0, 0)
_gp12 = gp_near(0, 1, 0)
_gp21 = gp_near(1, 0, 0)
_gp22 = gp_near(1, 1, 0)
;
  _disp_0 = 0.5*(gp_xdisp(_gp11) + gp_xdisp(_gp12))
  _disp_1 = 0.5*(gp_xdisp(_gp21) + gp_xdisp(_gp22))
  Lateral_strain = -(_disp_0 - _disp_1)/1.0
  ;
  _disp_0 = 0.5*(gp_ydisp(_gp11) + gp_ydisp(_gp21))
  _disp_1 = 0.5*(gp_ydisp(_gp12) + gp_ydisp(_gp22))
  Ax_strain = (_disp_0 - _disp_1)/1.0

    my_bulk     =   z_prop(_zp1, 'bulk')
    my_shear    =   z_prop(_zp1, 'shear')
    my_young    =   z_prop(_zp1, 'young')
    my_poisson  =   z_prop(_zp1, 'poisson')
    my_SL       =   z_prop(_zp1, 'SL')
    my_SS       =   z_prop(_zp1, 'SS')
    my_ssmaxi   =   z_prop(_zp1, 'SSMax')
    my_S1S3     =   z_prop(_zp1, 'S1-S3max')

    my_sigma1   =   z_sig1(_zp1)
    my_sigma3   =   z_sig3(_zp1)
    _sig_zz     =   z_szz(_zp1)
    _sig_xx     =   z_sxx(_zp1)
    _sig_yy     =   z_syy(_zp1)
    Shearstress =   z_syy(_zp1)-(0.5*(z_sxx(_zp1)+z_szz(_zp1)))
    _voluStrain     =   z_vsi(_zp1)

end
; --- histories ---
hist nstep 100
hist Ax_strain
```

```
hist Lateral_strain
hist _voluStrain
hist Shearstress
hist unbal
hist my_bulk
hist my_shear
hist my_young
hist my_poisson
hist my_SL
hist my_SS
hist my_ssmaxi
hist my_S1S3
his  my_sigma1
hist my_sigma3
his  _sig_xx
his  _sig_yy
his  _sig_zz
; --- test ---
title 'Triaxial Test on Density Sand (Medium, 280kPa) after Gomez 2002'
plot  hist -4 vs 1 alias 'stress-strain model response' yla ' Deviator
stress (kPa)' xla 'Axial Strain (m/m)'
plot  add hist -3 vs 1 alias 'Volumetric strain-axial strain' yla
'Volumetric Strain (m3/m3)' xla 'Axial Strain (m/m)'
plot  add hist 6, 7, 8 vs 1 alias 'Elastic Moduli' yla 'Moduli (kPa)'
xla 'Axial Strain (m/m)'
step 100000
hist write 1 2 3 4 file GomezMediumSand280.txt
save MediumSand280.sav
```

B2: SAMPLE OF INPUT DATA FOR ROUGH STRIP FOOTING ON A COHESIONLESS MATERIAL

```
Config cppudm
model load hyperDuncanSelig
title
Hyperbolic Model validation-Footing proble,
;  generate geometry
gen zone brick  p0 2.44,0,0  p1  22.44,0,0  p2 2.44,12.44,0   p3
2.44,0,20  &
                size 15,7,15 ratio 1.1,1,0.9 group SOIL

gen zone reflect norm 0,0,-1  ori 0,0,20
gen zone brick  p0 0,0,0  p1  2.44,0,0  p2 0,12.44,0   p3 0,0,20  &
                size 4,7,15 ratio 1,1,0.9 group SOIL
Plot create model
plot add axes
plot add surface
plot add block group
plot show
pause
; Assign Hyperbolic model to soil (stress units: kPa)
model hyper range group soil
prop Pa=14.7, KL=300, Lmod=0.55, Rf=0.83 ;coh = 0.001; KUL = 480
prop pois = 0.35  fric=35.5 S3max = 5 Emin = 1.47
;prop Kmin=1863.92 VolMax = 0.10 fric=32 S3max = 80 Emin = 10.13
;-----------------------------------------------
;Initial Conditions             |
;-----------------------------------------------
ini dens 0.065
set grav 0 0 -1

;Boundary Conditions
fix x y z range z -0.001, 0.001
fix x     range x 0.01 -0.01
fix x     range x 2.43,2.45 z= 20,40
fix y     range y 12.43, 12.45
fix y     range y 0.0001 -0.0001
fix z     range x=0,2.441 z=19.8,20.2
ini zvel 1e-5 range x=0,2.441 z=19.8,20.2
def p_load
    pnt = gp_head
    pload = 0.0
    n = 0
    loop while pnt # null
        if gp_zpos(pnt) > 19.8 then
            if gp_xpos(pnt) < 2.441 then
                pload = pload + gp_zfunbal(pnt)
                n = n + 1
            end_if
        end_if
        pnt = gp_next(pnt)
    end_loop
pload = pload/30.3536
p_load = pload
pdis0 = gp_near(0.0,0.0,20.0)
pdis1 = gp_near(2.44,0.0,20.0)
c_disp = gp_zdisp(pdis0)
c_disp1 = gp_zdisp(pdis1)
end
```

```
hist n 50
hist p_load
hist c_disp
hist c_disp1
hist unbal
step 200000
pause
;Histories
define Locates_

;Footing Displacement

    out_1   = gp_near(0.61,6.22,20)
    mid_2   = gp_near(1.22,6.22,20)
    innn_3  = gp_near(1.83,6.22,20)

end
Locates_
define D_Surf

    Outtyy    =  gp_zdisp(out_1)
    Middllu   =  gp_zdisp(mid_2)
    Inny      =  gp_zdisp(innn_3)

    D_Surf  =  gp_zdisp(out_1)


end
hist unbal
hist gp zdisp id =4451
hist gp  zdisp id =4453
hist gp  zdisp id =4451
hist D_Surf
hist Outtyy
hist Middllu
hist Inny
call myhyperv2.fis
hyper_ini
solve
save insituEquli.sav
hist write 1 2 3 4 5  file Displ_insitu.txt
apply szz add -2.5 range x=0,2.44 z=20.4,20.6
solve
hist write 2 3 4 5 6 7 8 file Displ_1.txt
save layer25.sav
apply szz add -2.5 range x=0,2.44 z=20.4,20.6
solve
hist write 2 3 4 5  file Displ_2.txt
save layer5.sav
apply szz add -2.5 range x=0,2.44 z=20.4,20.6
solve
hist write 2 3 4 5  file Displ_3.txt
save layer75.sav
apply szz add -2.5 range x=0,2.44 z=20.4,20.6
solve
hist write 2 3 4 5  file Displ_4.txt
save layer10.sav
```

```
apply szz add -2.5 range x=0,2.44 z=20.4,20.6
solve
hist write 2 3 4 5 file Displ_5.txt
save layer125.sav
apply szz add -2.5 range x=0,2.44 z=20.4,20.6
solve
hist write 2 3 4 5  file Displ_6.txt
save layer15.sav
apply szz add -2.5 range x=0,2.44 z=20.4,20.6
solve
hist write 2 3 4 5  file Displ_7.txt
save layer175.sav
apply szz add -2.5 range x=0,2.44 z=20.4,20.6
solve
hist write 2 3 4 5  file Displ_8.txt
save layer20.sav
apply szz add -2.5 range x=0,2.44 z=20.4,20.6
solve
hist write 2 3 4 5 file Displ_9.txt
save layer1225.sav
apply szz add -2.5 range x=0,2.44 z=20.4,20.6
solve
hist write 2 3 4 5 6 7 8 file Displ_10.txt
save layer250.sav
apply szz add -2.5 range x=0,2.44 z=20.4,20.6
solve
hist write 2 3 4 5  file Displ_11.txt
save layer275.sav
apply szz add -2.5 range x=0,2.44 z=20.4,20.6
solve
hist write 2 3 4 5  file Displ_12.txt
save layer300.sav
apply szz add -2.5 range x=0,2.44 z=20.4,20.6
solve
hist write 2 3 4 5  file Displ_13.txt
save layer325.sav
apply szz add -2.5 range x=0,2.44 z=20.4,20.6
solve
hist write 2 3 4 5  file Displ_14.txt
save layer350.sav
apply szz add -2.5 range x=0,2.44 z=20.4,20.6
solve
hist write 2 3 4 5 file Displ_15.txt
save layer375.sav
apply szz add -2.5 range x=0,2.44 z=20.4,20.6
solve
hist write 2 3 4 5  file Displ_16.txt
save layer400.sav
apply szz add -2.5 range x=0,2.44 z=20.4,20.6
solve
hist write 2 3 4 5  file Displ_17.txt
save layer425.sav
apply szz add -2.5 range x=0,2.44 z=20.4,20.6
solve
hist write 2 3 4 5  file Displ_18.txt
save layer450.sav
apply szz add -2.5 range x=0,2.44 z=20.4,20.6
```

```
solve
hist write 2 3 4 5  file Displ_19.txt
save layer475.sav
apply szz add -2.5 range x=0,2.44 z=20.4,20.6
solve
hist write 2 3 4 5  file Displ_20.txt
save layer500.sav
apply szz add -2.5 range x=0,2.44 z=20.4,20.6
solve
hist write 2 3 4 5  file Displ_21.txt
save layer525.sav
apply szz add -2.5 range x=0,2.44 z=20.4,20.6
solve
hist write 2 3 4 5  file Displ_22.txt
save layer550.sav
apply szz add -2.5 range x=0,2.44 z=20.4,20.6
solve
hist write 2 3 4 5  file Displ_23.txt
save layer575.sav
my_table
```

B3: SAMPLE OF INPUT DATA FOR CIRCULAR FLEXIBLE PIPE BURIED IN SILTY-SAND SOIL

```
Config cppudm
model load hyperDuncanSelig
title
Hyperbolic Model validation
;
; Set Geometry Parameter
;*************************
;set echo off
define Geometry_parameter
;Pipe parameter (meters)
;;;;  Input properties
;;;;;;;;;;;;;;;;;;;;;;;;;;;;;;;;;;;;;;;;

Pipe_Dia      = 0.61
Depth_cover   = 6.1
gamma_        = 18.0 ; unit weight of soil
Max_H         = 6.1 ; max height of soil
;;;;;;;;;;;;;;;;;;;;;;;;;;;;;;;;;;;;;;;;;;;;;;;;;;;;;;;;;;;;;;;;;;;;;;;;;;;;

  p_rad         = Pipe_Dia/2
  p_rad_1       = -p_rad
  p_rad6        = 6*p_rad
  densy         = (gamma_)/10
  HC_max        = Max_H
  ny        = round(13.5*(Depth_cover-6.1)/2)
  if Depth_cover > Max_H then
    diff_ = Depth_cover - Max_H

    xtra_stress = -1*diff_*gamma_

    else
        xtra_stress = 0

  end_if
end
set echo on
Geometry_parameter
;  generate geometry
gen zon cshell  p0 0,0,0   p1  0.366,0,0   p2  0,0.061,0
p3  0,0,0.366   &
                p4 0.366,0.061,0   p5  0,0.061,0.366 p6
0.366,0,0.366  p7  0.366,0.061,0.366   &
                p8 0.305,0,0   p9  0,0,0.305   p10
0.305,0.061,0   p11 0,0.061,0.305     &
                size  1,1,20,5 group backpack
gen zon radcyl  p0 0,0,0   p1  0.61,0,0   p2  0,0.061,0
p3  0,0,0.61   &
```

```
                p4 0.61,0.061,0   p5  0,0.061,0.61 p6
0.61,0,0.61  p7  0.61,0.061,0.61   &
                p8 0.366,0,0   p9  0,0,0.366   p10
0.366,0.061,0   p11 0,0.061,0.366     &
                size  6,1,20,4
gen zone brick  p0 0.61,0,0  p1  1.830,0,0  p2 0.61,0.061,0
p3 0.61,0,0.61  &
                size 10,2,10  ratio 1.1,1,1
gen zone brick  p0 0,0,0.61  p1  0.61,0,0.61  p2
0,0.061,0.61   p3 0,0,1.22  &
                size 10,1,7  ratio 1,1,1.1
gen zone brick  p0 0.61,0,0.61  p1  1.830,0,0.61  p2
0.61,0.061,0.61   p3 0.61,0,1.22  &
                size 10,1,7  ratio 1.1,1,1.1
gen zone reflect norm 0,0,-1  ori 0,0,0
attach face range x = 0.609 0.6101
attach face range z = 0.609 0.6101
attach face range z = -0.609 -0.6101
plot create model
plot add axes
plot add surface
plot show
pause
;  Add PE Pipe
sel shell range cyl end1 0 0 0 end2 0,0.061,0 rad p_rad
sel shell prop iso 7.579e5 0.45 thick 0.029
sel node fix y xr zr range y 0.0001 -0.0001
sel node fix y xr zr range y 0.06099 0.06101
sel node fix x yr zr range x 0.001 -0.001
plot create model
plot add axes
plot add surface
plot add block group
plot add sel geo shell black yellow
plot show
;-----------------------------------------------
;Initial Conditions             |
;-----------------------------------------------
ini dens densy
set grav 0 0 -10

;Boundary Conditions
fix x y z range z -1.2199 -1.2201
fix x     range x 0.001 -0.001
fix x     range x 1.8299 1.8301
fix y     range y 0.0001 -0.0001
fix y     range y 0.06099 0.06101
```

```
; Assign Hyperbolic model to soil (stress units: kPa)
model hyper
prop Pa=101.3, KL=480, Lmod=0.44, Rf=0.75 coh = 57 ;KUL =
480
prop KB=80 ULmod = 0.38 fric=30 S3max = 50 Emin = 10.13
;prop Kmin=1863.92 VolMax = 0.10 fric=32 S3max = 80 Emin =
10.13
;Histories
define Locates_

;Pipe Displacement

    v30  = -p_rad*cos(30*pi/180)
    h30  = p_rad*sin(30*pi/180)
    v150 = p_rad*cos(30*pi/180)


    top_pipe    = gp_near(0,0.061,p_rad)
    pipe_150    = gp_near(h30,0.061,v150)
    pipe_30     = gp_near(h30,0.061,v30)
    sprline_pipe = gp_near(p_rad,0.061,0)
    bot_pipe    = gp_near(0,0.061,p_rad_1)
    grd_sur     = gp_near(0,0.061,HC_max)
;Horizontal Stresses
    hor_0 = p_rad
    hor_1 = p_rad + 0.061
    hor_2 = p_rad + 0.183
    hor_3 = p_rad + 0.305
    hor_4 = p_rad + 0.61
    hor_5 = p_rad + 0.915
    hor_6 = p_rad + 1.22
    phor_0 = z_near(hor_0,0,0)
    phor_1 = z_near(hor_1,0,0)
    phor_2 = z_near(hor_2,0,0)
    phor_3 = z_near(hor_3,0,0)
    phor_4 = z_near(hor_4,0,0)
    phor_5 = z_near(hor_5,0,0)
    phor_6 = z_near(hor_6,0,0)
    phor_7 = z_near(p_rad6,0,0)

;Vertical Stresses
    vert_1 = 4*p_rad
    vert_2 = 4*p_rad - 0.1525
    vert_3 = 4*p_rad - 0.305
    vert_4 = 4*p_rad - 0.4575
    vert_5 = 4*p_rad - 0.61
    vert_6 = 4*p_rad - 0.915
```

```
    vert_7 = p_rad
    pvert_1  = z_near(0,0,vert_1)
    pvert_2  = z_near(0,0,vert_2)
    pvert_3  = z_near(0,0,vert_3)
    pvert_4  = z_near(0,0,vert_4)
    pvert_5  = z_near(0,0,vert_5)
    pvert_6  = z_near(0,0,vert_6)
    pvert_7  = z_near(0,0,vert_7)
end
Locates_
define D_Surf

    D_180   =  gp_zdisp(top_pipe)
    D_150   =  gp_zdisp(pipe_150)
    D_90    =  gp_zdisp(sprline_pipe)
    D_30    =  gp_zdisp(pipe_30)
    D_0     =  gp_zdisp(bot_pipe)
    D_Surf  =  gp_zdisp(grd_sur)

    Percent_Deflect = abs(100*(D_0 - D_180)/ Pipe_Dia)
    hx_0    = z_sxx(phor_0)
    hx_1    = z_sxx(phor_1)
    hx_2    = z_sxx(phor_2)
    hx_3    = z_sxx(phor_3)
    hx_4    = z_sxx(phor_4)
    hx_5    = z_sxx(phor_5)
    hx_6    = z_sxx(phor_6)
    hx_7    = z_sxx(phor_7)
    v_1 = z_szz(pvert_1)
    v_2 = z_szz(pvert_2)
    v_3 = z_szz(pvert_3)
    v_4 = z_szz(pvert_4)
    v_5 = z_szz(pvert_5)
    v_6 = z_szz(pvert_6)
    v_7 = z_szz(pvert_7)

end
hist unbal

hist D_180
hist D_0
hist sel node zdisp id =41
hist sel node zdisp id =81
hist sel node zdisp id =42
hist sel node zdisp id =82
hist Percent_Deflect
hist sel node xdisp id =41
```

```
hist sel node xdisp id =42
hist sel node xdisp id =81
hist sel node xdisp id =82


hist D_Surf
hist D_150
hist D_90
hist D_30
hist hx_0
hist hx_1
hist hx_2
hist hx_3
hist hx_4
hist hx_5
hist hx_6
hist hx_7
hist v_1
hist v_2
hist v_3
hist v_4
hist v_5
hist v_6
hist v_7
define my_table

    table(1,1) = D_180
    table(1,2) = D_150
    table(1,3) = D_90
    table(1,4) = D_30
    table(1,5) = D_0
    table(1,6) = gp_zdisp(grd_sur)
    table(1,7) = Percent_Deflect
    table(2,1) = hx_0
    table(2,2) = hx_1
    table(2,3) = hx_2
    table(2,4) = hx_3
    table(2,5) = hx_4
    table(2,6) = hx_5
    table(2,7) = hx_6
    table(2,8) = hx_7
    table(3,1) = v_1
    table(3,2) = v_2
    table(3,3) = v_3
    table(3,4) = v_4
    table(3,5) = v_5
    table(3,6) = v_6
```

```
    table(3,7) = v_7

end
Table 1 name Displacement_
Table 2 name Hor_Stress_
Table 3 name Vert_stress_
; stress recovery ...
sel recover surf surfx 1 2 3
; A depth factor of +1.0 corresponds to the outer shell
surface,
; in the direction of the shell's +ve z-axis (which is the
inside of the pipe).
; A depth factor of -1.0 corresponds to the inner shell
surface (the outside of the pipe).
sel recover stress depth_fac 1.0
call myhyperv2.fis
hyper_ini
solve
save insituEquli.sav
hist write 2 3 4 5 6 file Displ_insitu.txt
apply szz add -5.04 range z=1.2199, 1.2201
solve
hist write 2 3 4 5 6 7 8 file Displ_15.txt
save layer15.sav
apply szz add -27.9 range z=1.2199, 1.2201
solve
hist write 2 3 4 5 6 7 8 file Displ_30.txt
save layer30.sav
apply szz add -13.5 range z=1.2199, 1.2201
solve
hist write 2 3 4 5 6 7 8 file Displ_38.txt
save layer38.sav
apply szz add -14.4 range z=1.2199, 1.2201
solve
hist write 2 3 4 5 6 7 8 file Displ_46.txt
save layer46.sav
apply szz add -27.0 range z=1.2199, 1.2201
solve
hist write 2 3 4 5 6 7 8 file Displ_61.txt
save layer61.sav
my_table
```

APPENDIX C:
DESIGN CHARTS FOR HDD INSTALLATION

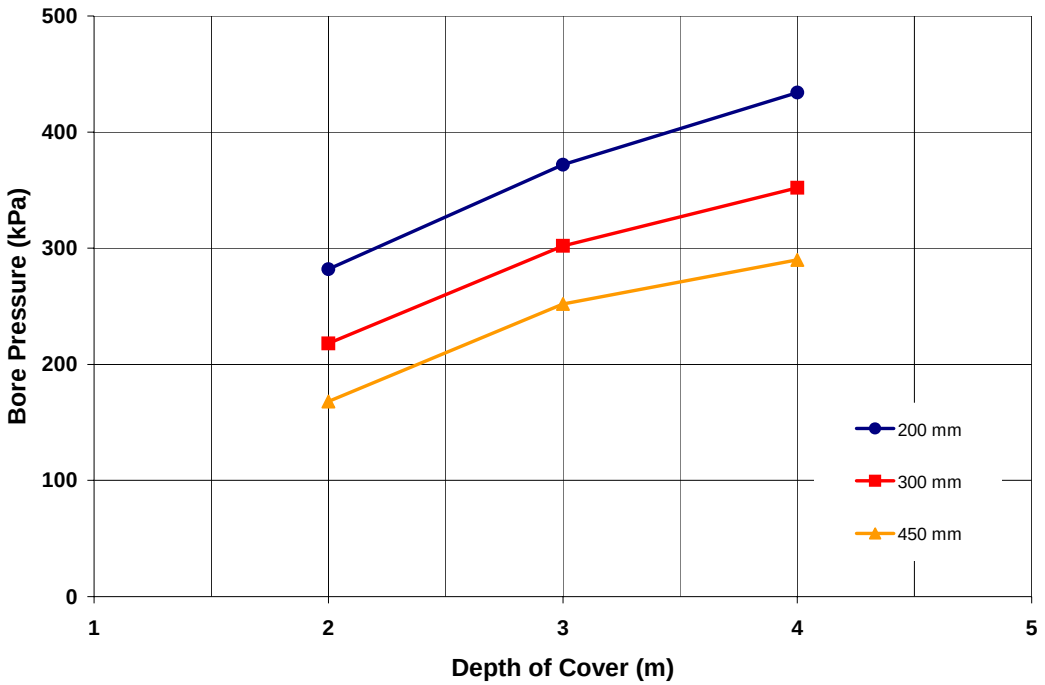

Figure C.1: Bore pressure-depth of cover relationship for initiating 12.5mm displacement at the bore wall in cohesionless subgrade with friction of 35°

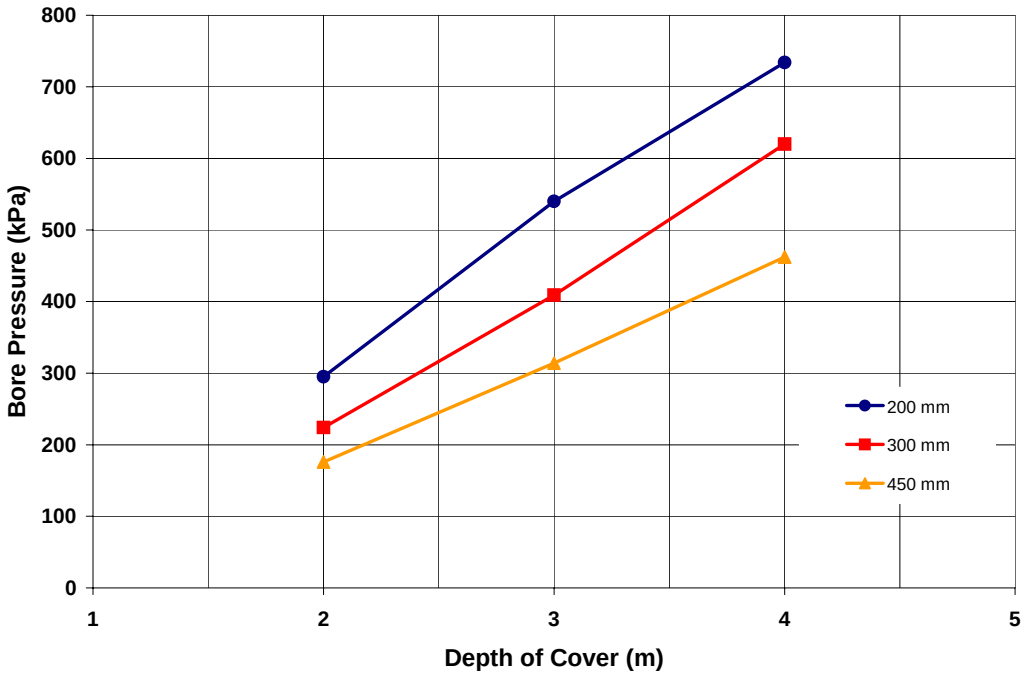

Figure C.2: Bore pressure-depth of cover relationship for propagating 12.5mm vertical displacement to 25% of depth of cover above the crown of bore in cohesionless subgrade with friction of 35°

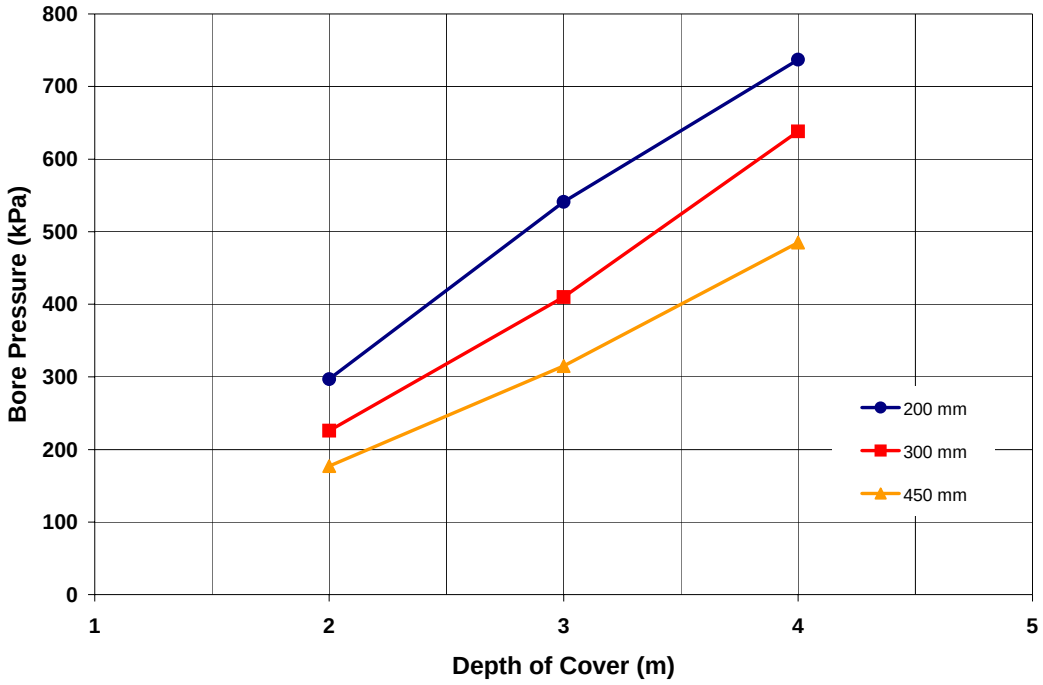

Figure C.3: Bore pressure-depth of cover relationship for propagating 12.5mm vertical displacement to 50% of depth of cover above the crown of bore in cohesionless subgrade with friction of 35°

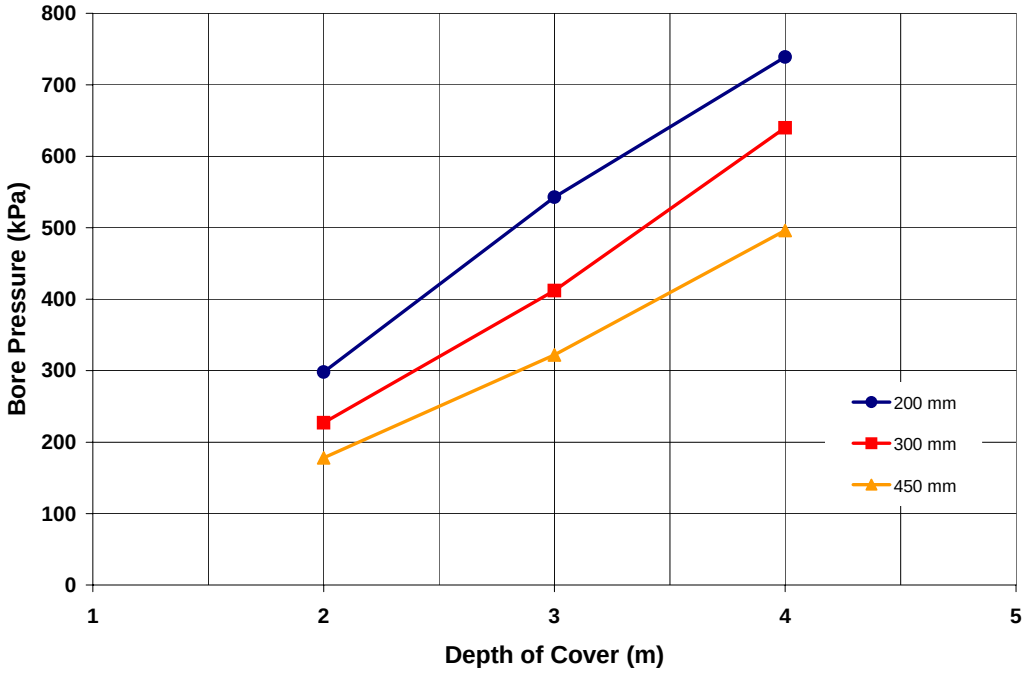

Figure C.4: Bore pressure-depth of cover relationship for propagating 12.5mm vertical displacement to pavement surface in cohesionless subgrade with friction of 35°

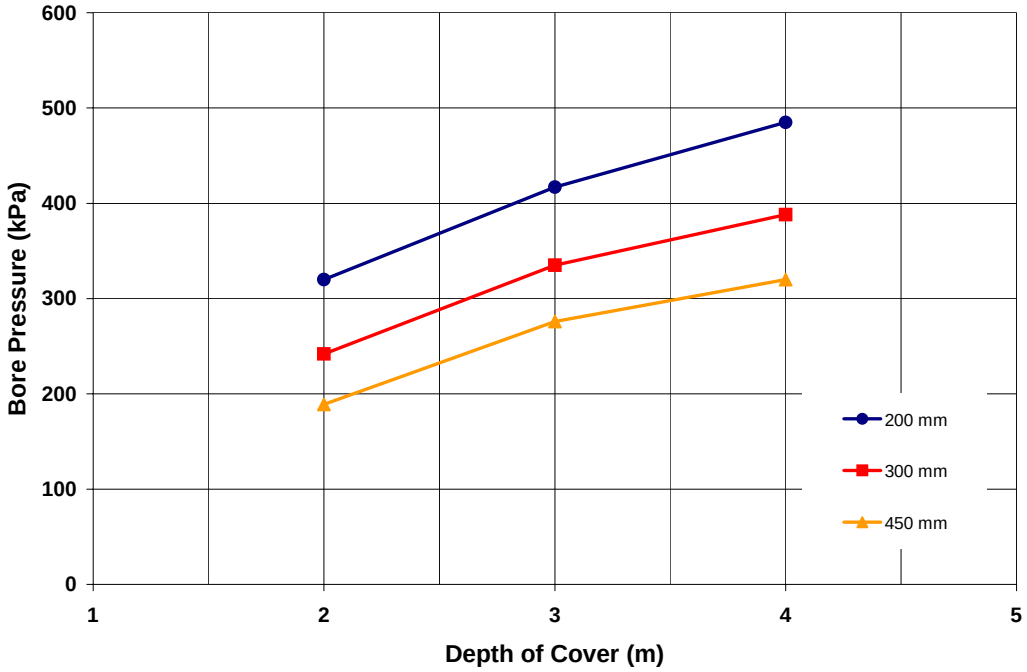

Figure C.5: Bore pressure-depth of cover relationship for initiating 12.5mm displacement at the bore wall in cohesionless subgrade with friction of 40°

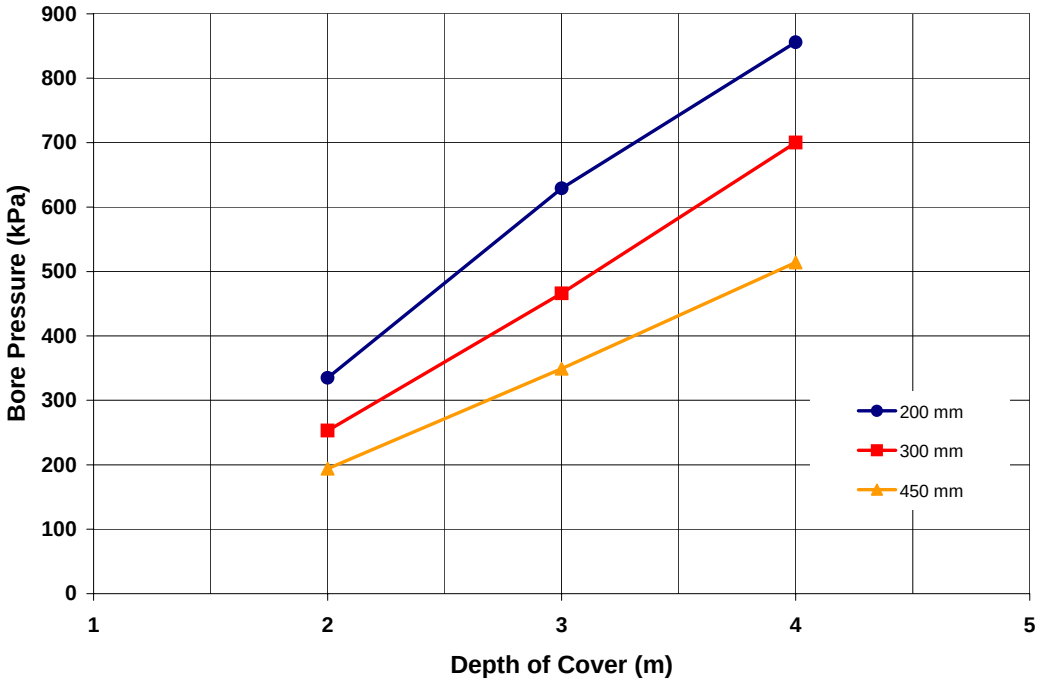

Figure C.6: Bore pressure-depth of cover relationship for propagating 12.5mm vertical displacement to 25% of depth of cover above the crown of bore in cohesionless subgrade with friction of 40°

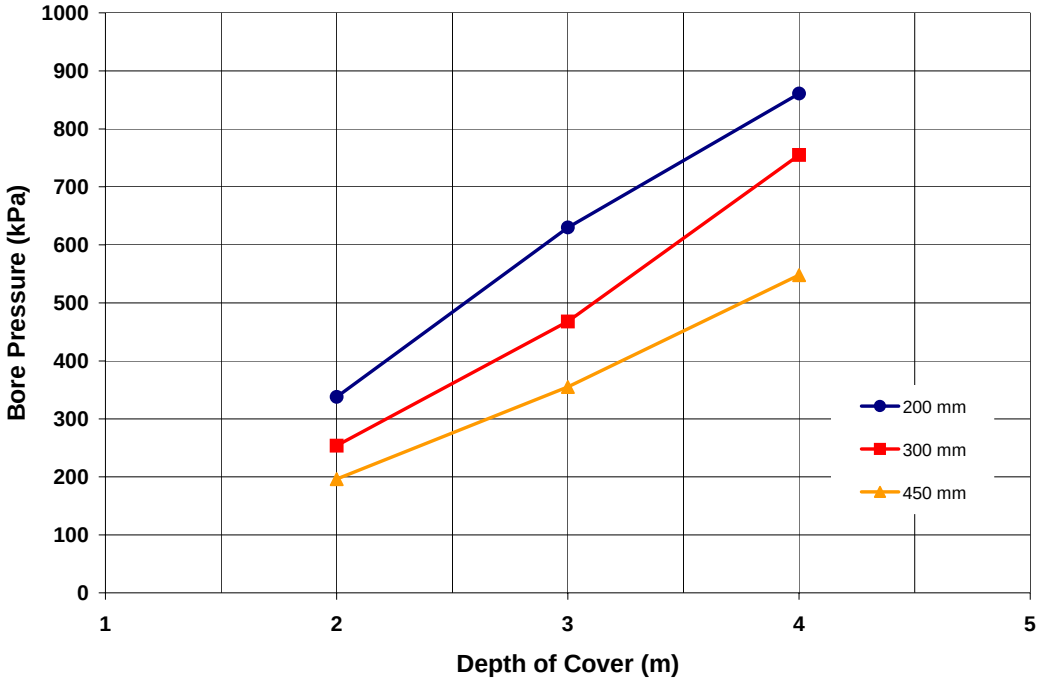

Figure C.7: Bore pressure-depth of cover relationship for propagating 12.5mm vertical displacement to 50% of depth of cover above the crown of bore in cohesionless subgrade with friction of 40°

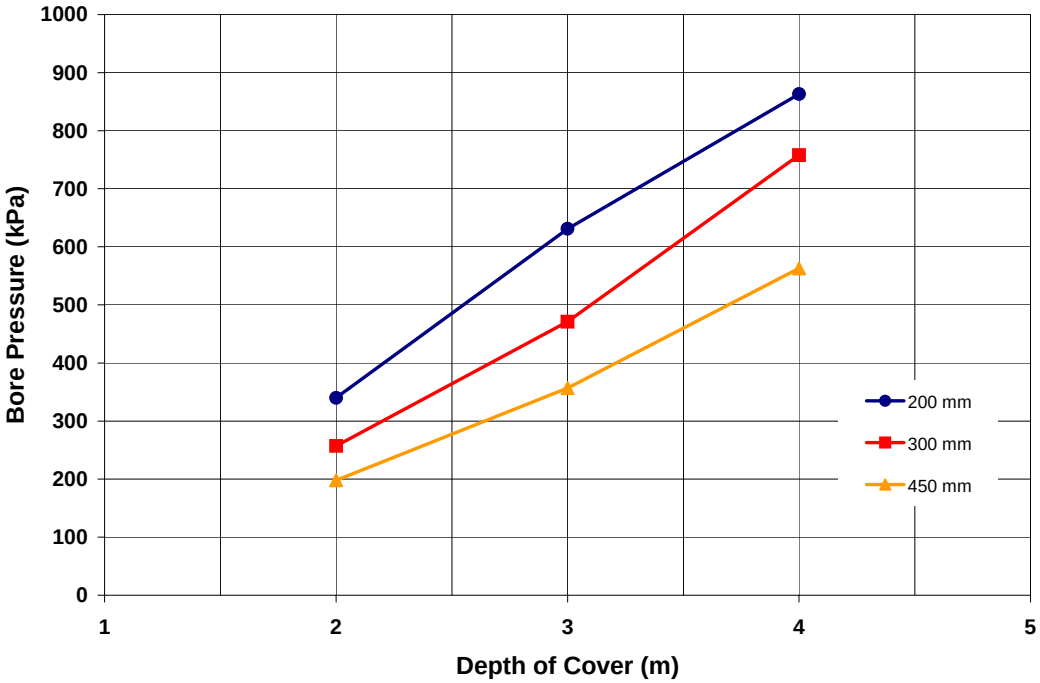

Figure C.8: Bore pressure-depth of cover relationship for propagating 12.5mm vertical displacement to pavement surface in cohesionless subgrade with friction of 40°

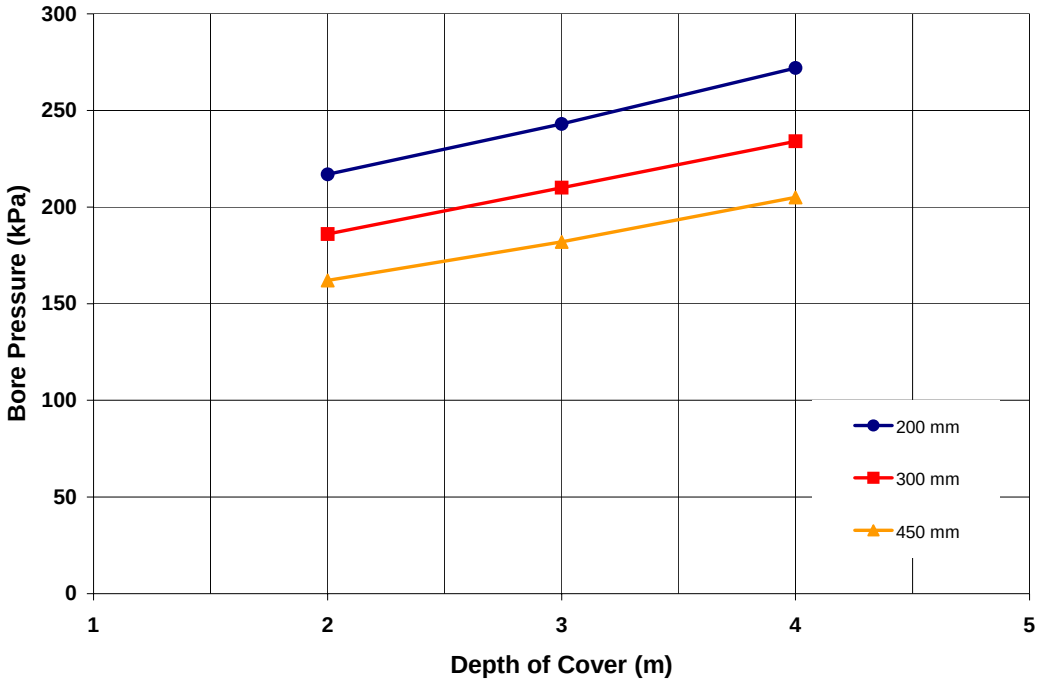

Figure C.9: Bore pressure-depth of cover relationship for initiating 12.5mm displacement at the bore wall in cohesive subgrade with friction of 25°

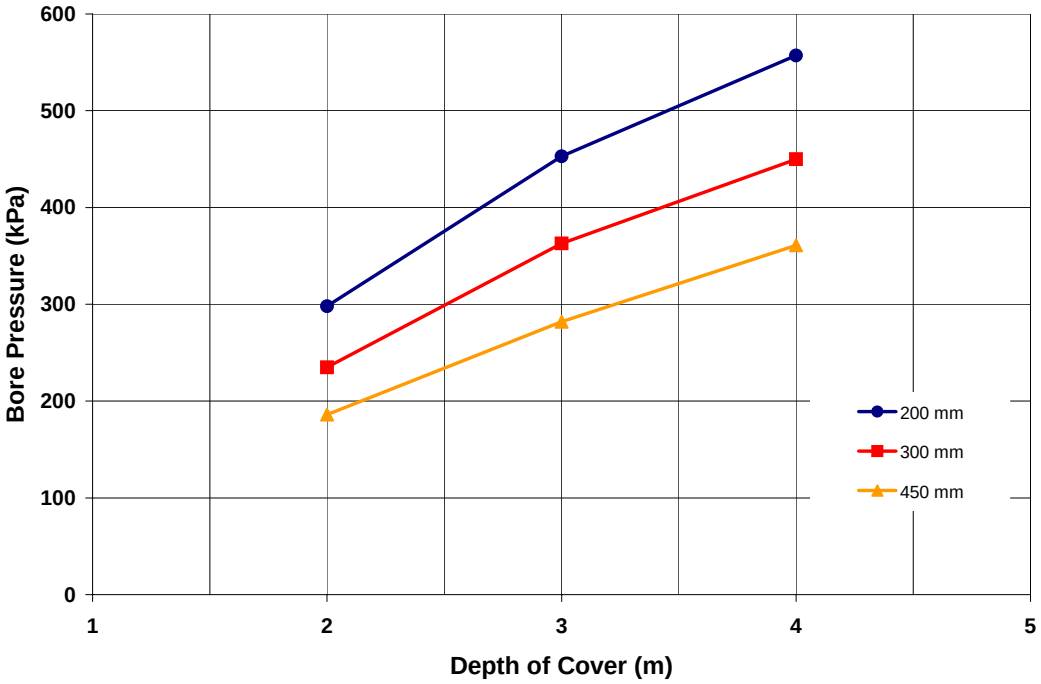

Figure C.10: Bore pressure-depth of cover relationship for propagating 12.5mm vertical displacement to 25% of depth of cover above the crown of bore in cohesive subgrade with friction of 25°

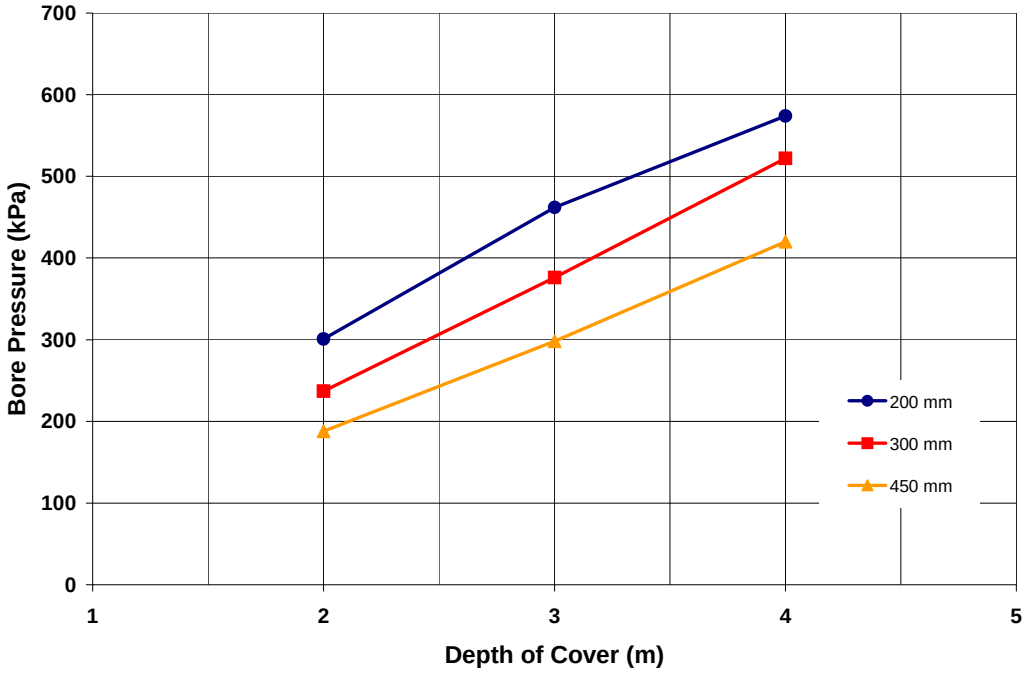

Figure C.11: Bore pressure-depth of cover relationship for propagating 12.5mm vertical displacement to 50% of depth of cover above the crown of bore in cohesive subgrade with friction of 25°

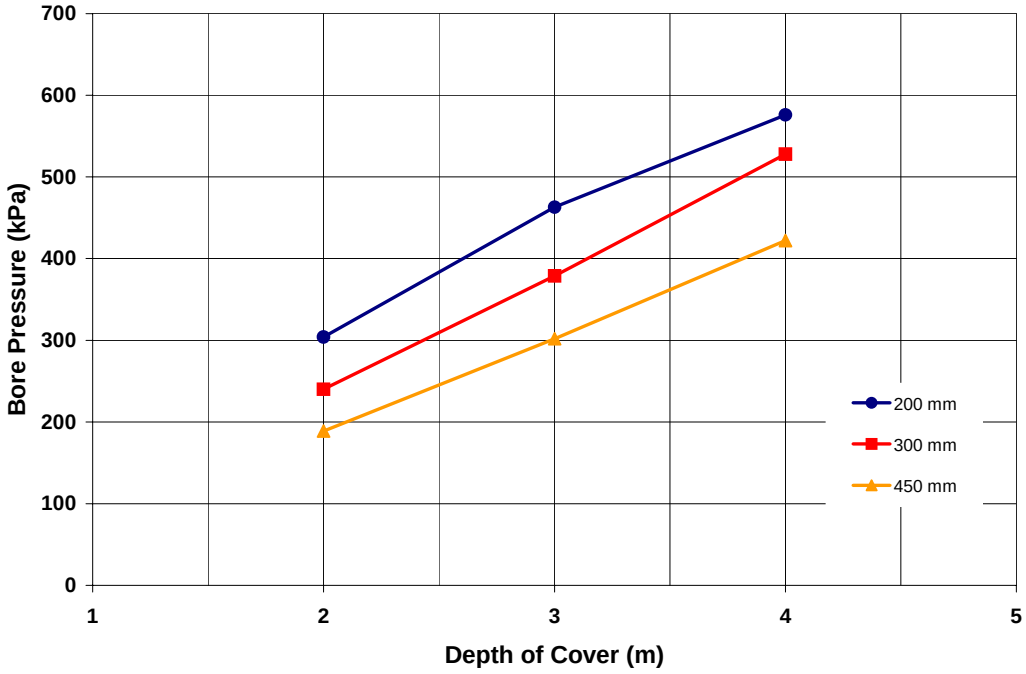

Figure C.12: Bore pressure-depth of cover relationship for propagating 12.5mm vertical displacement to pavement surface in cohesive subgrade with friction of 25°

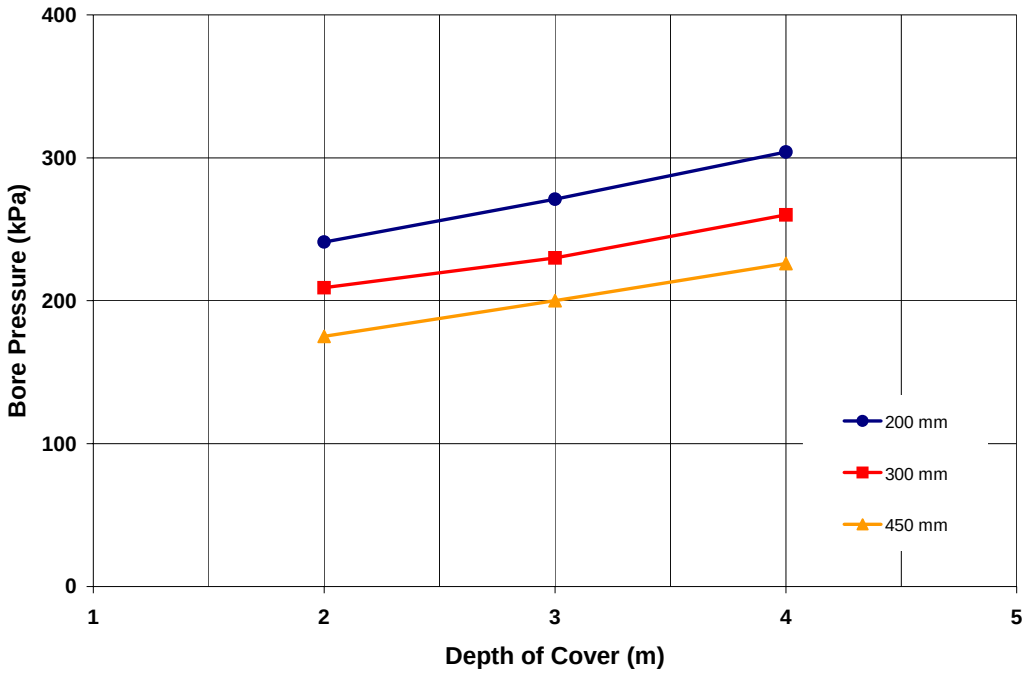

Figure C.13: Bore pressure-depth of cover relationship for initiating 12.5mm displacement at the bore wall in cohesive subgrade with friction of 30°

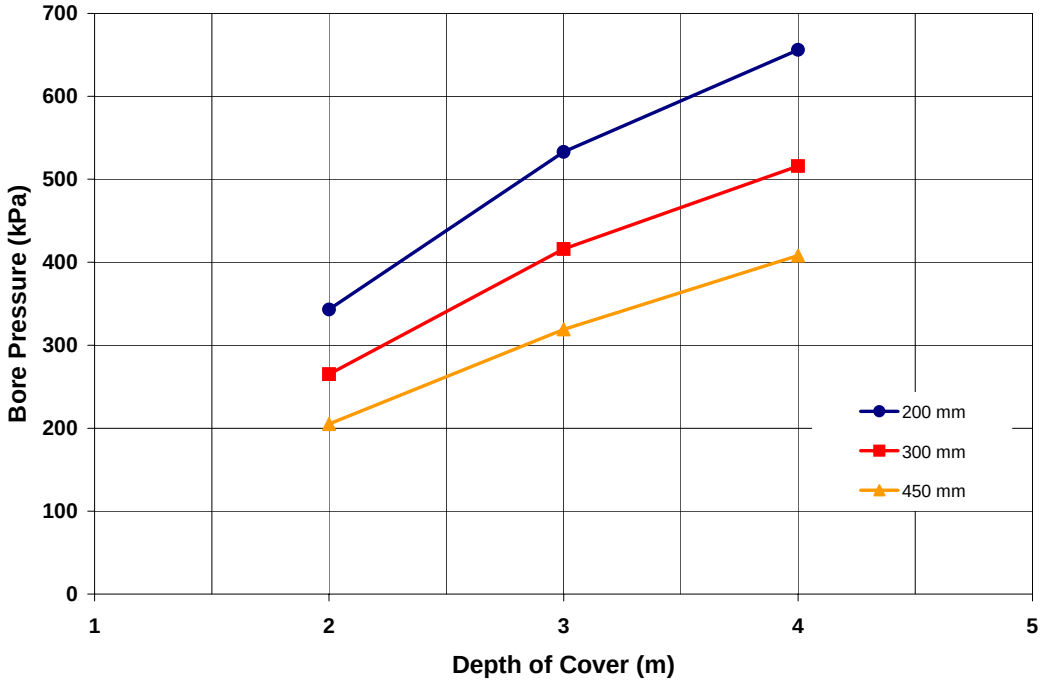

Figure C.14: Bore pressure-depth of cover relationship for propagating 12.5mm vertical displacement to 25% of depth of cover above the crown of bore in cohesive subgrade with friction of 30°

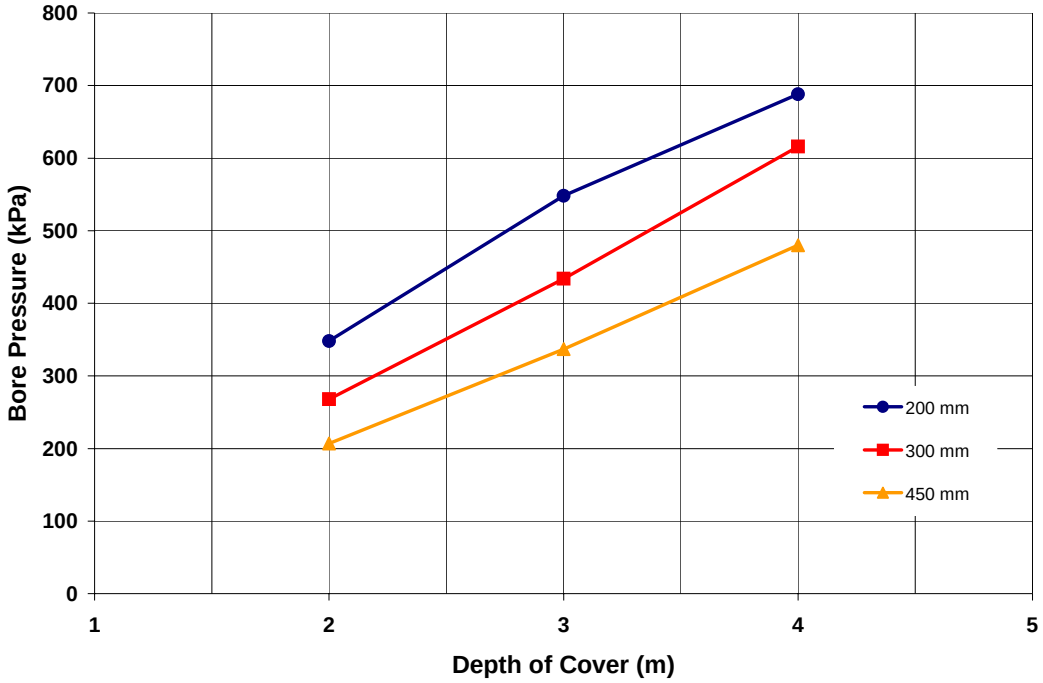

Figure C.15: Bore pressure-depth of cover relationship for propagating 12.5mm vertical displacement to 50% of depth of cover above the crown of bore in cohesive subgrade with friction of 30°

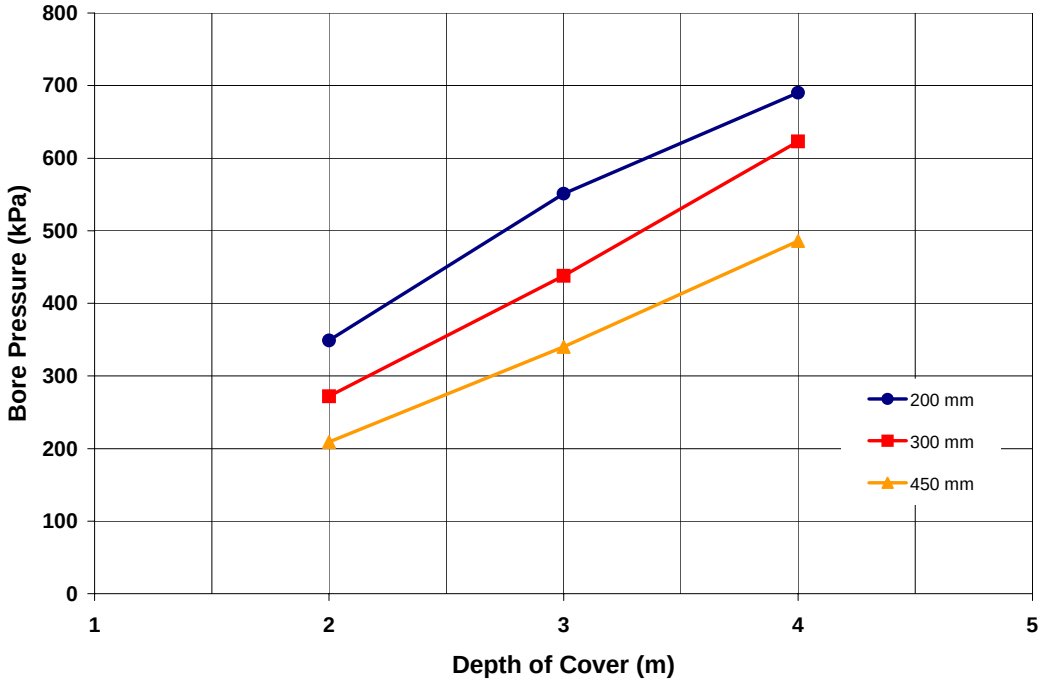

Figure C.16: Bore pressure-depth of cover relationship for propagating 12.5mm vertical displacement to pavement surface in cohesive subgrade with friction of 30°